Julio César Pacio

Multiscale thermo-hydraulic modeling of cryogenic heat exchangers

Thesis for the degree of Philosophiae Doctor

Trondheim, January 2012

Norwegian University of Science and Technology
Faculty of Engineering Science and Technology
Department of Energy and Process Engineering

NTNU – Trondheim
Norwegian University of
Science and Technology

NTNU
Norwegian University of Science and Technology

Thesis for the degree of Philosophiae Doctor

Faculty of Engineering Science and Technology
Department of Energy and Process Engineering

ISBN 978-82-471-3231-9 (printed ver.)
ISBN 978-82-471-3233-3 (electronic ver.)
ISSN 1503-8181

Doctoral theses at NTNU, 2012:2

Printed by NTNU-trykk

To all those who support
the public education system

Preface

This thesis was submitted to the Norwegian University of Science and Technology, in partial fulfillment of the requirements for obtaining the degree of Philosopiae Doctor (Dr. Ing).

The present work was performed at the Department of Energy and Process Engineering, Faculty of Engineering Science and Technology, in the period November 2008 - November 2011. Prof. Carlos Dorao was the main advisor of this project, with the co-supervision of Profs. Maria Fernandino and Jostein Pettersen.

Abstract

The cryogenic industry has experienced a continuous growth in the last decades, partially sustained by the worldwide development of Liquefaction of Natural Gas (LNG) projects. LNG technology provides an economically feasible way of transporting natural gas over long distances, and currently accounts for nearly 30% of the international trade of this resource. The economic feasibility of these projects, in terms of both capital and operating costs, is to a large extent controlled by the performance of the main cryogenic two-phase flow heat exchanger. This industrial scenario provides then the motivation for a detailed study of the heat exchanger from a design perspective.

On the one hand, it is widely accepted that a highly detailed analysis is required at a micro scale to properly take account of the two phase heat transfer process. On the other hand, a process-level description corresponds to larger time and space scales. In general, determining the proper methodology for considering these scales and their interaction remains a challenging problem. For this reason, current techniques focus in only one particular scale. The main objective of this project is then to develop a multiscale model applicable for two-phase flow heat exchangers.

In this context, a three-scale framework is postulated. This thesis was divided into macro, meso (medium) and micro scale analysis. First, a macroscopic analysis provides a broad description in terms of overall heat transfer and pressure drop, using simple models without taking into account the details of physical phenomena at lower scales. Second, at mesoscale level, flow in parallel channels is considered following a homogenization approach, thus including the effects of flow maldistribution and partial mixing. Third, the microscopic description conceives a phenomenological representation of boiling flows, following multifluid formulations, for two specific flow patterns: annular-mist and post-dryout regimes. Finally, a multiscale design algorithm is proposed.

Acknowledgments

I take this opportunity to acknowledge the assistance of all the staff at the Department of Energy and Process Engineering. Special thanks are given to my main supervisor Prof. Carlos Dorao for his guidance throughout this project. He provided me with both advice and freedom to work independently. The discussions with him and my two co-supervisors Profs. Maria Fernandino and Jostein Pettersen helped to shape this thesis.

This three-year project would not have been possible without the support of family and friends. To those back home who backed me throughout this journey. To the people I met here and made this experience so enjoyable. And to Claudia, who makes my life happier everyday and everywhere. To all of you, thanks for your company and support.

Julio César Pacio
Trondheim, Norway
November 22, 2011

Contents

List of Figures

List of Tables

Nomenclature

Roman letters

$\bar{A}$	Interfacial area density [$m^2/ m^3 = m^{-1}$]
$\mathbf{A}$	Matrix term in system of algebraic equations, see equation (4.9), page 67
$\mathbf{a}$	Coefficients in the spectral approximation, see equation (4.7), page 67
A	Cross sectional area [m^2]
C	Heat capacity flow rate, see equation (2.4), page 30 [W K^{-1}]
C^*	Heat capacity flow ratio (as used in the $\varepsilon - NTU$ method), see equation (2.10), page 32 [-]
C_D	Droplet concentration in the gas core [kg m^{-3}]
c_p	Specific heat capacity at constant pressure [J kg^{-1} K^{-1}]
d	Droplet diameter [m]
D_i	Inner diameter [m]
D_o	Outer diameter [m]
D_{eq}	Equivalent diameter, see equation (5.7), page 97 [m]
D_h	Hydraulic diameter [m]
$\mathcal{E}$	Numerical error, see equation (4.24), page 71
e	Specific energy, see equation (8.3), page 173 [J kg^{-1}]
$\mathfrak{f}$	Generic source-term vector
f	Generic scalar function, or trial function
F	Correction factor for mean temperature difference, see equation (2.8), page 31 [-]

f_i	Interfacial (film-gas) friction factor, see equation (9.21), page 202
f_s	Smooth tube wall friction factor
f_W	Wall friction factor, see equation (9.21), page 202
F_{fc}	Correction factor for forced convection heat transfer coefficient, see equation (3.6), page 57 [-]
F_{pb}	Correction factor for pool boiling heat transfer coefficient, see equation (3.6), page 57 [-]
G	Mass flux [kg m^{-2} s^{-1}]
g	Acceleration of gravity [m s^{-2}]
h	Specific enthalpy [J kg^{-1}]
$\hat{h}$	Local heat transfer coefficient [W m^{-2} K^{-1}]
$\hat{h}_{fb}$	Flow boiling heat transfer coefficient, see equation (3.6), page 57 [W m^{-2} K^{-1}]
$\hat{h}_{fc}$	Forced convection heat transfer coefficient, see equation (3.6), page 57 [W m^{-2} K^{-1}]
$\hat{h}_{pb}$	Pool boiling heat transfer coefficient, see equation (3.6), page 57 [W m^{-2} K^{-1}]
$\mathcal{H}$	Jacobian matrix operator, see equation (6.7), page 113
$\mathcal{H}^*$	Importance operator, see equation (6.9), page 114
i, j, k	Generic indeces
j	Superficial velocity [m s^{-1}]
k_{dep}	Deposition coefficient [m s^{-1}]
ℓ	Laplace length , see equation (10.21), page 236 [m]
$\mathcal{L}$	Generic problem operator
L	Tube length [m]
$\dot{m}$	Mass flow rate [kg s^{-1}]
$\dot{m}'$	Cross mixing mass flow per unit length [kg m^{-1} s^{-1}]
$\mathfrak{m}$	Generic system of partial differential equations, see equation (6.1), page 112

MW	Molecular weight [kg mol^{-1}]
N	Number of nodes/elements
n_p	Number of parameters
$\mathbf{p}$	Generic vector of problem parameters, see equation (6.1), page 112
P	Approximation order in spectral methods
P	Temperature effectiveness (as used in the $P-NTU$ method) , see equation (2.15), page 33 [-]
p	Pressure [Pa, bar]
$\mathcal{Q}$	Generic integral response, see equation (6.2), page 112
Q	Thermal power / Heat duty (total heat transferred) [W]
q'	Linear heat flux [W m^{-1}]
q''	Surface heat flux [W m^{-2}]
$\bar{R}$	Universal specific gas constant = 8.314 J mol^{-1} K^{-1}
$\mathbf{r}$	Generic position vector in the domain Ω
$\mathcal{R}$	Numerical residual, see equation (4.2), page 65
$\mathcal{R}_{LS}$	Least squares residual, see equation (4.23), page 71
R	Heat capacity flow ratio (as used in the $P-NTU$ method) , see equation (2.14), page 32 [-]
R	Radius [m]
r	Radial coordinate
$\mathfrak{s}$	Generic source term in the GPT formulation
S	Specific entropy [J kg^{-1} K^{-1}]
S_r	Slip ratio
$\hat{s}_j$	Dimensionless sensitivity coefficient for the parameter p_j, see equation (6.44), page 131 [-]
s_j	Sensitivity coefficient for the parameter p_j, see equation (6.5), page 113
T	Temperature [K]

t_W	Wall thickness [m]
$\mathfrak{u}$	Generic solutions vector
$\mathfrak{u}^*$	Importance function in the GPT formulation
U	Overall heat transfer coefficient [W m^{-2} K^{-1}]
u	Fluid velocity [m s^{-1}]
$\mathfrak{u}^A$	Analytical (exact) solutions vector
$\mathfrak{u}^N$	Numerical (approximate) solutions vector
$\mathbf{v}$	Vector term in system of algebraic equations, see equation (4.9), page 67
$\mathcal{V}$,$\mathcal{V}'$	Generic vector space of functions, infinite dimension
$\mathcal{V}^N$	Approximation vector space of functions, finite dimension
$\mathfrak{W}$	Weigthing function for defining integral responses, see equation (6.2), page 112
$\mathfrak{w}$	Generic function in the vector space $\mathcal{V}$
$\mathfrak{w}^N$	Generic function in the vector space $\mathcal{V}^N$
W	Quadrature weighting function
w	Quadrature weight coefficient
W	Crossed mass flux [kg m^{-2} s^{-1}]
W	Mechanical power [W]
Wp	Pumping power [W]
x	Vapor mass content (quality) [-]
x_{dy}	Dryout quality [-]
x_{th}	Thermodynamic quality [-]
z	One dimensional position coordinate

Abbreviations and acronyms

APD	Axial power distribution
C3MR	Propane–precooled mixed refrigerant process

CHE	Cryogenic heat exchanger
CHF	Critical heat flux
CWHE	Coil–wound heat exchanger
DPM	Distributed parameters models
FDM	Finite differences method
FMD	Flow maldistribution
FVM	Finite volumes method
GPT	Generalized Perturbation Theory
HE	Heat exchanger
HIL	Heat in–leakage
HP	High pressure
HTC	Heat transfer coefficient
LH2	Liquid Hydrogen
LHC	Longitudinal heat conduction
LNG	Liquefied Natural Gas
LP	Low pressure
LPM	Lumped parameters models
MR	Mixed refrigerant
NTU	Number of Thermal Units (as used in the $P-NTU$ method) , see equation (2.13), page 32 [-]
NTU	Number of Thermal Units (as used in the $\varepsilon-NTU$ method) , see equation (2.9), page 32 [-]
NBP	Normal boiling point
NG	Natural gas
PFHE	Plate–fin heat exchanger
RMS	Root mean square
SEM	Stream evolution model

SMR Single mixed refrigerant process

WRF Weighted residual formulation

Greek letters

α Volume/void fraction [-]

Δh_{LV} Specific heat of evaporation: $\Delta h_{LV} = h_V - h_L$ [J kg^{-1}]

ΔT Local temperature difference [K]

ΔT_m Effective mean temperature difference, see equation (2.6), page 31 [K]

ΔT_{lm} Logarithmic mean temperature difference, see equation (2.7), page 31 [K]

Δ Difference, variation

δ Film thickness [m]

ε Heat exchanger effectiveness, see equation (2.9), page 32 [-]

$\varepsilon_{W,D}$ Droplet evaporation efficiency [-]

κ Non-equilibrium parameter

λ Thermal conductivity [W m^{-1} K^{-1}]

μ Dynamic viscosity [kg m^{-1} s^{-1}]

μ Maldistribution parameter, see equation (7.5), page 155 [-]

Ω Generic computational domain

π_e Dimensionless entrainment parameter, see equation (9.17), page 201

$\varphi_{G,D}$ Gray-body factor for gas-to-droplets radiation heat transfer [-]

$\varphi_{W,D}$ Gray-body factor for wall-to-droplets radiation heat transfer [-]

$\varphi_{W,G}$ Gray-body factor for wall-to-gas radiation heat transfer [-]

ϕ General scalar function of one or more variables

Φ_j Test function, in the weighted residual formulation, see Section 4.1

φ_j Generic basis function, or trial function

Φ^2 Two–phase multiplier, see equation (5.4), page 96 [-]

Ψ	Dimensionless effective mean temperature difference (as used in the $\Psi - P$ method), see equation (2.19), page 33 [-]
ρ	Fluid density [kg m^{-3}]
ρ_h	Homogeneous density [kg m^{-3}]
σ	Surface tension [kg s^{-2}]
σ_{SB}	Stefan-Boltzman constant for radiation heat transfer = 5.67 10^{-8} [W m^{-2} K^{-4}]
τ	Shear stress [N m^{-2}]
θ	Non–dimensional temperature, see equation (4.28), page 73

Non-dimensional numbers

Bo	Boiling number number = $q''_W/(G\Delta h_{LV})$
Nu	Nusselt number = $\hat{h}L/\lambda$
Pr	Prandtl number = $c_p\mu/\lambda$
Re	Reynolds number = $\rho u L/\mu$
We	Weber number = $\rho u^2 L/\sigma$

Subscripts

cold	Refers to the lower temperature level
crit	Critical value
D	Droplets
dep	Refers to the deposition process
ent	Refers to the entrainment process
evap	Refers to the evaporation process
G	Refers to the gas phase
hot	Refers to the higher temperature level
in	Refers to the inlet value of the variable
L	Refers to the saturated liquid state
max	Maximum value

min	Minimum value
ref	Reference value
S	Refers to shell-side stream
T	Refers to tube-side stream
tph	Refers to the two–phase flow
V	Refers to the saturated vapor state
W	Wall

Material produced in this work

A list of the additional material produced during this thesis is presented in this section. It is divided into two categories: peer-reviewed publications and other materials. The articles in the first category are included in Appendix A.

Peer-reviewed publications

This category includes articles that were accepted after a review process. A distinction is made between papers in journals and in conference proceedings as follows.

Papers in journals

In chronological order of submission date, these articles are:

- Pacio J.C. and Dorao, C.A. (2010) *A study of the effect of flow maldistribution on heat transfer performance in evaporators*. Nuclear Engineering and Design **240**(11), pp. 3868-3877. `doi:10.1016/j.nucengdes.2010.09.004`.

- Pacio J.C. and Dorao, C.A. (2010) *A comparative analysis of computational models for solving one-dimensional heat exchangers problems*. Submitted to the International Journal of Refrigeration (under review).

- Pacio J.C. and Dorao, C.A. (2011) *A review on heat exchanger thermal hydraulic models for cryogenic applications*. Cryogenics **51**(7), pp. 366-379. `doi:10.1016/j.cryogenics.2011.04.005`.

Papers in conference proceedings

Also in chronological order of submission date, the following articles were published in conference proceedings.

- Pacio J.C. and Dorao, C.A. (2009) *Application of high order methods for the simulation of heat exchanger models*. In Skallerud, B. and Andersson, H.I. (Eds.): Mekit'09, Fifth national conference on Computational Mechanics, Trondheim 26-27 May 2009, Tapir Academic Press, pp. 341-351.

- Pacio J.C., Dorao, C.A. and Fernandino M. (2009) *Sensitivity analysis of heat exchangers models using perturbation theory.* In Hesthaven, J.S. and Rønquist, E.M (Eds.): Spectral and High Order Methods for Partial Differential Equations, Selected papers from the ICOSAHOM'09 conference, June 22-26, Trondheim, Norway. Volume 76 of Lecture Notes in Computational Science and Engineering. Springer-Verlag, Berlin Heidelberg. ISBN: 978-3-642-15336-5, pp. 275 - 282.

- Pacio J.C. and Dorao, C.A. (2010) *Numerical analysis of the effect of two.phase flow maldistribution on heat transfer performance.* In Transactions of the American Nuclear Society, Vol. 102, pp. 599-600. 10-17 Jun 2010.

- Pacio J.C. and Dorao, C.A. (2010) *A homogenization approach for studying two-phase heat exchanger performance.* In Proceedings of the 8$^{\text{th}}$ International Topical Meeting on Nuclear Thermal-Hydraulics, Operation and Safety (NUTHOS-8), October 10-14, 2010, Shanghai, China. Paper ID: N8P0131.

- Pacio J.C. and Dorao, C.A. (2011) *Modeling two-phase heat exchanger performance in the annular-mist flow regime considering entrainment and deposition phenomena.* In Proceedings of ASME-JSME-KSME Joint Fluids Engineering Conference 2011, July 24-29, 2011, Hamamatsu, Shizuoka, Japan. Paper ID: AJK2011-10013.

- Pacio J.C. and Dorao, C.A. (2011) *Design considerations for the sizing of high-effectiveness two-phase flow heat exchangers.* In Proceedings of the 23$^{\text{rd}}$ IIR International Congress of Refrigeration, August 21-26, 2011, Prague, Czech Republic. Paper ID: 476.

Other material

This second category includes scientific works presented at international conferences and workshops *without* an exhaustive review process. In other words, the following articles were accepted for presentation based on a reviewed abstract, and were not published. In particular, they are separated into two groups: oral and poster presentations.

Oral presentations

- Pacio J.C. and Dorao C.A. (2009) *Optimization of two phase heat exchangers*, International Conference on Computational Methods for Thermal Problems, 8-10 September, Naples, Italy.

- Pacio J.C. and Dorao C.A. (2010) *Modeling of heat transfer phenomena in annular–mist flow considering entrainment and deposition*, Workshop on Multiphase Flows. Simulation, Experiment and Application. 22-24 June 2010. Dresden-Rossendorf

Poster presentations

- Pacio J.C. and Dorao C.A. (2009) *Optimization of a LNG thermal process. Case study: the PRICO® cycle.*. First Trondheim Gas Technology Conference, 21 - 22 October, Trondheim

Chapter 1

Overview

► A brief synopsis is depicted in the present chapter, comprising the motivation, objectives, scope and structure of this thesis.

This introductory chapter is divided in five sections. The motivation and proposed research approach (further detailed in part I), is briefly described in Section 1.1. A summarized list of objectives is given in Section 1.2. Section 1.3 deals with the scopes and limitations of the present work. The structure of this thesis is given in Section 1.4, including a short description of each chapter. Finally, practical recommendations to simplify the reading of this manuscript are given in Section 1.5.

1.1 Motivation and approach

The world energy demand is rapidly increasing and natural gas is one of the most competitive primary sources. However, natural gas market shares have been historically restricted by the transportation costs. Over the past decades, developments in Liquefaction of Natural Gas (LNG) technology made possible the transportation over great distances where pipeline investment and operational costs are unpractical. On the one hand, since LNG specific volume is about 600 times smaller than natural gas, transportation costs are much more favorable. On the other hand, the liquefaction process requires huge capital investments and is very energy demanding. Therefore, a feasibility analysis of such a project must include both operating and capital expenses.

LNG processes operate in the cryogenic temperature range (that is, below 120K). Previous experience from cryogenic systems, such as the liquefaction of industrial gases (including air separation), indicate that the overall performance of these processes is highly dependent on the heat exchanger network. In fact, the cryogenic heat exchangers are main components in the LNG industry, in terms

of both investment costs and technical challenges. Consequently, an accurate description of this equipment is mandatory for the overall success of the project.

It is usually forgotten in this type of analysis that improving the predicting capabilities of a model has a cost, known as *the cost of the calculation* (Leinhard V and Leinhard IV, 2011, page 128), which must be weighted along with other expenses. In other words, in some systems it might be more convenient to adopt a rather large design margin, than to extend indefinitely the calculation costs. However, in this particular case, as detailed in background presented in Chapter 2, the design engineer faces a narrow window for the analysis. On the one hand, if the design margin is large, the main heat exchanger becomes too expensive, thus seriously affecting the economic feasibility of the project. On the other hand, if it is undersized, the ultimate objective of the process (that is, to obtained liquefied natural gas at the outlet) might not be fulfilled. Therefore, an accurate description is mandatory for this case.

In this thesis, a multiscale approach is proposed for the thermal-hydraulic analysis of cryogenic heat exchangers. This methodology, further described in Chapter 3, consists on identifying the relevant physical phenomena occurring over different length and time scales and focusing the modeling upon their interaction. The main advantage of this technique is that it allows to take advantage of scale separation and consider their coupled behavior in a reduced extent. For this reason, it is widely considered in different areas of physical sciences and engineering, and the list of applications is continuously expanding.

The multiscale nature of the heat exchanger, i.e. the interaction of several length and time scales, makes the modeling a challenging task. This multiscale coupling can be found at different levels. For example:

- The heat transfer coefficient, which is a main parameter in the macroscopic flow analysis, is controlled by the microscopic heat transfer processes in the evaporation interface, in addition to the forced convective terms.
- In shell-type geometries, the flow structure in a labyrinthine arrangement of tubes is usually represented following a porous media approach.
- Large pieces of equipment, with multiple parallel channels, are sometimes represented in terms of one or a few representative tubes, for example one close to the center and another one in the outer region. This description involves a multiscale formulation, as it includes the assumption that all other channels behave similarly and the overall performance is therefore evaluated from an analysis at a lower scale.

A simultaneous resolution of all scales is not practical. While the traditional approach is based on focusing on the scale of interest and disregarding other effects, useful tools and concepts for dealing with multiscale modeling and coupling are developed in the present work. A three-scales framework is defined and modeling

and simulation results are presented for each individual scale. In addition, a proper overall simulation setting is proposed.

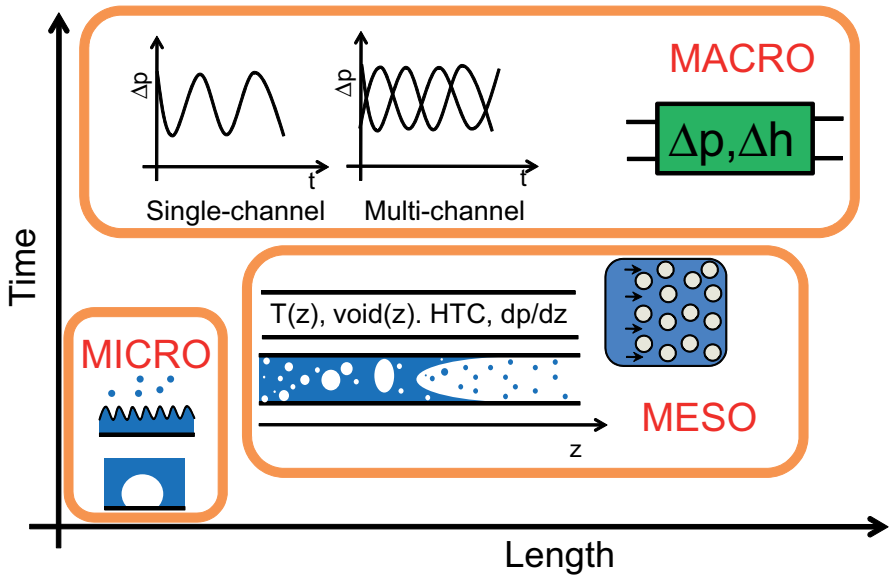

Figure 1.1: Physical effects in a two-phase flow heat exchanger occur over different time and length scales.

1.2 Objectives

Considering the scenario described in the previous section, the main objective of this thesis can be summarized as follows.

1. Evaluate the state-of-the-art in heat exchanger modeling from a design perspective, specially for cryogenic and other high-efficiency applications. The main problems for obtaining an accurate description are identified and consequently a research methodology based on a multiscale formulation for solving these issues is proposed.

2. Develop a multiscale framework, identifying the most relevant physical phenomena and bridging parameters. While in strict terms all these phenomena are coupled, a proper setup must be defined in order to exploit efficiently the separation of different scales.

3. Postulate modeling and simulation tasks in order to improve the current understanding of heat exchanger performance for each individual scale defined

in the previous step. Keeping this final objective in mind, macroscopic effects are analyzed first and further modeling and simulations activities in this project include phenomena occurring at the lower scales.

4. Take into account smaller-scale effects, including the consequences of flow maldistribution, and a phenomenological description of two-phase flow heat transfer.

5. Investigate practical aspects of the implementation of the postulated multiscale scheme. Specifically, an overall simulation algorithm is proposed.

1.3 Scope of the Work

The main idea is to develop a thermo-hydraulic model applicable to the cryogenic heat exchangers used in the LNG industry, mainly spiral wound and to a lesser extent plate-fin type. Therefore, the geometry and operating conditions in the cases studied in this work are selected following those used in LNG processes. Overall, the modeling and simulation activities presented in this work are restricted to the following conditions.

- Steady state operation is considered in order to simplify the analysis. Transient effects, although they might have serious consequences in the performance, do not belong to the first stage of design and therefore are not included in the present analysis and constitute a key element of the recommendations for future works depicted at the end of this thesis.

- A one-dimensional description is conceived for the evolution of cold and hot streams within the heat exchanger. This formulation is representative of intube flow in spiral wound geometries and in some cases also for the plate-fin. Elements of flow mixing and flow maldistribution in parallel channels are incorporated in an homogenization approach.

- High efficiency (ε) applications are considered. For cryogenic systems, this is usually above 90% and for this reason some results are better understood in terms of the *inefficiency* $1 - \varepsilon$.

- Special emphasis is placed on gas-liquid two-phase flow systems. Both boiling and condensing flows are included in the analysis. In this context, while mixture models can be applied to the macroscopic formulations, the microscopic description must account for the individual evolution of each phase. In both cases, state-of-the-art constitutive relations are incorporated.

- Thermodynamic equilibrium is assumed in both liquid and gas phases. This means that, although they can have different temperatures, non-equilibrium effects such as shock waves are disregarded.

- In most of the cases, pure-fluid hydrocarbon refrigerants are the working fluids, around room temperature or slightly colder. Water cases at high temperature are also included in view of the available experimental data for comparison.

- Round-tube geometry with diameters larger or around 8 mm (normal-size channels) is considered in all cases. In general, several criteria have been defined for establishing the transition between channel sizes[1]. Throughout this thesis, a threshold value of 8 mm was considered as a safe figure for normal-size channels.

1.4 Thesis structure

In addition to the present chapter, the remaining of this thesis is divided into five parts, as summarized in Fig. 1.2. Part I presents introductory concepts, including a literature review and some comparative analysis for determining the best research path for this project. Modeling and simulation results at macro, meso and micro scales are the main topic of Parts II to IV. Finally, Part V deals with the conclusion of this thesis and recommendations for future work. In addition, publications and other material produced during this project are included in the appendix.

A short overview of each chapter is presented as follows.

Part I: Introduction

This introductory part covers the fundamental background information for this thesis. In addition to a thorough review of the current state-of-the-art, some comparative analysis are presented for determining the optimum research path for this project. In particular, through the following three chapters, a multiscale framework and different numerical techniques are proposed.

- **Chapter 2: Background and motivation**. The motivation for this thesis, revised in this chapter, is given by the leading role of heat exchangers in cryogenic science and technology. After an extensive review on heat exchanger modeling, a discussion on the state-of-the-art is presented.

- **Chapter 3: A multiscale approach for two-phase flow**. In this chapter, the characteristics of gas-liquid flows and cryogenic heat exchangers are analyzed from a multiscale perspective. The most important bridging parameters are identified and a three-scale framework is proposed (macro, meso, and micro) for the remaining of this thesis.

[1] See Chen et al. (2006, and references therein) and Kandlikar and Grande (2003).

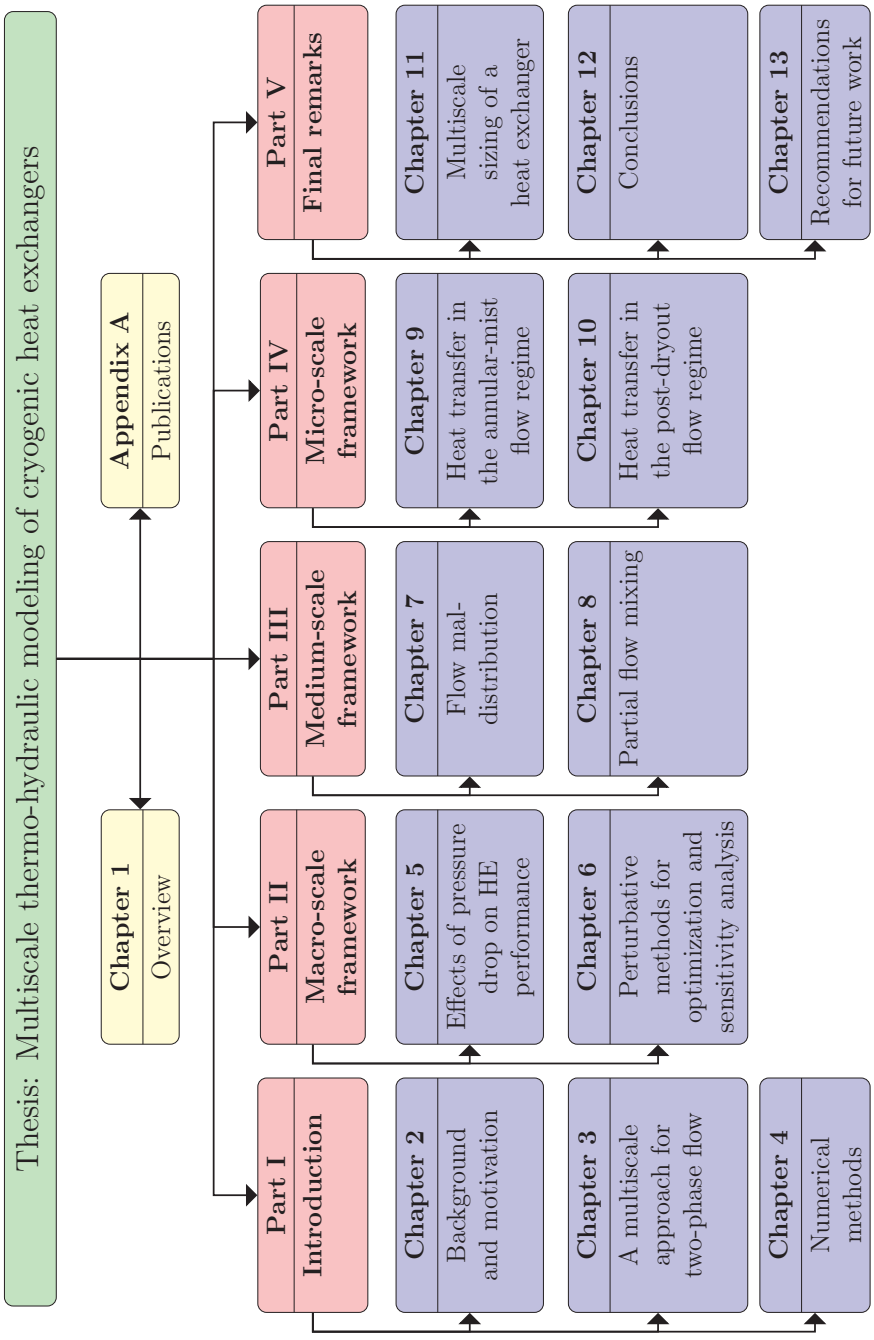

Figure 1.2: Structure of this thesis

- **Chapter 4: Numerical methods**. This chapter deals with the different numerical techniques applicable for this problem. A comparative analysis is performed and the most convenient method is selected. In particular, the Least Squares Spectral Element Method provides some interesting advantages and is recommended for complex problems.

Part II: Macro-scale framework

As a starting point, the modeling and simulation activities in this thesis are first performed at a macroscopic level, that is considering the largest scale. In particular, simple one-dimensional models are selected for evaluating the overall performance of two-phase flow high-efficiency heat exchangers, in terms of both total heat transferred and pressure drop. This part consists of two chapters, as follows.

- **Chapter 5: Effects of pressure drop on HE performance**. Simulation examples are presented and different models are compared in this chapter. In general, neglecting this effect results in serious mispredictions for high-effectiveness applications.

- **Chapter 6: Perturbative methods for optimization and sensitivity analysis**. A simulation tool, widely used in other areas of engineering but not so extensively in this context, is presented in this chapter for the sensitivity analysis and optimization of heat exchangers. The mathematical formulation is described and two examples are presented. In addition, a possible optimization algorithm is postulated and tested.

Part III: Medium-scale framework

This two-chapters part deals with medium-scale effects, that is, including details that were neglected in part II. Then, instead of simple tube-in-tube geometries, more complex geometries with parallel-channel arrangements can be studied. A homogenization approach is postulated, representing the heat exchanger in terms of several layers. In this framework, different physical phenomena are analyzed in these two chapters as follows.

- **Chapter 7: Flow maldistribution**. This chapter deals with simulation analysis of the consequences of the flow maldistribution in parallel channels of large heat exchangers. In particular, the pressure coupling between parallel channels is emphasized.

- **Chapter 8: Partial flow mixing**. Throughout this short chapter, an homogenization approach is postulated for the analysis of multiple-channel heat exchangers and two numerical examples are analyzed: geometrical and mass flow rate differences between the channels.

Part IV: Micro-scale framework

This part deals with the description of the smallest scale. In particular, this analysis is focused on the individual evolution of gas and liquid phases for diabatic intube flow. Considering that in boiling and condensing flows the vapor content is not constant and several flow regimes are found along the tube length, it is important to establish which flow structure is considered. In this context, modeling and simulations results are compared with experimental observations reported in the open literature in the following two chapters.

- **Chapter 9: Heat transfer in the annular-mist flow regime**. A phenomenological model is derived for the prediction of dryout in annular flow. The validation of this model indicates good agreement with experimental data. Similarly, partial dryout in horizontal flow is analyzed.

- **Chapter 10: Heat transfer in the post-dryout flow regime**. In this chapter, post-dryout heat transfer is analyzed. The individual evolution of liquid droplets and the gas core, are described within a two-fluid formulation, coupled with state-of-the-art constitutive relations. This model is then validated against experimental data for power-controlled system, in terms of wall temperature profiles. Both water and hydrocarbon refrigerant cases are studied. Overall, good agreement is observed between predicted and measured wall temperatures. In addition, possible future improvements are discussed.

Part V: Final remarks

Some comments regarding the results from this thesis are summarized in this final part. In general, these are analyzed from a design perspective. In other words, the lessons learned in this work and recommendations for future research are focused on mechanisms for improving the description of heat exchangers in cryogenic and LNG processes. This part comprises three chapters as described next.

- **Chapter 11: Multiscale sizing of a heat exchanger**. An overall multiscale algorithm for the design and sizing of two-phase flow heat exchanger is postulated in this chapter. Modeling results and guidelines from previous chapter are coupled together, thus achieving a complete multiscale scheme. This postulated formulation is applied in this chapter to a practical case, presenting simulation results.

- **Chapter 12: Conclusions**. In this chapter, the objectives of this work presented in Section 1.2 are revised. In addition, a multiscale algorithm for the thermalhydraulic design of a heat exchanger is postulated, and the major contributions from this thesis are summarized.

- **Chapter 13: Recommendations for future work**. This last chapter deals with perspectives for future activities arising from this work. Recommendations for future research at both experimental and modeling levels are derived from the lessons learned in this work. In addition, the possibilities for extending the scope of the current analysis are discussed.

Publications

This appendix comprises the transcript of peer-reviewed publications produced during this work. In total, nine articles are included as follows.

Article 1. Pacio J.C. and Dorao, C.A. (2009) ***Application of high order methods for the simulation of heat exchanger models.*** **In Skallerud, B. and Andersson, H.I. (Eds.): Mekit'09, Fifth national conference on Computational Mechanics, Trondheim 26-27 May 2009, Tapir Academic Press, pp. 341-351.** In the context of a national conference on computational mechanics, this paper investigates practical aspects of the implementation of high-order numerical techniques for the solution of heat exchanger problems.

Article 2. Pacio J.C., Dorao, C.A. and Fernandino M. (2009) ***Sensitivity analysis of heat exchangers models using perturbation theory.*** **In Hesthaven, J.S. and Rønquist, E.M (Eds.): Spectral and High Order Methods for Partial Differential Equations, Selected papers from the ICOSAHOM'09 conference, June 22-26, Trondheim, Norway. Volume 76 of Lecture Notes in Computational Science and Engineering. Springer-Verlag, Berlin Heidelberg. ISBN: 978-3-642-15336-5, pp. 275 - 282.** The ICOSAHOM series of conferences represent a worldwide forum for discussion on current and prospective applications of high order and spectral methods. In this framework, this articles presents the application of perturbative theory for the sensitivity analysis of heat exchangers (which is the main topic on Chapter 6), using the Least Squares Spectral Element Method for the numerical solution of the governing equations.

Article 3. Pacio J.C. and Dorao, C.A. (2010) ***Numerical analysis of the effect of two.phase flow maldistribution on heat transfer performance.*** **In Transactions of the American Nuclear Society, Vol. 102, pp. 599-600. 10-17 Jun 2010.** This short paper deals with the consequences of maldistribution in two-phase flow systems, and was presented at the annual meeting of the nuclear engineering community in the United States.

Article 4. Pacio J.C. and Dorao, C.A. (2010) ***A study of the effect of flow maldistribution on heat transfer performance in evaporators.***

Nuclear Engineering and Design 240(11), pp. 3868-3877. doi:10.1016/j.nucengdes.2010.09.004. This paper accepted for publication in an international journal is an extended version of Article 3. Further analysis of the consequences of maldistribution is detailed in Chapter 7.

Article 5. Pacio J.C. and Dorao, C.A. (2010) ***A homogenization approach for studying two-phase heat exchanger performance.*** **In Proceedings of the 8th International Topical Meeting on Nuclear Thermal-Hydraulics, Operation and Safety (NUTHOS-8), October 10-14, 2010, Shanghai, China. Paper ID: N8P0131.** The effects of partial flow mixing are analyzed in this paper by means of a homogenization approach. The results presented in this article are further discussed in Chapter 8.

Article 6. Pacio J.C. and Dorao, C.A. (2010) ***A comparative analysis of computational models for solving one-dimensional heat exchangers problems.*** **Submitted to the International Journal of Refrigeration (under review).** This paper comprises results obtained in Chapter 4, concerning the performance of different numerical techniques for the analysis of single-phase and two-phase heat exchangers. The main conclusion is that the LSSEM is the most efficient technique for complex problems, while the finite difference formulation is more advantageous in the case of explicit scenarios such as in a co-current flow arrangement. Submitted on August 23th 2010, it is currently under review.

Article 7. Pacio J.C. and Dorao, C.A. (2011) ***A review on heat exchanger thermal hydraulic models for cryogenic applications.*** **Cryogenics 51(7), pp. 366-379.** doi:10.1016/j.cryogenics.2011.04.005. An extensive review on the state-of-the-art is presented in this article, following the background described in Chapter 2.

Article 8. Pacio J.C. and Dorao, C.A. (2011) ***Modeling two-phase heat exchanger performance in the annular-mist flow regime considering entrainment and deposition phenomena.*** **In Proceedings of ASME-JSME-KSME Joint Fluids Engineering Conference 2011, July 24-29, 2011, Hamamatsu, Shizuoka, Japan. Paper ID: AJK2011-10013.** A phenomenological model for predicting the dryout quality in the annular-mist flow regime is presented and validated in this paper. Further details of this models and its predicting capabilities are analyzed in Chapter 9.

Article 9. Pacio J.C. and Dorao, C.A. (2011) ***Design considerations for the sizing of high-effectiveness two-phase flow heat exchangers.*** **In Proceedings of the 23rd IIR International Congress of Refrigeration, August 21-26, 2011, Prague, Czech Republic. Paper ID: 476.** In this

article, a one-dimensional formulation is considered for the macroscopic description of heat exchangers. Several models are compared and the consequences of pressure drop on thermal performance are investigated. An extended description of this analysis can be found in Chapter 5.

1.5 For an easier reading of this thesis

The following items are included in order to simplify the reading of this thesis.

- A short introduction is given at the beginning of each of the parts I to V.
- Without exception, all the chapters start with a highlighted abstract and an unnumbered introduction. The main idea behind this scheme is that each chapter can be read independently.
- In addition, a summary (roughly one-page long) is included at the end of every chapter, including analysis of results and conclusions.

Part I

Introduction

The fundamental background information useful for understanding this thesis is covered in this introductory part. During the following three chapters, an overview of the motivation and proposed approach is provided.

Chapter 2 presents the current status of cryogenic science and technology as background information for this thesis. From this analysis, the industrial motivation for this work becomes clear: heat exchangers play a major role in cryogenic processes and therefore accurate models are required. Present models and advanced trends reported in the open literature are analyzed. After an extensive review, a discussion on the state-of-the-art is presented, highlighting those areas where further improvement is necessary.

In Chapter 3, the postulated multiscale approach is described. As the relevant physical phenomena occur over widespread time and length scales, the analysis of a cryogenic two-phase flow heat exchanger is indeed a multiscale problem. Present multiscale formulations, as well as the characteristics of gas-liquid flows, are analyzed. Consequently, the most important bridging parameters, such as the heat transfer coefficient, are identified. Following this analysis, a multiscale modeling framework is postulated, based on the separation into three scales: macro, meso and micro. This framework is essential for the remaining of this thesis, focused on the analysis of each individual scale.

As a necessary step before leaping from modeling to simulation activities, different numerical methods are evaluated in Chapter 4. A weighted residuals formulation is selected for the generic mathematical description of the different techniques analyzed in this chapter. Special emphasis is placed in the performance of the Least Squares Spectral Elements Methods, due to its very appealing theoretical advantages, such as the fast convergence and inherent ability to provide an error estimator even when no analytical solution is available. These potential advantages are tested with two numerical examples: a single-phase heat exchanger (with analytical solution) and an evaporator. The main conclusion from this chapter is that the LSSEM is the preferred technique for generic and potentially complex problems, while the traditional finite differences approach yields the best performance in the case of explicit scenarios, such as those analyzed in Chapters 9 and 10.

Chapter 2

Background and motivation

► In this chapter, the current status of cryogenic science and technology is briefly overviewed. Special emphasis is placed on the decisive role of the heat exchangers in cryogenic processes, the most common geometries and the main challenges for their modeling and analysis.

Present models for heat exchanger design and current advanced trends reported in literature are analyzed in this chapter. The generic problem of modeling and designing heat transfer equipment is very old, dating back to the beginnings of the industrial revolution. Nevertheless, a final state of research has not yet been achieved, particularly for cryogenic and two phase flow systems. Due to the very demanding requirements in terms of efficiency and overall costs, accurate models are needed. For this reason, some physical phenomena that are normally neglected, such as flow maldistribution, longitudinal heat conduction and heat exchange to the surroundings, must be included in the analysis. After an extensive review, a discussion on the state-of-the-art is presented.

In the last fifty years the cryogenic industry has experienced a sustained growth, mainly based on two pillars: the extension in the use of superconductors, and liquefaction of natural gas. Superconductive materials working at low temperatures are used for constructing the large magnets required for magnetic resonance, magnetic levitation vehicles and research in nuclear physics (Wolsky et al., 1989). Liquefaction of natural gas makes the transportation of this energetic resource economically feasible over long distances.

The economics of cryogenic processes are dominated to a certain extent by the energy requirements of the compressors, which are related to the overall thermodynamic efficiency of the system. Thermodynamic considerations emphasize the need for very small temperature difference in the heat exchangers, resulting in large heat transfer equipment with high effectiveness requirements (Robertson, 1983). For this reason, heat exchangers are major pieces of equipment that affect

the overall performance of these processes. In particular, the main cryogenic heat exchanger (CHE) represents roughly 10% of the total investments in the LNG chain.

The following sections comprise a review on the industrial applications of cryogenics, the importance of using efficient heat exchangers, their challenging features and how present models deal with them.

2.1 Cryogenic science and technology

The word *cryogenic* comes from the Greek *κρῦος*, cryos (frost), and *γίνομαί*, genomae (to produce) (Scurlock, 1992). In short, this means the science and art of producing cold. This definition, however correct, is rather ambiguous, and the prefix *cryo-* has been used in the XIX century for referring to the artificial production of ice, beer brewery and meat transportation (Scurlock, 1990).

The starting point of modern cryogenic engineering can be established in 1877 with the first transitory condensation of oxygen by Cailletet in France and Pictet in Italy, and the permanent production of liquid air by Wroblewski and Olszewski in Poland six years later (Foerg, 2002). Since then, the term has been generally applied related to the liquefaction of the so-called *permanent gases*, that is the group of gases with critical temperature below ambient, which means that they cannot be condensed from ambient conditions by the sole effect of pressure. It was not until 1969 that a recommended upper temperature boundary was settled at 120 K (Kurti, 1970). According to this definition, Liquefied Natural Gas (LNG) is included as a cryogenic fluid, while liquid ethylene is excluded. The group of pure cryogenic fluids is then limited to those listed in Table 2.1. While Table 2.1 is limited to single–component fluids, two important mixtures are worth mentioning: air (78% N_2, 21% O_2 and 1% others, mainly argon) and LNG (roughly 90% CH_4 and 10% other hydrocarbons and N_2)[1].

2.1.1 Industrial applications

The production of cryogenic fluids at industrial scale started in the last quarter of the XIX century as a consequence of the requirements of pure oxygen for the steel industry. Cryogenic technology has evolved significantly since then, and present industrial applications can be divided into three broad categories (Kellner and Scurlock, 1971): cooling purposes, separation and distillation of gas mixtures, and liquefaction for transportation and storage.

[1]These compositions are approximated and given in terms of atomic content

Fluid	Chemical formula	NBP [K]	T_{crit} [K]	p_{crit} [bar]
Helium	He	4.22	5.2	2.3
Hydrogen	H_2	20.3	33.0	12.9
Neon	Ne	27.1	44.4	27.1
Nitrogen	N_2	77.3	126.2	34.0
Carbon monoxide	CO	82.0	136.8	35.0
Fluorine	F_2	85.2	144.0	55.7
Argon	Ar	87.3	150.7	48.7
Oxygen	O_2	90.2	154.6	50.4
Methane	CH_4	111.7	190.7	46.3

Table 2.1: Normal boiling point (NBP) and critical point for cryogenic fluids. Source: Flynn (2005, §3.3).

Cooling at low temperature

The worldwide production of cryogenic fluids is currently dominated by the use of liquid nitrogen for refrigeration. Given its relatively inexpensive production from air, it is widely used in applications including superconductive magnets, sensor cooling (Mukhopadhyay, 2007), cryogenic metal hardening (Baldissera and Delprete, 2008) and treatment of biological samples (Gage, 1998).

Liquid helium is used for cooling of high current superconductive magnets and research in low temperature physics below 4K. For temperatures in the range 20-50 K, liquid hydrogen (LH2) is used; while liquid neon, being chemically inert and having a higher volumetric heat capacity, seems to be an interesting alternative in the near future (Jha, 2006, §1.7).

Distillation and separation

Liquefaction of air provides a relatively simple and inexpensive method for separation of its main components: nitrogen, oxygen and, in minor quantities, argon. Other noble gases, such as helium and neon, are only found in small quantities and therefore not produced from air but from distillation of natural gas at low temperatures. Carbon monoxide is recovered from partial oxidation of natural gas by cryogenic separation.

Liquefaction of fuels and oxidizers

When these *permanent gases* are condensed through the use of cryogenic processes, a large reduction of specific volume (increase in density) is achieved, ranging between 600 (LNG) and 1400 (neon) times compared to room temperature conditions. This feature has lead to the liquefaction of normally gaseous fuels and oxidizers for combustion and transportation purposes, including:

- *Liquid oxygen* is the most commonly used liquid oxidizer for rocket engines, combined with hydrocarbon fuels or LH2.
- *Liquid fluorine* provides the highest specific impulse when combined with LH2 (Gall, 1957). However, it is highly toxic and corrosive, and its use was dropped after some pilot tests.
- The advantages of *LH2* as a fuel are that it has more than twice the energy density (per unit mass) than normal gasoline and its only combustion product is water steam. However, its production requires more energy input than achieved with its combustion, then it should not be considered as a natural energy source, but rather as an energy carrier. It has been used as fuel for rocket engines, submarines and vehicles; and as energy storage for peak–shaving production of electricity.
- *LNG* has a density roughly 600 times larger than room-temperature natural gas, making economically feasible the production in remote locations and transportation over long distances, being usually regasified at a receiving terminal. In 2009, the shipping of LNG amounted to 242 billion standard cubic meters, that is 27.7% of international trade of natural gas (BP, 2010). The direct use of LNG as fuel has also been considered and applied in small scale in recent years for public transportation (Arcadis Geraghty & Miller, 1998, §4.2) and trucks (Wegrzyn and Gurevich, 2000), as well as aviation fuel (Duffy and Kandalov, 1996)

The high growth in production of LNG in the last decades (see Fig. 2.1) has motivated extensive research in cryogenic processes and equipment. A special feature of LNG processes is the condensation of a multicomponent mixture (natural gas, with varying composition). In addition, over 95% of the base–load plants operate on mixed refrigerant (MR) processes in order to improve the cycle efficiency and consequently reduce the power consumption (Venkatarathnam, 2008, §6). The complexity of the LNG process is reflected in the design of heat exchangers and other equipment.

2.2 Heat exchangers in cryogenic processes

While the so–called *condensable gases* can be liquefied by the sole effect of pressure, the production of low temperature is required for the cryogenic fluids listed in Table 2.1. If these temperatures were to be achieved by direct expansion from room temperature (the ideal thermodynamic process, computed using REFPROP[2] is depicted in Fig. 2.2 for air and natural gas), working pressure over 10000 bar

[2]REFPROP is a software developed by the National Institute of Standards and Technology that evaluates thermodynamic properties on the base of empirical correlations. For further details and technical documentation, see (Lemmon et al., 2007).

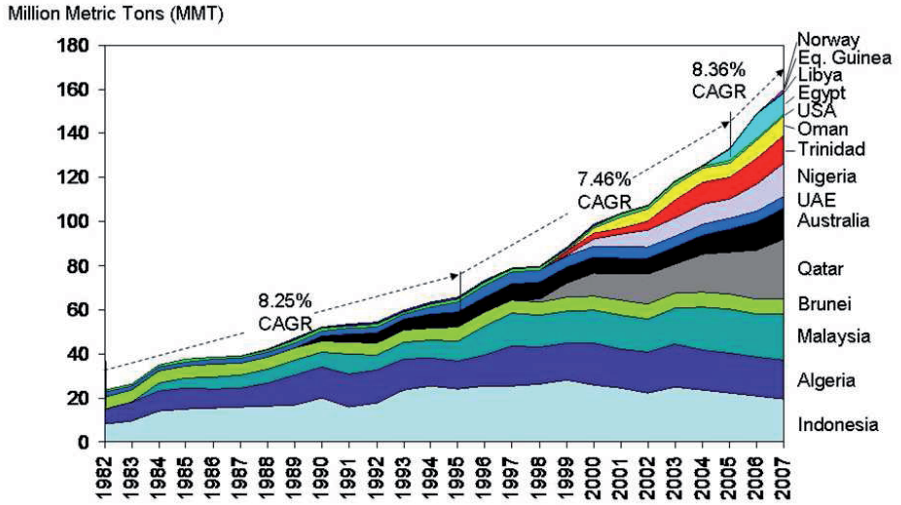

Figure 2.1: World LNG production in the years 1982–2007. CAGR = compound annual growth rate. Source: LNGpedia (2010).

would be required, which is extremely complicated to realize in practice. This means that the use of heat exchangers (HE) at low temperature is fundamentally necessary for the liquefaction of cryogenic fluids.

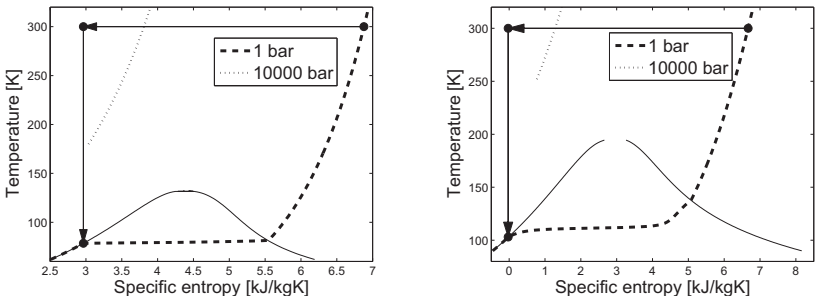

(a) Air: 78.12% N_2, 20.96% O_2, 0.92% Ar (b) NG: 90% CH_4, 5% C_2H_6, 5% N_2

Figure 2.2: Ideal isothermal compression and isoentropic expansion process in T-S diagrams for air and natural gas

2.2.1 High effectiveness HE are required

The importance of HE for cryogenic systems can be illustrated by analyzing a simple process. Figure 2.3 describes the Linde cycle for liquefaction of air, first used by Carl von Linde in 1895 (Scurlock, 1992). Atmospheric air is compressed and cooled to room temperature. The high pressure (HP) gas is expanded after being cooled by the low pressure (LP) gas obtained as flash at the valve outlet.

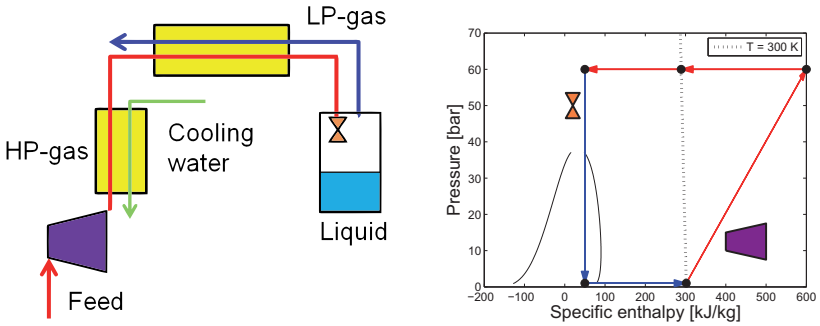

(a) Process diagram (b) Pressure-enthalpy diagram

Figure 2.3: Linde cycle for liquefaction of air

Figure 2.3(b) shows that relatively large amounts of energy must be transferred in order to enter the two–phase region. This scenario makes the process very sensitive to the performance of the HE. For example, Kanoglu et al. (2008) predicted a reduction of 22% in the production of liquid if the HE effectiveness (ε) departs from the ideal value of 100% to a more reasonable one to achieve in practice of 96.5%. In the case of liquefaction of helium, Atrey (1998) calculated that 12% less liquid is obtained if ε is reduced from 97% to 95%, and Barron (1985) stated that no liquid is produced if $\varepsilon < 85\%$. Consequently, cryogenic HE typically operate in the high-efficiency range $\varepsilon > 90\%$ (Venkatarathnam and Sarangi, 1990).

In order to compensate for these reductions, modifications in the process may become necessary in order to restore the refrigeration capacity to the desired level. For example, the pressure ratio can be increased, resulting in a higher power consumption in the compressor. The minimum ideal power input per unit of heat removed in a refrigeration circuit, given by the inverse Carnot cycle (Çengel and Boles, 1994, §11.2) can be computed according to Eq. (2.1).

$$\frac{W}{Q} = \frac{T_{hot} - T_{cold}}{T_{cold}} \tag{2.1}$$

Then, every unit of heat that is not internally transferred must be removed externally, thus implying an increase in the power input, at least as given by

Eq. (2.1). Analyzing Eq. (2.1), it is observed that the power consumption represents a major concern in cryogenics due to the low cold temperature level (T_{cold}). The specific power input (per refrigeration capacity) for several cryogenic fluids is listed in Table 2.2, considering a reference hot temperature level (T_{hot}) of 300 K.

Fluid	T_{cold} [K]	W/Q
Helium	4.2	70.43
Hydrogen	20.3	13.78
Nitrogen	77.3	2.88
Methane	111.7	1.69

Table 2.2: Thermodynamical minimum input of mechanical power per unit of thermal power removed for selected cryogenic fluids

In short, if the HEs have low performance, the production rate of liquid is reduced and large amounts of extra mechanical power are required in order to restore it to the desired level. This sets the need for high effectiveness heat exchangers.

2.2.2 Cryogenic heat exchangers for LNG

For small scale and laboratory applications, simple geometries such as concentric tubes HE can be used with the advantages of building and maintenance simplicity (Shah and Sekulić, 2003, §1.5). However, for larger scale applications, the high effectiveness requirement for CHE and the use of complex processes for LNG, including multiple streams exchanging heat simultaneously, result in the development of complex equipment.

Fredheim and Heiersted (1996) compared data from different authors regarding cost breakdown of LNG facilities, concluding that the HE represent 20–30% of the capital costs of a liquefaction unit, which in turn accounts for half of the total investments in the LNG chain (DiNapoli, 1986; Finn et al., 1999). More recently, Thonon (2005) reported that the main HE represents 5.6–8.4% of the total project costs. In short, it can be sustained that a relevant part of the investments is covered by this sole equipment.

The selection of the main CHE for LNG processes is currently dominated by the use of plate–fin and spiral–wound geometries (Finn et al., 1999). They are illustrated in Fig. 2.4 and compared in the following subsections.

Coil–wound heat exchanger (CWHE)

The coil–wound heat exchanger (CWHE), also known as Giauque–Hampson HE, was first used by Linde in 1895 in Germany and shortly thereafter by Hampson in England (Abadzic and Scholz, 1972). Layers of tubes are coiled around a central mandrel, which provides mechanical stability. Several tube–side streams can

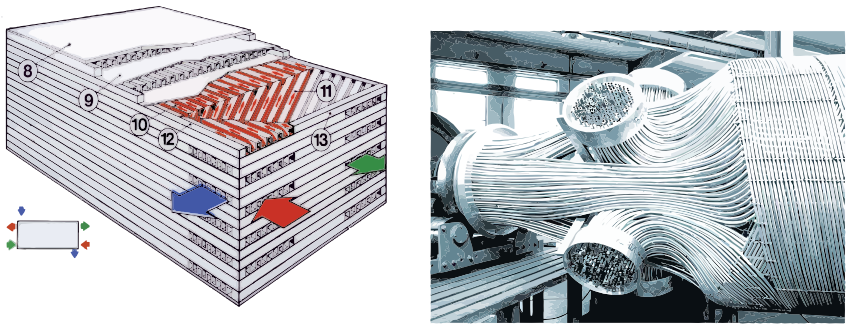

(a) Plate–fin (b) Coil–wound

Figure 2.4: HE geometries used for LNG processes. Illustrations from Linde.

be used in the different layers (two or three being common in LNG processes), exchanging heat with a common shell–side stream. They are used as main CHE in most of the present LNG production plants, and their selection is based on the advantages of multistream capability, high area–to–volume ratio, efficient heat transfer and mechanical robustness considering fast transients in temperature and pressure (Fredheim, 1994).They can be constructed in very large units, only limited in size by transportation issues (McKeever et al., 2008). The main disadvantage is that they are proprietary and expensive equipment, only produced by Air Products and Chemicals, Inc. (APCI) and Linde Group (Tariq, 2004)

Plate–fin heat exchanger (PFHE)

Plate–fin heat exchangers (PFHE) are very compact equipment, with the possibility of handling up to 10 streams in the same unit. In addition, very low temperature differences can be achieved. This results in lower capital and operating costs compared to traditional shell–and–tube–type HE (Linde, b). For this reason they are used in several industries, covering large ranges of temperature and pressure, and many manufacturers produce them around the world, grouped in the *Brazed Aluminum Plate–Fin Heat Exchanger Manufacturers' Association* (ALPEMA, 2000). The use of fins results in a large density of heat transfer area, although their mechanical stability is more sensitive to operational transients.

Both geometries are used in LNG processes. A comparison between them given by Linde[3] is presented in Table 2.3. It is worth mentioning that the reported cost for PFHE does not include the installation of manifolds and connecting equipment. PFHE are more limited in size than CWHE, making necessary the use of parallel units with the corresponding manifolding and assembly, that can represent more than double the cost of the actual HE cores (Crawford and Eschenbrenner, 1972).

[3]Linde Group is the only manufacturer that produces both PFHE and CWHE.

	PFHE	CWHE
Main feature	Extremely compact	Extremely robust
Heating surface density	300–1000 m^2/m^3	50–150 m^2/m^3
Fluid conditions	Very clean, non–corrosive	Less restrictive
Applications	Smooth operation	High T or p gradients
Relative price	25–35%	100%

Table 2.3: Comparison of plate–fin and coil–wound HE. Source: Linde (a).

In addition, Crawford and Eschenbrenner (1972) remarked that, while PFHE have lower cost for a given refrigeration duty, CWHE are more advantageous in other features such as maintenance, pressure and size limitations.

2.2.3 CHE for small–scale/laboratory applications

Small scale equipment is usually designed on a different basis than for larger scale applications. Simplicity and maintenance issues are sometimes more important than the relative cost per unit heat removed, since the amount of heat is small. Although this thesis is focused on industrial applications, these geometries are included here for reasons of completeness. Two main types are described: perforated–plates and regenerators.

Perforated–plate heat exchangers (PPHE)

A comprehensive review on the history and applications of PPHE was given by Venkatarathnam and Sarangi (1990). This geometry consists of several parallel perforated plates separated by spacers. The periodic disruption of the flow gives high heat transfer coefficients but also a relatively large pressure drop.

Heat exchange between the usually counter–current streams occurs laterally through the high–conductivity plates (usually copper or aluminum) which act as fins. Axial heat conduction is avoided, to some extent, with the use of low-conductivity material, such as stainless steel, for the spacers.

Regenerators

The design of a regenerator is conceptually different from all the other geometries, which can be grouped under the name of recuperators. In a regenerator, both fluids occupy alternately the same space and the heat is transferred in and out of a packing material, called the matrix. A review on their historical development and extensive applications in cryogenic systems was given by Ackermann (1997).

Their main advantages are given by the very high area density, as large as 6500 m^2/m^3, relatively low cost and simplicity to build and maintain. The major

limitations consist on their maximum size, and the residual amount of mixing between streams.

2.3 Challenges in the modeling of CHE

Heat exchangers used in cryogenic applications, in particular for LNG processes, present some peculiarities that make their modeling a challenging task. These can be divided into two main categories: the complexity of the processes, and the fact that some effects that are usually neglected for high–temperature applications, cannot be disregarded for CHE.

2.3.1 Complex processes

The aim for overall economic optimization of LNG production resulted in the development of complex liquefaction processes that represent roughly half of the plant capital costs (Finn et al., 1999). Brendeng and Hetland (2004) provide a comprehensive review of natural gas liquefaction technologies. Around 80% of the installed capacity uses a propane–precooled mixed refrigerant process (C3MR) licensed by APCI (Barclay and Denton, 2005). Other cycles include optimized cascade, single mixed refrigerant (SMR) and natural gas expanders. The Snøhvit project, in northern Norway, employs a mixed fluid cascade process, developed by Statoil/Linde.

Figure 2.5 shows a simplified schematic diagram of two processes: (a) C3MR with a propane cycle and a MR cycle, and (b) SMR with one single mixed refrigerant cycles. Both processes have a throttle expansion in the end where LNG is separated from the so-called flash gas, usually used as fuel. These are simplified diagrams, the actual processes involve several pressure level cycles.

As a consequence of the mentioned processes, the CHE operate in challenging conditions, such as large temperature ranges and the use of multiple streams of multicomponent mixtures experiencing boiling and condensation. In addition, the separation of heavier hydrocarbons from the natural gas flow results in flow removal and injection within the main CHE.

2.3.2 Non–negligible effects

Traditional heat exchanger models neglect some effects (Shah and Sekulić, 2003, ch 3.2) since they are not relevant for the typical required engineering accuracy. However, the high–effectiveness requirements for CHE make necessary to take these effects into account. They include: changes in fluid properties, heat exchange with the surrounding, longitudinal thermal conduction in the wall, flow maldistribution and effects of pressure drop on heat transfer. Their relevance, in terms of the degree of accuracy for which they must be considered, is illustrated in Fig. 2.6.

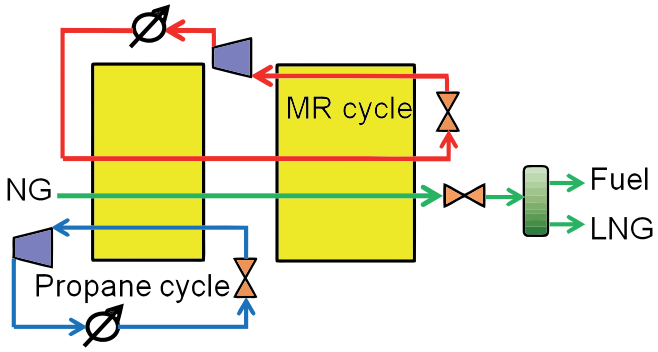

(a) C3MR

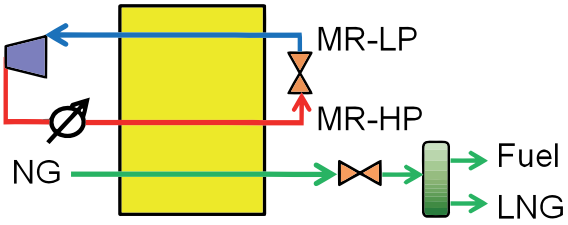

(b) Single mixed refrigerant

Figure 2.5: LNG processes

The dark bars in Fig. 2.6 illustrate the effectiveness threshold below which these effect can be disregarded.

Some of these effects have been addressed in literature for rating the performance of HE in simple processes involving single–phase flow, as described later in Section 2.5. However, no reports were found on applications to complex processes as those used for production of LNG.

Changes in fluid properties

Barron (1999) stated that the main distinctive feature of cryogenic heat transfer is that *all constants become variables*. For the analysis of high–temperature HE, Kays and London (1964) suggested the use of a constant value, corresponding to the physical properties evaluated at a mean temperature. However, this approach is not applicable for cryogenic applications, as noticed by several authors. Soyars (1991) stated that the use of this approximation for simulation of HE with helium below 15 K leads to mispredictions of 30–100% of heat load. Oonk and Hustvedt (1986) found underpredictions of up to 12% on performance of helium HE between 4 and 20 K. Chowdhury and Sarangi (1984a) proposed the use of an harmonic mean instead, resulting in differences up to 20% in the effective size.

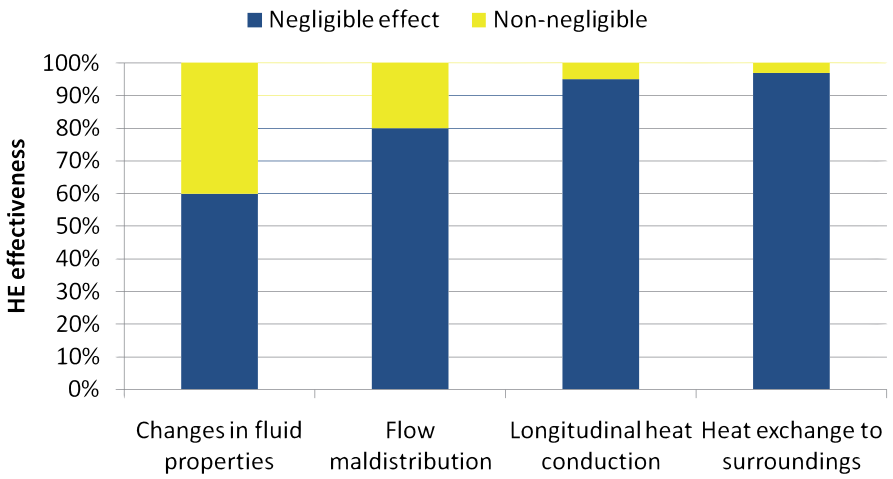

Figure 2.6: Relevant physical effects for a given design effectiveness. The color bars indicate if the effect can be neglected or not.

Heat in–leakage

Since cryogenic processes operate at much lower temperature than ambient, cryogenic equipment exchange heat with the surroundings. The development of multilayer insulations in the 1960s, with apparent thermal conductivity as low as 10–100 $\mu W/(m\ K)$ (Tien and Cunnington, 1973) has reduced the heat–leakage to a practical minimum. However, when high–effectiveness equipment is required, this effect has to be considered. Several authors (Ameel and Vitharana, 1999; Chowdhury and Sarangi, 1984b; Gupta and Atrey, 2000) have considered this effect when rating the performance of single–phase heat exchangers, but it is not currently considered for design. Ameel (2000) considered the effect of heat transfer from a constant–temperature surroundings for co–current and counter–current flow, concluding that the first arrangement is more sensitive to this effect. More recently Al-Dini and Zubair (2008) presented analytical and graphical solutions for the Effectiveness-NTU method considering ambient heat leakage as a distributed heat source, thus allowing to extend the model to include chemical or electrical generated heat inputs.

Longitudinal thermal conduction

This effect reduces the local temperature difference between the working fluids and the separating wall, thus deteriorating the heat transfer. In the extreme case of an infinitely large thermal conductivity, the wall temperature would remain uniform,

since any gradient is dumped by axial conduction. Then, the performance of a balanced counterflow HE is reduced roughly by half, matching the parallel flow case (Hesselgreaves, 2001, §6). Kroeger (1967) presented an analytical solution for the constant–properties single–phase case. The analysis by Venkatarathnam and Narayanan (1999) included the conduction in the wall separating the fluids from the environment. These effects are more significant in small systems (with short conduction lengths and therefore larger gradients) than in the large CWHE ad PFHE.

Flow maldistribution

In many scenarios, the flow distribution can deviate from design conditions, which is usually homogeneous. Mueller and Chiou (1988) presented a comprehensive review on the causes of maldistribution. They include mechanical issues such as fouling, fabrication tolerances, bypass and poor header performance; two–phase instabilities; and heat–transfer induced as a consequence of changes in viscosity or density. Flow maldistribution results in a reduction of performance of single–phase HE (Chowdhury and Sarangi, 1985; Fleming, 1967; Jung and Jeong, 2007), although this effect is only relevant for high efficiency equipment such as those used in cryogenics (Mueller and Chiou, 1988). The effect on two–phase flow systems is more complex, with both reduction (Rabas, 1985; Srihari et al., 2005) and increase (Aganda et al., 2000; Timoney and Foley, 1994) in performance noticed.

Effect of pressure drop on heat transfer

Changes in working pressure affect the fluid physical properties and consequently, the heat transfer performance. While single–phase fluid properties are mainly dependent on the temperature, that is not always the case for two–phase flow. Of special interest for boiling and condensation applications are variations in the saturation temperature.

2.4 Present models for heat exchanger design

This section deals with the present models used for thermalhydraulic design of HE. A complete analysis of a heat exchanger must consider mechanical and corrosion effects. In addition, fabrication and shipping procedures should be taken into account. However, this analysis escapes the scope of this work.

Heat exchanger thermalhydraulic modeling involves the solution of two problems: rating and sizing (Shah and Sekulić, 2003). Rating consists on evaluating the performance of an existing HE. Since all the relevant information is given (geometry, flow conditions), detailed models can be used. Sizing refers to the opposite problem, that is to select the proper HE geometry, flow arrangement and size to

meet the specified performance within some given constraints. The geometry is still unknown, and for that reason simpler models are required.

A summary of the present HE models used for sizing is presented in Fig. 2.7. They can be grouped into three main categories: lumped parameters, distributed parameters and stream evolution, which are further explained in detail in the following subsections. Finally, a review of these models and their ability to consider relevant physical effects is presented in Table 2.4.

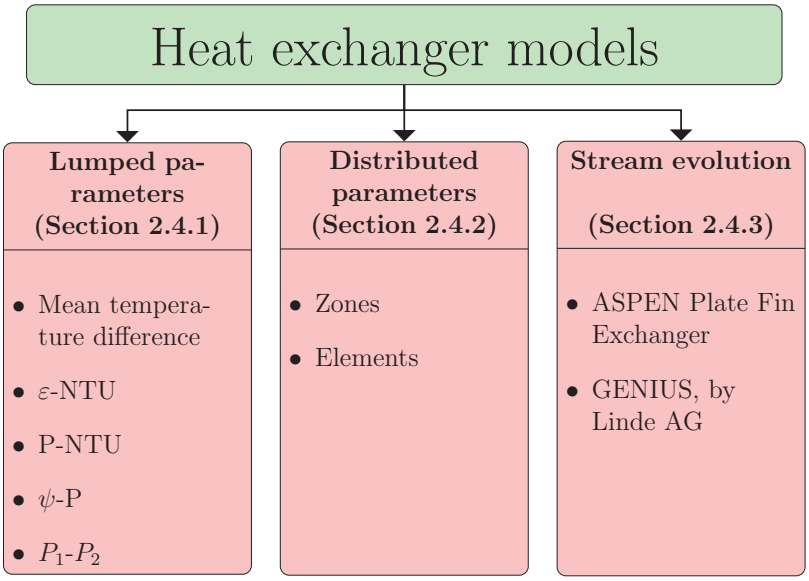

Figure 2.7: Summary of models for sizing heat exchangers

2.4.1 Lumped parameters models (LPM)

These models represent the basic design theory for HEs and can be found in most textbooks (Kakaç and Liu, 2002; Kuppan, 2000; Shah and Sekulić, 2003). They are based on the following energy balances for two single–phase streams:

$$C_{cold}\ dT_{cold} = U\ dA\ \ (T_{hot} - T_{cold}) \tag{2.2}$$

$$C_{hot}\ dT_{hot} = -U\ dA\ \ (T_{hot} - T_{cold}) \tag{2.3}$$

where the heat capacity flow rate (C), defined as the mass flow rate ($\dot{m}$) times the specific heat (c_p) is used.

$$C = \dot{m} c_p \tag{2.4}$$

Equations (2.2) and (2.3) are integrated considering the following assumptions:

1. Steady–state operating conditions
2. No heat transfer with the surroundings
3. Longitudinal heat conduction is negligible
4. Constant overall heat transfer coefficient
5. Constant heat capacity

Following this integration, the HE is represented with two parameters: one for the physical size and another for the thermal performance. This category includes five different models (Shah and Sekulić, 2003, §3.5-3.10): mean temperature difference, $\varepsilon-NTU$, $P-NTU$, $\Psi-P$ and P_1-P_2. All these lumped parameters models (LPM) yield the same results, since they solve the same equations under identical assumptions. The only difference between them is the selection of the parameters. In general, lumped parameters models are meant to be used for single–phase flow with constant properties.

Mean temperature difference (MTD)

The local differential heat flux (dq) between streams is given by the product of local temperature difference (ΔT), differential area (dA) and an overall heat transfer coefficient (U), that is:

$$dq = U\ \Delta T\ dA \tag{2.5}$$

Integrating Eq. (2.5) and considering a constant heat transfer coefficient (HTC), an effective mean temperature difference (ΔT_m) can be considered as acting through the total area (A)

$$\Delta T_m = \frac{Q}{U\ A} \tag{2.6}$$

In the case of co–current or counter–current flow, the integration results in a logarithmic mean temperature difference, defined as in Eq. (2.7).

$$\Delta T_{lm} = \frac{T_h - T_c|_{hot\ end} - T_h - T_c|_{cold\ end}}{\ln\left(\dfrac{T_h - T_c|_{hot\ end}}{T_h - T_c|_{cold\ end}}\right)} \tag{2.7}$$

For this reason, this method is sometimes referred-to as the Logarithmic Mean Temperature Difference (LMTD). In the case of other geometries, a correction factor F, defined in Eq. (2.8), is employed.

$$F = \frac{\Delta T_m}{\Delta T_{lm}} \longrightarrow Q = U\ A\ F\Delta T_{lm} \tag{2.8}$$

ε – NTU

This method is widely used and it is found in most textbooks on heat transfer. The thermal performance is expressed in a dimensionless manner using an effectiveness (ε) defined as the ratio of actual heat duty (Q) and the maximum achievable with the given inlet conditions (Q_{max}).

$$\varepsilon = \frac{Q}{Q_{max}} \tag{2.9}$$

This model uses two dimensionless parameters: the ratio of heat capacity flow rate of both fluids (C^*) and a number of thermal units (NTU) that relates the HTC and physical size area with the minimum heat capacity flow rate.

$$NTU = \frac{U\ A}{C_{min}} \tag{2.10}$$

$$C^* = \frac{C_{min}}{C_{max}} \tag{2.11}$$

Basic forms of the solution are available in literature for both rating and sizing problems for a given flow arrangement, as in Eqs. (2.12a) and (2.12b), respectively.

$$\varepsilon = \phi\left(NTU, C^*, \text{flow arrangement}\right) \tag{2.12a}$$

$$NTU = \phi\left(\varepsilon, C^*, \text{flow arrangement}\right) \tag{2.12b}$$

P – NTU

This method employs two individual parameters for each stream. The first parameter, a number of thermal units (NTU), is defined for each stream as:

$$NTU_{hot} = \frac{U\ A}{C_{hot}} \quad , \quad NTU_{cold} = \frac{U\ A}{C_{cold}} \tag{2.13}$$

The second parameter is a heat capacity flow ratio (R) for each stream:

$$R_{hot} = \frac{C_{hot}}{C_{cold}} \quad , \quad R_{cold} = \frac{C_{cold}}{C_{hot}} \tag{2.14}$$

The thermal performance of the HE is evaluated with individual temperature effectiveness (P) defined as:

$$P_{cold} = \frac{Q}{C_{cold}\Delta T_{max}} \quad , \quad P_{hot} = \frac{Q}{C_{hot}\Delta T_{max}} \longrightarrow \varepsilon = \max\left(P_{cold}, P_{hot}\right) \tag{2.15}$$

The temperature effectiveness P is related to ε as given by Eq. (2.16)

$$P_{cold} = \varepsilon \frac{C_{min}}{C_{cold}} \quad , \quad P_{hot} = \varepsilon \frac{C_{min}}{C_{hot}} \tag{2.16}$$

In general, for a given flow arrangement, P depends on the HE size, the heat capacity flow ratio, that is:

$$P_{cold} = \phi_{cold}\left(NTU_{cold}, R_{cold}, \text{flow arrangement}\right) \tag{2.17}$$

$$P_{hot} = \phi_{hot}\left(NTU_{hot}, R_{hot}, \text{flow arrangement}\right) \tag{2.18}$$

The comparative advantage of the $P - NTU$ method is that, with the use of individual parameters, it is not necessary to identify the stream with C_{min}.

$\mathbf{\Psi - P}$

This method, first proposed by Mueller (1967), introduces the parameter Ψ that represents a dimensionless effective mean temperature difference.

$$\Psi = \frac{\Delta T_m}{\Delta T_{max}} \tag{2.19}$$

This parameter is related to the previous models as:

$$\Psi = \frac{\varepsilon}{NTU} = \frac{P_{cold}}{NTU_{cold}} = \frac{P_{hot}}{NTU_{hot}} \tag{2.20}$$

$\mathbf{P_1 - P_2}$

Roetzel and Spang (1990) proposed this method as a simpler way of graphical representation of the HE performance. It does not introduce new parameters, but recommends the use of the temperature effectiveness of both streams.

Other efficiencies

Clayton (1974) proposed the use of a HE efficiency η and a *new effectiveness* E_n.

The first one is the ratio of the actual heat transfer rate to the one that would be achieved if both fluids had an infinitely large specific heat capacity and it is always $\eta < 1$. Its use is advantageous for small–size exchangers, since in this case $\eta \to 1$, while $\varepsilon \to 0$, thus reducing the relative sensitivity to uncertainties.

A *new effectiveness* is defined as the ratio of the actual heat transfer to the one obtained by direct mixing. According to this definition, it can take values larger than unity. In particular, an infinite co–current flow HE would have $E_n = 1$, and a balanced infinitely large counter–current flow case would give $E_n = 2$.

2.4.2 Distributed parameters models (DPM)

These models consist on dividing the HE in elements of variable size and applying a lumped parameters model in each of them, being $\varepsilon - NTU$ and mean temperature difference the most common ones. The application of a LPM is then restricted to a small region where the assumptions, such as constant fluid properties, are better fulfilled. They are widely used for applications with complex flow arrangements, such as air conditioning systems and heat pumps. This can be done at two different levels: zones or elements (Iu et al., 2007).

Zones

Evaporators and condensers are usually divided into three zones: single–phase liquid, two–phase and single–phase vapor. This approach applies a lumped parameter model over the whole two–phase region, where its assumptions (listed in Section 2.4.1) are not strictly valid. In particular, the assumption of constant HTC is only applicable to a certain extent in scenarios where the thermal resistance is dominated by the single–phase stream. For this reason, this approach has been used by several authors for modeling air–cooled condensers and air–heated evaporators (Costa and Parise, 1993; Fischer and Rice, 1981; Mullen et al., 1997). As a possible solution, Orth et al. (1993) further divided each zone into elements.

Elements

The heat exchanger is divided in elements of some given physical length, in a geometry–oriented approach. This formulation is useful for complex geometries like air conditioning and heat pump systems with multiple tube passes in several directions (Domanski and Didion, 1983; Liang et al., 2001).

Since this model is not flow–oriented, the transition between the single– and two–phase regions is not intrinsically considered, which may lead to some numerical problems. These issues can be solved by reducing the element size to a tube–segment, as proposed by several authors (Iu, 2007; Ragazzi and Pedersen, 1991; Vardhan and Dhar, 1998), therefore reducing the size of the transition element.

2.4.3 Stream evolution models (SEM)

This category of models is based on steady–state one dimensional mass, momentum and energy balance equations for each individual stream, thus they are appropriate for multi–stream heat exchangers. The inclusion of the mass balance allows to evaluate the individual compositions of vapor and liquid in boiling and condensation of mixtures, and the momentum equation is used to evaluate the pressure drop. While a one–dimensional analysis is simple and fast, heterogeneous behavior through the cross section is neglected.

These models are usually implemented into proprietary software, and their know-how is mainly related to the correlations used for fluid properties and heat transfer and pressure drop characteristics. Two proprietary programs are reviewed in this section: *Aspen Plate Fin Exchanger* ®, offered by AspenTech® and *GENIUS*, developed by Linde AG. In some cases, such as the COIL model proposed by Fredheim et al. (2000), these schemes are designed user–defined–subroutine integrated into a process simulator.

Aspen Plate Fin Exchanger ®

ASPENTech (2010) offers this commercial software for simulation of PFHE, that can be integrated into its proprietary process simulator. Some relevant features include:

- Pressure drop is evaluated in detail, including the localized effects in distributors, headers and nozzles. However, its consequences on heat transfer are not considered.
- Flow maldistribution can be considered to a certain extent in a layer–by–layer simulation mode. The evolution of each layer is modeled individually, imposing a linear or parabolic flow distribution profile. It should be noticed that the usual flow distributions for plate–type geometries are cosine or hyperbolic cosine profiles, as reported by Bassiouny and Martin (1984a; b).

GENIUS, by Linde AG

This program, presented by Steinbauer and Hecht (1996), was developed an tested by Linde AG to model CWHE. Although this program is not commercially available, its review is interesting since it is used by one of the only two manufacturers of CWHE. Some important features include:

- Local coefficients are used for both heat transfer and pressure drop, evaluated with the local fluid properties. However, the HTC is only dependent on the local enthalpy and the wall temperature, neglecting the effects of changes in pressure (inlet value is assumed).
- Heat losses and heat feed can be considered.
- Cross–sectional averaged temperatures are used. In addition, a mean fluid velocity is considered. This means that the HE is modeled at a stream–by–stream level, an not layer–by–layer.

The first version was released in 1993 and since then large efforts were focused on developing and testing correlations against reported literature and measurements performed in Linde AG laboratories. Although this gives an extensive level of validation to the code, it implies that all the physical effects that are not considered by the model, are implicitly taken into account by the correlations.

2.4.4 Summary. Features for cryogenic applications

Effect	LPM	Distributed		Distributed	
		Zones	Elements	HYSIS	Genius
Single–phase flow	Yes	Yes	Yes	Yes	Yes
Two–phase flow	No	Yes	Yes	Yes	Yes
Flow mixing (partial)	No	No	No	No	No
Flow mixing (complete)	Yes	Yes	Yes	Yes	Yes
Changes in fluid properties	No	No	Yes	Yes	Yes
Multiple streams	No	No	No	Yes	Yes
Multi-component mixtures	No	Yes	Yes	Yes	Yes
Flow injection/removal	No	No	Yes	Yes	Yes
Heat in-leakage	No	No	No	No	Yes
Axial thermal conduction	No	No	No	No	Yes
Flow maldistribution	No	No	No	Yes	No
Effects of Δp on heat transfer	No	No	No	No	No

Table 2.4: Review of HE models and their evaluation of interesting effects for cryogenic and LNG applications

Table 2.4 summarizes the HE models introduced in this section and their consideration of physical effects relevant for cryogenic applications. Some important conclusions can be extracted from this table:

1. All models are capable of modeling complete flow mixing. This can be simply done by using averaged values in a one–dimensional analysis. However, flow mixing is not always complete, and an analysis of partial mixing would require a two– or three–dimensional model, which none of them considers. The consequences of partial flow mixing are the main topic of Chapter 8.

2. The consequences of pressure drop on heat transfer are neglected in all cases. The relevance of this effect is further studied in Chapter 5.

3. The most advanced models (stream evolution category) are proprietary. Furthermore, some of them are not commercially available.

4. The model given by ASPENTech (2010) is the only one that considers flow maldistribution in a layer–by–layer approach. All layers are considered to be identical except for the mass flow rate.

In summary, present heat exchanger models are not capable of considering all physical effects relevant for cryogenic and LNG applications. Some of these effects have been addressed in literature, as is reviewed next in Section 2.5.

2.5 Advanced models reported in literature

Several authors have developed advanced models to overcome the limitations of formulations presented in Section 2.4. Their research has been focused in the main relevant effects listed in Section 2.3.2, that is changes in fluid properties, flow maldistribution, longitudinal heat conduction and heat exchange to the surroundings. The available literature is reviewed in the following subsections. Finally, they are summarized in Table 2.5.

2.5.1 Changes in fluid properties

For single–phase flow heat exchangers, the two most relevant effects are given by variations in the specific heat capacity and heat transfer coefficient. The vast majority of the available literature is focused in only one of them separately. The research on their combined effect is rather limited (Peters, 1970; Roetzel, 1969; 1974), with no general conclusion.

Specific heat capacity

Some authors suggested the use of an average value. This simple approach gives good results if the variation factor (ratio of larger to smaller values) is small. Evaluating the fluid properties at the mean temperature, as proposed by Kays and London (1964) for high–temperature applications, is valid up to a variation factor of 2. In cryogenic systems, however, the temperature range gives larger variations. Chowdhury and Sarangi (1984a) studied supercritical hydrogen in the range 300-40 K (specific heat increases four times), and suggested the use of a harmonic mean value, except for unbalanced, high NTU cases. The use of a harmonic mean has also been suggested by Sahoo and Sarangi (1985) for the analysis of regenerators.

This average–value approach gives misleading results for complex scenarios. For example, if the design is close to balanced in terms of heat capacity flow rate (as is usually the case for cryogenic systems), the ratio C_h/C_c can change from a value larger than unity to one lower than unity, or vice versa. In this case, points of minimum temperature difference, known as pinch points, may occur. The average–value approach, however, fails to predict the location of pinch points, as noticed by Kumar and Sarangi (1991), since it postulates smooth profiles. In the case of distributed parameter model (DPM, see Section 2.4.2), the variations of specific heat may lead to a wrong identification of the stream with C_{min}, required by the $\varepsilon - NTU$ method. For this reason, Soyars (1991) recommends the use of the Mean Temperature Difference (MTD) method over the $\varepsilon - NTU$ for the analysis of close-to-balanced heat exchangers.

Heat transfer coefficient

An earlier review on the topic was presented by Gardner and Taborek (1977). Two simple methods stand out, based on an average value of the product of heat transfer coefficient and temperature difference. In both cases, this average can be computed on the basis of the extreme values. For counter–current flow arrangements, the method given by Colburn and de du Pont (1933) (logarithmic mean) is recommended. In the case of general multipass flow arrangements, the use of an arithmetic mean was proposed by Bowman et al. (1940) and validated by later authors (Gardner, 1941; Tiller et al., 1963) within 10% accuracy. Both methods assume that the overall heat transfer coefficient is a linear function of temperature.

For general functional forms of the HTC, the solution of coupled, non–linear energy balances is required (Kao, 1975). Recently, Sharqawy and Zubair (2010) studied polynomial and power-law dependencies of HTC on the local temperature difference. They recommend the use of a four-points numerical integration which predicts the required surface area within 1% uncertainty.

2.5.2 Flow maldistribution (FMD)

The consequences of a poor flow distribution on heat exchanger performance have been first studied by Fleming (1967). He considered a counterflow HE divided in two sections: a fraction F_L of the channels in one stream has a lower–than–average flow, and a fraction $1-F_L$ with higher–than–average flow. Thus, an initial balanced design is divided into two unbalanced sections, which are less effective. In this framework, the overall performance is given by a combination of both sections. The main conclusion of his work is that, for high–effectiveness cryogenic HE, there is very little to be gained from increasing the size if the flow distribution is poor. In addition, if the uniform stream is completely and continuously mixed (an idealization of shell–and–tube geometry), a more homogeneous temperature profile is obtained, thus improving the performance. A similar effect is obtained when transverse heat conduction is considered (Jung and Jeong, 2007). This latter conclusion is of interest for the design of anisotropic geometries, such as PPHE.

FMD produces different velocities in each channel, which affect the local HTC. Ranganayakulu et al. (1996) incorporated this effect for the study of a cross–flow HE, resulting in a 2% difference in ε compared to the simpler model given by Fleming (1967). Rao and Das (2004); Rao et al. (2002; 2005; 2006) included this effect for the analysis of plate–type HE in single–phase laminar flow as well as condensers. They concluded that there is an optimum number of plates that gives the maximum efficiency, and a further increase results in a large reduction of performance due to maldistribution.

2.5.3 Longitudinal heat conduction (LHC)

Traditionally, axial conduction in a single–phase fluid is neglected, except in the case of very low Prandtl number, typical for liquid metals (Hennecke, 1968). In regenerators, however, LHC in the fluid affects the eddy thermal conduction given by the flow through porous media (Sarangi and Baral, 1987). The performance of regenerators is also reduced by LHC in the matrix. Das and Sahoo (1999) recommended increasing the charging time to an optimum value. This modification, however, would reduce their maximum heat duty.

A comprehensive review on the effect of LHC in the separating wall of recuperators is given by Shah (1994). In co–current flow arrangements, the effect is negligible, due to the small temperature gradient in the wall. Extensive research has been focused in cross–flow HE, where the temperature profile is two–dimensional. However, this arrangement is usually used for lower performance, usually $\varepsilon < 0.8$. Then, the consideration of LHC for cryogenic applications is most relevant in counter–current flow arrangement.

The pioneer work by Kroeger (1967) is a comprehensive analysis for a wide range of operating conditions. The reduction of performance as a consequence of LHC (up to 5% in ε) is maximum for balanced, high NTU exchangers. This research was confirmed and followed by later authors (Chowdhury and Sarangi, 1983; Narayanan and Venkatarathnam, 1998; Venkatarathnam and Narayanan, 1999).

2.5.4 Heat in–leakage (HIL)

In cryogenic systems, heat exchange to the surroundings gives a net heat input (heat in–leak) to the HE streams. If only one stream receives heat in–leak, as in the case of a double–tube geometry, heat transfer to the cold fluid has a more pronounced effect on performance (Barron, 1984; Chowdhury and Sarangi, 1984b). In other geometries, such as micro HE with thin insulation layers, both streams can interact with the surroundings simultaneously. In this case, a counter–current flow arrangement is less affected by HIL, since the local temperature difference is rather uniform (Ameel, 2000; Ameel and Vitharana, 1999).

Some authors have studied this effect in terms of a uniformly distributed heat load applied to one or both streams (Al-Dini and Zubair, 2008; Nellis and Pfotenhauer, 2005). They presented analytical results, which provide useful guidelines for more complex problems. However, the situation is better represented by heat exchange to a constant–temperature medium, or a third stream that represents the surroundings (Seetharamu et al., 2004).

Recently, Mathew and Hegab (2010a; b; 2011) presented an analysis for high-temperature micro channel HE with heat leakage, reporting conclusions that can be easily extended for cryogenic systems. Considering the P-NTU method, they noticed that the temperature effectiveness of one fluid increases, while the other

one decreases. This situation indicates that the use of only one efficiency (as in the $\varepsilon - NTU$ method), does not describe the problem completely. In addition, the results in terms of overall performance depend on which fluid has the lowest heat capacity flow. If the most sensitive stream (cold fluid in cryogenics, hot fluid in high-temperature systems) has the highest heat capacity flow rate, there is an optimum value of NTU that gives a maximum effectiveness.

2.5.5 Combined effects

Most of the available literature is focused in only one of the four effects mentioned above. The research on the combination of two or more of these effects is scarce and no general conclusion can be derived from it. In other words, it is not clear how they interact.

On the one hand, Ranganayakulu and Seetharamu (1999) studied the combined effect of FMD and LHC. They concluded that the effects on the HE performance tend to eliminate each other in regions of high NTU, and to augment each other for lower values of NTU. In all cases, the effectiveness is reduced, up to 30%. On the other hand, Nellis (2003) studied LHC, HIL and property variations, and concluded that their effect on HE performance can be computed separately, within 10% difference respect to a full model.

The combination of LHC and HIL has attracted the most attention from researchers. Venkatarathnam and Narayanan (1999) studied the LHC of a tube–in–tube heat exchanger, concluding that the degradation of performance is lower as compared to LHC in the inner wall, and the model by Kroeger (1967) holds. Gupta and Atrey (2000) observed that, while increasing NTU reduces the effect of LHC, it increases the heat in–leakage, thus an optimum value of NTU is found to exist.

Table 2.5: Summary of advanced models reported in literature

Effect	**Method**	**Observations**	**Reference(s)**
c_p	Use c_p at mean temperature	Up to a factor 2 variation	[172]
c_p	Harmonic mean (recuperators)	Up to a factor 4 variation. Misleading results for unbalanced, high NTU	[60]
c_p	Harmonic mean (regenerators)	Predicts well ε, but not the temperature profiles	[277]
c_p	Distributed parameters	LMTD preferred over $\varepsilon - NTU$	[293]

Continued on Next Page...

Table 2.5 – Continued

Effect	**Method**	**Observations**	**Reference(s)**
c_p	Finite–difference	Identifies pinch points	[182]
HTC	Review (1977)	Widely studied for single-phase	[112]
HTC	Logarithmic mean of $U \times \Delta T$	For linear functions $U(T_c, T_h)$ in counter–flow arrangement	[65]
HTC	Arithmetic mean of $U \times \Delta T$	For linear functions $U(T_c, T_h)$ in multipass flow arrangements	[40; 111; 315]
HTC	Four-points integration	For polynomial or power-law functions $U(\Delta T)$, 1% uncertainty	[291]
HTC	Non–linear energy equations	General functions $U(T, \Delta T)$	[167]
FMD	Divide the HE in two sections, step profile	Flow mixing improves performance	[93]
FMD	Heat transfer coefficient depends on fluid velocity	2% change in ε compared to [93]	[260]
FMD	Transverse heat conduction	Similar effect to flow mixing in [93]	[160]
FMD	Plate condensers	Optimum number of plates	[262–265]
LHC	Review (1994)	Most relevant in counter–current	[289]
LHC	Pioneer work, non–dimensional	Maximum effect for balanced, high NTU.	[181]
LHC	Regenerators	In the fluid, affects eddy thermal conduction. There is an optimum charging time	[72; 281]
HIL	Heat exchange to only one stream	Some graphical results. For cryogenics, heat exchange to the cold fluid is more severe	[31; 59; 250; 285]
HIL	Heat exchange to both streams	Counter–current flow arrangement is less affected	[12; 13]

Continued on Next Page...

Table 2.5 – Continued

Effect	Method	Observations	Reference(s)
HIL	Uniform heat source	Analytical solution, useful as a guideline.	[8; 234]
HIL	P–NTU method	For high temperature, if $C_c < C_h$, an optimum NTU exists	[213–215]
	FDM and LHC	Tend to eliminate each other for high NTU, and augment each other for low NTU	[259]
	LHC and HIL	LHC in outer wall is not severe as in inner wall	[328]
	LHC and HIL	Optimum NTU is found to exist	[124]
	FDM, HIL, and properties variation	Their effects can be computed separately within 10% accuracy	[233]

2.6 Discussion on the state of the art

The advanced models presented in Section 2.5 incorporate some effects that present models used for sizing, described in Section 2.4, neglect. In general, the state of the art can be divided into two categories of models: non–dimensional analysis and discretized equations.

Non–dimensional analysis is a powerful tool that allows the simple modeling of complex problems. In this context, it is used for defining axial conduction parameters and flow distribution profiles, allowing a simple understanding of LHC and FMD. Although this analysis is very useful in early stages of design, it is only applicable to simple idealized cases in single-phase flow.

Most of the advanced models, indeed, are based on the numerical solution of discretized energy balances. The variations in fluid properties are straightforwardly considered by this approach. With the inclusion of energy balances in the wall, more effects such as LHC and HIL can be considered. Then, following the same trend as in Table 2.4, discretized numerical models are more complete. An underlying question in this approach is the selection of the numerical method. As more physical effects are included and the models grow more complex, the computational costs become more demanding and advanced numerical methods, more efficient than the traditional finite–difference formulation, will be needed. This

aspect is discussed later in Chapter 4.

Although these advanced models include, to some extent, several relevant physical effects, two points are currently not being considered: the effects of pressure drop on heat transfer and incomplete flow mixing.

Changes in pressure affect all fluid properties, with consequences on heat transfer. As opposite to single–phase flow, where fluid properties are mainly dependent on temperature, this situation is more complex for two–phase flow. In particular, for boiling and condensation applications, variations in the saturation temperature can separate or bring closer the temperature profiles, thus affecting the total heat transferred. In short, this effect can be negligible for single–phase flow, but not in the case of two–phase flow. Chapter 5 deals with this topic in further detail.

Flow mixing can play an important role in HE performance, as observed by Fleming (1967) in his study of maldistribution. However, some authors neglect it, while others assume a complete and continuous mixing. The practical case is an intermediate situation, which cannot be easily modeled by a one–dimensional formulation. The effects of flow mixing are further studied in Chapter 8.

In this thesis, a multiscale approach is proposed for tackling these issues. Further detail are given in Chapter 3.

2.7 Summary

Liquefaction of Natural Gas represents one of the major foundations for the sustained growth of cryogenic science and engineering in the last decades. This technology provides an economically feasible way of transporting natural gas over long distances. The economics of LNG processes, which allow for this possibility, are to some extent controlled by the performance of the main cryogenic heat exchangers. Not only the HE efficiency largely controls the overall plant performance, but also they represent a substantial fraction of the capital costs. This industrial scenario provides then the motivation for continuous efforts oriented towards improving the current understanding and predicting capabilities of heat exchanger models.

In general, the major challenges in the modeling of heat exchangers for cryogenic applications can be divided into two categories: complex processes and non-negligible physical effects. State-of-the-art liquefaction techniques include several refrigeration cycles, with multicomponent mixtures as working fluids and multiple interacting streams within a single heat exchanger unit. Non-negligible effects include changes in fluid properties, flow maldistribution, longitudinal heat conduction and heat exchange to the surroundings. These effects, which are normally disregarded for traditional high-temperature applications, must be included in the analysis due to the requirements for high efficiency.

An extensive review on current heat exchanger models is presented in this chapter. In general, they can be divided into those used for design (sizing) and those for rating. On the one hand, the sizing problem involves more unknowns and

therefore requires simpler models. On the other hand, more accurate descriptions can be used for rating existing equipment.

The sizing models were grouped into three categories: lumped parameters, distributed parameters and stream evolution formulations. These were described in detail and their performance for cryogenic applications was compared. In general, stream evolution models are the most complete ones.

More advanced models reported in the open literature for the rating of heat exchangers were also analyzed. An extensive review indicates that the non-negligible effects described above have been individually studied by previous authors in simple cases such as single-phase flow with constant physical properties. The available literature on two-phase flow, which is the major focus of this thesis, is rather limited.

Finally, a discussion on the state of the art is presented. Two physical effects stand out as unaccounted for by present models. These are the consequences of pressure drop on heat transfer, and the extent of partial flow mixing in shell-type geometries. Further analysis on these topics is described in Chapters 5 and 8, respectively.

Chapter 3

A multiscale approach for two-phase flow

► A multiscale problem is simply a situation where the relevant phenomena are widely spread in terms of characteristic length and time. In this context, most problems in engineering (and not few in social sciences) have indeed multiscale features. While multiscale models have extended to several applications in the last decade, this work deals with a novel multiscale approach for the analysis of two-phase flow in heat exchangers.

This chapter includes a throughout description of present multiscale models and their applications. Current techniques are mostly based on homogenization or multigrid formulations. For this particular case, however, only a heterogeneous description is suitable. The characteristics of gas-liquid flows and cryogenic heat exchangers are analyzed from a multiscale perspective. Consequently, the most important bridging parameters, such as the heat transfer coefficient, are identified. Following this analysis, a three-scale framework is proposed (macro, meso, and micro), which is the ground base for the remaining of this thesis.

Most problems in science and engineering involve physical phenomena occurring over different temporal and spatial scales. In general, they range from quantum mechanics and molecular dynamics to continuum and system-level descriptions. Not all of them are necessarily relevant for a particular problem, and traditional formulations are focused in the particular scale of interest (usually called macroscale) and neglecting all others.

The Navier–Stokes equation in fluid mechanics represents a textbook example of this type of formulation (E and Engquist, 2003). The microscopic processes are physically governed by molecular dynamics, while in the macroscopic continuum description, they are represented by an equation of state that defines new fluid properties such as the viscosity, and linear constitutive equations. These empirical

closure laws are not always justified or understood in other complex systems, such as two–phase flow. Then, although this continuum formulation describes well the dynamics of simple liquids, it does not perform as good in large complex systems. The reason for this is probably that physical effects occurring at lower scales (micro-, or meso-scales) might have a large influence in the macroscopic evolution.

In the particular case of cryogenic heat exchangers, the models reviewed in Chapter 2 are focused on the top scales. The lumped-parameters models, see Section 2.4.1, relate inlet and outlet temperatures in an integral form, thus giving a system-level description. Distributed parameters models and stream evolution models (described in Sections 2.4.2 and 2.4.3) represent the HE in terms of temperature and pressure profiles, represent continuum formulation. The advanced models described in Section 2.5 include, with some limitations, effects occurring at lower scales, such as flow maldistribution. However, the interaction between scales is not considered.

The complete solution of the problem in a fully detailed microscopic description is, in most cases, impractical. For this reason, a multiscale formulation might be required for some problems. In this chapter, the current applications and models are presented. In addition, their applicability to two-phase flow and heat exchanger problems is analyzed.

3.1 Current applications

Multiscale models consider the separation and interaction between scales in both upwards and downwards directions. They have gained lot of attention in the last decade, with exponential growth in the number of publications and the creation of several journals dedicated to this topic (Horstemeyer, 2010).

In general these models are used in problems where the smallest and the largest scales are separated by several orders of magnitude. Current applications include, but are not limited, to the following list.

- **Biology and medicine**. A tissue, which is usually the macroscopic level of analysis, is a collection of a large number of cells. In addition, the evolution of tumors depends on processes at cellular and subcellular levels, which are the microscales. Since these scales are very separated from each other but also present strong interaction among them, this problem can be represented by a multiscale formulation (Anderson, 2007).

- **Solid mechanics**. The macroscopic variables of interest are usually elastic and plastic properties such as yield stress. However, the evolution of some processes such as fracture propagation in brittle or ductile behavior depend on the individual interaction of atoms. Continuum and atomistic descriptions are separated by more than six orders of magnitude and then multiscale

models become necessary (Liu et al., 2006, §9). This analysis is specially relevant for heterogeneous materials with directional properties.

- **Transport of particles**. This category includes the transport of neutrons in nuclear reactors, radiative heat transfer in terms of transport of photons, sedimentation of particles in atmospheric dispersions and diffusion of matter and energy. In this case, the multiscale behavior is given by different local and global characteristics for heterogeneous systems. Then, the global coefficients (for example in the diffusion equation) present sharp local variations (Ganapathysubramanian and Zabaras, 2008).

- **Fluid mechanics**. Many problems in fluid mechanics involve different scales. For instance, the analysis of turbulence in terms of averages and perturbation in the variables (velocities) is another example of local and-global scales (Hughes et al., 2000). Collis (2001) later extended this analysis to a three-scale framework. This is also the case for flow through porous media, as in subsurface flow (Jenny et al., 2003). Bubbly flows have also been analyzed from a multiscale perspective in the last decade (Deen et al., 2004; Takada and Tomiyama, 2006; Zun, 2002).

3.2 Current models

The extensive list of applications described in Section 3.1 has led to the formulation of different models for multiscale problems. Although the term *multiscale models* is commonly used to refer to the numerical techniques, this is only one of three types. The other categories are homogenization approaches (volume averaging) and the heterogeneous multiscale method. These are explained in further detail in the following subsections. Their advantages and disadvantages are summarized in Table 3.1. An early review has been presented by Brandt (2001). However, the models have evolved significantly since then.

Method	Advantage(s)	Disadvantage(s)
Volume averaging	Gives coarse-scale description. Performs well for periodic structures	Only upscaling: smaller scales are not solved
Multiscale numerical techniques	All scales solved together. Compromise between accuracy and computational costs	Same physical model is assumed in all scales
Heterogeneous multiscale method	Allows different physical models in each scale and exploits scales separation	Precomputed solutions at high computational cost

Table 3.1: Comparison of different multiscale methods

3.2.1 Homogenization approach

This methodology is used for upscaling, that is moving from smaller scales to larger ones. The microscopic problem is solved first and the solution is volume–averaged to obtain coefficients that can be implement in the coarse–scale description (Allen, 2001), and no *downscale* interaction is considered.

Following this definition, this approach can only be applied in the strict sense to situations where the same physical model can be applied to both scales, considering the evolution of the same physical variables. Example of these situations are meteorology and CO_2 injection in subsurface flow, where the physical variables are velocities, mass concentrations, pressure and temperature in all scales. Nevertheless, it is also applied in practice to problems where this condition is not satisfied, for example in the computation of heat transfer coefficients (HTC), later discussed in Section 3.3.3. This is a parameter defined in the macroscopic description to account for lower–scale effects. In the case of laminar single–phase flow, it is obtained as the result of averaging, considering temperature and velocity profiles (Incropera and DeWitt, 1996). For more complex cases, such as turbulent or multiphase flow, this analytical procedure is not possible. However, the macroscopic analysis is still based upon this HTC, computed on the base of empirical correlations, thus masking the interaction between scales.

The homogenization procedure can be done using different techniques, and its selection usually depends on the characteristics of the particular problem (Engquist and Runborg, 2002). In the case of periodic micro–structures, or assuming a parametrized profile, averaged equations can be obtained analytically (Bourgat, 1979; Yue and E, 2005). If the problem presents rapid changes at the microscale, which are expected to have a random component, the high- and low-frequency terms can be separated using a wavelet projection (Brewster and Beylkin, 1995; Dorobantu and Engquist, 1998). For generic problems, numerical averaging is required, thus resulting in the techniques described in Section 3.2.2.

3.2.2 Multigrid/multiscale numerical methods

The numerical description of the physical effects occurring at small scale requires the use of fine grids. However, as mentioned earlier, the complete solution of the problem at a microscopic level is not practical. The use of different grids, that is a multigrid formulation, can solve this difficulty (Hackbusch, 1985).

The two preferred numerical methods for this formulation are Finite Volumes (Hajibeygi et al., 2008) and Finite Elements (Hou and Efendiev, 2009). Both of them are later described in more detail in Chapter 4. These approaches are usually called plainly *multiscale models*, since the finite elements method involves the use of different sets of basis functions, see Section 4.1.2, at local and global levels and not necessarily different discretization schemes (grids).

Ultimately, all scales are solved simultaneously and both micro and macroscopic

descriptions are obtained. The use of different and coupled numerical schemes results in a good compromise between accuracy and computational costs. Extensive research has been focused in the optimization of these procedures, for both finite volume (Lunati et al., 2011) and finite elements (Jiang et al., 2010) approaches.

Nevertheless, it should be noted that the same governing equations are solved in each grid. In other words, the same physical model is assumed to be valid in all scales. Then, although this formulation is more effective than homogenization techniques from a numerical perspective, its applicability is restricted to a smaller number of problems.

3.2.3 Heterogeneous multiscale method

This generic description presented by E and Engquist (2003) is destined to those situations where the two previous formulations are not applicable. As a starting point, it should be reminded that the description of interest is usually at a macroscale level. Then, this approach starts by setting a proper macroscopic scheme, and estimating the missing data from microscopic models.

The term heterogeneous refers to the possibility to incorporate different physical models for each scale. From this perspective, it is different to the previous multiscale approaches (Brandt, 2001) which, in opposition, are homogeneous.

In addition, this formulation allows a complete separation of scales. The microscale problem is then solved only once in a computationally intensive stage, giving high microscopic resolution. These results are then used to estimate the necessary parameters for the macroscale problem. The main disadvantage of this formulation is that usually the microscale problem is affected by the solution of the larger scale. Although this inconvenience can be solved in an iterative procedure, the simultaneous solution of both problems is not practical. For this reason, the lower–scale problem is usually solved *a priori* for selected values of the macroscopic variables. This approach is commonly known as the *offline–online* technique, and it allows a fast solution of the macroscopic problem on the base of precomputed solutions for the underlying lower scales. This feature is very important for iterative and non–linear problems, since the *online* stage is relatively fast.

Due to its generality, this approach is the only one applicable to the particular problem of two–phase flow in heat exchangers. Further details are presented in the following sections.

3.3 Hydrodynamics of gas–liquid flows

Multiphase flows, and in particular gas–liquid systems which are relevant for heat exchanger analysis, present rather complex structures. Since the phase boundaries are not static but constantly evolving, a straightforward continuum mechanics description in terms of field balance equations and constitutive relations is not ap-

plicable. Then, the investigation of local properties and the use of proper averaging become necessary (Ishii and Hibiki, 2006).

It will be shown in the following subsections that the modeling of gas–liquid flow presents some characteristics which make it indeed a multiscale problem.

3.3.1 Void fraction and slip ratio

A basic information required for the analysis of gas-liquid flows is the amount and distribution of each phase. In general, at given position $\mathbf{r}$ and at a time t there can be either gas or liquid. This could be expressed in mathematical terms using a phase identifier that takes binary values. However exact, this description lacks practical importance because the required accuracy exceeds the possibilities of current experimental measurement techniques.

For this reason, a volume–averaged void fraction (that is, a volume fraction of gas) α is defined as in Eq. (3.1).

$$\alpha(\mathbf{r},t) = \frac{\text{Volume of gas in a control volume around } (\mathbf{r},\text{t})}{\text{Total volume in a control volume around } (\mathbf{r},\text{t})} \tag{3.1}$$

As mentioned earlier, if the control volume considered in Eq. (3.1) is small enough, then α is either zero or one. For practical purposes, a larger control volume is considered. In the case of internal flow, this average can be performed throughout the cross-sectional area, resulting in a one-dimensional description. Then, the area–averaged void fraction for the axial coordinate z is given by Eq. (3.2).

$$\alpha(z,t) = \frac{\text{Cross–sectional area occupied by gas at (z,t)}}{\text{Total cross–sectional area gas at (z,t)}} = \frac{A_G}{A_L + A_G} \tag{3.2}$$

The use of Eq. (3.2) instead of (3.1) is a clear example of *upscaling*. The three–dimensional effects (microscale) are disregarded and only a one–dimensional (macroscopic) analysis is considered. Although this description is sufficient in most internal flow applications, this is not always the case. For examples, Gill et al. (1964) observed that for low $\alpha(z)$, the gas tends to collect in the wall, while for higher values, it concentrates in the center of the flow channel. Considering that both phases have different densities and consequently different moderating capabilities, this result is of interest for the design of water cooled nuclear reactors. In such cases where this microscopic description is required, it can be recovered using a *downscaling* technique. Since this information was lost during the *upscaling*, some assumptions are required for downscaling. For example, the flow structure is assumed on the basis of parametrized flow pattern maps, see Section 3.3.2.

Two phase flow models can be grouped into two categories: mixture–type and separated–fields formulations. The first type of models consider total field balance equations for both phases as if they were completely mixed, allowing for

different velocities. Although this condition is not generally satisfied, they give good approximate results in a wide range of applications. Separated–field models, in the second category, consider individual balance equations for each phase. Their general mathematical description is rather complex, and practical results can only be obtained if a given flow pattern is assumed as in Chapters 9 and 10.

In mixture models, homogeneous effective properties are defined as a weighted average of the gas and liquid values (Awad and Muzychka, 2008). For volume–based properties, such as density, they are averaged using the void fraction α as in Eq. (3.3), obtaining an homogeneous density ρ_h.

$$\rho_h = \alpha\rho_G + (1-\alpha)\rho_L \tag{3.3}$$

In addition to the void fraction, the relative amount of vapor is also described by the flow quality x, defined as in Eq. (3.4). This variable represents the mass vapor fraction, and its use is advantageous for the analysis of mass–intensive properties, such as energy and momentum.

$$x = \frac{\dot{m}_G}{\dot{m}_G + \dot{m}_L} \tag{3.4}$$

The relation between quality x and void fraction α is given by Eq. (3.5) (Ghiaasiaan, 2007, §3.4), where S_r is the slip ratio, that is the ratio of gas and liquid velocities.

$$\frac{x}{1-x} = \frac{\alpha}{1-\alpha}\frac{\rho_G}{\rho_L}S_r \qquad \text{with } S_r = \frac{u_G}{u_L} \tag{3.5}$$

The most simple mixture model, that is the homogeneous model, assumes that both phases travel at the same velocity, thus giving a slip ratio of 1. This description is only accurate for high–pressure flows, when liquid and gas phases present similar characteristics. In most practical cases, the larger differences in densities and viscosities make the phases slip (that is, travel at different velocities) for several reasons, including buoyancy, velocity–profile and acceleration effects (Tong and Tang, 1997, §3.3). All these effects make the lighter phase (usually gas) have a larger velocity, resulting in slip ratios larger than 1. Drift–flux models (Zuber and Staub, 1966) describe the flow in terms of an homogeneous mixture with two different velocities.

Although some theoretical models exist for simplified flow structures, the slip ratio is usually computed on the basis of empirical correlations, extensively reviewed by Woldesemayat and Ghajar (2007). Some selected models are presented in Table 3.2. In general, the proper selection of this correlation depends on the particular flow regime. However, the one proposed by Premoli et al. (1970) can be applied in a wide range of operating conditions.

The use of this slip ratio is another example of upscaling averaging, condensing the information from the lower scales. If it is correlated from experimental data, as it is usually the case, this upscaling is imposed, while the microscopic description

Model	Slip ratio S_r	Recommended use
Homogeneous	1	High pressure
Zivi(1964)	$\sqrt[3]{\rho_L/\rho_G}$	Annular flow
Premoli et al. (1970)	Function of quality, Reynolds and Weber numbers	Viscosity ratio $\mu_L/\mu_G < 1000$
Chisholm(1973)	$\sqrt{\rho_L/\rho_h}$	High mass flow

Table 3.2: Selected slip ratio models. For a complete list, refer to Woldesemayat and Ghajar (2007).

was never considered. This lack of consideration for lower-scale physical effects is the dominant reason why the empirical correlations fail when applied outside their validity range.

3.3.2 Flow patterns

The two–phase flow structure is, though complex, not necessarily chaotic. Different flow patterns, see schematic in Fig. 3.1, can be recognized by visual observations.

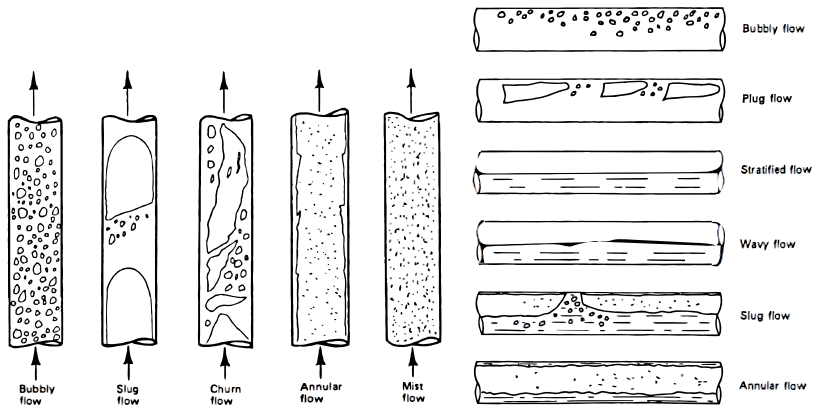

(a) Vertical flow (b) Horizontal flow

Figure 3.1: Flow patterns in gas–liquid flows. Source: Tong and Tang (1997).

These are, in increasing order of gas mass flow rates:

- **Dispersed bubbles**. For relatively low gas content (typically $x < 0.3$) the lighter phase tends to group in isolated bubbles, which are dispersed in the continuum liquid. The bubbles size and their distribution depend on several factors. For example in the case of boiling flows, the bubbles are originated near the wall and a boundary layer is formed. In the case of adiabatic air–water flow, velocity–profile effects make the bubbles concentrate in the center

of the channel. In general, bubbly flows can be well represented, under some conditions, by an homogeneous mixture model.

- **Slug/plug**. When the gas content is increased and bubbles grow large enough to cover the channel cross section, the flow becomes a sequence of gas plugs and liquid slugs. This flow pattern occurs at moderate void fractions and relatively low flow velocity. It is important for the analysis of long pipelines since the inertial effects of liquids slugs may affect some receiving equipment. Further increasing the gas velocity results in instabilities leading to an intermittent churn flow.

- **Stratified and wavy**. In horizontal arrangements, gravitational effects can make the liquid collect at the bottom while the gas flows at the top. This condition is found for low velocities over a wide range of void fraction. An increase in the velocity initially produces waves in the interface, and eventually the disruption of this flow pattern.

- **Annular flow**. At high void fractions and flow velocities, a continuous thin and relatively slow liquid film is found along the wall, and a gas core covers most of the cross section. Dispersed droplets can be found in the gas core, as well as bubbles in the liquid film. This flow pattern is particularly relevant for heat exchanger applications, since it is found over a wide range of practical operating conditions (Wattelet, 1994). In stable subcooled film boiling an, *inverse annular flow* is found, with a thin gas film in the wall surrounded by a liquid core. This regime, nevertheless, is usually not found in heat exchanger applications.

- **Mist flow**. Additional increase in the gas flow results in the disruption of the liquid film. The liquid phase is then found in the form of droplets dispersed in the continuous gas flow.

The identification of the flow pattern becomes then a key element for bridging the different scales. If the flow is known to be characterized by one of these regimes, the microscopic structure can be recovered from macroscopic variables such as void fraction and total mass flow, depending on physical parameters such as bubbles or droplets size, film thickness or slug length.

Flow pattern maps provide then a very useful tool for the analysis of gas–liquid flows. However, they should be used with caution for several reasons (Bell, 1988). First, the transitions between regimes that are usually represented as solid lines should be interpreted as occurring over a broad range of the flow variables. Second, most maps are expressed in terms of dimensional variables and therefore are only applicable for a given fluid, geometry and operating conditions. There are some non–dimensional maps based on theoretical transition criteria. The two most widely used are those of Scott(1963) and Taitel-Dukler (1976), for both see

Tong and Tang (1997, §3.2). Nevertheless, they are mostly based on adiabatic air–water or steam–water experimental data. Therefore their applicability for fluids very different from water, such as hydrocarbons, should be questioned.

Finally, flow patterns and their transition mechanisms in boiling and condensation applications may differ substantially from adiabatic cases. In the case of condensing flow, the liquid is generated near to the cold wall and therefore the annular flow regime is dominant. In boiling flows, the heat input produces vapor generation in the wall and, for example, reduces the extent of annular flow (Kattan et al., 1998).

3.3.3 Heat transfer models

In both condensing and boiling processes, both heat and mass transfer phenomena between the different phases and the channel wall are involved. In general, they can be represented by Figs. 3.2(a) and 3.2(b), respectively. Although the change of phase can also occur in stagnant liquids or gases, this situations are not relevant for heat exchanger applications. The following subsections are then focused on forced convection two-phase heat and mass transfer.

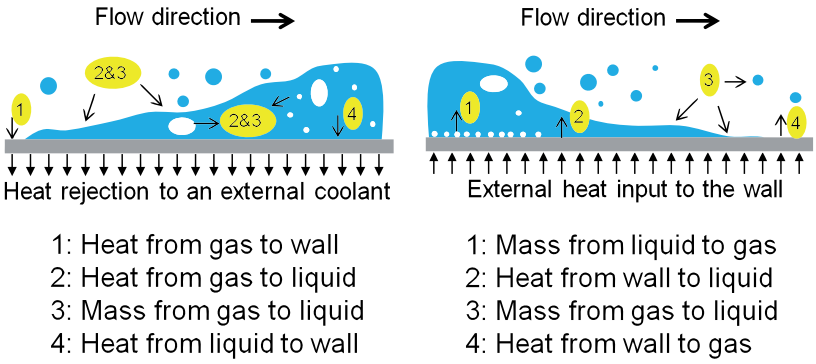

(a) Condensing flow (b) Boiling flow

Figure 3.2: Generic heat and mass transfer mechanisms in two–phase flow

Forced convective condensation

Cooling a gas flow below its saturation temperature results in the formation of liquid at the cold wall, either in form of individual droplets or a continuous film. In forced convection systems, the first type is rare and film condensation is the main physical mechanisms. Therefore, the annular flow regime and stratified in

horizontal arrangement are dominant, with some trapped bubbles at low void fractions.

The Nusselt film theory, dating from 1916, provides an analytical solution for a laminar film flow and stationary vapor (Whalley, 1987). This model was extended by later authors incorporating effects of liquid subcooling, changes in fluid properties and interfacial drag (Collier and Thome, 1994, §10.4.2). For design purposes, the effects of turbulence should not be neglected, and completely empirical methods are generally used, typically modifications of the Dittus-Bolter single-phase forced convection correlation. Different correlations are compared in Fig. 3.3. All the correlations follow the same trend, indicating that the heat transfer coefficient is larger at high void fractions, due to the high velocities. They present nonetheless large differences between each other, which exceed in some cases 100% of the predicted HTC. Collier and Thome (1994) recommended the use of the model given by Akers et al. (1959) for low flow rates, and the one by Shah (1979) for high flow rates.

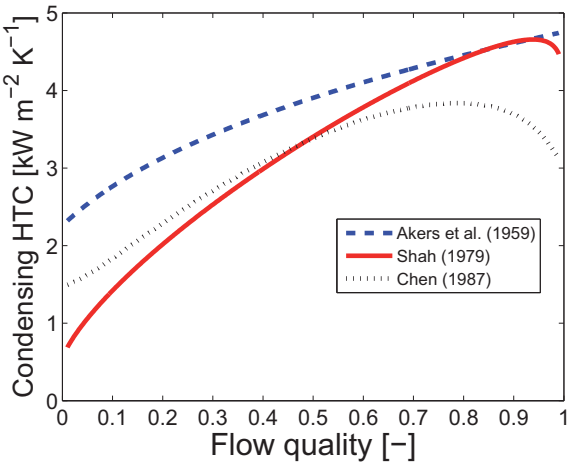

Figure 3.3: Forced convection condensation heat transfer models. Study case: refrigerant R134a at 3 bar. Mass flux: 200 kg m^{-2} s^{-1} inside a 5mm round tube.

While the previous models apply for pure vapors, the heat transfer performance is largely reduced in the case of gas mixtures. The existence of gases that do not condense at the given temperature (such as air in steam–water flow), even in a low concentration, affects the mass diffusion from gas to liquid phase and the heat transfer process becomes gas-side limited. The presence of only 1% mass of a noncondensable gas in the bulk vapor can result in reduction over 50% of the condensation rates.

Forced convective boiling

Two mechanisms contribute to boiling heat transfer: nucleation of bubbles and convection of liquid and gas phases in the wall. The nucleation of bubbles implies the creation of a gas–liquid interface. Due to surface tension effects, a certain extent of overheating in the liquid is required, determined by the surface conditions and fluid properties. This means that stable bubbles can only be formed and grow if the liquid is locally heated slightly above its saturation temperature. As a consequence of this microscopic condition, different boiling regimes can occur depending on the heat input. In increasing order of heat flux these are:

- **Single–phase convection**. If the heat flux is low and the heat length is not large enough, the required overheating may not be achieved. In that case, although the fluid may reach its saturation temperature, bubbles cannot be nucleated and the flow remains single–phase liquid.

- **Saturated flow boiling**. Increasing the heat flux, bubbles start forming in a boundary layer near the wall, while the bulk liquid flows at saturation temperature, hence its name. Bubbles grow and detach from the wall, that is rewetted with liquid. This process results in relatively large heat transfer rates. This is an extensive regime, covering all the different flow patterns presented in Section 3.3.2 until the occurrence of a boiling crisis, which may result in film boiling or dispersed droplets regimes.

- **Subcooled flow boiling**. For high–enough heat fluxes, the nucleation of bubbles can begin before reaching saturation conditions. In other words, the boundary layer is overheated, while the bulk liquid is subcooled. This regime covers a short length until the total mass flow rate reaches saturated conditions and only exist in the bubbly flow pattern. Overall, the heat transfer performance is increased by this effect, and therefore neglecting its existence is a conservative assumption for design.

- **Film boiling**. Further increase in the heat input results in a larger generation of bubbles in the subcooled regime. At some point, this generation rate might become large enough to prevent the rewetting of the wall, which is then covered by a thin film of gas. This regime is characterized by an inverted annular flow pattern. The study of film boiling regime is important for the safety analysis of heat–flux–controlled systems such as nuclear reactors, since the poor heat transfer characteristics of the gas film might results in extremely high temperatures in the wall. However, it is very rare in temperature–controlled systems, only to be found transiently during the quenching of steels.

Most empirical boiling heat transfer models refer only to the saturated boiling regime. However, the analysis of subcooled boiling is relevant for the evolution

of void fraction, which then takes positive values before reaching bulk saturated conditions, up to roughly 10% for low–pressure water systems (Ghiaasiaan, 2007, 12.8). In particular, the three–regions model given by Kandlikar (1997) is considered in this work for the subcooled boiling region.

Saturated flow boiling models must account for both forced convection and bubble nucleation. In principle, each of these mechanisms can be modeled individually from pool boiling and single–phase convection analysis, respectively. However, it is not yet clear how these processes interact. Different approaches have been proposed over the last half century. Figure 3.3 presents a comparison of six different correlations. Large differences can be found among them, giving an uncertainty in the order of 100%. In addition, not all of them yield the same conceptual results. Some of them, predict a maximum HTC during the phase-change region, which physically corresponds to the dryout mechanism (later described in Chapter 9), while others do not account for this phenomena.

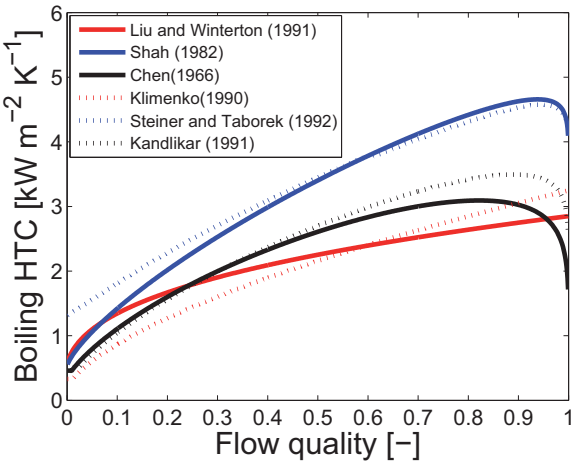

Figure 3.4: Forced convection boiling transfer models. Study case: refrigerant R134a at 3 bar. Mass flux: 200 kg m^{-2} s^{-1} inside a 5mm round tube.

The flow boiling heat transfer coefficient (HTC) $\hat{h}_{fb}$ is computed in all cases on the basis of a pool boiling HTC ($\hat{h}_{pb}$) and a forced convection HTC ($\hat{h}_{fc}$), along with corresponding correction factors F_{pb} and F_{fc}. In general, all the proposed models can be represented by a power–law combination of these two HTC, as in Eq. (3.6).

$$\hat{h}_{fb} = \left[\left(\hat{h}_{pb}\ F_{pb} \right)^n + \left(\hat{h}_{fc}\ F_{fc} \right)^n \right]^{1/n} \tag{3.6}$$

The power n then indicates the transition between both mechanisms. A value of $n = 1$ indicates a direct summation of both heat transfer coefficients. This approach was first proposed by Chen (1966), who suggested that the bubble nucleation is reduced (then $F_{pc} < 1$ is a suppression factor) and forced convection is improved (then $F_{fc} > 1$ is an enhancement factor) by their interaction. Further improvements to his original correlation were proposed by Gungor and Winterton (1986), who one year later presented a simplified version.

Higher values of n result in a smooth transition between a nucleate–boiling dominated to a forced–convection controlled regime. For example, Kutateladze (1961) and later Liu and Winterton (1991) suggested $n = 2$, while Steiner and Taborek (1992) presented an asymptotic model with $n = 3$. This approach becomes reasonable when analyzing the different flow patterns. On the one hand, in bubbly flow, typical of low void fractions, the contribution of convection is rather small and mainly the generation of bubbles determines the heat transfer rates. On the other hand, in annular flow, found at high void fractions, the situation is opposite and thermal conduction through the thin liquid film is the main mechanism for heat transfer.

The extreme case of $n = \infty$ results in the selection of the highest of both HTC. Although this formulation does not accurately represents the transition between both regimes, acceptable predictions of experimental data were obtained. Examples of this type of correlations are the models given by Shah (1982), Klimenko (1990) and Kandlikar (1990).

Recent research over the last decade has been focused on developing heat transfer models for a particular flow pattern. In this context, Sun et al. (2004) studied horizontal slug/plug flow and proposed the evaluation of the HTC as a time average of those corresponding to the liquid slugs and the gas plugs, each of them computed using a Chen–type correlation. In this same framework, Thome and coworkers presented an asymptotic analysis ($n = 3$) for annular and stratified flows of refrigerants in microchannels. Although these models present a rather high accuracy, this analysis does not consider the uncertainties of the flow pattern maps upon which they are based.

All the models listed in Table 3.3 rely on the fitting of experimental data. This procedure consists on proposing a functional dependence on the physical properties and obtaining values for some parameters that give the best possible representation of the measurements. Then, these correlations should be used with caution, since if many parameters are involved, the functional dependence may not represent the actual physical phenomena, as illustrated in Fig. 3.3: some models predict a maximum HTC at high void fractions, while others do not.

Correlation	Type	Developed for
Kutateladze (1961)	$n = 2$	Water in vertical flow
Chen (1966)	$n = 1$	Water and organic fluids in vertical flow
Shah (1982)	$n = \infty$	Water and refrigerants, vertical and horizontal flow
Gungor and Winterton (1986; 1987)	$n = 1$	Water, refrigerants and ethylene-glycol in vertical flow
Klimenko (1990)	$n = \infty$	Water, freons, organic and cryogenic fluids
Kandlikar (1990)	$n = \infty$	Water, refrigerants and cryogenic fluids
Liu and Winterton (1991)	$n = 2$	Water, refrigerants and hydrocarbons
Steiner and Taborek (1992)	$n = 3$	Vertical flow of water, refrigerants, hydrocarbons, cryogenic fluids and ammonia
Sun et al. (2004)	$n = 1$	Refrigerant in horizontal slug-plug flow
Thome (2005)	$n = 3$	Horizontal annular and stratified-wavy flow of refrigerants in microchannels

Table 3.3: Comparison of different flow boiling correlations. The correlation type refers to the value of n in Eq. (3.6).

3.4 Multiscale modeling of heat exchangers

Although a strict definition of the term *scale* was not provided (for a mathematical definition, refer to Yang and Marquardt (2009)), it has become somehow clear throughout this chapter that the underlying physical phenomena in a heat exchanger occur over different scales. The most relevant physical effects are summarized in Table 3.4 and Fig. 3.5.

The analysis of a heat exchanger at system–level considers the HE as a *black box* connected to other equipment such as a compressors or a valve, forming part of a larger process. At this level, the internal behavior is disregarded and the relevant variables are simply changes in pressure (Δp) and enthalpy (Δh) for each stream. Some examples of this type of analysis are the lumped–parameters models described in Section 2.4.1. This level of description also includes the analysis of flow instabilities. This phenomena, reviewed by Kakaç and Bon (2008), occurs both in single-channel and multiple-channel systems and leads to temporal oscillations in the mass flow rate and the pressure drop.

A more detailed description that includes the physical effects occurring within

the HE must account for its actual geometry. For industrial applications, the large required surface area results in the use of many parallel channels, see Section 2.2.2. This situations leads to flow across tube banks and some extent of flow mixing in shell–type geometries, as well as a non–homogeneous distribution of temperatures and velocities. The study of these effects implies a multi–channel formulation.

Single–channel analysis remains a fundamental step towards understanding the overall HE behavior and performance. In a one–dimensional continuum description of each stream, axial profiles are obtained for pressure, temperature, void fractions, densities and other flow variables. This formulation relies on variables such as the HTC, that condenses the effects occurring at lower scales. Present heat transfer models, described in Section 3.3.3, are based on empirical correlations and do not allow a reconstruction of the microscopic structures.

Identifying the different flow patterns, in principle, is not relevant from a process– or equipment–oriented perspective. It is, however, relevant for understanding the different microscopic physical effects that interact and affect the overall performance. Nucleation of bubbles, flow stratification, film convection and behavior of droplets are the basic mechanisms that contribute to the macroscopic flow behavior, and their evolution depends on structure of the flow.

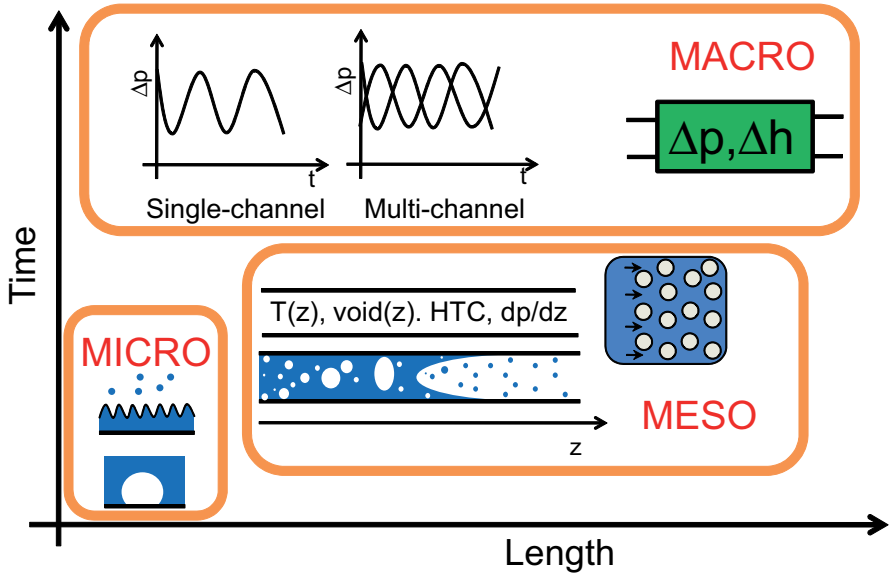

Figure 3.5: Physical effects in a two-phase flow heat exchanger occur in different time and length scales.

Phenomena	Characteristic length	Scale
Film convection	Film thickness	10^{-6}–10^{-3} m
Slug/plug flow	Slug length	10^{-3}–10^{0} m
Dispersed droplets and bubbles	Particle diameter	10^{-7}–10^{-5} m
Identifying flow pattern	Tube diameter	10^{-4}–10^{-2} m
Continuum description	Axial position	10^{-3}–10^{1} m
Single–channel instabilities	Tube length	10^{0}–10^{1} m
Parallel–channel instabilities	Tube length	10^{0}–10^{1} m
Flow across bank of tubes	HE diameter	$\approx 10^{0}$ m
Flow maldistribution in parallel channels	HE diameter	$\approx 10^{0}$ m

Table 3.4: Characteristic length and scale for different phenomena

3.5 Summary

Over the last decade, multiscale modeling has gained extensive recognition in the scientific community as an efficient approach to tackle complex problems. The list of applications is continuously evolving, ranging from biology and medicine to fluid mechanics.

The complex hydrodynamics of boiling and condensing flows, and design considerations from different perspectives, make the analysis of two–phase flow heat exchangers indeed a multiscale problem. The relevant physical phenomena take place over different scales from the behavior of bubbles and droplets with sizes in the order of some micrometers to flow insatiabilities occurring over the entire length of several meters.

Most current multiscale models deal with problems governed by one unique physical law with two or more clearly separated scales. This is hardly the case in two–phase HE. Different physical models apply for each scale, thus resulting in a heterogeneous multiscale approach. Then, all scales are studied individually and they are connected by *bridging* parameters such as the heat transfer coefficient.

In this work, three different scales are considered: macro, meso, and micro. Parts II to IV present modeling and simulation results in each of them. These three scales are highlighted in Fig. 3.5. Finally, some comments on their coupling are presented in Chapter 12.

Chapter 4

Numerical methods

► The main objective of this chapter is to evaluate different numerical methods and compare their performance for the analysis of heat exchangers. As the physical models for two-phase flow are intrinsically complex, they usually lead to the numerical solution of partial differential equations. Therefore, this study is a necessary preliminary step in order to improve practical aspects of later simulations.

In particular, the traditional approach for this problem is based on first-order finite difference methods (FDM), and advanced techniques reported in literature include first-order and spectral Galerkin finite element formulations and orthogonal collocation concepts. In this context, the Least Squares Spectral Element Method (LSSEM) is an interesting alternative, engaging some theoretical comparative advantages such as providing an error estimator in all cases, and a high-order exponential convergence for smooth problems. The mathematical description of all these method is presented in this chapter in a generic weighted residuals formulation and two examples are analyzed. In general, FDM are the most convenient for explicit problems, and LSSEM for more complex and implicit scenarios. For this reason, LSSEM is selected for the simulations in Chapters 5 to 8, and FDM for Chapters 9 and 10.

The evolution of heat exchanger modeling has led to the numerical solution of partial differential equations. Then, a comparative analysis of different methods and their application to the particular problem of heat exchangers becomes necessary as a preliminary study.

The traditional approach to this problem is based on first-order finite–differences or finite–volumes formulations. These methods consist on a discretization of the domain in nodes or control volumes. They are simple to implement and are widely used for lots of applications. However, they usually require a large number of discretization points, due to their convergence rates and stability requirements. This situation is particularly demanding for phase–change problems, which present some

extent of discontinuities.

For these reasons, different numerical approaches have been proposed in recent years for the solution of heat exchanger problems. In particular, three formulations stand out as the most relevant:

First–order Galerkin-type finite elements. This method has obtained increasing recognition in the last decades, and their applications include the analysis of heat exchanger for single–phase flow (Mikhailov and Özişik, 1981; Ravikumaur et al., 1988), as well as evaporators and condensers (Harshbarger and Bullard, 2000; Quadir et al., 2002). Within this formulation, other effects such as longitudinal heat conduction (Ranganayakulu and Seetharamu, 1999; Ranganayakulu et al., 1997) and heat exchange with the surroundings (Seetharamu et al., 2004) were incorporated.

Spectral elements methods. This approach consists on representing the solution as a combination of high–order polynomials. In this framework, Amon and Mikic (1991) solved two–dimensional Navier–Stokes equations in a periodic exchanger, and Jen et al. (2002) evaluated the performance of a heat pipe evaporator and condenser for drilling applications, using a one–dimensional model.

Orthogonal collocation. These schemes are particular formulations of the spectral methods where the governing equations are evaluated in selected points (Villadsen and Stewart, 1967). These techniques were used for the transient analysis of evaporators in high-temperature (Stefanov and Hoo, 2003; 2004) and cryogenic systems (Rodríguez and Díaz, 2007). In his steady–state thermal analysis of evaporators, Thyageswaran (2008; 2009) concluded that this approach presents some improvements regarding computational costs compared to Runge–Kutta and finite–difference methods.

In addition to the three methods mentioned above, the Least Squares Spectral Elements Method (LSSEM) is presented in this chapter as an interesting alternative. A comprehensive review on its current applications is given by Kayser-Herold and Matthies (2005), including computational fluid dynamics (Jiang and Povinelli, 1990; Proot and Gerrtisma, 2002), electromagnetics (Jiang, 1998; Maggio et al., 2004), and neutron transport (Manteuffel and Ressel, 1998). Since the publication of this review, the list of applications has extended and covers radiative heat transfer (Zhao and Liu, 2007), population balance (Dorao and Jakobsen, 2008) and reactor modeling (Dorao et al., 2009).

The application of LSSEM can provide some comparative advantages for the solution of heat exchanger problems. This method always provides an estimation of error, at both local and global levels with no further calculations (Eason, 1976). In addition, the convergence rate is typical of high–order methods and, for smooth solutions, it is exponential (Maerschalck and Gerritsma, 2008).

This chapter presents a mathematical description of all these methods in terms of a general weighted residual formulation, see Section 4.1. In addition, their performance is compared for the solution of single (Section 4.2) and two-phase (Section 4.3) flow heat exchangers. Finally, a summary of this chapter, including the conclusions of this analysis, is detailed in Section 4.4.

4.1 Weighted residual formulation (WRF)

Although the numerical methods considered in this work (finite difference, finite volumes, Galerkin and LSSEM) present some important differences between each other, they all can be considered to be particular cases of a general weighted residuals formulation. A thorough mathematical description

Let Eq. (4.1) represent a generic ordinary different equation problem.

$$\mathcal{L}\mathfrak{u}(\mathbf{r}) = \mathfrak{f}(\mathbf{r}) \qquad \text{for} \quad \mathbf{r} \in \Omega \tag{4.1}$$

where $\mathcal{L} : \mathcal{V} \rightarrow \mathcal{V}'$ is the problem operator[1], $\mathfrak{u}$ the unknown solution vector and $\mathfrak{f}$ a known source term in the computational domain Ω. The residual $\mathcal{R}$ of the problem in Eq. (4.1) is defined as:

$$\mathcal{R}(\mathfrak{u}) = \mathcal{L}\mathfrak{u} - \mathfrak{f} \tag{4.2}$$

With this definition, the residual $\mathcal{R}$ represents the accuracy of the solution. For example, if the exact analytical solution $\mathfrak{u}^A$ is obtained then $\mathcal{R}(\mathbf{u^A}) = \mathbf{0}$. In general, for other numerical solutions $\mathfrak{u}^N$, the residual is not zero, that is $\mathcal{R}(\mathbf{u^N}) \neq \mathbf{0}$.

The weighted residual formulation is based on canceling this residual only with respect to certain test functions Φ_j, as expressed in Eq. (4.3), where $\langle , \rangle_{\mathcal{V}(\Omega)}$ is the canonic inner product in the space function $\mathcal{V}(\Omega)$.

$$\langle \mathcal{R}, \Phi_j \rangle_{\mathcal{V}(\Omega)} = \int_\Omega \mathcal{R}\Phi_j d\Omega = 0 \longrightarrow \langle \mathcal{L}\mathfrak{u}, \Phi_j \rangle_{\mathcal{V}(\Omega)} = \langle \mathfrak{f}, \Phi_j \rangle_{\mathcal{V}(\Omega)} \tag{4.3}$$

In this framework different numerical methods can be considered as particular cases of the weighted residual formulation. The differences between them are the given by the selection of test functions Φ_j as listed in Table 4.1.

The two first methods listed in Table 4.1 represent a point-discretization approach, while the last three are based on a spectral approximation. Both types of methods are explained in the following subsections.

[1]The notation $\mathcal{L}$ stands for linear operator. Further in the text, the mathematical formulation continuous with the assumption of linearity.

Method	Type	Test function
Finite differences	Point discretization	$\Phi_j(\mathbf{r}) = \delta(\mathbf{r} - \mathbf{r}_j)$
Finite volumes	Point discretization	$\Phi_j(\mathbf{r}) = 1$ if $\mathbf{r} \in \Omega_j$, $\Phi_j(\mathbf{r}) = 0$ otherwise
Orthogonal collocation	Spectral approximation	$\Phi_j(\mathbf{r}) = \delta(\mathbf{r} - \mathbf{r}_j)$
Galerkin	Spectral approximation	$\Phi_j(\mathbf{r}) = \varphi_j$
Least-Squares	Spectral approximation	$\Phi_j(\mathbf{r}) = \mathcal{L}\varphi_j$

Table 4.1: Test functions used by different weighted residual methods. $\{\varphi_j\}$ is a complete set of basis functions, and δ represents the Dirac delta function.

4.1.1 Point discretization methods

These methods are usually presented in the open literature in a different and more straightforward way. However, with the use of local test functions Φ_j, they represent special cases of the WRF. They are based on the discretization of the domain, and the local evaluation of the problem operators. Furthermore, the partial derivatives are approximated with discrete values. For the solution of ordinary differential equations in Cartesian coordinates, both finite–differences and finite–volumes methods result in the same system of algebraic equations.

Finite differences method (FDM)

This formulation is maybe the most intuitive from a mathematical perspective. A set of N selected points $\mathbf{r}_j$ are established in a square grid in the domain Ω. With the use of delta functions as test functions $\varphi_j = \delta(\mathbf{r} - \mathbf{r}_j)$, the governing system of equations is only applied to those points, that is for $j = 1, \ldots, N$:

$$\text{Eq. (4.3) and } \varphi_j = \delta(\mathbf{r} - \mathbf{r}_j) \longrightarrow \mathcal{L}\mathfrak{u}(\mathbf{r}_j) = \mathfrak{f}(\mathbf{r}_j) \tag{4.4}$$

Finite Volumes Method (FVM)

This approach represents the numerical implementation of the physically–based control volumes techniques. Most balance equations, such as mass, momentum and energy conservation in fluid mechanics, consider fluxes going into and out of an elementary control volume. In the FVM, the governing equation is locally integrated in a set of N finite volumes Ω_j. Then, for $j = 1, \ldots, N$:

$$\text{Eq. (4.3) and } \varphi_j = \begin{cases} 1 & \text{if } \mathbf{r} \in \Omega_j \\ 0 & \text{otherwise} \end{cases} \longrightarrow \int_{\Omega_j} \mathcal{L}\mathfrak{u}(\mathbf{r}) d\Omega_j = \int_{\Omega_j} \mathfrak{f}(\mathbf{r}) d\Omega_j \tag{4.5}$$

4.1.2 Spectral methods

While point-discretization methods consider a local formulation of the problem, the spectral approach gives a global representation. The solution is represented as a linear combination of some basis functions $\{\varphi_j\}$.

In general, the unknown solution $\mathfrak{u}$ is an arbitrary function in the vector space $\mathcal{V}$. If no additional considerations are included $\mathcal{V}$ has an infinite dimension. This means that an infinite number of basis functions φ_j are necessary to obtain an *exact* representation of $\mathfrak{u}$, as expressed in Eq. (4.6). Then, for practical reasons an approximate space $\mathcal{V}^N$ is defined (the superscript N stands for numerical) and the numerical solution $\mathfrak{u}^N$ is given by Eq. (4.7). In this framework, the approximate solution is completely defined by a set of $P+1$ unknown coefficients $\{\mathbf{a}_j\}_{j=0}^{P}$ and selected basis $\{\varphi_j\}_{j=0}^{P}$. In this case, P represents the approximation order.

$$\mathfrak{u}(\mathbf{r}) = \sum_{j=0}^{\infty} \mathbf{a}_j \varphi_j(\mathbf{r}), \qquad \mathfrak{u} \in \mathcal{V} = span\,\{\varphi_j\}_{j=0}^{\infty} \tag{4.6}$$

$$\mathfrak{u}(\mathbf{r}) \approx \mathfrak{u}^N(\mathbf{r}) = \sum_{j=0}^{P} \mathbf{a}_j \varphi_j(\mathbf{r}), \qquad \mathfrak{u}^N \in \mathcal{V}^N = span\,\{\varphi_j\}_{j=0}^{P} \tag{4.7}$$

The generic WRF equation (4.3) is then applied to $\mathfrak{u}^N$, resulting in Eq. (4.8).

$$\int_\Omega \mathcal{L}\mathfrak{u}^N(\mathbf{r})\Phi_j(\mathbf{r})d\Omega = \int_\Omega \mathfrak{f}(\mathbf{r})\Phi_j(\mathbf{r})d\Omega \qquad \forall j = 1,\ldots,N \tag{4.8}$$

If the problem operator $\mathcal{L}$ is linear[2], the system of algebraic equations for the coefficients $\{\mathbf{a}\}_{k=0}^{P}$ depicted in Eq. (4.9) is obtained. The solution of Eq. (4.9) then allows to recover the numerical solution $\mathfrak{u}^N$ by means of Eq. (4.7).

$$\sum_{k=0}^{P} \mathbf{a}_k \underbrace{\int_\Omega \mathcal{L}\varphi_k(\mathbf{r})\Phi_j(\mathbf{r})d\Omega}_{\mathbf{A}_{j,k}} = \underbrace{\int_\Omega \mathfrak{f}(\mathbf{r})\Phi_j(\mathbf{r})d\Omega}_{\mathbf{v}_j} \longrightarrow \mathbf{A}\mathbf{a} = \mathbf{v} \tag{4.9}$$

This spectral representation allows an accurate description of smooth functions. For sufficiently smooth functions $\mathfrak{u}(\mathbf{r})$, the convergence rate with polynomial enrichment is exponential (Canuto et al., 2006). In the case of problems with some extent of discontinuity, as might be the case in phase–change flows, it is convenient to represent the spectral approximation in an elemental approach. This consists on dividing the domain Ω into N non–overlapping elements $\{\Omega_j\}_{j=1}^{N}$ as expressed in Eq. (4.10).

[2]Although in the general case $\mathcal{L}$ is not necessarily linear, this condition can be approximated in an iterative procedure.

$$\Omega = \bigcup_{j=1}^{N} \Omega_j, \qquad \Omega_i \cap \Omega_j = \emptyset \quad \forall i \neq j \tag{4.10}$$

Then, a local solution $\mathbf{u}_j^N(\mathbf{r})$ is defined in each element Ω_j as a combination of local basis $\{\varphi_{j,k}(\mathbf{r})\}_{k=0}^{P_k}$, as in Eq. (4.11). The global solution is obtained by gluing together the local elements.

$$\mathbf{u}_j^N(\mathbf{r}) = \sum_{k=0}^{P_k} \mathbf{a}_{j,k}\varphi_{j,k}(\mathbf{r}) \text{ in } \Omega_j \longrightarrow \mathbf{u}^N(\mathbf{r}) = \bigcup_{j=1}^{N} \mathbf{u}_j^N(\mathbf{r}) \tag{4.11}$$

Selection of approximation space and basis functions

In general, there is no restriction in the selection of the approximation space $\mathcal{V}^N$. In addition, an infinite number of sets of basis functions $\{\varphi_j\}_{j=0}^{P}$ can be defined for a given $\mathcal{V}^N$. The performance of a given set is determined by the number of basis functions (this means, the approximation order) required in order to obtain an acceptable approximation. In this context the optimum selection depends on the particular problem to be solved. However, there are some types of basis function sets that perform well for most problems, as will be shown next. As a broad classification, the selection of basis can be divided into two categories: modal and nodal.

Modal basis The term modal is derived from the fact that each basis function represents one type of solution. Then, for example, in a cosine expansion each function represents a given frequency, similar to a Fourier analysis. In general, hierarchical expansion sets can be defined from a mathematical point of view as in Eq. (4.12). This means that an expansion set of order $P-1$ is contained in the set of order P. In other words, high order expansions are built from low-order sets (Karniadakis and Sherwin, 2005).

$$\{\varphi_j(\mathbf{r})\}_{j=0}^{P} = \{\varphi_j(\mathbf{r})\}_{j=0}^{P-1} \bigcup \varphi_P(\mathbf{r}) \tag{4.12}$$

Examples of modal basis in a one–dimensional domain $z \in [-1, 1]$ including (4.13a) polynomials, (4.13b) cosine and (4.13c) hyperbolic trigonometric functions. This approach is very practical for self–adjoint problems. In that case, the basis functions $\{\varphi_j(\mathbf{r})\}_{j=0}^{P}$ represent the eigenfunctions and the coefficients $\{\mathbf{a}_j\}_{j=0}^{P}$ are the eigenvalues of the problem operator $\mathcal{L}$.

$$\{\varphi_j(z)\}_{j=0}^{P} = \left\{1, z, z^2, \ldots, z^P\right\} \tag{4.13a}$$

$$\{\varphi_j(z)\}_{j=0}^{P} = \{1, \cos(\pi z), \cos(2\pi z), \ldots, \cos(P\pi z)\} \tag{4.13b}$$

$$\{\varphi_j(z)\}_{j=0}^{P} = \{1, \sinh(\pi z), \cosh(\pi z), \ldots, \sinh(P\pi z), \cosh(P\pi z)\} \tag{4.13c}$$

Nodal basis This type of functions represent the continuous extension of a discrete approach. Some selected points $\{\mathbf{r}_i\}_{i=0}^{P}$ called nodes are defined in the domain Ω, and nodal basis are defined so that they take zero-values in all of these points but one, as in Eq. (4.14).

$$\varphi_i(\mathbf{r}_i) = \begin{cases} 1 & \text{if } i \neq j \\ 0 & \text{if } i = j \end{cases} \qquad \forall i, j = 1, \ldots, P \tag{4.14}$$

This discrete approach is extended into a continuous formulation by the use of Lagrange interpolant polynomials. In a one–dimensional domain, this is represented by Eq. (4.15), for which $\varphi_j(z_j) = 1$.

$$\varphi_j(z) = \frac{\prod_{i=0, i\neq j}^{P}(z - z_i)}{\prod_{i=0, i\neq j}^{P}(z_j - z_i)} \tag{4.15}$$

Once again, the selected nodes $\{\mathbf{r}_i\}_{i=0}^{P}$ can be arbitrary. However, a proper selection of these nodes provides additional advantages. The use of quadrature sets allows the approximation of integrals by means of arithmetic operations and the local evaluation of the functions of interest. This feature is relevant for the numerical calculation of the integrals in Eq. (4.9).

In general, the integration of a generic function $f(\mathbf{r})$ with a weight function $W(\mathbf{r})$ can be approximated as in Eq. (4.16). In this context, the nodes $\{\mathbf{r}_i\}_{i=0}^{P}$ are called quadrature points, and the coefficients $\{w_i\}_{i=0}^{P}$ are quadrature weights.

$$\int_{\Omega} W(\mathbf{r}) f(\mathbf{r}) d\Omega \approx \sum_{j=0}^{P} w_i f(\mathbf{r}_i) \tag{4.16}$$

In particular, the Gauss-Lobatto-Legendre quadrature (Parter, 1999) is considered in this work. This formulation considers a unity weight function, that is $W(\mathbf{r}) = 1$, which allows a straightforward integration of the function of interest. In addition, the quadrature points include the borders of the domain Ω. In this context, the boundary conditions can be directly incorporated into the problem operator. Other quadrature sets might be convenient for integrating function with local singularities, although this case is not considered in the present work.

This framework (nodal basis and quadrature sets) gives a general formulation that can be applied to an arbitrary problem operator $\mathcal{L}$. For this reason, they are widely used for different problems. In this general spectral approach, three methods are presented: Orthogonal Collocation, Galerkin and Least Squares, which use different test functions Φ_j as listed in Table 4.1.

Orthogonal collocation

This method represents a mixed approach. On the one hand, it includes some elements of a spectral approximation, that is Eq. (4.8). On the other hand, it

presents some characteristics of point discretization schemes, using the same local test functions as in FDM: $\Phi_j(\mathbf{r}) = \delta(\mathbf{r}-\mathbf{r}_j)$. Introducing this expression in Eq. (4.9) gives the following system of algebraic equations.

$$\sum_{k=0}^{P} \mathbf{a}_k \underbrace{\mathcal{L}\varphi_k(\mathbf{r}_j)}_{\mathbf{A}_{j,k}} = \underbrace{\mathfrak{f}(\mathbf{r}_j)}_{\mathbf{v}_j} \tag{4.17}$$

As described above, Eq. (4.9) implies the cancellation of the residual respect to the selected basis. Then, with the selection of delta point test function, the solution of Eq. (4.17) gives the exact solution in the selected points $\{\mathbf{r}_j\}_{j=0}^{P}$, as expressed in Eq. (4.18). However, no information is obtained concerning the accuracy of the continuous solution $\mathfrak{u}(\mathbf{r})$ in the rest of the domain.

$$\text{Solving Eq. (4.17)} \longrightarrow \mathfrak{u}^N(\mathbf{r}_j) = \mathfrak{u}^A(\mathbf{r}_j) \tag{4.18}$$

Galerkin finite elements

The Galerkin approach consists on considering test functions and basis functions to be equal, that is $\Phi_j = \varphi_j$. Then, Eq. (4.9) results into Eq. (4.19).

$$\sum_{k=0}^{P} \mathbf{a}_k \underbrace{\int_\Omega \mathcal{L}\varphi_k(\mathbf{r})\varphi_j(\mathbf{r})d\Omega}_{\mathbf{A}_{j,k}} = \underbrace{\int_\Omega \mathfrak{f}(\mathbf{r})\varphi_j(\mathbf{r})d\Omega}_{\mathbf{v}_j} \tag{4.19}$$

Furthermore, if nodal basis and quadrature sets are considered, the integrals can be approximated by summations, obtaining the coefficients for the algebraic equations listed in Eqs. (4.20a) and (4.20b).

$$\mathbf{A}_{j,k} \approx \sum_{i=0}^{P} w_i \mathcal{L}\varphi_k(\mathbf{r}_i)\varphi_j(\mathbf{r}_i) \tag{4.20a}$$

$$\mathbf{v}_j \approx \sum_{i=0}^{P} w_i \mathfrak{f}(\mathbf{r}_i)\varphi_j(\mathbf{r}_i) \tag{4.20b}$$

Least squares method

Following this general weighted residual formulation, the least squares method is a particular case which considers test functions $\Phi_j = \mathcal{L}\varphi_j$, resulting in Eq. (4.21).

$$\sum_{k=0}^{P} \mathbf{a}_k \underbrace{\int_\Omega \mathcal{L}\varphi_k(\mathbf{r})\mathcal{L}\varphi_j(\mathbf{r})d\Omega}_{\mathbf{A}_{j,k}} = \underbrace{\int_\Omega \mathfrak{f}(\mathbf{r})\mathcal{L}\varphi_j(\mathbf{r})d\Omega}_{\mathbf{v}_j} \tag{4.21}$$

Considering nodal basis and quadrature sets, the coefficients for the algebraic equations are derived as in Eqs. (4.22a) and (4.22b).

$$\mathbf{A}_{j,k} \approx \sum_{i=0}^{P} w_i \mathcal{L}\varphi_k(\mathbf{r}_i)\mathcal{L}\varphi_j(\mathbf{r}_i) \tag{4.22a}$$

$$\mathbf{v}_j \approx \sum_{i=0}^{P} w_i \mathfrak{f}(\mathbf{r}_i)\mathcal{L}\varphi_j(\mathbf{r}_i) \tag{4.22b}$$

It is worth noticing in Eq. (4.22a) that the exact same expression is obtained if the indeces j and k are interchanged, that is $\mathbf{A}_{j,k} = \mathbf{A}_{k,j}$ for any given operator $\mathcal{L}$. This means that the resulting system of equations is symmetric and therefore it can be efficiently solved by iterative algorithms. This is a comparative advantage respect to the Galerkin approach, since the condition of symmetry in Eq. (4.20a) is only obtained for self–adjoint operators $\mathcal{L}$.

From a different perspective, the least squares formulation can be presented as a minimization problem. The objective of this approach is to minimize the L^2 norm (square integral) of the residual, denoted by $\mathcal{R}_{LS}$ as in Eq. (4.23).

$$\mathcal{R}_{LS}(\mathfrak{u}) = \langle \mathcal{R}(\mathfrak{u}), \mathcal{R}(\mathfrak{u}) \rangle_{\mathcal{V}(\Omega)} = \int_{\Omega} (\mathcal{L}\mathfrak{u} - \mathfrak{f})^2 \, d\Omega \tag{4.23}$$

In addition, the boundary conditions can be incorporated in the definition of $\mathcal{R}_{LS}$. Then, the boundary conditions are imposed in a *weak* approach, as part of the minimization problem. It can be shown that if the problem is well–posed[3], the numerical solution $\mathfrak{u}^N$ that minimizes $\mathcal{R}_{LS}$ also represents a minimum value for the numerical error $\mathcal{E}$, given by Eq. (4.24).

$$\mathcal{E}(\mathfrak{u}^N) = \left\langle \mathfrak{u}^N - \mathfrak{u}^A, \mathfrak{u}^N - \mathfrak{u}^A \right\rangle_{\mathcal{V}(\Omega)} = \int_{\Omega} \left(\mathfrak{u}^N - \mathfrak{u}^A\right)^2 d\Omega \tag{4.24}$$

This means that the minimization of $\mathcal{R}_{LS}$ gives the best approximate solution (the one with minimum error) from a least squares perspective. If $\mathfrak{u}$ is a local minimum of $\mathcal{R}_{LS}$, then the value of the residual is lower than in the surroundings. In other words, an infinitesimal perturbation in any direction $\mathfrak{w} \in \mathcal{V}$ must result in a null variation of the residual. In mathematical terms this is represented by Eq. (4.25).

$$\lim_{\epsilon \to 0} \frac{\partial}{\partial \epsilon} \mathcal{R}_{LS}(\mathfrak{u} + \epsilon \mathfrak{w}) = \lim_{\epsilon \to 0} \frac{\partial}{\partial \epsilon} \int_{\Omega} [\mathcal{L}(\mathfrak{u} + \epsilon \mathfrak{w}) - \mathfrak{f}]^2 \, d\Omega = 0 \tag{4.25}$$

[3]Jiang (1998, §4) defined a well–posed problem as one with a unique solution $\mathfrak{u}$ that depends continuously on the source term $\mathfrak{f}$. This condition is fulfilled if $\mathcal{L}$ is a linear.

Furthermore, if the the operator $\mathcal{L}$ is linear, Eq. (4.26) is derived with some algebra from Eq. (4.25).

$$\int_{\Omega} (\mathcal{L}\mathfrak{u} - \mathfrak{f})\, \mathcal{L}\mathfrak{w} d\Omega = 0 \qquad \forall \mathfrak{w} \in \mathcal{V} \tag{4.26}$$

Equation (4.26) is a general representation of the least squares formulation. For the numerical implementation, the search space $\mathcal{V}$ which has an infinite dimension is replaced by $\mathcal{V}^N = span\,\{\Phi_j\}_{j=0}^{P}$. Then, the generic perturbation in Eq. (4.26) is considered respect to an arbitrary direction $\mathfrak{w}^N \in \mathcal{V}^N$.

Since $\mathcal{V}^N$ has a finite dimension $P+1$, Eq. (4.26) can be replaced by a set of $P+1$ equations as Eq. (4.27), which is evaluated for each individual basis $\Phi_j = \mathcal{L}\varphi_j$.

$$\int_{\Omega} \mathcal{L}\mathfrak{u}^N \mathcal{L}\varphi_j d\Omega = \int_{\Omega} \mathfrak{f}\mathcal{L}\varphi_j d\Omega \quad \forall j = 0, \ldots, P \tag{4.27}$$

Finally, using an spectral approximation for $\mathfrak{u}^N$ as in Eq. (4.7), the algebraic system in Eq. (4.21) is recovered.

$$\sum_{k=0}^{P} \mathbf{a}_k \underbrace{\int_{\Omega} \mathcal{L}\varphi_k(\mathbf{r})\mathcal{L}\varphi_j(\mathbf{r}) d\Omega}_{\mathbf{A}_{j,k}} = \underbrace{\int_{\Omega} \mathfrak{f}(\mathbf{r})\mathcal{L}\varphi_j(\mathbf{r}) d\Omega}_{\mathbf{v}_j} \tag{4.21}$$

This alternative formulation indicates that the least squares method is, in fact, a minimization problem in the search space $\mathcal{V}^N$. In other words, the LSSEM provides the best approximation $\mathfrak{u}^N \in \mathcal{V}^N$ to the solution within this space, through the minimization of the least squares residual $\mathcal{R}_{LS}$ in the space $\mathcal{V}'$. This situation can be represented by Fig. 4.1.

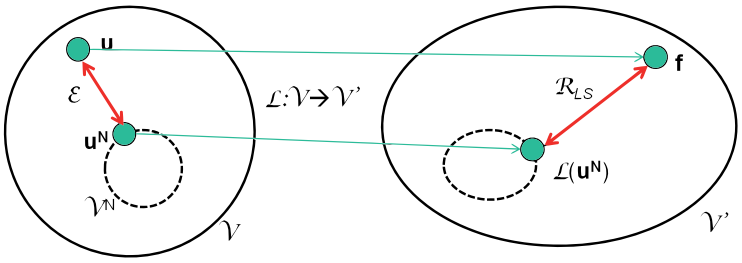

Figure 4.1: For linear operators $\mathcal{L}$, the least squares residual $\mathcal{R}_{LS}$ and the numerical error $\mathcal{E}$ are equivalent.

This means that the accuracy of the solution is also provided by the method, even in the case where the analytical solution is unknown, by means of the least squares residual $\mathcal{R}_{LS}$, which can be computed according to Eq. (4.23). In the case

of the subdivision of the domain into elements, $\mathcal{R}_{LS}$ is obtained at both local and global levels. This feature of the LSSEM is further evaluated in Section 4.3.

4.2 A single–phase heat exchanger

The general mathematical formulation from Section 4.1 is applied now to a practical case. The analysis of a one–dimensional single–phase heat exchanger with constant fluid properties provides an interesting example with analytical solution, allowing to compare the performance of different numerical methods. Their mathematical description for this particular case and a convergence analysis are presented in the following subsections. In addition, the evolution of the least squares residual and the stability requirements of the FDM are studied.

4.2.1 Mathematical description

Figure 4.2 presents an schematic of a one–dimensional heat exchanger for both (a) co–current and (b) counter–current flow. While the counter–current flow arrangement is more effective, the co–current scheme results in a rather uniform wall temperature and for that reason is selected in chemical processes.

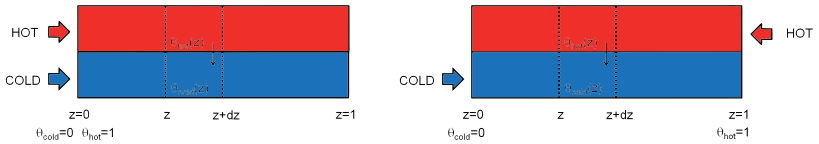

(a) Co–current flow (b) Counter–current flow

Figure 4.2: Scheme of a one–dimensional heat exchanger

A non–dimensional temperature $\theta(z)$ is defined as in Eq. (4.28), where $z \in [0, 1]$ is the relative axial position. With this definition, the boundary conditions are $\theta_{cold} = 0$ and $\theta_{hot} = 1$ at the inlets.

$$\theta(z) = \frac{T(z) - T_{cold,in}}{T_{hot,in} - T_{cold,in}} \tag{4.28}$$

This problem is governed by energy balances for both cold and hot streams. As discussed in Section 2.4.1, these balances can be represented with non–dimensional temperatures and two parameters that indicate the HE size and design characteristics. These two parameters can be selected from different sets and in all cases lead to the same results. Following the $P - NTU$ approach (see Section 2.4.1), which defines individual number of thermal units NTU_{cold} and NTU_{hot}, the energy balances are then given by Eqs. (4.29) and (4.30).

$$\frac{\partial \theta_{cold}}{\partial z} + NTU_{cold}\left(\theta_{cold} - \theta_{hot}\right) = 0 \tag{4.29}$$

$$\pm\frac{\partial \theta_{hot}}{\partial z} + NTU_{hot}\left(\theta_{hot} - \theta_{cold}\right) = 0 \tag{4.30}$$

The $\pm$ sign in Eq. (4.30) allows to account for both co–current and counter–current flow arrangements. Table 4.2 summarizes the analytical solutions for Eqs. (4.29) and (4.30) for different conditions.

Case	$\theta_{cold}(z)$	$\theta_{hot}(z)$
Co–current	$\dfrac{1-e^{-NTU_{cold}(1+R_{cold})z}}{1+R_{cold}}$	$1-\dfrac{1-e^{-NTU_{cold}(1+R_{cold})z}}{1+R_{hot}}$
Counter–current $NTU_{hot} \neq NTU_{cold}$	$\dfrac{e^{NTU_{cold}(R_{cold}-1)z}-1}{R_{cold}e^{NTU_{cold}(R_{cold}-1)}-1}$	$\dfrac{R_{cold}e^{NTU_{cold}(R_{cold}-1)z}-1}{R_{cold}e^{NTU_{cold}(R_{cold}-1)}-1}$
Counter–current $NTU_{hot} = NTU_{cold}$	$\dfrac{NTUz}{NTU+1}$	$\dfrac{NTUz+1}{NTU+1}$

Table 4.2: Analytical solutions for single–phase constant–properties cases

The mathematical description of the WRF was presented in Section 4.1 for a generic problem. In this particular problem, the mathematical operator and variables described in Section 4.1 are given by Eq. (4.31). The unknown solutions vector $\mathfrak{u}$ contains the two dimensionless temperatures, as in Eq. (4.31a). In addition, the problem operator $\mathcal{L}$, given by Eq. (4.31b), is linear, since it results from the combination of two linear elements. With these considerations, the assumptions described in Section 4.1 are fulfilled.

$$\mathfrak{u} = \begin{bmatrix} \theta_{cold} \\ \theta_{hot} \end{bmatrix} \tag{4.31a}$$

$$\mathcal{L} = \begin{bmatrix} NTU_{cold} & -NTU_{cold} \\ -NTU_{hot} & NTU_{hot} \end{bmatrix} + \begin{bmatrix} \frac{\partial}{\partial z} & 0 \\ 0 & \pm\frac{\partial}{\partial z} \end{bmatrix} \tag{4.31b}$$

$$\mathfrak{f} = \begin{bmatrix} \mathbf{0} \\ \mathbf{0} \end{bmatrix} \tag{4.31c}$$

$$\Omega = [0, 1] \tag{4.31d}$$

So far, the different numerical techniques have been presented as particular cases of a generic WRF and their resulting algebraic equations were developed in Section 4.1. In this section, both FDM and FVM are developed for this particular single–phase example. The application of spectral methods follows straightforward from Eqs. (4.17) to (4.21) and therefore it is not included in this section.

FDM Replacing Eq. (4.31) into Eq. (4.4) gives for this case:

$$\left.\frac{\partial \theta_{cold}}{\partial z}\right|_{z=z_j} + NTU_{cold}\left[\theta_{cold}(z=z_j) - \theta_{hot}(z=z_j)\right] = 0 \tag{4.32a}$$

$$\pm \left.\frac{\partial \theta_{hot}}{\partial z}\right|_{z=z_j} + NTU_{hot}\left[\theta_{hot}(z=z_j) - \theta_{cold}(z=z_j)\right] = 0 \tag{4.32b}$$

Although Eq. (4.32) is exact and general, it cannot be solved if no further assumptions are considered. The FDM considers a first–order approximation for the derivative as in Eq. (4.33).

$$\left.\frac{\partial \mathfrak{u}}{\partial z}\right|_{z=z_j} \approx \frac{\mathfrak{u}(z=z_{j+1}) - \mathfrak{u}(z=z_j)}{z_{j+1} - z_j} \tag{4.33}$$

Furthermore, defining $\Delta z = z_{j+1} - z_j$ the algebraic system in Eq. (4.34) is obtained for $j = 1, \ldots, N$.

$$\theta_{cold}(z_{j+1}) = \theta_{cold}(z_j) + \Delta z NTU_{cold}\left[\theta_{hot}(z_j) - \theta_{cold}(z_j)\right] \tag{4.34a}$$

$$\theta_{hot}(z_{j+1}) = \theta_{hot}(z_j) \pm \Delta z NTU_{hot}\left[\theta_{cold}(z_j) - \theta_{hot}(z_j)\right] \tag{4.34b}$$

FVM Replacing the mathematical operators for this problem from Eq. (4.31), into the general FVM formulation on Eq. (4.5) gives:

$$\theta_{cold}(z=z_{j+1}) - \theta_{cold}(z=z_j) + NTU_{cold}\int_{\Omega_j}\left[\theta_{cold}(z) - \theta_{hot}(z)\right]dz = 0 \tag{4.35a}$$

$$\pm\left[\theta_{hot}(z=z_{j+1}) - \theta_{hot}(z=z_j)\right] + NTU_{hot}\int_{\Omega_j}\left[\theta_{hot}(z) - \theta_{cold}(z)\right]dz = 0 \tag{4.35b}$$

The solution of Eq. (4.35) requires the calculation of some integrals. The FVM approximates the solution considering a constant value in each finite volume $\Omega_j = [z_j, z_{j+1})$, that is:

$$\mathfrak{u}(z) \approx \mathfrak{u}(z_j) \forall z \in [z_j, z_{j+1}) \longrightarrow \int_{z=z_j}^{z=z_{j+1}} \mathfrak{u}(z)dz \approx \mathfrak{u}(z_j) \times \Delta z_j \tag{4.36}$$

Introducing this approximation into Eq. (4.35), Eq. (4.34) is recovered. Then, as postulated in Section 4.1.1, both FDM and FVM result in the same system of algebraic equations.

$$\theta_{cold}(z_{j+1}) = \theta_{cold}(z_j) + \Delta z NTU_{cold}\left[\theta_{hot}(z_j) - \theta_{cold}(z_j)\right] \tag{4.34a}$$

$$\theta_{hot}(z_{j+1}) = \theta_{hot}(z_j) \pm \Delta z NTU_{hot}\left[\theta_{cold}(z_j) - \theta_{hot}(z_j)\right] \tag{4.34b}$$

4.2.2 Convergence analysis

As the number of discretization points or the approximation order are increased, a more accurate numerical solution is obtained. The convergence analysis refers then to the relation between the obtained numerical error $\mathcal{E}$ and the total number algebraic unknowns, also called number of degrees of freedom (dof).

Figure 4.3 presents a convergence analysis for different methods in both (a) co–current and (b) counter–current flow arrangements. The numerical results correspond to the conditions $NTU_{cold} = 4$, $NTU_{hot} = 5$, from which are derived $R_{cold} = 1.25$ and $R_{hot} = 0.8$. Since both FDM and FVM result in the same system of algebraic equations, only FDM is analyzed. In addition, two approaches are presented for the spectral methods. On the one hand, the h–approach[4] consists on increasing the number of elements while keeping the approximation order constant (in this case $P = 3$). On the other hand, in the p–approach the number of elements is constant (in this case only one element) and the approximation order P is increased.

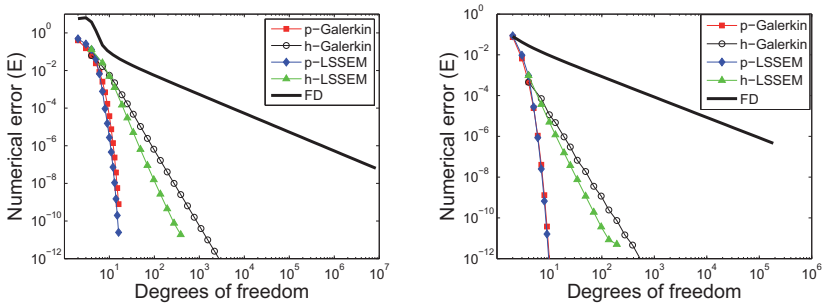

(a) Co–current flow (b) Counter–current flow

Figure 4.3: Convergence plots for FDM, Galerkin and LSSEM in a double logarithmic scale

A first unconverged regime for the FDM is noticed in Fig. 4.3(a), with numerical errors larger than unity. This regime is a consequence of the stability requirements of the method for initial value problems (Richtmyer, 1967), and is further studied in the following subsections.

In these log-log plots, the FDM, h–LSSEM and h–Galerkin approaches present a linear convergence. The slopes are -1 for FDM and -P for both spectral methods. This can be represented in mathematical terms as in Eq. (4.38).

[4]The letter h is commonly used in literature to refer to the element size.

$$\mathcal{E}_{FDM} \propto \text{dof}^{-1} \tag{4.38a}$$

$$\mathcal{E}_{Galerkin} \propto \text{dof}^{-P} \tag{4.38b}$$

$$\mathcal{E}_{LSSEM} \propto \text{dof}^{-P} \tag{4.38c}$$

The fastest convergence rate is found for the p–LSSEM and p–Galerkin approaches. As postulated in Eqs. (4.38b) and (4.38c) the slope is proportional to P and an exponential convergence rate is observed. This result is consistent with the description of Canuto et al. (2006), who stated that for smooth solutions (such as those listed in Table 4.2) the approximation with polynomial gives exponential convergence.

This fast exponential convergence rate leads to the reduction of the numerical error $\mathcal{E}$ to very low values, as observed in Fig. 4.3. However, this type of accuracy is usually not required in engineering applications. In general, the numerical tolerance is directly related to the accuracy of the physical model. In short, the error introduced by the computational solution of the governing equations should be negligible compared to the error given by their formulation, that is, the physical model. Considering that these simple models can have uncertainties in the order of roughly 10%, the numerical tolerance should be two order of magnitudes lower, around 10^{-3}=0.1%. Keeping this in mind, the results of this convergence analysis are summarized in Table 4.3, which presents the required number of degrees of freedom to reduce the numerical error below a prescribed numerical tolerance.

Tolerance	Co–current flow				Counter–current flow			
	10^{-2}	10^{-3}	10^{-4}	10^{-5}	10^{-2}	10^{-3}	10^{-4}	10^{-5}
p–LSSEM	6	7	8	10	3	4	5	6
p–Galerkin	6	8	10	11	3	4	5	6
h–LSSEM	10	19	25	34	4	4	7	10
h–Galerkin	10	19	34	70	4	4	7	13
FDM	65	725	5794	65537	12	92	1025	11586

Table 4.3: Required number of degrees of freedom in order to reduce error below a given tolerance

As observed in Table 4.3, LSSEM and Galerkin present similar performance. and they both require a much lower number of degrees of freedom compared to FDM. This reduction ranges between one and four orders of magnitude.

However, the results presented in Fig. 4.3 and Table 4.3 do not represent completely the performance of different methods. While both Galerkin and LSSEM involve solving a matrix system of algebraic equations, expressed by Eqs. (4.19) and (4.21), this is not always necessary for the FDM. In the case of co–current flow, the temperature in each new position z_{j+1} can be obtained from previous

known values in z_j as given by Eq. (4.34). This approach, known as explicit FDM, allows a faster computation for the same number of degrees of freedom, although it is only applicable for initial-value problems. In the case of counter–current flow, the Eq. (4.33) results in the solution of a matrix system of equations. This second approach is known as implicit FDM.

With these considerations, the overall figure of merit is then the numerical accuracy that can be obtained at a certain CPU time. These results are presented in Fig. 4.4 and summarized in Table 4.4, where the times are presented relative to the p–LSSEM approach.

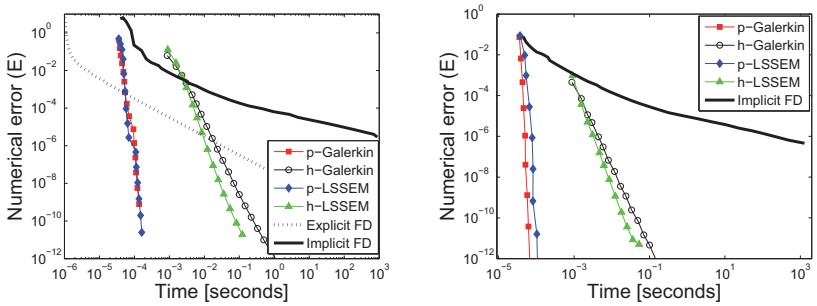

(a) Co–current flow (b) Counter–current flow

Figure 4.4: Numerical error obtained at a given computational time for different methods

Figure 4.4(a) and Table 4.4 indicate that the explicit FDM is several orders of magnitude faster than the implicit FDM. In addition, for low–accuracy solutions, it is even faster than the spectral methods. However, it cannot be used for counter–current flow, and its use in the co–current flow should consider its stability requirements.

Tolerance	Co–current flow				Counter–current flow			
	10^{-2}	10^{-3}	10^{-4}	10^{-5}	10^{-2}	10^{-3}	10^{-4}	10^{-5}
p–LSSEM	1	1	1	1	1	1	1	1
p–Galerkin	1.37	0.96	1.09	1.65	0.79	0.80	0.70	0.65
h–LSSEM	41.7	67.0	77.3	103	18.5	17.0	23.8	29.2
h–Galerkin	42.3	67.3	105	211	17.7	16.3	23.8	38.6
Explicit FDM	0.08	0.63	4.26	47.8	NOT APPLICABLE			
Implicit FDM	14.1	191	4297	$2.0\ 10^6$	4.09	22.4	300	24320

Table 4.4: Relative times. Reference, in all cases: p–LSSEM = 1.

For a low accuracy requirement ($\mathcal{E} \approx 10^{-2}$) the implicit FDM and LSSEM show a comparable computational cost (in the same order of magnitude) and there is no

significant advantage in the use of spectral methods in this case. The reason for this is that, in the LSSEM, the assembly of the problem matrix, i.e. computing the integrals in Eq. (4.22), takes a big part of the total time. In fact, Proot (2003) showed that it may represent half of the total computational cost.

However, for higher accuracies the differences become significant. For example, for $\mathcal{E} \approx 10^{-5}$, the implicit FDM results in roughly twenty thousand times more computational cost for counter–current flow and two millions times for co–current flow. In general, for $10^{-3} < \mathcal{E} < 10^{-4}$, a reduction from one to three orders of magnitudes in computational time is obtained with the use of LSSEM.

4.2.3 Stability analysis

The FDM presents some stability requirements for initial–value problems. In this case, an stable solution for the co–current flow arrangement is such that the temperature difference $\theta_{hot}(z) - \theta_{cold}(z)$ is continuously reduced and remains positive. Considering this condition in the FDM system in Eq. (4.34), it gives:

$$0 < \frac{\theta_{hot}(z_{j+1}) - \theta_{cold}(z_{j+1})}{\theta_{hot}(z_j) - \theta_{cold}(z_j)} = [1 - \Delta z_j \, (NTU_{cold} + NTU_{hot})] < 1 \tag{4.39}$$

Furthermore, if the numerical step Δz_j is uniform, the condition in Eq. (4.40) is obtained. For the example presented in this section, with $NTU_{cold} = 4$ and $NTU_{hot} = 5$, a minimum of dof > 10 is required to obtain an stable solution.

$$\frac{1}{\Delta z_j} = \text{dof} - 1 > NTU_{cold} + NTU_{hot} \tag{4.40}$$

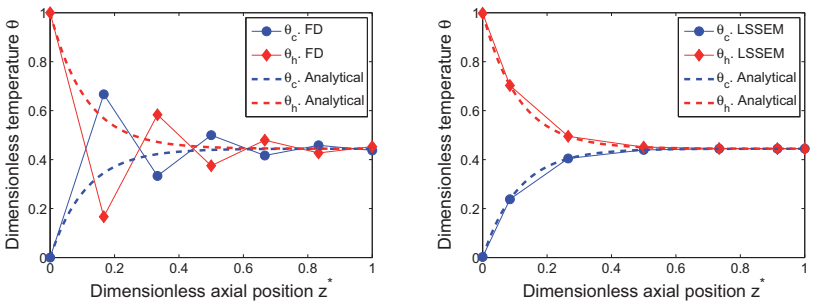

(a) FDM. Temperature cross

(b) LSSEM. Stable solution

Figure 4.5: Numerical temperature profiles for the co–current flow case.

Figure 4.5 presents numerical temperature profiles in the case where this condition is not fulfilled. While the FDM results in temperature crosses, the solution

obtained with the same number of degrees of freedom using LSSEM is stable and accurate.

This situation leads to the conclusion that FDM should not be used with few discretization points. Furthermore, if more points are used, the LSSEM and Galerkin result in lower computational costs.

4.2.4 The least squares residual

So far this analysis has been focused in numerical convergence, in terms of degrees of freedom and computational times. From these perspectives, Galerkin and LSSEM have similar performances.

In Section 4.1, the LSSEM was alternatively presented as a minimization problem. In this context, this method provides an error estimator, that is the least squares residual $\mathcal{R}_{LS}$. The evolution of this residual with the number of degrees of freedom is presented in Fig. 4.6 along with the numerical error $\mathcal{E}$ for both (a) co–current and (b) counter–current flow arrangements.

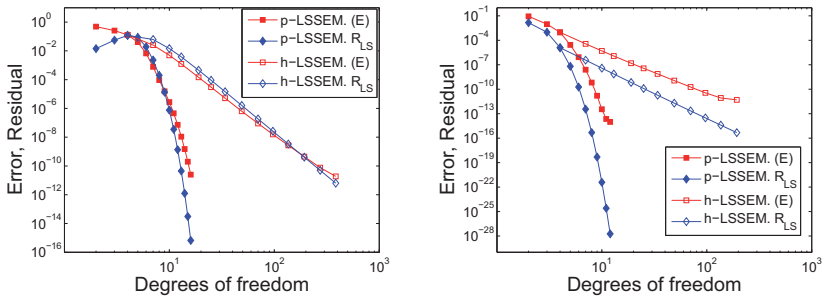

(a) Co–current flow

(b) Counter–current flow

Figure 4.6: Numerical error $\mathcal{E}$ and least squares residual $\mathcal{R}_{LS}$

In Section 4.1 it was postulated that $\mathcal{E}$ and $\mathcal{R}_{LS}$ are *equivalent*, meaning that finding the solution that minimizes the residual also results in the minimum numerical error. This situation can be observed in Figs. 4.6(a) and 4.6(b), where $\mathcal{E}$ and $\mathcal{R}_{LS}$ run in roughly parallel curves. In other words, the convergence of the residual implies the convergence of the numerical error. This feature has been demonstrated theoretically by Jiang (1998, §4) and Fig. 4.6 shows the results for this particular example.

4.3 A two-phase heat exchanger

The occurrence of phase–change, either boiling or condensation, leads to different behavior within the same equipment. For this reason, two–phase–flow heat

exchangers cannot be accurately represented in a generic non–dimensional formulation as sketched in Section 4.2.1 and Fig. 4.2. In this case, a particular geometry must be selected *a priori*. The typical geometries for cryogenic processes were described in Section 2.2. For simplicity, a tube–in–tube geometry is selected for this example, with the cold stream flowing in the inner tube and the hot stream in the annuli. Nevertheless, the present analysis can be extended to other geometries. A schematic diagram is depicted in Fig. 4.7, indicating energy balances in a control volume $[z, z + dz)$.

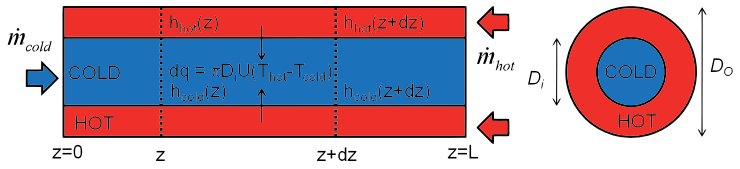

Figure 4.7: Scheme of a tube–in–tube heat exchanger considered in this example

Although Fig. 4.7 shows a counterflow arrangement, where the cold fluid enters in $z = 0$ and the hot one in $z = L$ and they flow in opposite directions, the co–current arrangement is also considered. Assuming that heat losses to the surroundings and axial conduction effects are negligible, a general steady-state energy balance may be formulated for each fluid in terms of the evolution of the specific enthalpy h. Equations (4.41) and (4.42) must be solved with proper initial–value boundary condition.

$$\dot{m}_{cold}\frac{\partial h_{cold}}{\partial z} = \pi D_i U(z)\left[T_{hot}(z) - T_{cold}(z)\right] \tag{4.41}$$

$$\pm\dot{m}_{hot}\frac{\partial h_{hot}}{\partial z} = \pi D_i U(z)\left[T_{cold}(z) - T_{hot}(z)\right] \tag{4.42}$$

In terms of the general WRF, the mathematical operators for this problem are given by Eq. (4.43). Once again, the problem operator $\mathcal{L}$ is linear, thus fitting the assumption of the spectral elements methods. The source term $\mathfrak{f}$ depends on the local temperature difference, which is related to the local solution $\mathfrak{u}(z)$. Then, they are not known *a priori* and an iterative solution is required.

$$\mathfrak{u} = \begin{bmatrix} h_{cold} \\ h_{hot} \end{bmatrix} \tag{4.43a}$$

$$\mathcal{L} = \begin{bmatrix} \dot{m}_{cold}\frac{\partial}{\partial z} & 0 \\ 0 & \pm\dot{m}_{hot}\frac{\partial}{\partial z} \end{bmatrix} \tag{4.43b}$$

$$\mathfrak{f} = \begin{bmatrix} \pi D_i U \left[T_{hot}(z) - T_{cold}(z)\right] \\ \pi D_i U \left[T_{cold}(z) - T_{hot}(z)\right] \end{bmatrix} \tag{4.43c}$$

$$\Omega = [0, L] \tag{4.43d}$$

The variable U is the overall heat transfer coefficient, which takes into account the geometry and flow conditions. In a steady–state analysis, it can be computed as a combination of thermal resistances. For this tube–in–tube geometry, and neglecting fouling resistances, U can be computed from Eq. (4.44). The first two terms in Eq. (4.44) represent convective thermal resistance on the cold and hot fluids, respectively, and the last term is the resistance given by thermal conduction in the wall.

$$\frac{1}{\pi D_i U(z)} = \frac{1}{\pi D_i \hat{h}_{cold}(z)} + \frac{1}{\pi \left(D_i + 2t_w\right) \hat{h}_{hot}(z)} + \frac{\ln(1 + 2t_w/D_i)}{2\pi\lambda_w} \tag{4.44}$$

Generally, an empirical or semi–empirical correlation is used to compute the local heat transfer coefficients $\hat{h}_{cold}$ and $\hat{h}_{hot}$, which are dependent on the fluid properties, velocity and geometry. Different models were presented in Section 3.3.3. The following correlations were considered in this work. For both streams in the single–phase regions (liquid and gas) two correlations are used, depending on the range of Reynolds number: Petukhov-Popov for fully developed turbulent flow and Gnielinski for the transition regime (for both, see Ghiaasiaan (2007)). For the boiling HTC, the simplified version of the Gungor and Winterton was used. It is applicable in all the two–phase flow range $h_L < h < h_V$ and its use is recommended by Collier and Thome (1994). In addition, the subcooled boiling model proposed by Kandlikar (1997) is incorporated.

With all these considerations, Eqs. (4.41) and (4.42) do not have an analytical solution. Therefore, the performance of the different numerical methods cannot be compared as in Section 4.2. Instead, only the LSSEM is considered and the evolution of the least squares residual $\mathcal{R}_{LS}$ is studied in the following subsections.

The particular case of an evaporator is studied in this section. The cold stream (refrigerant R134a) flows in the inner tube, entering in liquid state at 270 K and 3 bar. The hot fluid is water, and enters the annuli at 290 K and 1 bar. The mass flow rates are $\dot{m}_{cold} = 5\ 10^{-3} kgs^{-1}$ and $\dot{m}_{hot} = 2\ 10^{-2} kgs^{-1}$ for the refrigerant and water, respectively. The geometry considered is the tube–in–tube sketched in Fig. 4.7, with $L = 2m$, $D_i = 6mm$ and $D_o = 10mm$. The tube wall is $t_w = 1mm$ thick and the material is copper ($\lambda_w = 401\ Wm^{-1}K^{-1}$). For these conditions the conductive thermal resistance of the wall becomes negligible.

4.3.1 Local error estimator

The least squares residual $\mathcal{R}_{LS}$ as defined in Eq. (4.23) can be interpreted at a local level performing the integration in each element Ω_j instead of the global domain Ω. This description allows to identify which element has the largest local residual, that is where the governing equations are solved less accurately.

Figure 4.8 presents the temperature profiles for (a) co–current and (b) counter–current flow, computed using 20 elements and approximation order $P = 3$. In addition, the residual $\mathcal{R}_{LS}$ in each element is indicated in the right–hand vertical axis using a logarithmic scale.

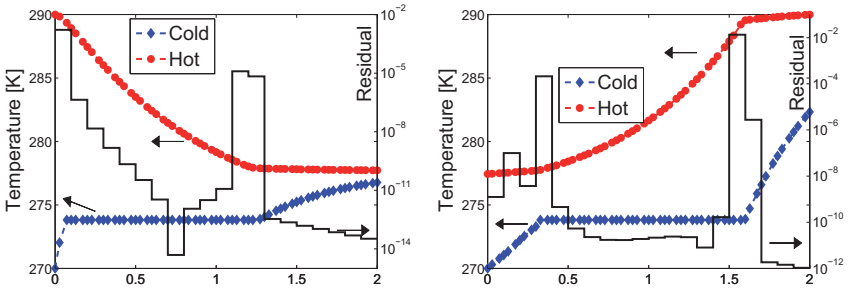

(a) Co–current flow

(b) Counter–current flow

Figure 4.8: Temperature profiles and least squares residual $\mathcal{R}_{LS}$

The plateau in the cold–stream temperature profile corresponds to the two–phase flow region. In this region, the specific enthalpy is increasing, while the temperature remains at its saturation value. Finally, when full evaporation is reached, the cold–stream temperature increases again in the gas–flow region.

In both Figs. 4.8(a) and 4.8(b) the dominant contribution to the residual is located in the transition element. At these points there is a sharp discontinuity in the temperature curves, which represent the source term in Eqs. (4.41) and (4.42). As a consequence, the solution of the problem is not smooth. Therefore, the approximation of the solution with polynomials does not necessarily provide an accurate description (Maerschalck and Gerritsma, 2008) in these elements. In the rest of the domain, the solution is smooth and the local residual is several orders of magnitude lower.

Considering that $\mathcal{R}_{LS}$ is equivalent to the numerical error $\mathcal{E}$, the information provided by Fig. 4.8 is useful for improving the accuracy. An adaptive strategy could take advantage of the location of elements with relatively large error, in this case in the surroundings of the phase transition for the cold fluid. This feature is further studied in Section 4.3.3, which presents a possible adaptive strategy that could be applied to this problem.

4.3.2 Global error estimator

Considering the least squares residual in a global sense, that is integrated over the entire domain Ω, it is an estimator of the quality of the solution. Then, the LSSEM allows to perform a convergence analysis in terms of $\mathcal{R}_{LS}$. In particular, it reflects how good the governing equations hold. As studied in Sections 4.1 and 4.2, the reduction of this estimator directly implies a decrease in the numerical error.

The results of this convergence analysis for this two–phase flow example are depicted in Fig. 4.9 for (a) co–current and (b) counter–current configurations. This analysis includes variations of both the number of elements (vertical axis, logarithmic scale) and the approximation order (horizontal axis, linear scale). The results are then presented in terms of contour lines for $\log_{10}(\mathcal{R}_{LS})$. In all cases, equal size and equal order elements were considered.

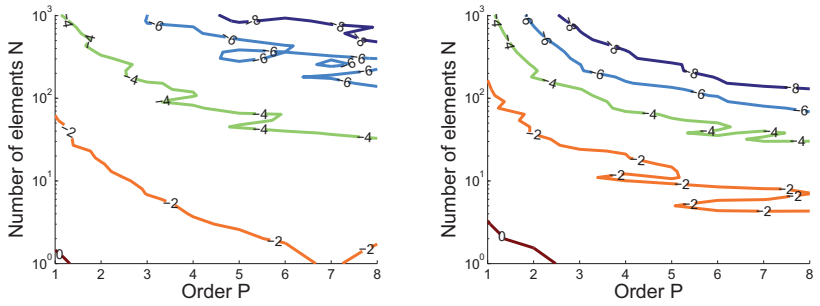

(a) Co–current flow

(b) Counter–current flow

Figure 4.9: Global convergence. Contour plots for $\log_{10}(\mathcal{R}_{LS})$.

Some instabilities can be noticed in Figs. 4.9(a) and 4.9(b). These occur as a consequence of the discontinuities in the solution studied in Section 4.3.1. With the existence of such discontinuities, an increase in the order or total number of elements does not guaranty a reduction of the residual, since it is dominated by the uncertainties in the boundary element. Nevertheless, the overall convergence of the method is appreciated in Fig. 4.9, since the total residual is largely reduced in eight orders of magnitude when moving from bottom–left to top–right.

Finally, the convergence plots indicate that, for high–accuracy, the contour plots are rather horizontal lines, specially in the case of Fig. 4.9(b), that is, for counter–current flow. This means that further increase of the approximation order beyond a critical value does not improve significantly the numerical performance, and more efficient results would be obtained considering a larger number of elements instead.

4.3.3 Adaptive strategy

The instabilities in Fig. 4.9 indicate that the h–LSSEM and p–LSSEM approaches do not guaranty a continuous convergence. In other words, increasing the number of elements at a fixed approximation order, or vice versa, does not always results in a lower residual. For this reason, an alternative adaptive strategy is presented in this section. The main objective is to achieve a discretization technique that allows a reasonable accuracy with less degrees of freedom than a h–LSSEM approach.

The following adaptive strategy is considered in this section. After a coarse–scale solution with few elements, the residual is evaluated at local level. If the residual in one element is higher than the average, it is split into two smaller elements (of equal size). In addition, if two neighboring elements present both a residual much lower than average (a ratio of 1 to 1000 was considered), they are joined together. After these procedures, a new simulation is performed and the process is repeated. In all cases, the approximation order P is kept constant.

Table 4.5 compares the performance of the h–LSSEM approach and the postulated adaptive strategy for several approximation orders. In all cases, the adaptive strategy achieves the required numerical tolerance of $\mathcal{R}_{LS}$ which much less degrees of freedom than h–LSSEM. This difference is more notorious at low orders. The ratio between both schemes ranges between 5.3 (for high order) and 6.8 (for low order).

Order	Co–current flow		Counter–current flow	
	Adaptive	h–LSSEM	Adaptive	h–LSSEM
1	192	1264	258	1761
2	53	863	69	609
3	49	646	46	544
4	57	609	53	365
5	46	456	56	381
6	61	325	55	385
7	57	316	57	379
8	57	361	57	305

Table 4.5: Required number of degrees of freedom to achieve $\mathcal{R}_{LS} < 10^{-4}$

The results in Table 4.5 indicate that the information provided by the LSSEM can be used to improve the numerical performance. However, it should be noticed that this strategy implies several steps of calculations and then it is not necessarily faster.

As indicated in Section 4.3.2, an increase in the order of approximation does not necessarily imply a reduction of the residual. This is reflected in Table 4.5, which indicates that the required degrees of freedom remains roughly constant for approximation orders $P \geq 4$.

4.4 Summary

In this chapter, different numerical methods are presented and compared for two heat exchanger examples. This preliminary study is important for the remaining of this thesis, since the following analysis includes the numerical solution of differential equations. Then, it is convenient to identify at an early stage which method is most convenient.

The mathematical description of the different methods is presented in Section 4.1, following a generic weighted residual formulation. In general, they can be grouped into two categories: point–discretization and spectral–elements. The first type includes FDM and FVM, which are traditionally used for lots of applications. Orthogonal collocation, Galerkin finite–elements and LSSEM are examples of the second category. These spectral methods give a global continuous representation of the solution.

The LSSEM presents some potential advantages that make it an interesting alternative to other methods. For smooth solutions, it presents high order convergence rate. The least squares residual $\mathcal{R}_{LS}$ is an error estimator provided by this method even for problems without analytical solution. Other features are the possibility to include the boundary conditions in the minimization problem as a weak formulation, and the proper numerical characteristics of the resulting system of equations for computational solving.

A first example is presented in Section 4.2 for a single–phase flow heat exchanger case with constant properties. It has an analytical solution and then, the performance of different methods can be compared. Both LSSEM and the Galerkin spectral elements method present exponential convergence rates and for typical accuracy requirements, they are between one and three orders of magnitudes faster than the implicit FDM. In the case of initial–value problems, such as the co–current flow arrangement, the explicit FDM is a fast technique since it does not involve solving a matrix system of algebraic equations. In fact, for low accuracy requirements, it is faster than LSSEM. However, caution is required, since it may lead to unstable solutions (in this example, with temperature crosses which are not physical) if few discretization points are used. Finally, the evolution of the least squares residual $\mathcal{R}_{LS}$ indicates that it is equivalent to the numerical error $\mathcal{E}$. In other words, $\mathcal{R}_{LS}$ is an alternative estimator of the accuracy of the solution, and if no analytical solution exists, is the only one available.

That is the case of the second example, presented in Section 4.3, for a two–phase flow HE, in particular, an evaporator. Only the LSSEM is considered, and the least squares residual is studied at both local and global levels. At a local level, the regions with higher error are easily identified close to the phase-change boundaries, where both the temperature and the heat transfer coefficient are non-smooth functions of the specific enthalpy. At a global level, the overall convergence of the solution is noticed. However, this convergence is not smooth and shows some instabilities, as a consequence of the discontinuities in the solution. Taking

advantage of the information provided by the least squares residual, this situation can be improved using an adaptive strategy. Then, only the elements with high error are further discretized resulting in roughly six times less degrees of freedom than a non–adaptive for achieving a proper solution.

The results from this chapter indicate that the LSSEM performs well and its use implies some advantageous for the solution of heat exchanger problems. For this reason, it is the selected numerical method applied in most of the following chapters. Only in the case of explicit initial—value problems the FDM is selected. Such is the case of Chapters 9 and 10.

Part II

Macro-scale framework

Following the multiscale description presented in Chapter 3, some elements of modeling and simulation at macroscopic level are presented. The prefix *macro* is generally used for referring to the largest scale in a given context. In the particular case of a heat exchanger, the broadest description is given in terms of heat duty (total amount of heat transferred) and overall pressure drop in each stream. Keeping this final objective in mind, simple models are used in this macro-scale framework, without taking into account the details of physical phenomena at lower scales. For this reason, the following two chapters are focused on simple one-dimensional formulations for evaluating the heat exchanger performance.

Chapter 5 analyzes the consequences of pressure drop in the sizing and design of two-phase flow heat exchanger, specially for high-efficiency applications as those required in cryogenic processes. For this reason, the results are perhaps better understood in terms of the ineffectiveness $1 - \varepsilon$. The variations in the saturation temperature largely affect the performance and failing to account for this effect results in a serious misprediction of the required size. This scenario confirms the approach selected in this thesis of proposing a multiscale formulation for an accurate description of the heat transfer and pressure drop. Three numerical examples are studied: an evaporator, a condenser and a mixed system with both boiling and condensation, and three models are compared.

In Chapter 6, perturbation theory is proposed for studying the sensitivity of the heat exchanger performance to the different operating and geometrical parameters at the design stage. This method is used in other areas of engineering, and a thorough introduction is given in this chapter, including an example with analytical solution. In summary, this technique is based on the solution of an importance problem and, with one additional simulation, provides the derivative of an integral response to *all* the parameters involved in the governing equations. Therefore, perturbative methods are very efficient for evaluating the sensitivity at the design stage, and can be implemented into an optimization algorithm. An evaporator example is studied in terms of four responses: heat duty, individual pressure drop for each stream and pumping power.

Chapter 5

Effects of pressure drop on HE performance

► In this chapter, the consequences of pressure drop in the sizing and design of high-efficiency heat exchanger are investigated. For two-phase flow systems, the variations in the saturation temperature largely affect the performance. This scenario confirms the approach selected in this thesis of proposing a multiscale formulation for an accurate description of the heat transfer and pressure drop.

Three numerical examples are studied: an evaporator, a condenser and a mixed system with both boiling and condensation. In all of them, three models previously presented in Chapter 2 are compared. The results from this examples indicate that neglecting the coupling between momentum and energy equations results in an underprediction of the performance (conservative assumption) for an evaporator, and the opposite for a condenser. In this last case the performance is overpredicted (non-conservative assumption) and therefore, at the design stage, the heat exchanger is undersized. Considering that high-efficiency equipment are required for cryogenic applications, the extent of these consequences is better understood in terms of the ineffectiveness $1 - \varepsilon$. Finally, a comparative analysis indicates that, over a wide range of operating conditions, the co-current flow arrangement can yield higher performance than counter-current.

As reviewed in Chapter 2, heat exchangers (HE) are main equipment in refrigeration processes, and for cryogenic applications, high efficiency HE are usually required. However, an accurate description of high–effectiveness heat transfer equipment is rather limited, in particular for two–phase flow applications. Then, the sizing of these equipment results a challenging task due to two main reasons.

First, the prediction of two–phase heat transfer coefficients is based on empirical models, described in Section 3.3.3, with a large extent of uncertainties. Second, different physical phenomena which are usually neglected must be considered. The

discussion on the state–of–the–art presented in Section 2.6 indicates that, while advanced models reported in literature incorporate individually some of these effects for simple cases, two of them remain unconsidered: the effects of pressure drop and of flow mixing on heat transfer performance. The first effect is the topic of this chapter, while the second one is considered in Chapter 8.

The effects of pressure drop are included in this chapter with the incorporation of a momentum equation coupled to the energy balances. The governing equations for this stream–evolution model are presented in Section 5.2 and are based on the pressure drop models introduced in Section 5.1. The results from this formulation are compared with those of two methods based only on energy balances: lumped–parameters and distributed–parameters models, described previously in Sections 2.4.1 and 2.4.2, respectively.

Three cases are considered in Section 5.3 and the sizing predictions of the different models are compared. On the base of these results, the consequences of undersizing in the final effectiveness are discussed in Section 5.4. Finally, optimal geometrical and physical design characteristics are investigated in Section 5.5.

In the multiscale framework of this thesis, this analysis represents a macroscopic description. A continuum formulation is used and the attention is focused in the overall changes in pressure and enthalpy. Despite the selection of a particular geometry for the numerical examples presented in Section 5.3, the formulation presented in this chapter is general and applicable to any given heat exchanger.

5.1 Pressure drop models

Changes in pressure occur due to four different effects:

- Localized effects flow disturbances, such as bends
- Body forces, usually the only one present is gravity
- Flow acceleration due to changes in density, area or mass flow rate
- Friction in the wall and other solid surfaces

Local disturbances to the flow produce an irreversible drop in pressure and loss of mechanical energy into heat. The flow behavior in sudden expansions and contractions, bends, and other perturbations, is complex and multidimensional. For this reason, it is usually modeled in the case of single–phase analysis as a lumped resistance, originated a pressure drop proportional to the flow inertia. Although the situation can result even more complex for two–phase flow, the same methodology is usually considered, with the use of empirical coefficients.

Body forces are well represented by means of the homogeneous mixture density defined in Eq. (3.3). Then, the pressure gradient in the axial direction z due to this effect is given by Eq. (5.1), where g is the acceleration of gravity in the flow

direction. For downward flow, g takes positive values and an increase in pressure is noticed, while for upward flow, g is negative and a pressure drops.

$$\left.\frac{dp}{dz}\right|_{\text{gravity}} = \rho_h g = \left[\alpha\rho_G + (1-\alpha)\rho_L\right] g \tag{5.1}$$

When the flow is accelerated, its momentum changes and this is reflected inversely in the pressure. Since both phases may have different velocities, the individual accelerations of liquid and gas should be considered. However, this can be approximated for high flow and low void fraction conditions (Tong and Tang, 1997, 3.5) using the homogeneous density ρ_h and the total mass flux G, as in Eq. (5.2). The extension of this model to the entire two–phase region introduces some error, which is negligible considering that the larger contribution to the total pressure drop is given by frictional term. In boiling flows the vapor content is increasing, and thus the homogeneous density is reduced, resulting in a net pressure drop due to acceleration. The opposite occurs in the case of condensation, and this effect results in an increase in pressure.

$$\left.\frac{dp}{dz}\right|_{\text{acceleration}} = -\frac{d}{dz}\left[\rho_L u_L^2 (1-\alpha) + \rho_G u_G^2 \alpha\right] \approx -\frac{d}{dz}\left(\frac{G^2}{\rho_h}\right) \tag{5.2}$$

Flow friction against solid surfaces, such as the tube–wall, represents the largest component of pressure drop. It is related to the relative perimeters, expressed in terms of an hydraulic diameter D_h, and the shear forces τ in the wall, as in Eq. (5.3). For two–phase flow applications, τ is usually represented with empirical correlations on the basis of single–phase results, as described in Section 5.1.1.

$$\left.\frac{dp}{dz}\right|_{\text{friction}} = \frac{4}{D_h}\tau \qquad \text{with } D_h = 4\frac{\text{Cross–sectional area}}{\text{Wetted perimeter}} \tag{5.3}$$

5.1.1 The two–phase multiplier

While an homogeneous model can be used to describe gravity and acceleration effects, it fails to account accurately for the frictional term, which is usually the most relevant one. Some attempts have been made to define an homogeneous mixture viscosity, although it is not clear if the liquid and gas values should be averaged using the quality or void fraction as weighting factors (Ghiaasiaan, 2007, 8.2). In both cases, the physical meaning of this effective viscosity is not clear, since this is not a fluid physical property but a proportionality constant defined for laminar flow and their is no theoretical basis for its use in the analysis of two–phase flows.

The use of separated–field models method to model pressure drop is too complex for the general case, and their application is limited to known flow patterns

that can be represented by simplified structures (Quibén and Thome, 2007). This approach is followed in Chapters 9 and 10 for annular and dispersed-droplets flow regimes, respectively.

An intermediate solution consist in the use of a two–phase multiplier Φ^2, first defined by Lockhart and Martinelli (1949) as in Eq. (5.4). This variable relates the pressure gradient to that which would be obtained if the flow was all in liquid or gas states, based on empirical correlations for laminar and turbulent flow regimes.

$$\Phi_L^2 = \frac{dp/dz|_{tph}}{dp/dz|_L} \quad ; \quad \Phi_G^2 = \frac{dp/dz|_{tph}}{dp/dz|_G} \tag{5.4}$$

According to this definition, $\Phi_L^2 = 1$ and $\Phi_G^2 = 0$ for single–phase liquid and $\Phi_L^2 = 0$ and $\Phi_G^2 = 1$ for single–phase gas. Several empirical correlations have been proposed by different authors for either of these multipliers in the two–phase region. They have been reviewed by Whalley (1987), Tribbe and Mller-Steinhagen (2000) and Didi et al. (2002), and each of them recommended a different correlation. Overall, the Friedel (1979) correlation predicts reasonably well the experimental data and has the most extensive application range.

Finally, it should be noticed that all empirical models are based in experimental data for adiabatic flow, usually in air–water systems. Then, they should be used with caution for boiling and condensation systems, since it is not clear how the heat and mass transfer mechanisms affect the momentum interaction between phases and overall pressure drop. Tarasova et al. (1966), see Tong and Tang (1997, 3.5.3), noticed that heat input to the wall increases the pressure drop in a few percent, and proposed a dimensional correlation for high pressure water, which can hardly be extended to other flow systems.

5.2 The governing equations

Lumped- and distributed-parameters models represent the basic design theory for heat exchanger design, as described in Section 2.4. They are useful tools for the sizing of HE, since they allow to estimate the required surface area without previously establishing a given geometry. They do, however, consider several assumptions on the behavior and characteristics of the flow which are usually not applicable for boiling or condensation cases. Then, a one–dimensional continuum description, hitherto called stream–evolution model (SEM), is suitable.

In general, one–dimensional models can be considered as extensions of nodal formulations, hence the usual references to them as fully–distributed models. The main difference is that SEM allow the inclusion of both continuity and momentum equations, thus accounting for changes in velocity and pressure. Since these models require an established geometry, flow arrangement and size, they have been applied for transient analysis of heat pump systems (Jia et al., 1995; Judge and Radermacher, 1997; Nyers and Stoyan, 1994), but not for sizing and design.

The application of a steady–state SEM in this chapter consists on the iterative search of the required size to fit a target performance. The governing equations are then stationary mass, momentum and energy balances. However, the mass balance has then a trivial solution, that is a constant mass flux $G = \rho\, u$, where ρ is the fluid density and u its velocity. Then, it can be considered implicitly and the problem is governed by momentum and energy balances for the cold and hot fluids as in Eqs. (5.5) and (5.6).

$$\frac{d}{dz}\left(\frac{G^2}{\rho}+p\right)_{cold} + \rho_{cold}(z)g + \frac{4}{D_{h,cold}}\tau_{cold}(z) = 0 \tag{5.5a}$$

$$\pm\frac{d}{dz}\left(\frac{G^2}{\rho}+p\right)_{hot} + \rho_{hot}(z)g + \frac{4}{D_{h,cold}}\tau_{hot}(z) = 0 \tag{5.5b}$$

$$G_{cold}\frac{dh_{cold}}{dz} = \frac{4}{D_{eq,cold}}U(z)\left[T_{hot}(z) - T_{cold}(z)\right] \tag{5.6a}$$

$$\pm G_{hot}\frac{dh_{hot}}{dz} = -\frac{4}{D_{eq,hot}}U(z)\left[T_{hot}(z) - T_{cold}(z)\right] \tag{5.6b}$$

Several remarks about Eqs. (5.5) and (5.6) must be clarified before further analysis. These are described in the following paragraphs.

First, the $\pm$ sign in Eqs. (5.5b) and (5.6b) allows to consider both co–current (+) and counter–current (-) flow arrangements in the same formulation.

Second, the required local physical properties, such as density and temperature, and secondary variables as the heat transfer coefficient can be obtained for each fluid from its thermodynamic state (p, h).

Third, the equivalent diameter D_{eq} in the energy balances represents the heated perimeters in a similar way as the hydraulic diameter D_h represents the wetted perimeter for the momentum equation. Then, D_{eq} is defined as in Eq. (5.7).

$$D_{eq} = 4\,\frac{\text{Cross–sectional area}}{\text{Heated perimeter}} \tag{5.7}$$

Fourth, the shear stress τ is modeled using a two–phase multiplier Φ_L^2 previously presented in Section 5.1.1. In particular, the Friedel correlation is used for Φ_L^2. This formulation also requires an empirical correlation for the single–phase liquid shear stress τ_L, which is represented using a friction factor f_L given by the Haaland formula (White, 1986, §6.4) for smooth tubes. Ultimately, the shear stress τ is computed according to Eq. (5.8).

$$f_L = \left[1.8\log\left(\frac{G\ D_h}{6.9\mu_L}\right)\right]^{-2} \rightarrow \tau_L = f_L\frac{G^2}{2\rho_L} \rightarrow \tau = \tau_L\Phi_L^2 \tag{5.8}$$

Fifth, the overall heat transfer coefficient U is the only physical variable whose description depends on the actual geometry, since it regulates the thermal resistance on both streams. In general, the same methodology as in Section 4.3 is followed. Without loss of generality a tube–in–tube geometry, see schematic in Fig. 4.7, is considered and in that case the overall HTC is computed according to Eq. (4.44).

Finally, with all these considerations, the governing equations are solved numerically with proper inlet–value boundary conditions for pressure and specific enthalpies. Based on the comparison of different numerical techniques presented in Chapter 4, the least–squares spectral elements method (LSSEM) is used. Although the same results should be obtained using any numerical method, the LSSEM presents some advantages which make it preferable for this problem.

5.3 Numerical examples

This section presents simulation results for three examples. First, a water–cooling evaporator is studied, where the hot stream is a single–phase liquid (water), while the cold stream (refrigerant R134a) is boiling. The second example presents the opposite case, that is a water–cooled condenser. Finally, a mixed boiling-condenser system is analyzed in the third example.

In all three cases the established geometry is a double-pipe HE, see Fig. 4.7, in counter-current flow arrangement. The tube wall material is copper, which has a high thermal conductivity ($\lambda_{copper} = 410$ W m^{-1} K^{-1}), thus resulting in a negligible wall thermal resistance. The input parameters for the different cases, listed in Table 5.1, were selected in a balanced design. The mass flow rates are low, in the order of a few grams per second, because this geometry is usually selected for small-capacity such as laboratory applications.

The results from this analysis are compared to those of lumped-parameters and distributed-parameters models. Both methods require the estimation of averaged flow properties within a HE element, which depend on the thermodynamic state (p, h). These are evaluated at the inlet pressure and average enthalpy. In addition, the discretization of HE is first made into zones according to the fluid phase, and each zone is further divided into elements, as recommended by Orth et al. (1995) to obtain a stable solution.

5.3.1 Water–cooling evaporator

Figure 5.1 presents simulations results for this case, where the evaporating refrigerant is used for cooling water. Keeping in mind that this analysis is focused on high–effectiveness HE, the temperature profiles for $\varepsilon = 0.99$ are indicated in Fig. 5.1(a) and these results are highlighted in Fig. 5.1(b).

	Variable	Case 5.3.1	Case 5.3.2	Case 5.3.3
Cold stream	Working fluid	R134a	Water	R134a
	Inlet temperature [K]	275	283	280
	Inlet pressure [bar]	3.5	1.0	4.0
	Saturation temperature at inlet pressure [K]	278	373	282
	Mass flow rate [g s^{-1}]	5.0	20.0	2.0
	Mass flux [kg m^{-2} s^{-1}]	250	400	100
Hot stream	Working fluid	Water	R134a	Propane
	Inlet temperature [K]	303	303	293
	Inlet pressure [bar]	1.0	6.7	7.0
	Saturation temperature at inlet pressure [K]	373	298	286.5
	Mass flow rate [g s^{-1}]	20.0	5.0	1.1
	Mass flux [kg m^{-2} s^{-1}]	400	250	16
Geometry	Inner diameter [mm]	5.0	5.0	5.0
	Outer diameter [mm]	10.0	10.0	10.0
	Wall thickness [mm]	0.5	0.5	0.5
	Stream in inner tube	Cold	Hot	Cold
	Flow direction	Horizontal	Horizontal	Vertical

Table 5.1: Input parameters for the three numerical examples

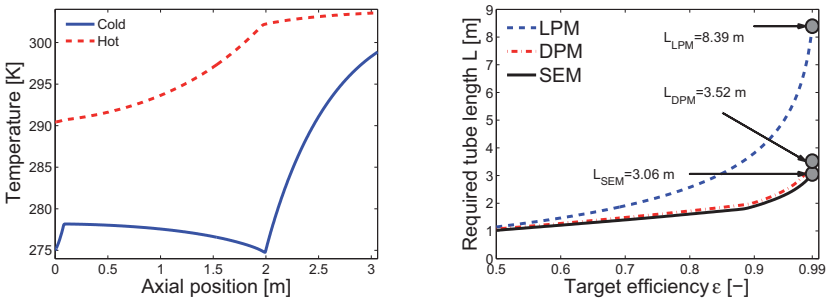

(a) Temperature profiles for $\varepsilon = 0.99$ (b) Required length for a given performance

Figure 5.1: Simulation results for the water-cooling evaporator

The main effect of pressure drop is given by the changes in saturation temperature. This results in a temperature glide during the phase-change region of Fig. 5.1(a) of over 3K, lowering the cold-stream temperature even below its inlet value. As a consequence, the local temperature difference is larger than in a zero-pressure-drop scenario, and thus the heat transfer performance is increased. Then, the same target efficiency of $\varepsilon = 0.99$ can be obtained with a smaller HE:

Fig. 5.1(b) indicates that DPM predict a tube length 15% larger than SEM.

The same trend is observed in Fig. 5.1(b) over the entire range $0.5 \leq \varepsilon \leq 0.99$: the tube length predicted by SEM is always lower than the other models. The DPM curve follows the predictions of SEM quite closely. The differences become larger for $\varepsilon > 0.9$, which corresponds to the full evaporation of the refrigerant. Further heat transfer occurs in the single-phase gas region, characterized by a reduction in the temperature difference, and a larger area (tube length) is required. Then, a sharp increase in the slope of both curves is noticed in Fig. 5.1(b). Nevertheless, the use of DPM is conservative, since it predicts a larger length, and the differences are limited up to 15%. Then no significant error is introduced by the use of DPM.

Although the use of LPM is also conservative, it should not be used for this case, since the differences are very large, predicting more than twice the required length than SEM, specially for high values of ε. In addition, the predictions of LPM are given by a smooth curve, not accounting for the sharp increase for $\varepsilon > 0.9$. This smooth curve is obtained from the basic solution of the $\varepsilon - NTU$ method for evaporators and condensers, as in Eq. (5.9).

$$NTU = \ln\left(\frac{1}{1-\varepsilon}\right) \longrightarrow L_{LPM} = \frac{C_{min}}{\pi D_{in} U} NTU = \frac{C_{min}}{\pi D_{in} U} \ln\left(\frac{1}{1-\varepsilon}\right) \tag{5.9}$$

According to Eq. (5.9), the required length L_{LPM} is inversely proportional to the overall heat transfer coefficient. Observing Fig. 5.1(b), if the required length is overpredicted, this can be a consequence of an underprediction of U. The large variations of two-phase HTC, studied in Section 3.3.3, indicate that it cannot be represented accurately by an average value as proposed by LPMs.

5.3.2 Water–cooled condenser

In a condenser the hot fluid enters as a gas and exits as a liquid. During the phase-change region, the temperature is kept at its saturation temperature, which depends on the local pressure. As in the previous case, a temperature glide of over 3K is observed in the temperature profile, given by Fig. 5.2(a)[1]. This effect reduces the local temperature difference and consequently the heat transfer performance. Then, a larger tube length is required to obtained the same target efficiency, as indicated by Fig. 5.2(b).

The opposite behavior as the previous case is observed in Fig. 5.2(b). For any given value of ε, the DPM predicts a lower length than SEM and, for the extreme highlighted case of $\varepsilon = 0.99$, the relative difference between models is 18%. For lower efficiencies, the differences are smaller. Nevertheless, the use of DPM is not conservative and will lead to the undersizing of the HE. In other words, the desired performance will not be achieved. This effect is further studied in Section 5.4, and

[1]In this figure, as in the previous profile, the cold stream flows from left to right and the hot stream from right to left.

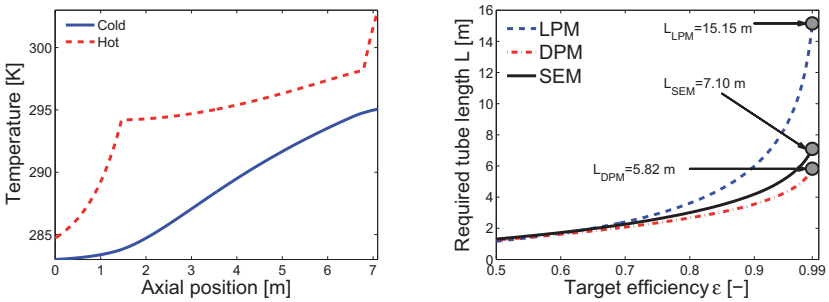

(a) Temperature profiles for $\varepsilon = 0.99$ (b) Required length for a given performance

Figure 5.2: Simulation results for the water-cooled condenser

leads to the conclusion that the consequences of pressure drop on heat transfer should not be neglected.

The use of lumped-parameters models is once again not recommended. Although they are conservative, the overpredictions of required length are too large, over double those by SEM.

5.3.3 Mixed boiler-condenser

The results presented in Sections 5.3.1 and 5.3.2 motivate the analysis of a mixed boiler-condenser system. These type of system are found in LNG and other liquefaction processes where boiling refrigerants, which provide large heat transfer rates, are used to condensate other streams.

In this case, both streams experience a change of phase and their saturation temperatures are affected by pressure drop. Then, the prediction of the overall effect on the heat exchanger performance is not straightforward. The vertical flow configuration is particularly interesting, since gravitational effects produce a pressure increase for a stream flow downwards, and a decrease if it is flowing upwards. Then, in a counter-current flow arrangement one saturation temperature rises and the other one is lowered.

Then, if the cold stream flows downward and the cold upward, the temperature curves get closer to each other and the heat transfer performance is reduced. This is reflected in Fig. 5.3(a), indicating that a larger length is required to fit any given performance in the range $\varepsilon > 0.5$, compared to the prediction of DPM, which neglects the effects of pressure drop. In the extreme case of $\varepsilon = 0.99$, there is a difference of 11.5%. As a consequence, the use of DPM leads to an undersizing of the HE, further studied in Section 5.4.

The opposite behavior is noticed in Fig. 5.3(b), which presents results for the case with the cold stream flowing upward, and the hot stream downwards. In this case, the heat transfer performance is increased and a smaller tube length is

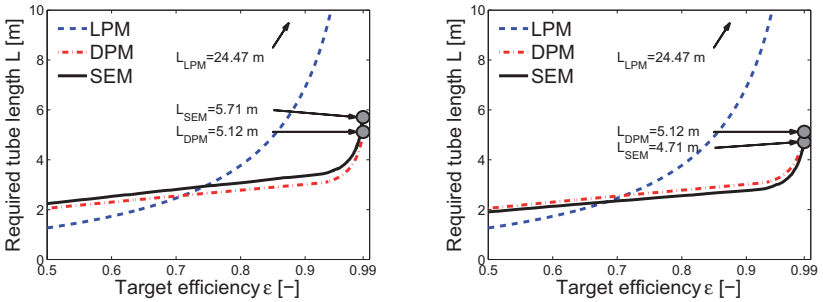

(a) Cold downward, hot upward

(b) Cold upward, hot downward

Figure 5.3: Simulation results for the mixed boiler-condenser. Required length for a given performance.

required. For the extreme case of $\varepsilon = 0.99$, the SEM predicts an 8% smaller length. This difference is not large, and the use of DPM results then in a conservative assumption for this case.

Both LPM and DPM do not account for effects of pressure drop and therefore give exactly the same results for both configurations. The LPM, considering an average heat transfer coefficient, give misleading results that exceed those of distributed models by more than 400%, and therefore is not recommended. The DPM, which considers the variations of fluid properties and heat transfer coefficients, gives more accurate results, within ±10% of SEM. Although this difference is not large, in the case of the hot stream flowing downward, it results in undersizing. Then, this small difference becomes important because the design performance is not achieved.

The analysis using stream-evolution models allows to identify which configuration gives better performance. A smaller tube length is required with the cold stream flowing upward for any given performance, and the difference is 1 meter, that is roughly 20% for $\varepsilon = 0.99$. This increase in performance is achieved by making *good use* of the available pressure drop. In single-phase applications, this statement is usually understood in terms of larger velocities, which result in larger heat transfer coefficients. In two-phase flow scenarios, as this example shows, it should be understood in terms of changes in the saturation temperature.

5.4 Consequences of undersizing

The numerical examples presented in Section 5.3 indicate that neglecting the effects of pressure drop on heat transfer performance leads to an erroneous sizing of the HE. The LPM introduces large errors due to the assumption of constant properties, in particular a uniform heat transfer coefficient. Since this method

presents differences over 100% in predicted tube length with those of SEM, its use is not recommended and therefore is not analysed in this section.

The results from DPM follow the same trend and are similar to those of stream-evolution models, which consider the effects of pressure drop. The differences between models in terms of predicted tube length are limited to maximum of 20%. In some cases, such as the evaporator studied in Section 5.3.1, the DPM overpredicts the tube length. Then its use, neglecting the consequences of pressure drop, is a conservative assumption and the design efficiency is nontheless achieved. However, in other cases, such as the condenser studied in Section 5.3.2, the DPM underestimates the size of the HE, and the desired performance is not obtained.

The consequences of undersizing on heat exchanger performance for the condenser example are summarized in Table 5.2 for selected values of the design efficiency. These values can also be extracted from Fig. 5.2(b). The use of DPM results in a reduction of efficiency of only a few percent. These differences, although small in absolute terms, can result important for high-effectiveness applications, since it has been shown in Chapter 2 that a small degree of underperformance may have a large effect on the overall system behavior, negatively affecting the power consumption or liquefaction rate.

For this reason, these results are better understood in terms of the HE *ineffectiveness* $1-\varepsilon$. The percentual variations in this ineffectiveness are included in the last column of Table 5.2. These results indicate that the consequences of undersizing, in terms of ineffectiveness, are more relevant for high-effectiveness applications, leading to more than triple the design value of $1-\varepsilon$.

Design efficiency	L_{SEM} [m]	L_{DPM} [m]	ε_{DPM}	$\frac{1-\varepsilon_{DPM}}{1-\varepsilon}-1$
$\varepsilon = 0.5$	1.311	1.251	0.4835	3.30 %
$\varepsilon = 0.6$	1.728	1.621	0.5765	5.88 %
$\varepsilon = 0.7$	2.266	2.078	0.6682	10.60 %
$\varepsilon = 0.8$	3.008	2.670	0.7589	20.55 %
$\varepsilon = 0.9$	4.185	3.547	0.8529	47.10 %
$\varepsilon = 0.95$	5.244	4.336	0.9091	81.80 %
$\varepsilon = 0.99$	7.100	5.820	0.9673	227.00 %

Table 5.2: Effects of undersizing for selected design efficiencies. Results for the condenser example presented in Section 5.3.2.

A similar analysis for the mixed boiler-condenser system with the cold stream flowing downwards and the hot stream downwards, is presented in Table 5.3, which corresponds to the plots in Fig. 5.3(a). In this case the consequences on the HE performance are larger, with absolute variations larger than $\Delta\varepsilon = 0.1$, which means that the total heat transferred is reduced in more than 10% of Q_{max}.

The reason why the changes in performance are larger in this case than in the condenser example, is because the sizing curve $L(\varepsilon)$ in Fig. 5.3(a) has a lower slope

Design efficiency	L_{SEM} [m]	L_{DPM} [m]	ε_{DPM}	$\frac{1-\varepsilon_{DPM}}{1-\varepsilon}-1$
$\varepsilon = 0.5$	2.238	2.051	0.4565	8.7 %
$\varepsilon = 0.6$	2.531	2.302	0.5520	19.5 %
$\varepsilon = 0.7$	2.807	2.543	0.6037	32.1 %
$\varepsilon = 0.8$	3.074	2.779	0.6908	54.6 %
$\varepsilon = 0.9$	3.353	3.014	0.7754	124.6 %
$\varepsilon = 0.95$	3.629	3.270	0.8640	172.0 %
$\varepsilon = 0.99$	5.710	5.120	0.9862	38.0 %

Table 5.3: Effects of undersizing for selected design efficiencies. Results for the mixed boiler-condenser example with cold stream flowing downward and hot upward presented in Section 5.3.3.

than in Fig. 5.2(b), except for very large effectiveness $\varepsilon > 0.95$. This behavior is given by the larger overall heat transfer coefficient, since both streams are going through two-phase flow, which gives larger local HTC than single-phase flow, as indicated in Section 3.3.3. For $\varepsilon > 0.9$, the cold stream is full evaporated and some part of the heat is transferred in the single-phase region, thus resulting in the continuous reduction of the temperature difference and a larger slope in the curve $L(\varepsilon)$.

Then in the range $\varepsilon \leq 0.9$, small variations in the predicted length (that is, the vertical axis), represent a larger effect on the effectiveness (horizontal axis). The increases in the HE ineffectiveness $1-\varepsilon$ exceed 100%. For large efficiencies, the situation is reverted, and the consequences of undersizing are smaller, resulting in a 38% increase in ineffectiveness for the extreme case of $\varepsilon = 0.99$.

In short, the use of a DPM, neglecting the effects of pressure drop, results in an undersized HE for these two examples. In both cases, this means that for any given design effectiveness, it is not achieved and the reduction in performance is better understood in terms of the HE ineffectiveness.

5.5 Flow arrangement

For single-phase flow applications it is rather well established that the counter-current flow arrangements gives the best heat transfer performance. In fact, an infinitely large counter-current HE would have an effectiveness of 100% ($\varepsilon = 1.0$), which means that the maximum possible heat is transferred from the hot stream to the cold one, and this condition cannot be achieved with any other arrangement (Incropera and DeWitt, 1996).

For two-phase flow problems, the flow arrangement is considered irrelevant by energy-balance models, since the heat capacity flow rates are infinitely large and the fluid temperature is assumed to be constant at its saturation value. However,

pressure drop affects the saturation temperature as indicated in the temperature profiles presented in Figs. 5.1(a) and 5.2(a). In the particular case of the evaporator, it is noticed that the cold fluid temperature is decreasing during the phase-change region, while its enthalpy is increasing. This situation could be interpreted as a negative heat capacity, although the changes in temperature are not directly related to those in enthalpy, but to the pressure variations.

The HE models based on energy-balances only, described in Sections 2.4.1 and 2.4.2, implicitly consider a positive heat capacity. The inclusion of a negative c_p would alter their conclusions. In fact, the temperature profiles in Fig. 5.1(a), which correspond to a counter-current flow arrangement, are rather similar in the phase-change region $z < 2m$ to those expected from a co-current configuration flowing from right to left.

These considerations motivate the comparative analysis of co- and counter-current evaporators. Figure 5.4(a) presents temperature profiles for a 1.8 m long evaporator with the input parameters described in Table 5.1. In the co-current arrangement (solid lines), the temperature difference is initially large providing large heat transfer rates and a rapid increase in the vapor content. This leads to a larger pressure drop and the consequent reduction of saturation temperature, even below its inlet value, which occurs earlier for co-current (at roughly 1.5 m from the inlet) than in counter-current (1.8 m) flow arrangement. The larger temperature difference gives a higher heat transfer performance which is reflected in the effectiveness, which is increased in a 2.4% from $\varepsilon = 0.885$ to $\varepsilon = 0.909$. In terms of the HE ineffectiveness $1 - \varepsilon$, this means a 26.4% difference. This results indicates that, for this particuar case, the co-current flow arrangement is preferable.

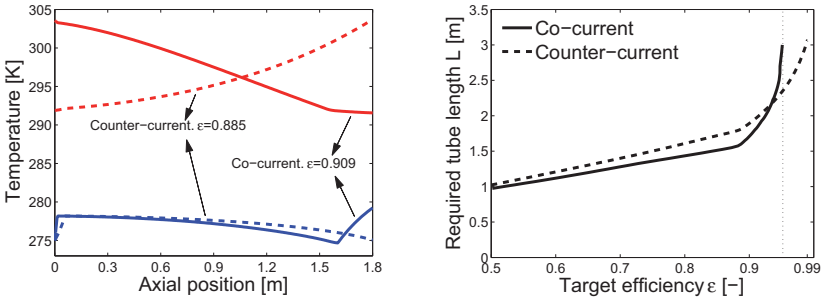

(a) Temperature profiles

(b) Required length to fit a performance

Figure 5.4: Simulation results for the evaporator example in co- and counter-current flow arrangements

Following the same procedure as in Section 5.3, the sizing prediction for a given performance in the range $\varepsilon \geq 0.5$ are presented in Fig. 5.4(b). The results for counter-current flow (dashed line) correspond to those presented earlier in

Fig. 5.1(b). Over a wide of ε, the co-current flow arrangement requires a smaller tube length. In addition the curve $L(\varepsilon)$ for co-current flow has a lower slope which, as discussed in Section 5.4, is related to a higher HTC, given by the rapid increase in vapor content.

The situation is reversed in the high-effectiveness region, and a higher performance is obtained using a counter-current flow arrangement. This can be explained by the fact that, after full evaporation of the cold fluid (which occurs roughly for $\varepsilon = 0.9$), the problem becomes one of purely single-phase HE. Then, this well-known result is recovered and the slope of $L(\varepsilon)$ in Fig. 5.4(b) is higher for co-current flow, and the curves intersect at $\varepsilon = 0.934$. Finally, it should be noticed that, while an infinitely large counter-current HE would achieve 100% effectiveness, this is not possible in co-current flow which is limited by an asymptotic value of $\varepsilon = 0.955$. Therefore, if higher efficiency equipment is required, a counter-current flow arrangement is necessary.

Table 5.4 summarizes the results from Fig. 5.4(b). For selected values of the design efficiency ε the predicted length for counter-current arrangement is presented. In addition, the performance of a co-current HE with the same size is included in the third column. These results are analyzed in terms of variations of ε and the ineffectiveness $1 - \varepsilon$.

Design efficiency	L_{cf} [m]	ε_{pf}	$\varepsilon_{pf} - \varepsilon$	$\frac{1-\varepsilon_{pf}}{1-\varepsilon} - 1$
$\varepsilon = 0.5$	1.023	0.5346	0.0346	-6.92 %
$\varepsilon = 0.6$	1.208	0.6561	0.0561	-14.03 %
$\varepsilon = 0.7$	1.399	0.7768	0.0768	-25.60 %
$\varepsilon = 0.8$	1.608	0.8883	0.0883	-44.15 %
$\varepsilon = 0.9$	1.892	0.9166	0.0166	-16.60 %
$\varepsilon = 0.95$	2.329	0.9412	-0.0088	17.60 %
$\varepsilon = 0.99$	3.060	0.9514	-0.0386	386.00 %

Table 5.4: Comparison of results for the evaporator example in co- and counter-current flow arrangements. The subindices cf and pf stand for counterflow and parallel flow (co-current).

The same conclusions can be obtained from Table 5.4: the co-current flow arrangement gives a better performance, except for high-effectiveness conditions in which case it should be avoided. The increase in performance can be quite large, reducing the ineffectiveness in more than 40%.

5.6 Summary

Changes in pressure affect the fluid physical properties. The main effect for evaporators and condensers is given by the variations in saturation temperature. Then,

the local temperature difference between hot and cold streams is affected, with some consequences on the overall heat exchanger performance.

Three numerical examples are considered in this chapter: an evaporator, a condenser and a mixed boiler-condenser system, described in Section 5.3. Simulation results are presented for lumped- and distributed-parameters models (LPM and DPM), which are based on integrated energy balances, and a stream-evolution model (SEM) that includes a coupled momentum balance equation. The frictional contribution to pressure drop is represented with empirical correlations using the concept of a two-phase multiplier, while acceleration and gravitational effects are modeled in terms of an homogeneous mixture density. The LPM is presented for comparative purposes only, and it should be reminded that its assumptions (constant fluid properties and heat transfer coefficient) are not fulfilled for two-phase flow problems.

In the case of an evaporator, where the cold stream is the one experiencing a phase-change, pressure-drop effects tend to increase the local temperature difference, thus resulting in a higher performance. From a sizing perspective, this leads to a roughly 10 to 15% difference in the required size to fit a given HE performance. Nevertheless, in this case the use of a DPM, ignoring the variations is pressure, is conservative.

An opposite behavior is noticed for the condenser example. In this case, the hot stream is going through a two-phase flow region, and then the variations in its saturation temperature result in a reduction of the local temperature difference. As a consequence, the overall performance is reduced, and from the sizing point of view, this means that a larger tube length is required to fit the specified efficiency. Then, the use of DPM is not recommended, since it would lead to an undersizing of the heat exchanger.

The consequence of undersizing using a DPM is a reduction of the HE effectiveness only a few percent below its design value. However, it should be reminded that for low-temperature systems, a small variation of ε might have a large impact in the overall system performance, thus affecting global variables such as liquefaction rate or power consumption. For this reason, the results are better understood in terms of the HE ineffectiveness $1 - \varepsilon$. From this perspective, the ineffectiveness can be more than tripled for the extreme case of $\varepsilon = 0.99$.

Finally, the characteristics of different flow arrangements are analyzed for the evaporator example. This study was motivated by the temperature profiles presented in Fig. 5.1(a) which, although they correspond to a counter-current arrangement, are similar to those that can be expected from a co-current system. Comparing both configurations, it is noticed that the co-current arrangement gives a better performance (or, from a sizing perspective, requires a smaller equipment for the same performance) over a wide range of design efficiency. This situation is explained by the large initial temperature difference which leads to a rapid generation of vapor. As a consequence, the pressure drop is increased, with positive feedback on the heat transfer performance. The situation is reversed for high-

effectiveness applications, since the co-current flow arrangement is limited by an asymptotic value of $\varepsilon = 0.955$. For higher performance, a counter-current configuration is required.

The results from the analysis in this chapter indicate that the inclusion of pressure drop effects is essential for a macroscopic description of two-phase flow heat exchangers. In the general multiscale framework of this thesis, where the relevant parameters for the larger scales are obtained from microscopic descriptions, this leads to the motivation of an accurate prediction of pressure drop from the analysis of physical effects occurring at lower scales.

Chapter 6

Perturbative methods for optimization and sensitivity analysis

► The main purpose of this chapter is to investigate the applicability of perturbation theory for studying the sensitivity of the heat exchanger performance to the different operating and geometrical parameters at the design stage. As this method is not extensively used in process engineering, a thorough introduction is given, including an example with analytical solution (single-phase heat exchanger). The main advantage of perturbative formulations is that they provide the derivative of an integral response respect to all the working parameters with only one additional simulation.

This formulation is also applied in this chapter to the analysis of an evaporator. Although in this case, the mathematical description becomes more sophisticated, the complexity of the final system of differential equations to be solved is comparable to that of the original physical model. This example is studied in terms of four responses: heat duty, individual pressure drop for each stream and pumping power. For each response, the sensitivity coefficients respect to all parameters (ten in total) are obtained with one additional simulation. This method can be implemented in an optimization algorithm, and two examples are presented.

From a macroscopic perspective and in a process-level formulation, the heat exchanger and any other equipment can be considered as black boxes. In other words, continuum descriptions such as temperature and pressure profiles may be irrelevant and the attention is focused on integral responses. As described in Section 3.4, the most relevant responses are the changes in the pressure and energy of the streams.

In this framework, the optimization and sensitivity analysis represents a fun-

damental stage of design. It consists on studying the effects of different design parameters on selected integral responses. Then the relevant parameters can be identified and design margins and fabrication tolerances can be established.

The traditional formulation for this problem is based on the construction of response surfaces. A set of individually representative values is selected for each parameter and every relevant combination of them is studied. For each of these combinations, the required evolution of a certain objective function is obtained from experiments or simulations. This approach gives a detailed description and allows a straightforward identification of the optimum design. However, this formulation is only applicable in practice to very simple problems, since the required number of simulations grows exponentially with the number of parameters. For example, considering ten individual values for each parameter, a total of 10^6 (one million) simulations are required in the case of six parameters and 10^9 (one billion, that is one thousand millions) in the case of nine.

An interesting alternative to the direct calculation is the methodology of sensitivity and uncertainty analysis. The term *sensitivity* usually concerns the determination of optimal conditions in the design process, while *uncertainty* refers to the measurement errors of parameters which are experimentally obtained. Both techniques consist on estimating the variations of the integral response as a consequence of perturbations in the parameters. In general, these consequences cannot be easily predicted and may in some cases defy intuition for large and complex systems (Cacuci, 2010).

Perturbative methods, further described in Section 6.1 make use of a known solution at a given working point, and the local sensitivity to all parameters can be obtained with only one extra simulation. Sections 6.2 and 6.3 cover their application to two examples: a single-phase and a two-phase heat exchanger, respectively. Finally, the implementation of this technique into an optimization algorithm is discussed in Section 6.4. A summary of this chapter is presented in Section 6.5.

6.1 Perturbative methods

These techniques were initially developed for the analysis of nuclear reactors and have been widely applied in the field of nuclear engineering (de Andrade Lima et al., 1998, and references therein). The list of applications has extended to include the analysis of atmospheric flows (Gabriel et al., 1998; Giménez et al., 2003; Ustinov, 2001) and dynamical systems (Baker et al., 2006; Marchuk et al., 2005). In the field of fluid flow and heat transfer, perturbative methods have been used for research on heat conduction (Pupko, 1966), water hammer (Balio et al., 2001) and other thermalhydraulic phenomena (de Andrade Lima et al., 1993; Oblow, 1978) in single-phase flow, as well as adiabatic air-water flows (Castrillo, 2004).

Three different formulations have been proposed for the development of pertur-

bative methods, although all of them result in the exact same expressions (Gandini, 2001). While differential and variational descriptions are focused on the mathematical perspective, the heuristic generalized perturbation theory (Gandini, 1967; 1987) is more physically oriented and is presented in this section.

6.1.1 The basic idea

The generalized perturbation theory (GPT) is based upon the conservation and balance equation for an importance function, defined in Lewins (1965). The physical significance of this importance function is the contribution of a local perturbation to the integral response of interest. For example, in the analysis of in-tube flow and observing the response in terms of overall pressure drop, the importance function would be higher in the regions where the velocity gradients are larger.

The basic procedure for sensitivity analysis by means of GPT consists on three consecutive steps as follows.

1. Solve the original problem at a given working point, obtaining a continuum description for all the variables.

2. Select an integral response of interest. It is usually not simple to define a unique figure of merit to establish the meaning of an optimum design. For this reason many problems result in a multiobjective optimization process. Nevertheless, perturbative methods are based on individual responses which can later be combined. Once the response is selected, the next step is the solution of the importance problem, which is closely related to the original one, and a continuum description for the importance function is obtained.

3. Finally, sensitivity coefficients for all the parameters can be computed from both solutions obtained in steps 1 and 2.

The main advantage of this technique is that relevant information for all the parameters can be obtained with only one additional simulation, given by the importance problem. On the negative side, the information provided by this method is strictly local around the operating point. The differences between GPT and the traditional formulation are summarized in Table 6.1.

6.1.2 Mathematical formulation of the GPT

Consider a generic problem as presented earlier in Section 4.1, as follows.

$$\mathcal{L}\mathfrak{u}(\mathbf{r}) = \mathfrak{f}(\mathbf{r}) \qquad \text{for} \quad \mathbf{r} \in \Omega \tag{4.1}$$

In general, both the problem operator $\mathcal{L}$ and the known source term $\mathfrak{f}$ depend on a set of n_p parameters $\{p_j\}_{j=1}^{n_p}$ which can be expressed in vector form as $\mathbf{p}$. For reasons of compactness, the problem given Eq. (4.1) is condensed in terms of

	Traditional approach	Perturbative methods with GPT
Basic mechanism	Construction of a response surface	Sensitivity coefficients
Obtained result	Local value of the response at the selected operating conditions	Local value and gradient of the response at the operating conditions
Number of simulations	With one additional simulation for each parameter, an approximate gradient can be obtained	The exact gradient is obtained with only 2 simulations
Applicability	In practice, only for small problems with few parameters	Only for linear problems (or linearized in an iterative scheme), due to the complex algebra

Table 6.1: Comparison of traditional and GPT formulations for sensitivity analysis

the governing system of equations $\mathfrak{m}$ as defined in Eq. (6.1), which includes the boundary conditions by making proper use of delta functions.

$$\mathfrak{m}(\mathfrak{u}(\mathbf{r}), \mathbf{p}) \equiv \mathcal{L}\mathfrak{u}(\mathbf{r}, \mathbf{p}) - \mathfrak{f}(\mathbf{r}, \mathbf{p}) = \mathbf{0} \quad \text{for } \mathbf{r} \in \Omega \tag{6.1}$$

The GPT is focused on integral responses $\mathcal{Q}$ which can be expressed in terms of the inner product $\langle , \rangle_{\mathcal{V}(\Omega)}$ of the solution $\mathfrak{u}(\mathbf{r})$ and a weighting function $\mathfrak{W}(\mathbf{r}, \mathbf{p})$ as in Eq. (6.2). In this context, the information about the response is summarized in the weighting function $\mathfrak{W}(\mathbf{r}, \mathbf{p})$.

$$\mathcal{Q} = \langle \mathfrak{u}(\mathbf{r}), \mathfrak{W}(\mathbf{r}, \mathbf{p}) \rangle_{\mathcal{V}(\Omega)} \tag{6.2}$$

The definition given in Eq. (6.2) is very general and thus allows to consider several types of responses. For example, considering the inner product related to the L_∞ norm, the maximum value of $\mathfrak{u}(\mathbf{r})$ in the domain Ω can be evaluated. Such analysis is interesting for the study of safety transients, for example observing the maximum temperature achieved in a given material. However, this analysis exceeds the scope of this chapter. Therefore, and only the canonic inner product is considered, represented simply by the integral of the product, as in Eq. (6.3), where $\mathfrak{w}_1^t$ is the transpose of $\mathfrak{w}_1$.

$$\langle \mathfrak{w}_1, \mathfrak{w}_2 \rangle_{\mathcal{V}(\Omega)} = \int_\Omega \mathfrak{w}_1^t \mathfrak{w}_2 d\Omega \qquad \forall\ \mathfrak{w}_1, \mathfrak{w}_2 \in \mathcal{V}(\Omega) \tag{6.3}$$

Following this definition of the inner product, two simple examples of integral responses are presented in Eq. (6.4). With a uniform weighting function, the mean

value can be evaluated as in Eq. (6.4a). Using localized weighting functions the local value at a given point can be considered as in Eq. (6.4b).

$$\mathcal{Q} = \text{Mean value } = \frac{\int_\Omega \mathfrak{u}(\mathbf{r}) d\Omega}{\text{Volume of } \Omega} \longrightarrow \mathfrak{W}(\mathbf{r}, \mathbf{p}) = \frac{1}{\text{Volume of } \Omega} \tag{6.4a}$$

$$\mathcal{Q} = \mathfrak{u}(\mathbf{r}_0) = \int_\Omega \mathfrak{u}(\mathbf{r}) \delta(\mathbf{r} - \mathbf{r}_0) d\Omega \longrightarrow \mathfrak{W}(\mathbf{r}, \mathbf{p}) = \delta(\mathbf{r} - \mathbf{r}_0) \tag{6.4b}$$

The sensitivity analysis consists on studying the variations in the response $\mathcal{Q}$ as a consequence of perturbations in the parameter p_j. Then, individual sensitivity coefficients s_j are defined as in Eq. (6.5).

$$s_j = \frac{\partial \mathcal{Q}}{\partial p_j} = \left\langle \underbrace{\frac{\partial \mathfrak{u}}{\partial p_j}(\mathbf{r})}_{\text{unknown}}, \underbrace{\mathfrak{W}(\mathbf{r}, \mathbf{p})}_{known} \right\rangle_{\mathcal{V}(\Omega)} + \left\langle \underbrace{\mathfrak{u}(\mathbf{r})}_{known}, \underbrace{\frac{\partial \mathfrak{W}}{\partial p_j}(\mathbf{r}, \mathbf{p})}_{known} \right\rangle_{\mathcal{V}(\Omega)} \tag{6.5}$$

Once the original system of equations $\mathfrak{m}$ was solved for $\mathfrak{u}(\mathbf{r})$, all the terms in Eq. (6.5) are known, except for $\frac{\partial \mathfrak{u}}{\partial p_j}(\mathbf{r})$. In general, the problem $\mathfrak{m}$ is solved numerically and an analytical expression for $\mathfrak{u}(\mathbf{r})$ may be unavailable and therefore this derivative cannot be obtained directly.

A governing equation for this unknown term can be obtained from a variational analysis. The effect of a perturbation δp_j on the parameter in the original system $\mathfrak{m}(\mathbf{r}, \mathbf{p})$ is expressed as in Eq. (6.6). This equation represents the total derivative respect of p_j following the chain rule.

$$\frac{\partial \mathfrak{m}}{\partial p_j} = \mathcal{H} \frac{\partial \mathfrak{u}}{\partial p_j} + \frac{\partial \mathfrak{m}}{\partial p_j} = \mathbf{0} \tag{6.6}$$

The Jacobian matrix $\mathcal{H}$ includes the Fréchet derivative (Stickel, 1987) of each equation in $\mathfrak{m}$ respect to each variable $\mathfrak{u}(\mathbf{r})$[1]. Then, for a system of N equations with the same number of variables it results in Eq. (6.7).

$$\mathcal{H}_{i,j} = \frac{\bar{\partial} \mathfrak{m}_i}{\bar{\partial} \mathfrak{u}_j} \forall\ i, j = 1, \ldots, N \longrightarrow \mathcal{H} = \begin{bmatrix} \frac{\bar{\partial} \mathfrak{m}_1}{\bar{\partial} \mathfrak{u}_1} & \cdots & \frac{\bar{\partial} \mathfrak{m}_1}{\bar{\partial} \mathfrak{u}_N} \\ \vdots & \ddots & \vdots \\ \frac{\bar{\partial} \mathfrak{m}_N}{\bar{\partial} \mathfrak{u}_1} & \cdots & \frac{\bar{\partial} \mathfrak{m}_N}{\bar{\partial} \mathfrak{u}_N} \end{bmatrix} \tag{6.7}$$

[1]The traditional calculus derivative $\partial f / \partial x$ represents the variation in a function f produced by changes in the variable x, and the result is a new function. In simple terms, the Fréchet derivatives $\bar{\partial} f / \bar{\partial} g$ are an extension of this concept in the case where f results from the application of a transformation onto g. Therefore, they account for the variations in a function f given by a perturbation in another function g, and the result is a linear or non-linear operator.

Equation (6.6) can be solved individually for each parameter p_j. Then, introducing the solution in Eq. (6.5), individual sensitivity coefficients would be obtained. This approach implies the solution of n_p systems of partial differential equations.

The GPT, making use of the importance function allows the computation of sensitivity coefficients for all the n_p parameters with only one extra simulation. This formulation was first developed for the analysis of neutron and other particles density distribution. In this context, the importance is understood as the contribution to the integral response, of individual particles inserted in the position $\mathbf{r}$, hence the name *importance*. In general terms, the influence of an external source $\mathfrak{s}(\mathbf{r})$ on the response the response is obtained by weighting it with the importance function $\mathfrak{u}^*$, that is $\langle \mathfrak{u}^*, \mathfrak{s} \rangle$.

It can be observed in Eq. (6.6) that the source term for the field $\dfrac{\partial \mathfrak{u}}{\partial p_j}$ is $\mathfrak{s} = -\dfrac{\partial \mathfrak{m}}{\partial p_j}$. Then, following the concept of importance described above, its contribution to the integral response is given by:

$$\left\langle \frac{\partial \mathfrak{u}(\mathbf{r})}{\partial p_j}, \mathfrak{W}(\mathbf{r}, \mathbf{p}) \right\rangle_{\mathcal{V}(\Omega)} \equiv \left\langle \mathfrak{u}^*(\mathbf{r}), -\frac{\partial \mathfrak{m}(\mathbf{r}, \mathbf{p})}{\partial p_j} \right\rangle_{\mathcal{V}(\Omega)} \tag{6.8}$$

The main advantage of this description is that the dependence of the right-hand-side on the different parameters is reduced to a known term, that is the derivative of the system equations $\mathfrak{m}$ respect to each parameter p_j. Then, introducing Eq. (6.8) into Eq. (6.5), all sensitivity coefficients are described in terms of only one unknown term, the importance function $\mathfrak{u}^*(\mathbf{r})$, which is unique and not dependent on the selected parameter.

At this point, the only remaining issue is to obtain a governing equation for the importance function. Following the concept of conservation of importance (Usachev, 1964), $\mathfrak{u}^*$ satisfies Eq. (6.9), which is hitherto referred to as the importance problem. It can be deduced from Eq. (6.9) that the importance function is directly related to the selected integral response, characterized by the weighting function $\mathfrak{W}(\mathbf{r}, \mathbf{p})$. In other words, the importance is defined respect to a given response.

$$\mathcal{H}^* \mathfrak{u}^* = \mathfrak{W} \tag{6.9}$$

The importance operator $\mathcal{H}^*$ can be obtained directly from $\mathcal{H}$ following some reversion rules (Gandini, 1987). These rules only apply for linear operators and they include transposing matrix elements, changing the sign of odd-order derivatives, as well as transposing the order of operators and the location of delta functions.

Finally, once Eq. (6.9) is solved for $\mathfrak{u}^*$, the sensitivity coefficient for all parameters can be computed according to Eq. (6.10).

$$s_j = \frac{\partial \mathcal{Q}}{\partial p_j} = \left\langle \mathfrak{u}(\mathbf{r}), \frac{\partial \mathfrak{W}}{\partial p_j}(\mathbf{r}, \mathbf{p}) \right\rangle_{\mathcal{V}(\Omega)} - \left\langle \mathfrak{u}^*(\mathbf{r}), \frac{\partial \mathfrak{m}}{\partial p_j}(\mathbf{r}, \mathbf{p}) \right\rangle_{\mathcal{V}(\Omega)} \tag{6.10}$$

The procedure described in this section is summarized in Fig. 6.1. It consists of basically three steps: original problem, importance problem, and calculation of sensitivity coefficients. It should be noted that a given parameter p_j is not selected until the final step, that is after all simulations were performed. Consequently, all the sensitivity coefficients can be obtained with only one extra simulation, that is the solution of the importance problem.

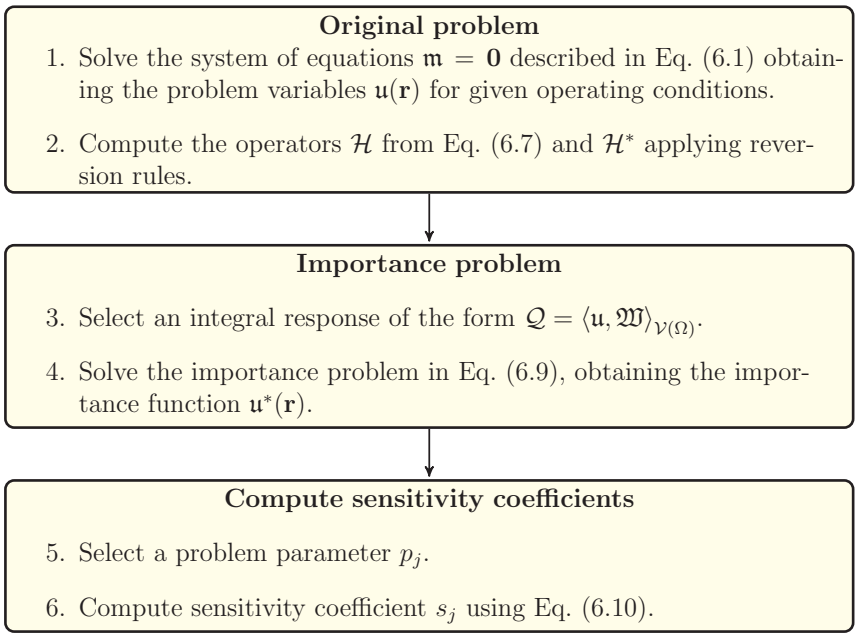

Figure 6.1: Sequential steps in the calculation of sensitivity coefficients using GPT

6.2 Simple case with analytical solution

In order to clarify the mathematical description from Section 6.1.2 a simple example with analytical solution and only one parameter is provided in this section.

Consider a balanced counter-current single-phase heat exchanger as described in Section 4.2. This problem is governed by the energy balance given by Eq. (6.11) for both cold and hot streams, where θ indicates non-dimensional temperatures.

$$\frac{\partial \theta_{cold}}{\partial z} + NTU\,(\theta_{cold} - \theta_{hot}) = 0 \tag{6.11a}$$

$$-\frac{\partial \theta_{hot}}{\partial z} + NTU\,(\theta_{hot} - \theta_{cold}) = 0 \tag{6.11b}$$

The inlet boundary conditions for Eqs. (6.11a) and (6.11b) are $\theta_{cold}(z=0)=0$ and $\theta_{hot}(z=1)=1$, respectively. Following the scheme described in Fig. 6.1, the application of GPT to a particular problem consists of basically three steps, which are described in the following subsections.

6.2.1 Original problem

The GPT formulation implies the inclusion of the boundary terms into the governing equations by making proper use of delta functions. In this case, this scenario is represented by Eq. (6.12).

$$\mathfrak{m}_{cold} = \frac{\partial \theta_{cold}}{\partial z} + NTU\,(\theta_{cold} - \theta_{hot}) + \theta_{cold}(z)\delta(x) = 0 \tag{6.12a}$$

$$\mathfrak{m}_{hot} = -\frac{\partial \theta_{hot}}{\partial z} + NTU\,(\theta_{hot} - \theta_{cold}) + [\theta_{hot}(z) - 1]\,\delta(x-1) = 0 \tag{6.12b}$$

The generic mathematical formulation in Eq. (6.1) corresponds in this case to the operators listed in Eq. (6.13). This is a very simple case and the only parameter in this problem is the number of transfer units, that is NTU.

.

$$\mathfrak{u} = \begin{bmatrix} \theta_{cold} \\ \theta_{hot} \end{bmatrix}, \mathfrak{m} = \begin{bmatrix} \mathfrak{m}_{cold} \\ \mathfrak{m}_{hot} \end{bmatrix} \tag{6.13a}$$

$$\mathbf{r} = z \in \Omega = [0,1]\,, \mathbf{p} = NTU \tag{6.13b}$$

The solutions of the direct problem were listed in Table 4.2, and for this particular counter-current balanced case result as in Eq. (6.14).

$$\theta_{cold}(z) = z\,\frac{NTU}{NTU+1} \tag{6.14a}$$

$$\theta_{hot}(z) = z\,\frac{NTU}{NTU+1} + \frac{1}{NTU+1} \tag{6.14b}$$

The next step is the computation of the Jacobian matrix $\mathcal{H}$, which includes the Fréchet derivatives of the problem operator $\mathfrak{m}$ respect to the variables $\mathfrak{u}$. In simple cases such as Eq. (6.12), it can be computed directly in a similar way as traditional calculus derivatives, resulting in Eq. (6.15).

$$\mathcal{H} = \frac{\bar{\partial}\mathfrak{m}}{\bar{\partial}\mathfrak{u}} = \begin{bmatrix} \dfrac{\partial}{\partial z} + \delta(x) + NTU & -NTU \\ -NTU & -\dfrac{\partial}{\partial z} + \delta(x-1) + NTU \end{bmatrix} \tag{6.15}$$

An associate importance operator $\mathcal{H}^*$ is obtained from $\mathcal{H}$, applying some reversion rules. These rules include changing the sign of odd-order derivatives, transposing matrix elements and altering the location of delta functions from one border to the other and result in the expression in Eq. (6.16).

$$\mathcal{H}^* = \begin{bmatrix} -\dfrac{\partial}{\partial z} + \delta(x-1) + NTU & -NTU \\ -NTU & \dfrac{\partial}{\partial z} + \delta(x) + NTU \end{bmatrix} \tag{6.16}$$

6.2.2 Importance problem

As discussed in Section 6.1.2, several integral responses $\mathcal{Q}$ can be defined for a given problem. In this particular case, the most interesting result is the total heat transfer Q or, in dimensionless terms, the HE effectiveness ε. Recalling Eq. (6.2), and defining the response in terms of a weighting function $\mathfrak{W}(\mathbf{r}, \mathbf{p})$, the expression in Eq. (6.17) for ε is obtained.

$$\mathcal{Q} = \varepsilon = \int_{z=0}^{z=1} NTU\,[\theta_{hot} - \theta_{cold}]\,dz \longrightarrow \mathfrak{W}(\mathbf{r}, \mathbf{p}) = \begin{bmatrix} -NTU \\ NTU \end{bmatrix} \tag{6.17}$$

The importance problem given by Eq. (6.9) is specific for each response, since the weighting function $\mathfrak{W}(\mathbf{r}, \mathbf{p})$ represents the source term. Then, after establishing this response as the HE effectiveness, the governing equations for the importance function $\mathfrak{u}^*$ are indicated in Eq. (6.18).

$$-\frac{\partial \theta^*_{cold}}{\partial z} + NTU\,(\theta^*_{cold} - \theta^*_{hot}) = -NTU \tag{6.18a}$$

$$\frac{\partial \theta^*_{hot}}{\partial z} + NTU\,(\theta^*_{hot} - \theta^*_{cold}) = NTU \tag{6.18b}$$

The boundary conditions for Eqs. (6.18a) and (6.18b) are derived from the delta functions in the operator $\mathcal{H}^*$, see Eq. (6.16). Then in this case they are $\theta^*_{cold}(z = 1) = 0$ and $\theta^*_{hot}(z = 0) = 0$, respectively. It is important to notice that these boundary conditions are usually homogeneous and located in opposite border than the original ones.

An important characteristic of the importance problem is that it is always as well-posed as the original one. Then, this problem also has an analytical solution for the cold and hot importances as given by Eq. (6.19).

$$\theta^*_{cold}(z) = \frac{NTU}{NTU+1}(z-1) \tag{6.19a}$$

$$\theta^*_{hot}(z) = \frac{NTU}{NTU+1}z \tag{6.19b}$$

Three observations can be made from Eqs. (6.19a) and (6.19b):

- The importance of the cold temperature is always negative for any given position with an homogeneous boundary condition, that is $\theta^*_{cold} \leq 0$. This means that a positive perturbation in the local cold temperature has always a negative effect in the response. In physical terms, the local temperature difference is reduced, thus lowering the HE effectiveness ε.
- Similarly, the importance of the hot temperature is always positive, in other terms $\theta^*_{hot} \geq 0$ and this is explained for the same reasons.
- The net importance $\theta^*_{hot} - \theta^*_{cold}$ is constant for any value of z. This occurs because the local temperature difference $\theta_{hot} - \theta_{cold}$, and consequently the local heat flux, are also uniform.

6.2.3 Sensitivity coefficient

At this point, the two relevant systems of differential equations (direct and importance problems) are already solved. Then, the sensitivity coefficient respect of any parameter (in this particular case there is only one) can be computed according to Eq. (6.10) on the basis of the results obtained in Sections 6.2.1 and 6.2.2.

$$s_j = \frac{\partial \mathcal{Q}}{\partial p_j} = \left\langle \mathfrak{u}(\mathbf{r}), \frac{\partial \mathfrak{W}}{\partial p_j}(\mathbf{r},\mathbf{p}) \right\rangle_{\mathcal{V}(\Omega)} - \left\langle \mathfrak{u}^*(\mathbf{r}), \frac{\partial \mathfrak{m}}{\partial p_j}(\mathbf{r},\mathbf{p}) \right\rangle_{\mathcal{V}(\Omega)} \tag{6.10}$$

Replacing $\mathfrak{u}(\mathbf{r})$ from Eq. (6.14), $\mathfrak{W}(\mathbf{r},\mathbf{p})$ from Eq. (6.17), and $\mathfrak{u}^*$ from Eq. (6.19) into Eq. (6.10) the following expression for the sensitivity coefficient is obtained.

$$\begin{aligned}
\left.\frac{\partial \varepsilon}{\partial NTU}\right|_{GPT} &= \left\langle \begin{bmatrix} \theta_{cold} \\ \theta_{hot} \end{bmatrix}, \begin{bmatrix} -1 \\ 1 \end{bmatrix} \right\rangle - \left\langle \begin{bmatrix} \theta^*_{cold} \\ \theta^*_{hot} \end{bmatrix}, \begin{bmatrix} \theta_{cold} - \theta_{hot} \\ \theta_{hot} - \theta_{cold} \end{bmatrix} \right\rangle \\
&= \int_{z=0}^{z=1} \left[\frac{1}{NTU+1} \right] dz - \int_{z=0}^{z=1} \left[\frac{NTU}{(NTU+1)^2} \right] dz \\
&= \frac{1}{(NTU+1)^2}
\end{aligned} \tag{6.20}$$

The calculation of Eq. (6.20) includes the computation of two integrals of known functions. This result can be compared to the analytical derivative of ε, defined in by Eq. (6.17), respect to the parameter NTU, as in Eq. (6.21).

$$\begin{aligned}\left.\frac{\partial \varepsilon}{\partial NTU}\right|_{analytical} =& \frac{\partial}{\partial NTU}\left\{\int_{z=0}^{z=1} NTU\left[\theta_{hot}(z)-\theta_{cold}(z)\right] dz\right\} \\ =& \frac{\partial}{\partial NTU}\left[\frac{NTU}{NTU+1}\right] \\ =& \frac{1}{(NTU+1)^2}\end{aligned} \tag{6.21}$$

Comparing Eqs. (6.20) and (6.21), it is observed that the GPT method gives the exact value of the sensitivity coefficient. On the one hand, Eq. (6.20) can always be applied even when the solutions for $\mathfrak{u}(\mathbf{r})$ and $\mathfrak{u}^*(\mathbf{r})$ were obtained numerically and are only known at discrete points. On the other hand, the direct analytical computation as in Eq. (6.21) is usually not possible, since an analytical description is generally not available. In this difference lays the main advantage of the GPT formulation and perturbative methods in general.

6.3 A two-phase heat exchanger

The example presented in this section further increases the completeness of this framework of sensitivity analysis accounting for two-phase flow. The physical model is governed by momentum and energy balances for cold and hot streams, as given by Eqs. (5.5) and (5.6). These expressions are rather general and some assumptions are required in order to reduce the complexity of the importance problem, which might otherwise in some cases become overwhelming.

1. The study case corresponds to an evaporator. Then, the cold stream enters as a liquid, goes through a phase-change region and exits as a gas, while the hot stream remains in single-phase flow.

2. A counter-current flow arrangement is considered, and tube-in-tube geometry presented in Fig. 4.7 is selected, with the cold stream in the inner tube.

3. The flow orientation is horizontal and therefore, gravitational effects in the momentum equation can be disregarded.

4. All single-phase physical properties are assumed to be constant, at their saturated values for the cold stream, and at the inlet value for the hot stream.

5. The energy balance for the boiling stream is represented in terms of the specific enthalpy h. In the case of the hot stream, the evolution of the temperature is studied, considering a constant specific heat capacity c_p.

6. The local temperature of the cold stream depends on both the fluid enthalpy and pressure. In the single-phase region, it is only dependent on the enthalpy, and it is computed on the basis of an specific heat capacity. For two-phase flow, the temperature is fixed at its saturation value, which depends on the local pressure. Considering that the variations in pressure are relatively small, the changes in the saturation temperature can be approximated using the Clausius-Clapeyron relation (Çengel and Boles, 1994), as in Eq. (6.22).

$$\begin{aligned} T_{sat}(p) &\approx T_{sat}(p_{in}) + (p - p_{in}) \left.\frac{\partial T_{sat}}{\partial p}\right|_{p_{in}} \\ &\approx T_{sat}(p_{in}) + \frac{p - p_{in}}{p_{in}} \frac{\bar{R}}{MW} \frac{T_{sat}^2(p_{in})}{\Delta h_{LG}} \end{aligned} \tag{6.22}$$

The variables MW, $\bar{R}$ and Δh_{LV} are the molecular weight, specific universal gas constant and specific heat of evaporation, respectively. Then, the local temperature is given by a three-branches function as in Eq. (6.23).

$$T_{cold} = \begin{cases} T_{cold,in} + \dfrac{h_{cold} - h_{in}}{c_{p,cold,L}} & \text{for } h_{cold} < h_L \\ T_{sat}(p) \text{ as in Eq. (6.22)} & \text{for } h_L \leq h_{cold} \leq h_V \\ T_{sat}(p) + \dfrac{h_{cold} - h_V}{c_{p,cold,V}} & \text{for } h_{cold} > h_V \end{cases} \tag{6.23}$$

7. An homogeneous mixture model is considered for the two-phase flow region. Then, the cold fluid density ρ_{cold} is given by Eq. (6.24), where the mass quality x can be computed (assuming thermal equilibrium) directly from the enthalpy as $x = (h - h_L)/\Delta h_{LV}$.

$$\rho_{cold} = \begin{cases} \rho_L & \text{for } h_{cold} < h_L \\ \rho_h = \left[\dfrac{x}{\rho_G} + \dfrac{1-x}{\rho_L}\right]^{-1} & \text{for } h_L \leq h_{cold} \leq h_V \\ \rho_G & \text{for } h_{cold} > h_V \end{cases} \tag{6.24}$$

In addition, the two-phase multiplier takes into account the changes in density, and in this homogeneous description results in $\Phi_L^2 = \rho_{L,cold}/\rho_{cold}$. As in Section 5.2, the Haaland formula is selected for the single-phase friction factor f_L. Then, the shear stress for the cold stream results in:

$$\tau_{cold,L} = f_{cold,L}\frac{G_{cold}^2}{2\rho_L} \rightarrow \tau_{cold} = \tau_{cold,L}\Phi_{cold,L}^2 = f_{cold,L}\frac{G_{cold}^2}{2\rho_{cold}} \tag{6.25}$$

8. For the selected geometry, the overall heat transfer coefficient U can be computed according to Eq. (4.44). Since the boiling HTC is much larger than in single-phase forced convection, the dominant heat transfer resistance is located in the hot stream side. Then, for this special case, U can be considered equal to $\hat{h}_{hot}$, that is the hot-side HTC. Furthermore, recalling assumption number 4, the overall HTC is also constant.

With all these considerations a perturbative analysis for this problem is presented following the same structure as in the previous examples. Then, the direct problem is analyzed in Section 6.3.1 for given operating conditions. In Section 6.3.2, the importance problem is studied for different integral responses, and the sensitivity coefficient for all the parameters are discussed in Section 6.3.3.

6.3.1 Direct problem

Considering all the assumptions described above, the governing equations are given by the momentum and energy balances presented in Eqs. (6.26) to (6.29). For their later analysis with GPT, the inlet boundary conditions were incorporated with proper delta functions, and the equations were normalized to the derivative term. In addition, the relative axial position $z \in [0, 1]$ is considered, allowing to account explicitly for the tube length L as an additional parameter. The cold fluid enters in $z = 0$, and the hot stream in $z = 1$, flowing in opposite directions.

$$\begin{aligned}\mathfrak{m}_{p,cold} =& \frac{\partial p_{cold}}{\partial z} + 2\frac{L}{Dh_{cold}}\frac{f_{cold}G_{cold}^2}{\rho_{cold}(z)} + G_{cold}^2\frac{\partial}{\partial z}\left(\frac{1}{\rho_{cold}}\right) \\ &+ [p_{cold} - p_{cold,in}]\,\delta(z) = 0 \end{aligned} \tag{6.26}$$

$$\mathfrak{m}_{p,hot} = -\frac{\partial p_{hot}}{\partial z} + 2\frac{L}{Dh_{hot}}\frac{f_{hot}G_{hot}^2}{\rho_{hot}} + [p_{hot} - p_{hot,in}]\,\delta(z-1) = 0 \tag{6.27}$$

$$\begin{aligned}\mathfrak{m}_{h,cold} =& \frac{\partial h_{cold}}{\partial z} + \frac{4U}{G_{cold}}\frac{L}{Deq_{cold}}[T_{cold}(z) - T_{hot}(z)] \\ &+ [h_{cold} - h_{cold,in}]\,\delta(z) = 0 \end{aligned} \tag{6.28}$$

$$\begin{aligned}\mathfrak{m}_{T,hot} =& -\frac{\partial T_{hot}}{\partial z} + \frac{4U}{G_{hot}c_{p,hot}}\frac{L}{Deq_{cold}}[T_{hot}(z) - T_{cold}(z)] \\ &+ [T_{hot} - T_{hot,in}]\,\delta(z-1) = 0 \end{aligned} \tag{6.29}$$

The problem variables and equations are summarized in Eq. (6.30).

$$\mathfrak{u} = \begin{bmatrix} p_{cold} \\ p_{hot} \\ h_{cold} \\ T_{hot} \end{bmatrix}, \mathfrak{m} = \begin{bmatrix} \mathfrak{m}_{p,cold} \\ \mathfrak{m}_{p,hot} \\ \mathfrak{m}_{h,cold} \\ \mathfrak{m}_{T,hot} \end{bmatrix} \tag{6.30}$$

The study case corresponds to the evaporator example described earlier in Section 5.3.1, and the selected values for the parameters were listed in Table 5.1. These are as follows:

- Physical properties of the hot stream, such as ρ_{hot}, μ_{hot} and $c_{p,hot}$. For a given working fluid, they depend on the inlet temperature

- Saturated physical properties of the cold stream including $\rho_{cold,L}$, $\rho_{cold,V}$, $\mu_{L,cold}$, $c_{p,cold,L}$, $c_{p,cold,V}$, Δh_{LV}, $T_{sat}(p_{cold,in})$ and others that might be relevant for computing the heat transfer coefficient. For a given fluid (R134a), with a given molecular weight (in this case MW=0.102 kg mol^{-1}), these properties depend on the inlet pressure $p_{cold,in}$.

- Both hydraulic and equivalent diameters (Dh and Deq, respectively) and the cross-sectional areas are determined by three physical parameters: inner tube diameter D_i, tube wall thickness t_w and outer tube diameter D_o. In addition, the tube length L=4 m has also been included explicitly in the governing equations.

- The mass flow rate of each fluid is characterized by their mass flux. In this case, they are G_{cold}=250 kg m^{-2} s^{-1} and G_{hot}=400 kg m^{-2} s^{-1}.

- In strict terms, the overall heat transfer coefficient is a complex function of all the parameters listed above. For simplicity, a constant value of U=1000 Wm^{-2}K^{-1} is considered, and it is included as an individual parameter. This value was obtained from a Dittus-Bolter correlation for the hot water, slightly reduced by additional heat transfer resistance in the boiling stream.

Figure 6.2 presents the solution of the direct problem for the (a) momentum and (b) energy equations.

As a consequence of having constant fluid properties, the pressure gradient for the hot stream is constant, thus giving a linear pressure profile, with a total pressure drop of $\Delta p_{hot} = 0.164$ bar. In the case of the hot stream, the homogeneous density is reduced during the two-phase region, thus giving an increasingly larger friction, and an acceleration component of pressure drop. Then, the pressure profile is better represented by a quadratic function, until full evaporation is reached at $z > 0.90$, and the pressure gradient is once again constant and rather large. The overall pressure drop for the cold stream is $\Delta p_{cold} = 1.038$ bar, that is roughly 30% of the inlet value.

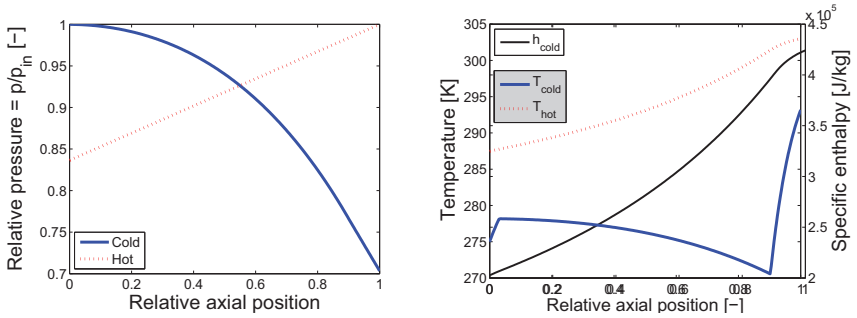

(a) Pressure profiles (b) Temperature profile

Figure 6.2: Solution to the direct problem in an evaporator

The solutions for the energy equation are presented in Fig. 6.2(b) in terms of both temperature and enthalpy profiles. The temperature glide during the two-phase region is over 7.5 K and is a consequence of pressure drop and its effect on the saturation temperature. The profiles for $h_{cold}(z)$ and $T_{hot}(z)$ indicate that the heat flux during the two-phase region is exponential, as would be expected from a co-current flow arrangement. Finally, the local heat flux (given by the gradient of the specific enthalpy) is largely reduced after full evaporation, as a consequence of the reduction in the temperature difference.

After the solution of the direct problem for the given operating conditions (that is, the selected values for the parameters), the Jacobian matrix $\mathcal{H} = \frac{\partial \mathfrak{m}}{\partial \mathfrak{u}}$ can be obtained as in Eq. (6.31). For reasons of compactness, some coefficients k_1 to k_8 are defined as in Eqs. (6.32a) to (6.32h).

$$\mathcal{H} = \begin{bmatrix} \frac{\partial}{\partial z} + \delta(z) & 0 & k_1 + k_2\frac{\partial}{\partial z} & 0 \\ 0 & -\frac{\partial}{\partial z} + \delta(z-1) & 0 & 0 \\ k_3 & 0 & \frac{\partial}{\partial z} + \delta(z) + k_4 & k_5 \\ k_6 & 0 & k_7 & -\frac{\partial}{\partial z} + \delta(z-1) + k_8 \end{bmatrix} \tag{6.31}$$

$$k_1 = 2f_{cold}\frac{L}{Deq_{cold}}G_{cold}^2\frac{\partial}{\partial h_{cold}}\left(\frac{1}{\rho_{cold}}\right) \qquad \Rightarrow [k_1] = \frac{kg}{m^3} \tag{6.32a}$$

$$k_2 = G_{cold}^2\frac{\partial}{\partial h_{cold}}\left(\frac{1}{\rho_{cold}}\right) \qquad \Rightarrow [k_2] = \frac{kg}{m^3} \tag{6.32b}$$

$$k_3 = 4\frac{L}{Deq_{cold}}\frac{U}{G_{cold}}\frac{\partial T_{cold}}{\partial p_{cold}} \qquad \Rightarrow [k_3] = \frac{m^3}{kg} \tag{6.32c}$$

$$k_4 = 4\frac{L}{Deq_{cold}}\frac{U}{G_{cold}}\frac{\partial T_{cold}}{\partial h_{cold}} \qquad \Rightarrow [k_4] = - \tag{6.32d}$$

$$k_5 = -4\frac{L}{Deq_{cold}}\frac{U}{G_{cold}} \qquad \Rightarrow [k_5] = \frac{J}{kg\ K} \tag{6.32e}$$

$$k_6 = -4\frac{L}{Deq_{hot}}\frac{U}{G_{hot}c_{p,hot}}\frac{\partial T_{cold}}{\partial p_{cold}} \qquad \Rightarrow [k_6] = \frac{K}{Pa} \tag{6.32f}$$

$$k_7 = -4\frac{L}{Deq_{hot}}\frac{U}{G_{hot}c_{p,hot}}\frac{\partial T_{cold}}{\partial h_{cold}} \qquad \Rightarrow [k_7] = \frac{K}{J/kg} \tag{6.32g}$$

$$k_8 = 4\frac{L}{Deq_{hot}}\frac{U}{G_{hot}c_{p,hot}} \qquad \Rightarrow [k_8] = - \tag{6.32h}$$

The relevant derivatives of the specific volume ($1/\rho$) and local temperature of the cold stream, required for the calculation of some of these coefficients, can be obtained following the assumptions listed in Section 6.3. Their analytical expressions are listed in Table 6.2 for different ranges of the specific enthalpy, in other words, for the liquid, two-phase and vapor regions.

Range	$\frac{\partial}{\partial h_{cold}}\left(\frac{1}{\rho_{cold}}\right)$	$\frac{\partial T_{cold}}{\partial h_{cold}}$	$\frac{\partial T_{cold}}{\partial p_{cold}}$
$h_{cold} < h_L$	0	$\frac{1}{c_{p,cold,L}}$	0
$h_L \leq h_{cold} \leq h_V$	$\left(\frac{1}{\rho_V} - \frac{1}{\rho_L}\right)\frac{1}{\Delta h_{LV}}$	0	$\frac{\bar{R}}{MW}\frac{T_{sat}(p_{cold,in})}{p_{cold,in}\Delta h_{LV}}$
$h_{cold} > h_V$	0	$\frac{1}{c_{p,cold,V}}$	$\frac{\bar{R}}{MW}\frac{T_{sat}(p_{cold,in})}{p_{cold,in}\Delta h_{LV}}$

Table 6.2: Partial derivatives of specific volume and local temperature for different ranges of the specific enthalpy

Finally, applying reversion rules to the Jacobian matrix $\mathcal{H}$, the importance operator $\mathcal{H}^*$ is obtained as in Eq. (6.33). This operator is necessary for the solution of the importance problem, as discussed in Section 6.3.2.

$$\mathcal{H}^* = \begin{bmatrix} -\dfrac{\partial}{\partial z} + \delta(z-1) & 0 & k_3 & k_6 \\ 0 & \dfrac{\partial}{\partial z} + \delta(z) & 0 & 0 \\ k_1 - k_2\dfrac{\partial}{\partial z} & 0 & -\dfrac{\partial}{\partial z} + \delta(z-1) + k_4 & k_7 \\ 0 & 0 & k_5 & \dfrac{\partial}{\partial z} + \delta(z) + k_8 \end{bmatrix} \tag{6.33}$$

6.3.2 Importance problem

As described in Section 6.1.2 the importance problem is specific for each selected integral response $\mathcal{Q}$. Four responses are selected in this example: the total heat duty Q, the pressure drop in each stream Δp_{cold} and Δp_{hot}, and the pumping power Wp, as studied in the following subsections.

All responses are evaluated in terms of inlet and outlet values of the solution $\mathfrak{u}$ obtained for the direct problem in Section 6.3.1. In mathematical terms, this can be represented by using a combination of delta functions as the weighting function $\mathfrak{W}(\mathbf{r}, \mathbf{p})$. For this purpose, it is useful to recall that, being $\mathcal{H}^*$ a linear operator, the summation rule in Eq. (6.34) can be applied. This property results very useful for the solution of the importance problem.

$$\mathcal{H}^* (\mathfrak{u}_1 + \mathfrak{u}_2) = \mathcal{H}^* \mathfrak{u}_1^* + \mathcal{H}^* \mathfrak{u}_2^* \tag{6.34}$$

Total heat duty Q

The term heat duty refers to the total heat transferred, and its reference value for the given operating conditions is Q_{ref} =1088.1 W. It can be obtained from an energy balance for either stream. In particular, considering this balance for the specific enthalpy of the cold stream, the response is represented by Eq. (6.35).

$$Q = \dot{m}_{cold} \left[h_{cold}(z=1) - h_{cold,in} \right] \Rightarrow \mathfrak{W} = \underbrace{\begin{bmatrix} 0 \\ 0 \\ \dot{m}_{cold}\delta(z-1) \\ 0 \end{bmatrix}}_{\mathfrak{W}_1} - \underbrace{\begin{bmatrix} 0 \\ 0 \\ \dot{m}_{cold}\delta(z) \\ 0 \end{bmatrix}}_{\mathfrak{W}_2} \tag{6.35}$$

Recalling that $\mathcal{H}^*$ is a linear operator and the summation rule from Eq. (6.34), the solution $\mathfrak{u}^*$ is divided in two components $\mathfrak{u}_1^*$ and $\mathfrak{u}_2^*$, thus resulting in two independent importance problems as in Eq. (6.36).

$$\mathfrak{u}^* = \mathfrak{u}_1^* - \mathfrak{u}_2^* \longrightarrow \begin{cases} \mathcal{H}^* \mathfrak{u}_1^* = \mathfrak{W}_1 \\ \mathcal{H}^* \mathfrak{u}_2^* = \mathfrak{W}_2 \end{cases} \tag{6.36}$$

The solution for the second component is the result $\mathfrak{u}_2^* = \mathbf{0}$ in the domain $[0, 1]$. From a mathematical perspective, this result is the consequence of the null boundary conditions imposed (by use of delta functions in $\mathcal{H}^*$ and $\mathfrak{W}_2$) at both ends for the importance of the cold specific enthalpy, that is $h^*_{cold,2}(z = 0) = h^*_{cold,2}(z = 1) = 0$. Then, it follows that the only possible solution for this second component is that all the importance variables are zero. The physical meaning of this result is that the solution has zero importance respect to the response given by $\mathfrak{W}_2$, which represents the inlet boundary condition. In other words, the inlet value is not affected by the solution and therefore the importance is zero.

After solving for $\mathfrak{u}_2^*$, the problem is then reduced to the first component $\mathfrak{u}_1^*$. The solution is presented in Fig. 6.3 for both (a) momentum and (b) energy equations. According to Eq. (6.10), the importance function $\mathfrak{u}^*$ has units of the response (in this case W), divided by those of the system of equations $\mathfrak{m}(\mathbf{r}, \mathbf{p})$. In Section 6.3.1, the system of equation $\mathfrak{m}$ was normalized to have units of the direct variables $\mathfrak{u}(\mathbf{r})$. Then, p^*_{cold} and p^*_{hot} have units of W Pa^{-1}, h^*_{cold} is measured in W/(J kg^{-1})=kg s^{-1} and T^*_{hot}, in W K^{-1}.

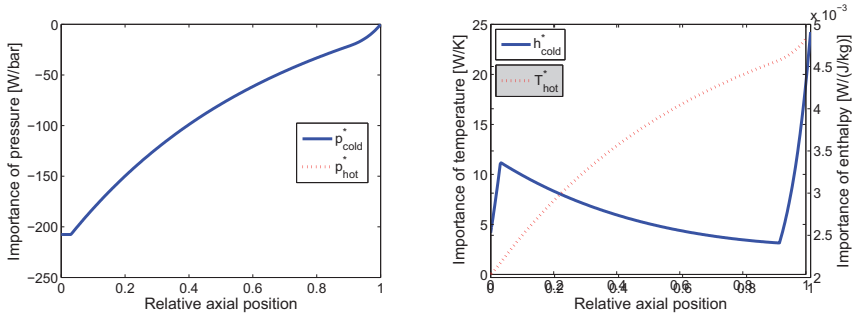

(a) Pressure profiles

(b) Temperature profile

Figure 6.3: Solution to the importance problem in an evaporator analyzing the response in terms of total heat duty

On the one hand, Fig. 6.3(a) indicates that $p^*_{hot}(z) = 0$ throughout the entire length. In other words, the solution for the hot stream pressure is not important for analyzing the total heat duty Q. On the other hand, the cold stream pressure has a negative importance, that is $p^*_{cold}(z) \leq 0$. This means that a local positive perturbation in the cold stream pressure affects negatively the total heat duty. The physical reason for this behavior is given by the increase in saturation temperature. It can also be observed in Fig. 6.3(a) that, in absolute terms, this importance is

larger close to the inlet than to the outlet. This implies that a perturbation closer to the inlet has a larger impact, since it affects the entire heat transfer performance downstream of the perturbation.

Regarding the importance for the energy balance equation, Fig. 6.3(b) indicates that both the hot stream temperature and the cold stream enthalpy have a positive importance, that is $T^*_{hot}(z) \geq 0$ and $h^*_{cold}(z) \geq 0$, although for different reasons.

A positive local perturbation in the specific enthalpy has two effects: one downstream and another one upstream in the cold flow direction, that is from left to right in Fig. 6.3. Both contributions are positive and therefore the importance $h^*_{cold}(z)$ is always positive throughout the entire length.

First, the specific enthalpy is increased downstream, thus increasing the vapor content. As a consequence of the lower density, the pressure drop is larger, reducing the saturation temperature and increasing the heat transfer.

Second, the local temperature difference and heat flux are reduced at this point. Then, the hot stream temperature remain higher. Since both streams flow in different directions, this effect increases the heat flux upstream for the cold fluid. In addition, this effect is more relevant in the regions where the temperature difference is lower, thus explaining the profile of h^*_{cold}, which is exactly the opposite of the temperature difference in Fig. 6.2(b).

In the case of the hot stream temperature, the importance T^*_{hot} is positive because a local perturbation results in a larger temperature difference and a larger heat duty. The importance is then larger close to the inlet (located at the right end), since it affects a larger length downstream.

Hot stream pressure drop Δp_{hot}

For the given operating conditions selected as reference, the value of this response is $\Delta p_{hot,ref}$ =0.137 bar. From a GPT perspective, this response is obtained by means of delta functions at inlet and outlet applied to the hot stream pressure, as represented by Eq. (6.37).

$$\mathcal{Q} = \Delta p_{hot} = p_{hot,in} - p_{hot}(z=0) \Rightarrow \mathfrak{W} = \underbrace{\begin{bmatrix} 0 \\ \delta(z-1) \\ 0 \\ 0 \end{bmatrix}}_{\mathfrak{W}_1} + \underbrace{\begin{bmatrix} 0 \\ -\delta(z) \\ 0 \\ 0 \end{bmatrix}}_{\mathfrak{W}_2} \tag{6.37}$$

Following the same procedure as with the total heat duty, the importance function $\mathfrak{u}^*$ is divided in two components $\mathfrak{u}^*_1$ and $\mathfrak{u}^*_2$ and, with the same considerations, the first component results zero, as in Eq. (6.38).

$$\mathfrak{u}^*|_{\mathcal{Q}=\Delta p_{hot}} = \mathfrak{u}^*_1 + \mathfrak{u}^*_2 \longrightarrow \begin{cases} \mathcal{H}^*\mathfrak{u}^*_1 = \mathfrak{W}_1 \longrightarrow \mathfrak{u}^*_1 = \mathbf{0} \\ \mathcal{H}^*\mathfrak{u}^*_2 = \mathfrak{W}_2 \end{cases} \tag{6.38}$$

Then once again, the problem is reduced to the second component of $\mathfrak{u}^*$. In this particular case, since the variable p^*_{hot} is uncoupled from the rest of the variables in the importance problem (see $\mathcal{H}^*$ in Eq. (6.33)), these other variables have zero importance. This result indicates that the pressure drop in the hot stream is not influenced neither by the energy balance, nor by the pressure profile in the cold stream. In addition, an analytical solution is available, given by Eq. (6.39).

$$\mathfrak{u}^*|_{\mathcal{Q}=\Delta p_{hot}} = \begin{cases} p^*_{cold}(z) = 0 \\ p^*_{hot}(z) = -1 \\ h^*_{cold}(z) = 0 \\ T^*_{hot}(z) = 0 \end{cases} \tag{6.39}$$

The constant value of -1 for the importance simply indicates that a local positive perturbation to the pressure reduces in the same amount the pressure drop, as could be expected.

Cold stream pressure drop Δp_{cold}

The reference value for this response, obtained at the given operating conditions, is $\Delta p_{cold,ref}$ =1.038 bar. Once again, this response is analyzed by GPT using delta functions as in Eq. (6.40).

$$\mathcal{Q} = \Delta p_{cold} = p_{cold,in} - p_{cold}(z=1) \Rightarrow \mathfrak{W} = \underbrace{\begin{bmatrix} \delta(z) \\ 0 \\ 0 \\ 0 \end{bmatrix}}_{\mathfrak{W}_1} + \underbrace{\begin{bmatrix} -\delta(z-1) \\ 0 \\ 0 \\ 0 \end{bmatrix}}_{\mathfrak{W}_2} \tag{6.40}$$

The same procedure is then applied to this response: $\mathfrak{u}^*$ is divided in two components $\mathfrak{u}^*_1$ and $\mathfrak{u}^*_2$. For the same reasons as for $\mathcal{Q} = \Delta p_{hot}$ the first component is zero, as indicated in Eq. (6.41), and the problem is then reduced to the second component of the importance function.

$$\mathfrak{u}^*|_{\mathcal{Q}=\Delta p_{cold}} = \mathfrak{u}^*_1 + \mathfrak{u}^*_2 \longrightarrow \begin{cases} \mathcal{H}^*\mathfrak{u}^*_1 = \mathfrak{W}_1 \longrightarrow \mathfrak{u}^*_1 = \mathbf{0} \\ \mathcal{H}^*\mathfrak{u}^*_2 = \mathfrak{W}_2 \end{cases} \tag{6.41}$$

The solution to this importance problem is presented in Fig. 6.4 for both (a) momentum and (b) energy equations. The first conclusion that can be obtained from these plots is that the solutions follow the same trend as for the total heat duty, presented in Fig. 6.3. This situation occurs because an increase in heat duty results in a larger pressure drop (due to the larger vapor content and lower density) and vice versa (because of the reduction in saturation temperature).

It has been shown in the previous analysis for $\mathcal{Q} = \Delta p_{hot}$ that the inherent importance of pressure regarding Δp is -1, since a local positive perturbation increases the outlet value (and thus reduced the pressure drop) in the same amount.

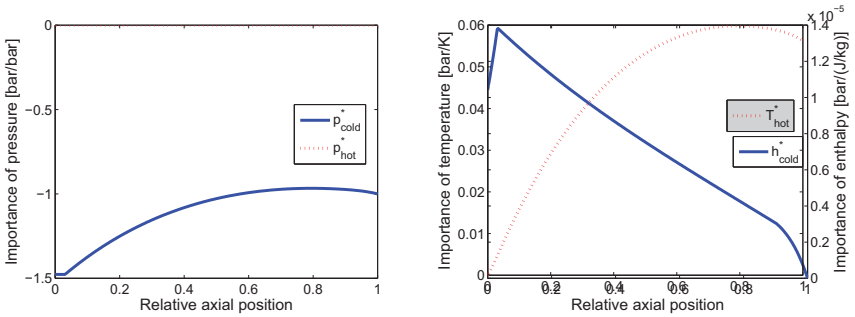

(a) Momentum equation (b) Energy equation

Figure 6.4: Solution to the importance problem in an evaporator analyzing the response in terms of the pressure drop in the cold stream

In this case, analyzing $\mathcal{Q} = \Delta p_{cold}$ the importance is larger (in absolute terms), as a consequence of the feedback with heat transfer. Then, a positive perturbation to p_{cold} further reduces the saturation temperature downstream and thus the heat duty and pressure drop. Due to this effect, the importance is up to 50% larger in absolute terms close to the inlet, since all the flow length downstream is affected.

The importance solution for the energy equation can be explained by this coupling between heat transfer and pressure drop. Then, the same trend as in Fig. 6.3(b) is obtained with the only difference of homogeneous boundary conditions at $z = 1$.

Pumping power Wp

While the analysis in terms of pressure drop is relevant for determining the feasibility and requirements of different equipment, the operating costs related to this phenomena are given by the pumping power Wp, defined as in Eq. (6.42). For the given operating conditions the pumping power is Wp_{ref} =0.729 W. This reference value is rather small due to the low mass flow rates and the fact that both streams enter as liquids with relatively large densities. In larger equipment, with multiple parallel channels, the pumping power increases roughly proportionally to the number of tubes.

$$Wp = \frac{\dot{m}_{cold}}{\rho_{cold,in}} \Delta p_{cold} + \frac{\dot{m}_{hot}}{\rho_{hot,in}} \Delta p_{hot} \tag{6.42}$$

Since Wp is a linear combination of both pressure drops and recalling that $\mathcal{H}^*$ is a linear operator, the importance solution can also by means of a linear combination, as given by Eq. (6.43).

$$\mathfrak{u}^*|_{\mathcal{Q}=Wp} = \frac{\dot{m}_{cold}}{\rho_{cold}}\,\mathfrak{u}^*|_{\mathcal{Q}=\Delta p_{cold}} + \frac{\dot{m}_{hot}}{\rho_{hot}}\,\mathfrak{u}^*|_{\mathcal{Q}=\Delta p_{hot}} \tag{6.43}$$

The importance solution for this response is represented in Fig. 6.5. It can be observed that the importance solution to the energy equation in Fig. 6.5 corresponds to the one presented in Fig. 6.4(b), normalized by $\dot{m}_{cold}/\rho_{cold,in}$.

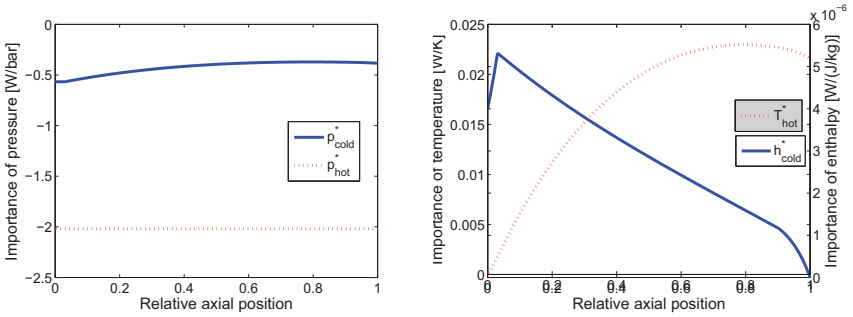

(a) Pressure profiles

(b) Temperature profile

Figure 6.5: Solution to the importance problem in an evaporator analyzing the response in terms of total pumping power

It is worth noticing in Fig. 6.5(a) that, in absolute terms, the hot-stream pressure has a larger importance than the cold-stream pressure. This result is a consequence of the larger mass flow rate ($\dot{m}_{hot}$=20.1 g s^{-1}, while $\dot{m}_{cold}$=4.9 g s^{-1}), and the lower density ($\rho_{hot,in}$=995.7 kg m^{-3}, and $\rho_{cold,in}$=1278.0 kg m^{-3}).

6.3.3 Sensitivity coefficients

Based on the solution for the direct ($\mathfrak{u}$) and importance ($\mathfrak{u}^*$) problems, the sensitivity of the response $\mathcal{Q}$ respect to a parameter p_j can be computed according to Eq. (6.10). At this point all the required variables are known and the integrals can be computed numerically.

$$s_j = \frac{\partial \mathcal{Q}}{\partial p_j} = \left\langle \mathfrak{u}(\mathbf{r}), \frac{\partial \mathfrak{W}}{\partial p_j}(\mathbf{r},\mathbf{p}) \right\rangle_{\mathcal{V}(\Omega)} - \left\langle \mathfrak{u}^*(\mathbf{r}), \frac{\partial \mathfrak{m}}{\partial p_j}(\mathbf{r},\mathbf{p}) \right\rangle_{\mathcal{V}(\Omega)} \tag{6.10}$$

Table 6.3 presents the coefficients s_j for the four responses studied in Section 6.3.2. The ten parameters p_j are divided into two categories: the first six represent physical variables, while the last four represent the thermodynamic state at the inlet which affects the physical properties of the fluids, such as their densities and specific heat capacity. Each column of ten sensitivity coefficient for a given response in Table 6.3, was obtained with only one additional simulation.

p_j	Unit	$\mathcal{Q} = Q$ [W]	$\mathcal{Q} = \Delta p_{cold}$ [bar]	$\mathcal{Q} = \Delta p_{hot}$ [bar]	$\mathcal{Q} = Wp$ [W]
G_{cold}	[kg m^{-2}s^{-1}]	2.316	0.0013	0	0.0021
G_{hot}	[kg m^{-2}s^{-1}]	0.605	0.0019	6.74 10^{-4}	0.0029
D_i	[mm]	216.176	-0.8298	0.0553	-0.1094
D_o	[mm]	75.606	0.2410	-0.0553	0.0841
L	[m]	102.388	0.4261	0.0409	0.2463
U	[kW m^{-2} s^{-1}]	358.857	0.6921	0	0.2658
$p_{cold,in}$	[bar]	-201.337	-0.8590	0	-0.3299
$p_{hot,in}$	[bar]	-0.016	-5.0 10^{-5}	-8.1 10^{-6}	-3.6 10^{-5}
$h_{cold,in}$	[kJ kg^{-1}]	-2.379	0.0104	0	0.0040
$T_{hot,in}$	[K]	23.550	0.0562	-0.0012	0.0192

Table 6.3: Sensitivity coefficients s_j for all four responses and ten parameters

The results presented in Table 6.3 have the units of the response $\mathcal{Q}$ divided by those of the parameter p_j. Then, the sensitivity of different parameters cannot be compared in terms of s_j, since they have different units. Therefore, the only general conclusions that can be obtained from Table 6.3 are related to the signs of the coefficients, such as the following.

- As a consequence of the positive feedback between heat duty and the pressure drop of the cold stream, their sensitivity coefficients respect to most parameters have the same sign. There are only two exceptions: the inner diameter D_i and the cold inlet specific enthalpy $h_{cold,in}$. In the first case, a larger diameter reduces the friction and, at a constant mass flux, results in a larger mass flow rate and thus larger heat duty.

- Regarding the pressure drop in the hot stream, its sensitivity respect to G_{cold}, $p_{cold,in}$, $h_{cold,in}$ and U is zero. Since the pressure drop in this single phase fluid is not affected by heat transfer, it is not influenced by any of these parameters related to the interaction with the cold stream.

In order to allow for a simple way of determining which parameter is *more important* regarding its consequences on the response, non-dimensional sensitivity coefficients $\hat{s}_j$ are defined as in Eq. (6.44). They represent the relative change in the response $\mathcal{Q}$ as a consequence of a unit relative perturbation in the parameter p_j. Then, for example, for $\hat{s}_j = 1$, a 10% increase in the parameter will result in a 10% increase in the response. Such is the case of Δp_{hot} respect to the tube length.

$$\hat{s}_j = \frac{\partial \mathcal{Q}}{\partial p_j} \frac{p_j}{\mathcal{Q}} = s_j \frac{p_j}{\mathcal{Q}} \tag{6.44}$$

Table 6.4 presents the results for this example in terms of the non-dimensional sensitivity coefficients.

p_j	$\mathcal{Q} = Q$	$\mathcal{Q} = \Delta p_{cold}$	$\mathcal{Q} = \Delta p_{hot}$	$\mathcal{Q} = Wp$
G_{cold}	0.5320	0.3185	0	0.7210
G_{hot}	0.2223	0.7429	1.6472	1.1527
D_i	0.9934	-3.9969	1.6910	-0.7506
D_o	0.6948	2.3216	-3.3819	1.1531
L	0.3764	1.6422	1.0000	1.3512
U	0.3298	0.6668	0	0.3646
$p_{cold,in}$	-0.6476	-2.8964	0	-1.5839
$p_{hot,in}$	-1.3 10^{-5}	-4.8 10^{-5}	-4.9 10^{-5}	-4.8 10^{-5}
$h_{cold,in}$	-0.4428	2.0316	0	1.1110
$T_{hot,in}$	6.5580	16.4122	-2.1863	7.9843

Table 6.4: Non-dimensional sensitivity coefficients $\hat{s}_j$ for all four responses and ten parameters

Two additional remarks can be derived from this non-dimensional approach:

- Since the hot momentum balance is uncoupled from the other equations, the inlet pressure of the hot stream $p_{hot,in}$ has very little influence in the responses. The only effect is given by changes in the hot fluid physical properties (c_p, ρ, μ) resulting in a non-dimensional sensitivity coefficient several orders of magnitude smaller than the rest.

- In non-dimensional terms, the total heat duty Q is more sensitive to the tube length L than to the overall heat transfer coefficient U. In lumped-parameter models for single phase (LPM, see Section 2.4.1) they are grouped together in a number of thermal units (NTU) and an equal contribution is assumed. In this evaporator example, however, the difference is given by the larger pressure drop in the cold stream, which has a feedback in the heat duty.

6.3.4 Accuracy of the GPT

It is important to recall that during the mathematical description of the GPT method, presented in Section 6.1.2, the only assumption was that high order effects are negligible. Then, the obtained sensitivity coefficients are the exact values of the derivatives from a strictly mathematical perspective, that is considering infinitely small perturbations to the parameters.

The practical application of GPT is given by its ability to predict the consequences on the response $\mathcal{Q}$ of a *finite* perturbation in the parameters. These prediction can be approximated by means of the sensitivity coefficient as in Eq. (6.45).

$$\mathcal{Q}(p_j + \Delta p_j) \approx \mathcal{Q}(p_j) + s_j \Delta p_j \tag{6.45}$$

This approximation is only exact if $\mathcal{Q}$ is a linear function of p_j, that is, if the sensitivity coefficient is constant for any operating conditions. In such a case, like the dependence of Δp_{hot} on the tube length L, the solution is straightforward and there is no practical advantage in the application of the complex mathematical formulation of GPT. In a general case, the accuracy of Eq. (6.45) is related to how well this behavior can be represented by a straight line.

Two representative examples are presented in Fig. 6.6, where the direct solution and the prediction of GPT are compared within ±10% variations in the parameter. In Fig. 6.6(a), the effect of the tube length on the cold pressure drop is well approximated, while that is not the case for (b) the consequences in the heat duty of perturbations to the inner diameter.

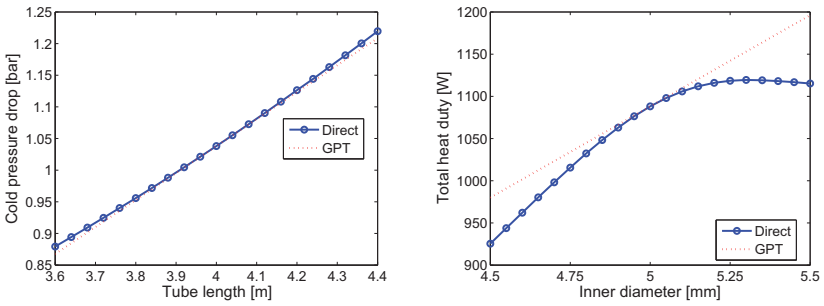

(a) Δp_{cold} against tube length L (b) Q against inner diameter D_i

Figure 6.6: Integral responses obtained by direct solution and prediction by GPT

On the one hand, the results for the direct solution (blue solid lines in Fig. 6.6) required twenty-one simulations, that is one for each value of the parameter. On the other hand, the linear predictions of the GPT method required only two, that is one for the direct problem and another for the importance. This reduction in the number of simulations, at the expense of introducing some error in the predictions, is justifiable for Fig. 6.6(a) but not acceptable in Fig. 6.6(b). Then, it is interesting to further investigate the accuracy of this approximation. For this analysis, the relative error $\mathcal{E}_{GPT}$ is defined as in Eq. (6.46).

$$\mathcal{E}_{GPT} = \frac{[\mathcal{Q}_{ref} + s_j \Delta p_j] - \mathcal{Q}(p_j + \Delta p_j)}{\mathcal{Q}_{ref}} \tag{6.46}$$

Figure 6.7 presents the evolution of this relative error for all four responses and the six physical parameters, that is both mass fluxes, inner and outer diameters, tube length and overall heat transfer coefficient. In all cases, the larger error is

given by the inner and outer diameters, reaching up to 15% of the reference value of the response. These two parameters are the less accurate because their effect in the responses is clearly not linear, as in Fig. 6.6(b).

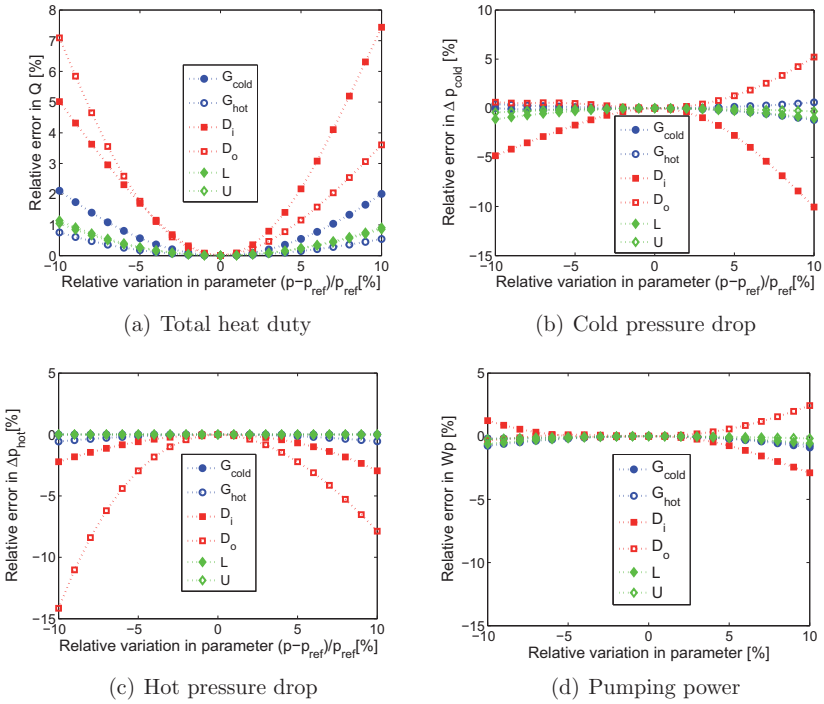

(a) Total heat duty

(b) Cold pressure drop

(c) Hot pressure drop

(d) Pumping power

Figure 6.7: Relative error in the prediction using GPT for six physical parameters

For the other four parameters, the relative error is lower than 2% considering a ±10% perturbation. This error is rather small and then the application of GPT is acceptable within this range. For D_i and D_o, this range should be reduced to ±2%. In any case, the relative error can always be reduced to acceptable levels by considering small enough perturbation to the parameters.

The inlet boundary conditions are complex parameters, since they affect the physical properties of the fluid. For this reason, their relative error $\mathcal{E}_{GPT}$ is presented separately in Fig. 6.8.

Regarding the cold (a) inlet pressure and (c) enthalpy, the GPT method overpredicts the heat duty and underpredicts the cold pressure drop. This is also the case for the other six parameters presented in Fig. 6.7. The perturbations to $p_{cold,in}$ were considered over a wide range of ±1 bar, resulting in a relative large error. Nevertheless, the error is rather small if the perturbations are reduced to a few

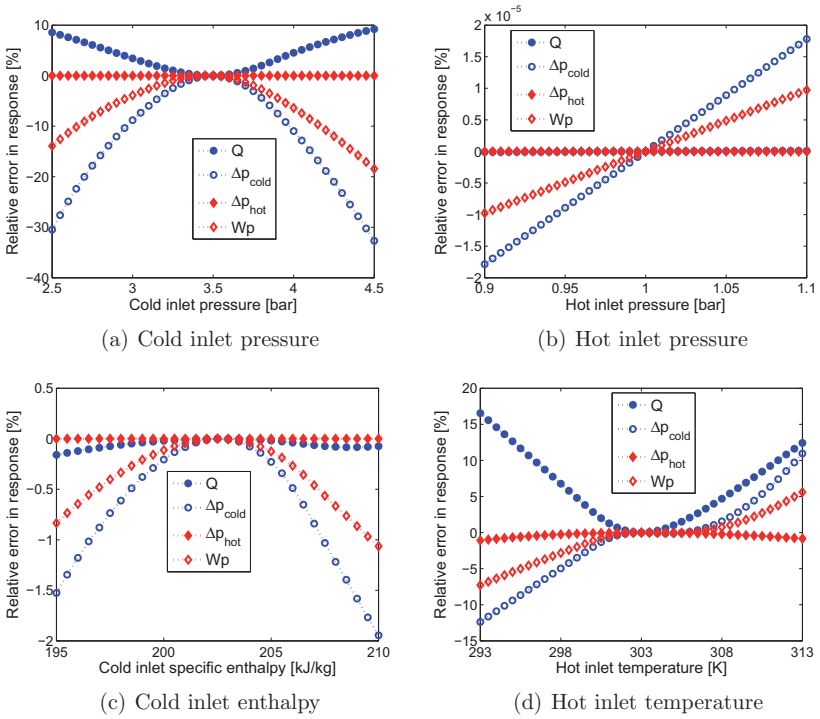

(a) Cold inlet pressure

(b) Hot inlet pressure

(c) Cold inlet enthalpy

(d) Hot inlet temperature

Figure 6.8: Relative error in the prediction using GPT for the inlet conditions

kPa=0.01 bar. In the case of (c), smaller perturbation were considered, including single-phase liquid and two-phase conditions at the inlet, with a rather small error for all four responses.

As discussed in Section 6.3.3, the hot inlet pressure has very little effect in the responses, given by the changes in the fluid properties. For this reason, the error presented in Fig. 6.8(b) is also very small. The hot inlet temperature does not only affect the physical properties but also the temperature difference, which is the driving force for the heat transfer. This is reflected in the large sensitivity coefficient presented in Tables 6.3 and 6.4. An increase in $T_{hot,in}$ produces a faster generation of vapor, and a reduction of the boiling region. This effect is not linear and therefore the relative error presented in Fig. 6.8(d) is rather larger. Perturbations in the hot inlet temperature should then be restricted to a few degrees Kelvin.

6.4 An optimization algorithm

The term optimization refers to the process of finding the most convenient operating conditions in terms of maximizing or minimizing an objective response $\mathcal{Q}$, depending on the problem. Different techniques have been extensively reviewed in the open literature (Andradóttir, 2007; Fu et al., 2005; Tekin and Sabuncuoglu, 2004) and they include gradient-based formulations, stochastic, heuristic and statistical methods, among others.

The first type of methods consists on the continuous search of better operating conditions following the direction of gradient. In this category, the GPT formulation stands out as an efficient technique, since the derivative respect of all the parameters (that is, the gradient), are computed with only one additional simulation. This is a comparative advantage over the finite difference method, which requires one additional simulation for each parameter and only provides approximate values for the derivatives.

With these considerations, a possible optimization algorithm is presented in this section, as summarized in Fig. 6.9.

Starting from the physical model and constraints, a search space is defined. In other words, minimum and maximum values are established for each parameter. An initial set of values for $\mathbf{p}$ is selected and an iterative procedure is started, which will eventually lead to the optimum solution.

Each iteration step k comprises two computationally intensive stages: the solution of the direct and importance problems, from which sensitivity coefficients can be computed. A local optimum is found if the gradient (given by the sensitivity coefficients) is zero or, for practical purposes, below a predefined tolerance.

In the case that this tolerance is not yet reached, meaning that the solution can be further optimized, a new set of parameters $\mathbf{p}^{k+1}$ is defined following the direction of the gradient as in Eq. (6.47). The coefficient ω is a constant which determines the relative step in the parameters, and has the same sign as $\mathcal{Q}^k$ for maximization problems and the opposite if the objective is to minimize the response. The accuracy analysis from Section 6.3.4 indicated that the prediction of GPT are not reliable for large perturbations in the parameters. For this reason, the constant coefficient ω should not be too large, usually around $|\omega| \approx 0.1$.

$$p_j^{k+1} = p_j^k + \hat{s}_j^k \; p_j^k \; \omega \qquad \forall \; j = 1, \ldots, n_p \tag{6.47}$$

It is important to remark that, since the direction of the gradient is followed, the solution is always improved in each step. The integral response as predicted by GPT is modified following the sign of ω, as indicated by Eq. (6.48).

$$\mathcal{Q}_{GPT}^{k+1} - \mathcal{Q}^k = \omega \; \mathcal{Q}^k \; \sum_{j=1}^{n_p} \left(\hat{s}_j^k\right)^2 \tag{6.48}$$

Not all problems present a local optimum withing the search space, as in the

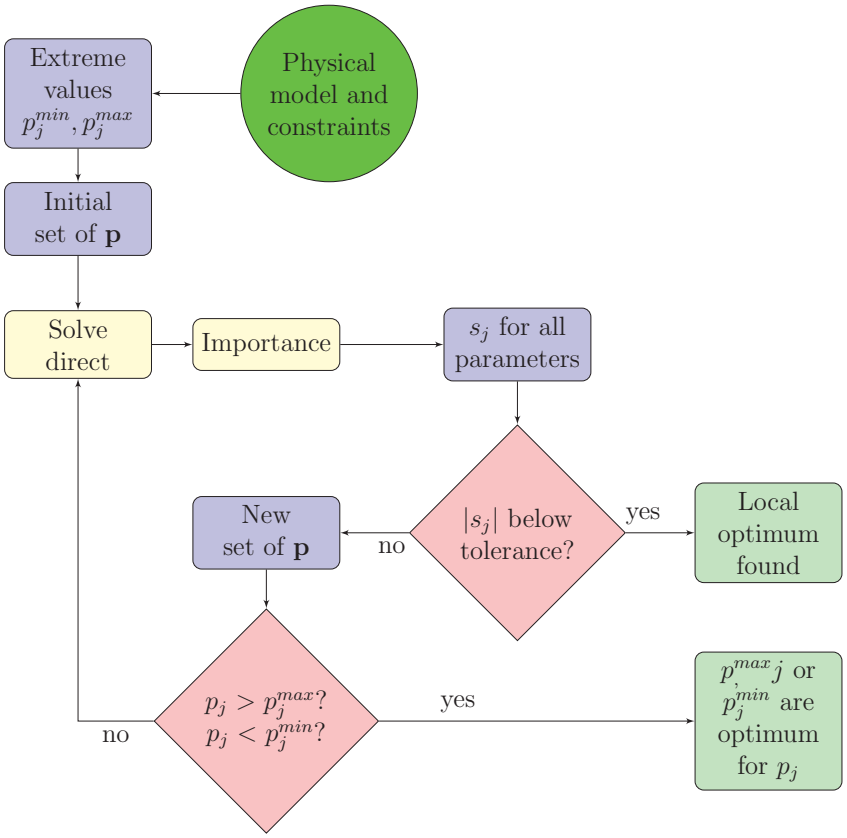

Figure 6.9: Proposed optimization algorithm using using GPT

analytical example presented in Section 6.2. In this example, the effectiveness increases continuously with the heat exchanger size, and the optimal solution is given by constructing the HE as large as possible. In such cases, the gradient line would eventually predict a value p_j^{k+1} outside the established limits. Then, the iteration for this parameter is stopped and its optimal value is determined to be p_j^{max} or p_j^{min}, and the procedure continues with the other parameters.

6.4.1 Application to the evaporator example

The evaporator example presented Section 6.3 involves ten different parameters. In this section, a reduced version with only two parameters is considered for illustrative purposes. For a given heat exchanger geometry (thus establishing D_i, D_o, L and U) and inlet thermodynamic conditions ($p_{cold,in}$, $p_{hot,in}$, $h_{cold,in}$ and $T_{hot,in}$),

the two variable parameters are the cold and hot mass fluxes G_{cold} and G_{hot}.

A search space is defined for these two parameters as $100 < G_{cold} < 400$ and $200 < G_{cold} < 600$, both with units of kg m^{-2} s^{-1}. This range is divided in a 100x100 grid and a response surface is constructed with 10000 simulations. An optimization algorithm is started from the lower values, regarding two different responses: the total heat duty and a compromise with the pumping power.

Maximizing heat duty

This section deals with the process of finding the maximum heat duty that can be obtained from a given HE . The optimization results are presented in Fig. 6.10 in terms of (a) the response surface and (b) convergence scheme.

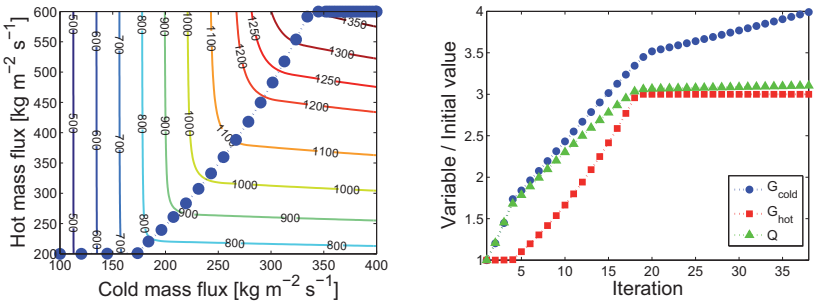

(a) Contour plot of the response surface

(b) Convergence analysis

Figure 6.10: Maximization of heat duty

The contour plot of the response surface in Fig. 6.10(a) indicates that this problem does not have a local maximum, and the optimal solution is found at one corner of the search space. In other words, the heat duty is maximized by setting both mass fluxes as large as possible. Then, the successive operating points proposed by the optimization algorithm according to Eq. (6.47), cross the different level curves following the direction of the gradient and locate the optimum at the top right corner.

A convergence analysis presented in Fig. 6.10(b) indicates that the heat duty is increased in each step, as predicted by Eq. (6.48). In addition, the evolution of the optimization algorithm is initially fast, reaching the final value for G_{hot} and within 1.5% of the optimal heat duty after 19 iterations. The final stage is rather slow, since another 19 iterations are required in order to locate the final optimum. This behavior with two clearly different convergence rates is a consequence of considering a constant value for the coefficient ω in Eq. (6.47), in this case $\omega = 0.2$. Although better results could be obtained with an adaptive strategy, this section

intends to demonstrate the feasibility of using GPT as part of an optimization algorithm, with no further investigation regarding its performance.

Compromise of heat duty and pumping power

A new figure of merit can be defined, accounting for a penalization given by the operating costs related to pumping power. Then, the integral response given by Eq. (6.49) represents a compromise of heat duty and pumping power.

$$\mathcal{Q} = Q - 250Wp \tag{6.49}$$

The level curves for this response, presented in Fig. 6.11(a) indicate that there is a local optimum within the search space. Then, the optimization algorithm is stopped at the first decision step in Fig. 6.9, that is, when the non-dimensional sensitivity coefficients are reduced below a specified tolerance of 10^{-2}.

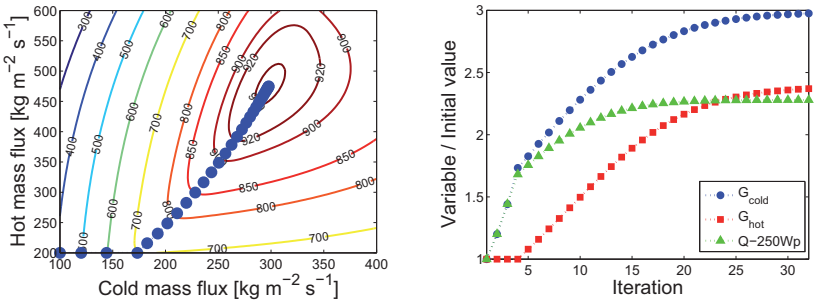

(a) Contour plot of the response surface (b) Convergence analysis

Figure 6.11: Optimization of a compromise between heat duty and pumping power

This optimum solution is determined by the algorithm to be located at the conditions $G_{cold} = 297.5$ and $G_{hot} = 474.0$, both in kg m^{-2} s^{-1}, as indicated by the solid points in Fig. 6.11(a) that represents the successive operating conditions. At this point, the maximum value for the response is $\mathcal{Q}_{opt} = 942.8$W.

Figure 6.11(b) presents the convergence analysis for this optimization process. Once again, the selected response increases in each step. Although the direction of the gradient is followed, this condition is only fulfilled if the coefficient ω is not larger than some critical value which cannot be predicted *a priori*. For this reason, the rather small value of $\omega = 0.2$ was selected. However, a small value for this coefficient results in a slow convergence in the last stages of the optimization process. In the region where the gradients are smaller, that is close to the optimum, the variations in the parameters proposed by Eq. (6.47) are consequently also small. Then, as indicated in Fig. 6.11(b), more than half of the required iterations take place in the neighborhood of the maximum.

6.5 Summary

Optimization and sensitivity analysis represent a fundamental stage in the design of a heat exchanger as well as other equipment from a macroscopic perspective. At a system-level description, the design engineer is not necessarily interested in a continuum formulation, but is rather focused on integral responses and how they are affected by the different design parameters.

In this framework, perturbative methods discussed in this chapter represent an interesting alternative to the traditional approach, based upon the computation of response surfaces. Based on the concept of the importance function, these methods provide the sensitivity of the selected response respect to all relevant parameters at a given operating conditions, with only one additional simulation. The information provided by perturbative methods, described in this chapter in terms of the Generalized Perturbation Theory (GPT), is very useful for design. The relevant parameters can be identified and design margins and fabrication tolerances can be established in an uncertainty analysis. In addition, the optimal operating conditions can be obtained by means of these sensitivity analysis.

The mathematical description of the GPT is presented in Section 6.1. In physical terms, it is based on the concept of conservation of the importance function. This importance function represents the consequences on the response of local perturbation to the variables. The process of obtaining this importance function involves the solution of the so-called importance problem, which is closely related to the direct one. Sensitivity coefficients can be computed from the results of the direct and importance problems. Two examples are presented in this chapter to clarify this concept: a single-phase heat exchanger and an evaporator.

First, a single-phase example with analytical solution is analyzed in Section 6.2. This example allows to apply the mathematical expression from Section 6.1 and observe that the sensitivity coefficient obtained by the GPT method is an exact representation of the partial derivative of the selected response (in this case, the effectiveness) with respect to the parameters (in this case, the HE size represented by a number of thermal units). The results for a balanced counter-current flow arrangement indicate that the effectiveness increases towards the asymptotic value of one, which would correspond to an infinitely large heat exchanger.

Second, a counter-current evaporator is studied in Section 6.3 in terms of both momentum and energy balances. The physical model for this example has been presented earlier in Chapter 5. Its key feature is given by the coupling between pressure drop and heat transfer in the boiling region. The changes in pressure affect the saturation temperature and therefore also the local heat flux. In addition, the heat flux affects the flow density with consequences in the pressure drop. Although this problem does not have a simple analytical solution due to the discontinuities given by the change of phase, it is linear and fulfills the mathematical conditions required for the application of GPT.

This complex problem involves ten different parameters, including the inlet

conditions, geometry and mass fluxes. Sensitivity analysis results are presented for four different responses: the total heat duty, pressure drop for both cold and hot streams, and pumping power. Although the obtained results are exact in terms of the derivative, the accuracy of its use for the prediction of the consequences of finite perturbations in the parameters, depends on the how well this response can be approximated by a linear function. For example, the variations of pressure drop with regard to the tube length are rather well approximated, while that is not the case for the heat duty and the inner diameter. An accuracy analysis was performed for all the responses and parameters and, in general, the accuracy is always improved when smaller perturbations to the parameters are considered, with good results for variations of a few percent.

Finally, an iterative optimization algorithm is presented in Section 6.4, as sketched in Fig. 6.9. This algorithm is based on the use of GPT in each step for determining the gradient, that is the partial derivatives of the response respect of the parameters. Using this information, a new set of operating conditions is postulated following the direction of the gradient, thus guaranteeing that the response is improved in each step. Results are presented for two examples, based on the evaporator problem in Section 6.3. In the first example, the response (the heat duty) does not have a local maximum and the optimum is located at one of the corners of the search space. In the second example, a local optimum is found for a compromise of heat duty and pumping power. A convergence analysis for both examples indicates that the response is indeed improved in each step.

Part III

Medium-scale framework

The macroscopic framework presented in part II (Chapters 5 and 6) is focused on a continuum one-dimensional analysis for predicting overall effects, such as heat transfer performance and pressure drop. Numerical examples were presented for a tube-in-tube geometry, which is a simple case with only one channel. The direct application of this macroscopic framework to more complex geometries with multiple channels would imply assuming that the entire geometry can be represented by a single channel. In other words, a unique set of parameters such as tube length, diameter, and flow rate, would be considered. Such an assumption would be rarely justified in practice. In the following two chapters, this framework is extended to include physical effects occurring at a so-called mesoscale, or medium scale.

In this part, modeling and simulation results in a meso-scale framework are presented, considering geometries with multiple parallel channels. A homogenization approach is postulated for dealing with complex geometries. This methodology results in an interesting compromise of accuracy and computational costs. In particular, a shell-and-tube geometry is represented in terms of several radial layers. This approach could also be extended to plate-type geometries, considering horizontal or vertical layers instead.

Chapter 7 deals with the consequences of the flow maldistribution (that is different flow rates in two or more parallel channels) in the performance of evaporators and other two-phase flow systems. Including an equal pressure-drop boundary condition, a secondary maldisitribution is observed. This means that if one of the streams is maldistributed, the other stream will also be affected, roughly doubling the negative consequences in the thermal performance.

In Chapter 8, this homogenization approach is extended and partial flow mixing in the shell-side is incorporated to the model, with contributions from both turbulent mass exchange and pressure-differences driven cross flow. In this framework, the effects of possible heterogeneities between the layers are investigated. For example, small differences in the diameter or mass flow rate result in interesting flow mixing profiles, following the trend of experimental observations reported in the open literature. In addition, it is observed that allowing for flow mixing, the negative impact of flow maldistribution is slightly reduced.

Chapter 7

Flow maldistribution

► This chapter deals with the consequences of the flow distribution in parallel channels deviating from the (usually homogeneous) design conditions, on heat exchanger performance. The available literature, reviewed in Chapter 2, is dominated by single-phase applications and there is limited information for two-phase flow systems. In order to simplify the analysis, the selected geometry (shell–and-tube) is represented in terms of several layers.

In particular, the pressure coupling between parallel channels is emphasized. The results presented in this chapter indicate that this boundary conditions imposed by the connections at inlet and outlet header produces a secondary maldisitribution. This means that if one of the streams is maldistributed, the other stream will also be affected. In the case of neglecting this effect, the negative consequences in the total heat duty would be underestimated.

In industrial cryogenic applications the required surface area in the main heat exchangers is very large, in the order of several thousand square meters (Bach et al., 2001). For this reason, the most used heat exchanger geometries, described in Section 2.2.2 present a parallel channels configuration. On the positive side, this design allows to accommodate a large heat-transfer area in a limited space. On the negative side, however, it also leads to problems related to flow distribution.

When designing power-controlled systems, the flow is distributed according to the heat generation rate in order to keep a rather uniform temperature. Then, for example in nuclear reactors the flow rate is larger in the inner regions than close to the outer wall. In heat exchangers, which are wall temperature-controlled system, there is no fundamental reason to determine that some channel might need a larger flow rate than others. For this reason, in order to keep a balanced and smooth operation, the stationary design flow distribution is homogeneous. However, in many scenarios it can deviate from these usually homogeneous design conditions. Different causes, reviewed by Mueller and Chiou (1988) might lead to

flow maldistribution. These can be categorized as:

- A deficient performance of devices designed to distribute and collect the flow among parallel channels, that is the inlet and outlet headers. These devices make use of area changes and flow restrictions in order to provide a homogeneous distribution, which is never perfect. In addition, off-specifications inlet conditions might result in a large reduction in their performance.

- In shell-and-tube type geometries such as the coil-wounded HE, the flow in the shell-side can deviate from its path due to effects known as leakage and bypass (Shah and Sekulić, 2003), given by the imperfect mechanical assembly of the shell and baffle plates.

- Other mechanical reasons, such as differences between the channels due to fouling or corrosion, as well as fabrication tolerances in the tube length or diameter. These disparities lead to diverse pressure drop characteristics for each channel, thus affecting the flow distribution.

- In the case of flows with variable properties, the application of different heat loads may lead to problems of flow distribution. For a homogeneous flow distribution, a larger heat flux results in a higher temperature. As a consequence, there will be channels with different physical properties such as density and viscosity, affecting the pressure drop characteristics. Finally, considering that all channels are connected at both inlet and outlet, and consequently their pressure drop are related, the respective mass flow rates are affected. Such is the case of highly viscous single-phase fluids, as well as boiling and condensing flows.

- An unstable situation can also be originated with an homogeneous heat flux. Given the influence of the heat input in the flow physical properties and consequently the friction characteristics, two or more channels can have the same pressure drop with different flow rates. This situation may trigger flow instabilities (such as the Ledinegg instability), and the flow rate does not reach an stationary value (Kakaç and Bon, 2008).

The analysis of the consequences of flow maldistribution on heat transfer performance has been focused on single-phase applications, as described in Section 2.5.2. In this case, a reduction of performance is always noticed as a consequences of the reduction in the average temperature difference (Fleming, 1967). This effect is small (less than 5%) for most practical cases, with the exception of large-efficiency exchangers such as those used in cryogenic applications (Mueller and Chiou, 1988). The consequences of flow maldistribution are more relevant for power-controlled systems (Lalot et al., 1999), since they may lead to extremely high local temperatures and mechanical failure due to thermal stresses.

For two-phase applications, the analysis has been mostly focused on the flow distribution in manifolds, and their design. The vast list of reports in literature was reviewed by Marchitto et al. (2008) and continued to extend ever since (Ablanque et al., 2010; Ahmad et al., 2009; Byun and Kim, 2011; Wen et al., 2008). The general conclusion of these studies indicate that the heavier phase (liquid) tends to flow preferably in the inner channels, while the lighter phase (gas) deviates towards the most outer tubes, as a consequence of inertial effects. Nevertheless, a generic two-phase flow distribution profile has not yet been proposed.

Regarding the thermal performance of two-phase flow heat exchanger with maldistribution, both evaporators and condensers have been considered by previous researchers. On the one hand, the total heat duty is always reduced in condensers (Rabas, 1985; Rao et al., 2006; Srihari et al., 2005). On the other hand, in the case of cross-flow air-heated evaporators some increase in thermal performance has been observed in experiments.

These models are based on the solution of energy balances assuming a given flow distribution (see Section 7.2). In the single-phase case, an average temperature difference and heat transfer coefficient are considered (Lalot et al., 1999; Mueller and Chiou, 1988). For two-phase flow, this averaging procedure becomes too cumbersome and a two-dimensional model is used instead (Rao et al., 2006). The momentum equation is studied uncoupled from the energy balance, and pressure drop is generally computed a posteriori.

Therefore, present models do not consider neither the coupling of channels at inlet and outlet by means of pressure equalizing mechanisms (it is assumed to be implicitly considered by the selected flow distribution model), nor the feedback between pressure drop and heat transfer described in Chapters 5 and 6.

Since pressure drop for all channels are interrelated, the existence of flow maldistribution in one stream can affect the distribution on the other stream, as has been experimentally noticed by Aganda et al. (2000). This secondary maldistribution is expected to affect the thermal performance, with a positive or a negative effect depending on its relation with the primary one.

The multichannel heat exchanger problem is presented in Section 7.1, based on energy and momentum balances for each individual channel. Since this model involves individual boundary conditions, different flow distribution profiles are discussed in Section 7.2. This framework is then applied to three study cases, as indicated in Fig. 7.1. A reference homogeneous case is presented in Section 7.3, and two cases with flow maldistribution in the tube-side are analyzed according to two different models in Sections 7.4.1 and 7.4.2 and compared in Section 7.4.3. Finally, a summary is presented in Section 7.6.

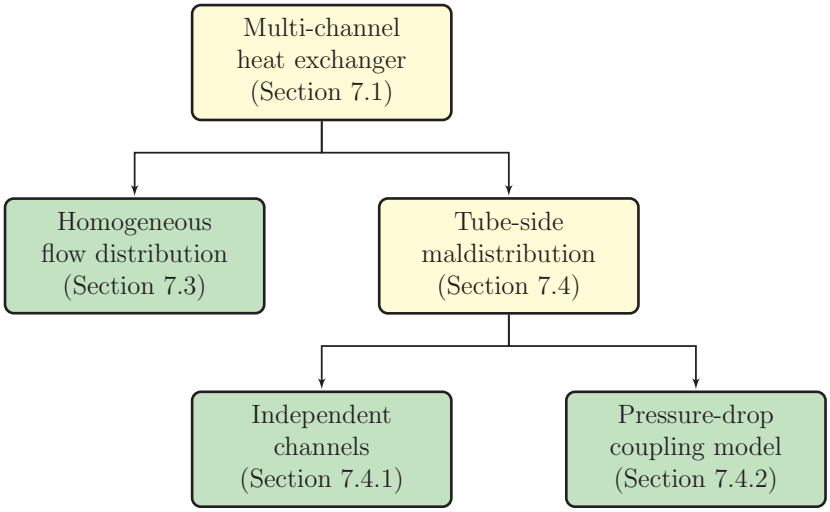

Figure 7.1: Three cases, highlighted in green, are considered in this chapter

7.1 The multichannel one-dimensional heat exchanger problem

The physical model presented in part II (Chapters 5 and 6) considered single-channel geometries, in particular a tube-in-tube heat exchanger. Considering multiple parallel channels, more complex geometries can be modeled. In particular, a countercurrent shell-and-tube heat exchanger, sketched in Fig. 7.2, is analyzed. Nevertheless, the analysis described in this chapter can be easily extended to other geometries and flow arrangements.

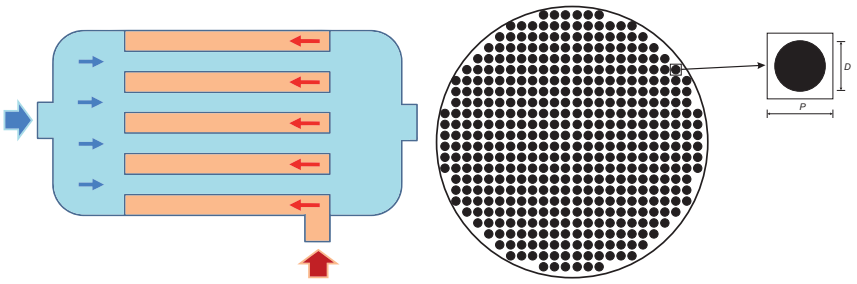

(a) Side view (b) Front view

Figure 7.2: Scheme of a counterflow shell-and-tube heat exchanger

The following simplifying assumptions are considered

1. A steady-state analysis is performed. Then, stationary operating conditions are assumed and temporal variation given, i.e. flow instabilities are disregarded.

2. The working fluids are single-components, not mixtures.

3. Mixing between channels does not occur. This means that they do not exchange mass nor momentum.

4. An elemental geometry can be identified where hot and cold stream exchange energy, and the interaction with other channels is negligible. In other words, the heat exchanger can be divided in smaller subunits. For the selected shell-and-tube geometry, this is indicated in Fig. 7.2(b).

Then, considering these assumptions, the physical model described in Chapter 5 can be applied to each individual subunit. For this case, a mass balance equation is not required since, for steady-state conditions and single-component fluids, it gives a trivial result, that is a constant mass flux in each channel.

The governing equations are given by momentum and energy balances for both tube and shell streams in each channel j, as in Eqs. (7.1) and (7.2), respectively, where the subindices S and T stand for shell- and tube-side streams. Since no local interaction between channels are considered, each set of Eqs. (7.1) and (7.2) is independent and can be solved separately. Both the shear stress τ and the overall heat transfer coefficient U are described in terms of empirical correlations presented in Chapters 4 and 5.

$$\frac{d}{dz}\left(\frac{G_{T,j}^2}{\rho_{T,j}} + p_{T,j}\right) + \rho_{T,j}(z)g + \frac{4}{D_{h,T,j}}\tau_{T,j}(z) = 0 \tag{7.1a}$$

$$\pm\frac{d}{dz}\left(\frac{G_{S,j}^2}{\rho} + p_{S,j}\right) + \rho_{S,j}(z)g + \frac{4}{D_{h,S,j}}\tau_{S,j}(z) = 0 \tag{7.1b}$$

$$G_{T,j}\frac{dh_{T,j}}{dz} + \frac{4}{D_{eq,T,j}}U(z)\left[T_{S,j}(z) - T_{T,j}(z)\right] = 0 \tag{7.2a}$$

$$\pm G_{S,j}\frac{dh_{S,j}}{dz} + \frac{4}{D_{eq,S,j}}U(z)\left[T_{T,j}(z) - T_{S,j}(z)\right] = 0 \tag{7.2b}$$

The consideration of individual balance equations for each heat exchanger subunit j allows to take into account all type of heterogeneities, like differences in geometrical parameters or inlet conditions. In addition, this approach is also applicable to multi-stream heat exchangers by selecting different working fluids in each channel. In this chapter, the only differences between channels are given by the flow rates: a flow distribution profile is imposed according to the models discussed in Section 7.2.

7.2 Flow distribution models

As described in Section 7.1, the solution of the multichannel heat exchanger problem requires the input of individual parameters for each channel. In particular, an individual mass flow rate is required, in other words, a flow distribution profile must be imposed. Extensive research in this topic has been reported in literature concerning the design of plate headers. These models are described in Section 7.2.1.

Current research on two-phase flow distribution in manifolds indicates that the gas and liquid phase are not equally disseminated in the parallel channels. In particular, depending on the flow pattern at the inlet, the flow distribution can be rather homogeneous (intermittent churn flow) or preferably more liquid can go through the inner tubes (downward annular flow) or viceversa (upward annular), as observed by Vist and Pettersen (2004). In this chapter, however, single-phase flow is considered at the inlet. In this context, a simple distribution profile applicable to a a shell-and-tube geometry is proposed in Section 7.2.2.

7.2.1 Classical models for plate headers

Traditional models identify the header design as the main cause for flow maldistribution. The two most common geometries for plate headers, that is the U-type and Z-type, are presented in Figs. 7.3(a) and 7.3(b), respectively. In both figures, the fluid enters at the bottom and exits at the top, with the flow channels oriented in the z direction, and the headers distribute the flow among the channels along the y direction.

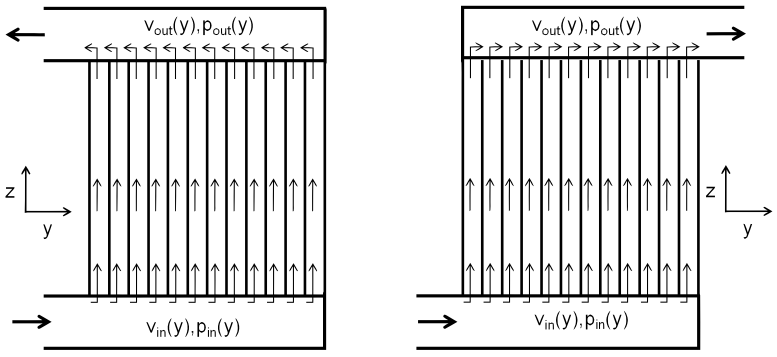

(a) U-type (b) Z-type

Figure 7.3: Plate header geometries

In a steady-state analysis, the total pressure drop between inlet and outlet nozzles is the same for all the flow path. However, due to inertial and friction effects in the inlet header, where the flow is distributed, the pressure $p_{in}(y)$ at the inlet

of the channels is not uniform. Similarly, in the outlet header, where the flow is collected, the pressure $p_{out}(y)$ is also not uniform for the same reasons. In general, this situation leads to a different net pressure drop for each channel $\Delta p(y) = p_{in}(y) - p_{out}(y)$. Considering that the flow is driven by pressure differences, this condition results in a flow maldistribution.

The inertial effects in both manifolds play a major role as causes of flow maldistribution. In the inlet header, the flow rate in the y direction is depleted as the fluid is distributed among the channels, thus resulting in a pressure increase due to a lower velocity v. The opposite effect occurs at the outlet header. Considering these effects, the ratio of maximum to average velocities can be approximated (Fraas, 1989) as in Eq. (7.3), where u and v represent the flow velocities in the z and y direction, respectively.

$$\frac{u_{max}}{u_{avg}} \approx \sqrt{1 + \frac{\rho v_{in}^2}{\Delta p_{avg}}} \tag{7.3}$$

Equation (7.3) indicates that the flow maldistribution can only be neglected if the pressure drop in the channels Δp_{avg} is much larger than the inertial effects. In the general case, the flow distribution can be obtained from a control volume analysis as presented in Fig. 7.4. The five variables (v_{in},v_{out},p_{in},p_{out} and u) are obtained from the same number of equations: mass and momentum balances at the inlet and outlet headers, and the pressure drop characteristics of each channel.

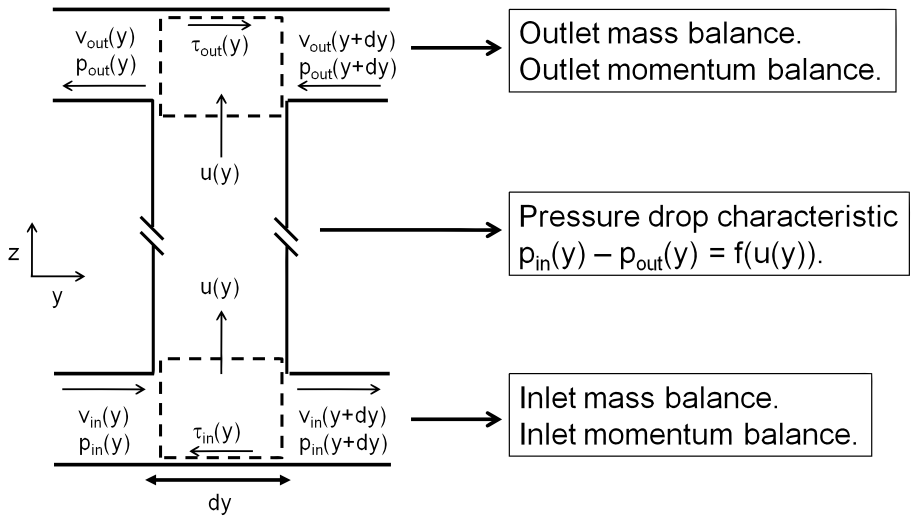

Figure 7.4: Control volume analysis of plate headers

Some analytical and numerical results have been reported for applications in-

volving incompressible liquids and identical channels. In general, this analysis facilitates the design of manifolds in order to achieve a well-distributed flow. However, its extension to a more complex situation such as boiling flow is not practical. In the case of two-phase flow, the fluid physical properties at the inlet and outlet headers are different, and depend on the solution of the flow distribution. Therefore, they cannot be successfully applied to two-phase heat exchangers, which are the subject of the present study.

The pioneer work by Bassiouny and Martin (1984a;b) remains today as the most widely used distribution profile for this geometry. Considering only inertial effects and neglecting friction in the manifolds, the authors represented the flow distribution in terms of a single parameter, related to the cross-sectional areas, for both U- and Z-type headers. However, the assumption of negligible friction is only applicable for short manifolds.

In the case of large headers, the frictional terms might dominate over the inertial effects. Following this premise, Maharudrayya et al. (2005) and Kee et al. (2002) incorporated the frictional term for their analysis of fuel cell manifolds. While the first neglected inertial effects completely, the second one incorporated them, although assuming equal inlet and outlet flow areas. Then, their analysis can not be applied to a generic case. More recently, Wang (2008; 2010) provided analytical results for the generic problem including both inertial and frictional effects. The author also showed that all previous models are particular cases of this general expressions.

7.2.2 Selected profile for this geometry

While the traditional models for plate headers, described in Section 7.2.1, predict exponential-type flow distribution profiles, the situation is somehow different for a shell-and-tube heat exchanger, given the radial geometry. In a way, the manifold system is similar to the U-type presented in Fig. 7.3(a), since the flow enters in the centerline, is distributed along the outer channels and is once again collected in the center at the outlet. In another way, the main difference is given by a variable flow area in the headers, characteristic of radial geometries. Finally, analyzing the symmetry of this geometry, it can be concluded the flow rate should either be maximum or minimum at the centerline.

These considerations lead to propose a parabolic profile for the mass flux, as in Eq. (7.4), being maximum at the center ($r = 0$) and minimum at the outer wall ($r = R_{shell}$).

$$\frac{G(r)}{G_{avg}} = 1 + \mu \left[1 - \left(\frac{r}{R_{shell}} \right)^2 \right] \tag{7.4}$$

The coefficient μ represents a maldistribution parameter, defined as in Eq. (7.5), representing the maximum deviation from an homogeneous distribution. In prin-

ciple, since additional causes for maldistribution may be present, it does not have a direct relation to the headers flow areas, and it is considered as an additional degree of freedom.

$$\mu = \frac{G_{max} - G_{avg}}{G_{avg}} = \frac{G_{max}}{G_{avg}} - 1 \tag{7.5}$$

In order to avoid the individual analysis of each channel, since the number of tubes can be rather large, a simplifying approach is undertaken. Those channels with similar flow rate are grouped together, and the exchanger is modeled on the basis of several of these groups. In particular, assuming axial symmetry, N radial layers are considered, as illustrated in Fig. 7.5. This approach can also be applied to plate-type geometries, considering slabs instead of radial layers.

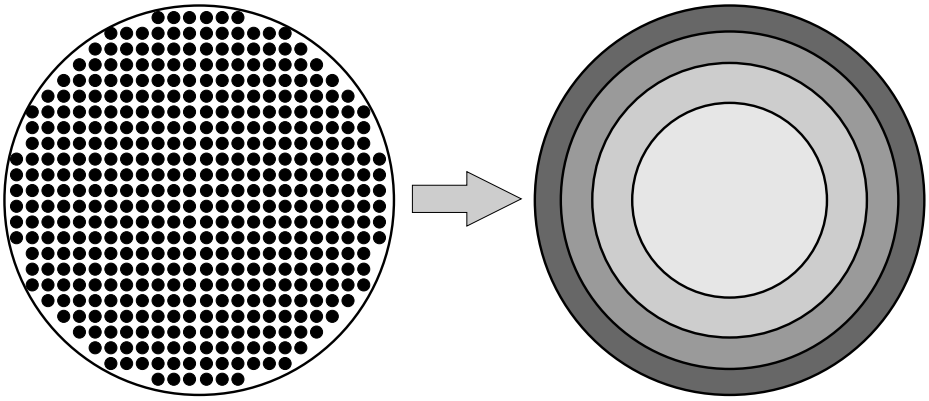

Figure 7.5: Shell-and-tube heat exchanger divided in radial layers

Furthermore, equal cross-sectional area layers are considered. Therefore each layer includes the same number of tubes. This is achieved by defining the outer radius R_j of each layer j as in Eq. (7.6). They are numbered continuously from $j = 1$ (for the most inner layer) until $j = N$ (for the most outer one).

$$R_j = R_{shell}\sqrt{\frac{j}{N}} \tag{7.6}$$

Finally, considering the proposed mass flux and the grouping of channels in layers, the mass flow rate in each layer $\dot{m}_j$ results from the integration of Eq. (7.4), obtaining the expression in Eq. (7.7). It should be noted that a linear profile is obtained with two degrees of freedom: the maldistribution parameter μ and the number of layers N.

$$\dot{m}_j = \frac{\dot{m}_{total}}{N}\left[1 + \mu\left(1 - \frac{2j-1}{N}\right)\right] \tag{7.7}$$

7.3 Results for an homogeneous case

A case with homogeneous distribution in both streams is studied in this section. this analysis provides reference results for further comparison of two the maldistributed cases presented in Section 7.4.

This reference homogeneous case can be completely defined by three sets of parameters, related to the geometry, working fluids and inlet conditions.

- A shell-and-tube geometry is considered, as described in Fig. 7.2. It consists of 600 tubes, 8.0 mm in diameter and 5m in length, arranged in a square-lattice array with a 10.4 mm pitch. The flow orientation is horizontal.
- Inside the tubes, condensing propane flows at a rate of 1.24 kg s^{-1}. In the shell-side, 2.31 kg s^{-1} of boiling R134a flow in the opposite direction, in a countercurrent arrangement. These conditions were selected to imitate the liquefaction process of LNG, where a boiling refrigerant flows in the tube-side, where a hydrocarbon is condensing in the shell-side, with close-to-balanced heat capacity flow rates.
- The inlet conditions are selected close to ambient temperatures, which could be more easily reproduced in laboratory scale. Then, the propane enters at 290 K and a pressure of 7 bar, and the cold refrigerant at 280 K and 4 bar.

Since this is an homogeneously distributed case, all the channels are indistinguishable from each other. Therefore, the number of layers is irrelevant and the governing equations described in Section 7.1 need to be solved only once. The reference solution is presented in Fig. 7.6 in terms of (a) temperature and (b) pressure profiles. This is a countercurrent arrangement, and the tube-side fluid enters at $z = 0$, thus flowing from left to right, and the opposite applies for the shell-side stream, entering at $z/L = 1$.

In general, the conclusions that can be withdrawn from Fig. 7.6 are similar to those expressed in Section 5.3.3. The roughly horizontal lines in the temperature profile correspond to saturation temperature of each fluid. The variations in pressure which, according to Fig. 7.6(b) are limited to a 1.5%, affect this saturation temperature. These variations have consequences in the heat transfer performance, as described in Chapter 5. Figure 7.6(a) also indicates that the propane (tube-side) reaches full condensation, and R134a (shell-side) is fully evaporated.

In addition to the profile solutions, some integral results are of interest for quantifying the performance. These results are useful for comparing the maldistributed cases in Section 7.4. In particular, three responses are studied:

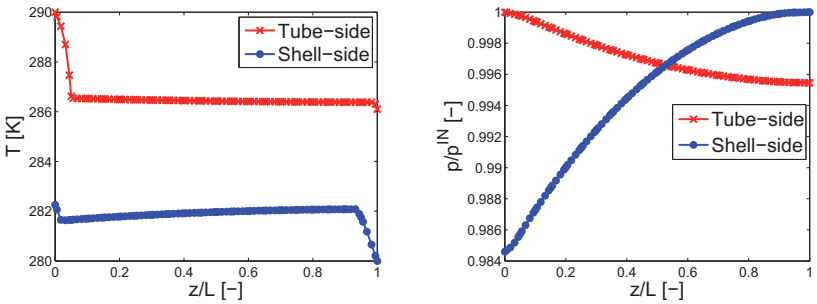

(a) Temperature profiles

(b) Relative pressure profiles

Figure 7.6: Profile solution for the reference homogeneous case

- Total heat duty Q_{ref}=449.92 kW
- Tube-side pressure drop $\Delta p_{T,ref}$=3.184 kPa
- Shell-side pressure drop $\Delta p_{S,ref}$=6.161 kPa

7.4 Tube-side maldistributed cases

Two cases with flow maldistribution in the tube-side are studied in this section, as described in Fig. 7.1, according to the flow distribution profile proposed in Section 7.2.2 and two models for the evolution of the shell-side stream. First, no interaction between the channels is considered, and they are assumed to be independent in Section 7.4.1. Finally, the results of a second model which incorporates an equal outlet pressure constraint are presented in Section 7.4.2.

7.4.1 First model. Independent channels

A first approach for evaluating the effects of maldistribution consists in solving the governing Eqs. (7.1) and (7.2) for each layer separately with no interaction between them. In particular, a homogeneous distribution is assumed for the shell-side stream, and flow maldistribution is considered for the tube-side according to the profile given by Eq. (7.7). For simplicity, a case with N=2 layers is studied first and is later extended in a parametric analysis.

Study case: μ_T=0.2 and N=2 layers

Figure 7.7 presents profile solutions for a case characterized by a maldistribution coefficient μ_T=0.2 and only two layers for both the tube- (red, warm) and shell-side

(blue, cold) streams. This means that 60% of the total tube-side flow go through the inner layer and the rest (40%) in the outer layer.

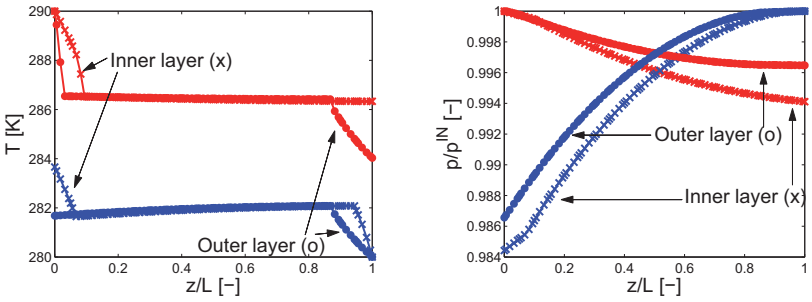

(a) Temperature profiles

(b) Relative pressure profiles

Figure 7.7: Profile solutions of the first maldistribution model for a case with $\mu_T = 0.2$ and $N = 2$ layers

The consequences of maldistribution in the energy balances are illustrated in the temperature profiles in Fig. 7.7(a). When the flow is maldistributed between two layers, both subunits are unbalanced in terms of heat capacity flow rate. Then, in the inner layer the tube-side exits as a two-phase mixture, while in the outer layer, full condensation is reached. As a consequence, the heat duty in each layer is different as Eq. (7.8) indicates. This value for the total heat duty is 3.95% lower than the reference corresponding to the homogeneous case studied in Section 7.3.

$$\left.\begin{array}{l} Q_{inner} = 226.50\ kW \\ Q_{outer} = 205.64\ kW \end{array}\right\} Q = Q_{inner} + Q_{outer} = 432.14\ kW \tag{7.8}$$

Regarding the momentum balance equation, the pressure profiles illustrated in Fig. 7.7(b) indicate some differences between the layers. In the case of the tube-side, the pressure drop is larger in the inner layer, due to larger flow rate. Since this stream is maldistributed, this difference in pressure drop is allowed, since they can be the original cause for maldistribution (Mueller and Chiou, 1988).

Some pressure differences are also observed for the shell-side stream. In this case, since this flow is homogeneously distributed, the differences in pressure drop cannot be too large for a steady-state analysis. These differences are given in Eq. (7.9), representing 13.9% of the reference value ($\Delta p_{S,ref}$=6.161 kPa).

$$\left.\begin{array}{l} \Delta p_{S,inner} = 6.231\ kPa \\ \Delta p_{S,outer} = 5.373\ kPa \end{array}\right\} \Delta p_{S,inner} - \Delta p_{S,outer} = 0.858\ kPa \tag{7.9}$$

At first sight, equal pressure drop is expected in steady-state because the different channels are connected at both inlet and outlet. However, there is experimental

evidence (Chandraker et al., 2002) of pressure differences between parallel channels in the outlet header in the order of a few times the inertial term G^2/ρ. In this case, these inertial terms are $(G^2/\rho)_{S,inner}$=0.251 kPa and $(G^2/\rho)_{S,outer}$=0.094 kPa. Then, for this particular case, the pressure differences in the shell-side could be acceptable for a steady-state analysis.

Parametric analysis

Extending this model to N layers, a parametric analysis on μ_T is presented in Fig. 7.8 in terms of (a) variations in the heat duty and (b) differences in the shell-side pressure drop. A maximum maldistribution coefficient of $\mu_T = 0.4$ is considered, and the differences in the tube-side pressure drop are disregarded since this stream is maldistributed.

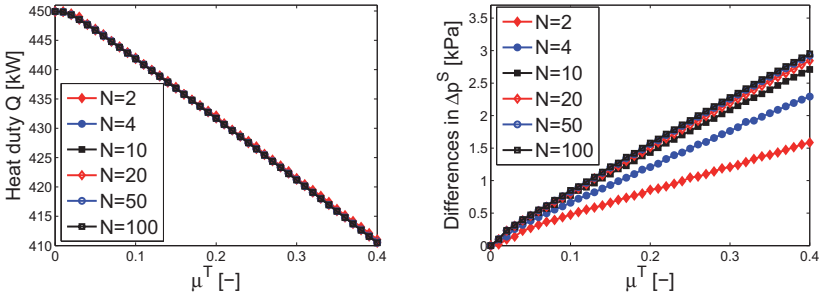

(a) Total heat duty

(b) Differences in shell-side pressure drop

Figure 7.8: Parametric analysis on μ_T and number of layers for the independent-channels model

The evolution of heat duty, presented in Fig. 7.8(a) is not influenced by the number of layers considered (N). This results is expected, since the different independent subunits do not interact with each others. In all cases, the performance is further reduced when increasing the maldistribution coefficient, up to a maximum reduction of 39.44 kW, that is a 8.77% of the reference value.

In the case of Fig. 7.8(b) the situation is different, where differences in shell-side pressure drop are strongly dependent on N. This pressure drop depends on both the mass flow rate (which in the shell-side is uniform) and the heat flux. In a heat exchanger, this heat flux is influenced by the heat capacity flow rate in the other stream, that is the tube-side. As a consequence, the differences in Δp_S are strictly related to the differences in the tube-side flow rate $\dot{m}_T$. According to the flow distribution profile proposed in (7.7), these differences are proportional to $1/N$. This condition is reflected as an asymptotic behavior in Fig. 7.8(b), and the results are indistinguishable for $N > 50$.

This parametric analysis indicates that these differences in Δp_S increase with μ_T and asymptotically also with N. In general, they can result much larger than the inertial term G^2/ρ =0.251 kPa that could be expected inside the header. This means that these differences cannot be allowed in a steady-state analysis, providing the motivation for incorporating some interaction between layers related to pressure drop, as proposed in Section 7.4.2.

7.4.2 Second model. Pressure-coupled channels

The results from the first model presented in Section 7.4.1 predict large differences in the shell-side pressure drop which cannot be allowed in a steady-state description. A more complete model must account for the coupling between channels: since they are all connected at both inlet and outlet headers, a homogeneous shell-side pressure drop constraint is incorporated, as given by Eq. (7.10).

$$\Delta p_{S,j} = \text{ constant } = \Delta p_S \quad \forall j = 1, \ldots, N \tag{7.10}$$

It should be remarked that this steady-state pressure drop is not necessarily equal to the reference value for a homogeneous flow distribution and in the general case $\Delta p_S \neq \Delta p_{S,ref}$. In order to evaluate the new pressure drop incorporating this constraint, some other conditions must be relaxed. In particular, the shell-side mass flow is expected to redistribute between the channels with a profile that is unknown *a priori*.

Then, this problem has a total of $N + 1$ unknowns: the pressure-drop level Δp_S and N values for $\dot{m}_{S,j}$. In order to obtain the values for these variables, the same number of algebraic equations is required for solving the system. As in any pressure-driven flow system, the steady-state solution is given by the intersection of internal and external pressure-drop characteristic curves $\Delta p(\dot{m})$. In other words, a solution is reached when the pressure difference provided by the external pump or other device compensates exactly for the pressure drop in the channel.

The internal characteristic pressure-drop curve for gas-liquid flow depends on both the mass flow rate $\dot{m}_{S,j}$ and the imposed heat flux. For a given geometry and inlet conditions, the heat flux in a HE depends on both tube- and shell-side mass flow rates. This situation is represented by a set of N equations as follows, where ϕ_{int} is the internal characteristic of the system.

$$\Delta p_{S,j} = \phi_{int}\left(\dot{m}_{T,j}, \dot{m}_{S,j}\right) \tag{7.11}$$

Figure 7.9 presents the evolution of Δp_S according to the internal characteristic function ϕ_{int} respect to (a) both flow rates and for individual variations in (b) $\dot{m}_{S,j}$ and (c) $\dot{m}_{T,j}$, at selected constant values of the other stream flow rate. A more detailed resolution is provided around the reference values.

For some values of $\dot{m}_{T,j}$ (which represents the heat flux for shell-side), a slightly N-shaped curve is noticed in Fig. 7.9(b). In particular, this is noticed

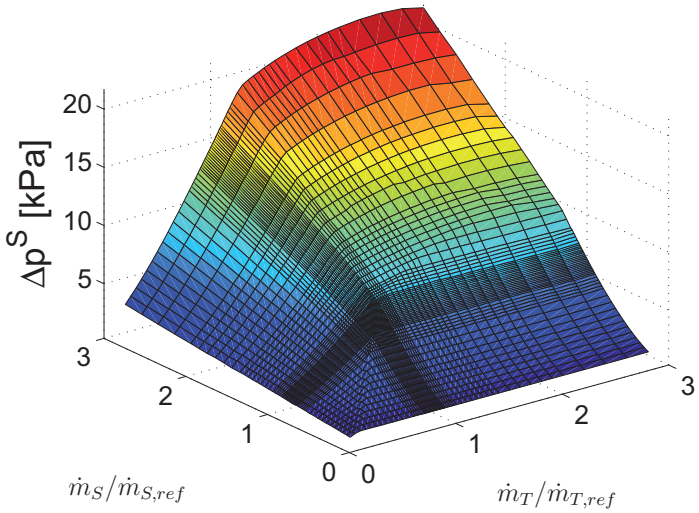

(a) Surface plot presenting dependencies on both tube- and shell-side flow rates

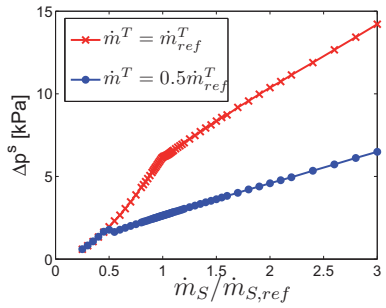

(b) Constant tube-side flow

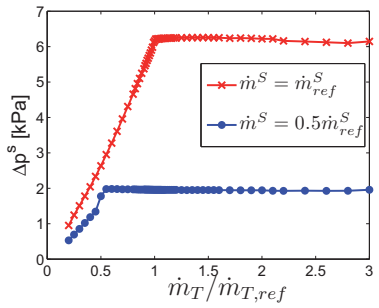

(c) Constant shell-side flow

Figure 7.9: Evolution of shell-side pressure drop respect to tube- and shell-side mass flow rates, representing the internal characteristic pressure drop curve ϕ_{int}

for $\dot{m}_{T,j} = 0.5\dot{m}_{T,ref}$ and $\dot{m}_{S,j} \approx 0.5\dot{m}_{S,ref}$. This N-shaped curve implies that the same pressure drop can be obtained with three different values of the shell-side flow rate, thus providing a necessary condition for Ledinegg instability (Kakaç and Bon, 2008). In addition, this condition might represent a possible cause for flow maldistribution for the shell-side, since different layers can have different flow rate with the same pressure drop.

Increasing the tube-side flow represents an increase in the heat flux for the shell-side. Then, the vapor content is increased, giving a larger pressure drop, as

represented in Fig. 7.9(c). After reaching full evaporation, Δp_S remains roughly constant because the heat exchanger efficiency is close to 100% and therefore the heat flux cannot be further increased.

The external characteristic relation between Δp_S and $\dot{m}_S$ is given by the flow-driving device and consider only the total mass flow rate, disregarding the parallel-channels configuration. This situation, represented by Eq. (7.12), provides the additional equation required for solving the system.

$$\phi_{ext}\left(\Delta p_S, \sum_{j=1}^{N} \dot{m}_{S,j}\right) = 0 \tag{7.12}$$

Three extreme functional forms for ϕ_{ext} are sketched in Fig. 7.10. On the one hand, an extreme case would be (a) the use of high and low pressure tanks, thus providing a constant Δp_S, independent of the flow rate. On the other hand, the opposite extreme is given by (b) a constant flow. This situation would be achieved if the exchanger is part of a large system where the total pressure drop is dominated by other components, such as an expansion valve. Then, with the same mass flow rate for all processes, this results independent of Δp_S. An intermediate situation is found in case that (c) a pump is used as a driving force and the pressure drop is given mainly by the exchanger.

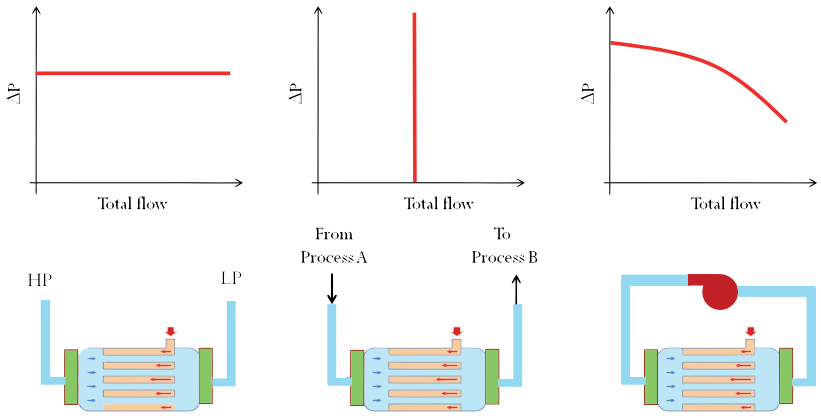

(a) Pressure tanks (b) Process (c) Pump

Figure 7.10: Three example cases of external pressure drop characteristic curve

In this section the constant mass flow rate scenario, represented by Fig. 7.10(b), is selected, because it is considered to be applicable to a large number of practical situations. In particular, for refrigeration processes, the overall pressure drop is largely dominated by the expansion valves, who regulate the flow rate and therefore it is constant respect to the operation of the heat exchanger.

With all these considerations, this model can be solved following these steps:

1. Given the tube-side flow distribution profile $\dot{m}_{T,j}$, a set of N curves $\Delta p_{S,j}$ as a function of $\dot{m}_{S,j}$ can be obtained individually for each layer from Eq. (7.11) or Fig. 7.9. Some examples are indicated in Fig. 7.9(b).

2. These curves can then be added for developing a curve of total mass flow rate as a function Δp_S, representing the internal characteristic ϕ_{int} of the heat exchanger.

3. The solution is given by the intersection of the internal and external characteristic curves. In this case, a constant flow line is selected. This intersection gives the solution for the values of Δp_S and the total shell-side flow.

4. Finally, once Δp_S is known, the shell-side flow rate in each layer can be evaluated from the individual internal characteristic (ϕ_{int}) curves obtained in the first step.

This procedure is first applied to a case with μ_T= 0.2 and N=10 layers, and later extended in a parametric study.

Study case: μ_T=0.2 and N=10 layers

Figure 7.11 presents the results for this study case in terms of (a) flow distribution and (b) temperature profiles for the inner (j=1) and outer layer ($j = N$).

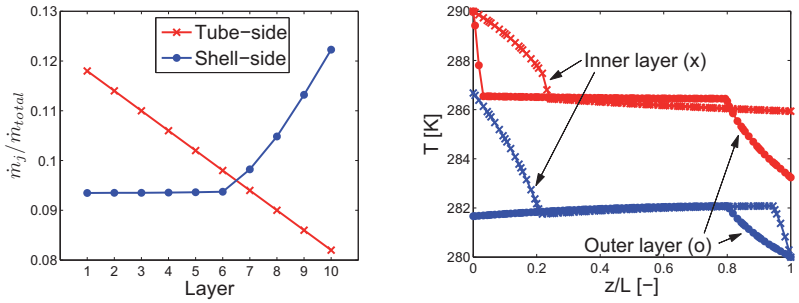

(a) Flow distribution

(b) Temperature profiles

Figure 7.11: Results for the coupled-channels model. Study case: μ_T=0.2 and N=10 layers.

Observing Fig. 7.11(a), it is noticed that less shell-side flow goes through the inner layer (with the larges tube-side flow) than in the others. This situation arises because the largest tube-side flux represents the highest heat flux and frictional effects. As a consequence, the vapor content on the inner layers is increased,

and the opposite occurs in the outer layers. Similar consequences can be drawn observing Fig. 7.11(b), which indicates that full evaporation in the shell-side is reached in the inner layer, while in the outlet layer, the shell-side fluid exits at saturation temperature in $z = 0$.

This secondary maldistribution in the shell-side is opposite to the tube flow profile: the shell-side flow is larger in the layer where the tube-side flow is lower. As a consequence, the heat exchanger is further unbalanced in terms of heat capacity flow rate. Then, the heat transfer performance is further reduced, and the heat duty is 33.35 kW (7.41%) lower than the reference case. This reduction is rougly twice as large as the one predicted by the first model (independent channels) presented in Section 7.4.1.

In addition to the reduction in heat transfer performance, the shell-side pressure drop has also been reduced by this secondary maldistribution resulting in Δp_S=5.6 kPa, that is a 9% lower than the reference homogeneous case. It should be reminded that in this example, it was assumed that the total mass flow rate is constant for any value of Δp_S. This assumption is strictly valid only within certain operating range. For refrigeration processes, this range is indeed large, since the overall pressure drop is dominated by other equipment. Nevertheless, in the general case, this assumption should be reviewed in view of the variations observed in Δp_S.

Parametric analysis

The results from a parametric analysis respect to the maldistribution coefficient μ_T and the number of layers N is presented in Fig. 7.12 for the evolution of (a) the total heat duty and (b) the pressure drop in the shell-side stream.

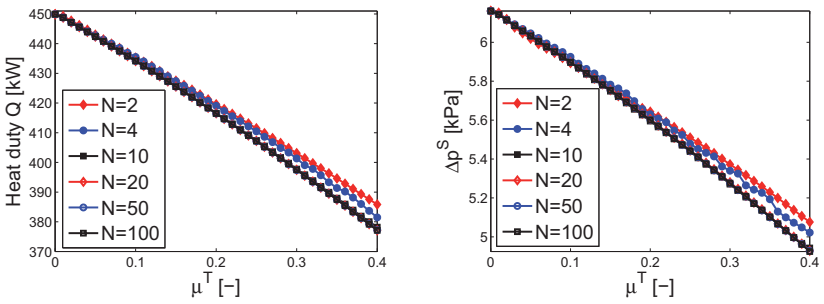

(a) Total heat duty (b) Shell-side pressure drop

Figure 7.12: Parametric analysis on μ_T and number of layers for the coupled-channels model

Increasing the maldistribution coefficient μ_T, a larger reduction in the heat

duty is observed in Fig. 7.12(a). Although this result is dependent on the number of layers, they approach asymptotically to a single-curve, since the differences are negligible for $N > 10$. The maximum reduction observed in heat duty is of 72.84 kW (16.2% of the reference value), that is roughly twice as large as predicted by the first model. This larger effect in the heat transfer performance is a consequence of the secondary maldistribution in the shell-side stream. In addition, while the first model (independent channels) predicts the same heat duty for any number of layers, the situation is different for this second model which takes into account the pressure-coupling between channels. This situation is further studied in Section 7.4.3.

The shell-side pressure drop is also reduced with increasing μ_T and number of layers, with a minimum value of 4.924 kPa, that is 20.08% lower than the reference value. This result can be explained by analyzing the internal characteristic pressure drop curves presented in Fig. 7.9. In particular Fig. 7.9(c) presents the dependence of Δp_S on $\dot{m}_T$ at a constant shell-side mass flow rate. For example, consider the case of $\dot{m}_{S,j} = \dot{m}_{S,ref}$. On the one hand, a reduction of 10% on $\dot{m}_T$ from its reference value, produces a reduction on Δp_S of 0.788 kPa. On the other hand, a similar increase of 10% produces a much smaller change in Δp_S, increasing it in only 0.071 kPa. These differences in Δp_S must be fixed by a re-distribution of shell-side flow, and the final value for Δp_S is stabilized at an intermediate value between both extremes. Since the effect of reduction in Δp_S is larger, this final value is lower than the original reference value.

7.4.3 Comparing both models

Each of the above models presents some advantages and disadvantages. On the one hand, the first model (independent channels) is rather simple and provides a straightforward solution, although it predicts unrealistic pressure differences. On the other hand, the second model (coupled channels) account for the equal-pressure coupling between channel and is more computationally intensive since it implies the construction of an internal characteristic response surface as in Fig. 7.9(a). Therefore it is important to establish the applicability range of the first model and the differences between both approaches.

The predicted reduction in heat duty according to both models is compared in Fig. 7.13 in a parametric study of the maldistribution coefficient μ_T. Since the results of the second model, discussed in Section 7.4.2 depend on the number of layers, two extreme cases are presented: $N = 2$ and $N = 100$. At this point it should be reminded that these results are asymptotic and the differences are negligible for $N > 50$.

The first conclusion that can be drawn from Fig. 7.13 is that in all cases a reduction in the heat transfer performance is observed, and the second model predicts a larger effect, as a consequence of the secondary maldistribution. In this study, the results are compared respect to the predictions of the second model

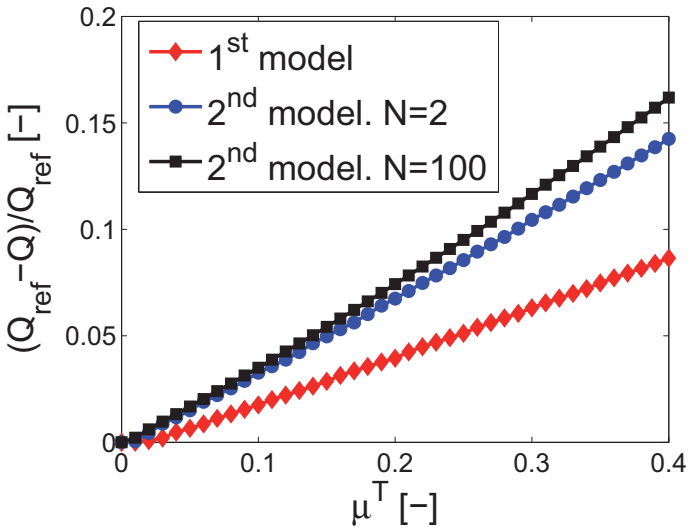

Figure 7.13: Schematic of a counterflow shell-and-tube heat exchanger

with the larger number of layers, since these can be considered the most reliable ones as this is the most complete model.

In this context, it is observed in Fig. 7.13 that these reference predictions are roughly twice as large as those of the first model. In order to quantify this relation, the average of the ratio between both prediction over the range $0 < \mu_T < 0.4$ is presented in Eq. (7.13). This value of 2.0955 indicates that, in average, the most reliable results for the reduction in performance are 110% larger than those predicted by the simple independent-channels model. This large difference, related to the occurence of a secondary maldistribution in the shell-side, is rather large and should discourage the use of this first model, described in Section 7.4.1.

$$\text{Average of } \left(\frac{Q_{ref} - Q_{\text{second model, 100 layers}}}{Q_{ref} - Q_{\text{first model}}} \right) = 2.0955 \tag{7.13}$$

Focusing then on the use of the second model (pressure-coupled channels), it is interesting to investigate the dependence of the results on the selected number of layers. As stated earlier in this chapter, the flow distribution profile given in Eq. (7.7) presents a slight dependence on the number of layers N as a consequence of the integration procedure in the setup of a layers scheme discussed in Section 7.2.2. The differences in the flow rate of two neighboring layers is proportional to μ/N^2. Then, as the number of layers becomes larger, these differences are smaller. The consequences in heat transfer performance, presented in Fig. 7.12(a),

indicate that an asymptotic behavior is noticed and a number of layers $N \geq 20$ is large enough to consider a converged solution.

In this framework, the error introduced by the use of an unconverged solution is investigated. The two extreme curves presented in Fig. 7.13 present very similar results for low values of μ_T, and they deviate notoriously for $\mu_T > 0.2$. In average, as presented in Eq. (7.14), the predicted reduction in heat duty using 100 layers is 13.15% larger than with only 2 layers. This deviation present a minimum value of 6.8% for $\mu_T = 0.06$ and it increases with the maldisitrubion coefficient beyond this point.

$$\text{Average of } \left(\frac{Q_{ref} - Q_{\text{second model, 100 layers}}}{Q_{ref} - Q_{\text{second model, 2 layers}}} \right) = 1.1315 \tag{7.14}$$

Although this difference can be considered acceptable in view of the inherent uncertainties of the empirical models, it is important to remark that there is no significant advantage in the use of few layers. Analyzing the solution procedure described in Section 7.4.2, it can be concluded that the largest contribution to the total computational cost is given by the evaluation of the internal characteristic curve of the shell-side pressure drop as a function of the shell-side flow rates which depends on the tube-side flow in each individual layer, as given by Eq. (7.11) and represented in Fig. 7.9(b).

In principle, since an individual characteristic curve must be obtained for each layer, selecting $N = 2$ instead of $N = 100$ might represent a considerable simplification. However, in the practical application of this procedure, the best performance is obtained by first constructing a response surface as in Fig. 7.9(a), reducing the online computation stage to arithmetic operations on the basis of these precomputed results, avoiding a new solution of the governing differential equations. Therefore in practice, the complexity of handling 100 layers is very similar to that of only two, and this simplification is not justifiable.

7.5 Discussion

Two different models were presented Section 7.4 for describing the consequences of flow maldistribution on the thermal performance. The major difference between them is given by the considerations regarding the pressure drop in each individual channel. While the first model assumed the parallel channels to be independent on each other, the second one imposed an equal pressure drop boundary conditions. In general, when these models where compared in Section 7.4.3, the second formulation was considered to be the most accurate one. However, they were not compared against experimental data, due to the general lack of empirical information in two-phase flow systems. For this reason, a suitable discussion is included in the present section.

In a steady-state description, the equal pressure drop condition seems rather reasonable. However, in practice strictly stationary conditions are not achieved, and some differences in the order of the inertial terms have been observed. In addition, the analysis of plate headers described in Section 7.2.1 indicates that in fact the inlet and outlet pressure in each tube are not identical. Therefore, some small differences in the pressure drop must be allowed. Nevertheless, the approach selected in this analysis should be further investigated.

On the one hand, it is advised from this analysis that future experimental setups should include measurements inside the headers. Although this situation can be difficult to achieve in practice for compact geometries, it might contribute to a breakthrough in the modeling capabilities.

On the other hand, CFD analysis might help to determine the extent of these differences, and whether they can be completely arbitrary or not. In other words, it can be investigated if perhaps a given pressure profile is established or, as assumed in this chapter, the individual pressure drops are completely independent on each other.

7.6 Summary

Heat exchanger used in industrial applications require large heat transfer surface areas. For this reason, the usual geometries employ a parallel-channels configuration, allowing the construction of compact equipment, but also leading to problems related to flow maldistribution. In many scenarios the flow distribution can deviate from design conditions (Mueller and Chiou, 1988), in particular for two-phase flow, with possible negative consequences in the overall heat transfer performance.

While extensive research has been devoted to the single-phase problem, from the pioneer work by Fleming (1967), current models for two-phase flow fail to account for all relevant phenomena. In particular, all of them are based on energy balances, disregarding the pressure coupling between parallel channels connected at both ends. The heat exchanger model evaluated in this chapter, described in Section 7.1 considers coupled momentum and energy balances for each stream, on the basis of the macroscopic model described in Chapter 5, with an imposed distribution profile.

Traditional flow distribution profile models have been focused upon the design of plate-type manifolds. In this context, theoretical models were developed for plate-heat exchanger assuming single-phase flow with constant physical properties, as reviewed in Section 7.2.1. In this chapter, a shell-and-tube geometry is studied. Taking into account radial symmetry, a layers-approach is proposed as in Fig. 7.5 for condensing similar channels into groups, avoiding the need of evaluating each individual channel, since the number of tubes can be rather large. In addition, a maldistribution coefficient μ is defined as in Eq. (7.5).

In this context, three cases are analyzed, as indicated in the diagram in Fig. 7.1:

one homogeneous which serves as a reference solution case and two scenarios with flow maldistribution in the tube-side. Two different models are considered for the flow maldistribution: independent channels and pressure-coupled channels.

In the first model, presented in Section 7.4.1, the governing equations are solved for each layer separately with no interaction, initially for a study case with only two layers and later extended in a parametric analysis. This model predicts that the heat transfer performance is reduced in all cases, up to maximum value of roughly 8% in the selected range. The major limitation of this model is that large differences in the shell-side pressure drop are observed. In a steady-state analysis, very small pressure differences can be allowed, related to inertial effects. This situation then provides the motivation for incorporating some interaction between parallel channels.

Then in the second model, Section 7.4.2, an equal pressure drop constraint is incorporated. In order to allow for this imposed constraint, some other conditions must be relaxed. In particular, the shell-side flow rate is expected to redistribute, according to the intersection of both internal and external pressure drop characteristics curves. In particular, a constant mass-flow rate scenario was considered. This condition produces a secondary maldistribution in the shell-side, which further reduces the heat transfer performance up to a maximum of approximately 16% for the same range.

Comparing both models, the first one is simple and straightforward, while the second is more complex in particular for the determination of the flow redistribution profile in the shell-side. In addition, the first model predicts unreasonable differences in the pressure drop, while the second one account for this constraint and predicts a secondary maldistribution. Analyzing the results in terms of heat transfer performance, the second model predicts a reduction roughly twice as large as the independent-channels approach. With these considerations, the use of the coupled model with a sufficiently large number of layers is recommended for two-phase heat exchanger applications. The use of few layers is not justifiable by a reduction in complexity, since this simplification is not significant in practice. Similarly, the use of the independent-channels model is discouraged because the predictions in heat transfer performance and pressure drop are not realistic.

Chapter 8

Partial flow mixing

► In this short chapter, a homogenization approach is proposed for the analysis of multiple-channel heat exchangers, based upon the representation in terms of layers previously presented in Chapter 7. This technique consists basically on a weighted averaging procedure. In this framework, the effects of possible heterogeneities between the layers are investigated. Partial flow mixing is included in the model considering two contributions: turbulent mass exchange and pressure-differences driven flow.

Two numerical examples are analyzed: geometrical and mass flow rate differences between the layers. In both cases, rather intriguing flow mixing profiles are observed. In particular, it is suggested that a larger flow rate is directed towards the layer with larger friction characteristics. Although this result might defy first-sight intuition, the same trend was noticed in experimental observations reported in literature. An interesting discussion on the validity of the equal pressure drop boundary condition is included in the analysis of these results.

In Chapter 2 the current state-of-the-art for heat exchanger modeling was reviewed, indicating that two effects stand out as not considered by present models. These are the consequences of pressure drop on heat transfer performance, analyzed in Chapter 5, and the influence of partial flow mixing, which is the main topic of the present chapter.

Traditionally, one of two extreme scenarios is considered for flow mixing in heat exchangers. On the one hand, separated and independent channels can be considered for flows distributed among several tubes. On the other hand, a continuous and complete mixing is usually considered as an idealization of in-shell or external flow, as in air-heated evaporators or water-cooled condensers. In practice, an intermediate situation between 0% (no mixing) and 100% (complete, continous mixing), that is partial flow mixing, is most likely to occur. However, there are currently no reports on the implementation of a predicting model to determine the

extent of flow mixing in heat exchanger applications.

The basic idea in the present chapter is to extend the mesoscale framework developed previously in Chapter 7, based on the description of the heat exchanger in terms of several groups of channels, in order to incorporate the effects of flow mixing. In this analysis, similar channels in the HE are grouped in several layers. This is an intermediate solution between a macroscopic description (only one channel) and the individual evolution of each flow passage (hundreds or thousand of channels), hence the term mesoscale. This approach allows for an interesting compromise between accuracy and computational cost.

In this context, neighboring channels are allowed to interact exchanging mass, momentum and energy in an homogenization approach as formulated in Section 8.1. With this formulation, the differences between layers can be incorporated simply and straightforward. In particular, two numerical examples are presented. First, the effects of a larger shell-side hydraulic diameter in the outer layer is studied in Section 8.2. Second, the consequences of a tube-side flow maldistribution, is analyzed in terms of interactions between the channels in Section 8.3. Finally, the results are discussed in Section 8.4 and a summary of this chapter is given in Section 8.5.

8.1 A homogenization approach

Since the number of parallel channels can be rather large (hundreds or thousands) it is not convenient to analyze each of them individually at the design stage. For this reason, usually a few representative channels are considered instead. These could be selected based upon geometrical criteria (for example inner and outer channels) or the expected heat and/or flow distribution (for example an average channel and the one with the largest heat flux). In any case, the formulation of the heat exchanger problem in terms of representative channels leaves out of consideration most of the channels, which operate at some intermediate conditions.

With a homogenization approach, all channels can be included in the analysis by means of proper averaging. This technique consists on modeling the heat exchanger in terms of several layers, as sketched in Fig. 7.5 for a shell-and-tube geometry. Each layer represents then a groups of channels (which, being closely located, have similar operating conditions) with integrated extensive properties like flow rate and area, and mass-averaged intensive properties like density and velocity.

As the heat exchanger involves the simultaneous solution of two streams, two matching sets of layers are considered. In other words, for this geometry each layer j includes a tube-side and a corresponding shell-side flow sub-stream. In a steady-state analysis, the problem is governed by mass, momentum and energy balances for each of them.

For the tube-side stream, as different layers cannot mix, the mass balance

gives a trivial results, that is a constant mass flux $G_{T,j}$ in each layer j. Then, the evolution of the tube flow is is governed by momentum and energy equations, given by Eqs. (8.1) and (8.2), respectively.

$$\frac{\partial}{\partial z}\left(p_{T,j}+\frac{G_{T,j}^2}{\rho_{T,j}}\right)=-\rho_{T,j}g-\frac{4}{Dh_{T,j}}\tau_{T,j} \tag{8.1}$$

$$G_{T,j}\frac{\partial e_{T,j}}{\partial z}=\frac{4\times U}{D_{eq,T,j}}(T_{S,j}-T_{T,j}) \tag{8.2}$$

The specific energy e includes enthalpy, gravitational and inertial terms, as in Eq. (8.3).

$$e=h+gz+\frac{1}{2}u^2 \tag{8.3}$$

In the shell-side there is no separating wall and neighboring layers exchange mass, momentum and energy. As a consequence, an additional source term appears in the balances Eqs. (8.4) to (8.6), related to cross flow rate from layer, denoted as $\dot{m}'_{ij}$. Since this mixing only occurs between neighboring channels, the only non-zero terms are for $i=j-1$ and $i=j+1$.

$$\frac{\partial G_{S,j}}{\partial z}=\frac{1}{A_{S,j}}\sum_{i\neq j}\dot{m}'_{ij}-\dot{m}'_{ji} \tag{8.4}$$

$$\frac{\partial}{\partial z}\left(p_{S,j}+\frac{G_{S,j}^2}{\rho_{S,j}}\right)=-\rho_{S,j}g-\frac{4}{Dh_{S,j}}\tau_{S,j}+\frac{1}{A_{S,j}}\sum_{i\neq j}\dot{m}'_{ij}u_{S,i}-\dot{m}'_{ji}u_{S,i} \tag{8.5}$$

$$\frac{\partial}{\partial z}(G_{S,j}e_{S,j})=\frac{4\times U}{D_{eq,S,j}}(T_{T,j}-T_{S,j})+\frac{1}{A_{S,j}}\sum_{i\neq j}\dot{m}'_{ij}e_{S,i}-\dot{m}'_{ji}e_{S,j} \tag{8.6}$$

This gives a total of five differential equations for each layer, coupled with constitutive equations. The empirical models for the shear stress τ and heat transfer coefficient U have been described in previous chapters. An additional model is required for the description of $\dot{m}'_{ij}$. This cross flow has been studied for flow in porous media (Sha et al., 1984) and subchannel analysis (Todreas and Kazimi, 1990, and references therein), and several model are available for single-phase flow.

In general, there are two contributions for this cross flow. First, some mixing between neighboring channels or layers occurs due to turbulent effects, usually represented as a fraction β (very small, in the order of $\beta\approx 0.005$) of the average mass flux. The second contribution is given by mass flow driven by pressure differences between the layers. Then, if $p_{S,i}>p_{S,j}$ there is a net flow from layer i to j, according to a distributed flow resistance K . Considering these two contributions,

the cross flow is given by Eq. (8.7), where Per_{ij} is the contact perimeter between both layers.

$$\frac{\dot{m}'_{ij}}{Per_{ij}} = \underbrace{\beta \frac{G_{S,i}A_{S,i} + G_{S,j}A_{S,j}}{A_{S,i} + A_{S,j}}}_{\text{Turbulent mixing}} + \underbrace{\frac{1}{K}\rho_{S,i}\sqrt{\frac{p_{S,i} - p_{S,j}}{\rho_{S,i}}}}_{\text{Pressure-difference driven}} \tag{8.7}$$

This model is applied to a reference case in Section 8.1.1.

8.1.1 Solution to a reference case

In this section, a reference case with only one layer is solved for comparison purposes. Given the governing equations (8.1) to (8.6) and its associated constitutive laws and physical models, the problem is completely defined by identifying the working fluids, flow arrangement and problem parameters. Then, N sets of parameters for each layer j must be defined as in Eq. (8.8), which include inlet values and geometrical aspects.

$$\text{Problem parameters: } \{G_T, G_{S,in}, p_{T,in}, p_{S,in}, h_{T,in}, h_{S,in}, D_{h,T}, D_{h,S}, A_T, A_S\}_j \tag{8.8}$$

A homogenization approach is implicit in the definition of these parameters, since they are the result of an averaging over the region they represent. The objective of this section is to study a reference case where all layers are assumed to be identical (and therefore they can be integrated into one unique layer), establishing the basis for Sections 8.2 and 8.3, that deal with the results of scenarios where the homogenization approach leads to differences between the layers.

In particular, the horizontal counter-flow of condensing propane in the tube-side (entering at 290 K and 7 bar) and boiling R134a in the shell side (280K, 4 bar) is studied and the total mass flow rates are 1.5 and 3.0 kg/s, respectively. The geometry consists in 800 aluminum tubes, 8.0 mm in inner diameter, 0.25 mm thickness and 5 m in length, in a 335 mm in diameter shell with a square-lattice array (10.4 mm pitch).

Figure 8.1 presents profile solutions for this case in terms of (a) temperature and (b) relative pressure, which represent the energy and momentum balances, respectively. Regarding the mass balance, there is no net cross flow and both tube- and shell-side mass flux remain constant at their inlet values. Since this is a counter-flow arrangement, the shell-side enters in the position $z = 0$, and the tube-side in z=L, i.e. $z/L = 1$.

The plots presented in Figs. 8.1(a) and 8.1(b) serve as a reference for comparison in the following sections. In addition to these profile solutions, the total heat duty is studied, with a reference value of $Q_{ref} = 553.09$ kW.

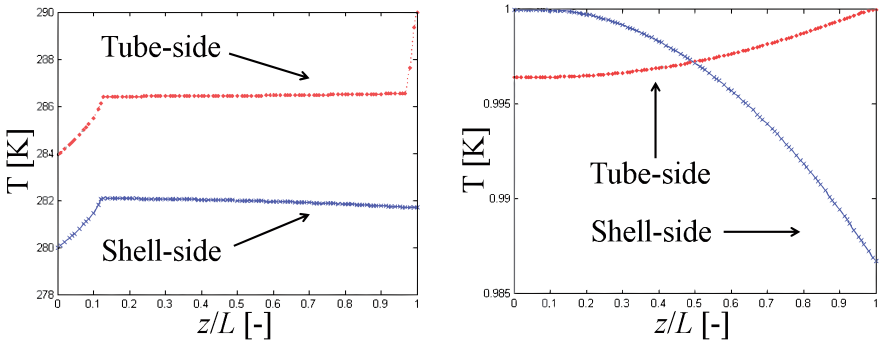

(a) Temperature (b) Relative pressure

Figure 8.1: Profile solutions for a reference case

8.2 Shell-side hydraulic diameter

This section intends to reflect the consequences of geometrical heterogeneities in a shell-and-tube heat exchanger. In general, these difference can be related to several possible causes, including fabrication tolerances, corrosion or channel blockage during operation. However, these effects cannot not be located in a particular layer *a priori* and therefore a homogenization approach is not applicable for their analysis, thus they escape the scope of this chapter.

Nevertheless, one particular geometrical heterogeneity can be identified at the design stage. As the tube array deviates from the ideal square lattice, some differences in the shell-side hydraulic diameter $D_{h,S,j}$ can occur. This constant deviation can be identified in the most outer layer, where the proximity to the wall does not allow the location of some tubes and therefore $D_{h,S,outer}$ is slightly larger. Consequently, this outer layer has less flow resistance, since Eqs. (8.1) and (8.5) indicate that the contribution of friction to pressure drop is indeed smaller, thus providing the conditions for cross flow in the shell stream.

An interesting exercise to understand the cross flow mechanisms that could be expected for adiabatic single-phase flow is an analogy with an electric circuit as presented in Fig. 8.2. The red lines (bottom) represent the inner layers (higher resistance), and the outer layer is in blue (top, lower resistance). For a laminar flow regime, the pressure drop is proportional to the flow rate, analog to the electric potential and the current through a resistance.

On the one hand, in (a) a closed circuit (analog to parallel channels connected at inlet and outlet with an equal pressure drop boundary condition) a larger current (analog to mass flow rate) goes through the lower resistance path (blue, top). On the other hand, if (b) the circuit is open (the pressure drop of different layers are not related), then the channel with lower resistance would get continuously

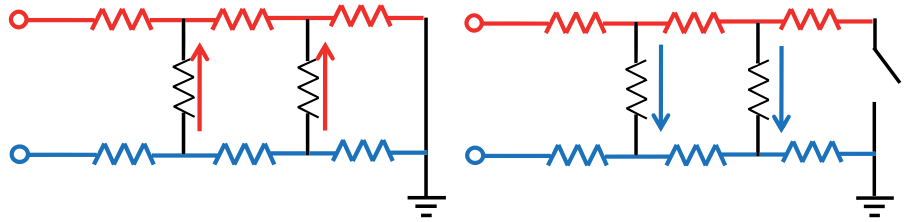

(a) Closed circuit (b) Open circuit

Figure 8.2: Analogy with an electric circuit: two parallel channels, bottom (red) with larger resistance than the top one (blue).

depleted and more flow rate (analog to electric current) goes through the inner layers, which have a larger resistance.

This boundary condition has been previously discussed in Section 7.4.1. In principle, an equal pressure drop can be assumed in a steady state analysis, represented by a closed circuit in Fig. 8.2(a). However, some differences in the outlet pressure have been noticed, originated by inertial effects, in the order of a few times G^2/ρ. Then relatively small pressure differences are allowed and, following this analogy, an open circuit is originally considered as in Fig. 8.2(b), and this model is switched to a closed circuit if the resultant differences are excessively large.

Naturally, there are some marked differences between laminar adiabatic single-phase flow and two-phase heat exchanger applications as the reference case analyzed in Section 8.1.1. In short, the relation between pressure drop and flow rate is not linear. Moreover, it is not necessarily monotonic. This means that an increase in the flow rates does not necessarily result in a larger pressure drop, as can be observed in the slightly N-shaped curve presented in Fig. 7.9(b). Then, the flow mixing profiles may differ substantially from those depicted in Fig. 8.2.

Figure 8.3 presents profiles solutions in the shell-side, considering two layers, the outer one (red) having a slightly larger hydraulic diameters. A small difference of only 1% is considered first and later extended in a parametric analysis.

According to Eq. (8.7), there are two contributions to flow mixing: turbulence effects and pressure driven flow. The first effect gives the same flow in both directions, and therefore leads only to a partial homogenization in momentum and energy and does not produce a net mass exchange. Then, the mass flux profiles presented in Fig. 8.3(a) can only be explained by the second effect, that is the differences in pressure. In order to understand this predicted profile, the following issues should be considered.

- Initially, in the single-phase liquid region, the pressure drop is larger in the inner layer because its hydraulic diameter is smaller and all other flow prop-

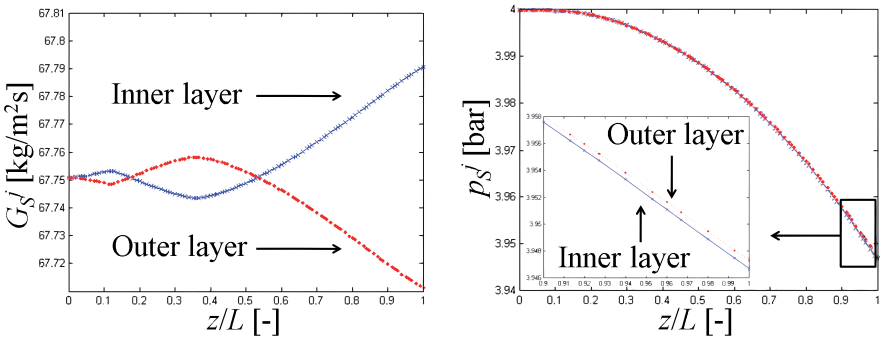

(a) Mass flux (b) Pressure

Figure 8.3: Profile solutions for the shell-side when $D_{h,S}$ in the outer layer is increased in 1%.

erties are equal. This pressure difference produces a net cross flow towards this inner layer, as in the open circuit represented in Fig. 8.2(b).

- As the flow evolves downstream, the heat exchange with the tube side produces further differences between both layers. In the outer layer, with a lower mass flow rate, the two phase region starts earlier and the vapor generation is faster. It is important at this point to remind that the frictional contribution to pressure drop is computed follows.

$$\frac{4\tau}{D_h} = 2f_L \frac{G^2}{\rho_L} \Phi_L^2 \tag{8.9}$$

  There are two opposite contributions in Eq. (8.9). First, a lower mass flux G gives a lower shear stress following a quadratic law, representing an inertial effect. Second, the flow is lower and the vapor generation is larger, producing a sharp increase in the two-phase multiplier Φ_L^2. In addition, the generation of vapor results in a reduction of density and an inertial contribution to pressure drop. Then, the overall pressure gradient is larger in the outer layer. As a consequence, for $z/L > 0.12$ the scenario changes and $p_{S,outer} > p_{S,inner}$, thus giving a net cross flow in the opposite directions, that is from the inner towards the outer layer.

- Eventually, the inertial effect dominates over the two-phase multiplier and for $z/L > 0.37$ the direction of the cross flow is once again reversed. This situation occurs as a consequence of the N-shaped relation between pressure gradient and mass flow rate (represented earlier in Fig. 7.9(b)), which is a necessary condition for the occurrence of some instabilities in two-phase flow

(Kakaç and Bon, 2008). Finally, the mass flux at the exit is 0.05% lower in the outer layer, that is the one with the larger hydraulic diameter, which in single-phase flow would represent a lower flow resistance.

This numerical example presents some interesting cross flow profiles, although it should be regarded rather as an academic exercise. Nevertheless, similar results have been reported by Teyssedou et al. (1989) from their experiments with laterally interconnected channels. Figure 8.4 presents mass flux profiles when a blockage is inserted in of them, representing (a) a small and (b) a large fraction of the cross sectional area. The two changes in direction of the crossflow are a consequence of the N-shaped relation of pressure drop and mass flow rate, as previously discussed.

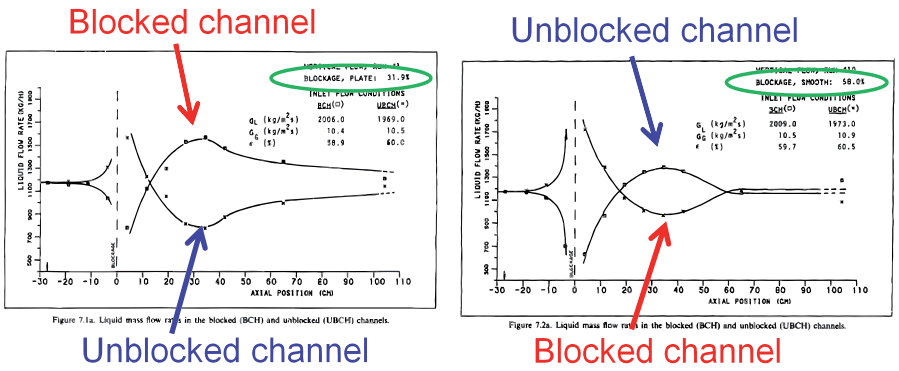

(a) Small blockage

(b) Large blockage

Figure 8.4: Mass flow profiles for two laterally connected channels. Source: Teyssedou et al. (1989).

This study is further extended in a parametric analysis up to a 10% difference in the hydarulic diameter in Fig. 8.5, in terms of (a) differences in mass flux, (b) differences in outlet pressure and (c) overall heat duty, considering 2 and 3 layers.

As could be expected, the effects are larger with increases differences in $D_{h,S}$. Nevertheless, these effects are still small with a mass flux variation up to 0.27% and a reduction in heat duty not larger than 0.14%. From these results it can be concluded that, for the selected range, the differences in hydraulic diameter, although they present interesting mixing profiles, can be neglected during the design stage.

Regarding the differences in the outlet pressure, indicated in Fig. 8.5(b), they increase in this parametric analysis up to roughly 10% of the average value for Δp_S. Nevertheless, this value is still less than 5 times the inertial head G^2/ρ and therefore they are allowed. Then, in this range, the assumption of an open circuit is valid and there is no justification for changing this model to a closed circuit.

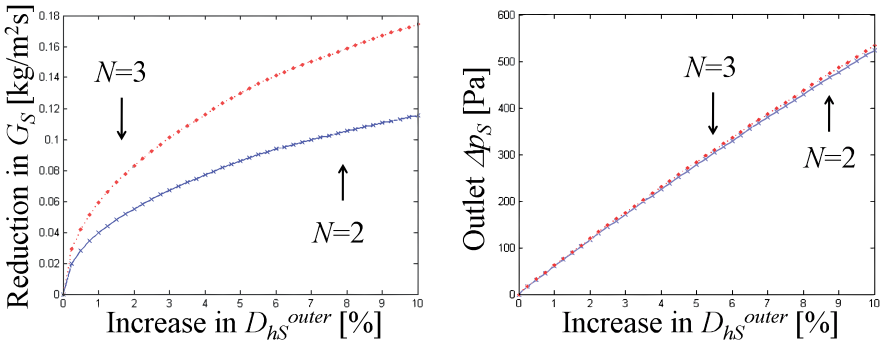

(a) Differences in mass flux

(b) Differences in outlet pressure

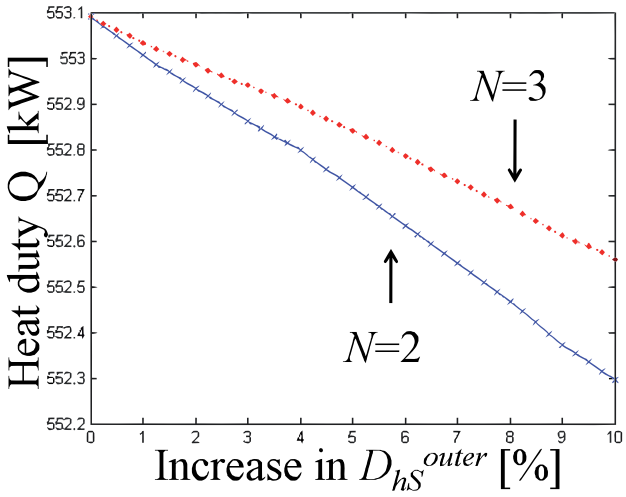

(c) Overall heat duty

Figure 8.5: Parametric analysis of differences in the shell-side hydraulic diameter

The inclusion of one additional layer does not alter the results significantly. For the same heat exchanger, some internal effects are now interpreted as mixing between layers. Then, the cross mass flux is larger, and the consequences in heat duty are lower. The effects of partial flow mixing in heat duty are better understood in the example described in Section 8.3, considering the consequences of flow maldistribution.

8.3 Tube-side flow maldistribution

This scenario is the main topic of Chapter 7 and the possible causes that may lead to flow maldistribution were discussed there. The main objective in the current section is to incorporate the effects of partial flow mixing according to the model described in Section 8.1.

Following the model approach presented in Section 7.2.2, the coefficient μ, defined as in Eq. (7.5), is used for quantifying the extent of flow maldistribution. In addition, the flow distribution profile given by Eq. (7.7) is considered to determine the mass flow rate in each layer j.

$$\mu = \frac{G_{max} - G_{avg}}{G_{avg}} = \frac{G_{max}}{G_{avg}} - 1 \tag{7.5}$$

$$\dot{m}_j = \frac{\dot{m}_{total}}{N}\left[1 + \mu\left(1 - \frac{2j-1}{N}\right)\right] \tag{7.7}$$

In this context, a simple case with only two layers is studied first and later extended in a parametric analysis. In particular, a tube-side maldistribution of $\mu_T = 0.1$ is analyzed. This means that the inner-layer tube-side has a mass flow 10% larger than the average (that is 55% of total), and the outer layer 10% less than the average (that is 45% of total). Figure 8.6 shows profile solutions for both tube-side (red, from right to left) and shell-side (blue, from left to right) indicating (a) temperature and (b) relative pressure for each layer.

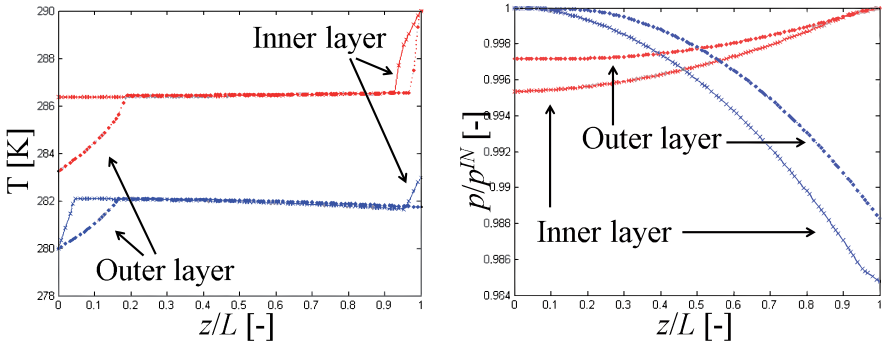

(a) Temperature (b) Relative pressure

Figure 8.6: Profile solutions for $\mu_T = 0.1$

At first sight, these profiles do not present substantial differences with those presented in Fig. 7.7. However, in this scenario considering flow mixing, the shell-side pressure profiles (blue in Fig. 8.6(b)) indicate the direction of the cross flow.

In particular, as a larger tube-side flow is imposed in the inner, the heat flux to the shell-side is larger, leading to a faster generation of vapor and increased pressure drop. For this reason, there is a net cross-flow from the outer towards the inner layer, exiting with a mass flux 0.87% higher than the inlet value.

This result is interesting because it contributes to the rebalancing of the heat exchanger. As discussed in Chapter 7, flow maldistribution leads to a reduction in the overall heat transfer performance mainly because the balance between streams, in terms of heat capacity flow rate, is disturbed. In this context, with the inner layer having 10% more flow than average in the tube-side and 0.87% more in the shell-side, the imbalance between tube and shell streams (main cause for reduction in performance) is reduced in an 8.7%.

In addition, flow mixing without net mass exchange is also known to reduce the consequences of flow maldistribution (Kroeger, 1967). This mechanisms leads to an homogenization in both momentum and energy by means of turbulent partial mixing, thus reducing the negative consequences in the heat transfer performance. In the ideal case of complete mixing, the effects of heat capacity flow imbalance partially disappears and the overall performance would be less affected. The present model considers partial flow mixing due to turbulence effects as given by Eq. (8.7).

The results for this example indicate that both layers exchange mass at a rate of roughly 0.27 kg s^{-1} m^{-1}. This means that 18% of the average mass flow rate is exchanged in each meter and integrating this value over the entire tubelength, 90% of the shell-side mass flow rate is at some point mixed between both inner and outer layers.

These two effects mitigate the consequences in the overall heat transfer performance. For this case, the heat duty is reduced in only 5.34 kW, that is 0.97% of the reference value. For the same operating conditions, the models presented in Chapter 7 would predict reductions of 1.75% (independent channels, as open circuit) and 3.5% (coupled channels, as closed circuit) in heat duty[1]. This result indicates that the inclusion of flow mixing greatly attenuates the consequences in heat duty, reducing this effect in more than 40%.

The effect on heat duty is further study in a parametric analysis, and the results are presented in Fig. 8.7 for 2, 3, and 4 layers.

An interesting observation in Fig. 8.7 is the initial plateau for $\mu_T < 10\%$, as the reduction in heat transfer performance is limited below 1%. This plateau was not observed in the analysis presented in Chapter 7 (see Fig. 7.13), confirming the conclusion that mixing mitigates the reduction in heat duty. This plateau indicates that for low maldistributions, the differences between the layers are almost completely eliminated by means of mass exchange in the shell side.

When more layers are considered the consequences in heat duty are further reduced. This situation occurs mainly for two reasons. First, for a given value of the maldistribution coefficient μ_T, the absolute differences between neighboring

[1]These values can be read from Figs. 7.8 and 7.12, respectively

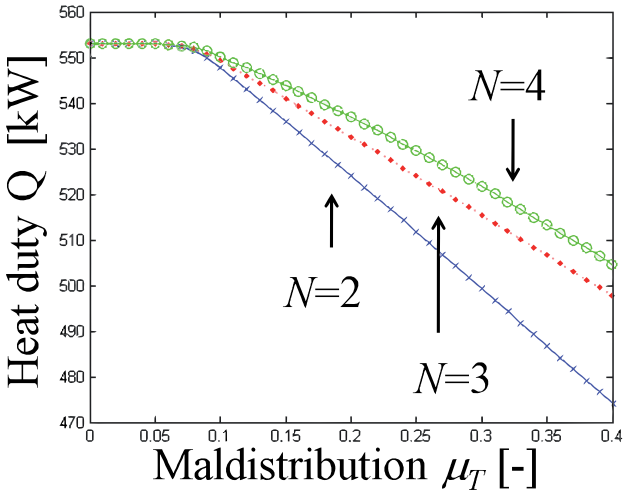

Figure 8.7: Parametric analysis of the total heat duty respect to the maldistribution coefficient for 2, 3, and 4 layers

layers become smaller. Second, as the number of layers is increased and initially large layers are subdivided, additional mixing paths in the shell side are included. Finally, the parametric analysis presented in Fig. 8.7 indicates that the consideration of only two layers is a conservative assumption, as it leads to the most pessimistic predictions.

8.4 Analysis of results

The key element that is incorporated in this chapter to the mesoscale modeling framework first developed in Chapter 7 is the consideration of partial flow mixing, with two contributions. First, pressure differences drive a net cross flow from one layer to another. Second, turbulent effect produce a mass exchange between neighboring layers or subchannels at equal rates in both directions, allowing for a partial homogenization in terms of momentum and energy. The relative individual contribution of each mechanism becomes more clear with the analysis of two numerical examples.

In the first example, presented in Section 8.2, the consequences of one layer having a lower flow resistance (represented by a slightly larger hydraulic diameter) than the others are analyzed. For this scenario, the turbulent mixing does not play a major role because the differences between the layers are rather small. The pressure-driven cross flow, however, produces some interesting axial mass flux profiles. As a consequence of the non-linearities in the relation between mass flow

rate and pressure gradient, the direction of this cross flow changes twice along the flow length. In particular, for this boiling case, this relation is N-shaped, as presented earlier in Fig. 7.9(b).

Following an analogy with an electric circuit, more flow goes through the layer with the highest resistance if an open circuit is considered, and the opposite occurs if the circuit is closed. However, since the differences in outlet pressure are small and acceptable in a steady-state analysis, there is no motivation to replace the model into a closed circuit. Extending this study in a parametric analysis, the effects are larger with increases differences in the hydraulic diameter. Nevertheless, the consequences in the mass flux distribution and heat transfer performance are rather small (the changes in outlet mass flux or total heat duty are below 1%) and then this scenario could be neglected during the design stage, despite the interesting mixing profiles.

The second example, presented in Section 8.3, deals with the consequences of flow maldistribution in the tube-side stream. As this topic was first discussed in Chapter 7, the main objective in this example is to investigate the influence, if any, of partial flow mixing in the shell-side stream. In particular, the analysis is focused in the negative consequences in the overall heat transfer performance. It has been discussed previously that flow maldistribution results in a reduction in the total heat duty, mainly because of the imbalance between the streams in terms of heat capacity flow rate. In this context, the two mass exchange mechanisms incorporated in the present chapter have a positive influence as follows.

- Pressure-driven cross flow contributes to a heat capacity flow rate balance between the streams, as more flow goes in the shell-side through the layer with the largest tube-side flow. However, this effect is small, since for a 10% maldistribution in the tube-side, only a 0.87% variation in the shell-side flow is observed.

- Turbulent mixing reduces the differences between layers, as this mechanism provides a homogenization in terms of momentum and energy. In the selected example, roughly 90% of the shell-side flow is exchanged between the layers at some point along the flow length. Although this value is relatively high, it is far from the usual assumption of a complete and continous mixing. In fact, less than 1% of the flow is being continuously mixed, as represented by the turbulent parameter β.

Both effects contribute to mitigate the reduction in the heat transfer performance. A parametric analysis presents a plateau, as the total heat duty remains within 1% of its reference value for maldistribution coefficients in the tube side in the range $\mu_T \leq 10\%$. This plateau, which was not found in the previous analysis described in Chapter 7, is a consequence of flow mixing. Then, for cases with relatively low maldistribution, their consequences in the heat transfer are almost completely dumped mass exchange due to turbulent effects.

Finally, including a larger number of layers in the model (that is, considering a lower number of individual tubes in each layer) further reduces the consequences in heat duty, although the plateau in Fig. 8.7 is not affected. This last observation seems to indicate that the most notorious effect is an increase in turbulent mixing, while the net cross mass flow remains roughly unchanged.

8.5 Summary

Partial flow mixing is currently not included in state-of-the-art heat exchanger models. Instead, present description consider either fully separated non-interacting channels (as in parallel tubes), or a complete and continuous mixing as an idealization of shell-side flows. The practical situation is an intermediate case between these two extreme scenarios. Considering the multiscale framework postulated in thesis, see Fig. 3.5, this phenomenon can be categorized as a mesoscale effect and is the main topic of this chapter.

The homogenization approach described Chapter 7 is extended in this chapter in order to include the effects of flow mixing. The one-dimensional evolution of several radial layers is described in terms of mass, momentum and energy balances. The main contribution in this chapter is given by the inclusion of a cross-flow between neighboring layers in the shell-side. This cross flow has two contributions: turbulent mixing and net mass exchange driven by local pressure differences. While the first mechanism contribute to a homogenization in terms of momentum and energy, the second one further increases the differences between neighboring layers.

This model is applied to two examples. First, the consequences of small differences in the shell-side hydraulic diameter are studied. Second, a flow maldistribution in the tube side is postulated, and the effects on the thermal performance are evaluated. In both examples, the results are compared to a reference case.

A larger hydraulic diameter is identified in the shell-side outer layer, since the tube array deviates from the ideal lattice due to the presence of the wall. In general, a larger hydraulic diameter represents a lower friction and therefore a small pressure drop. An analogy with an electric circuit is presented and the validity of the equal pressure drop boundary condition is once again discussed. If all channels must have the same pressure drop (analog to a closed electric circuit), more flow is expected to be derived towards the layer with the larger hydraulic diameter, that is the lower friction characteristics. However, the opposite situation is expected to occur if this boundary condition is relaxed and pressure difference within a certain range are allowed in the outlet (analog to an open electric circuit). In addition, the relation between pressure drop and mas flow rate in a boiling system is clearly non-linear. In addition, it is not necessarily monotonic and therefore a larger mass flow rate is not always related to a larger pressure drop.

With all these consideration, some interesting flow mixing axial profiles are observed in the example described in Section 8.2. These profiles follow the trend

of experimental observations reported in the open literature. Nevertheless, the overall consequences in the thermal performance are very small in the selected range. Therefore, this phenomenon can be disregarded at a first stage of design.

The consequences of a flow maldistribution in the tube-side were studied in Section 8.3. While this is the main topic of Chapter 7, it was observed that partial flow mixing has a positive effect, attenuating the negative impact on the total heat duty. In fact, both flow mixing mechanisms contribute towards this effect. On the one hand, as the shell-side pressure drop is larger in the layers with the larger tube-side flow rate (that is, the larger heat flux), the net crossflow contributes to reduce the imbalance in terms of heat capacity flow rate, which is the main cause for the reduction of performance. On the other hand, turbulent mixing produces a partial homogenization of temperature, velocities and densities. A parametric analysis presents an initial plateau. This means that for low maldistributions in the tube-side (roughly up to $\mu_T = 0.1$), the overall thermal performance remains basically unaffected.

The results presented in this chapter lead again to an open question regarding the validity of the equal pressure drop boundary condition. As the pressure differences observed in these examples were small (in the order of the inertial term G^2/ρ), this condition was relaxed. Further research is needed at both experimental and modeling levels in order to clear identify under which conditions this requirement must be imposed.

Part IV

Micro-scale framework

Following the multiscale description presented in Chapter 3, some elements of modeling and simulation at microscopic level are presented in this part. The previous formulations presented in parts II and III considered the evolution of intube flow only in terms of lumped parameters that represent the interaction with the surrounding fluid. In other words, the longitudinal evolution of two-phase flow has been so far described in terms of a mass flux G, pressure p and specific enthalpy h, thus accounting for mass, momentum and energy balances. Furthermore, the heat transfer coefficient was hitherto evaluated using empirical correlations in terms of these three variables.

A microscopic analysis is presented in this part, based on a phenomenological description of diabatic gas-liquid flows, following a multifluid formulation. In other words, this analysis is focused on the different physical phenomena that determine the individual evolution of each phase.

As discussed in Chapter 3 the vapor contents in boiling and condensing flows is constantly changing, leading to the formation of different flow patterns. An accurate description at a microscopic levels must account for the different flow regimes. In this context, and considering the most relevant patterns for heat exchanger applications, Chapters 9 and 10 deal with heat transfer in the annular-mist and post-dryout flow regimes, respectively.

Chapter 9 deals with heat transfer in the annular-mist flow regime for two-phase heat exchanger applications. Special emphasis is placed on understanding the physical phenomena leading to the occurrence of dryout, resulting in a large reduction of the heat transfer coefficient. A three-fluid model is proposed for describing the individual evolution of the vapor core, liquid film and liquid droplets. Good agreement is observed with experimental observations from the open literature, analyzed in terms of the dryout quality. In addition, partial dryout in horizontal flow is studied, considering the film to be thicker at the bottom than the top due to gravitational effects.

The post-dryout flow regime is the main topic in Chapter 10. This chapter then comprises the continuation of the analysis of annular-mist flow presented in Chapter 9. Following the same methodology, a two-fluid formulation is postulated for describing the individual evolution of liquid and gas phases. This approach allows to extend the current experience from power-controlled systems into HE applications. The main aim of this chapter is to predict the heat transfer coefficient in this liquid-deficient regime. For this purpose, the different underlying physical phenomena should be understood and included in the model. These effects include: wall-to-gas heat transfer, droplet collisions against the hot wall, evolution of the droplet size, among others. Selecting proper constitutive relations, these effects are included in the phenomenological description. Validation results in terms of wall temperature profiles are presented for water and other fluids. In addition, a discussion regarding possible future improvements is included.

Chapter 9

Heat transfer in the annular-mist flow regime

► The annular-mist is the dominant flow regime in two-phase heat exchanger applications and is the main topic of the present chapter. Throughout this forced convection- dominated flow regime, the boiling heat transfer coefficient is very large. This situation changes drastically when the boiling crisis known as dryout occurs and the wall is no longer wetted by the liquid phase. Considering this scenario, the main objective in this chapter is to understand the physical phenomena leading to the occurrence of dryout and to develop a model for predicting the critical quality.

A steady-state three-fluid model is proposed, thus allowing to account for the individual evolution of the vapor core, liquid film and liquid droplets. State-of-the-art models are selected for the constitutive relations. This model was validated with 81 experimental data points from literature for water and hydrocarbons, predicting the dryout quality with an RMS error of 13.7%. In general, the water data provided the best results, within ±10% in all cases. Based on this model, a parametric analysis is presented, thus investigating the influence of heat and mass flux, diameter and pressure in the dryout quality. Finally, partial dryout in horizontal flow is studied, resulting in good agreement with experimental data from literature.

As discussed in Section 3.3.2, the structure of intube two-phase flow can be characterized by some distinguishable regimes, including bubbly, slug/plug, stratified, annular flow. Their occurrence depends on the tube geometry, mass flux and vapor content, which for the case of boiling and condensation systems is continuously evolving. The identification of the flow pattern represents a key element for bridging the different scales and reconstructing the microscopic flow structure from larger-scale observations. In particular, the annular-mist flow pattern is found in

a wide range of operating conditions (Ishii and Hibiki, 2006) and is particularly relevant for heat exchanger design (Wattelet, 1994). The presence of a thin liquid film adjacent to the tube wall provides large heat transfer rates. However, this performance is deteriorated with the occurrence of dryout given by the depletion of this film. This boiling crisis might have serious consequences, such as:

- Large reduction of the boiling heat transfer coefficient (HTC), given the lower thermal conductivity of the vapor phase. While in power-controlled systems, like nuclear reactors, this crisis is followed by a large increase in the wall temperature leading to the meltdown or mechanical failure of the tube material, such is not a concern in heat exchanger applications, which are temperature-controlled systems. Then, in a heat exchanger the consequences of dryout are observed in terms of a reduction in the heat duty, that is the total heat transferred.

- As dryout occurs at a quality somewhat lower than unity, some liquid may be present at the outlet in spite of the bulk vapor being overheated. This situation presents a mechanical issue for other equipment in a refrigeration cycle, since most compressors do not accept gas-liquid mixtures in the inlet. For this reason, some modifications in the process might be required such as the inclusion of a separator, or the specification of a minimum overheating that results in a demanding constraint for the heat exchanger design.

The occurrence of dryout is then a highly relevant transition for heat exchanger design. An accurate prediction of this phenomenon involves a deep analysis of the thermal and hydrodynamics of the annular-mist flow regime. The historical development of theoretical models for annular-mist flow is summarized in Fig. 9.1

Early theoretical models, dating back nearly one century to the pioneer works by Nusselt and others, assume that the liquid phase flows as a thin smooth film at the wall with a vapor core covering most of the tube cross-sectional area. These simple models fail to predict overall effects such as heat transfer and pressure drop. Moreover, the film thickness predicted by these methods differs largely from experimental observations.

Nearly half a century later, with the worldwide growth of nuclear power plants in the 1960s, extensive research has been focused on the development of more realistic models. A major breakthrough during these years was the consideration of part of the liquid carried away by the gas core, flowing as entrained droplets, although the physical mechanisms leading to this phenomenon were not identified until some fifteen years later. In this framework, large proprietary experimental databases were constructed for this entrained fraction in equilibrium conditions for air-water and steam-water systems. Nevertheless, this approach is not applicable to diabatic flows, since the heat and mass transfer processes lead to the continuous evolution of the distribution of both phases, in a non-equilibrium scenario.

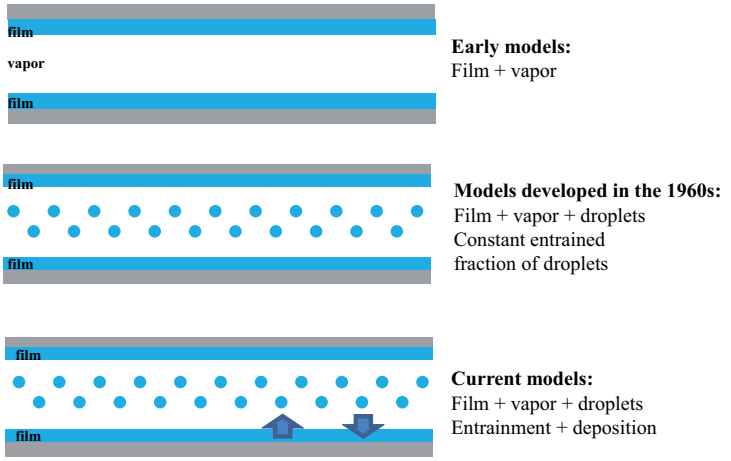

Figure 9.1: Historical evolution of annular-mist flow models

Finally, individual entrainment and deposition rates were incorporated to this framework, allowing the analysis of departure from equilibrium conditions. In this context, multi-fluid formulations, first reported by Saito et al. (1978), study the individual evolution of each flow field (droplets, film and vapor) with empirically-based constitutive models to account for their interaction in terms of mass, momentum and energy exchange. The selection of the most adequate constitutive model represents the most sensitive point of this formulation (Jiao et al., 2009).

This framework was extended by later authors with different degrees of success to incorporate transient one-dimensional annular flow (Sami, 1988; Sugawara, 1990), hydraulic jump in stratified horizontal flow (Stevanovic and Studovic, 1995), droplet number density (Alipchenkov et al., 2004) and multidimensional analysis (Kishore and Jayanti, 2004; Mitsutake et al., 1990). In addition, four-field two-fluid models, reviewed by Lahey and Drew (2001) and Lahey (2005) consider dispersed and continuous liquid and vapor flows, and are used for multidimensional direct numerical simulation.

In general, the most satisfactory results have been obtained for the analysis of Critical Heat Flux (CHF) for high heat and mass flux conditions, characteristic of nuclear reactor applications, as recently reviewed by Jiao et al. (2009). These operating conditions present two main differences respect to heat exchanger applications: the relative importance of the mass transfer mechanisms and the Axial Power Distribution (APD).

The first condition can be explained by analyzing a simple one-dimensional mass balance for the liquid film as in Eq. (9.1), first proposed by Whalley et al. (1974), where the subscripts *dep*, *ent* and *evap* stand for deposition, entrainment

and evaporation respectively and G and W are the axial and crossed mass fluxes.

$$\frac{D}{4}\frac{dG_F}{dz} = (W_{dep} - W_{ent}) - W_{evap} \tag{9.1}$$

If the heat flux is large enough, the net deposition-entrainment term can be negligible compared to the evaporation effect. As a consequence, the CHF (that is, the value of the heat flux that leads to boiling crisis for the given conditions) can be accurately predicted regardless the uncertainties of the entrainment and deposition models, although this situation does not imply that all the relevant dryout characteristic can be predicted with the same accuracy. Then, for example, Kawara et al. (1998) compared 9 correlations for entrainment and 11 for deposition, ranging several orders of magnitude, and predicted the CHF within 10% accuracy using different combinations of them. However, using the same correlations Kolev (2007, §5-6) found large differences in the film thickness and dryout locations for the experimental dataset of Bennett et al. (1968).

Second, the axial power distribution, which is notoriously different for heat exchanger and reactor applications, might have a large influence in the occurrence of dryout (Adamsson and Anglart, 2010). In general, shifting the power distribution towards the outlet results in a lower CHF, and for refrigerant in evaporator applications might result in a 50% reduction in this value compared to a uniform heat flux profile (Yang et al., 2006).

In this chapter, the evolution of annular-mist flow is studied using a multi-fluid formulation, presented in Section 9.1. This approach is very sensitive to the selected constitutive models, and the most convenient ones for heat exchanger applications are discussed. The accuracy of the predictions given by this model model against experimental data is investigated in Section 9.2. Two numerical examples are presented in Section 9.3: the sensitivity of the dryout quality to the input parameters is studied in Section 9.3.1, and the influence of the axial power distribution is investigated in Section 9.3.2 for heat flux profiles typically found in heat exchangers. Section 9.4 deals with the occurrence of partial dryout in horizontal boiling flow. Finally, Section 9.5 presents a summary of this chapter.

9.1 Mathematical formulation

The present model is based on a steady-state one-dimensional analysis of boiling flow in a round tube (although it could be easily extended to other geometries), and it relies on the following assumptions:

- The temperature remains constant at its saturation value corresponding to the inlet pressure, that is $T(z) = T_{sat}(p_{in})$. As a consequence, axial conduction in the fluid and the wall are neglected. This assumption implies thermal equilibrium and is valid until the occurrence of dryout which results in the overheating of the vapor phase.

- In a one-dimensional formulation, all variables are only dependent on the axial position and in particular a uniform value for the pressure p is considered over the cross-section.
- A representative constant value for the droplet diameter d is considered. This is a simplification, as a wide spectrum a droplet size is found in practice. In Chapter 10 this assumption is relaxed and the droplet diameter is allowed to evolve downstream.

This mathematical formulation is divided into four subsections. The governing equations for this problem are presented in Section 9.1.1. Different criteria for determining the occurrence of dryout are discussed in Section 9.1.2. Finally, constitutive models for mass transfer and shear stresses are presented in Sections 9.1.3 and 9.1.4, respectively.

9.1.1 Governing equations

As thermal equilibrium is assumed, an energy balance is implicitly accounted for. This model considers then the axial evolution of seven variables: the volume fraction α_k and velocity u_k for each phase represented by the subindex $k = D, F, G$ (D=droplets, F=film, G=gas) and the system pressure p. In order to obtain this solution, the same number of equations is required, given by Eqs. (9.2) to (9.4) as follows.

- Mass balances for droplets, film and gas

$$\frac{d}{dz}\left(\alpha\rho u\right)_D = \bar{A}_{F,G}\left(W_{ent} - W_{dep}\right) \tag{9.2a}$$

$$\frac{d}{dz}\left(\alpha\rho u\right)_F = \bar{A}_{F,G}\left(W_{dep} - W_{ent}\right) - \frac{4}{D}W_{evap} \tag{9.2b}$$

$$\frac{d}{dz}\left(\alpha\rho u\right)_G = \frac{4}{D}W_{evap} \tag{9.2c}$$

- Momentum balance for droplets, film and gas

$$\frac{d}{dz}\left(\alpha\rho u^2 + \alpha p\right)_D = \bar{A}_{F,G}\left(W_{ent}u_F - W_{dep}u_D\right) + \bar{A}_{D,G}\tau_{D,G} - \alpha_D\rho_D g \tag{9.3a}$$

$$\frac{d}{dz}\left(\alpha\rho u^2 + \alpha p\right)_F = \bar{A}_{F,G}\left(W_{dep}u_D - W_{ent}u_F\right) - \frac{4}{D}W_{evap}u_F + \bar{A}_{F,G}\tau_i - \frac{4}{D}\tau_W - \alpha_F\rho_F g \tag{9.3b}$$

$$\frac{d}{dz}\left(\alpha\rho u^2 + \alpha p\right)_G = \frac{4}{D}W_{evap}u_F - \bar{A}_{D,G}\tau_{D,G} - \bar{A}_{F,G}\tau_i - \alpha_G\rho_G g \tag{9.3c}$$

- Closure law

$$\alpha_D + \alpha_F + \alpha_G = 1 \tag{9.4}$$

In addition to these differential equations, some constitutive relations are required. First, the phase densities ρ are fixed at their saturation values, that is $\rho_D = \rho_F = \rho_L$ and $\rho_G = \rho_V$. The empirical models for mass transfer W and shear stresses τ are described later in Sections 9.1.3 and 9.1.4. Finally, the interfacial area densities $\bar{A}$, with units of $\mathrm{m}^2/\mathrm{m}^3$, are given by Eq. (9.5), where d is the droplet diameter and δ the film thickness.

$$\bar{A}_{F,G} = \frac{\pi\,(D - 2\delta)}{\pi D^2/4} = \frac{4}{D}\left(1 - 2\frac{\delta}{D}\right) \tag{9.5a}$$

$$\bar{A}_{D,G} = \alpha_D\,\frac{\pi d^2/4}{\pi d^3/6} = \frac{3}{2}\,\frac{\alpha_D}{d} \tag{9.5b}$$

In a round-tube geometry the film thickness δ can be computed from the problem variables as in Eq. (9.6).

$$\frac{\delta}{D} = \frac{1 - \sqrt{1 - \alpha_F}}{2} \tag{9.6}$$

Regarding the initial conditions for Eqs. (9.2) to (9.4), it is important to keep in mind that the present model is only valid for annular-mist flow and is not applicable for other flow regimes. Then, the initial conditions should be set at the onset of annular flow or any other location downstream where the problem variables are known. At this respect, extensive research, reviewed by Cheng et al. (2008), has been focused on the prediction of the transition quality x_0 which is related to the problem variables as given by Eq. (9.7).

$$x_0 = \frac{G_G}{G_D + G_F + G_G} = \frac{(\alpha\rho u)_G}{\sum_k (\alpha\rho u)_k} \tag{9.7}$$

Several correlations have been proposed for this flow pattern transition, and the two most widely used for the prediction of dryout (Jiao et al., 2009) are those of Wallis (1969) and Mishima and Ishii (1984), given by Eqs. (9.8) and (9.9), respectively. The first one is purely empirical, and the second one presents a theoretical approach for this flow pattern transition, based on the destruction of large slugs by means of entrainment or deformation.

$$x_0 = \frac{0.6 + 0.4\sqrt{\rho_F\,(\rho_F - \rho_G)}\sqrt{gD}/G}{0.6 + \sqrt{\rho_F/\rho_G}} \tag{9.8}$$

$$x_0 = \frac{\rho_G}{G}\left[\frac{\sigma g\,(\rho_F - \rho_G)}{\rho_G^2}\right]^{1/4}\left[\frac{\rho_F \sigma}{\mu_F^2}\sqrt{\frac{\sigma}{g\,(\rho_F - \rho_G)}}\right]^{0.1} \tag{9.9}$$

Equations (9.8) and (9.9) were both developed on the basis of experimental data for adiabatic air-water flow. Therefore, they should be avoided for the analysis of boiling flows, since the flow pattern maps can be rather different in diabatic conditions (Dukler and Taitel, 1986). Taking this situation into account, the flow pattern transition model developed by Kattan et al. (1998) for boiling horizontal flow of refrigerants is considered. The authors postulated that the onset of annular flow occurs at a fixed value of the Lockhart-Martinelli parameter X_{tt} (Lockhart and Martinelli, 1949). With a fitted value of $X_{tt} = 0.34$ this result is translated into the quality as:

$$x_0 = \left[1 + 0.2914 \left(\frac{\rho_G}{\rho_F} \right)^{-1/1.75} \left(\frac{\mu_F}{\mu_G} \right)^{-1/7} \right]^{-1} \tag{9.10}$$

Another important parameter to determine the initial conditions is the entrained fraction at the onset of annular flow, that it how much of the liquid is initially flowing in the form of droplets. Although the prediction of dryout is very sensitive to this parameter (Govan et al., 1988), the available literature is rather limited: there is no experimental data available for this variable because it is not simple to measure, and there is little theoretical research in this area. In general, it is empirically estimated and each author usually selects the value that best fits their experimental data, according to their own models and constitutive equations. In addition, rather successful results have been achieved assuming an equilibrium value for the initial entrained fraction (Lee et al., 2000; Okawa et al., 2004).

For this problem a total of seven initial conditions are required, that is one for each differential equation. The inlet pressure p and total mass flux G are established as problem parameters. Furthermore, the initial quality x_0 is computed according to Eq. (9.10). The initial volume fractions α_k and velocities u_k are set as equilibrium results from an adiabatic analysis, that is, without evaporation. In other words, the governing equations are solved for adiabatic flow, restricted to the condition expressed in Eq. (9.11), and the stationary solution is considered as initial values.

$$\frac{d\alpha_k}{dz} = \frac{du_k}{dz} = 0 \text{ for } k = D, F, G \quad \text{with } W_{evap} = 0 \tag{9.11}$$

9.1.2 Occurrence of dryout

The main objective of this analysis is to predict the conditions under which the film is disrupted and stops wetting the wall. Therefore, a proper criterion for the occurrence of dryout is essential. However, the complex structure of the liquid film, indicated in Fig. 9.2, leads to the transient production of local dry patches (Marathe and Webb, 2008) produced by disturbance waves, and the exact location of dryout is difficult to determine.

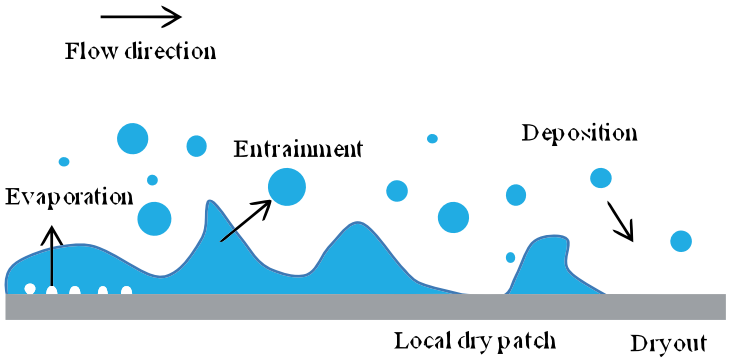

Figure 9.2: Structure of annular-mist flow indicating mass transfer mechanisms

A common approach is to assume that the film flow rate is zero or negligible small. For example, Lee et al. (2000) specified the dryout condition when the film flow rate is less than 1% of the initial value. However, some authors have measured a significant film flow at the dryout point (Milashenko et al., 1989; Ueda and Isayama, 1981). These observations imply that under some conditions (Adamsson (2009) observed that this does not occur for large tube lengths) there is a critical film thickness δ_{crit} where the film may suddenly break up and dryout occurs. Different approaches have been proposed for estimating δ_{crit}, including:

- The use of a constant value for δ_{crit} has been proposed by several authors for the analysis of evaporating refrigerants in microchannels, although presenting differences up to nearly two orders of magnitude between them. As extreme value, Dupont et al. (2004) found the best predictions for their database with $\delta_{crit} = 0.3\mu m$, while Saitoh et al. (2007) recommended $\delta_{crit} = 15\mu m$. An intermediate value was suggested by Shiferaw et al. (2009) as the average wall roughness, which in their study was $\delta_{crit} = 1.3\mu m$.

- As the disturbance waves play a major role in this boiling crisis, Revellin et al. (2008) postulated that the critical film thickness is equal to the amplitude of these waves, given by Eq. (9.12), where R is the tube radius. This correlation predicts reasonably well experimental data for CO_2 and refrigerants in horizontal flow in microchannels.

$$\frac{\delta_{crit}}{R} = 0.15 \left(\frac{\mu_G}{\mu_F}\right)^{-3/7} \left[\frac{gR^2\left(\rho_F - \rho_G\right)}{\sigma}\right]^{-1/7} \tag{9.12}$$

  However, recalling the wavy flow structure indicated in Fig. 9.2 the value given by Eq. (9.12) should be rather considered as an upper limit. In other

words, when the film thickness is reduced below the amplitude of the waves, local dry patches occur, but the wall can be rewetted.

- An analysis based on dimensionless groups including the influence of the wall heat flux q'' was presented by Chun et al. (2003). The authors proposed the empirical formula given by Eq. (9.13) for boiling water in round-tube and annular geometries in small channels ($3mm < D < 37.5mm$).

$$\delta_{crit} = \left(\frac{q''}{\Delta h_{LV} G_F} \right)^{0.35} \left(\frac{1}{\rho_G} - \frac{1}{\rho_F} \right) \frac{\mu_F^2}{\sigma} 10^{8.8(\mu_G/\mu_F)^{0.617}} \tag{9.13}$$

As a general comment, the above models fail to account for all relevant effects. For example, Eq. (9.12) does not include the effect of heat flux and Eq. (9.13) is missing the influence of the tube diameter. In addition, two lines of research can be identified: boiling water for reactor applications and horizontal flow of refrigerants in microchannels. Both of them present some similarities and some differences for their application in cryogenic and LNG applications.

9.1.3 Mass transfer models

The constitutive models for W_{dep}, W_{ent} and W_{evap} are described in this section. Extensive research has been devoted to the development of entrainment and deposition models, as reviewed by Jiao et al. (2009), with rather successful results in terms of the prediction of Critical Heat Flux. However, Kolev (2007, §5-6) indicated that all correlations predicted the occurrence of dryout further downstream of the experimental observations, and concluded that present models tend to overestimate the deposition and underestimate the entrainment. This result is probably a consequence of present models being developed for adiabatic conditions. In the case of boiling flows, the bubble nucleation and departure tends to enhance the entrainment and reduce the deposition rate (Milashenko et al., 1989; Peng, 2008).

The direct measurement of pure entrainment rates are a challenging task, since this phenomenon cannot be physically separated from deposition[1]. For this reason, most authors have focused their research on the modeling of equilibrium (and developing) entrained fractions, which can be more easily obtained experimentally and are more useful for adiabatic conditions than boiling flow. In addition, the entrainment rate is measured as equal to the deposition in equilibrium conditions. As a consequence, correlations for entrainment are always connected to a deposition model.

[1]The opposite situation, that is pure deposition without entrainment, can be achieved in practice by continuously draining the film at the wall

Droplets deposition

Experimental results for deposition of a mist flow indicate that the mass flow rate of droplets decays roughly exponentially. For this reason, the rate of droplet deposition is usually considered to be proportional to the liquid concentration in the gas core C_D. A deposition coefficient k_{dep} is then defined as in Eq. (9.14).

$$W_{dep} = k_{dep} C_D \tag{9.14}$$

According to this definition, k_{dep} is measured in units of m s^{-1}, and represents the average radial velocity at which the droplets are deposited from the gas core due to turbulent diffusion. The values of k_{dep} are much lower for high-pressure steam-water flows than in low-pressure air-water, mainly due to the reduced surface tension (Hewitt, 1982). In addition, several authors found a slight dependence of this coefficient on the droplet concentration. In this context Hewitt and Govan (1990) collected experimental data for air-water and steam-water systems from different sources as in Fig. 9.3 and proposed the correlation given by Eq. (9.15).

$$k_{dep}\sqrt{\frac{D\rho_L}{\sigma}} = \begin{cases} 0.1815 & \text{if } C_D/\rho_G < 0.3 \\ 0.083\,(C/\rho_G)^{-0.65} & \text{if } C_D/\rho_G > 0.3 \end{cases} \tag{9.15}$$

Considering the large scatter present in the experimental data, represented by the typical error bar indicated in Fig. 9.3, and the lack of a physical basis for the above discontinuity, Okawa et al. (2002) proposed a single-line correlation based on the same experimental data, as in Eq. (9.16).

$$k_{dep}\sqrt{\frac{D\rho_L}{\sigma}} = 0.0632\left(\frac{C_D}{\rho_G}\right)^{-0.5} \tag{9.16}$$

Equations (9.15) and (9.16) have approximately the same accuracy either one of them can be used. It is also observed in Fig. 9.3 that the experimental uncertainties, represented by the typical error bar, exceed 30%, and the scatter in the data is at least twice this value.

Droplets entrainment

Ishii and Grolmes (1975) identified the disruption of disturbance waves as the main mechanism for entrainment. The authors proposed an inception criteria for droplet entrainment, considering a critical gas superficial velocity $j_{G,crit}$, correlated with the film Reynolds number Re_F and a viscosity number. Although in the case of boiling flow other mechanisms such as bubble-induced entrainment can be significant (Milashenko et al., 1989), better results were obtained neglecting these effects than including them (Azzopardi, 1996).

Based on this mechanism Okawa and Kataoka (2005) suggested that the entrainment rate can be well correlated with a dimensionless parameter π_e, given

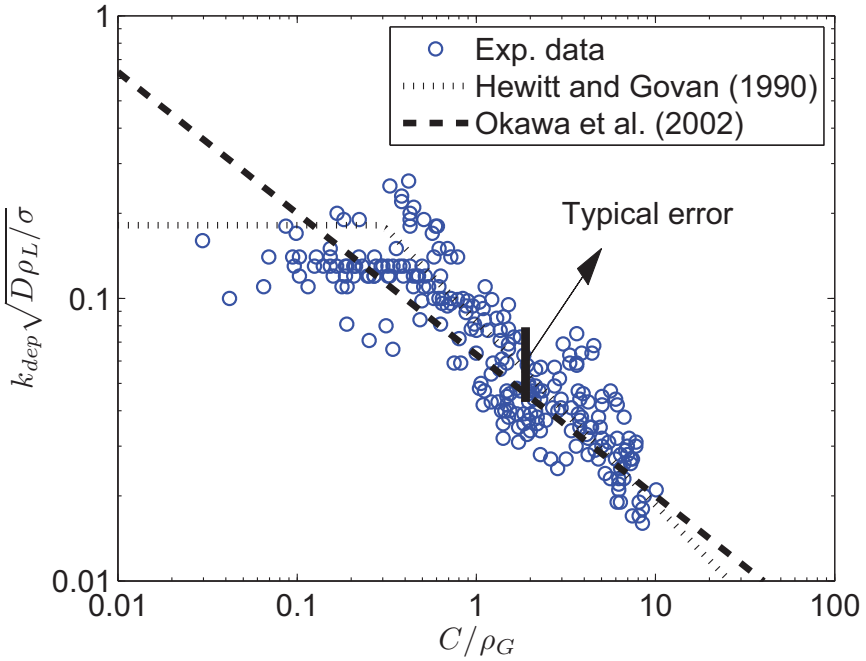

Figure 9.3: Deposition coefficient as a function of droplets concentration. Experimental data collected from different sources by Hewitt and Govan (1990).

by Eq. (9.17), where f_i is the interfacial film-gas friction factor, further studied in Section 9.1.4. This entrainment parameter expresses the ratio of interfacial shear stress (in excess of the critical value) and surface tension forces.

$$\pi_e = \frac{f_i \rho_G \left(j_G^2 - j_{G,crit}^2\right)}{\sigma/\delta} \tag{9.17}$$

On the basis of an extensive experimental database for air-water (more than one thousand points) and steam-water (250), the authors developed the three-lines empirical correlation given by Eq. (9.18). This model has been found to give the best results for boiling water reactor operating conditions (Secondi et al., 2009), that is steam-water flow at a pressure of roughly 70 bar.

$$\frac{W_{ent}}{\rho_F} = \begin{cases} 3.8\ 10^{-3}\ m\ s^{-1}\ \pi_e & \text{if } \pi_e < 0.1 \\ 1.2\ 10^{-3}\ m\ s^{-1}\ \pi_e^{0.5} & \text{if } 0.1 < \pi_e < 1 \\ 1.2\ 10^{-3}\ m\ s^{-1} & \text{if } \pi_e > 1 \end{cases} \tag{9.18}$$

In addition to a critical gas flow, there is experimental evidence of a threshold

film flow rate below which entrainment does not occur. In their model, Okawa et al. (2004) considered a critical film Reynolds number of $Re_{F,crit} = 320$.

Other authors, such as Dallman et al. (1984); de Bertodano et al. (1997) and Hewitt and Govan (1990) considered the entrainment rate to be given by the excess film flow over the threshold value. In particular, the empirical model by Hewitt and Govan (1990), given by Eq. (9.19), has achieved extensive experimental validation with air-water data. However, its use is discouraged for this analysis since it does not include a critical gas flow criteria.

$$\frac{W_{ent}}{G_G} = 5.75\ 10^{-5} \left[\left(G_F - G_{F,crit}\right)^2 \frac{D\rho_F}{\sigma \rho_G^2} \right]^{0.316} \tag{9.19a}$$

$$Re_{F,crit} = \frac{G_{F,crit} D}{\mu_F} = \exp\left(5.8504 + 0.4209 \frac{\mu_G}{\mu_L} \sqrt{\frac{\rho_F}{\rho_G}} \right) \tag{9.19b}$$

Considering the above discussion, the empirical models of Okawa and coworkers are selected in this analysis. That is, the deposition rate is given by Eq. (9.16) and the entrainment is computed according to Eq. (9.18).

Evaporation rate

Finally, the evaporation is given by the wall heat flux q''_W as in Eq. (9.20). This simple expression indicates that in non-homogeneous axial power distributions, the evaporation rate is also not constant.

$$W_{evap} = \frac{q''_W}{\Delta h_{LV}} \tag{9.20}$$

9.1.4 Interfacial and wall friction

In this section, the different shear stresses between the different phases are analyzed. In particular, the interfacial shear τ_i and wall friction τ_W are usually modeled in terms of friction factors f_i and f_W according to Eqs. (9.21) and (9.22), respectively.

$$\tau_i = \frac{1}{2} f_i \rho_G \left(u_G - u_F\right)^2 \tag{9.21}$$

$$\tau_w = \frac{1}{2} f_W \rho_F u_F^2 \tag{9.22}$$

Given the usual turbulent flow regime, these friction factors are generally computed from empirical correlations. A widely used model for the interfacial friction

factor is the one developed by Wallis (1969) that accounts for the disturbance waves in the film using a sand roughness concept as in Eq. (9.23), where f_s represents the smooth tube friction factor. While originally Wallis (1969) postulated the use of a constant value of 0.005 for f_s, later authors (Lee and No, 2007; Saito et al., 1978; Sami, 1988; Stevanovic and Studovic, 1995; Sugawara, 1990; Yao and Ghiaasiaan, 1996) recommended the use of friction factors corresponding to laminar and turbulent flow correlations. Nevertheless, as a value of $f_s = 0.005$ was selected by Okawa and Kataoka (2005) for the development of their entrainment model, the same value is considered for computing τ_i.

$$f_i = f_s \left(1 + 300 \frac{\delta}{D} \right) \tag{9.23}$$

Regarding the wall friction, several correlations were recently compared by Lee and No (2007), who recommended the use of a modified Blasius equation (White, 1986, §6.4), as in Eq. (9.24).

$$f_W = \max \left\{ \frac{16}{Re_F}, 0.001375 \left(1 + \frac{1}{Re_F^{1/3}} \right) \right\} \tag{9.24}$$

Finally, the drag forces at the droplet-gas interface can be modeled according to the Stoke's law for laminar flow across a solid sphere (Clift et al., 1978), considering their small diameter and consequently low Reynold number of the flow. Then, Eq. (9.25) applies for the shear stress $\tau_{D,G}$.

$$\tau_{D,G} = \frac{12 \mu_G \left(u_G - u_D \right)}{d} \tag{9.25}$$

9.2 Validation of the model

In Section 9.1 a complete three-fluid model was formulated for the evolution of annular-mist flow on the basis of some constitutive relations, and model closure was achieved without introducing arbitrary constants. The accuracy of this model to predict experimental data is investigated in the present section.

Most of the experimental observations reported in the open literature regarding the occurrence of dryout are expressed in terms of the Critical Heat Flux (CHF). However, as discussed above, this variable alone may be insufficient to determine the performance of the model. As the heat flux becomes large (like in typical CHF conditions), the magnitude of the evaporation rate makes it the dominant mass transfer mechanism, thus masking the usually large uncertainties in the description of the entrainment and deposition processes. Then, an accurate prediction of CHF does not imply that other relevant variables, such as the dryout quality and the local film thickness or velocity, are predicted with the same accuracy as observed by Kawara et al. (1998) and Kolev (2007, §5-6).

For this reason, the selected variable for the validation of the model is the dryout quality x_{dy}, that is the mass vapor content at which dryout occurs. Four data sets were obtained from the open literature, as summarized in Table 9.1.

Case	A	B	C	D
Fluid	R22,R410a	Water	R134a	Pentane
Pressure p [bar]	5.8, 9.3	3, 30-90	13-24	3-10
Tube diameter D [mm]	8, 13.4	10.0	17.04	25.4
Mass flux G [kg m^{-2} s^{-1}]	17-57	400-1400	52-75	30-100
Number of points	23	29	24	5
Flow direction	Horizontal	Upward	Upward	Upward
Source	[346]	[133; 350]	[193]	[29]

Table 9.1: Four experimental datasets for the validation of the annular-mist flow model

As in cases B, C and D the authors did not report the flow pattern at which the boiling crisis occurs, their data was filtered and only cases with $x_{dy} > 0.55$ (conservative figure, always large than the transition quality predicted by Eq. (9.10)) were considered, in order to assure that the data refers to annular film dryout and not other burnout mechanism. Figure 9.4 presents the results for this validation in terms of the predicted and measured dryout quality x_{dy}. In this figure, the horizontal lines represent the experimental uncertainties of the measured values as reported in the references listed in Table 9.1. This analysis allows to determine under which conditions the model performs best.

A statistical analysis of these 81 points gives a mean relative error of 0.55%, indicating that, in general, the model does not tend neither to underpredict nor to overpredict the occurrence of dryout. The overall accuracy of the model is better represented by the absolute mean and root-mean-square (RMS) relative errors, which are 11.01% and 13.68%, respectively. These results are encouraging, considering that the uncertainties of the experimental values range between 2% and 8%, although there is still plenty of space for improvement.

In addition, some individual conclusions can be obtained for each dataset A to D as follows.

- Nearly all the points corresponding to case A are shifted upward in Fig. 9.4, including one point overpredicted by roughly 45%. In other words, dryout occurs in the experiments earlier than predicted, and therefore the application of this model gives non-conservative (that is, not safe) results. It should be noted that case A corresponds to horizontal flow. In this case, gravitational effects tend to produce assymetries in the film, which is thicker at the bottom than at the top. As a consequence, dryout starts earlier at the top of the tube. In fact, the authors stated that dryout occurs over a wide range of quality, and the reported value in Fig. 9.4 corresponds to the lower limit.

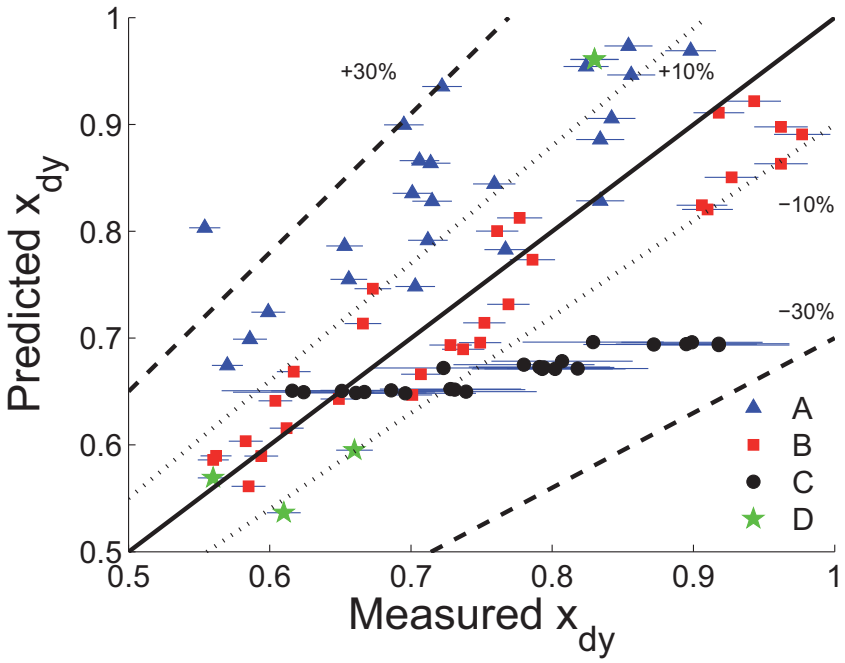

Figure 9.4: Predicted and measured dryout quality for cases A to D in Table 9.1

Furthermore, the selected crtical film thickness criterion for the determination of the occurrence of dryout is not applicable for horizontal flow. These effects are further studied in detail in Section 9.4.

- The dataset B, which includes experimental observations for boiling water flow, gives the best results. Nearly all the points are predicted within ±10% error, and the RMS relative error for these 29 cases is 6.27%, that is less than half than the overall value. At this point, it should be recalled that the selected constitutive relations for entrainment and deposition, were developed originally for air-water and steam-water flows.

- Case C presents the largest experimental uncertainties, given by the horizontal lines in Fig. 9.4. These 24 experimental points correspond to three different pressure levels (with small variation in the wall heat flux), and the model predicts basically one single value of x_{dy} for each of them. In average, these cases are underpredicted.

- For both cases C and D, the error in the predictions are larger than for the

water dataset. The working fluids for C and D are hydrocarbons, which have a lower surface tension than water. In the mathematical formulation presented in Section 9.1 the surface tension is expected to affect the entrainment and deposition processes, as well as the critical film thickness at which dry-out occurs. Then, the application of this empirical models for hydrocarbons is outside their validity range.

Finally, in order to locate the weaknesses of the model, these results are filtered in Fig. 9.5 according to four different parameters: (a) wall heat flux, (b) tube diameter, (c) mass flux and (d) surface tension.

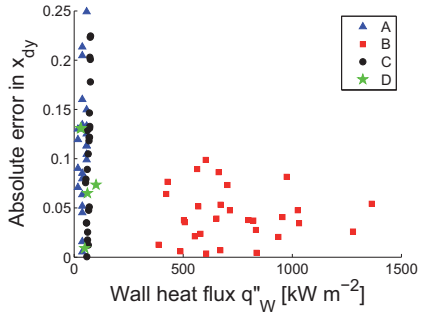

(a) Effect of q''_W

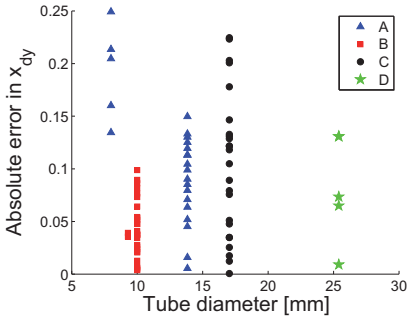

(b) Effect of D

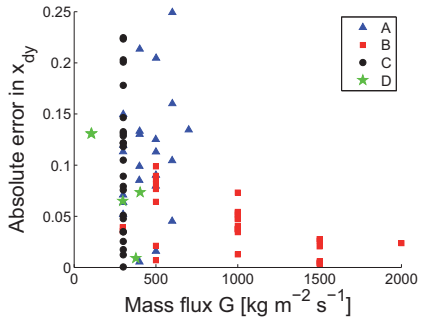

(c) Effect of G

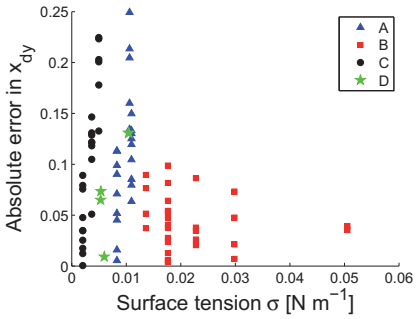

(d) Effect of σ

Figure 9.5: Parametric analysis of the accuracy of the annular-mist flow model. Cases A to D refer to Table 9.1.

It can be concluded from Fig. 9.5 that the only parameter that is *not* correlated with the error in x_{dy} is the tube diameter, at least in the selected range between 8.0 and 25.4 mm, since the plot in Fig. 9.5(a) does not show any clear trend. Regarding the other parameters, the largest errors are found at.

- Low heat flux q''_W, as observed in Fig. 9.5(a)

- Low mass flux G, see Fig. 9.5(c)
- Low surface tension σ, represented in Fig. 9.5(d)

The large errors in these cases are explained by their location outside the validity range of the empirical models selected for the constitutive relations, most remarkably entrainment and deposition. These models were originally developed for air-water and steam-water systems (which have larger surface tension than hydrocarbons) at relatively large heat and mass fluxes. The uncertainties of these models become more clear at lower heat flux, as the evaporation rate is reduced and the other mass transfer mechanisms gain relative importance. Therefore if the accuracy of the present model for these conditions is to be improved, specific constitutive relations based on relevant experimental data are necessary.

9.3 Numerical examples

The three-fluid model formulated in Section 9.1 and validated in Section 9.2, is applied in the present section to two numerical examples. First, a uniform heat flux case is considered and the sensitivity of the dryout quality x_{dy} to the input parameters is studied in Section 9.3.1. Finally, the effects of the axial power distribution are investigated in Section 9.3.2 for heat flux profiles relevant to heat exchanger applications.

An operating condition from dataset B (see Table 9.1) is selected as the reference case. The working fluid is water at a pressure of 70 bar with a mass flux of 1000 kg m^{-2} s^{-1} in a 10 mm round tube, subject to an external heat input of 387 kW m^{-2}. For these conditions, the measured dryout quality is $x_{dy} = 0.786 \pm 0.016$, while the present model predicted a value of 0.773, that is within the experimental uncertainty range.

9.3.1 Qualitative sensitivity analysis

For the given reference case described above, the sensitivity of x_{dy} to four parameters is studied in this section. Figure 9.6 presents the evolution of the dryout quality when varying the mass flux G, heat flux q''_W, tube diameter D and working pressure p, individually between half and twice their reference values.

All four parameters produce the same qualitative effect (increasing them reduces the dryout quality), and this behavior can be explained for each of them by analyzing the constitutive relations for the mass transfer processes, presented in Section 9.1.3, as follows.

Keeping all other variables constant, a larger heat flux q''_W increases the evaporation rate. In addition, according to the selected criterion for the occurrence of dryout (see Section 9.1.2), the critical film thickness δ_{crit}, given by Eq. (9.13), is also increased. This means that dryout occurs at larger film thickness, which is

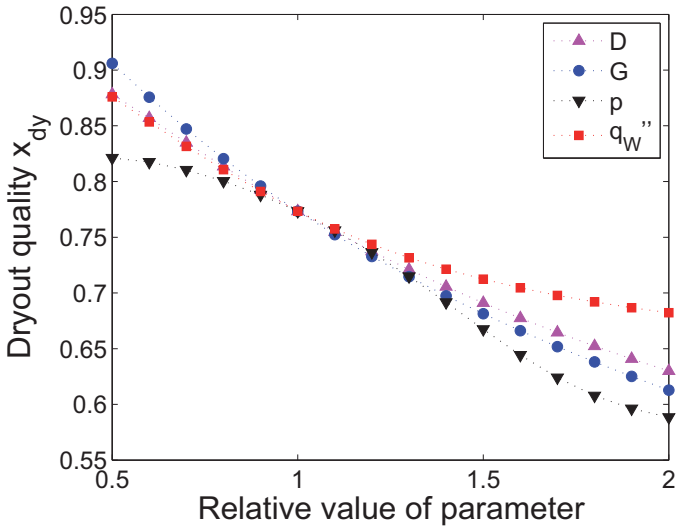

Figure 9.6: Sensitivity analysis of dryout quality to the input parameters

also depleted more rapidly due to the higher evaporation. As a consequence, the dryout quality x_{dy} is reduced by an increase in the heat flux.

According to Eq. (9.18) a larger mass flux G results in a larger entrainment rate W_{ent}. Similarly, the deposition rate W_{dep}, given by Eq. (9.16), is lower when the tube diameter is larger. Both effects result in an increase in the net entrainment rate (that is the difference $W_{ent} - W_{dep}$), thus reducing the film thickness more rapidly. In addition, since equilibrium initial conditions were considered, the initial film is thinner. For these reasons, keeping all other variables constant, a larger mass flux and a larger diameter lead to an earlier dryout.

In the case of the working pressure p, this variable affects all the saturated fluid properties at the same time. In particular, the largest effect is given by changes in the the surface tension σ and the latent heat of evaporation Δh_{LV}. First, a higher pressure gives a lower σ, leading to an increase in the entrainment rate. Second, for a constant heat flux, the evaporation rate is increased as a consequence of a lower Δh_{LV}. Both effects contribute to the reduction in the dryout quality x_{dy} that can be observed in Fig. 9.6.

Beyond the qualitative analysis, it can be concluded from Fig. 9.6 that the dryout quality is very sensitive to the input parameters. For examples, variations as large as ± 0.12 (that is 15% of the reference predicted value $x_{dy} = 0.773$) for the studied changes in the mass flux.

9.3.2 Application to a HE heat flux distribution

As discussed earlier, the axial power distribution (APD) is known to influence the occurrence of the boiling crisis known as dryout (Adamsson and Anglart, 2010; Yang et al., 2006). While both Sections 9.2 and 9.3.1 deal with a uniform heat flux distribution, different APD relevant to heat exchanger applications are considered in the present section.

In general, the local heat flux in a HE is given by the temperature difference and overall heat transfer coefficient as in Eq. (9.26a), and the APD can take arbitrary complex forms. However, some simplifying assumptions can be considered for the particular case of an evaporator. First, the overall heat transfer coefficient U is given by a combination of thermal resistances, which for a tube geometry is given by Eq. (4.44). Prior to the occurrence of dryout, it is dominated by the convection resistance in the single-phase stream, which is much larger than in the boiling refrigerant. As a consequence, the overall HTC can be considered (as a first approximation) to be roughly constant. Second, the local temperature difference is only affected by the temperature of the hot single-phase stream T_{hot}, as the evaporating fluid temperature T_{cold} remains at its saturation value. The evolution of T_{hot} can be obtained from the energy balances expressed in Eq. (9.26b).

$$q''_W = U\left(T_{hot} - T_{cold}\right) \tag{9.26a}$$

$$q''_W = -\frac{\left(\dot{m}c_p\right)_{hot}}{\pi D}\frac{\partial T_{hot}}{\partial z} \tag{9.26b}$$

The solution to Eq. (9.26) depends on the flow arrangement, and the results are summarized in Table 9.2. In a crossflow arrangement, which is characteristic of air-heated evaporators, the single-phase temperature can be considered to be uniform for a given tube. Consequently, the APD is also uniform. In the case of one-dimensional arrangements, such as co-current and counter-current conditions, the APD is exponential.

Flow arrangement	$\frac{q''_W(z)}{q''_{W,average}}$	Comments	Predicted x_{dy}
Cross-flow	1	Uniform	0.773
Co-current	$\frac{NTU\left(e^{-NTUz/L}\right)}{1-e^{-NTU}}$	Inlet-peaked	0.823
Counter-current	$\frac{NTU\left(e^{-NTU(1-z/L)}\right)}{1-e^{-NTU}}$	Outlet-peaked	0.731

Table 9.2: Heat flux axial power distributions relevant to heat exchanger applications

As the axial power distribution depends on the heat exchanger size, represented by the number of thermal units (NTU), a case with $NTU = 1.0$ is studied first

and later extended in a parametric analysis. For comparison purposes, the mass flux and mass transfer profiles are presented in Fig. 9.7 for APD corresponding to (a) co-current, (b) cross-flow and (c) counterflow arrangements. Since the initial conditions are given by an equilibrium state for an adiabatic cases, they are the same for all three cases, regardless the APD. For the same reason, the initial entrainment rate is equal to the deposition rate.

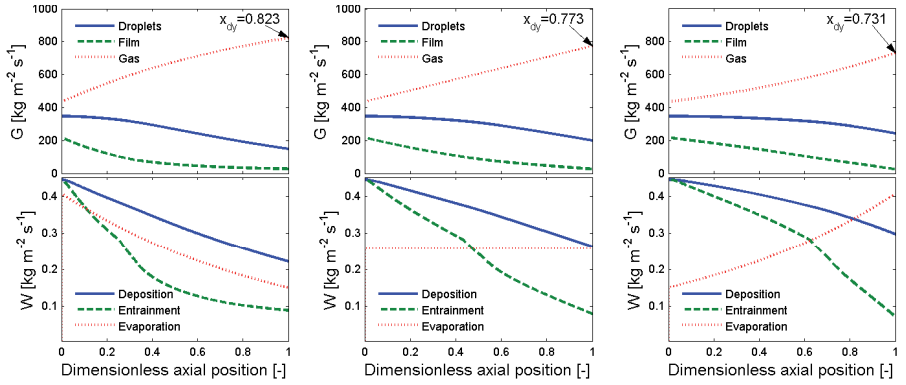

(a) Co-current (b) Uniform heat flux (c) Counter-current

Figure 9.7: Longitudinal evolution for different axial power distribution typical of heat exchangers

Some characteristic elements of Fig. 9.7 are common to all three cases. As the film mass flux G_F is reduced due to evaporation, the entrainment rate becomes lower, thus giving a net deposition of liquid. This is the only physical mechanisms responsible the the removal of droplets and consequently reducing the amount of liquid present at the dryout location and therefore increasing x_{dy}. In other words, the dryout quality is largely influenced by this net deposition rate.

The film mass flux is monotonously decreasing, indicating that the film is continuously being depleted because the evaporation rate is larger than this net deposition. For a co-current flow arrangement, the evaporation rate close to the dryout location is rather low, see Fig. 9.7(a). Then, the net deposition compensates almost completely for evaporation and the film is *slowly* depleted, leading to a dryout quality ($x_{dy} = 0.823$) that is 6.5% higher than for a uniform APD ($x_{dy} = 0.773$). In a counter-current flow arrangement, the opposite situation occurs, and the film is more *rapidly* depleted, leading to a dryout quality ($x_{dy} = 0.731$) 5.4% lower than in the homogeneous case. In addition, it should be noted that as the local heat flux is lower, thin films become more stable and the critical film thickness δ_{crit} is reduced, contributing to the differences in the dryout quality.

A parametric analysis of the effect of APD is presented in Fig. 9.8. According to the heat flux profiles summarized in Table 9.2, an increase in the number of

thermal units NTU results in a further deviation from a homogeneous profile. Therefore, it is expected that the difference between co-current and counter-current flow arrangements become larger with increasing NTU.

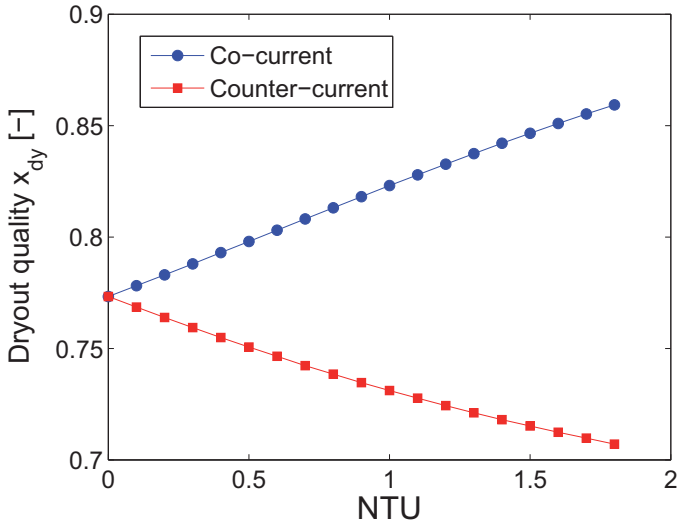

Figure 9.8: Dryout quality for different heat exchanger sizes

The predicted dryout quality presents differences up to ±10% with the reference value in the selected range $NTU \leq 1.8$. At larger values of NTU, early local dryout occurs in the co-current case due to the initially high heat flux and the results are not comparable, since the average heat flux imposed in the annular-mist flow regime would not be the same.

In summary, the results from this section indicate that the axial power distribution can have a large influence in the occurrence of dryout. For heat flux profiles relevant to evaporators, changes up to ±10% in the dryout quality are noticed.

9.4 Partial dryout in horizontal flow

The present three-fluid model was validated with experimental data in Section 9.2, and large uncertainties were observed for horizontal flow (dataset A in Table 9.1 and Figs. 9.4 and 9.5). In particular, the dryout quality is overpredicted in 22 out of 23 cases, by an average of 16%. This means that in experimental observations the boiling crisis known as dryout occurs earlier than predicted by the model, and then its use for this scenario is not conservative.

It can be concluded from this analysis that the selected criterion for determining the occurrence of dryout (described in Section 9.1.2 and based on a critical film thickness) is not applicable in horizontal flow. In their experiments, the authors (Wojtan et al., 2005a) observed that in horizontal flow, gravitational effects make the film thicker at the bottom and thinner at the top, where it is disrupted first. Then, the dryout of the wall is not a local phenomena but rather a process occurring over a finite range of vapor content. In this context, and following the framework first developed by Mori et al. (2000), they presented individual vapor qualities for the onset and end of dryout[2].

An extended model is developed in this section, including the following simplified flow regimes (indicated in Fig. 9.9) in the analysis: annular-mist, dryout or partial dryout, and mist flow.

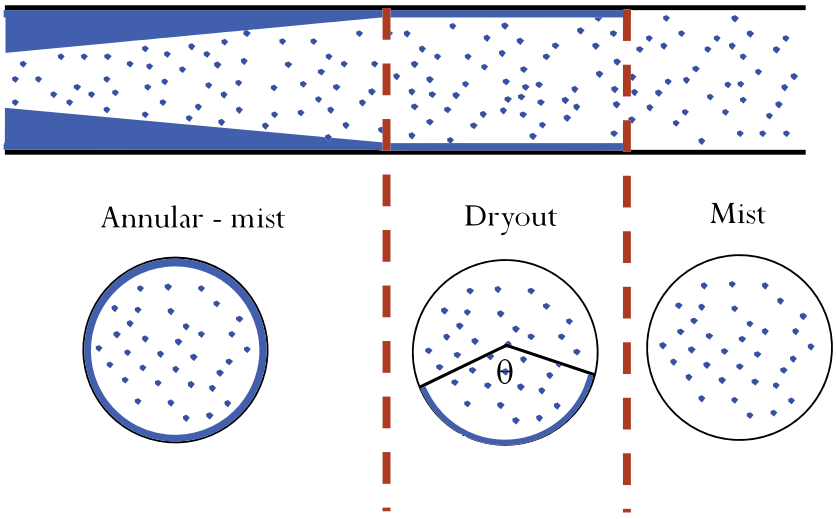

Figure 9.9: Flow regimes in horizontal boiling flow

In the annular-mist flow pattern, which is the regime discussed in the previous sections throughout this chapter, the wall is completely wetted by a thin liquid film, with entrained droplets in the gas core that covers most of the cross section. This flow regime extends from the onset of annular flow, given by Eq. (9.10), until the onset of dryout, according to the criterion presented in Section 9.1.2, that is when the film thickness reaches a critical value δ_{crit}. The multifluid formulation developed in Section 9.1 can be directly applied in the annular-mist flow pattern.

[2]The value considered for model validation in Section 9.2 was the one corresponding to the onset of dryout, as this represents the location at which the heat transfer coefficient is reduced. Then, the occurrence of dryout over a finite range represents a possible cause for the overprediction of the dryout quality.

As the liquid film is disrupted earlier at the top of the tube than at the bottom, a partial dryout flow pattern (also identified as dryout flow regime by other authors, such as Wojtan et al. (2005b)) is developed. During this flow regime, the film thickness is assumed to be constant at $\delta = \delta_{crit}$, with the upper part of the wall and the lower part wet, represented by a wet angle $\theta \in [0, 2\pi)$. At this point, some additional interactions between the different phases and the tube wall become relevant in this multifluid formulation.

- The deposition of droplets is driven mainly by turbulent fluctuations and therefore is is distributed homogeneously in all directions. Then, a fraction represented by the wet angle θ is deposited in the liquid film, and a complementary fraction of these droplets collide with the dry wall. During this collision with the dry wall, some evaporation occurs. In particular, it is assumed that, due to the large heat transfer rates, each droplet that collides with the wall is fully evaporated[3].

- As a consequence of direct heat transfer with the dry wall, the vapor phase becomes overheated, thus resulting in a departure from thermal equilibrium. A single-phase gas heat transfer coefficient is considered for this process.

- The departure from thermal equilibrium results in heat transfer between vapor and liquid phases, as their temperatures are different. In particular, the evaporation of droplets becomes relevant due to the large density of interfacial area.

Finally, further heat input results in a continuous reduction of the film flow rate until the wall becomes completely dry. This last two-phase flow regime is known as post-dryout or mist flow and is the main topic of Chapter 10. In the absence of a liquid film, only two phases are present: dispersed liquid as droplets and a continuous overheated vapor flow.

To sum up, the mass transfer mechanisms included in this extended model are summarized in Fig. 9.10. They are basically the same ones as described previously in Section 9.1, with the incorporation of droplet evaporation in the partial dryout and mist flow regimes.

In the following subsection 9.4.1 this extended model is applied to and the predicted heat transfer coefficient is compared with experimental observations.

9.4.1 Prediction of the heat transfer coefficient

The heat transfer coefficient (HTC) $\hat{h}$ is perhaps the most important parameter for bridging the results from this study with the analysis of larger scales. This parameter relates the heat flux and the temperature difference between the wall and the fluid as in Eq. (9.27). For internal flow, the fluid is represented by the

[3]Limited by the external heat input proportional to the dry angle $2\pi - \theta$.

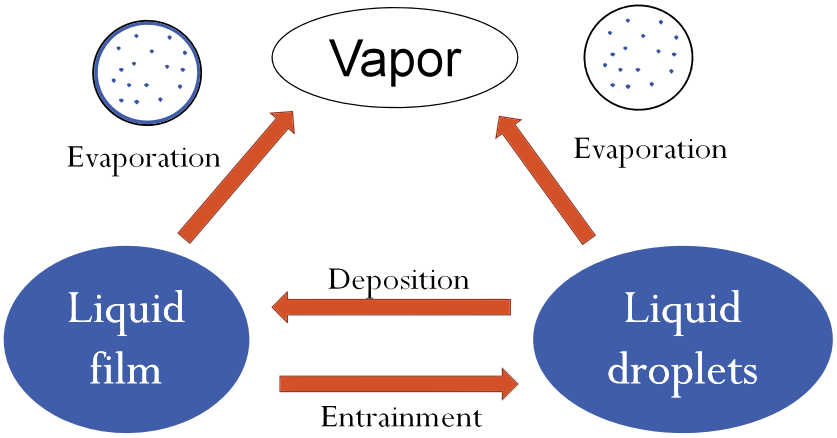

Figure 9.10: Mass transfer mechanisms in partial dryout flow

mean temperature T_m (Incropera and DeWitt, 1996, §8). This is the temperature that would be achieved if the flow is mixed and completely homogenized or, in other words, the equilibrium temperature.

$$\hat{h} = \frac{q''_W}{T_W - T_m} \tag{9.27}$$

During the annular-mist flow regime, both bubble nucleation and film convection contribute to the HTC. Then, some of the boiling heat transfer models described in Section 3.3.3 can be applied for determining the film boiling HTC $\hat{h} = \hat{h}_F$. In particular, the model given by Steiner and Taborek (1992) is used.

After the onset of dryout, the HTC is reduced continuously from the large values given by the thin film convection to the lower one corresponding to single-phase vapor convection. This behavior can be represented by a proper average of these two extreme values, weighted with the wetting angle θ (see Fig. 9.9) as in Eq. (9.28). In the post-dryout flow regime (studied in further detail in Chapter 10) the wall is completely dry ($\theta = 0$) and the HTC reaches the value for single-phase vapor ($\hat{h} = \hat{h}_G$).

$$\hat{h} = \frac{\theta}{2\pi}\hat{h}_F + \frac{2\pi - \theta}{2\pi}\hat{h}_G \tag{9.28}$$

With all these considerations, one test case is studied and compared with experimental data reported by da Silva Lima et al. (2009). For a given working fluid (in this case the refrigerant R134a) the problem is completely defined by four parameters. These are the tube diameter $D = 13$ mm, total mass flux $G = 500$ kg m^{-2} s^{-1}, working pressure $p = 5.8$ bar (corresponding to a saturation temperature of five

degrees Celsius) and heat flux $q''_W = 7.5$ kW m^{-2}. The experimental and predicted heat transfer coefficient as a function of the actual quality x_a (that is, the mass vapor content) are presented in Fig. 9.11.

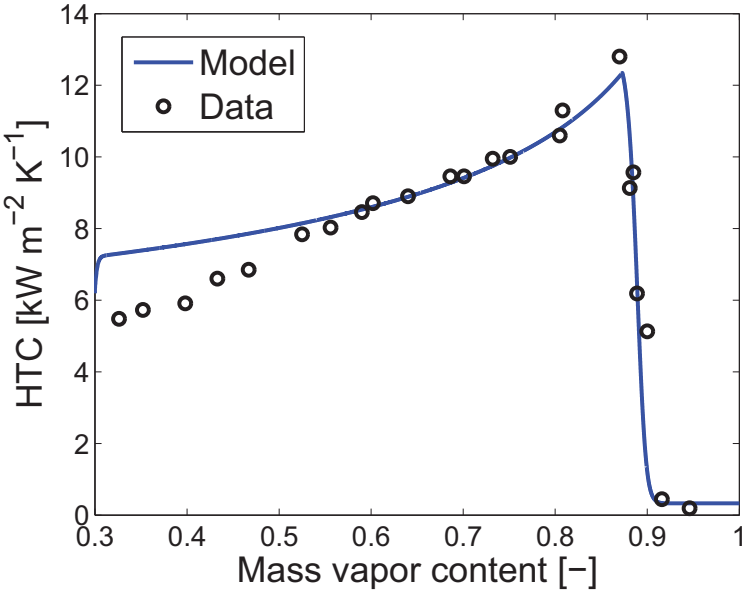

Figure 9.11: Heat transfer coefficient in horizontal boiling flow. Experimental data from da Silva Lima et al. (2009).

At first sight, the following conclusions can be obtained from Fig. 9.11.

- In the annular mist flow regime, the model captures the trend in the evolution of the HTC as it increases with the quality, mainly due to the continuous reduction in the film thickness. The predicted HTC deviates no more than ±20% from the experimental value throughout this regime. This accuracy is typical of the empirical model for HTC in two-phase flow analyzed in Section 3.3.3, indicating that the present model does not introduce significant error in the predicition of relevant flow parameters such as the film thickness. Further work in this area should be focused in the improvement of forced convection correlations for film flow, as the selected model presents an asymptotic description and this region is convection-dominated.

- According to Eq. (9.10), the onset of annular flow for these conditions is given at $x = 0.375$. This situation explains the rather large differences between

experimental data and model predictions for low quality (on the left side of Fig. 9.11). It is indeed very likely that these points do not correspond to the annular-mist flow regime, but to slug pattern instead. It should also be reminded that the experimental data used for the model validation in 9.2 was filtered considering only those cases with $x > 0.55$. In this region, the is very good agreement between empirical and predicted values of the heat transfer coefficient.

- The experimental observations indicate that the partial dryout flow regime occurs over a very narrow range of quality. The phenomenological model presented in this chapter predicted the extent of this regime rather well. This means that the film evaporation rate and its disruption are well represented.

- Finally, it should be mentioned that each experimental data point in Fig. 9.11 corresponds to an individual run. In other words, the experimental setup does not involve a long test section with several measurement locations, as assumed in this model. Instead, the test section is short and the flow is preconditioned to the desired vapor content. Therefore, there is a large degree of thermal equilibrium, which is not necessarily found in other applications. The extent of non-equilibrium is further discussed in Chapter 10.

9.5 Summary

A microscopic analysis intends to achieve an accurate description of the heat transfer coefficient in order to bridge the different scales. In this context, perhaps the most relevant transition in boiling flows is the occurrence of dryout in the annular-mist regime, leading to a drastic reduction of the heat transfer performance. The historical evolution of predicting models was studied in this chapter. In general, the most satisfactory results have been obtained using multifluid formulations for the analysis of Critical Heat Flux in power-controlled systems with large heat and mass fluxes. These operating conditions present two main differences respect to heat exchanger applications: the relative importance of the mass transfer mechanisms and the axial power distribution.

In this chapter, a phenomenological model is presented for the analysis of annular flow in heat exchangers. The governing equations are mass, momentum and energy balances for each phase field: vapor core, liquid droplets and liquid film. Empirical constitutive relations are required in order to account for the mass and heat transfer mechanisms (deposition, entrainment, evaporation), shear stresses, and the disruption of the film leading to dryout. In general, different state-of-the-art models are compared and the most suitable ones for heat exchanger application in cryogenic systems are selected.

This model was validated with experimental observations for different fluids, including water and hydrocarbons. Considering a total of 81 data points, and RMS

error of 13.7% in the prediction of the dryout quality was obtained. In general, the water cases present the best results, in all cases within ±10% error. This result is a consequence of the empirical relations being based on experimental observations for air-water and steam-water systems. Analyzing the weaknesses of this model, it is observed that the largest errors are found at low heat and mass flux, and low surface tension. These conditions, typical of hydrocarbon applications, exceed the validity range of the selected constitutive relations. Therefore, it can be concluded that in order to improve the accuracy of the predictions for hydrocarbon systems, specific experimental observations and correlations are required for describing the entrainment and deposition processes.

In addition, two numerical examples were analyzed. First, a sensitivity analysis to the input parameters was performed. It was observed that increasing the heat flux, mass flux, tube diameter or working pressure, lead to an earlier dryout. These results are a consequences of the increase in the entrainment and evaporations rates, and/or the reduction of deposition, which have the same effect: a faster reduction of the film thickness. The second example considers axial power distributions relevant to heat exchanger applications. On the one hand, an inlet-peaked profile (characteristic of co-current flow arrangement) leads to a later dryout, mainly because the evaporation rate at the outlet is smaller and the film becomes more stable. On the other hand, the opposition scenario is observed for outlet-peaked profiles (relevant to counter-current configurations) and dryout occurs earlier. These differences become larger when increasing the size of the heat exchanger, as the APD further deviates from homogeneous conditions.

Finally, the occurrence of partial dryout in horizontal flow was studied. The previous validation of the model indicated that, in general, the dryout quality was overpredicted in these cases. This means that dryout occurs earlier in the experiments than predicted by the model. The main reason for this difference is that gravitational effects make the liquid film thicker at the bottom and therefore the wall becomes dry earlier at the top. In order to account for this effect, a partial dryout flow regime is considered, where the wall is dry at the top and wetted in the bottom. With these considerations, heat transfer coefficient predictions were compared with experimental data, showing good agreement. Further improvements in the model should account for some extent of thermal non-equilibrium, which is the main topic in Chapter 10.

Chapter 10

Heat transfer in the post-dryout flow regime

► After the occurrence of dryout, which is the main topic of Chapter 9, the heat transfer performance is largely reduced. On the one hand, in a power-controlled system, this phenomenon produces a sharp increase in the wall temperature. On the other hand, the consequences in a HE are given by a dramatic reduction in the heat transfer rate and overall thermal performance. Due to the significance of this effect, a detailed analysis of the post-dryout flow regime is presented in this chapter. The main aim is to predict the evolution of the heat transfer coefficient in this liquid-deficient regime.

The phenomenological model presented in this chapter is based on a two-fluid formulation. In this context, the individual evolution of both liquid and gas phases is analyzed, coupled with some constitutive relations for their interaction. The different coupling mechanisms considered in this model include wall-to-gas, wall-to-droplets and gas-to-droplets heat transfer, based on empirical correlations. This model was validated with 10 experimental data sets from the open literature for power-controlled systems. These cases were divided into two categories: water and other fluids. In general, good agreement between the measured and predicted wall temperature is observed. A discussion and analysis of these results is presented, highlighting the most sensitive issues and the possible application for a heat exchanger problem. In particular, the description of the influence of the droplets in the wall-to-gas heat transfer needs further improvement.

It has been discussed in the previous chapters that the heat transfer coefficient (HTC) is a key parameter for bridging physical phenomena occurring over different scales and obtaining an accurate description of the heat exchanger (HE) at the level of interest, usually called macroscale. In this context, the occurrence of dryout in the annular-mist flow regime (which is the main topic in Chapter 9), resulting in

a large reduction of the HTC, is a clear example of microscopic effects affecting the overall performance.

In the present chapter the heat transfer processes in the post-dryout regime, that is downstream of the boiling crisis, are investigated. This analysis is highly relevant for HE design because this region is characterized by a very small heat transfer coefficient, usually 10 to 30 times lower than during the annular flow regime (Thome, 2006, §18). This large drop in the HTC has serious consequences in the sizing of the HE because the required surface area per unit of heat transferred is increased in the same proportion. As this boiling crisis occurs in the high-quality region (typically in the last 10-20% of the enthalpy range), this means that perhaps more than half of the HE area may operate in this regime, thus largely reducing the performance per unit area.

Regardless the possible consequences on the required area (which is the primary result at a first stage of design), most refrigeration HE softwares do not take account of this flow regime transition (Thome, 2006, §18). This assumption is certainly based on the consideration that boiling crisis phenomena are irrelevant for heat exchanger applications because they operate at relatively low heat fluxes, significantly below the CHF limit. However, as noticed in Chapter 9, dryout in an evaporator can nonetheless occur due to hydrodynamic effects, since thin liquid film in the annular-mist flow regime can be disrupted. The film flow is particularly unstable when it receives a heat input from the wall.

The analysis of post-dryout heat transfer has been widely studied in power-controlled systems, particularly in the nuclear engineering community. In this context, this phenomenon is related to safety and therefore has received special attention. When the heat input in the wall is determined by an external factor and not related to the flow dynamics (as in nuclear or chemical reactors and electrically heated systems), a large reduction in the HTC implies a sharp increase in the wall temperature which may lead to the mechanical failure or meltdown of the tube material. This situation has led to the development of an extensive (although proprietary) experimental database, empirical correlations and, to a lesser extent, theoretical models. Although most of the experiments were carried out with water, some researchers have used hydrocarbon refrigerants, in order to reproduce the physical properties of high-pressure steam-water at conditions easier to handle at laboratory scale, that is more similar to room temperature and atmospheric pressure. The available literature is further reviewed in Section 10.1.

Notwithstanding the extensive research on this topic in the field of nuclear engineering, these models cannot be directly applied to the analysis of heat exchangers. In addition to being wall temperature-controlled systems instead of power-controlled, boiling flow in heat exchangers presents several differences, including the following:

1. The flow structure downstream of the boiling crisis depends on the operating conditions and the physical mechanisms that have led to this phenomenon.

As a consequence, different flow regimes can be found in the post-dryout region (Jeong and No, 1996). The two most relevant are:

- **Inverted annular**, characterized by a thin vapor film attached to the wall and a continuous liquid core flowing in the center of the channel. This flow pattern is formed after the occurrence of burnout, that is the formation of a vapor blanket due to the excessively rapid nucleation of bubbles. It is usually found at low qualities (or even subcooled flows) and large heat fluxes and therefore it can be found for operating conditions typical of nuclear reactors, but it is very rare for typical heat exchanger applications.
- **Dispersed droplets (mist flow)**, also known as liquid-deficient flow. In this regime the liquid phase is flowing as discrete droplets dispersed in a continuum gas core. It is originated as a consequence of dryout, that is the disruptance of the liquid film in the annular-mist regime, described in Chapter 9. Typically found at high qualities (usually, void fractions larger than 80%), it is the dominant post-dryout regime in evaporators.

As the dispersed-droplets regime is dominant for heat exchangers, the following analysis is restricted to this regime. Nevertheless, it should be noticed that as the flow evolves downstream and the vapor content is further increased, the inverted annular regime will eventually derive into a mist flow pattern. Therefore, the same analysis could in principle be applied at a considerable distance from the burnout location.

2. Evaporators are designed for receiving liquid at the inlet and delivering vapor at the outlet. Therefore the entire quality range from 0.0 to 1.0 is covered and dryout in the annular flow regime is expected to occur at some point even in stationary conditions[1]. Then, a steady-state description is applicable for this analysis. This situation is different from nuclear reactors, where a hot dry surface is rewetted during emergency transients following accident scenarios such as LOCA (Loss Of Coolant Accident) or power excursions. Therefore, while dynamic effects are relevant from a nuclear engineering perspective, they could, in principle, be disregarded for the analysis of heat exchangers.

3. As discussed in Section 9.3.2, the axial power distribution in heat exchangers is not uniform. Consequently, empirical correlations based on experimental

[1]Except perhaps for very low mass fluxes when gas velocity is not large enough to divert the liquid towards the wall and annular flow regime is not originated, as indicated in the flow pattern map given by Hewitt and Roberts (1969, presented by Ghiaasiaan (2007)). In addition, horizontal arrangements can be dominated by the stratified flow regimes over the entire quality range under low velocity conditions.

data from uniform heat flux conditions cannot be applied, and phenomenological model which take account of the flow history are required. In this context, most experiments are performed using electrical heating in one (resulting in a constant heat flux) or several steps (giving a step profile, usually with the objective of reproducing a cosine distribution, typical of nuclear reactor applications). The available experimental information on post-dryout flow heated by another fluid (that is, a HE) is rather limited and is further studied in detail in Section 10.4.2.

4. In most post-dryout flow experiments the wall temperature is rather high, usually several hundred degrees Kelvin above saturation levels. This situation is representative of power-controlled systems. Furthermore, some authors performed experiments at less than 100 K superheating, and referred to these conditions as the low-superheat range. In this context, the analysis of heat exchanger applications would fit into the description of *very low* wall-temperature superheat.

All these differences lead to one conclusion: in order to be able to apply correlations based on the current data to the analysis of heat exchangers, the different phenomena and underlying heat transfer processes must be understood and accounted for. This scenario provides then the motivation for developing a phenomenologically-based multifluid model, as described below.

The structure of this chapter is as follows. A thorough review of the available literature is presented in Section 10.1. Following the approach considered in Chapter 9, a two-fluid model for the analysis of post-dryout heat transfer is described in Section 10.2. The predictions of this model are compared with experimental data extracted from the open literature in Section 10.3. In total, ten cases are studied, grouped into two categories: water (Section 10.3.1) and other fluids (Section 10.3.2). Section 10.4 deals with the analysis and conclusions from these results. Finally, a summary of this chapter is presented in Section 10.5.

10.1 Literature review on post dryout models

It has become evident since the earliest experimental observations that, as the vapor is in direct contact with the hot wall, its temperature is increased beyond saturation conditions. Then, a thermal non-equilibrium scenario is achieved, since both phases have a different temperature. This situation leads to temperature profiles such as those presented in Fig. 10.1 for (a) uniform heat flux and (b) heat exchanger applications.

In the case of (a) power-controlled systems, the occurrence of dryout results in a sharp increase in the wall temperature. In addition, as a constant (and relatively large) heat flux is transferred to the vapor phase, its temperature also rises rapidly, while the actual quality (that is, mass vapor content) remains roughly constant

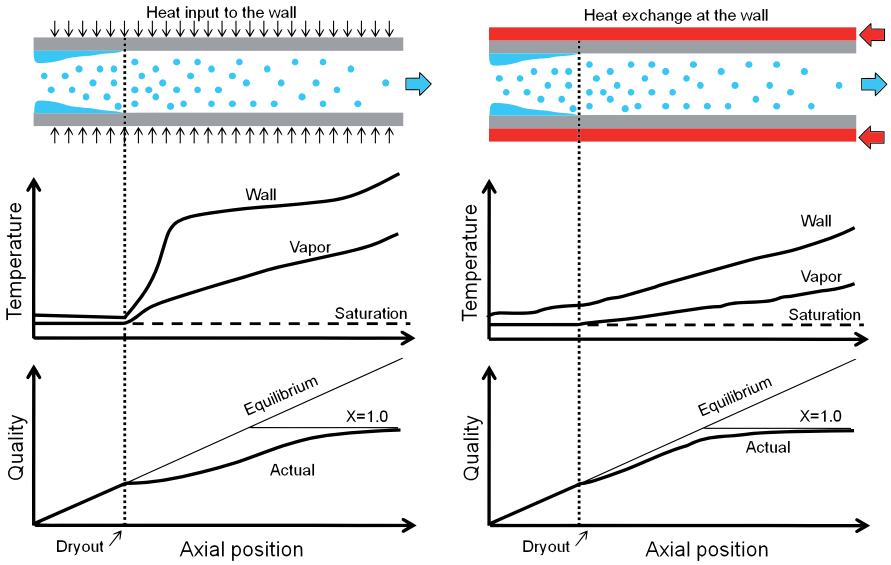

(a) Uniform heat flux (b) Counterflow heat exchanger

Figure 10.1: Schematic axial profiles for temperature and quality in the post-dryout regime

and departs from its equilibrium value. Eventually, all droplets will be evaporated and thermal equilibrium is achieved in the single-phase gas region.

On the other hand, the wall temperature and heat flux in (b) a heat exchanger depend on the interaction between cold and hot streams. Therefore, after the occurrence of dryout, the heat input to the boiling fluid is reduced (as observed in the experiments performed by Paske et al. (1992) and Yoo and France (1996)), since the wall temperature remains almost constant and the HTC is much lower. Consequently, the vapor temperature increases only slightly and this scenario is expected to be closer to thermal equilibrium, as represented in the quality profile.

In this review, the long list of available models for post-dryout flow are divided into two categories. First, the earliest approaches, based on local correlations are described in Section 10.1.1. Second, the state-of-the-art evolved towards axial history formulations with varied levels of details, presented in Section 10.1.2.

10.1.1 Early formulations

Groeneveld (1975), Wang and Weisman (1983)[2], Chen (1986) and later Andreani and Yadigaroglu (1994) presented up-to-date reviews on this topic. In general, they

[2]While other authors have mentioned the relevance of post-dryout analysis in cryogenic sys-

all agree that the models proposed during the 1960s and 1970s can be grouped in four categories as follows.

1. **Purely empirical** formulations, based on forced convective correlations, represented the first approach for the analysis of post-dryout flow. Although they are rather simple to use and describe accurately the experimental observations, their applicability range is very limited and their extrapolation should be avoided. As a consequence, a large number of correlations was proposed exclusively for water. For an extensive list, the reader is referred to Table 1 in Groeneveld (1975).

2. **Thermal equilibrium** models assume that the vapor remains at saturation temperature and the heat input to the wall is directed completely towards the evaporation of the liquid phase. As discussed above, this assumption is not clearly justified, since the liquid is not wetting the wall. Nevertheless, a sufficiently large mixing between both phases may lead to a situation rather close to equilibrium, under some conditions like high mass flow or inverse annular flow with entrained droplets in the thin vapor film. Anyway, these models give optimistic predictions, since they result in the highest possible value for the HTC and, in the case of power-controlled systems, give the lowest estimation for the wall temperature. In this regard, they do not guarantee safe operating conditions.

   The most representative example in this category is the model developed by Dougall and Rohsenow (1963), who proposed a Dittus-Bolter-type correlation based on the equilibrium quality. This correlation was postulated on the basis of experimental data for the refrigerant R-113 at very low quality, in the inverse-annular flow regime. Richlen and Condie (1976, reported by Chen (1986)) observed that its application for other operating conditions overpredicts the HTC by roughly 90%. Other examples are those proposed by Brevi and Cumo (1971) and Groeneveld (1972, reported in the open literature by Groeneveld and Delorme (1976)).

3. **Frozen droplets (no further evaporation)**. This approach considers a scenario of complete thermal non-equilibrium. In this context, it is assumed that the liquid droplets are not evaporated (hence the name, considering the actual quality constant at its dryout value) and do not participate in the heat transfer process. Therefore, the only relevant interaction is the vapor forced convection at the wall. Although this assumption is also not clearly justified, these models are useful since they provide the lowest estimation for the HTC (within the uncertainties of the selected single-phase correlations) and consequently the highest wall temperature in power-controlled systems,

tems, Wang and Weisman (1983) were the only ones to emphasize their importance in the case of LNG applications.

thus guaranteeing a safe operation. Nevertheless, the uncertainties can be rather large and this approach should only be used as a first approximation.

4. **Local correlations for the actual quality** consider the heat transfer process to be controlled by forced convection to the vapor phase. This formulation differs from the frozen-droplets approach since the vapor content is not constant. On the contrary, it is evaluated from a proper correlation based exclusively on local properties. These models represent the actual quality (x_a) in terms of the thermodynamic quality (x_{th}, also referred-to by several authors as equilibrium quality x_e), which can be computed directly from an energy balance.

   The first model in this category was given by Plummer (1974), who described the evolution of the vapor temperature in terms of a constant non-equilibrium parameter κ, obtained from the best fit of experimental data. Groeneveld and Delorme (1976) proposed a correlation with seven empirical parameters obtained as the best fit to water-steam data, thus limiting its extrapolation capabilities. The model given by Chen et al. (1979) (also known as the CSO correlation) introduces one unique empirical constant, related to the operating pressure, for determining the vapor generation rate. This model was later extended by Webb and Chen (1982) and Unal et al. (1991).

In general, the models grouped in the last category were the most accurate ones among the early formulations. However, as a general characteristic of all these models, their applicability range is rather limited.

The most relevant conclusion from the review presented in this subsection lays in the analysis of the models in the categories 2 and 3. In particular, they predict lower and upper limits for the wall temperature for a power-controlled system, respectively. In order to illustrate the relevance of this analysis, experimental wall temperature profiles are presented in Fig. 10.2 and compared with thermal-equilibrium and frozen-droplets predictions

In the case of (a) a large mass flux and low heat input, the experimental data from Nishikawa et al. (1983) is well represented by a thermal equilibrium model. The situation is different for (b) larger heat flux and lower mass flow, as the experimental observations from Becker et al. (1983, reported by Hoyer (1998)) are between 100 K and 200 K above the predictions based on the assumption of equilibrium. In general the degree of thermal non-equilibrium is mainly determined by the mass flux (Hynek et al., 1969).

In addition, it should be noticed that in both cases the frozen-droplets model establishes an upper limit largely above the experimental values. Then, this figure illustrates the result that the frozen-droplets formulation, despite its conservative predictions, should not be used for design, considering its low accuracy.

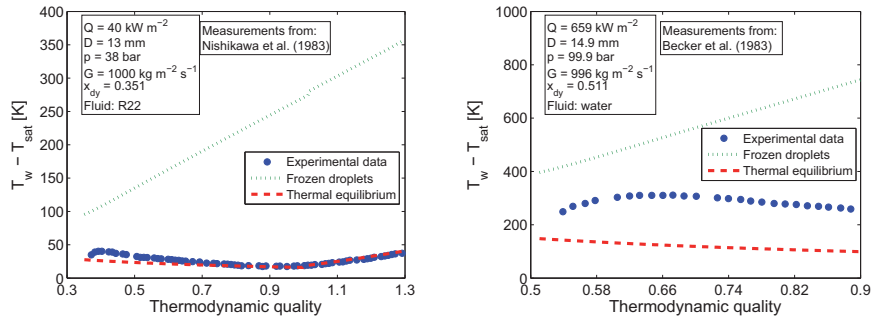

(a) Close to equilibrium (b) Large departure from equilibrium

Figure 10.2: Examples of experimental wall temperature profiles indicating different degrees of thermal non-equilibrium

10.1.2 Phenomenological models

Early formulations, described in Section 10.1.1, are only applicable in a narrow range of operating conditions similar to the ones developed in the laboratory. Therefore their predicting capabilities are rather limited and it soon became necessary to develop theoretical models for the analysis of post-dryout flow. In this context, phenomenological models include the underlying physical effects that shape the evolution of the flow and consequently they have a large potential for accuracy.

This approach was pioneered in the Heat Transfer Laboratory at the Massachussets Institute of Technology during the 1960s[3]. Laverty and Rohsenow (1964) first proposed a two-steps model in which the heat input at the wall is transferred completely to the vapor phase, which then exchanges heat with the liquid droplets by means of forced convection. Forslund and Rohsenow (1966) and Forslund (1967) further extended this analysis into a three-paths model, including direct heat transfer from the hot wall to the liquid droplets, as some of them are deposited towards the wall.

In general, the different heat and mass transfer mechanisms relevant for this analysis can be summarized as in Fig. 10.3. The two phases and the wall interact through three different paths as in Fig. 10.3(a). As the wall temperature increases after the occurrence of dryout, radiation heat transfer can becomes significant, since it is proportional to the fourth power of the temperature (Incropera and DeWitt, 1996, §12-13). In fact, Chung and Olafsson (1984) observed that including radiation in the analysis results in a reduction of 15% in the predicted wall temperature.

[3]This model was later derived independently by Bennett et al. (1968) at the Atomic Energy Research Establishment in the United Kingdom.

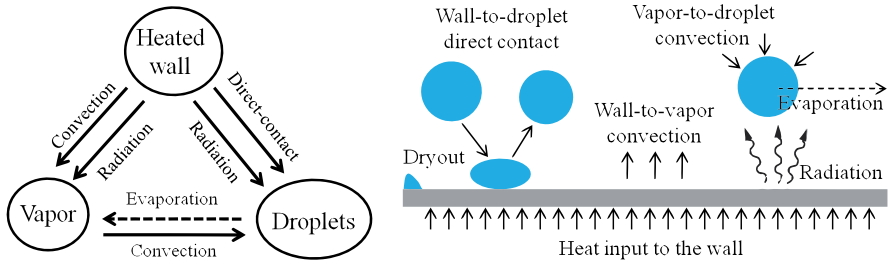

(a) Three-paths model (b) Schematic diagram

Figure 10.3: Heat and mass transfer mechanisms in post-dryout flow

Phenomenological models allow to describe the axial evolution of the flow based on field balance equations. For example, several authors (such as Chen et al. (1979) and Saha (1980)) defined a vapor generation rate Γ and studied the axial development of the mass distribution. Yoder (1980) included the momentum balance equation and obtained the local conditions based on a stepwise calculation downstream of the dryout location. Hill (1982) observed that this model could be reduced to two single uncoupled equations: one for the liquid velocity and another one for the actual quality x_a. Consequently, they represented the axial profiles in terms of a coefficient κ (based on the solution at the dryout location) and eliminated the necessity for the stepwise calculation.

In general, these models perform better than the early formulations described in Section 10.1.1. This result provides then the motivation for extending these phenomenological formulations into a multifluid description, including a more detailed analysis of the relevant physical effects. This approach, presented in Section 10.2, considers the individual evolution of each phase in terms of mass, momentum and energy balance equations.

10.2 Two-fluids formulation

Following the multi-fluid approach described in Chapter 9, a two-fluid formulation is presented in this section for the analysis of post-dryout flow. In this case, the axial evolution of dispersed droplets and continuous vapor phases are analyzed individually from an Eulerian perspective. This mathematical model relies on some general assumptions, included in the following list.

1. A steady state is considered. In other words, transient effects are neglected.

2. Longitudinal thermal conduction in the wall or the fluid are not included in this model. Under some extreme conditions, like large wall thickness

and/or sharp temperature gradients, this phenomenon can have significant consequences in the effective heat flux towards the flow, specially near the dryout location. In this analysis, the external heat input to the wall is assumed to be transferred completely to the flow, either to the liquid or vapor phases.

3. Superheat of liquid droplets is not included in this model, as this is a transient non-equilibrium effect. Therefore, the liquid phase temperature is fixed at its saturation value and heat transfer to the droplets results in evaporation.

4. This formulation presents a one-dimensional description of the flow in the axial direction z. Consequently, the problem variables are represented by uniform values throughout the cross section. Then, for example, a uniform pressure is considered for both the liquid and vapor phases. In addition, boundary-layer effects near the wall are not expressed directly, but included in the constitutive relations (based on empirical formulations).

5. Spherical droplets are considered. In general, the shape and size of droplets is determined by a balance between inertial, surface tension and buoyancy forces and different regimes are observed in the experiments. Several authors proposed non-dimensional correlations for the transitions between these regimes, as recently reviewed by Myint et al. (2007). Overall, all of them agree that the spherical regime is dominant for small droplet sizes, (as expected for hydrocarbons, given the low surface tension) as a consequence of the low Reynolds number.

6. In this context, the droplet diameter is a key parameter for this analysis. Due to the general lack of detailed experimental data, there is no motivation for including a polydispersed description. For this reason, a uniform droplet diameter is considered in Section 10.2.1. The axial evolution of this representative diameter is studied in Section 10.2.3.

10.2.1 Governing equations for a single-diameter model

This two-fluid formulation considers the axial evolution (in the direction z) of seven variables: volume fraction α_k and average fluid velocity u_k for each phase $k = D, G$ (droplets, gas), the system pressure p and the gas phase enthalpy (h_G)[4]. The same number of equations is then required. These are detailed in Eqs. (10.1) to (10.4) as follows.

[4]As the liquid droplets are assumed to remain at saturated conditions, their specific enthalpy is constant at $h_D = h_L$ and there is no need for an explicit liquid energy balance equation.

- Mass balance for droplets and gas (per unit of cross-sectional area)

$$\frac{d}{dz}(\rho_D u_D \alpha_D) = -\frac{4}{D} W_{evap} \tag{10.1a}$$

$$\frac{d}{dz}(\rho_G u_G \alpha_G) = \frac{4}{D} W_{evap} \tag{10.1b}$$

- Momentum balance for droplets and gas (per unit of cross-sectional area)

$$\frac{d}{dz}\left(\rho_D u_D^2 \alpha_D + \alpha_D p\right) = -\frac{4}{D} W_{evap} u_D + \bar{A}_{G,D} \tau_{G,D} \tag{10.2a}$$

$$\frac{d}{dz}\left(\rho_G u_G^2 \alpha_G + \alpha_G p\right) = \frac{4}{D} W_{evap} u_D - \bar{A}_{G,D} \tau_{G,D} - \frac{4}{D} \tau_{W,G} \tag{10.2b}$$

- Energy balance for the gas phase (per unit of cross-sectional area)

$$\frac{d}{dz}(\rho_G u_G \alpha_G h_G) = \frac{4}{D}\left(q''_{W,G} - q''_{G,D}\right) + \frac{4}{D} W_{evap} h_V \tag{10.3}$$

- Closure law

$$\alpha_D + \alpha_G = 1 \tag{10.4}$$

The evaporation rate W_{evap} is given by the total heat transferred to the liquid phase as in Eq. (10.5). In general, it has two contributions: one given by heat transfer from the wall ($q''_{W,D}$) and another one from the gas phase ($q''_{G,D}$). These two contributions are modeled according to some constitutive relations discussed in Section 10.2.2.

$$W_{evap} = \frac{q''_{W,D} + q''_{G,D}}{\Delta h_{LV}} \tag{10.5}$$

In addition, the frontal area density $\bar{A}_{G,D}$ in the momentum equation (10.2) was defined previously in Chapter 9 and is given by Eq. (9.5b), where d is the mean droplet diameter. In general, the droplet diameter evolves downstream of the dryout location, as investigated in Section 10.2.3.

$$\bar{A}_{G,D} = \alpha_D \, \frac{\pi d^2/4}{\pi d^3/6} = \frac{3}{2} \, \frac{\alpha_D}{d} \tag{9.5b}$$

10.2.2 Constitutive relations

As discussed in Chapter 9, multifluid formulations are very sensitive to the underlying constitutive relations. In this particular case, Andreani and Yadigaroglu (1992) observed that the main difficulties in modeling dispersed-droplets post-dryout flow are given by the the weaknesses of the constitutive relations, as they

intend to represent two-dimensional effects in a one-dimensional description. Although their review is already nearly twenty years old, this situation has not changed, as a consequence of the lack of detailed experimental information for validating the results of a multidimensional approach.

Therefore, the state of the art in multiflud formulations is limited (at least for the time being) to one-dimensional descriptions coupled with constitutive relations that represent (as accurately as possible) the underlying physical phenomena. In particular, five different effects must be included in the analysis, as detailed in the following subsections.

Gas-to-droplets heat transfer $q''_{G,D}$

The departure from thermal equilibrium results in a net heat transfer from the gas to the liquid phase as a consequence of the differences in temperature. In general there are two contributions for this heat transfer process: radiation and forced convection (dominant). When expressed per unit of wall area, it is given by Eq. (10.6), where $\varphi_{G,D}$ is the gray-body factor and σ_{SB}, the Steffan-Boltzman constant (Incropera and DeWitt, 1996, §12).

$$q''_{G,D} = \left(\bar{A}_{G,D} D\right) \left[\underbrace{\varphi_{G,D}\sigma_{SB}\left(T_G^4 - T_{sat}^4\right)}_{\text{Radiation}} + \underbrace{\hat{h}_{G,D}\left(T_G - T_{sat}\right)}_{\text{Forced convection}} \right] \tag{10.6}$$

The gray-body factor φ accounts for the view factors and lower-than-unity emission and absorption coefficients. As the liquid phase is very diluted and the droplet diameter is small, it represents a very thin optical medium, and therefore the gray-body $\varphi_{G,D}$ is expected to be very low. In fact, this term was included in their analysis by Guo and Mishima (2002), and they concluded that it can be neglected. Therefore, from this point onward it is assumed that $\varphi_{G,D} = 0$ and the gas-to-droplets heat transfer is purely given by forced convection.

The most widely used correlation for gas-droplets convection is the one given by Lee and Ryley (1968), as in Eq. (10.7), in terms of the dimensionless Nusselt number. The constant term (2) corresponds to the solution of laminar flow around a solid sphere. While the flow regime is expected to remain laminar (given the small diameter), the heat transfer is enhanced due to internal flow motion inside the droplets and possible slip between the phases. The Reynolds number Re_d is computed in terms of the relative velocity $u_G - u_D$ and the gas properties.

$$Nu_{G,D} = \frac{\hat{h}_{G,D} d}{\lambda_G} = 2 + 0.74 Re_d^{0.5} Pr_G^{0.33} \tag{10.7}$$

Some authors (for example, see Yuen and Chen (1978)) recommended the inclusion of a correction factor in order to account for a reduction in the heat transfer given by some shielding produced by evaporation. However, the overall effect in

the Nusselt number is not clear (Andreani and Yadigaroglu, 1992) and therefore is disregarded in the present analysis.

Wall-to-gas heat transfer $q''_{W,G}$

In this case both forced convection and radiation contribute significantly to the heat transfer from the wall towards the gas phase, and none of them can be neglected *a priori*. Then, Eq. (10.8) applies in this case.

$$q''_{W,G} = \underbrace{\varphi_{W,G}\sigma_{SB}\left(T_W^4 - T_G^4\right)}_{\text{Radiation}} + \underbrace{\hat{h}_{W,G}\left(T_W - T_G\right)}_{\text{Forced convection}} \tag{10.8}$$

For medium and high pressure systems, the vapor phase can be considered as an optically thick medium (Chung and Olafsson, 1984). This means that its overall transparency is low and absorbs nearly all the thermal radiation. Therefore, the gray-body factor is equal to the emissivity of the wall material, that is $\varphi_{W,G} = \epsilon_W$.

In principle, forced convection heat transfer can be modeled by a Dittus-Bolter-type correlation for single-phase flow as in Eq. (10.9). The constants a, b and c are derived from the best fit of empirical data, and the physical properties are evaluated at the average of wall and fluid temperatures. The two most widely used correlations in this category are summarized in Eq. (10.10). For other less widely used models, refer to table 3-1 in Yoder (1980).

$$Nu_{W,G} = \frac{\hat{h}_{W,G}D}{\lambda_G} = aRe_G^b Pr_G^c \tag{10.9}$$

On the one hand, Eq. (10.10a)[5] was developed for liquid water and its accuracy is around ±25% (Incropera and DeWitt, 1996, §8). On the other hand, Eq. (10.10b) is based on experimental data for superheated steam. Groeneveld and Delorme (1976) compared nine different correlations and recomended the use of Eq. (10.10b) because it presents the lowest root-mean-square error (6.7%).

$$\text{McAdams (1954)}: \quad a = 0.023, b = 0.8, c = 0.4 \tag{10.10a}$$

$$\text{Hadaller and Banerjee (1969)}: \quad a = 0.008348, b = 0.8774, c = 0.6112 \tag{10.10b}$$

Finally, it is worth noticing that the empirical models given by Eq. (10.9) were originally developed for single-phase flow. In the case of post-dryout flow, this heat transfer process can be affected by the presence of liquid droplets. In particular the liquid droplets can disturb velocity and temperature gradients in the boundary layer near the wall and the turbulent structure in the core. For this reason, Varone Jr. and Rohsenow (1986) introduced an *a posteriori* correction

[5]For discrepancies about the origins of Eq. (10.10a), see the discussion started by Winterton (1998) and followed by Williams (2011).

factor, ranging from 0.7 to 2.0. However, since this factor was not correlated with any of the problem variables and therefore it is not clear if the heat transfer is increased or reduced by the presence of droplets, it is not included in the present analysis.

Wall-to-droplets heat transfer $q''_{W,D}$

In general, for power-controlled systems, this heat transfer path represents less than 10% of heat input to the wall (Moose and Ganic, 1982), and in some cases even less than 5% (Varone Jr. and Rohsenow, 1986). For this reason some authors (e.g. Saha (1980) and Rohsenow (1988)) neglect this effect and consider that the entire heat flux is transferred to the gas phase.

In general, the experimental data presents a rather large scatter, with differences in the order of 15% for different authors performing experiments under nearly identical conditions (Moose and Ganic, 1982). Therefore, in principle, $q''_{W,D}$ could be neglected at a first stage of analysis. However, as discussed in the introduction of this chapter, the situation can be different for heat exchanger applications. Basically, in a HE the wall temperature superheat is lower and therefore the relative contribution of this heat transfer path is expected to be larger. Consequently, it must be included in the analysis.

Following the same formulation as in the previous subsections, a generic description of q''_{WD} must include the contribution of two mechanisms: radiation and direct-contact, as in Eq. (10.11).

$$q''_{W,D} = \underbrace{\varphi_{W,D}\sigma_{SB}\left(T_W^4 - T_{sat}^4\right)}_{\text{Radiation}} + \underbrace{W_{dep}\Delta h_{LV}\varepsilon_{W,D}}_{\text{Direct contact}} \tag{10.11}$$

It was discussed above that, regarding the heat transfer by thermal radiation, the liquid droplets form a very thin optical medium, since they are diluted in the gas core. In addition, this heat exchange path is blocked by absorption in the gas phase. For these reason, the overall gray-body factor is very low and it is assumed that $\varphi_{W,D} = 0$. This assumption is supported by the calculation performed by Guo and Mishima (2002), who observed that the contribution of this heat transfer mechanism is negligible.

Direct-contact heat transfer is given by the deposition of droplets from the turbulent gas core towards the wall. Therefore, it can be represented by the product of the deposition cross mass flux W_{dep} (previously studied in Section 9.1.3) and the total heat transfer per unit of deposited mass, as in Eq. (10.11). It should be noticed that the maximum possible heat transfer is given by the complete evaporation of the droplet. Therefore the actual heat transferred per unit mass can be represented by $\Delta h_{LV}\varepsilon_{W,D}$, where $\varepsilon_{W,D} \in [0, 1]$ is the evaporation efficiency, as introduced by Pederson (1967). Then, for example $\varepsilon_{W,D} = 0$ implies that no heat is transferred and $\varepsilon_{W,D} = 1$ represents full evaporation of the droplet. If the

liquid is subcooled, which is not the case in post-dryout flow, $\varepsilon_{W,D}$ might be larger than unity.

The overall droplet evaporation efficiency $\varepsilon_{W,D}$ depends on the mechanism controlling the interaction of the droplets with the wall. In general, two types of interactions can be distinguished as follows.

- **Dry collisions** occur when the normal velocity of the droplets towards the wall is not large enough for breaking through the vapor boundary layer. Therefore, the droplets bounce back and do not touch the wall (Wachters et al., 1966). Nevertheless, they exchange heat indirectly with the wall as they disturb the boundary layer. Kendall and Rohsenow (1978) indicated that evaporation efficiencies in the range of 10% to 20% can be observed for dry collisions. A detailed analysis for droplets that go though the vapor boundary layer and bounce back at the wall, based on an average residence time, was presented by Guo and Mishima (2002).

- **Wet collisions** consist on the rewetting of the wall when the impact velocity is large and the droplets break forming a liquid film. The heat transfer rates in this regime are large, with evaporation efficiencies close to unity, although somewhat lower because of partial bouncing (Holman et al., 1972).

Among all the factors that can affect the characteristics of the droplet-wall interaction, the single most important one is the wall temperature T_W. In general, dry collisions occur if the wall temperature is high, and low wall temperature allow for rewetting of the wall (Iloeje, 1975). Kendall and Rohsenow (1978) identified the transition wall temperature around $T_W = T_{sat} + 50\ K$.

Considering the large scatter in the experimental observations of different authors, Ganic and Rohsenow (1977) proposed Eq. (10.12) as a single-line correlation for determining the evaporation efficiency of droplets impacting the wall.

$$\varepsilon_{W,D}(T_W) = \exp\left[1 - (T_W/T_{sat})^2\right] \tag{10.12}$$

Although Eq. (10.12) is quite simple to use and captures correctly the overall behavior for large wall temperatures, it is not accurate when $T_W \approx T_{sat}$, as this would yield $\varepsilon_{W,D} = 1$, that is a full evaporation of the droplet with zero temperature difference. McGinnis III and Holman (1969) observed in their experiments that the maximum effectiveness ε_{max} occurs at a given wall superheat ΔT_{peak}, ranging between 170 and 220 K. Since this variable was not correlated by the authors, an average value of $\Delta T_{peak} = 200K$ is considered. The temperature dependence can then be better represented by a normal distribution as in Eq. (10.13), with a variance of $\Delta T_{variance} \approx 70K$. This formulation gives a more reasonable value of $\varepsilon_{W,D} = 0.05\varepsilon_{max}$ for $T_W = T_{sat}$.

$$\varepsilon_{W,D}(T_W) = \varepsilon_{max} \exp\left[\left(\frac{(T_W - T_{sat}) - \Delta T_{peak}}{\Delta T_{variance}}\right)^2\right] \tag{10.13}$$

The maximum effectiveness depends on several factors, including the droplet diameter and the impact velocity $u_{dep} = W_{dep}/\left(\rho_L \alpha_D\right)$. McGinnis III and Holman (1969) proposed a model for predicting the maximum effectiveness within ±10% uncertainty. This model was later extended by an Holman et al. (1972), who proposed Eq. (10.14), which is applicable over a wider range.

$$\varepsilon_{max} = 3.53\ 10^{-3} \left(\frac{\rho_L^2 u_{dep}^2 d}{\left(\rho_L - \rho_G\right) \sigma} \right)^{0.341} \tag{10.14}$$

In their study Ganic and Rohsenow (1977) also presented an interesting analysis on the effect of the droplet diameter in the evaporation process. In general, large droplets have enough inertia for breaking through the vapor boundary layer and can reach the wall, while small droplets cannot. In this context, they solved numerically the momentum balance equation for a liquid droplet in an undisturbed boundary layer. They obtained a cutoff diameter d_{crit}, concluding that if $d < d_{crit}$, the droplet does not reach the wall. Finally, assuming a given droplet size distribution (in a later study Moose and Ganic (1982) assumed a Gamma distribution), they defined a cumulative deposition factor representing the fraction of deposited liquid mass that actually touch the wall.

This interesting analysis was later described by Wang and Weisman (1983) as "*although theoretically appealing, impossible for designers to use it since it requires information on droplet size and distribution which is generally not available*". As this formulation cannot be validated with experimental data for post-dryout flow, it is not included in this analysis. In addition, it should be noticed that Ganic and Rohsenow (1977) considered an undisturbed boundary layer. In practice, the motion of droplets affects the turbulent structure of the flow, specially in the region near the wall. Therefore, it is expected that droplets smaller than d_{crit} can travel through this disturbed layer, resulting in a cumulative deposition factor rather close to unity. Consequently, the droplets evaporation efficiency is considered to be well represented by Eqs. (10.13) and (10.14).

Drag forces at the droplets-gas interface $\tau''_{G,D}$

These forces at the droplet-gas interface were considered previously in Chapter 9. Generally, they can be modeled according to the Stoke's law for laminar flow across a solid sphere (Clift et al., 1978), given their small diameter and consequently low Reynold number of the flow. Then, Eq. (9.25) applies for the shear stress $\tau_{G,D}$.

$$\tau_{G,D} = \frac{12 \mu_G \left(u_G - u_D\right)}{d} \tag{9.25}$$

Wall friction $\tau''_{W,G}$

The single-phase friction can be represented by a friction factor f_W as in Eq. (10.15). In particular, the Haaland formula (White, 1986, §6.4) for smooth tubes (used previously in Chapters 5 and 6), given by Eq. (10.16), is considered in this analysis.

$$\tau_{WG} = f_W \frac{\rho_G u_G^2}{2} \tag{10.15}$$

$$f_W = \left[1.8 \log \left(\frac{6.9}{Re_G} \right) \right]^{-2} \tag{10.16}$$

Evaluation of wall temperature or heat flux

In power-controlled systems, the total heat input to the fluid is independent of the wall temperature. Furthermore, considering that the axial conduction at the wall is negligible (as confirmed by Yoder (1980)), the contribution of wall-to-gas and wall-to-droplets heat transfer are equal to the external heat flux q''_W. Therefore, the wall temperature can be evaluated from the heat balance expressed in Eq. (10.17), which requires an iterative solution.

$$q''_W = q''_{W,D}(T_W) + q''_{W,G}(T_W) \tag{10.17}$$

The situation is different for HEs and the heat flux q''_W is not fixed and it depends on the solution for the wall temperature. In a steady-state analysis, the heat input to the boiling fluid (left-hand side in Eq. (10.18)) is equal to the heat flux from the hot fluid towards the wall (right-hand side in Eq. (10.18)). The solution of Eq. (10.18) gives then both the heat flux and wall temperature. If the heat transfer coefficient $\hat{h}_{hot}$ is sufficiently large, it can be assumed that $T_W = T_{hot}$.

$$q''_W(T_W) = q''_{W,D}(T_W) + q''_{W,G}(T_W) = \hat{h}_{hot} \left(T_{hot} - T_W \right) \tag{10.18}$$

10.2.3 Evolution of the droplet size

All the constitutive models describing the interaction of droplets with the wall and the gas phase, presented in Section 10.2.2, depend on the representative droplet diameter d. This single value represents a frontal-area average of a generally polydispersed size distribution. Therefore it is essential to be able to estimate the variation of the droplet size throughout the tube length, as this information is usually not available from experiments.

In this context, a key parameter is the initial droplet diameter at the onset of dryout d_0. The available experimental information for d_0 is more abundant and several correlations have been proposed. In general, they can be grouped into four categories as follows.

1. **Referred to the tube diameter** D. These models are based on an equilibrium between entrainment and deposition in the annular flow regime. This assumption allows to consider an extensive experimental database, mostly for air-water and steam-water systems. The two most cited correlations are summarized in Eqs. (10.19) and (10.20), where $We_{G,D} = \rho_G u_G^2 D/\sigma$ is the Weber number of the gas based on the tube diameter. The model proposed by Tatterson et al. (1977) incorporates the smooth friction factor f_s, which is expected to depend on the Reynolds number as $Re_{G,D}^{0.2}$. Therefore, both models present the same trend, only differing in the numerical value of the empirical constants.

$$\text{Tatterson et al. (1977):} \qquad \frac{d_0}{D} = 1.12\ 10^{-2} \left(f_s We_{G,D}/2\right)^{-0.5} \tag{10.19}$$

$$\text{Ueda (1979):} \qquad \frac{d_0}{D} = 5.8\ 10^{-3} \left[\frac{Re_{G,D}}{We_{G,D}} \left(\frac{\rho_G}{\rho_L}\right)^{1.25}\right]^{0.34} \tag{10.20}$$

   However, the linear dependence on the tube diameter D is not clearly justified. In particular, there is no obvious reason why larger droplets are formed in larger tubes, as this is not related with the droplet generation mechanism.

2. **Based on the Laplace length** ℓ, defined in Eq. (10.21), which takes into account two relevant variables for the stability of droplets: surface tension and density difference. The inclusion of the gravity g seems to respond more to its use as a dimensional constant than to the results of an analysis of forces-balance at the droplet surface.

$$\ell = \sqrt{\frac{\sigma}{g\left(\rho_L - \rho_G\right)}} \tag{10.21}$$

   Azzopardi (1985) observed that the drop sizes in annular flow are inversely proportional to the gas velocity and roughly independent of the tube diameter and postulated the correlation given by Eq. (10.22), where the gas Weber number $We_{G,\ell} = \rho_G u_G^2 \ell/\sigma$ is based on the Laplace length. The entrainment rate W_{ent} is included in order to account for the droplet concentration. Equation (10.22) is then only valid for equilibrium adiabatic annular flows, where the entrainment rate is constant and dryout does not occur.

   In the case of boiling flows, the entrainment rate is not constant and therefore Eq. (10.22) is not applicable. For this reason, Jayanti and Valette (2004) modified this model and replaced this second term for the liquid volume fraction α_D. In addition, they extended the experimental database including

the observations at large mass flux reported by Bennett et al. (1968), and proposed the correlation in Eq. (10.23).

$$\text{Azzopardi (1985)}: \quad \frac{d_0}{\ell} = 15.4We_{G,\ell}^{-0.58} + 3.5\frac{W_{ent}}{\rho_G u_G} \tag{10.22}$$

$$\text{Jayanti and Valette (2004)}: \quad \frac{d_0}{\ell} = 2.5We_{G,\ell}^{-0.58} + 0.1\alpha_D^{0.25} \tag{10.23}$$

3. Saha (1980) presented a **mixed approach**, referring the droplet diameter d_0 to both the tube diameter D and the Laplace length ℓ. Equation (10.24) presents a 5.34% root-mean-square error for the nearly 900 experimental data points from Bennett et al. (1968) and Ling et al. (1971).

$$\text{Saha (1980)}: \frac{d_0}{D} = 1.47\left(\alpha_G^2 We_{G,\ell}\right)^{-0.675} \tag{10.24}$$

4. Kataoka et al. (1983, cited by Guo and Mishima (2002)) included the droplet diameter in the **Weber number** of the gas and recommended the use of Eq. (10.25). This model does not include a reference length and the droplet diameter is defined only in terms of the flow properties.

$$\frac{G_G^2}{\sigma\rho_G} d_0 = 7.96\ 10^{-3} Re_{G,D}^{2/3} \left(\frac{\rho_G}{\rho_L}\right)^{-1/3} \left(\frac{\mu_G}{\mu_L}\right)^{2/3} \tag{10.25}$$

It should be noticed that the above models, given by Eqs. (10.19), (10.20) and (10.23) to (10.25) were developed based on air-water and steam-water entrainment data. Therefore, their application for the analysis of hydrocarbons (with a lower surface tension) is outside their validity range and, strictly speaking, none of them are valid. However, given the lack of experimental data for these conditions, it is worth evaluating the predictions of these models. In particular, the droplet diameters predicted by these models are compared with those observed in their experiments by the authors who postulated them.

In this context, the value for d_0 predicted by Eqs. (10.20), (10.23) and (10.24) is, in some of the cases later studied in Section 10.3, much larger than the maximum droplet diameter observed by the authors (roughly 100, 200 and 600 μm, respectively). On the other hand, the predictions of Eq. (10.25) are sometimes lower than the minimum observed droplet size (84 μm). Overall, the only correlation that remains in the same range of the experimental observations is the one proposed by Tatterson et al. (1977), given by Eq. (10.19).

The evolution of the droplet size distribution is controlled by different mechanisms, including break-up, coalescence and evaporation (Andreani and Yadigaroglu, 1992). Due to the general lack of experimental observations, strong assumptions are usually performed. Several authors (e.g. Saha (1980), Yoder (1980),

Hill (1982) and Varone Jr. and Rohsenow (1986)) consider that neither breakup nor coalescence occur and therefore the total number of droplet is constant. This approach represents a simplified analysis of the dynamics of droplets impacting the wall, considering that they are partially evaporated and a secondary droplet of smaller size is returned to the gas core. As a consequence, the representative diameter d is continuously reduced downstream of the dryout location.

Furthermore, if the number density of droplets is constant and the size distribution is not notoriously affected by the evaporation process, the front-area-averaged diameter d can be evaluated from the volume fraction α_D as in Eq. (10.26).

$$\frac{\alpha_D}{\alpha_{D,0}} = \frac{d^3}{d_0^3} \longrightarrow d = d_0 \left(\frac{\alpha_D}{\alpha_{D,0}} \right)^{1/3} \tag{10.26}$$

10.2.4 Summary

The necessary steps for applying this model are summarized in Fig. 10.4. Given the nature of the governing equations, this problem can be solved explicitly, moving forward in steps of length Δz from the onset of dryout until the end of the tube at $z = L$.

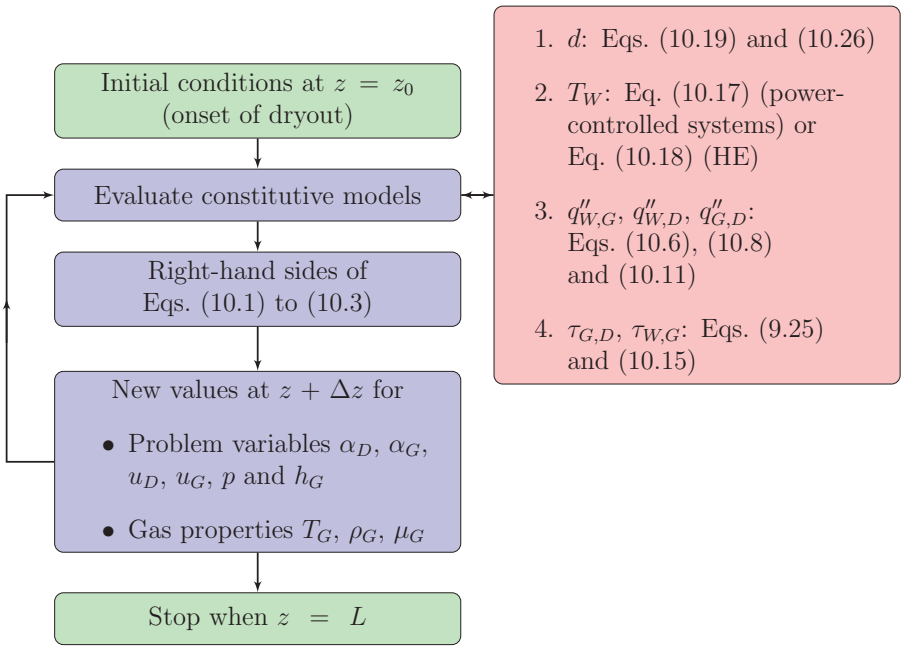

Figure 10.4: Sequential steps for the analysis of post-dryout flow

10.3 Validation of the model

A complete two-fluid formulation was presented in Section 10.2, describing the individual evolution of both liquid and gas phases. The governing equations, based on mass, momentum and energy balances, were defined in Section 10.2.1. State-of-the-art models were selected for the constitutive relations, summarized in Section 10.2.2. The inclusion of these effects provides model closure without including additional empirical coefficients. This generic formulation allows a detailed description of the flow evolution in terms of the mass vapor content, phase velocities and temperatures, pressure and heat transfer profiles, among others.

The validation of this model, however, cannot be performed at a high level of detail. On the contrary, it must be restricted to coarse variables which can be derived from experimental observations. In this context, the overall objective is to predict the heat transfer coefficient (HTC).

As a common feature, all the experimental work performed on this topic has so far been oriented towards power-controlled applications. In the few cases where a HE arrangement was used instead of direct electric heating (see Section 10.4), the overall intention was to imitate uniform axial power distribution conditions. For this reason, only uniform heat flux conditions are considered in this section. In this context, the selected variable for validation is the wall superheat $T_W - T_{sat}$.

Table 10.1 summarizes the experimental data sets selected for the validation of the model. For a given working fluid, the following input parameters are required from the experiments: pressure, heat and mass flux, diameter and dryout quality. In particular, this last parameter presents the largest uncertainty. In fact, although x_{dy} was reported with three significant digits, the experimental uncertainty of this parameter is usually around 5%.

The examples studied in this section, summarized in Table 10.1, are taken from different sources (nine in total). Only one representative data set is selected for each source. The only exception is the information reported by Bennett et al. (1968): two cases are studied because they present different trends. In general (with the only exception mentioned above), similar results as those described in Sections 10.3.1 and 10.3.2 are observed for all the data sets reported by each reference. For reasons of compactness, only representative examples of each source are presented in this section.

The cases described in Table 10.1 are grouped into two categories according to the working fluid. First, water cases are analyzed in Section 10.3.1. Second, other fluids are studied in Section 10.3.2.

10.3.1 Water cases

Considering that the constitutive relations selected for this model (described in Section 10.2.2) were developed based on adiabatic air-water and steam-water data, these cases are analyzed first. The results for these six water cases are presented in

Case	Fluid	p [bar]	q''_W [kW m^{-2}]	G [kg m^{-2} s^{-1}]	D [mm]	x_{dy} [-]	Source
1	Water	70.1	350	497	10.0	0.977	[139]
2	Water	70	545	394	12.6	0.920	[38]
3	Water	69	460	390	12.7	0.921	[38]
4	Water	69.6	840	1016	12.5	0.688	[148]
5	Water	185	720	1530	10.0	0.314	[226]
6	Water	70	900	2200	6.0	0.463	[90]
7	R22	38	40	1000.0	13	0.351	[235]
8	R113	3.08	21.3	898.3	10	0.698	[179]
9	N_2	1.4	23	45.0	10.2	0.690	[141]
10	R12	9.3	31.1	325.9	12.5	0.870	[216]

Table 10.1: Input parameters for the validation cases

Fig. 10.5. Predicted gas and wall temperatures (solid lines), along with measured values for the wall temperature, are presented against the thermodynamic quality x_{th}[6]. For reasons of compactness, the input data is referred to Table 10.1 and not explicitly included in the figures.

General remarks

In general, good agreement is obtained for cases 1 to 4, indicated in Figs. 10.5(a) to 10.5(d). The situation is different, however, for cases 5 and 6 in Figs. 10.5(e) and 10.5(f). As a common feature, these last two cases present the largest mass flux and earliest dryout. In addition, case 5 is at very high pressure, while case 6 involves a very small tube diameter.

The following considerations are the key elements for understanding the performance of the model in the different cases.

- The degree of thermal equilibrium determines the gas temperature and mass vapor content. Early formulations, introduced in Section 10.1.1, consider one of two extreme scenarios: 0% (frozen droplets) or 100% (complete equilibrium). The present phenomenological model allows to account for intermediate situations.

- Among all the constitutive relations, presented in Section 10.2.2, the wall-to-gas heat transfer q''_W is perhaps the least suitable to be described independently. In particular, the liquid droplets are expected to disturb this heat transfer process. For this reason, Varone Jr. and Rohsenow (1986) included a correction factor ranging from 0.7 to 2.0. On the contrary, the main philosophy of the present formulation is not to include additional *ad*

[6]Under uniform heat flux conditions, x_{th} depends linearly on the axial position z.

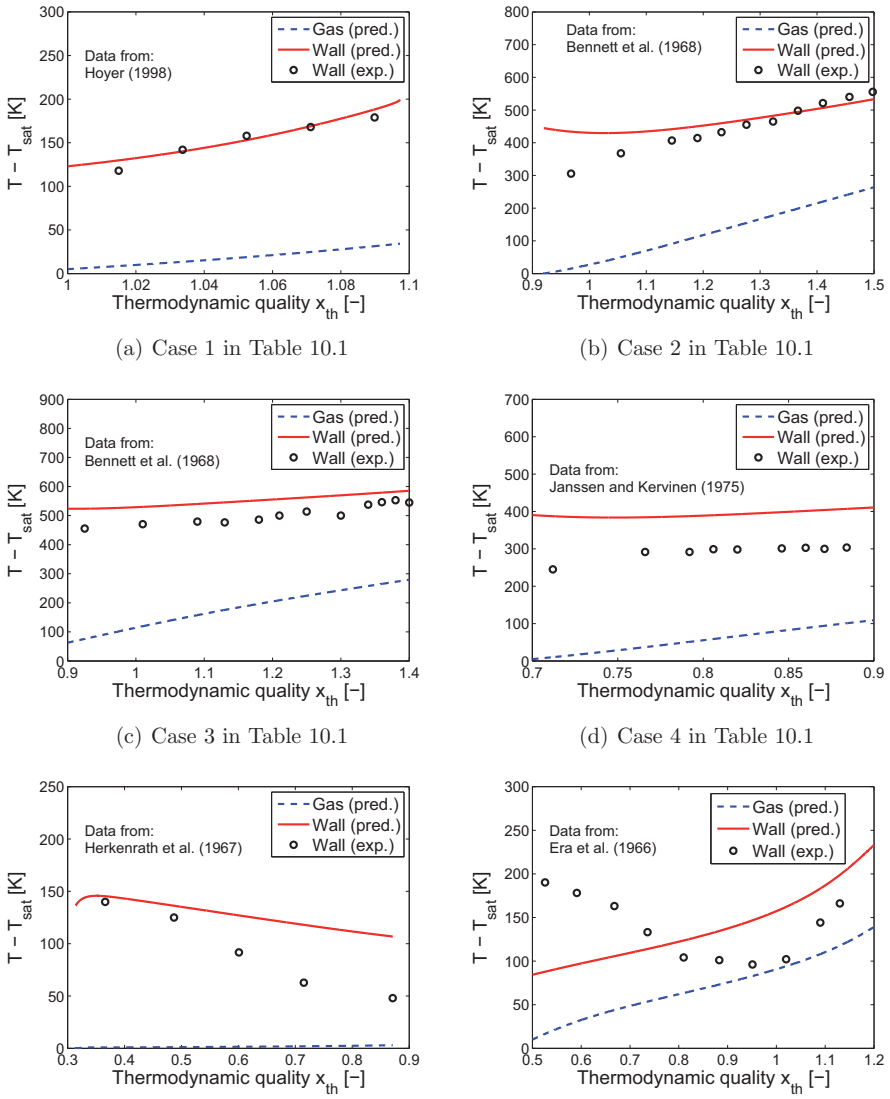

(a) Case 1 in Table 10.1

(b) Case 2 in Table 10.1

(c) Case 3 in Table 10.1

(d) Case 4 in Table 10.1

(e) Case 5 in Table 10.1

(f) Case 6 in Table 10.1

Figure 10.5: Results for post-dryout model validation in water cases

hoc constants. An inaccurate representation of this process might result in an offset between the predicted and measured wall temperature.

A more detailed analysis of Fig. 10.5 provides some interesting observations.

Some individual remarks for each case can be stated as follows.

Case 1: Fig. 10.5(a)

The special feature of this case is that dryout occurs very late ($x_{dy} = 0.977$). Therefore, this experimental data set corresponds almost completely to the single-phase gas flow. As the mass vapor content is very large, liquid droplets play a minor role in the heat transfer process. In this context, the data is well predicted by the model, represented by the single-phase heat transfer correlation given in Eq. (10.8). The gradual deviation of wall and gas temperature curves implies a slow reduction in the HTC. This effect is a consequence of the changes in the fluid physical properties, particularly the specific heat capacity c_p.

Case 2: Fig. 10.5(b)

This case has a much larger heat-to-mass flux ratio than the previous one (roughly twice as large). Considering the differences in the diameter, the equilibrium evaporation rate is still 55% larger in case 2 than in case 1. As a consequence, the phenomenological model predicts a large degree of thermal non-equilibrium close to the dryout location. Further downstream, droplets are slowly evaporated and the HTC of the gas phase is increased, reducing the temperature difference between the wall and gas.

Case 3: Fig. 10.5(c)

In this case, the overall trend is correctly predicted. However, a small offset is observed, as the predicted wall temperature is roughly 10% than the measured values. This result can have be interpreted in two different ways. On the one hand, it is an acceptably small error, within the reported uncertainties of the selected heat transfer correlations. On the other hand, this is a systematic error: the trend is to overestimate the temperature difference (which is equivalent to underpredicting the HTC). Therefore it should be kept in mind for further analysis.

Case 4: Fig. 10.5(d)

A similar result as in case 3 can be observed. The wall temperature superheat $T_W - T_{sat}$ is overpredicted by roughly 25 to 30%. This error is, although still restricted within an acceptable range, two to three times larger than in the previous case. Then, at this point a possible explanation for this trend is suitable. The wall-to-gas heat transfer $q''_{W,G}$ was modeled on the basis of a single-phase gas correlation, given by Eq. (10.8). This formulation does not consider the presence of dispersed droplets. It is expected that the droplets disturbe the gas boundary layer near the wall, affecting the velocity and temperature profiles. In particular, reducing the thickness of the boundary layer, the HTC is expeceted to be improved, therefore

reducing the temperature difference. This situation is discussed in further detail in Section 10.4.1.

Case 5: Fig. 10.5(e)

As reported by the authors, dryout occurs very early in this case: $x_{dy} = 0.314$. Therefore, the flow pattern at which the boiling crisis occurred is questionable. Since the experimental setup did not allow for visual observations (due to the very high operating pressure), it cannot be confirmed that the dryout mechanism is the disruption of the film as described in Chapter 9. In fact, it is very likely that the flow is operating in the inverted-annular regime, with entrained droplets near the wall. As a consequence, a large degree of thermal equilibrium would be achieved, thus accounting for the continuous reduction of the wall temperature.

This overall trend is satisfactorily captured by the present phenomenological model (which, in principle, is not applicable for this flow regime). The predicted gas temperature remains very close to its saturation value, indicating that the degree of non-equilibrium is indeed low. In addition, the predicted wall temperature is continuously reduced as a consequence of the increase in the HTC due to the larger velocities produced by further evaporation. This temperature gradient, however, is not as steep as observed in the experiments. In other words, the increase in the HTC predicted by the model is not as fast as indicated by the measurements. This situation can probably be explained due to the different flow regime. On the one hand, in the dispersed-droplets regime (assumed by this model), the liquid is not continuously in contact with the wall and the HTC is low. On the other hand, if the regime is inverted-annular, turbulent mixing might lead to a large heat transfer rate towards the liquid, thus reducing notoriously the wall temperature.

Case 6: Fig. 10.5(f)

In this case, the proposed model fails completely to predict the wall temperature profile. The experimental observations indicate that the wall temperature is continuously reduced until reaching $x_{th} = 1$, when it starts to rise again. This situation indicates a large degree of thermal equilibrium, which the model did not predict. In fact, the model postulates a rather constant temperature difference between the wall and the gas phase. This is an indication of a constant wall-to-gas HTC as a consequence of a rather uniform gas velocity. In other words, the model predicts a large degree of non-equilibrium, while the practical scenario is rather close to a full thermal equilibrium scenario. The causes for this inaccurate prediction can be found in the special characteristics of this case. In particular, the following two operating conditions are highlighted.

- Large mass flux: G =2200 kg m^{-2} s^{-1}. This value largely exceeds the upper limit of the selected constitutive relations. In general, all of them were

developed under conditions with G <1000 kg m^{-2} s^{-1}.

- Small diameter: D =6 mm. It was stated in the scopes and limitations of the present thesis (see Section 1.3), that the analysis is restricted to normal-size channels (around or more than 8 mm in diameter). In small channels, other effects become relevant (specially for boiling flow applications), affecting the turbulent structure of the flow.

Since these two parameters are outside the validity range of the selected constitutive relations, the following phenomena are not accurately represented.

- Wall-to-gas heat transfer. As observed in cases 3 and 4, the overall accuracy of the model is very sensitive to this effect.

- Gas-to-droplets heat transfer. An underestimation of this phenomenon results in a poor description of the vapor generation rate and its contribution towards thermal equilibrium.

- Deposition rate of droplets. This effect is clearly affected by the turbulence structure of the flow, which is expected to increase with the mass flux G. The deposition rate is one of the key factors determining the direct-contact heat transfer from wall to droplets $q''_{W,D}$, influencing on the evaporation rate.

An inaccurate description of these three phenomena is then the main reason why the model cannot reproduce the trend observed in the experimental data for this case. Nevertheless, it should be noticed that the operating conditions in this case are outside the validity range of the model and exceed the scope of this analysis.

10.3.2 Other fluids

The general scope of this thesis, described in Section 1.3, is oriented towards developing a multiscale thermalhydraulic model applicable to HE used in cryogenic and LNG processes. In this context, it is important to validate the present model against experimental data for hydrocarbons, in addition to the high-pressure water analyzed in the previous section.

Figure 10.6 presents the results for four cases with working fluids different than water, including nitrogen and three refrigerants. Once again, the results are presented in terms of temperature profiles for the gas (predicted) and the tube wall (predicted and measured). For details regarding to the input parameters for these examples, refer to cases 7 to 10 in Table 10.1.

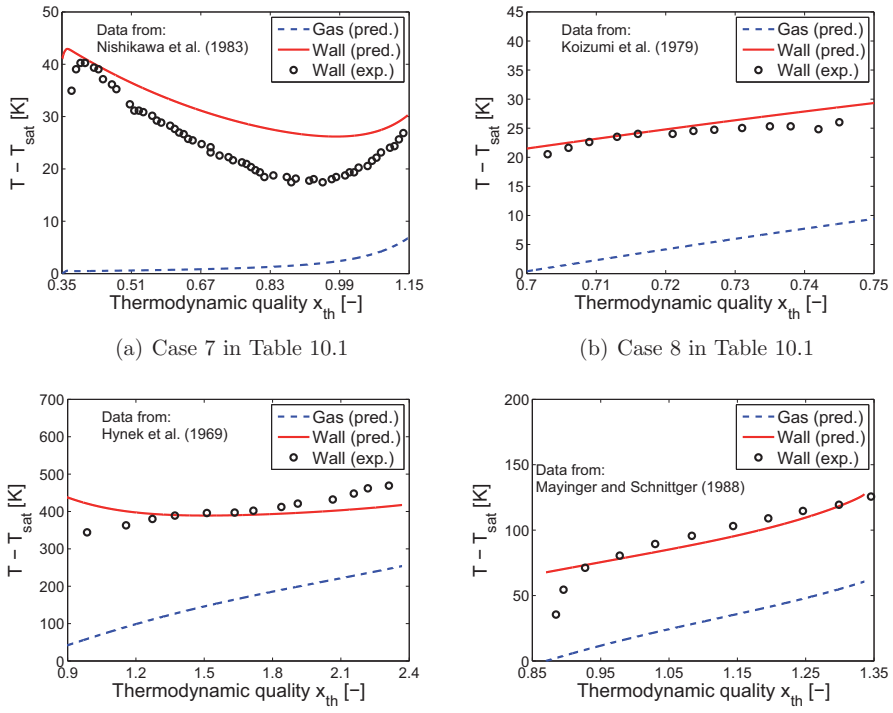

(a) Case 7 in Table 10.1

(b) Case 8 in Table 10.1

(c) Case 9 in Table 10.1

(d) Case 10 in Table 10.1

Figure 10.6: Results for post-dryout model validation in non-water cases

General remarks

Overall, Figs. 10.6(a) to 10.6(d) indicate good agreement between the predicted and measure values for the wall temperature. In broad terms, the model performs better for the hydrocarbon examples than for the water cases studied in Section 10.3.1. In addition, the performance for the nitrogen case, see Fig. 10.6(c), is rather similar than for water.

This situation can be better understood by means of a comparative analysis of the physical properties of each fluid, summarized in Table 10.2.

In particular, the three following observations can be derived from Table 10.2.

- Hydrocarbons (and also nitrogen) have a lower surface tension (σ) than high-pressure water. This variable affects the evolution of the liquid droplet through several mechanisms. The initial diameter d_0, deposition rate W_{dep} and evaporation efficiency $\varepsilon_{W,D}$ are controlled by this physical property.

- The specific evaporation enthalpy (Δh_{LV}) of water is one order of magni-

Fluid	Water	R22	R113	N_2	R12
Pressure [bar]	70	38	3.1	1.4	9.3
σ [10^{-3} kg s^{-2}]	17.63	1.1204	10.75	8.23	6.86
Δh_{LV} [10^{6} J kg^{-1}]	1.505	0.097	0.131	0.195	0.131
λ_L [10^{-3} W m^{-1} K^{-1}]	571.9	55.6	56.6	139..1	62.4
λ_G [10^{-3} W m^{-1} K^{-1}]	62.9	24.1	11.3	7.5	11.3
λ_L/λ_G[-]	9.09	2.30	5.01	18.47	5.53

Table 10.2: Comparison of selected physical properties for different working fluids

tude larger than for other fluids. However, cases 1 to 6 (water) present a larger heat-to-mass flux ratio than cases 7 to 10 (non-water), see Table 10.1. For this reason, the overall evaporation rate is better understood in terms of the Boiling number Bo, defined in Eq. (10.27). In simple terms, this non-dimensional number represents the fraction of the flow that would be evaporated (under equilibrium conditions) along a tube length of $D/4$.

$$Bo = \frac{q''_W}{G\Delta h_{LV}} \tag{10.27}$$

In this context, the nitrogen example (case 9, Fig. 10.6(c)) stands out with a high boiling number $Bo = 2.62\ 10^{-3}$. As a consequence the entire two-phase region occupies (once again, under equilibrium conditions) a total length of 95.4 diameters. This value is much lower than for water (272 to 919) and hydrocarbon (342 to 1385) cases.

- Both liquid and gas thermal conductivities are notoriously larger in the case of water than in other working fluids. Nevertheless, the most relevant variable for analysis the consequences of dryout is the ratio λ_L/λ_G. From this perspective, the largest conductivity ratio is found for nitrogen, followed by high-pressure water and later on the hydrocarbons. A lower value for this coefficient is one of the main reasons (together with the lower heat flux) why the wall temperature superheat in the post-dryout regime is not so extreme in the case of hydrocarbons.

In addition to these general remarks, some individual comments for each case are presented in the following subsections.

Case 7: Fig. 10.6(a)

After an initial and moderate rise in its value, the wall temperature is continuously reduced along the two-phase region. Further increase in the wall temperature is only observed beyond $x_{th} = 1$. Both characteristics are clear indications of a large extent of thermal equilibrium. As indicated in Fig. 10.2(a), this case can be

well represented by a complete-equilibrium model such as the early formulations described in Section 10.1.1.

The phenomenological model postulated in this chapter satisfactorily predicts this behavior. Within a small uncertainty, the locations of the minimum and maximum wall temperature are accurately predicted, providing a good description of the equilibrium characteristics. Finally, the lowest accuracy is found in the high-quality region. In particular, the wall temperature is overpredicted, which is equivalent to an underprediction of the HTC. A possible way to interpret this result is that the direct wall-to-liquid interaction is larger in experimental observations than predicted by the model.

Case 8: Fig. 10.6(b)

Very good agreement with the experiments is obtained in this case. A statistical analysis of the 13 data points indicates a mean error of 5.4% (1.3 K) and RMS relative error of 6.5% (1.6 K). In other words, the wall temperature is well predicted within the experimental uncertainties. Similar results can be obtained for the six data sets provided by this source (Koizumi et al., 1979).

It should be noticed that this case is characterized by a large mass flux and low heat input, see Table 10.1. In fact, the boiling number, Bo=1.80 10^{-4} (equivalent to the two-phase region extending over 1385 diameters), is the lowest one from the ten cases studied in this chapter. Perhaps for this reason, the present thermal and hydrodynamic phenomenological model performs best in this case.

Case 9: Fig. 10.6(c)

Some peculiarities about this nitrogen case have been discussed previously in the general remarks for non-water fluids. In general, this case is more similar to the water examples presented in Section 10.3.1 than to typical hydrocarbon applications. As discussed above, the boiling number and thermal conductivity ratio are very large. For these two reasons, large wall superheat temperatures ($T_W - T_{sat}$) are observed in the post-dryout regime.

Overall, the agreement between the model and the experimental data is good. However, it should be noticed that the wall temperature is initially overpredicted close to the dryout location, and underpredicted further downstream near the outlet (observe the large values of x_{th}). This result probably indicates that the degree of thermal equilibrium close to the dryout location is probably closer in the experiments than predicted by the model. As the measured wall temperature follows a profile rather parallel to the predicted gas temperature, it can be concluded that full evaporation is achieved rather early, and single-phase wall-to-gas heat transfer is the dominant mechanism.

Case 10: Fig. 10.6(d)

The results from the phenomenological model for this case are rather good, with a similar performance as in case 8, see Fig. 10.6(b). In particular, beyond the near-dryout region (that is, excluding the first two data points), the RMS error for the remaining 8 observation is only 5.6% (5.6 K). If these two data points are included, the RMS errors increases up to 31.7% (12.8 K).

This scenario (rather large errors near the location of dryout, and accurate predictions further downstream) is a direct consequence of one assumption of the present model. In particular, a sharp flow pattern transition from annular-mist to the post-dryout regime is considered. In practice, as discussed in Section 3.3.2, this passage is not instantaneous and occurs over a certain range of vapor quality. Such as smooth transition can be easily implemented when considering the coupling of the phenomenological formulation described in Chapters 9 and 10.

10.4 Discussion

This section comprises an analysis and discussion of the results described in Section 10.3. Based on the previous individual analyses, the following two topics are considered. First, the most sensitive issues of the postulated phenomenological model are discussed. Finally, some remarks on the general lack of experimental data applicable to heat exchanger applications are presented.

10.4.1 Sensitive issues

In general, multifluid formulations are sensitive to the constitutive relations that describe the underlying phenomena (Jiao et al., 2009). The selected model for the present analysis were described in Section 10.2.2. These include the different mass, momentum and heat transfer mechanisms. From the validation of the model for both water (Section 10.3.1) and non-water (Section 10.3.2) cases, it can be concluded that further improvement is required in the description of two phenomena. As further detailed in the following subsections, these are the wall-to-gas heat transfer and droplet collisions against the hot wall.

Wall-to-gas heat transfer

An underlying characteristic of this phenomenological formulation is that it considers each physical effect occurring separately. In other words, it does not account for the interaction of different phenomena. In this context, wall-to-gas heat transfer was described in terms of a single-phase correlation, given by Eq. (10.8). Under some conditions[7], this assumption has led to a certain offset between predicted and measured wall temperature profiles. This means that this correlation introduces

[7]Specifically, see cases 3 and 4 in Table 10.1, represented in Figs. 10.5(c) and 10.5(d).

not only a random error, but also a systematic (at least for the cases studied in this chapter) underprediction of the heat transfer coefficient.

The main reason for this offset can be found in the (neglected) consequences of the liquid droplets on the wall-to-gas heat transfer. In particular, the dense liquid droplets can disturb both velocity and temperature profiles in the gas core. Therefore, as this mechanism is controlled by boundary-layer profiles in the near-wall region, a large effect could be expected. Nevertheless, although other authors (Varone Jr. and Rohsenow, 1986) included a correction factor for this effect, it is not yet clear under which conditions the heat transfer rate towards the gas is enhanced or reduced.

In order to include an accurate description of this phenomenon, specific experimental observations are required. Experimental data is currently reported in terms of wall temperature and some qualitative intube observations, such as flow pattern identification. In this context, detailed information on the droplet phase for this scenario is not obtained. Nevertheless, relevant information can be derived, using current experimental techniques, from a similar scenario. Perhaps, future experiments in gas flow with solid particles can represent this phenomenon.

Wet and dry droplet collisions

As discussed in Section 10.2.2, direct-contact wall-to-droplets heat transfer can be represented by either one of two mechanisms: wet and dry collisions. On the one hand, wet collisions occur at low wall temperature superheat and are represented by intimate contact, large heat transfer and full evaporation of the droplets. On the other hand, in a dry collision (usually found at large temperatures) the droplet bounces back at the wall, and the heat transfer rate is low. The present model represents this phenomenon in terms of an evaporation efficiency $\varepsilon_{W,D}$. In addition, it was assumed (based on previous research reported in literature) that the main variable affecting this efficiency is the wall temperature.

A poor description of this phenomenon can be the cause for a particular systematic difference between predictions and experimental data. Near the dryout location, the wall temperature is overpredicted in some cases[8]. This means that the wall-to-droplets heat transfer was underpredicted. Perhaps the reason for this result is that a developing region must be included in the analysis and therefore the description only in terms of the wall temperature is not sufficient.

In addition, it should be noticed that present models for $\varepsilon_{W,D}$ were developed for individual droplets colliding against a heated plate. This experimental scenario does not involve fluid convection. In the practical case of intube forced convection, wet collisions are more likely to occur, thus providing larger heat transfer rates. Therefore, this is another example were the interaction of separate effects (forced convection and droplet collision) should be included in the analysis.

[8]See cases 2 (water), 9 (nitrogen) and 10 (R12) in Table 10.1, represented in Figs. 10.5(b), 10.6(c) and 10.6(d), respectively.

10.4.2 Data for heat exchangers

The scope of this thesis is oriented towards the study of heat exchangers. As stated above (see Section 10.1 and the unnumbered introduction of the present chapter), these applications are in some aspects different from power-controlled systems. Among other differences, the axial power distribution in a HE is not uniform, and the wall temperature cannot rise sharply since it is controlled by the other stream. This scenario, in addition to most of the experimental data being derived for power-controlled applications, provides the motivation to derive phenomenological models for the analysis of post-dryout flow.

In this context, the validation of the model in Section 10.3 was presented for uniform heat flux conditions. It would have been desirable to evaluate the performance of the postulated model also for heat exchanger applications. However, this evaluation was not possible, due to the lack of experimental information for this scenario. While most experiments were performed using direct electric heating, some authors selected a counter-current HE arrangement for their essays. Some representative references in this group are:

- George and France (1991): Boiling high-pressure water, heated with liquid sodium (16 data sets).
- Paske et al. (1992): Water-heated evaporating R-12 (10 data sets)
- Yoo and France (1996): Water-heated evaporating R-113 (19 data sets).

With this configuration, the authors could obtain low superheat data (below 70 K). In addition, using low pressure refrigerants, they could imitate the physical properties of high-pressure water in simpler experimental conditions. In this context, they tested different correlations and concluded that the model given by Plummer (1974) performs best. Nevertheless, it fails to accurately predict the wall temperature profiles.

Due to the selected experimental arrangement, these data sets should not be compared with simple correlations developed for power-controlled systems. On the contrary, this information should be directed towards the analysis of heat exchanger applications, more similar to the experimental conditions. Nevertheless, the reported data is insufficient for this purpose. In particular, relevant information regarding the hot fluid, such as mass flow rate and inlet conditions, is missing.

In summary, more detailed information for HE conditions is required. This data could be obtained following the trend by George and France (1991), Paske et al. (1992) and Yoo and France (1996). In general, the only possible way to exploit data from HEs or power-controlled systems and used them for either one of both applications, is by means of a phenomenological model as the one proposed in this chapter.

10.5 Summary

The post-dryout flow regime is characterized by a low heat transfer performance. It is found in the high-quality region, beyond the occurrence of dryout, described in detail in Chapter 9. As evaporators cover the entire quality range from 0.0 to 1.0, this regime is always found in typical heat exchanger applications (except in very low mass flux conditions). However, its analysis is not currently covered by state-of-the-art HE models.

Extensive research on this topic is found for power-controlled applications. In these systems, the boiling crisis produces a sharp increase in the wall temperature and therefore is relevant for overall safety considerations. Nevertheless, there are four main differences between both applications. First, the dominant flow pattern in HEs is the dispersed-droplets regime, while in power-controlled systems the inverted-annular structure can also be found. Second, transient effects are very relevant in emergency situations for uniform heat flux conditions, and they can be neglected in a first analysis of heat exchangers. Third, the axial power distribution in a HE is not necessarily uniform. Finally, the wall temperature profile in a heat exchanger is controlled by both cold and hot fluids. Therefore sharp variations are usually not found in HEs.

A literature review indicates that thermal non-equilibrium plays a major role in the evolution of post-dryout flow. Early formulations considered one of two extreme scenarios: 0% (frozen droplets) or 100% (complete thermal equilibrium). In general, these description present large unceratinties (although low heat-to-mass flux ratio scenarios can be well represented by a complete equilibrium model) and should only be used as a first approximation for establishing upper and lower limits for the wall temperature, respectively. In addition, axial evolution models have been proposed in the open literature, considering two or three heat transfer paths. Although they are more accurate than previous formulations, they do not include all the relevant effects.

In this context, a multifluid formulation was postulated, following the approach described in Chapter 9. A phenomenological model describes the evolution of both phases, using constitutive relations in order to account for their interaction. The relevant phenomena included in this model are, among others, wall-to-gas heat transfer, forced convection at the gas-droplets interface, wet and dry droplet collisions, shear stresses and the evolution of the representative droplet diameter. An overall summary of this method is presented in Section 10.2.4.

This model was validated against experimental data in Section 10.3. As only uniform heat flux data is available in the open literature, the selected variable for validation was the wall temperature profile. In total, 10 data sets (summarized in Table 10.1) were studied: six for water and four for other fluids, including hydrocarbon refrigerants and nitrogen. In general, good agreement is observed between predicted and measured wall temperatures. Some general remarks were presented along with a detailed analysis of each individual case. The hydrocarbon refrigerant

cases, with a lower heat-to-mass flux ratio, are well represented by this model, in some occasions within the uncertainties of the experimental measurements.

A detailed discussion on the performance of this model was presented in Section 10.4. Two issues are highlighted as the most sensitive ones: wall-to-gas heat transfer and droplet collisions at the wall. In both cases, it seems that these effects should not be described separated from others, and their interaction with other phenomena should be included. On the one hand, the presence of liquid droplets is expected to affect the thermal boundary layer with consequences in the wall-to-gas heat transfer, thus explaining the offset in the predictions presented in Figs. 10.5(c) and 10.5(d). On the other hand, the selected constitutive relation for describing the droplet collisions was derived from stationary conditions, without convection. In convective boiling, however, it is expected that wet collisions are more likely to occur than in other conditions.

Part V

Final remarks

An overall analysis of previous results is presented in this final part. A complete multiscale simulation example, including results from the previous chapter is presented. In addition, the final remarks are focused on deriving conclusions from this thesis and discussing possibilities for further investigations in this topic.

The interaction and coupling of physical phenomena at the different scales are studied on Chapter 11. A proper multiscale algorithm is postulated for the design and sizing of high-effectiveness heat exchangers. Simulation results are presented for a practical example (an evaporator).

Chapter 12 summarizes the major contributions of this work. The results are analyzed in view of the objectives defined in Chapter 1. In general, these objectives were satisfactorily fulfilled. The main conclusions derived from this work are discussed in this chapter. Following the overall intention of postulating a multiscale framework for improving the current understanding of cryogenic heat exchangers, a multiscale algorithm for this purpose is proposed.

The main topic in Chapter 13 is an analysis of the results with a focus on prospective future activities at both modeling and experimental levels. Describing the different lessons learned from the tasks performed throughout this thesis, some advices indicating possible research paths are included. In particular, further research should be focused on lower scale effects, such as the flow in parallel channels and an accurate phenomenological description of two-phase flow and heat transfer. In addition, a discussion is presented regarding the possibilities for extending the scope and limitations of the present work.

Chapter 11

Multiscale sizing of a heat exchanger

▶ The present chapter deals with the coupled analysis of the three scales (macro, meso, and micro) described throughout this thesis. An overall multiscale algorithm for the design and sizing of two-phase flow heat exchanger is postulated and applied to a practical example. The results from this example indicate that it is essential to include low-scale phenomena in the analysis at the design stage.

11.1 A multiscale algorithm

The main idea of this thesis was to investigate possibilities based on multiscale formulations, for improving the current understanding and design of heat exchangers. Following this concept, a possible multiscale algorithm for the design process is postulated in Fig. 11.1. It can be summarized as the following steps.

1. The design of a heat exchanger is strictly related to the operating conditions such as pressure, temperature and flow rates, and other specifications of the process. In other words, there is no such thing as a generic modeling scheme. Therefore, the particular characteristics of the given process where the HE is to be employed represent the starting point for this algorithm.

2. Based on previous experience and practical circumstances, several different geometries can be proposed, such as A, B and C in Fig. 11.1. This stage of design does not only concern thermalhydraulic considerations (Shah and Sekulić, 2003). Other aspects such as mechanical (e.g. high-pressure streams inside tubes) and manufacturing regards, selection of a chemically-compatible material, among others, must be included in the analysis. The

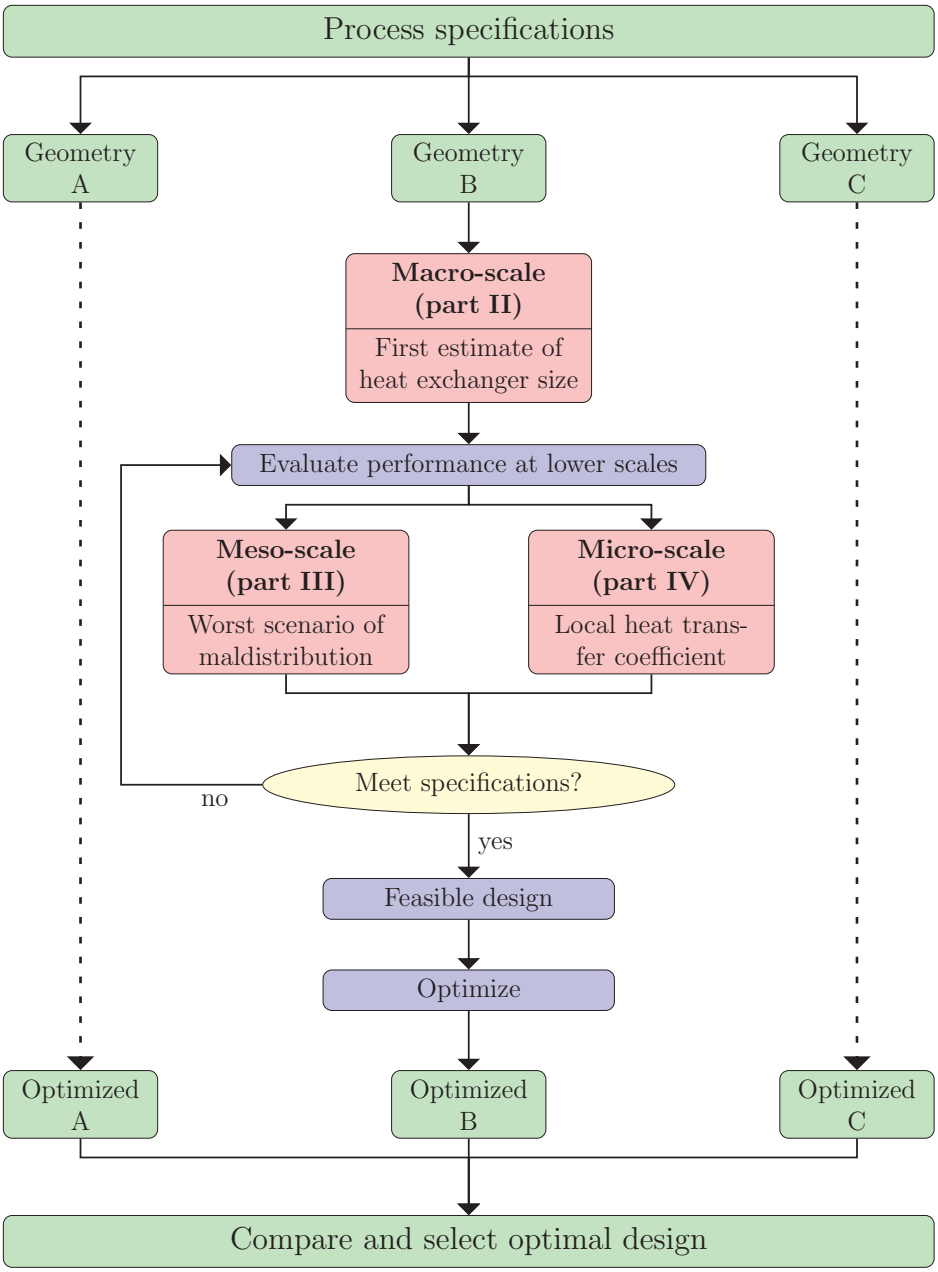

Figure 11.1: Multiscale algorithm for the design of a cryogenic heat exchanger

most commonly used geometries for cryogenic and LNG processes were reviewed in Section 2.2.

3. For a given geometry (the example in Fig. 11.1 is for case B), the thermal-hydraulic analysis starts at a macroscopic level. At this stage, a rough first estimate of the required heat exchanger size can be obtained using the rather simple model described in part II. As a result, a possible complete set of parameters like number of tubes, diameter and inlet velocities, is postulated.

4. Once a complete set of parameters is available, more complete models can be used for evaluating the performance. In particular, physical phenomena at lower scales can be incorporated. Throughout this thesis, two lower-scale frameworks are described as follows.

   - Meso-scale analysis comprises the heterogeneities in parallel-flow geometries. Perhaps the most important element to consider is the worst case scenario of flow maldistribution, which can largely reduce the thermal performance. It is important to achieve a design that would meet the process specifications under all realistic circumstances.
   - Micro-scale effects must be studied in order to accurately account for local variations of the heat transfer coefficient. As discussed in Chapters 9 and 10, the most important transition in boiling flows is the occurrence of dryout, degrading the heat transfer capability. In this work, phenomenological descriptions based on multifluid formulations were postulated for the microscopic analysis.

5. Once the performance is evaluated in detail, the next step consists on checking if this design meets the given specifications.

   - On the one hand, if the specifications are not met, a new set of parameters can be proposed and further iterations are required. A useful tool for proposing a new set of parameters that would yield a better performance is given by the perturbative method described in Chapter 6.
   - One the other hand, if the evaluated performance fulfills the process requirements, a feasible design was achieved. The next steps consists on optimizing this possible design. Once again, the perturbative formulation presented in Chapter 6, provide a suitable mechanism for the optimization procedure.

6. Steps 3 to 5 must be repeated for all the geometries proposed in step 2. Finally, all the optimized results should be compared for selecting the best design. Since this thesis is focused on round-tube geometries, this step exceeds the scope of the present work. Nevertheless, it should not be disregarded in more complete analyses.

11.2 Analysis of an example: an evaporator

The multiscale algorithm presented in Section 11.1 (and summarized in Fig. 11.1) is applied in the present section to a practical example. Throughout the following subsections, the same order described in Section 11.1 is followed.

11.2.1 Process specifications

As a starting point, the process specifications are summarized in Table 11.1. These specifications can be grouped into three categories: inlet conditions for both the cold and the hot streams, and the target performance. It should be observed that this is a high-effectiveness case ($\varepsilon \approx 96.9\% \Rightarrow 1-\varepsilon \approx 3.1\%$), following the general scope of this thesis.

	Variable	Symbol	Value	Unit
Cold stream	Working fluid		R134a	-
	Inlet temperature	T_{cold}^{in}	275	K
	Inlet pressure	p_{cold}^{in}	3.5	bar
	Saturation temperature at the inlet pressure	$T_{sat}(p_{cold}^{in})$	278	K
	Mass flow rate	$\dot{m}_{cold}$	4.6	kg s^{-1}
Hot stream	Working fluid		Water	-
	Inlet temperature	T_{hot}^{in}	303	K
	Inlet pressure	p_{hot}^{in}	1.2	bar
	Mass flow rate	$\dot{m}_{hot}$	20.0	kg s^{-1}
Performance	Total heat duty	Q	1000	kW
	Thermal effectiveness	ε	0.9687	-
	Maximum Δp_{cold}	Δp_{cold}^{max}	1.5	bar
	Maximum Δp_{hot}	Δp_{hot}^{max}	0.25	bar

Table 11.1: Specifications for the multiscale sizing example

At a process-level description, all the required information is included in Table 11.1. Further information is required at a lower level, as studied below.

11.2.2 Selecting the geometry

In general, several heat exchanger geometries can be selected for a given process (Shah and Sekulić, 2003, §1.5). Therefore, in strict terms, the following analysis should be repeated for each of these possible geometries. In this example, however, only a shell-and-tube evaporator is considered, following the general scope of this thesis. The possibilities for extending this analysis to other geometries are included in the recommendations for future works depicted in Chapter 13. In addition, only

plain tubes are studied and the description of baffles and flow distribution devices escapes the scope of this example.

Having selected the geometry, several parameters must be defined, listed in Table 11.2. The values of some of these parameters[1] can already be established at this stage, based on a preliminary analysis and *best-practice guidelines* derived from the results obtained in parts II to IV.

	Variable	Value	Unit
Geometry	Stream in the tube-side	Cold/Hot	-
	Flow arrangement	Co-current/Counter-current	-
	Cold flow direction	Horizontal/Upward/Downward	-
	Tube length	L	m
	Inner diameter	D_i	mm
	Tube pitch	P	mm
	Wall thickness	t_W	mm
	Number of tubes	N_t	-

Table 11.2: Required geometrical parameters in the multiscale sizing example

Stream in the tube-side

This variable is decided upon mechanical considerations. In simple terms, the higher-pressure stream should flow inside the tubes. Therefore, in this example the cold stream (evaporating R134a) is selected for the tube-side, and the hot stream (liquid water) in the shell-side.

Flow arrangement

Previous experience for single-phase flow (Incropera and DeWitt, 1996, §11.3) indicates that the counter-current arrangement yields the largest effectiveness ε. In the case of an evaporator, however, the analysis presented in Chapter 5 indicated that under some conditions, and up to a maximum effectiveness, the co-current arrangement might perform better.

Therefore, it is interesting to establish this maximum effectiveness at this stage of analysis in order to determine the optimum flow arrangement. This upper limit would be obtained with an infinitely large heat exchanger. In that case, both streams would leave at the same temperature. Consequently, this maximum efficiency can be computed from Eq. (11.1), setting a no-temperature-cross constraint.

[1] In fact, all of them except the tube length L and inner diameter D_i.

$$T_{cold}\left(p_{cold}^{in}, h_{cold}^{in} + \varepsilon \times \frac{Q_{max}}{\dot{m}_{cold}}\right) \leq T_{hot}\left(p_{hot}^{in}, h_{hot}^{in} - \varepsilon \times \frac{Q_{max}}{\dot{m}_{hot}}\right)$$
$$\Longrightarrow \varepsilon \leq 0.8865 \tag{11.1}$$

A slightly higher upper limit for the effectiveness when the reduction in saturation temperature (as a consequence of the maximum allowed pressure drop) is included in the analysis. In that case, this constraint results in Eq. (11.2).

$$T_{cold}\left(p_{cold}^{in} - \Delta p_{cold}^{max}, h_{cold}^{in} + \varepsilon \times \frac{Q_{max}}{\dot{m}_{cold}}\right) \leq T_{hot}\left(p_{hot}^{in}, h_{hot}^{in} - \varepsilon \times \frac{Q_{max}}{\dot{m}_{hot}}\right)$$
$$\Longrightarrow \varepsilon \leq 0.9295 \tag{11.2}$$

Therefore, even in the most optimistic case, the specificied target effectiveness is above the maximum efficiency ε. This result means that the co-current flow arrangement would not meet the specifications. Consequently, the counter-current flow arrangement is selected.

Cold flow direction

As mentioned in Chapter 5, the overall heat transfer coefficient is rather independent of the flow direction. Instead, the major effect of changing the flow direction is given by the gravitational pressure drop and its consequences on the saturation temperature. It has also been observed in Chapter 5 that a large pressure drop in the cold stream results in a better performance. With these considerations, the cold flow direction is selected as upwards. As a consequence, in a counter-current arrangement the hot stream flows downward, in a gravity dominated regime.

Tube pitch P

The distance between tubes (that is, the tube pitch) affects the shell-side hydraulic diameter. Due to vibration issues, industry standards (TEMA, 2007) recommend a minimum pitch of 1.25 times the tube outer diameter. In addition, the minimum gap between tubes should be 6 mm, in order to allow for cleaning. In this example, the tube pitch given by Eq. (11.3) is considered.

$$\text{Tube pitch:} \quad P = 1.4\,(D_i + 2 \times t_W) \tag{11.3}$$

Tube wall thickness t_W

Since this variable depends on other considerations that escape the thermalhydraulic analysis, a constant value of t_W =0.5 mm is selected, and it is not included in the optimization process.

Number of tubes N_t

This variable is controlled by the mass flow rates, which were specified in Table 11.1. Usually, an average velocity is considered, and the required number of tubes is consequently computed. In the case of boiling flows, as the density is not constant, an average mass flux G must be selected.

A preliminary analysis indicates that, in order to remain below the maximum allowed pressure drop, the mass flux should be around G_{cold} =300 kg m^{-2} s^{-1}. Based on this value, the number of tubes is computed as in Eq. (11.4), which depends on the inner diameter D_i.

$$\text{Number of tubes:} \quad N_t = \text{round}\left(\frac{4\dot{m}_{cold}}{\pi D_i^2 G_{cold}}\right) \tag{11.4}$$

11.2.3 Macroscopic analysis. First estimate of HE size

The selection of the geometry, discussed in Section 11.2.2, leaves only two independent parameters. These are the tube length L and inner diameter D_i.

In this context, the scheme summarized in Fig. 11.1 can be slightly reformulated as follows. The different geometries A, B and C would represent particular values of the tube diameter, and the required length is evaluated for each of them. For the particular case of D_i =8 mm, the macro-scale sizing solution is presented in Fig. 11.2, in terms of the thermal performance obtained at a given tube length.

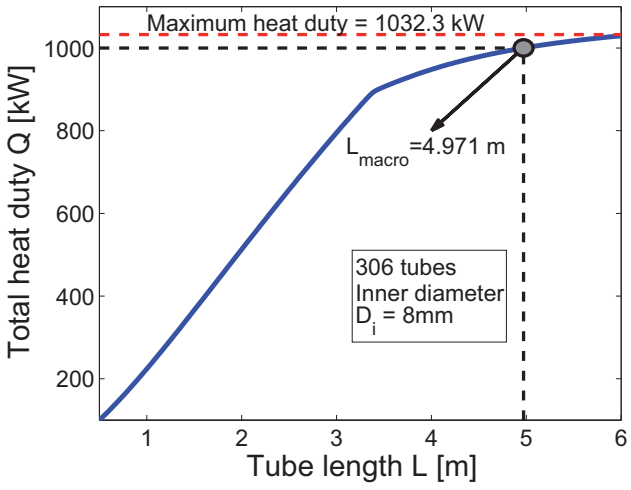

Figure 11.2: Solution the macroscopic sizing problem

A sharp change in the slope of the macroscopic sizing curve is noticed around $L \approx$3.4 m ($Q \approx$ 900 kW), as a consequence of the full evaporation of the cold stream. The heat flux in the boiling region is rather large (roughly 35 kW m^{-2} in average), and it is significantly reduced in the single-phase gas region (initially 17.5 kW m^{-2} and further decreasing downstream) due to both a lower HTC and temperature difference.

The required tube length for achieving the target performance is L =4.971 m. This result defines a complete set of geometrical parameter and therefore is the starting point for a more detailed analysis at lower scales, described in Section 11.2.4.

This process should be repeated for different values of the tube diameter, as later studied in Section 11.2.6. The selected figure of merit for comparing the heat exchanger size is the total surface area A, given by Eq. (11.5). For this case, a first estimate of the area is $A(D_i = 8mm)$=38.23m^2. The average heat flux is then 26.1 kW m^{-2}, that is 25% lower than in the two-phase region.

$$A\left(D_i\right) = N_t \pi L D_i \tag{11.5}$$

At this point, it should be verified whether the pressure drop for both streams remain below the upper limits specified in Table 11.1. On the one hand, the cold-side pressure drop is Δp_{cold}= 1.096 bar, which is an acceptable value. On the other hand, the pressure change in the hot stream is negative (Δp_{hot}= -0.378 bar), indicating that there is a net pressure rise. This result is a consequence of gravitational term in the momentum balance equation dominating over frictional and inertial terms for this single-phase stream.

11.2.4 Rating the performance at lower scales

As described in Section 11.1, once a complete geometry is defined (given by Sections 11.2.2 and 11.2.3), the thermal performance can be evaluated more accurately in a lower-scale analysis. In the three-scales framework selected for this thesis, two lower scales are considered: meso and micro. These analyses are detailed in the following subsections.

Medium-scale analysis. Worst case of maldistribution

The macroscopic analysis described in Section 11.2.3 considers one single tube and assumes that all channels present an identical behavior. As studied in part III (Chapters 7 and 8) the most notorious asymmetry between parallel channels is related to the problems of flow distribution. This phenomenon produces a reduction in the thermal performance, with a large impact in balanced (in terms of heat capacity flow rate) high-effectiveness applications.

In this context, the effects of maldistribution are studied in this section following the model presented in Section 7.4.2 (pressure-coupled channels). The results

of a parametric analysis are presented in Fig. 11.3, considering a flow maldistribution in the shell-side, characterized by the coefficient μ. The parameter n indicates the number of layers considered. As studied in Chapter 7, the predicted performance depends asymptotically on the number of layers, and no further changes are observed for $n \geq 100$.

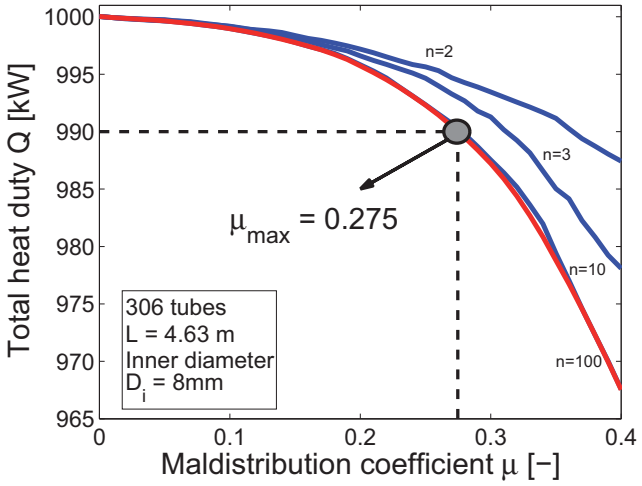

Figure 11.3: Reduction in the thermal performance due to flow maldistribution

Figure 11.3 confirms the larger negative impact on the performance with increasing maldistribution. At a first glance, this plot presents some slight differences with the parametric analysis presented in Chapter 7 (see Fig. 7.12(a)). In particular, the impact on the total heat duty is smaller (maximum reduction of 32.5kW=3.25% for μ=0.4), and it does not present a linear dependence on the coefficient μ. The cause for these differences is that the previous examples are rather balanced in terms of heat capacity flow rate. In the present example, the hot stream has such a capacity flow rate[2] (C_{hot}=83.8 W K^{-1}) more than twice as large as the cold stream (C_{cold}=36.9 W K^{-1}). For this reason, the negative impact on the heat duty is not as large as in the previous examples.

It is important to recall that the thermalhydraulic analysis is coupled with mechanical considerations, such as constraints in the design of the distribution

[2]In the case of phase-change flows (and variables properties cases in general), the representative heat capacity flow rate can be computed as in Eq. (11.6). The extreme values T_{min} and T_{max} are given by the inlet temperatures of the cold and hot streams, respectively.

$$C = \dot{m} \frac{h\left(p, T_{max}\right) - h\left(p, T_{min}\right)}{T_{max} - T_{min}} \tag{11.6}$$

devices. In this context, the worst-case scenario of maldistribution must be defined on the basis of the results presented in Fig. 11.3.

After establishing a maximum bearable reduction in performance (thermalhydraulic analysis), the largest allowed maldistribution μ_{max} (mechanical constraint) can be obtained from Fig. 11.3. For this example, considering that the target ineffectiveness is very low ($1 - \varepsilon \approx 3.1\%$) and that other neglected effects (such as longitudinal heat condution) might also contribute to deteriorate the performance, a maximum reduction in the heat duty as a consequence of maldistribution of only 1.0% (10 kW) is allowed. For these conditions, it can be read from Fig. 11.3 that the maximum acceptable flow maldistribution is given by a coefficient μ_{max}=0.275.

Micro-scale analysis. Local heat transfer coefficient.

A micro-scale description involves a detailed study of the intube flow. As discussed in the prologue to part IV, the larger scales (macro and meso) describe the thermalhydraulic behavior in terms of the evolution of macroscopic average variables such as enthalpy, pressure and mass flux. In addition, the interaction between the streams is represented using a heat transfer coefficient, based on simple correlations such as those studied in Section 3.3.3.

In this context, this analysis at a microscopic level is focused on the identification of different flow patterns in the boiling stream. Both annular and post-dryout flow regimes are studied in detail within a phenomenological framework according to the models described in Chapters 9 and 10, respectively.

Accounting for these flow pattern transitions, a more accurate evaluation of the thermal performance is possible. The implementation of this detailed description implies a larger computational cost. For this reason, it is only applicable in practice once a given geometry is established, as postulated in Sections 11.2.2 and 11.2.3.

Figure 11.4 presents the results of this micro-scale analysis in terms of axial profiles for (a) temperature and (b) quality of the cold stream. In both cases, the flow pattern transitions are indicated. Several observations can be derived from Fig. 11.4 for each particular flow regime.

At $z = 0$, the cold stream enters as a **single-phase liquid**, roughly 3 K below the saturation temperature. The **bubbly/slug** flow pattern is established at a short distance downstream from the inlet, as a consequence of subcooled boiling. This phenomenon results in a separation of the red (solid) and blue (dashed) lines in Fig. 11.4(b), corresponding to the mass vapor content and thermodynamic quality, respectively. In other words, there is a slight departure from thermal equilibrium. Bubbles are generated near the wall before the bulk reaches saturation conditions and represent up to 0.9% of the mass flux under subcooled conditions. Further downstream, the bubbly and slug regimes extend throughout the saturated boiling region until the onset of annular flow.

According to the criteria given by Eq. (9.10), the **annular-mist** flow regimes starts at $x_{th} = 0.307$. It covers a wide enthalpy range until the occurrence of dryout

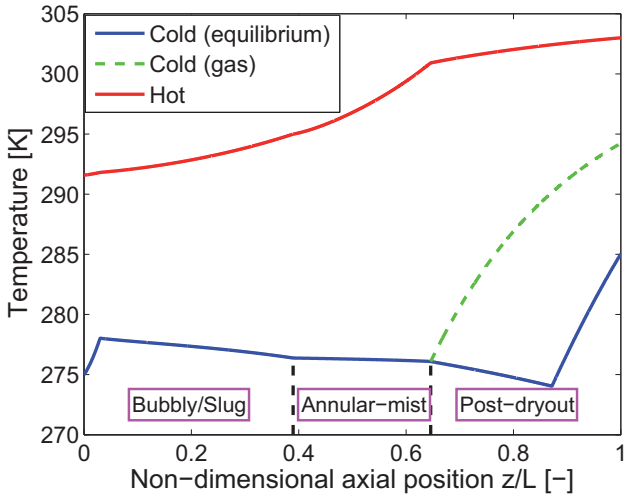

(a) Axial temperature profiles

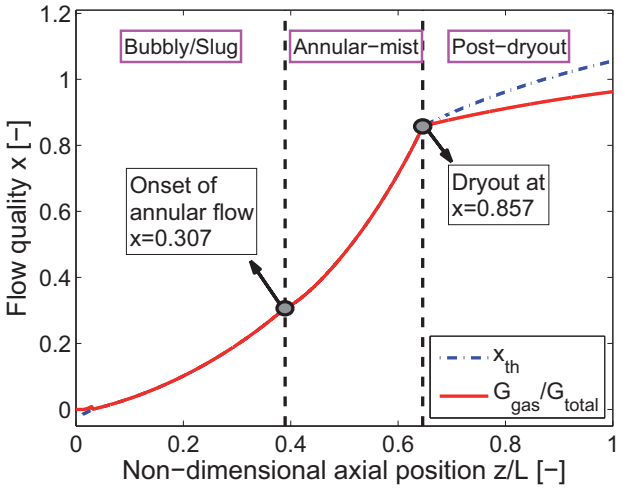

(b) Flow pattern transitions in the boiling cold stream

Figure 11.4: Micro-scale analysis including flow pattern transitions

at $x_{th} = 0.857$, that is more than half the total change in the thermodynamic quality. However, it only takes around 25% of the tube length. This is a clear indication that this regime is characterized by large heat transfer rates, twice the average value. For this reason, an accurate evaluation of this boiling crisis,

following the phenomenological model presented in Chapter 9, is essential for the overall sizing of the heat exchanger.

As described in Chapter 10, the **post-dryout** regime is characterized by a large degree of thermal non-equilibrium. The gas is in direct contact with the wall and becomes superheated, as can be observed in Fig. 11.4(a). The remaining liquid flows as dispersed droplets and is slowly evaporated. As a consequence, the flow does not reach full evaporation at the outlet in spite of the thermodynamic quality being larger than unity. In addition, the effective temperature difference is reduced roughly by half due to the gas superheat, and the heat transfer rates in this regime are very low. Only 18% of the enthalpy change is covered by this flow pattern, which extends over 35% of the tube length. This means that the heat flux in this region is half the overall average and roughly four times lower than in the annular-mist regime.

The main objective of this micro-scale analysis is to provide a more accurate evaluation of performance. In this case, the total heat duty is reduced to Q=955.16 kW (4.48% lower than the required specifications), mainly due to the superheating of the gas in the post-dryout region. Consequently, the thermal specifications are not met and a larger surface area (that is, a longer tube length) is required. This iterative design is analyzed in Section 11.2.5..

11.2.5 Iteration on the tube length

The evaluation of performance obtained from the lower-scale analysis in Section 11.2.4 indicates that the specified geometry does not fulfill the requirements. Consequently, a larger surface area A (which means a longer tube length L) is required. Considering that the microscopic analysis is computationally expensive, a parametric study as presented in the macroscopic description (see Fig. 11.2) cannot be applied in practice.

On the contrary, an iterative search scheme must be followed, on the basis of the rough estimates provided in Section 11.2.3. This sizing procedure indicates that the required tube length is L=7.174 m, which means a total area of A=55.18 m^2 (44.3% larger than predicted at a macro-scale description). The average heat flux under these conditions is q''_W=18.12 kW m^{-2}.

In short, the evaluation of performance at lower scales dictates that a considerably larger surface area is required. The main reason for this result is that the heat transfer rate in the post-dryout region is very low and is continuously reduced due to the vapor superheat. Therefore, while the original predicted tube length L=4.971 m resulted in a heat duty of Q=955.16 kW, an additional 2.2 m are necessary for achieving the specified performance (Q=1000 kW).

11.2.6 Iteration on the tube diameter

The final step in this multiscale design process is the selection of the tube diameter D_i. As described above, diverse values of D_i in this example represent the different geometries in the scheme in Fig. 11.1. The sizing results for five discrete values of this parameter are summarized in Table 11.3.

Tube diameter D_i [mm]	Number of tubes N_t [-]	Tube length L [m]	Total area A [m^2]
6.0	543	4.421	45.25
7.0	399	5.852	51.35
8.0	306	7.174	55.18
9.0	242	8.570	58.64
10.0	196	9.867	60.76

Table 11.3: Sizing results for different tube diameters

It can be concluded from Table 11.3 that a smaller diameter is more convenient, as the required surface are is lower. In a nutshell, this result is a consequence of the larger overall heat transfer coefficient. This situation arises because the local heat transfer coefficient on both streams is enhanced by a smaller diameter.

- According to single-phase heat transfer correlation, the HTC in the hot stream has a small dependency on the diameter. The Dittus-Bolter correlation consider a relation as $1/D_i^{0.2}$.
- In the case of the cold stream, a smaller diameter leads to an improvement of the heat transfer rate on both flow patterns:
  - In the annular-mist flow regime, a smaller dryout leads to a later occurrence of the boiling crisis, as observed in Chapter 9. Since the dryout is postponed toward larger qualities and the annular region is extended, the overall effective HTC is enhanced.
  - In the post-dryout regime, a larger deposition rate and wall-to-gas heat transfer capabilities as a consequence of the smaller diameter, lead to a larger extent of thermal equilibrium. Therefore, the gas superheat is reduced and the heat transfer rate increases.

11.3 Summary

This thesis considers a multiscale approach for the design of heat exchangers. In particular, three scales (macro, meso and micro) were defined and parts II to IV deal with each of them separately. The present chapter deals with the practical

implementation of a multiscale concept for the analysis of high-performance two-phase flow heat exchangers.

An overall multiscale algorithm for the sizing and design of HEs was postulated, as summarized in Fig. 11.1. The starting point for this scheme is given by the process specifications. From this point, several geometries can be selected, based on previous experiences and best-practice guidelines. Each of these geometries are then evaluated using a multiscale description. A macro-scale analysis provides a first estimate of the required HE size. A lower-scale evaluation determines the performance with a larger accuracy, including effects such as flow maldistribution (mesoscale) and flow pattern transitions (microscale). The final steps consist on optimizing each of these geometries, comparing them and selecting the most convenient design.

This algorithm was then applied in Section 11.2 to the practical example of an evaporator. The main conclusion from this example is that there can be a large difference between the total heat duty evaluated at a macroscopic level or considering a microscale description. As a consequence of the gas superheat in the post-dryout flow regime, the heat transfer rate is reduced and a considerable larger surface area is required.

Chapter 12

Conclusions

► The main conclusions derived from this work are discussed in this chapter. These remarks are analyzed in terms of the objectives defined in Chapter 1. In this context a generic multiscale algorithm, based on the three-scale framework utilized in this thesis, is postulated for the design of a two-phase flow heat exchanger.

The main purpose of this work was to investigate the implementation of a multiscale framework for the analysis of two-phase flow heat exchangers. A possible framework has been defined and modeling and simulations results were presented at different scales. While each chapter includes a summary of partial results, closing remarks are presented in this final part.

This chapter is structured as follows. The original objectives of this thesis are revised in Section 12.1. Section 11.1 deals with a design algorithm based on a multiscale framework, following the research methodology outlined in this work. Finally, the major contribution from this project are summarized in Section 12.2.

12.1 Reviewing the objectives

Considering the scenario described in the previous section, the main objectives of this thesis can be summarized as follows.

1. **Evaluate the state-of-the-art in heat exchanger modeling from a design perspective, specially for cryogenic and other high-efficiency applications. The main problems for obtaining an accurate description are identified and consequently a research methodology based on a multiscale formulation for solving these issues is proposed.**

   An extensive review on the state-of-the-art was presented in Chapter 2, and it is also the main topic of Article 7 in the Appendix. The main result of this analysis is that the modeling and design of cryogenic two-phase flow

heat exchangers is a complicated task mainly due to two reasons. First, as a consequence of the high-effectiveness requirements, additional physical effects must be studied. These effects include changes in the fluid properties, flow maldistribution, longitudinal thermal conduction and heat exchange with the surroundings. Second, two-phase flow and heat transfer are rather complex processes dominated by physical mechanisms spread over a wide range of time and length scales. While some of these effects have been already addressed individually in the open literature, the only formulation able to practically account for all of them is indeed a multiscale approach.

2. **Develop a multiscale framework, identifying the most relevant physical phenomena and bridging parameters. While in strict terms all these phenomena are coupled, a proper setup must be defined in order to exploit efficiently the separation of different scales.**

   The multiscale features of two-phase flow and heat exchangers were investigated in Chapter 3. In general the different scales are strongly coupled in both directions. In this context, a three-scale framework was proposed, as represented in Fig. 3.5. This thesis was then divided in macro, meso and micro scale analysis (parts II, III and IV, respectively). The most important variables that allow a bridging between the scales are the local void fraction, heat transfer coefficient and frictional pressure drop. In order to accurately represent these variables it is essential to identify the flow pattern.

3. **Postulate modeling and simulation tasks in order to improve the current understanding of heat exchanger performance for each individual scale defined in the previous step. Keeping this final objective in mind, macroscopic effects are analyzed first and further modeling and simulations activities in this project include phenomena occurring at the lower scales.**

   Macro-scale effects were studied in part II (Chapters 5 and 6). In this analysis, an elementary representation of the heat exchanger is considered in order to simply evaluate the performance. A one-dimensional description indicates that the overall accuracy relies on the ability to describe pressure drop and heat transfer, thus providing the motivation for investigating effects occurring at lower scales. In this macroscopic framework, perturbative methods are introducing for sensitivity and optimization analysis.

4. **Take into account smaller-scale effects, including the consequences of flow maldistribution, and a phenomenological description of two-phase flow heat transfer.**

   Lower-scale analysis was divided into medium (meso) and microscopic formulations. The meso-scale description was based on a homogenization approach

for analyzing heat exchangers with multiple parallel channels. In this context, the consequences of flow maldistribution and partial flow mixing on the overall thermal performance were studied. In the micro-scale framework, the boiling heat transfer rates in the annular-mist and post-dryout flow regimes were studied using a phenomenological multifluid formulation.

5. **Investigate practical aspects of the implementation of the postulated multiscale scheme. Specifically, an overall simulation algorithm is proposed.**

   The previous chapters were focused on the individual analysis of each scale. This information can only be useful for the design engineer if some additional comments on their coupling are included. A multiscale algorithm for the design of a two-phase flow heat exchanger is presented in Section 11.1

12.2 Contributions in this work

The major contributions from this work can summarized as follows.

- Extending the concept of multiscale modeling from current applications to the analysis of two-phase flow heat exchangers. In this context, a three-scale framework was proposed, and modeling and simulation results at each level were presented.
- Investigating the performance of different numerical methods for the analysis of heat exchanger problems. Special emphasis is placed on the potential advantages of the Least Squares Spectral Element Method. In fact, this technique is the mot convenient one for complex problems.
- Applying perturbative methods for sensitivity analysis and optimization of heat exchangers. These techniques have been applied before in other areas of engineering and provide an efficient way of determining the consequences of variations in the parameters.
- Describing complex geometries with multiple parallel channel by means of a homogenization approach. Following this concept, medium-scale effects such as flow maldistribution and partial mixing could be incorporated achieving an interesting compromise of accuracy and computational cost.
- Analyzing the individual evolution of each phase using phenomenological multifluid formulations. This type of description is currently not included in state-of-the-art heat exchanger models. In the multiscale framework of the present work, these formulations constitute a microscopic level of analysis.

In short, the techniques developed in this work contribute to improve the current understanding on high-efficiency two-phase flow heat exchangers.

Chapter 13

Recommendations for future work

▶ As closing remarks for this thesis, some advices for future research are included here based on the individual discussion and analysis of results presented in the previous chapters. The possibilities for extending the scope and limitations of the present work are also discussed.

As reviewed in Chapter 2, although the generic problem of modeling and designing heat transfer equipment is rather old, a final state of research has not yet been achieved, particularly for cryogenic and two phase flow systems. Extensive previous investigations have been so far focused on the scale of interest, usually called macro-scale. In this context, this thesis represents a contribution to the present state-of-the-art in terms of a multiscale description. Further research is required at different levels in order to improve the understanding and predicting capabilities of current models.

In this chapter, the recommendations for future work derived from this thesis are classified into two groups. Section 13.1 deals with the lessons learned in this work, derived from the individual discussion presented in each chapter. Possibilities for extending the scope of this analysis are described in Section 13.2.

13.1 Lessons learned

Throughout this thesis, modeling and simulation results were analyzed within a three-scales framework: macro, meso and micro. In general, the macroscopic description is rather complete and further improvements should be focused on the lower-scale effects. In particular, medium-scale phenomena are discussed in Section 13.1.1, while Section 13.1.2 deals with some advices for further developing the microscopic description.

13.1.1 Regarding flow in multiple parallel channels

Part III (Chapters 7 and 8) deals with the flow distribution and mixing in parallel-channels geometries, including the analysis of a shell-and-tube case. Following a homogenization approach, this geometry was described in terms of layers, and an interesting discussion was presented in Sections 7.5 and 8.4. In particular, further research at both experimental and modeling levels is required in order to investigate the following aspects.

- The validity of the equal pressure drop boundary condition. This scenario is usually assumed in a steady-state operation. However, this approach disregards that, in practice, stationary conditions are usually not achieved and transient effects are always present. As studied in part III of this thesis, relaxing this condition and allowing for some differences in the pressure drop within a certain range, results in interesting flow mixing and distribution profiles with consequences in the thermal performance.
- An analysis of flow distribution devices (inlet and outlet headers) in diabatic two-phase flow applications. So far, current models are based upon single-phase or adiabatic gas-liquid flows. Therefore, it is not clear the effect of heat transfer along the tube length in the performance of the distribution manifolds. In particular, different heat loads to parallel channels might result in larger departure of the flow distribution from the design conditions.

13.1.2 Phenomenological description of boiling flows

This area is the subject of extensive research in many industries. In this section, the most relevant research paths postulated in order to improve the predicting capabilities for this particular applications are highlighted as follows.

- Development of constitutive relations applicable at the operating conditions relevant to heat exchangers in cryogenic and LNG processes. As discussed previously in Chapters 9 and 10, the evolution of gas-liquid flows in heat exchangers presents some differences respect to power-controlled systems. In particular, further research is required in these topics.
  - Instabilities in the liquid film leading to the occurrence of dryout. In general, this boiling crisis is dependent on both the local conditions and the historical evolution of the flow, and it is largely influenced by disturbance waves in the film-gas interphase.
  - Droplet-wall interaction in the post-dryout flow regime. After the occurrence of dryout, deposited droplets interact directly with the hot wall. Present models are based upon high-wall temperature data, since they correspond to experiments relevant to power-controlled systems.

In the case of a heat exchanger, however, the wall temperature does not present sharp variations and consequently these models should not be directly extended to low-temperature conditions.

  - Specific entrainment and deposition correlations for hydrocarbons. Both processes are strongly dependent on the surface tension, and present models are based mostly on adiabatic air-water and steam-water experiments, with much larger surface tension. Therefore, if the overall accuracy is to be improved, specific experimental information is essential.

- Describing the evolution of the droplet size following a population balance approach. Since most constitutive relations depend on the droplet diameter, an accurate description of the distribution of sizes accounting for breakup and coalescence effects, would result in a better phenomenological description of the flow evolution. However, the large uncertainties in the understanding of the effects detailed above, and the general lack of experimental information, discourage the inclusion of a population balance formulation at the current stage of analysis.

13.2 Extending the scope of this work

The scope and limitations of this thesis were presented in Section 1.3. Future activities related to expand the extent of this analysis include

- Incorporating time-dependent effects. An interesting example in this category is the cool-down transient, that is the startup of the process from room temperature to cryogenic conditions. The study of this case should include effects of thermal inertial and heat conduction in the wall material, which were hitherto neglected.

- A phenomenological description of condensing flows at a microscopic level. The micro-scale analysis in this thesis was focused on boiling flows. A similar formulations can be applied for condensation.

- Extending the present formulation from pure fluid to multicomponent mixtures, as those used in LNG processes. In order to do so, the different mass transfer mechanism for each individual component should be added to the phenomenological description presented in Chapters 9 and 10.

- Analyzing the applicability of the present analysis to other geometries different from round tubes. The present description only allows a generalization in terms of hydraulic and equivalent diameters, that is the relation of cross-sectional area to the wetted and heated perimeters, respectively. A more

detailed analysis should include other effects such as the fin efficiency in plate-fin heat exchangers.

Appendix

Appendix A

Publications

This appendix comprises the following articles.

Article 6. Pacio J.C. and Dorao, C.A. (2010) *A comparative analysis of computational models for solving one-dimensional heat exchangers problems.* Submitted to the International Journal of Refrigeration (under review). Page 339

Article 7. Pacio J.C. and Dorao, C.A. (2011) *A review on heat exchanger thermal hydraulic models for cryogenic applications.* Cryogenics **51**(7), pp. 366-379. doi:10.1016/j.cryogenics.2011.04.005. ..... Page 367

Article 8. Pacio J.C. and Dorao, C.A. (2011) *Modeling two-phase heat exchanger performance in the annular-mist flow regime considering entrainment and deposition phenomena.* In Proceedings of ASME-JSME-KSME Joint Fluids Engineering Conference 2011, July 24-29, 2011, Hamamatsu, Shizuoka, Japan. Paper ID: AJK2011-10013. ..... Page 383

Article 9. Pacio J.C. and Dorao, C.A. (2011) *Design considerations for the sizing of high-effectiveness two-phase flow heat exchangers.* In Proceedings of the 23rd IIR International Congress of Refrigeration, August 21-26, 2011, Prague, Czech Republic. Paper ID: 476. ..... Page 395

Article 1

Pacio J.C. and Dorao, C.A. (2009)

Application of high order methods for the simulation of heat exchanger models

In Skallerud, B. and Andersson, H.I. (Eds.): Mekit'09, Fifth national conference on Computational Mechanics, Trondheim 26-27 May 2009, Tapir Academic Press, pp. 341-351.

Application of high order methods for the simulation of heat exchanger models

Pacio, J., Dorao*, C.A.
Department of Energy and Process Engeering. Faculty of Engineering Science
Norwegian University of Science and Technology
e–mail: carlos.dorao@ntnu.no

Summary
Heat exchanger design and optimization is a computationally expensive task, since usually multiple simulations are carried out. Therefore, an efficient numerical solver is required. In this work a high order method is proposed as an alternative of the traditional finite difference method for reducing the computational time while improving accuracy. The analysis of a simple case with analytical solution shows that the computational time required for a suitable solution can be improved in more than one order of magnitude. In addition, the application of the method to practical cases is discussed.

Introduction

The problem of heat exchanger (HX) design consists in seeking a structure of tubes that provides the maximum heat transfer for a set of technical and environmental constraints. Evaluating each constraint demands solving a set of first-order ordinary differential equations (ODEs) for determining the heat exchanged between the hot and cold fluids in the HX. This problem can become very difficult since multiple streams in different directions may be involved. In addition, complicated mathematical models are required for the physical processes underlying the heat transfer when mixtures flow or phase change are present.

Liquefied Natural Gas (LNG), natural gas processing and CO_2 capture industries are rapidly growing worldwide. The development of energy efficient and enviromentaly friendly processes in these industries turn the attention focus on the HX modeling and design problem.

Heat exchanger design involves solving many times the set of ODEs, for different operating conditions, and changing the problem parameters in the optimization process. For this reason, in order to avoid excessive computational costs, it is important to use efficient numerical methods, i.e. with acceptable accuracy at low CPU time, for solving these equations.

The traditional numerical approach for this problem is based on Finite Difference Method (FDM) or Finite Volume Method (FVM) formulations. Each stream is divided into nodes and the solution is approximated by a first order polynomial between the nodes. These methods are very simple to implement and are widely used for HX simulation [11, 5]. Commercial FDM and FVM codes are available for computation fluid dynamics (CFD) analysis. However, generally hundreds of discretization points are required for a suitable solution, resulting in a high computational cost. Many times, the high computational costs typical of FDM and FVM cannot be avoided, even assuming the lost in accuracy, because the unconverged solution may present numerical oscillations and instabilities, and for this reason a large number of points are usually required [11, 5, 2].

Not as widely as FDM and FVM, Galerkin–based Finite Element Methods (FEM) have also been used for HX design [7, 4]. Each stream is divided in elements, and the solution is approximated by first–order polynomials in each element. In a weighted residual formulation, the original equation is not required to hold except only with respect to certain test functions. The main advantage is that they allow to model more complex geometries, but the convergence rate

is similar to FDM, therefore they're not appropriate when many simulations are required, as in the case of modeling and optimization.

For this reason, higher order approximations are being considered for HX modeling, in order to reduce the computational time. For example, S. Thyageswaran [9, 10] used the orthogonal collocation approach in his analysis, and Amon [1] used a high–order spectral method. The advantage of high–order methods is that the solution can be well represented with few discretization points, reducing considerably the size of the problem to be solved.

As an effort for reducing the computational costs, a high order least squares (LS) formulation is presented in this work as a numerical alternative for this problem. The basis idea in the LS is to minimize the integral of the square of the residual over the computational domain.

The structure of this work is as follows. In section the LS method is discussed. The HX modeling problem is presented in section . Numerical examples are presented in section . Finally in section the main conclusions of this work are discussed.

Heat exchanger model

Heat transfer in a HX usually occurs through a separating wall, since mass transfer between the streams is avoided. Heat losses to the surroundings and axial conduction are usually neglected, since these effects are not relevant for typical engineering accuracy requirements. With these approximations, a general steady-state energy balance may be formulated for every stream as follows:

$$\dot{m}_i \frac{\partial h_i}{\partial z_i} = \sum_{j=1}^{N_s} (UP)_{ij} \, (T_j - T_i) \tag{1}$$

where N_s is the total number of streams, and eq. (1) holds for $i = 1, .., N_s$ with proper inlet boundary conditions. $\dot{m}$ is the mass flow rate [kg/s], T is the temperature [K], h the specific enthalpy [J/kg] and z_i refers to the i^{th}–stream flow direction.

$(UP)_{ij}$ is the overall heat transfer coefficient (HTC) per unit length between streams i and j [$\frac{W}{Km}$]. In a quasi–steady state analysis, it can be computed as a combinations of thermal resistances. Fig. 1 shows a sketch of the simplest HX configuration, i.e. two streams in parallel flow, e.g. a tube–in–tube HX.

In this simple one–dimensional case for single–phase flow, eq. (1) becomes, in $\Omega = (0, L)$

$$\dot{m}_c c_{p,c}(z) \, \frac{\partial T_c}{\partial z} = (UP)(z) \, (T_h - T_c) \quad T_c(z = 0) = T_{c_0} \tag{2}$$

$$\pm \dot{m}_h c_{p,h}(z) \, \frac{\partial T_h}{\partial z} = -(UP)(z) \, (T_h - T_c) \quad T_h(z = z_0) = T_{h_0} \tag{3}$$

Both co–current and counter–current cases are represented by eqs. (2) and (3). In the first case $z_0 = 0$ and the '$+$' sign applies; $z_0 = L$ and the '$-$' sign correspond to the counter–current case. Since fluid properties (c_p) and the HTC depend on the temperature, iteration over these parameters is required for the general case. For this configuration, the HTC can be computed as:

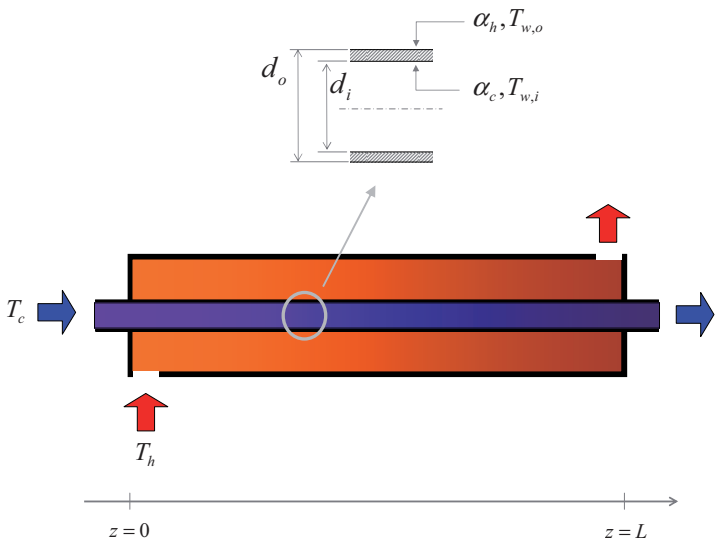

Figure 1: Parallel flow, two–streams tube–in–tube heat exchanger.

$$\frac{1}{UP} = \frac{1}{\pi d_o \alpha_h} + \frac{1}{\pi d_i \alpha_c} + \frac{log(d_o/d_i)}{2\pi\lambda_w} \tag{4}$$

The first two terms represent convective thermal resistance on the hot and cold side, respectively, being α $[\frac{W}{m^2K}]$ the convective HTC in each side. Generally, an empirical or semi–empirical correlation is used to compute α. The last term represent the wall–conduction thermal resistance, and λ_w is the wall material heat conductivity $[\frac{W}{mK}]$. Since α has a strong dependence on the fluid properties, an iterative solving is required.

Industrial tube type HX usually consist in an arrangement of hundreds of tubes. Therefore, a fully detailed simulation would require solving these equations hundreds of times. The usual approximation for avoiding this is to consider one [8] or a few representative tubes. The input data (flow rates, HTC, inlet temperatures) are selected as an average over all the tubes in the HX.

Analytical solutions for eq. (1) can only be found for simple cases with ideal conditions, i.e. single phase flow with constant thermo-physical fluid properties and constant HTC. Numerical simulations are then required for most practical applications.

The least squares formulation

The LSM is an interesting alternative to Galerkin–based methods which always leads to symmetric positive definite systems of equations which can be efficiently solved by standard iterative procedures.

The problem given by eq. (1) can be written as

$$\mathcal{L}\mathbf{u} = \mathbf{g} \quad in\ \Omega \tag{5}$$

$$\mathcal{B}\mathbf{u} = \mathbf{u}_\Gamma \quad on\ \Gamma \subseteq \partial\Omega \tag{6}$$

with $\mathcal{L} : X(\Omega) \to Y(\Omega)$ and $\mathcal{B} : X(\Gamma) \to Y(\Gamma)$ a partial differential operator and the boundary condition operator, respectively, being $X(\Omega)$ the space of functions $\Omega \to \mathrm{R}$. $\mathbf{g}$ and $\mathbf{u}_\Gamma$ are

known functions in Ω and Γ, respectively. The LSM consists in the minimization of the LS residual functional $\mathcal{J} : X(\Omega) \rightarrow \mathrm{R}$, defined as:

$$\mathcal{J}(\mathbf{u}) \equiv \| \mathcal{L}\mathbf{u} - \mathbf{g} \|^2_{Y(\Omega)} + \| \mathcal{B}\mathbf{u} - \mathbf{u}_\Gamma \|^2_{Y(\Gamma)} \tag{7}$$

It can be shown [3] that, if $\mathcal{L}$ and $\mathcal{B}$ are well–posed operators, both L^2 norms are equivalents, i.e. there are two positive real numbers C_1 and C_2 so that, for every $\mathbf{u} \in X(\Omega)$:

$$C_1 \| \mathbf{u} \|^2_{X(\Omega)} \leq \| \mathcal{L}\mathbf{u} \|^2_{Y(\Omega)} \leq C_2 \| \mathbf{u} \|^2_{X(\Omega)} \tag{8}$$

From eq. (8) it follows that

$$C_1 \mathcal{E}(\mathbf{u}^N) \leq \mathcal{J}(\mathbf{u}^N) \leq C_2 \mathcal{E}(\mathbf{u}^N) \tag{9}$$

with the the error functional $\mathcal{E}(\mathbf{u}^N)$ defined as $\mathcal{E}(\mathbf{u}^N) = \| \mathbf{u}^N - \mathbf{u}^A \|^2_{X(\Omega)}$, i.e. the difference between the numerical (N) and analytical (A) solutions. The minimization of $\mathcal{J}$ becomes, from a variational analysis:

$$\lim_{\epsilon \rightarrow 0} \frac{d}{d\epsilon} \mathcal{J}(\mathbf{u} + \epsilon\, \mathbf{v}) = 0 \quad \forall\, \mathbf{v} \in X(\Omega) \tag{10}$$

Eq. (10) results in the condition:

$$\mathcal{A}(\mathbf{u}, \mathbf{v}) = \mathcal{F}(\mathbf{v}) \quad \forall\, \mathbf{v} \in X(\Omega) \tag{11}$$

with

$$\mathcal{A}(\mathbf{u}, \mathbf{v}) = \langle \mathcal{L}\mathbf{u}, \mathcal{L}\mathbf{v} \rangle_{X(\Omega)} + \langle \mathcal{B}\mathbf{u}, \mathcal{B}\mathbf{v} \rangle_{X(\Gamma)} \tag{12}$$

$$\mathcal{F}(\mathbf{v}) = \langle \mathbf{g}, \mathcal{L}\mathbf{v} \rangle_{X(\Omega)} + \langle \mathbf{u}_\Gamma, \mathcal{B}\mathbf{v} \rangle_{X(\Gamma)} \tag{13}$$

Eq. (11) is the most general LS formulation and can be applied for lots of problems, but cannot be solved numerically, since $X(\Omega)$ is an infinite-dimensional space. A discretization is required, and this step consists in finding the solution in smaller space, i.e. finding $\mathbf{u}^N \in X^N(\Omega) \subseteq X(\Omega)$. The introduction of the boundary residual allows the use of spaces $X^N(\Omega)$ that are not constrained to satisfy the boundary conditions. Defining a set of basis $\mathbf{\Phi}_j$ for the space $X^N(\Omega)$, i.e. $X^N(\Omega) = span\{\mathbf{\Phi}_0, \ \ldots, \mathbf{\Phi}_P\}$, the approximate solution can be expressed as

$$\mathbf{u}^N = \sum_{j=0}^{P} u_j\, \mathbf{\Phi}_j \tag{14}$$

with P the approximation order. If $\mathcal{L}$ and $\mathcal{B}$ are both linear operators, we find a set of P+1 algebraic equations for u_j by introducing eq. (14) into eq. (11)

$$\mathbf{A}\bar{\mathbf{u}} = \mathbf{F} \tag{15}$$

with

$$\mathbf{A}_{ij} = \langle \mathcal{L}\mathbf{\Phi}_j, \mathcal{L}\mathbf{\Phi}_i \rangle_{X(\Omega)} + \langle \mathcal{B}\mathbf{\Phi}_j, \mathcal{B}\mathbf{\Phi}_i \rangle_{X(\Gamma)} \tag{16}$$

$$\mathbf{F}_i = \langle \mathbf{g}, \mathcal{L}\mathbf{\Phi}_i \rangle_{X(\Omega)} + \langle \mathbf{u}_\Gamma, \mathcal{B}\mathbf{\Phi}_i \rangle_{X(\Gamma)} \tag{17}$$

Solving eq. (15) for $\bar{\mathbf{u}}$ gives the numerical solution $\mathbf{u}^N$, and replacing it in eq. (7) we can find it's accuracy, even when no analytical solution if found.

Spectral finite element approximation

The computational domain Ω is divided into N_e non–overlapping sub–domains Ω_e, called spectral elements, such that

$$\Omega = \bigcup_{e=1}^{N_e} \Omega_e, \qquad \Omega_e \cap \Omega_l = \emptyset \quad e \neq l \tag{18}$$

Local basis $\mathbf{\Phi}_j^e$ are defined in each element Ω_e, and the overall numerical solution $\mathbf{u}^N$ is constructed by gluing the local approximations $\mathbf{u}_e^N$, i.e.

$$\mathbf{u}_e^N = \sum_{j=0}^{P} u_j^e \, \mathbf{\Phi}_j^e \Longrightarrow \mathbf{u}^N = \bigcup_{e=1}^{N_e} \mathbf{u}_e^N \tag{19}$$

Nodal basis

There is no constraint for choosing the basis $\mathbf{\Phi}_j$, and different sets can be used for different problems. Polynomials that interpolate the solution between certain points called nodes are usually chosen. The zeros of a Jacobi polynomial are usually chosen. The main advantage of this type of basis is that they provide a computationally efficient way to compute the integrals in eqs. (16) and (17). In this work,the Gauss-Legendre-Lobatto (GLL) quadrature sets $(\xi_q, w_q)^{GLL}$ to compute these integrals. In the reference domain $\hat{\Omega} = [-1, 1]$, they are approximated with the values of the function in Q+1 selected quadrature points ξ_q, as:

$$\int_{-1}^{1} f(\xi) d\xi \approx \sum_{q=0}^{Q} w_q f(\xi_q) \tag{20}$$

The weights w_q are the solution of the linear system:

$$\sum_{q=0}^{Q} w_q \xi_q^i = \int_{-1}^{1} W(x) x^i dx \quad for\ i = 0, ..., Q \tag{21}$$

The definition of w_q as the solution of eq. (21) means that eq. (20) is exact for $f \in \mathcal{P}^{2Q-1}$. In accordance to this quadrature set, the nodal basis are chosen as interpolants between the ξ_q points. For the GLL set, the proper basis are the Lagrangian interpolants. Figure 2 shows the 2^{nd} and 5^{th} order one–dimensional polynomials, as an example.

In the general case, $Q \neq P$, but all matrices become simpler if $P = Q$. In order for this LS spectral element formulation to make sense , the total number of residual equations must be equal or greater than the total number of unknown nodal values [3]. If the order of Gaussian quadrature (Q) is too low, the minimization problem becomes singular. On the other hand, Q should not be too high in order to avoid computational costs.

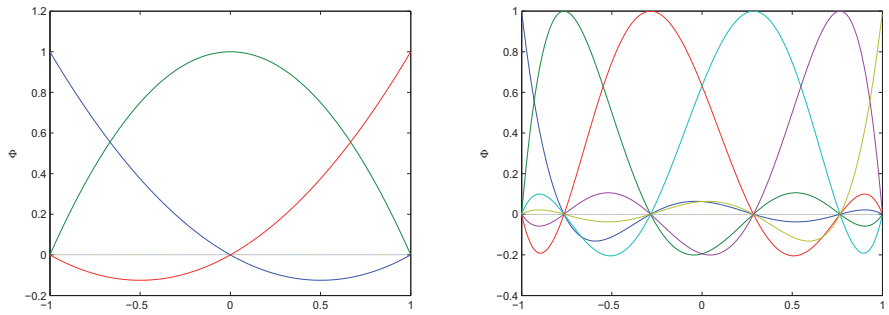

Figure 2: 2^{nd} and 5^{th} order Lagrangian interpolants in $\hat{\Omega} = [-1, 1]$

Numerical Examples

Simple case with analytical solution

As discussed in section , no analytical solution is required in order to test the LSM accuracy. It is required, however, if comparison against FDM is intended. For this reason the co–current case with constant parameters is presented here. The dimensionless analytical solution for this case is:

$$\theta_c^A = \frac{1}{r+1}(1 - e^{-a\tilde{z}}) \quad ; \quad \theta_h^A = 1 - \frac{r}{r+1}(1 - e^{-a\tilde{z}}) \tag{22}$$

with $\theta = \frac{T - T_{c_0}}{T_{h_0} - T_{c_0}}$ and $\tilde{z} = \frac{z}{L}$. Subscripts c and h stand for cold and hot, and $r = \frac{\dot{m}_c c_{p_c}}{m_h c_{p_h}}$ and $a = \frac{UPL}{\dot{m}_c c_{p_c}}(r+1)$ are properly defined dimensionless parameters. The asymptotic solution, for an infinetly large heat exchanger is $\theta_c^A = \theta_h^A = \frac{1}{r+1}$.

Since the parameter a determines how fast the temperature profile reaches the asymptotic solution, the numerical accuracy is expected to depend on this parameter. Figures 3 to 5 shows the solution and the LS convergence in terms of the total degree of freedom for $a = 0.2$, $a = 2$ and $a = 20$, respectively.

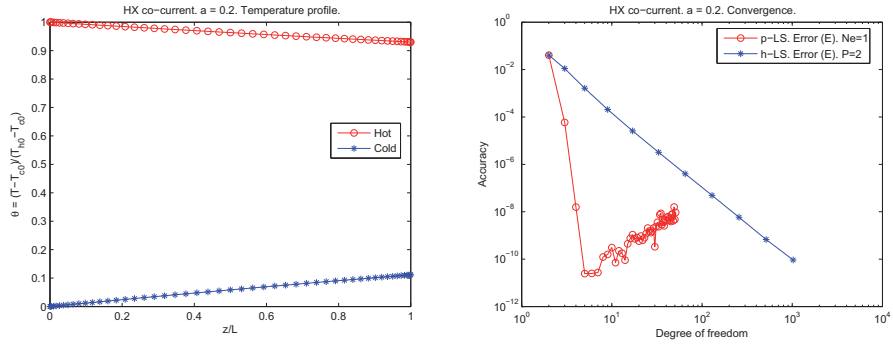

Figure 3: Solution and convergence for the co–current case. $a = 0.2$

A faster convergence rate is obtained for lower values of a, i.e. shorter heat exchangers. The reason for this is that, for larger values of a the temperature difference, which is the heat source

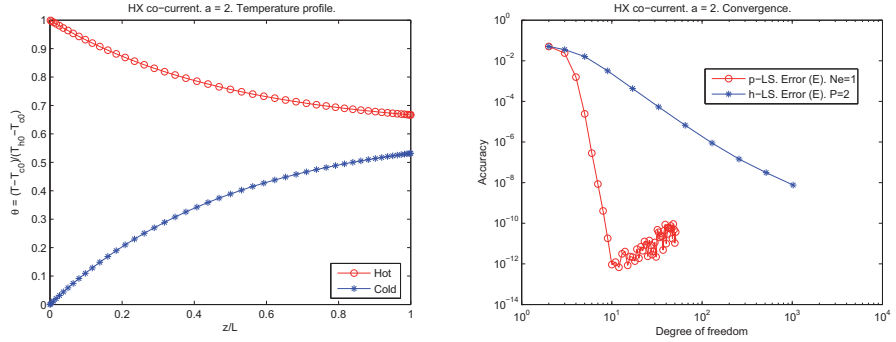

Figure 4: Solution and convergence for the co–current case. $a = 2$

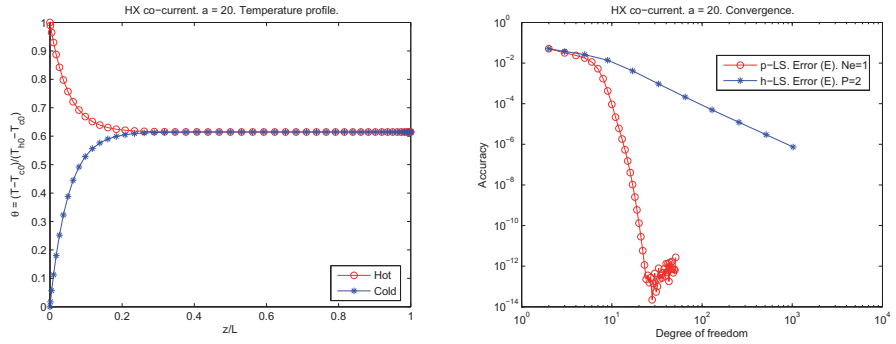

Figure 5: Solution and convergence for the co–current case. $a = 20$

for both streams, becomes very small. The *p*–LS approach convergence rate, i.e. changing the order of approximation at a fixed number of elements (in this case only one), is exponential, and this effect is not important since the computational precision ($\mathcal{E} \approx 10^{-10}$) is rapidly reached. In a *h*–LS approach, i.e. changing the number of elements at a fixed order of approximation (in this case P=2), the convergence rate is linear in a log–log plot, and the effect of a is important, since a high discretization is required for high values of a.

Figure 6 shows the convergence of the LS solution for $a = 1$, both in terms of $\mathcal{J}$ and $\mathcal{E}$, showing that they are equivalent for this particular case.

The interpretation of eq. (8) in these log–log plots, is that the $\mathcal{J}$ curve runs between two curves parallel to $\mathcal{E}$. A convergence analysis in terms of the total degree of freedom is shown in figure 7, comparing FDM and LSM.

As expected, in a log–log plot, the FDM shows a linear convergence, and the slope is proportional to the order of the approximation. The same tendency is observed in the *h*-LS approach, i.e. changing the number of elements at a fixed value of P, in this case P=3. The fastest convergence rate is found for the *p*-LS approach, i.e. changing the order of approximation at a fixed value of N_e, in this case only one element. In this case, when changing P, both the quadrature integral and the numerical solution are improved at the same time. The slope is then proportional to P and an exponential convergence rate is observed.

Since FDM usually leads to sparse–matrix sets of algebraic equations, it requires less computational time for solving systems of the same dof as the LSM. For this reason, the graph in figure

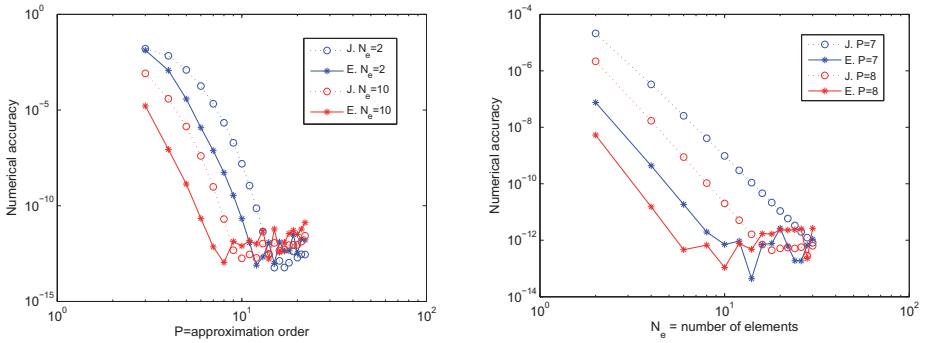

Figure 6: LS Numerical convergence in terms of $\mathcal{J}$ and $\mathcal{E}$.

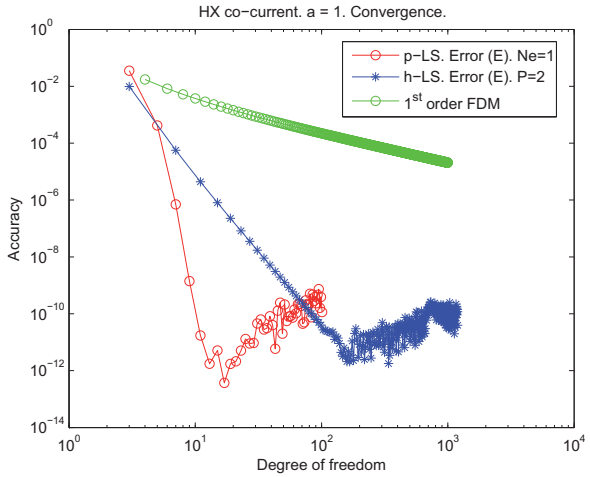

Figure 7: FDM and LS method convergence analysis.

7 shows the convergence tendencies, but is not good for comparing both methods. The overall figure of merit of the method is the numerical accuracy that can be obtained at a certain CPU time. This curve is presented in figure 8.

Figure 8 shows that, for low accuracies ($\approx 10^{-4}$), both FDM and LSM have similar computational costs, even though there is a large difference in the system's degree of freedom (see figure 7). The reason for this is that, in the LSM, the assembly of the problem matrix, i.e. computing the integrals in eqs. (12) and (13), takes a big part of the total CPU time. In fact, Proot [6] has shown that it may represent half the total computational cost.

Generally, better accuracy is required, and the CPU time required by FDM is much larger. This is because the convergence rate of the LS method is much faster, as shown in figure 7.

Single phase parallel flow two streams HX

In section a simple case with constant properties was studied. Of course, this is an idealized case, in general fluid properties and the HTC may change along the stream. In this section, the parallel flow of hot (outer tube) and cold (inner tube) water is studied. The proper correlations for the HTC in this geometry in forced–convection turbulent single–phase flow are Dittus Bolter

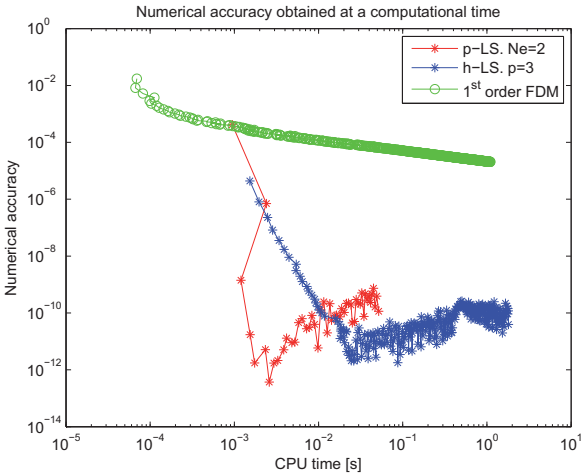

Figure 8: CPU time required for desired numerical accuracy.

for the inner tube (cold) and the Pethukov and Roizen for the outer one (hot):

$$Nu_c = 0.023 Re_c^{0.8} Pr_c^{0.3} \tag{23}$$

$$Nu_h = 0.023 Re_h^{0.8} Pr_h^{0.4}\ 0.86\ (\frac{d_e}{d_o})^{0.16} \tag{24}$$

with $Nu = \frac{\alpha}{d_h \lambda}$ the Nusselt number, $Re = \frac{\dot{m} d_h}{A\mu}$ the Reynolds number and $Pr = \frac{c_p \mu}{\lambda}$ the Prandtl number, being d_h the hydraulic diameter, d_e the external diameter, μ the dynamic viscosity and A the cross sectional area.

According to eqs. (23) and (24), the HTC depend on several fluid properties, and their dependencies on the temperature must be analyzed before tackling the numerical solving. Figure 9 shows how the water thermal conductivity and Prandtl number change with temperature. In the temperature range of interest (single phase liquid at atmospheric pressure) the Prandtl number changes in a factor 10, therefore iterative solving cannot be avoided. The pressure is assumed to be constant along the streams.

Figure 10 shows the dimensionless numerical solution for the counter–current cases for $a = 1$ and $a = 10$, solving with $P = 10$ and $N_e = 3$. This simple example shows that, in the HX design and optimization process, the problem ODEs must be solved several times, and that's the motivation for establishing an efficient numerical solver.

A convergence analysis in terms of $\mathcal{J}$ for the counter–current case is shown in figure 11. The fast convergence rate of the *p* approach shows that the problem is well–solved for $N_e = 3$ and $P = 10$.

Conclusions

A review on the numerical methods used for HX modeling was performed shows that FDM is the most widely used technique because of its simple implementation. The main drawback of nowadays methods is the high computational costs, that can be improved by using high order methods, and a high order least squares approach was proposed as an interesting alternative

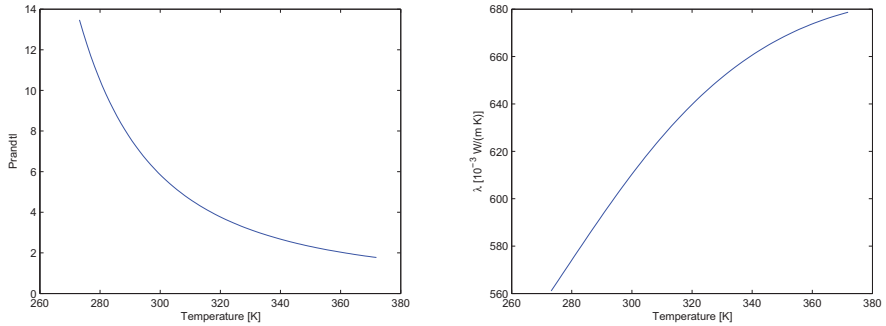

Figure 9: Water thermal conductivity (λ) and Prandtl number (Pr).

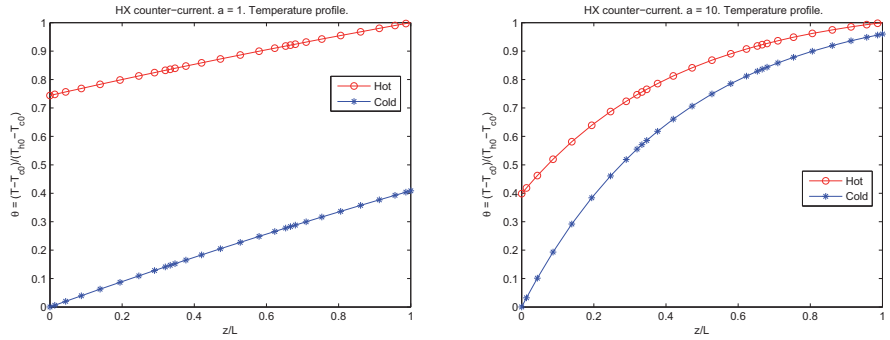

Figure 10: Counter–current numerical solution for a) $a = 1$ and b) $a = 10$.

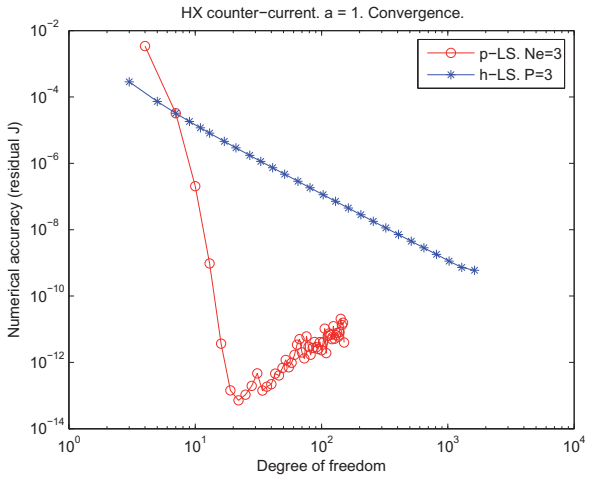

Figure 11: Convergence analysis in terms of $\mathcal{J}$ for counter–current case

An ideal case with analytical solution was studied and the different methods were compared. While FDM shows a linear convergence, the p-LS method convergence is exponential. Large differences are found in the CPU time required for a suitable solution.

Finally, the LSM was applied to a real one–dimensional case with variable properties. A simple change in one of the input parameters shows large differences in the temperature distribution, therefore multiple simulations are required at the design stage, and there relies the need for an efficient numerical method.

References

[1] C.Amon and B.Mikic Spectral element simulations of unsteady forced convective heat transfer: application to compact heat exchanger geometries *Numerical Heat Transfer Part A: Applications*, **vol.19**(1), 1–19, 1991.

[2] H.Jensen and S.Skogestad Optimal operation of a simple lng process *International Symposium on Advanced Control of Chemical Processes*, 2006.

[3] B.Jiang *The least-squares finite element method, theory and applications in computational fluid dynamics and electromagnetics* Springer, New York, 1998.

[4] Y.Kaptan and E.Buyruk Numerical investigation of fouling on cross-flow heat exchanger tubes with conjugated heat transfer approach *International Communications in Heat and Mass Transfer*, **vol.35**(9), 1153–1158, 2008.

[5] K.Nigam and M.Mridha Numerical studies of a tube-in-tube helically coiled heat exchanger *Chemical Engineering and Processing: Process Intensification*, **vol.47**(12), 2287–2295, 2008.

[6] M.Proot.

[7] G. A.Quadir and G. M.Krishnan Modeling of wire-on-tube heat exchangers using finite element method *Finite Elements in Analysis and Design*, **vol.38**(5), 417–434, 2002.

[8] R.Ribando and G.O'Leary General numerical scheme for heat exchanger thermal analysis and design *Computer Applications in Engineering Education*, **vol.5**(4), 231–242, 1997.

[9] S.Thyageswaran Analysis of multi-pass evaporators using orthogonal collocation *International Journal of Refrigeration*, **vol.31**, 204–216, 2008.

[10] S.Thyageswaran Thermo-hydraulic predictions for multi-pass evaporators by orthogonal collocation using a new flow pattern map *Applied Thermal Engineering*, **vol.29**(2–3), 601–606, 2009.

[11] Z.Li and M.Zheng Development of a numerical model for the simulation of vertical u-tube ground heat exchangers *Applied Thermal Engineering*, **vol.29**(5–6), 920–924, 2009.

Article 2

Pacio J.C., Dorao, C.A. and Fernandino M. (2009)

Sensitivity analysis of heat exchangers models using perturbation theory

In Hesthaven, J.S. and Rønquist, E.M (Eds.): Spectral and High Order Methods for Partial Differential Equations, Selected papers from the ICOSAHOM'09 conference, June 22-26, Trondheim, Norway. Volume 76 of Lecture Notes in Computational Science and Engineering. Springer-Verlag, Berlin Heidelberg. ISBN: 978-3-642-15336-5, pp. 275-282.

Is not included due to copyright

Article 3

Pacio J.C. and Dorao, C.A. (2010)

Numerical analysis of the effect of two-phase flow maldistribution on heat transfer performance

In Transactions of the American Nuclear Society, Vol. 102, pp. 599-600. 10-17 Jun 2010.

Numerical Analysis of the Effect of Two-Phase Flow Maldistribution on Heat Transfer Performance

Pacio, J.C. & Dorao, C.A.

Norwegian University of Science and Technology, Department of Energy and Process Engineering: Kolbjørn Hejes vei 1b, Trondheim, Norway, NO-7012, julio.pacio@ntnu.no

INTRODUCTION

In many scenarios the flow distribution can deviate from design conditions. A poor header design or off-specifications operating conditions, and channel blockage or size reduction due to differential thermal expansion are just some of the possible causes. This situation is more likely to occur (and in larger magnitude) in two phase applications, such as condensers, steam generators and boiling refrigeration channels. In these cases, phase stratification and two phase flow instabilities, e.g. Ledinegg or pressure drop instabilities, make the flow distribution control a challenging issue and can trigger flow excursions.

DESCRIPTION OF THE WORK

The objective of this work is to study the consequences on heat transfer performance. The pressure drop on different channels are not independent on each other, since usually they are connected by inlet/outlet plenums and, in some cases as shell side flow on heat exchangers, the connection is stronger, producing a net crossflow between channels as a consequence of local pressure and density differences. Since heat transfer and pressure drop are strongly coupled in two phase flow, heat transfer profiles are also expected to deviate from design, in most cases resulting in a reduction of refrigeration capacity, e.g. see fig 1.

Methodology

The underlying physical phenomenon has clearly a transient nature, since both plenums are connected by pressure waves. However, a complete model would results in overwhelming computational cost, since the wave velocity (speed of sound) shows large variations for two phase flow and is very dependent on the local void fraction.

For this reason, a steady state analysis is performed, i.e. the steady temperature and power profiles are searched after a given perturbation, such as maldistribution in the inlet conditions. The governing equations are then steady state one dimensional mass, momentum and energy balance equations for each channel considered. For this reason, similar channels are considered together as forming a group (substream).

Study case

The study case is for two phase heat exchanger applications, such as boilers and condensers, where one or all of the streams are going through phase change.

Extensive research has been done on single phase heat exchanger maldistribution [1], [2]. Two phase maldistribution has been widely studied for power controlled (given heat flux or wall temperature, as in subchannel analysis [3], [4]) or pressure drop driven systems (e.g. pump driven experiments where the test section represents the main contribution to pressure drop, [5]). However, none of these cases are representative of two phase heat exchangers, since in these applications the heat source depends on the flow rate, and the overall pressure drop is not fixed, adding one degree of freedom to the problem.

RESULTS

The following results belong to the simulation of a counterflow exchanger with boiling R134a and condensing propane. However, at this stage the results can be conceptually extended to any other working fluids.

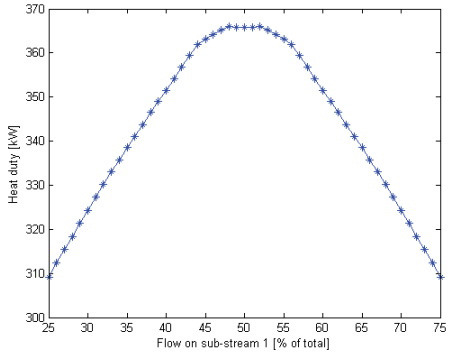

Fig. 1. Heat duty for different distributions of R134a.

Fig. 1 shows the effect of maldistribution when two groups of channels (i.e. substreams) are considered for the cold side. The heat duty (i.e. total powered transferred) is maximum when distribution is homogeneous.

Any deviation from homogeneous distribution results in a reduction of refrigeration capacity (or heating, depending on the application). This reduction is up to

15% for large maldistribution. Even larger maldistribution can be found in the case of two phase flow instabilities, when some channels can get almost dry.

REFERENCES

1. A.K.DWIVEDI & S.K.DAS. “Dynamics of plate heat exchangers subject to flow variations” *International Journal of Heat and Mass Transfer*, **50** (13-14), p. 2733-2743 (2007).
2. S.LALOT et al. “Flow maldistribution in heat exchangers”, *Applied Thermal Engineering*, **19** (8), p. 847-863 (1999).
3. N.E.TODREAS & M.S.KAZIMI. *Nuclear Systems II: Elements of Thermal Hydraulic Design*, Taylor & Francis, 1990.
4. J.YOO et al. “Subchannel analysis of supercritical light water-cooled fast reactor assembly”, Nuclear Engineering and Design, **237** (10), p. 1096-1105 (2007).
5. S.VIST & J.PETTERSEN, “Two-phase flow distribution in compact heat exchanger manifolds,” *Experimental Thermal and Fluid Science*, **28**, p. 209-215 (2004).

Article 4

Pacio J.C. and Dorao, C.A. (2010)

A study of the effect of flow maldistribution on heat transfer performance in evaporators

Nuclear Engineering and Design **240**(11), pp. 3868-3877.

Nuclear Engineering and Design 240 (2010) 3868–3877

Contents lists available at ScienceDirect

Nuclear Engineering and Design

journal homepage: www.elsevier.com/locate/nucengdes

A study of the effect of flow maldistribution on heat transfer performance in evaporators

Julio C. Pacio*, Carlos A. Dorao[1]

Department of Energy and Process Engineering, Norwegian University of Science and Technology, NO-7491 Trondheim, Norway

ARTICLE INFO

Article history:
Received 9 June 2010
Received in revised form 20 August 2010
Accepted 3 September 2010

ABSTRACT

The performance of a heat exchanger with parallel channels can be seriously affected by flow maldistribution. In two-phase flow applications, such as evaporators, this situation may lead to local dryout and off-specification products. However, due to the complexity of describing this effect, it is normally not considered in the design process.

Two models are proposed in this work for predicting the effect of maldistribution on performance. The first model neglects the interaction between channels, while the second one incorporates an equal pressure drop constraint. Both models analyze the geometry (shell-and-tube) in terms of radial layers. Here, the number of layers considered is irrelevant for the first model, while it affects the results of the second one.

All results were compared to a homogeneous reference case, and reduction of performance was noticed in all cases. The first model predicts unrealistic pressure differences at the outlet. This situation is controlled by the second model, which predicts a secondary maldistribution to fit the constraint that further reduces the performance. When both models are compared, the first one underestimates the reduction in performance roughly by half.

1. Introduction

Evaporators are widely used in industrial applications. In the power generation and thermal processing industries, they are used for vaporizing a heat-carrying fluid as in steam boilers. In addition, since boiling yields large heat transfer rates, evaporators play a major role in refrigeration processes.

The usual geometries (shell-and-tube, plate-type, tube-fin) use a parallel channels configuration, in order to accommodate a large heat-transfer area in a limited space. This allows the building of large capacity equipment within a reasonable size, but it also leads to problems related to flow maldistribution.

In many scenarios the flow distribution can deviate from design conditions, which is usually homogeneous. The possible causes include poor header design or off-specifications operating conditions, and channel blockage or size reduction due to differential thermal expansion or fouling. A comprehensive review on causes of maldistribution can be found in Mueller and Chiou (1988).

Single-phase maldistribution has been widely studied, both from a header design perspective (Bassiouny and Martin, 1984a,b; Wang, 2008) and its effect on thermal performance (Lalot et al., 1999; Srihari et al., 2005). A reduction in heat duty (defined as the total heat transfered) is found in all cases as a consequence of maldistribution. However, this effect is small (less than 5%) for most practical cases, with the exception of large-efficiency exchangers such as those used in cryogenic applications (Mueller and Chiou, 1988).

For two-phase applications, research has been focused on the flow distribution in manifolds, both experimentally (Vist and Pettersen, 2004) and by numerical modeling (Ahmad et al., 2009; Ablanque et al., 2010). The thermal performance analysis was limited to the effect of maldistribution on the single-phase streams, such as in condensers (Rabas, 1985; Bobbili et al., 2006) and evaporators (Timoney and Foley, 1994; Aganda et al., 2000; Chen et al., 2005). As in the single-phase case, a deterioration of performance is predicted in most situations, but there is some experimental evidence of an increase in thermal performance on air-heated evaporators (Timoney and Foley, 1994; Aganda et al., 2000).

These models are based on energy balances, assuming a given flow distribution, usually based on the model given by Bassiouny and Martin (1984a,b). An average temperature difference and heat transfer coefficient are considered in the single-phase case (Mueller

* Corresponding author. Tel.: +47 73593662; fax: +47 73591640.
E-mail addresses: julio.pacio@ntnu.no (J.C. Pacio), carlos.dorao@ntnu.no (C.A. Dorao).
[1] Tel.: +47 73598462.

0029-5493/$ – see front matter © 2010 Elsevier B.V. All rights reserved.
doi:10.1016/j.nucengdes.2010.09.004

Table 1
Nomenclature used in this work.

Nomenclature	
A	Cross-sectional area (m^2)
D	Tube diameter (m)
Dh	Hydraulic diameter (m)
f	Single-phase friction factor
f_{int}	Internal characteristic
f_{ext}	External characteristic
g	Gravitational acceleration (m/s^2)
G	Mass flux ($kg/m^2\,s$)
h	Specific enthalpy (J/kg)
L	Total tube length (m)
$\dot{m}$	Mass flow rate (kg/s)
p	Pressure (Pa)
Δp	Pressure drop (Pa)
R	Outer radius (J/kg)
q	Heat flux (W/m^2)
T	Temperature (K)
UP	Linear HTC (W/m K)
V	Velocity (m/s)
z	Axial position (m)
Greek symbols	
α	Local HTC ($W/m^2\,K$)
λ_w	Wall thermal conductivity (W/m K)
μ	Maldistribution parameter
ϕ	Two-phase multiplier
ρ	Density (kg/m^3)
τ	Shear stress (N/m^2)
Subscripts	
L	Liquid
V	Vapor
REF	Reference value
Superscripts	
S	Shell-side
T	Tube-side
MAX	Maximum value
AVG	Average value
TOT	Total value

and Chiou, 1988; Lalot et al., 1999). For two-phase flow this averaging becomes too cumbersome and a two-dimensional model is used instead (Bobbili et al., 2006).

Since no momentum equation is considered, pressure drop is generally computed *a posteriori*. This approach does not consider the coupling of channels at inlet and outlet headers and therefore gives misleading results. Since pressure drop must be the same for all channels, the flow distribution on the other stream is also affected, as has been experimentally noticed by Aganda et al. (2000). This secondary maldistribution is expected to affect the thermal performance.

The objective of this work is to study the relative importance of flow maldistribution in evaporators, and the coupling effect of interacting parallel channels. In order to do so, three study cases are considered. First, a homogeneous situation is studied which gives reference values for the performance. Second, a given flow maldistribution is assumed in one stream, and a homogeneous distribution in the other one, with no interaction between channels. Finally, an equal pressure drop constraint is considered and the flow redistribution on the secondary stream is studied.

The structure of this work is as follows. The multi-channel evaporator problem is introduced in Section 2, presenting the governing equations and their numerical treatment. The three study cases are presented in Section 3 and their results, in Sections 4–6. Analysis and discussion of these results are covered in Section 7, and final comments and conclusions are sketched in Section 8.

2. The multi-channel one-dimensional evaporator problem

In general, lots of geometries can be considered for heat exchangers which can include two or more streams (Shah and Sekulić, 2003). In particular, this work studies a two-streams shell-and-tube heat exchanger, sketched in Fig. 1.

The scope of this work is limited to practical situations that fit the following simplifying assumptions:

- A steady-state analysis is performed.
- All working fluid are single-component.
- Axial conduction, radiative heat transfer and heat leakage to the surroundings are negligible small.
- Mixing is not considered. This means that the parallel channels do not exchange mass and momentum.
- An elemental geometry can be identified where hot and cold stream exchange energy, and interaction with other channels is negligible. This is indicated for the chosen geometry in Fig. 1b.

The general modeling for the evolution of the streams is based on one-dimensional mass, momentum and energy balances for each channel j. However, with the above considerations, the mass-balance equation gives a trivial result, that is a constant flow rate in each channel. Then, the problem is governed by Eqs. (1)–(4) for each channel, which represent momentum and energy balances for both tube- and shell-side fluids. The nomenclature used in this work is listed in Table 1.

$$-\frac{\partial p_j^T}{\partial z} = G_j^T \frac{\partial V_j^T}{\partial z} + \frac{4\tau_j^T}{Dh_j^T} + \rho_j^T g \tag{1}$$

$$-\frac{\partial p_j^S}{\partial z} = G_j^S \frac{\partial V_j^S}{\partial z} + \frac{4\tau_j^S}{Dh_j^T} + \rho_j^S g \tag{2}$$

$$\frac{\partial h_j^T}{\partial z} + V_j^T \frac{\partial V_j^T}{\partial z} = \frac{q_j^T}{G_j^T A_j^T} - g \tag{3}$$

$$\frac{\partial h_j^S}{\partial z} + V_j^S \frac{\partial V_j^S}{\partial z} = \frac{q_j^S}{G_j^S A_j^S} - g \tag{4}$$

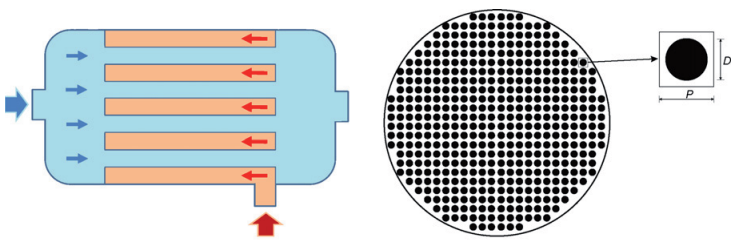

(a) Side wiew (b) Cross-sectional view

Fig. 1. Scheme of a multi-channels evaporator. Shell-and-tube geometry. (a) Side view and (b) cross-sectional view.

where G_j^T and G_j^S are constant at their inlet values. Both co-current (both streams flowing in the same direction) and counter-current (opposite directions) situations can be modeled by these equations with proper signs for the space derivatives. The acceleration term in Eqs. (1)–(4), and the coupling between enthalpy (h_j) and fluid properties, mainly the density (ρ_j) make the system non-linear and an iterative solution is required.

The inherent complexity of the governing equations leads to two practical approaches: design- and operation-oriented. A first approach, proper for design, is to consider only one channel for each stream, using design values for the problem parameters (Shah and Sekulić, 2003, chapter 3). The second approach, proper for an operational perspective, includes the modelling of large number of channels. In order to solve this problem within reasonable computational cost, some strong assumptions are usually made, e.g. fluid properties not affected by pressure drop, decoupling the momentum Eqs. (1) and (2) (Bobbili et al., 2006), and constant heat transfer coefficient (HTC) over wide ranges (Roetzel and Ranong, 1999).

These assumptions, however excessive for two-phase flow, are made for practical reasons, in order to avoid overwhelming computational cost. The traditional numerical approach for this problem is based on finite difference or finite volume methods. These formulations are simple to implement, but the convergence rate is not optimal. This means that lots of discretization points are usually required in order to get a suitable numerical solution (Li and Zheng, 2009; Kumar et al., 2008).

In this work, a least squares spectral elements method (Jiang, 1998) is used for solving the governing equations. It was selected due to its advantageous convergence rate. This method is based on error minimization and yields an exponential convergence for sufficiently smooth problems (Gerritsma and DeMaerschalck, 2010). Compared to the traditional method, this allows to improve the accuracy obtained at a given CPU time, and at the same time allows to reduce the computational cost when models with large relative errors are used. Then, with the use of a more efficient numerical solver, variables properties and heat transfer can be considered within reasonable computational cost.

Given that there is no local interaction between channels, all sets of Eqs. (1)–(4) are independent, and individual inlet boundary conditions are required. In addition, empirical or semi-empirical models for τ and q are required in order to solve these equations. The models used in this works are presented in the following subsections.

2.1. Frictional pressure drop models

The shear stress is modeled on the base of a two-phase multiplier, defined as $\phi = \tau/\tau_L$, and τ_L is computed on the base of a single-phase friction factor f_L, obtained according to the Haaland formula for smooth channels (White, 1986, chapter 5):

$$\tau_L = f_L \frac{G^2}{2\rho_L} \rightarrow \tau = \phi\tau_L \tag{5}$$

For single-phase liquid $\phi = 1$, and for single-phase gas $\phi = (f_V/f_L)(\rho_G/\rho_L)$. The correlation given by Friedel (1979) for ϕ is recommended by Whalley (1987) for using in the two-phase region.

2.2. Heat transfer models

Energy exchange is driven by temperature differences between both streams:

$$q_j^T = UP_j(T_j^S - T_j^T) \tag{6}$$

$$q_j^S = UP_j(T_j^T - T_j^S) \tag{7}$$

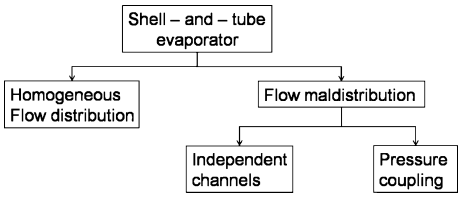

Fig. 2. Three study cases considered in this work.

where UP_j is the linear HTC between both streams for channels j. In a steady-state analysis, it can be computed on the base of thermal resistances (Incropera and DeWitt, 1996). Eq. (8) applies for the geometry shown in Fig. 1.

$$\frac{1}{UP_j} = \frac{1}{\pi D\alpha_j^T} + \frac{1}{\pi(D+2t)\alpha_j^S} + \frac{\ln(1+2t/D)}{2\pi\lambda_w} \tag{8}$$

with α_j^T and α_j^S the local HTC of the tube- and shell-side, respectively. They are computed with empirical or semi-empirical correlations. Several correlations were used in this work, for different enthalpy ranges.

For both streams in the single phase regions (liquid and gas) two correlations are used, depending on the range of Reynolds number: Petukhov–Popov for fully developed turbulent flow and Gnielinski for the transition regime (both (Ghiaasiaan, 2007)). The simplified version of the Gungor and Winterton correlation was used for boiling HTC and the one of Akers for condensation. Both are applicable in all the range $h_L \leq h \leq h_V$ and their use is recommended by Collier and Thome (1994, chaps. 7 and 10). In addition, the Kandlikar model for subcooled boiling (Kandlikar, 1997) is incorporated.

3. Study cases

Three study cases are considered in this work, depicted in Fig. 2. They include one case with homogeneous distribution in both streams, which is used as a reference for comparing further results. In addition, two cases with flow maldistribution in the tube-side are studied, according to two different models. First, no interaction between the channels is considered, and they are assumed to be independent. Finally, the second model incorporates an equal outlet pressure constraint that accounts for the pressure coupling in the headers.

3.1. Reference homogeneous case

The reference homogeneous case is completely defined by the geometry, the working fluids and the operating conditions. The geometry consists on 600 tubes, 8.0 mm in diameter and 5 m in length, in a square-lattice array with 10.4 mm pitch. Counter-flow of condensing propane in the tube-side (entering at 290 K and 7 bar) and boiling R134a in the shell side (280 K, 4 bar) is studied and the total mass flow rates are 1.24 and 2.31 kg/s, respectively.

The results for this case are shown in Section 4.

3.2. Cases with flow maldistribution

In this work, a simple approach to modeling of flow maldistribution is proposed. As an intermediate situation between an homogeneous case and the individual modeling of each channel, those with similar flow rate are grouped together, and the exchanger is modeled on the base of several of these groups. In particular, axial symmetry is assumed and N radial layers are considered, as illustrated in Fig. 3.

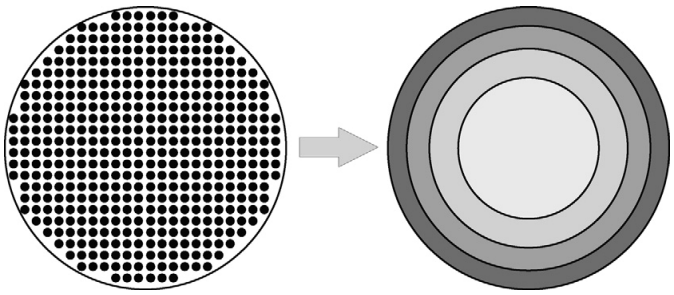

Fig. 3. Modelling of flow maldistribution. N radial layers.

For simplicity, equal cross-sectional area layers are considered, and each of them represent the same number of channels. This is done by defining the outer radius of each layer j, denoted R_j, as follows:

$$R_j = R_{shell}\sqrt{\frac{j}{N}} \tag{9}$$

In order to extend the analysis to maldistributed cases, individual inlet boundary conditions are required. This means that both a flow distribution profile and a parameter that quantifies the deviation from the homogeneous case must be define first.

The model given by Bassiouny and Martin (1984a,b) is commonly used for flow distribution in parallel-channels systems. This model identifies the header design as the main cause for maldistribution, and proposes two types of profiles: *cos*-type and *cosh*-type. In addition, a parameter given by the headers geometry is used for quantifying the deviation from the homogeneous case. However, this model was developed for plate heat exchanger headers with lots of parallel channels, and its not applicable for this work, where another geometry is analyzed and few layers are considered.

In this work, the causes of the maldistribution are not studied, and the chosen parameter is simply the maximum relative deviation from the average mass flux, i.e.:

$$\mu = \frac{G^{MAX} - G^{AVG}}{G^{AVG}} \tag{10}$$

In addition, a parabolic radial distribution of mass flux is proposed as:

$$\frac{G(r)}{G^{AVG}} = 1 + \mu\left[1 - 2\left(\frac{r}{R_{shell}}\right)^2\right] \tag{11}$$

By integrating the mass flux in each layer j, a linear profile is obtained for the mass flow rate as:

$$\dot{m}_j = \frac{\dot{m}^{TOT}}{N}\left[1 + \mu\left(1 - \frac{2j-1}{N}\right)\right] \tag{12}$$

where the layers are numbered from inside to outside.

In a maldistributed case, Eqs. (1)–(4) must be solved for each channel j. Within this framework, two different cases were studied, developed in the following subsection.

3.2.1. 1st maldistribution model. Independent channels

This case consists on evaluating the governing equations for each layer, with individual initial boundary condition according to the flow distribution profile proposed in Eq. (12). Then, all channels are assumed to be independent on each other and no interaction is considered. The results for this case are presented in Section 5.

3.2.2. 2nd maldistribution model. Pressure-coupled channels

This third study case accounts for the coupling between channels. Since all layers are connected at both inlet and outlet headers, the steady-state pressure drop must be the same for all of them. Then, this model includes a homogeneous shell-side pressure drop constraint, given by Eq. (13).

$$\Delta p_j^S = \text{constant} = \Delta p^S \qquad \forall j \in \left\{1, \ldots, N\right\} \tag{13}$$

In order to incorporate this situation, some other conditions must be relaxed. As a consequence of this constraint, the shell-side mass flow is expected to redistribute. Then, the shell-side mass flow on each layer $\dot{m}_j^S$ cannot be known *a priori*. This makes a total of $N+1$ unknowns: the pressure-drop level Δp^S and N values for $\dot{m}_j^S$.

The same number of equations are required for solving the system. A steady-state solution for Δp^S and $\dot{m}_j^S$ is reached when the pressure drop in the channels is the same as that provided by the pump or other differential-pressure flow driving device. In other terms, this is when the internal and external characteristics Δp vs. $\dot{m}$ curves intersect.

The internal characteristic pressure-flow relation f_{int} is dependent on the heat flux, given by the tube-side flow. This gives N equations as:

$$\Delta p^S = f_{int}(\dot{m}_j^S, \dot{m}_j^T) \qquad \forall j \in 1, \ldots, N \tag{14}$$

This function represents the response of the system, in terms of Δp^S, to variations in both mass flows. This internal characteristic is further studied in Section 6.

The external characteristic Δp vs. $\dot{m}$ relation f_{ext} does not take into account the parallel-channels configuration and only considers the total mass flow rate. This is expressed as:

$$\Delta p^S = f_{ext}\left(\sum_{j=0}^{N} \dot{m}_j^S\right) \tag{15}$$

Three extreme functional forms for f_{ext} are sketched in Fig. 4. On the one hand, if a high and low pressure tanks are used, the pressure difference in the equipment is independent of the flow. On the other hand, if the exchanger is part of a large system where other components dominate the total pressure drop, the mass flow rate can assumed to be constant, as given by the previous process. An intermediate situation is found when a pump is used as a driving force and the pressure drop is given mainly by the exchanger.

The constant mass flow rate situation was selected in this work, because it is considered to be applicable to a large number of practical situations. The results for this study case are presented in Section 6.

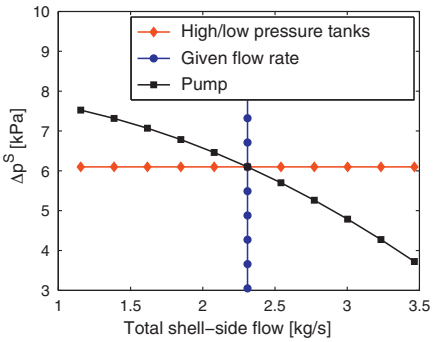

Fig. 4. Three cases of external characteristic Δp vs. $\dot{m}$ relations

4. Results for the homogeneous case

The mathematical model developed in Section 2 is applied in this section to a homogeneous case without flow maldistribution. Then, since all channels are identical, the governing Eqs. (1)–(4) are solved only once.

The profile solutions for this reference case are illustrated in Fig. 5. It should be noticed that, since a counter-flow arrangement is considered, the shell-side fluid enters the exchanger in the position $z=0$, and the tube-side inlet is located in $z=L$, i.e. $z/L=1$. The results for momentum and energy equations are shown in terms of (a) temperature and (b) dimensionless pressure (p/p^{IN}) profiles, respectively.

The roughly horizontal lines in Fig. 5a correspond to saturation temperature. As a consequence of pressure drop, there is a slight temperature drop during phase change, more notable for the shell-side fluid. This figure also indicates that the propane (tube-side) reaches full condensation, and R134a (shell-side) is fully evaporated. In addition to the profile solutions, some integral results are of interest for quantifying the performance. In particular, three responses are studied in this work:

- Heat duty, defines as the total heat transfered and computed by:

$$Q = \sum_j \int_{z=0}^{z=L} UP_j (T_j^T - T_j^S)\, dz \tag{16}$$

The reference value for the duty is $Q_{REF} = 449.92$ kW

- Tube-side pressure drop: the reference value is $\Delta p^T_{REF} = 3.184$ kPa
- Shell-side pressure drop: the reference value is $\Delta p^S_{REF} = 6.161$ kPa

The effect of maldistribution on performance is evaluated in the following sections in terms of these three integral results.

5. Results for the uncoupled-channels case

The first approach for evaluating the effect of maldistribution consists in solving the governing Eqs. (1)–(4) for each layer. In particular, tube-side maldistribution is considered according to the linear distribution profile given by Eq. (12), and a homogeneous distribution is assumed for the shell-side.

For simplicity, a case with 2 layers is considered first, and its then extended in a parametric study to N layers. The profile solutions for the case with 2 layers and $\mu^T = 0.2$ are displayed in Fig. 6, where the tube-side (in red) is warm and the shell-side (in blue) is cold. According to Eq. (12), this situation means that 55% of the total flow, i.e. 0.682 kg/s, go through the inner layer, and 45% of the total (0.558 kg/s) in the outer layer.

Flow maldistribution in the tube-side affects both the momentum and energy equations on this stream. In the first equation, a higher flow rate yields larger pressure gradient, as Fig. 6b indicates, since the tube-side pressure in the inner layer is always lower than in the outer layer. As a consequence, both layers have different outlet pressure. Although all channels are connected at both inlet and outlet plena, pressure differences in the outlet on tube-side are allowed, since they can be the original cause of flow maldistribution, as identified in Mueller and Chiou (1988).

The effect of flow maldistribution in the energy equation is that the variations in the specific enthalpy (h) are smaller for a higher flow rate. As a consequence, the fluid in the inner layer exits at saturation temperature in $z=L$; while full condensation is reached in the outer layer and the propane is subcooled at the exit.

Tube-side flow maldistribution also affects the evolution of the shell-side fluid, through heat transfer. A higher tube-side flow rate gives a higher HTC and this represents a higher heat source to the shell-side fluid. This is reflected in both temperature and pressure profiles.

Some differences in the outlet temperature of the shell-side fluid can be noticed in Fig. 6a. The inner-layer fluid exits as super-heated vapor at $z=0$, while the outer-layer is at saturation temperature. In fact, different amount of heat is transfered in each layer. These partial duties are:

$$Q_1 = \int_{z=0}^{z=L} UP_1 (T_1^T - T_1^S)\, dz = 226.50\ \text{kW} \tag{17}$$

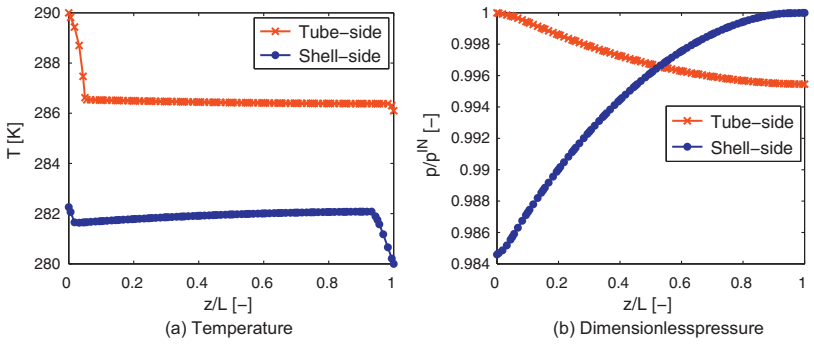

Fig. 5. Profile solutions for the reference case. (a) Temperature and (b) dimensionless pressure.

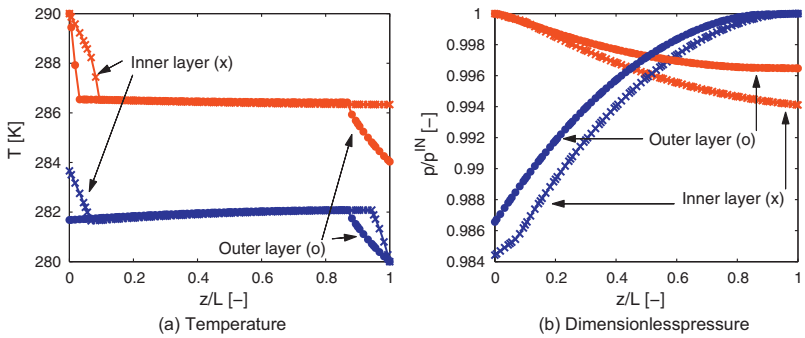

Fig. 6. Profiles for the uncoupled-channels case. $N = 2$ and $\mu^T = 0.2$. (a) Temperature and (b) dimensionless pressure.

$$Q_2 = \int_{z=0}^{z=L} UP_2(T_2^T - T_2^S)\,dz = 205.64\,\text{kW} \tag{18}$$

This makes a total heat duty of $Q = 432.14$ kW. This value is 17.78 kW (3.95%) lower than the reference value. The reduction in heat duty is further studied in a parametric analysis below.

The shell-side pressure profile is also affected, since a higher heat source increases the vapor content, producing a higher pressure gradient, as Fig. 6b indicates. As a consequence, both layers present a different pressure drop:

$$\Delta p_1^S = 6.231\,\text{kPa} \tag{19}$$

$$\Delta p_2^S = 5.373\,\text{kPa} \tag{20}$$

In this case, the difference in pressure drop cannot be explained by the maldistribution, since the flow distribution in the shell-side is homogeneous. At first sight, equal pressure drop is expected in steady-state because they are connected at inlet and outlet. However, there is experimental evidence (Chandraker et al., 2002) of pressure differences in the outlet header in the order of ρV^2. Nevertheless, in this case the pressure differences (0.858 kPa) are larger than this expected values, since $\rho_1 V_1^2 = 0.251$ kPa and $\rho_2 V_2^2 = 0.094$ kPa.

This model is extended to N layers and a parametric study of μ^T is performed. The evolution of the heat duty, and the differences in shell-side pressure drop are illustrated in Fig. 7. A maximum tube-side flow maldistribution of $\mu^T = 0.4$ was considered. Pressure differences in the tube-side outlet are not analyzed.

According to Fig. 7a the number of layers considered (N) has no effect on the prediction of performance, since all three curves overlap within the numerical accuracy. This is a logical and expectable result, since the different layers are considered as independent sets of tube-side and shell-side streams, and no heat exchange between layers is considered.

This is not the case of Fig. 7b, in which the differences in shell-side pressure drop are dependent on N. Pressure drop is dependent on mass flow rate (considered constant on shell-side) and heat flux. In a heat exchanger, the heat flux is related to temperature differences and mass flow rates on both sides. Therefore, the differences in Δp^S are a consequence of the differences in $\dot{m}^T$. According to Eq. (12), the relative differences in tube-side mass flow rate are proportional to $1/N$. This is reflected as an asymptotic behavior in Fig. 7b, since these differences become negligible for large values of N.

The parametric effect of rising μ^T is an increase in the differences between layers. This is reflected in the performance as a reduction of heat duty in all cases, with a maximum reduction of 39.44 kW, i.e. 8.77% of the reference value.

The differences in Δp^S also increase with μ^T, and they result much larger than the value of $\rho V^2 \approx 0.25$ kPa that is to be expected as steady-state pressure differences inside the header. In short, these differences cannot be allowed by a steady-state model, and this situation is the motivation for the analysis of a third study case, whose results are presented in Section 6.

6. Results for the pressure-coupled channels model

The large differences in outlet pressure predicted by the independent-channels model lead to the analysis of this final case where an equal pressure drop constraint is considered.

The analysis of this case includes a study of the internal characteristic response of pressure-drop vs. flow rate for this exchanger, illustrated in Fig. 8. Fig. 8a presents a map for this internal charac-

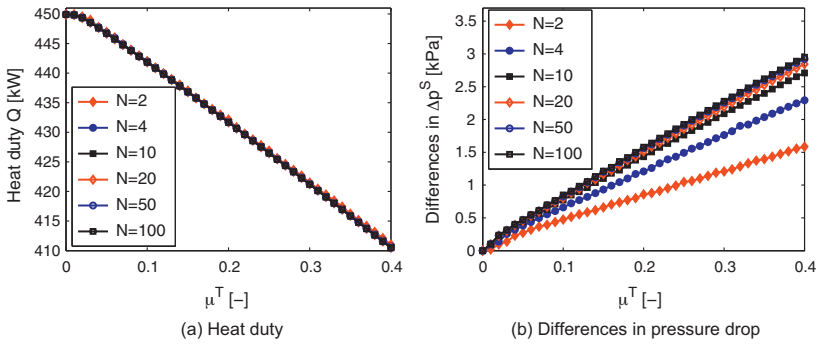

Fig. 7. Parametric study of μ^T for the independent-channels case. (a) Heat duty and (b) differences in pressure drop.

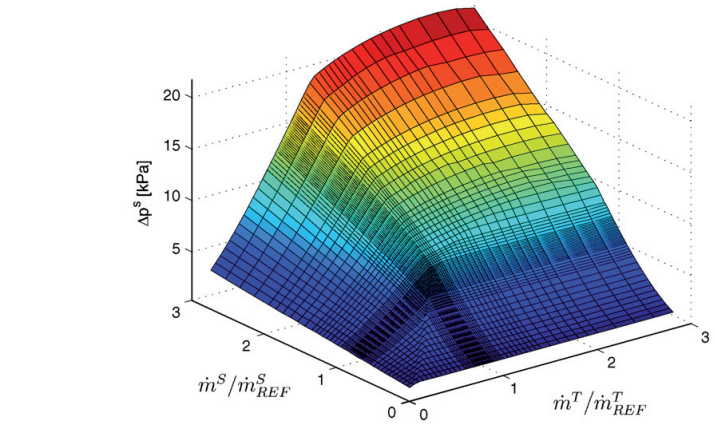

(a) Internal characteristic map for shell-side pressure drop

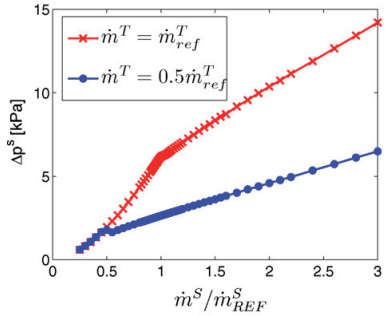

(b) Δp^s at constant values of $\dot{m}^T$

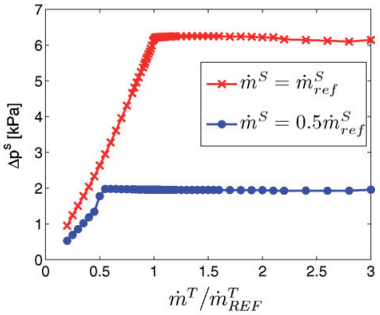

(c) Δp^s at constant values of $\dot{m}^S$

Fig. 8. Internal characteristic evolution Δp^S for $\dot{m}^S$ and $\dot{m}^T$. (a) Internal characteristic map for shell-side pressure drop, (b) Δp^S at constant values of $\dot{m}^T$, and (c) Δp^S at constant values of $\dot{m}^S$.

teristic f_{int}, defined in Eq. (14), obtained by solving the governing Eqs. (1)–(4) in a parametric study for $\dot{m}^S$ and $\dot{m}^T$. Higher resolution is shown around the reference values. In addition, planes at constant values of $\dot{m}^T$ and $\dot{m}^S$ are shown in Fig. 8b and c, respectively.

According to Fig. 8b, for some values of $\dot{m}^T$ (that represents the heat flux for shell-side), a slightly N-shaped curve is noticed. In particular, this is noticed for $\dot{m}^T = 0.5\dot{m}^T$ and values of $\dot{m}_S/\dot{m}_S^{REF}$ around 0.5. This gives three values of flow rate for the same pressure drop, and may lead to Ledinneg instability (Kakaç and Bon, 2008) if the system operates in the region with negative slope. It also represents a possible cause for flow maldistribution on the shell-side, since different layers can have the same pressure drop with different flow rate.

The effect of increasing $\dot{m}^T$ on Δp^S, sketched in Fig. 8c, is related to the increase in heat flux. This increases the vapor content, which gives a larger pressure drop. When full evaporation is reached, Δp^S remains roughly constant, since the shell-side fluid exits the exchanger almost at the tube-side inlet temperature, and the heat flux is not further increased.

With all these considerations, this model can be solved according to the following procedure.

1. Given the tube-side flow distribution $\dot{m}_j^T$, a set of N curves Δp^S vs. $\dot{m}_j^S$ can be obtained from Eq. (14) or Fig. 8. Some examples are indicated in Fig. 8b.
2. These curves can be added and develop a Δp^S vs. total mass flow curve that represents the internal characteristics of the exchanger.
3. This last curve is then intersected with the external characteristic, in this case, a constant flow line. This intersection gives the solution for the values of Δp^S and the total shell-side flow
4. Finally, once the value of Δp^S is known, the shell-side flow distribution can be evaluated from the individual Δp^S vs. $\dot{m}_j^S$ curves obtained in the first step.

This procedure was first applied to a case with $\mu^T = 0.1$ and $N = 10$ layers, and later extended in a parametric study. The results for this first case are illustrated in Fig. 9, which indicates the shell-side flow distribution and the temperature profiles for the inner ($j = 1$) and outer ($j = N$) layers.

According to Fig. 9a less shell-side flow goes through the inner layer than in the others. This most inner layer has a higher tube-side flow than the other, which represents a higher heat flux. This situation increases the vapor content on the inner layers, and the opposite occurs in the outer layers. This result can also be appreciated in Fig. 9b, that shows fast full evaporation on the shell-side for the inner layer, while in the outer layer, the shell-side fluid exits at saturation temperature in $z = 0$.

This secondary flow maldistribution affects the performance, giving a reduction of heat duty of 33.35 kW, i.e. 7.41% of the reference value. This reduction is roughly twice as large as the one

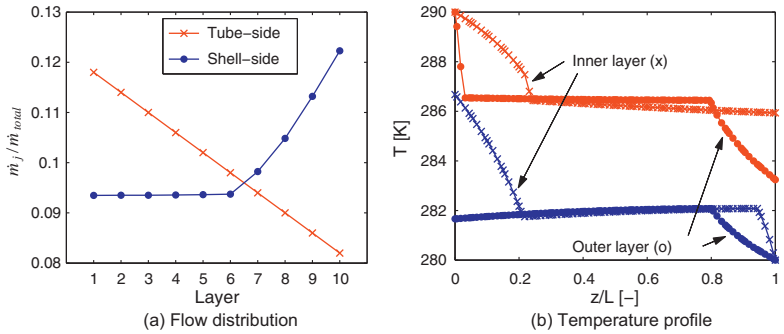

Fig. 9. Results for the coupled-channels case. $N = 10$ and $\mu^T = 0.2$. (a) Flow distribution and (b) temperature profile.

predicted by the independent-channels model presented in Section 5. Further discussion about the differences between the models is covered in Section 7.

In addition, the shell-side pressure drop is also affected by this flow re-distribution, resulting in $\Delta p^S = 5.595$ kPa, i.e. 9.19% lower than the reference value for the homogeneous case. This result can be explained by analyzing the internal characteristic pressure drop curves presented in Fig. 8. At a fixed value of shell-side flow, e.g. $\dot{m}^S = \dot{m}^S_{REF}$, Fig. 8c shows the dependence of Δp^s on $\dot{m}^T$. A reduction of 10% on $\dot{m}^T$ from the reference value, produces a reduction on Δp^S of 0.788 kPa, while an increase of 10% produces a much smaller change in Δp^S, increasing it in 0.071 kPa. The differences in shell-side pressure drop are fixed by re-distribution of shell-side flow, and Δp^S is stabilized to a value between both extremes. Since the effect of reduction of Δp^S is larger, the final value is lower than the original reference value.

The evolution of both streams is coupled by heat transfer, and for this reason the flow redistribution on the shell-side has a feedback effect on the tube-side. This situation is reflected in Fig. 9b as a noticeable temperature glide during condensation in the inner layer. This is a consequence of a large pressure drop, originated by a larger $\dot{m}^T_j$ and a lower $\dot{m}^S_j$, which produces less condensation and then increases the vapor content. In fact, there are large differences in the tube-side pressure drop, with $\Delta p^T_1 = 11.761$ kPa and $\Delta p^T_N = 1.983$ kPa, i.e. roughly 6 times larger in the inner layer. However, a deep analysis of pressure differences on the tube-side must take account of the original causes of maldistribution, which escapes the scope of this work.

A parametric study of the effect of rising μ^T on the reduction of heat duty and shell-side pressure drop is illustrated in Fig. 10 for different number of layers.

An increase in μ^T, thus increasing the maldistribution, results in a larger reduction of heat duty, giving a maximum reduction of 72.84 kW, i.e. 16.19% of the reference value. The shell-side pressure drop is also reduced, with a minimum value of 4.924 kPa, 20.08% lower than the reference value. This last result should be considered for checking the previous assumption of total mass flow as independent of the value of Δp^S.

Both Fig. 10a and b indicate that the results depend on N. When few layers are considered (e.g. $N = 2$), each of them represent an average over a large area (half of the channels), and the differences between them are dumped by the averaging procedure. When a larger number is considered, these differences are taken into account. Then, since the reduction of duty is a consequence of these differences, a larger reduction is noticed. An asymptotic behavior is appreciated in both figures, since the differences between the curves become negligible for large values of N.

7. Analysis of results

Although both maldistributed cases predict a reduction of heat duty with maldistribution, they differ in the magnitude of this effect. The results from the first model (independent channels) are not realistic, since they predict large differences in the shell-side outlet pressure. The second model (coupled channels) incorporates this constraints and therefore gives more reliable results.

However, this last model involves the large computational cost of developing the internal characteristic pressure drop map of Fig. 8. Then, it is interesting to quantify these differences, in order to conclude if the first model is applicable in any range.

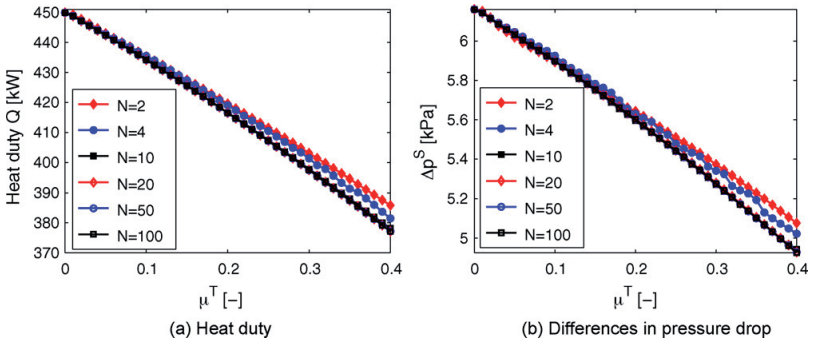

Fig. 10. Parametric study of μ^T for the coupled-channels case. (a) Heat duty and (b) differences in pressure drop.

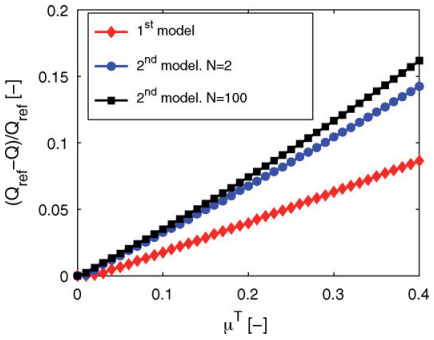

Fig. 11. Prediction of reduction in heat duty for both models.

7.1. Prediction of reduction in performance

The prediction of reduction in Q of both models is compared in Fig. 11 in a parametric study of μ^T. Since the second model is dependent on N, two extremes curves are shown: $N = 2$ and $N = 100$.

If we consider the second model with $N = 100$ as the most reliable results, the first model under-predicts roughly by half the reduction of heat duty. In fact, the average ratio of performance reduction is:

$$\text{average}\left(\frac{Q_{ref} - Q_{2^{nd}\,model,N=100}}{Q_{ref} - Q_{1^{st}\,model}}\right) = 2.0955 \quad (21)$$

This means that the prediction of reduction in performance given by the most reliable result is, in average, 110% larger than the one predicted by the first model. This ratio is lower at large maldistributions, with a minimum value of 1.84. Nevertheless, this minimum value is still very high, which indicates that the first model should not be used for predicting the reduction of performance because it largely underestimates it.

7.2. The effect of the number of layers

On the one hand, the first model considers the different layers to be independent on each other. On the other hand, the second model studies the coupling between layers, and the results are dependent on N, presenting an asymptotic behavior. As Fig. 10 indicates, the same trend is found for any number all layers. This means that the simple model with few layers is representative of the heat exchanger.

When more layers are considered, the effect of maldistribution is studied in more detail and a larger reduction of duty is noticed. The average ratio of this prediction of reduction by the model with $N = 100$ and $N = 2$ is:

$$\text{average}\left(\frac{Q_{ref} - Q_{2^{nd}\,model,N=100}}{Q_{ref} - Q_{2^{nd}\,model,N=2}}\right) = 1.1315 \quad (22)$$

In other words, the model with $N = 100$ predicts a reduction of heat duty 13.15% larger than the model with $N = 2$, in average. This ratio has a minimum value of 1.068 for $\mu^T = 0.06$, and then it increases with μ^T. In short, the second model with $N = 2$ also underestimates the reduction of performance, but the difference is quite small, especially for intermediate values of μ^T.

8. Conclusions

Previous works on maldistribution in heat exchangers predict a reduction in performance, although it is usually considered to be negligible (Mueller and Chiou, 1988). For two phase applications, the analysis has been limited to the effect of flow maldistribution on the single phase streams, such as in condensers and evaporators. However, these models do not take into account the impact on the momentum equation, which can not be neglected, since all channels are connected by inlet and outlet headers.

An homogeneous reference case was studied and then it was extended to cases with tube-side maldistribution according to two different models. Both of them consider the chosen geometry (shell-and-tube) in terms of radial layers. This approach allows to represent the exchanger with few layers, instead of considering all the channels individually. For extension to maldistributed cases, a maldistribution profile and parameter μ were proposed. A parametric study of μ was performed for both models.

A first model for flow maldistribution considers the different layers as independent. It predicts a reduction of performance in all cases. However, large outlet pressure differences on the shell-side are noticed, which is unrealistic for a steady-state analysis.

This situation is considered by the second model, which incorporates a constant pressure drop constraint. This leads to a flow redistribution in the shell-side, given by the solution of both internal and external characteristic curves for Δp vs. $\dot{m}$. This flow redistribution further decreases the performance. The results of this second model are affected by the number of layers considered, showing and asymptotic behavior.

Considering the second model with large number of layers as the most reliable result, the first model underestimates the reduction of performance roughly by half, which makes its use inappropriate. In addition, the consideration of few layers in the second model also under predicts the effect of maldistribution by an average of 13%.

Finally, a more complete model should include the pressure coupling on both streams. In this work, pressure differences in the tube-side were disregarded since the original causes of maldistribution are not studied. However, if they were known, a pressure coupling could be settled, having a feedback of flow redistribution in on both streams.

References

Ablanque, N., Oliet, C., Rigola, J., Pérez-Segarra, C., Oliva, A., 2010. Two-phase flow distribution in multiple parallel tubes. International Journal of Thermal Sciences 49 (6), 909–921.

Aganda, A.A., Coney, J.E.R., Sheppard, C.G.W., 2000. Airflow maldistribution and the performance of a packaged air conditioning unit evaporator. Applied Thermal Engineering 20 (6), 515–528.

Ahmad, M., Berthoud, G., Mercier, P., 2009. General characteristics of two-phase flow distribution in a compact heat exchanger. International Journal of Heat and Mass Transfer 52 (1–2), 442–450.

Bassiouny, M.K., Martin, H., 1984a. Flow distribution and pressure drop in plate heat exchangers. I. u-Type arrangement. Chemical Engineering Science 39 (4), 693–700.

Bassiouny, M.K., Martin, H., 1984b. Flow distribution and pressure drop in plate heat exchangers. II. z-Type arrangement. Chemical Engineering Science 39 (4), 701–704.

Bobbili, P.R., Sunden, B., Das, S.K., 2006. Thermal analysis of plate condensers in presence of flow maldistribution. International Journal of Heat and Mass Transfer 49 (25–26), 4966–4977.

Chandraker, D.K., Maheshwari, N.K., Saha, D., Raj, V.V., 2002. Experimental and analytical investigations on core flow distribution and pressure distribution in the outlet header of a phwr. Experimental Thermal and Fluid Science 27 (1), 11–24.

Chen, N., Xu, L., dong Feng, H., Yang, C.G., 2005. Performance investigation of a finned tube evaporator under the oblique frontal air velocity distribution. Applied Thermal Engineering 25 (1), 113–125.

Collier, J.G., Thome, J.R., 1994. Convective Boiling and Condensation. Clarendon Press/Oxford University Press, Oxford/New York.

Friedel, L., 1979. Improved frictional pressure drop correlations for horizontal and vertical two phase pipe flow. In: European Two Phase Flow Group Meeting, Ispra, Italy.

Gerritsma, M., DeMaerschalck, B., 2010. Least-squares spectral element methods in computational fluid dynamics. In: Advanced Computational Methods in Science and Engineering, vol. 71. Springer, Berlin, Heidelberg, pp. 179–227.

Ghiaasiaan, S.M., 2007. Two-Phase Flow, Boiling, and Condensation in Conventional and Miniature Systems. Cambridge University Press.

Incropera, F.P., DeWitt, D.P., 1996. Fundamentals of Heat and Mass Transfer, 4th ed. John Wiley and Sons, New York.
Jiang, B.-N., 1998. On the least-squares method. Computer Methods in Applied Mechanics and Engineering 152 (1–2), 239–257 (Containing papers presented at the Symposium on Advances in Computational Mechanics).
Kakaç, S., Bon, B., 2008. A review of two-phase flow dynamic instabilities in tube boiling systems. International Journal of Heat and Mass Transfer 51 (3–4), 399–433.
Kandlikar, S.G., 1997. Heat transfer characteristics in partial boiling, fully developed boiling, and significant void flow regions of subcooled flow boiling. Journal of Heat Transfer 120 (2), 395–401.
Kumar, V., Faizee, B., Mridha, M., Nigam, K., 2008. Numerical studies of a tube-in-tube helically coiled heat exchanger. Chemical Engineering and Processing: Process Intensification 47 (12), 2287–2295.
Lalot, S., Florent, P., Lang, S.K., Bergles, A.E., 1999. Flow maldistribution in heat exchangers. Applied Thermal Engineering 19 (8), 847–863.
Li, Z., Zheng, M., 2009. Development of a numerical model for the simulation of vertical u-tube ground heat exchangers. Applied Thermal Engineering 29 (5–6), 920–924.
Mueller, A.C., Chiou, J.P., 1988. Review of various types of flow maldistribution in heat exchangers. Heat Transfer Engineering 9 (2), 36–50.
Rabas, T., 1985. The effect of tubeside maldistribution on the thermal performance of condensers used in multistage flash distillation plants. Desalination 55, 515–528.
Roetzel, W., Ranong, C.N., 1999. Consideration of maldistribution in heat exchangers using the hyperbolic dispersion model. Chemical Engineering and Processing 38 (4–6), 675–681.
Shah, R.K., Sekulić, D.P., 2003. Fundamentals of Heat Exchanger Design. John Wiley and Sons, New Jersey.
Srihari, N., Rao, B.P., Sunden, B., Das, S.K., 2005. Transient response of plate heat exchangers considering effect of flow maldistribution. International Journal of Heat and Mass Transfer 48 (15), 3231–3243.
Timoney, D.J., Foley, P.J., 1994. Some effects of air flow maldistribution on performance of a compact evaporator with r134a. Heat Recovery Systems and CHP 14 (5), 517–523.
Vist, S., Pettersen, J., 2004. Two-phase flow distribution in compact heat exchanger manifolds. Experimental Thermal and Fluid Science 28 (2–3), 209–215 (The International Symposium on Compact Heat Exchangers).
Wang, J., 2008. Pressure drop and flow distribution in parallel-channel configurations of fuel cells: U-type arrangement. International Journal of Hydrogen Energy 33 (21), 6339–6350.
Whalley, P.B., 1987. Boiling, Condensation, and Gas–liquid Flow. Clarendon Press/Oxford University Press, Oxford/New York.
White, F.M., 1986. Fluid Mechanics, 2nd ed. McGraw-Hill, New York.

Article 5

Pacio J.C. and Dorao, C.A. (2010)

A homogenization approach for studying two-phase heat exchanger performance

In Proceedings of the 8th International Topical Meeting on Nuclear Thermal-Hydraulics, Operation and Safety (NUTHOS-8), October 10-14, 2010, Shanghai, China. Paper ID: N8P0131.

A Homogenization Approach for Studying Two-Phase Heat Exchanger Performance

Pacio, J.C. and Dorao, C.A.
Norwegian University of Science and Technology. Department of Energy and Process Engineering
Kolbjørn Hejes vei 1b, Trondheim, Norway, N-7041
julio.pacio@ntnu.no, carlos.dorao@ntnu.no

ABSTRACT

Two phase heat exchangers (TPHE) present a rather complex behavior. The physical mechanisms underlying multiphase flow and heat and mass transfer and the usual geometries (spiral wound, plate-fin, shell-and-tube condensers) make modeling and design a challenging task. A usual and simple approach consists on considering one representative channel and its longitudinal evolution, disregarding the inherent complexity of the system.

However, several coupled scales are present in this type of exchangers, and the overall performance is dependent on all of them and their interaction. The usual geometries can include parallel channels and some internal structures, such as tube plates. The channels structure allows mass, momentum and energy exchange.

The objective of this work is to extend the experience on multiscale modeling and homogenization from core analysis to two phase heat exchanger applications. The model developed is based on describing the heat exchanger in term of representative channels which can interact among them exchanging mass, momentum and energy. The final model is solved using a spectral element method based on a least squares formulation. Numerical examples in this work include geometrical and mass flow effects.

KEYWORDS

Two-phase flow, Heat exchanger, Homogenization, Numerical analysis.

1. INTRODUCTION

TPHE are widely used for heating and refrigerating processes, since they yield large heat transfer rates. In some industries, e.g., chemical processing, air separation and power generation, they are main equipments and the overall performance may rely on their optimal design.

The modeling of TPHE performance results a challenging task for two main reasons: physical and geometrical. First, the physical mechanisms underlying multiphase heat and mass transfer and pressure drop, e.g. bubble nucleation, convective transport and interfacial stress, are quite complex in nature and occur simultaneously [1,2]. In addition, as the vapor content changes, different flow patterns develop along the stream which control the dominant heat and mass transfer mechanisms [3,4]. However, the flow pattern transition cannot be easily predicted.

For practical reasons, the complexity inherent to the physical processes is usually disregarded

and strong simplifications are made. For example, the working pressure is considered to be constant [5,6] or only the inlet-outlet pressure drop is considered [7]. An average constant heat transfer coefficient (HTC) is considered over wide ranges and the fluid physical properties are not considered to be affected by pressure drop [8] These are strong assumptions, since both the pressure gradient and the HTC are known to be strongly dependent on the quality [1,2] and it presents large variations along the stream.

The second reason is geometrical. The parallel channels configuration allows accommodating large heat transfer areas in small volumes, but leads to the problems of maldistribution, which affects the performance [9]. Also some of the usual geometries, e.g. shell-and-tube type or plate-fin HE, incorporate internal structures and regions with cross flow. In other words, the problem deals with a heterogeneous three dimensional geometry.

However, since simple models are required, the usual approach consists on considering one representative channel and its longitudinal evolution, i.e. all channels are considered to be equal [10]. In addition, no physical insight is used for determining the representative parameters, e.g. diameters, inlet conditions, but design values are assumed instead.

In this work a new model for representing complex TPHE is presented. The model is based on describing the heat exchanger in term of several representative channels which can interact among them exchanging mass, momentum and energy. A homogenization approach is used for obtaining the representative parameters for each channel considered, i.e. they are obtained as a weighted average over the entire region they represent.

This approach is intended to reflect the multiscale nature of the problem, and has been previously applied to thermo hydraulic analysis of reactor core. A porous media approach for multiphase flow is presented in [11] and its application to the analysis of interacting channels and, particularly, sub-channel analysis can be found in [12]. The extension of this experience to the study of TPHE performance involves the challenges that both fluids might be boiling or condensing, and the heat source is dependent on the solution (since its driven by temperature differences and not externally controlled).

The governing equations are solved numerically using a least-squares spectral element method [13]. This method was preferred over the traditional Finite Difference Method (FDM) or Finite Volume Method (FDM) because of its advantages concerning convergence rate. FDM and FVM are widely used and easy to implement, but usually lots of discretization points are needed for a suitable solution. The LSSEM consists on a minimization formulation, and yields and exponential convergence for smooth problems [14]. With a more efficient numerical solver more physical effects can be incorporated for modeling the local pressure gradient and heat transfer, disregarding some of the assumptions mentioned above. At the same time, a high order method allows to reduce the computational cost when models with large relative errors are used.

The structure of this work is as follows. The TPHE problem and present model are introduced in section 2. A reference case is presented in section 3. Section 4 shows some results for different scenarios. Final remarks are summarized in section 5. The nomenclature used in this work is listed in appendix A.

2. THE TPHE STEADY-STATE PROBLEM AND PRESENT MODEL

The TPHE problem consists on rating the evolution of interacting streams within a given geometry. The scope of this work is limited to steady-state analysis, with single-component working fluids, and heat leakage to the surrounding; axial conduction and radiative heat transfer are neglected.

In particular, a shell-and-tube geometry is studied. Figure 1 shows a simplified cross section of the exchanger, i.e. the internal structures are not shown, with tube-side in black and shell-side in white. In a homogenization approach this model considers N radial layers and allows for mass, momentum and energy exchange within them on the shell-side. In addition, tube-side and shell-side exchange energy, driven by temperature differences.

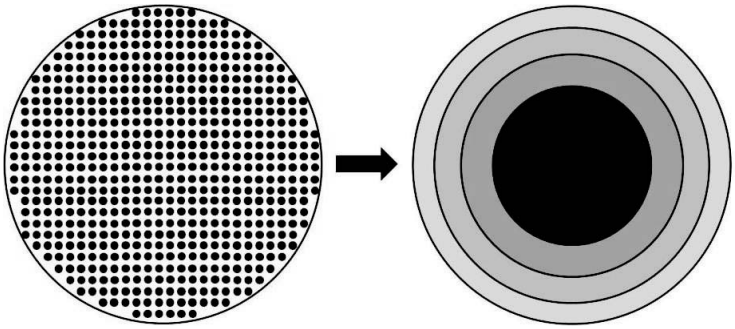

Fig. 1 Cross section of shell-tube HE and N radial layers scheme used in this work.

The governing equations are steady-state mass, momentum and energy balances for each stream on each layer. However, since the tube-side stream is closed and does not allow for mass exchange, the mass balance has a trivial solution, i.e. constant flow rate. Therefore, it is not considered, and the problem is governed by the following 5xN equations (for a complete list of the nomenclature used in this work, refer to table 1 in appendix A):

Tube-side:

$$G_T^j \frac{\partial V_T^j}{\partial z} + \frac{4\tau_T^j}{D_{hT}^{\ j}} + \rho_T^j g + \frac{\partial p_T^j}{\partial z} = 0 \tag{1}$$

$$G_T^j \frac{\partial e_T^j}{\partial z} = \frac{UP_{ST}^{\ j}}{A_T^j}(T_S^j - T_T^j) \tag{2}$$

Shell-side:

$$\frac{\partial G_S^j}{\partial z} = \frac{1}{A_S^j}\sum_{i\neq j} m'_{ij} - m'_{ji} \tag{3}$$

$$\frac{\partial (G_S^j V_S^j)}{\partial z} + \frac{4\tau_S^j}{D_{hS}^{\ j}} + \rho_S^j g + \frac{\partial p_S^j}{\partial z} = \frac{1}{A_S^j}\sum_{i\neq j} m'_{ij} V_S^i - m'_{ji} V_S^j \tag{4}$$

$$\frac{\partial (G_S^j e_S^j)}{\partial z} = \frac{UP_{ST}^{\ j}}{A_S^j}(T_T^j - T_S^j) + \frac{1}{A_S^j}\sum_{i\neq j} m'_{ij} e_S^i - m'_{ji} e_S^j \tag{5}$$

Both co-current and counter-current flow situations can be modeled by eqs. (1) to (5), with proper sign for the derivatives. These equations are coupled and require some constitutive

equations that relate the different variables, such as:

$$e = h + \tfrac{1}{2}V^2 + gz \tag{6}$$
$$G = \rho V \tag{7}$$

All fluid physical properties, e.g. density, and local temperature for each fluid are given by the thermodynamic state (*p,h*), as follows:

$$T = T(p,h) \tag{8}$$
$$\rho = \rho(p,h) \tag{9}$$

In addition, shear stress (τ), heat transfer (*UP*) and cross flow (*m'*) are modeled on the base of semi-empirical correlations that are further developed in the following subsections. Finally, the set of equations (1) to (5) are solved for p_T^j, h_T^j, G_S^j, p_S^j and h_S^j with proper inlet boundary conditions.

2.1. Pressure drop models

In order to accommodate the effects of multiphase flow, a two-phase multiplier $\Phi_L^2 = \tau/\tau_L$ is introduced for modeling the shear stress, and τ_L is computed on the base of a friction factor f_L, which is obtained according to the Haaland formula for smooth tubes [15].

$$\tau_L = f_L \frac{G^2}{2\rho_L} \rightarrow \tau = \tau_L \Phi_L{}^2 \tag{10}$$

For single-phase liquid $\Phi_L^2 = 1$ and for single-phase vapor $\Phi_L^2 = (f_G \rho_L)/(f_L \rho_G)$. The Friedel correlation for the two-phase multiplier [2] is used in the two-phase region.

2.2. Heat transfer models

In a steady-state analysis, the linear heat transfer coefficient (HTC) is computed on the basis of three linear thermal resistances: shell-side and tube-side convective heat transfer, and thermal conduction in the wall, i.e.:

$$\frac{1}{UP_{ST}} = \underbrace{\frac{1}{Per_{ST}\alpha_S}}_{\text{shell convection}} + \underbrace{\frac{1}{Per_{ST}\alpha_T}}_{\text{tube convection}} + \underbrace{\frac{t_W}{Per_{ST}\lambda_W}}_{\text{wall conduction}} \tag{11}$$

Different correlations were used for computing α_T and α_S, depending on the enthalpy range. In general, the formulas recommended by Collier and Thome [16] were used, namely Gnielinsky, and Pethukov-Popov for single phase flow (depending on Reynolds number range), simplified Gungor and Winterton for boiling flow, and Akers for condensation. In addition, the three-region subcooled boiling model by Kandlikar [17] was incorporated.

2.3. Cross flow models

The term m'_{ij} represents shell-side cross-flow from layer *i* to *j*. Since it carries mass, momentum

and energy it appears as a source in the right hand sides of eqs. (3) to (5). This cross-flow term has two main contributions: turbulent mixing and pressure difference-driven flow, and several models available for them can be found in [18].

The extension of these models to two-phase mixing is not simple and its study is strictly based on experimental data, only available for air-water and water-steam systems. In this work, a model based on simple constants that includes both contributions is used, as follows:

$$m'_{ij} = \underbrace{\beta \frac{G_S{}^i A_S{}^i + G_S{}^j A_S{}^j}{A_S{}^i + A_S{}^j} Per_{ij}}_{\text{Turbulent mixing}} + \underbrace{\frac{1}{K} \rho_S{}^i \sqrt{\frac{p_S{}^i - p_S{}^j}{\rho_S{}^i}} Per_{ij}}_{\text{Pressure difference-driven}} \tag{12}$$

Constant values are assumed for the mixing parameter (β) and distributed resistance (K). It should be noticed that the second term in eq. (12) is only applicable if $p_S{}^i > p_S{}^j$.

3. REFERENCE CASE

Given the governing equations (1) to (5) and its associated constitutive laws and physical submodels, the problem is completely defined by identifying the working fluids, flow arrangement and problem parameters. These parameters include inlet values and geometrical data for each layer j, i.e. N sets defined as:

$$\left\{ T_T^{IN}, G_S^{IN}, p_T^{IN}, p_S^{IN}, h_T^{IN}, h_S^{IN}, D_{hT}, D_{hS}, A_T, A_S \right\}_j \tag{13}$$

A homogenization approach is implicit in the definition of these parameters, since they are the result of an average over the region they represent. The objective of this section is to study a reference case where all layers are assumed to be identical, establishing the base for section 4 that deals with the results of scenarios where the homogenization approach leads to differences between the layers.

In particular, the horizontal counter-flow of condensing propane in the tube-side (entering at 290 K and 7 bar) and boiling R134a in the shell side (280K, 4 bar) is studied and the total mass flow rates are 1.5 and 3.0 kg/s, respectively. The geometry consists in 800 aluminum tubes, 8.0 mm in inner diameter, 0.25 mm thickness and 5 m in length, in a 335 mm in diameter shell with a square-lattice array (10.4 mm pitch).

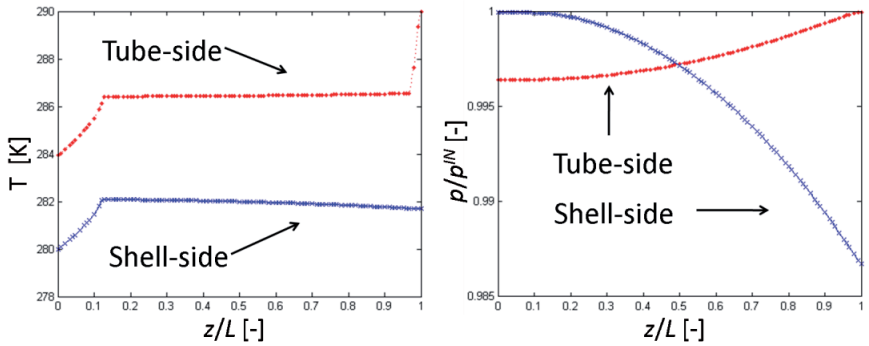

Fig. 2 Reference case profile solutions. (a) Temperature and (b) Dimensionless pressure.

Figure 2 (a) and (b) show the results for this reference case. Since all layers are identical, there is no net cross flow between them, and both the mass flux remain constant at their inlet values, i.e. G_T^{IN} = 37.30 and G_S^{IN} = 67.75 kg/m^{2}s. The results for momentum and energy equations are shown in terms of (a) temperature and (b) dimensionless pressure (p/p^{IN}) profiles. It should be noticed that, since it's a counter-flow arrangement, the shell-side enters in the position z=0, and the tube-side in z=L, i.e. z/L = 1.

In addition to the profile solutions, some integral results might be of interest. In this work, only the heat duty Q, defined as the total heat transferred between streams, is studied:

$$Q = \sum_j \int_0^L UP_{ST}^j (T_T^j - T_S^j) dz \tag{14}$$

The reference value for the heat duty is Q^{REF} = 553.09 kW.

4. RESULTS

The reference case presented in section 3 is ideal because all layers were supposed to be identical. In this section the consequences of some differences between layers, shell-side hydraulic diameter and tube-side flow maldistribution are discussed.

4.1. Shell-side hydraulic diameter

Differences in D_{hS}^j can occur when the tube array deviates from the ideal square lattice. This can be the consequence of fabrication tolerance, but this effect cannot be identified in a particular layer. However, a constant deviation can be identified in the most outer layer, since the proximity to the wall does not allow the location of some tubes. This results in a slightly larger hydraulic diameter for the shell-side.

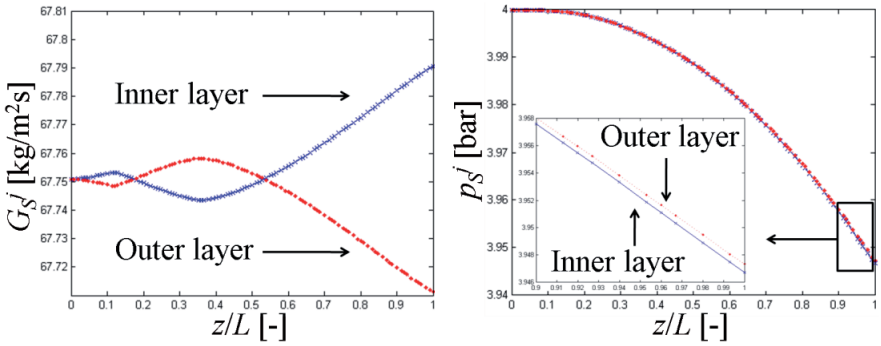

Fig. 3 Shell-side profiles. 1% increase in outer layer D_{hS}. (a) Mass flux and (b) Pressure

Figure 3 shows the profile solutions for shell-side mass flux and pressure when N=2 layers are considered and a 1% increase in hydraulic diameter is assigned to the outer layer. Since it's a small perturbation on the parameters, its effect on the solution is also small.

According to eq. (4), an increase in hydraulic diameter yields less friction and therefore, less pressure drop. This means that, initially $p_S^{outer} > p_S^{inner}$, and this produces an initial net

cross-flow to the inner layer as figure 3 (a) shows.

This cross-flow has a feedback on pressure drop, since it is strongly dependent on mass flux with two opposite contributions: first, a lower flux yields lower shear stress with a quadratic law (inertia effect, see eq. 10), and second, it also results in more generation of vapor, which increases the value of the two-phase multiplier (see also eq. 10). The relative contribution of both effects determines the pressure drop on both layer and the direction of the cross-flow.

The effect of the two-phase multiplier is dominant in the initial low-vapor content region and the inertia effects, in the last part of the exchanger (with high-vapor content). This means that the outer layer has a lower pressure drop, and then it gives a positive net cross-flow to the inner layer, which produces further lower pressure drop, i.e. with a positive feedback. Then both mass fluxes diverge and the outer layer flux at the exit is 0.04 kg/m^{2}s (0.051%) lower that at inlet. In other words, there is more flux at the exit in the layer with a smaller hydraulic diameter, i.e. larger flow resistance. The cross-flow that produces this differences in outlet mass flux is in the order of m'_{ij} = 0.02 kg/sm

As a result of this positive feedback, the pressure difference between layers also diverges. However, the difference is small, as fig. 3 (b) shows, and the outlet pressure of the outer layer is 60.0 Pa higher. At first sight, in a steady-state analysis, all outlet pressures should be identical. However, the equal-pressure-drop condition applies for all the flow paths between inlet and outlet, nozzles, including the flow inside the headers. Nevertheless, the study of the header exceeds the scope of this work. In addition, there is experimental evidence of outlet pressure differences of the order of 7-8 G_S^2/ρ_S [19] (in this case = 770-880 Pa). For this reason, these differences are allowed in this work with no further considerations, as long as they are negligible compared to the inlet-outlet pressure drop, as in this case (it represents 1.13% of it).

Figure 4 shows a parametric analysis of both effects, i.e. (a) reduction in outer layer mass flux and (b) differences in outlet pressure, varying the increase in the outer layer hydraulic diameter from 0 to 10%, considering N=2, and 3 radial layers.

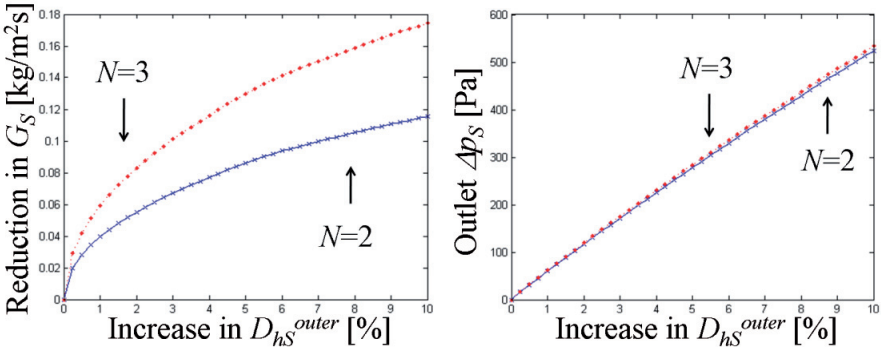

Fig. 4 (a) Reduction in mass flux and (b) Differences in outlet pressure for N=2, 3 layers

As expected, a larger increase in outer layer D_{hS} produces larger deviations in both outlet pressure and mass flux, since the layers are increasingly different. The consideration of one extra layer produces the same results.

As in the case with only 2 layers, as a consequence of the larger hydraulic diameter, the pressure drop on the outer layer is less than in the rest and, after an initial regime where the effect of the

two-phase multiplier is dominant, it results in a net flow to the adjacent layer, which increases its pressure drop, giving a positive feedback.

With the consideration of one extra layer, it also receives a net cross-flow from the most inner layer. This last contribution is small, because both layers have the same hydraulic diameter, but it is responsible for the differences between both curves shown in figures 4 (a) and (b).

The redistribution of mass fluxes has an effect on performance. The evolution of heat duty is shown in figure 5, for N=2 and 3 layers. A reduction of Q is noticed in all cases and, as expected, the effect is larger for larger increases in D_{hS}^{outer}. On the other hand, the consideration of one extra layer reduces the effect of the perturbation, showing an opposite behavior to figures 4. (a) and (b). This is simply a consequence of the fact that with N = 3, the outer layer represent a lower fraction of the total flow rate than with N = 2.

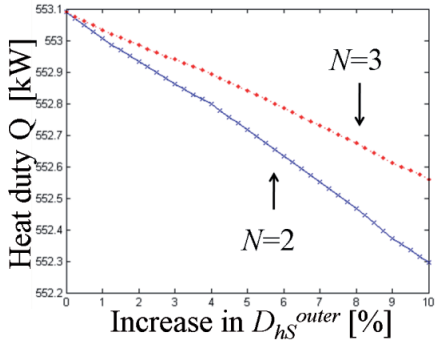

Fig. 5 Total heat duty N=2, and 3 layers

Nevertheless, its relative effect is negligible, with a maximum reduction of 0.14% compared to Q^{REF}. Therefore, the effect of increasing the outer layer hydraulic diameter is interesting since it produces a redistribution of mass flow in a rather complex manner, but has no relevant effect on the performance, in terms of heat duty. The effect of maldistribution on performance is further studied in section 4.2.

4.2. Tube-side flow maldistribution

In many scenarios the flow distribution can deviate from design conditions. A poor header design or off-specifications operating conditions, and channel blockage or size reduction due to differential thermal expansion are just some of the possible causes. Its effect on TPHE performance is not clear, since a reduction in duty is expected from single-phase experience [9], but there is experimental evidence of an increase in some two-phase applications [20].

As in section 4.1 this problem is first studied with N=2 layers with fixed values for the parameters listed in eq. (13), and it's further extended to more layers, in a parametric analysis. For the quantification of maldistribution, a maldistribution parameter μ is defined as the maximum deviation in mass flow rate from average values, i.e.:

$$\mu = \frac{(GA)^{MAX} - (GA)^{AVG}}{(GA)^{AVG}} \tag{15}$$

Figure 5 shows the results for N=2 layers and a tube-side maldistribution of μ_T = 0.1, where

more tube-side mass flow goes through the inner layer than the outer. This means that the inner-layer tube-side has a mass flow 10% larger than the average (i.e. 55% of total), and the outer layer 10% less than the average (i.e. 45% of total). Figure 5 shows both tube-side (red, from right to left) and shell-side (blue, from left to right) profile solutions.

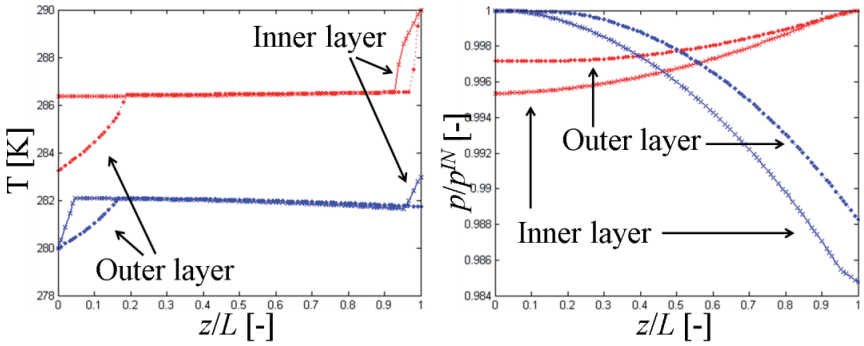

Fig. 6 Profile solutions for N=2 and μ_T = 0.1 (a) Temperature (b) Dimensionless Pressure

The maldistribution affects both the tube-side momentum and energy equations (eqs. 1 and 2). On the first one, a higher mass flux gives a higher pressure drop, as figure 6 (b) shows, since the shear stress is strongly dependent on it (eq. 10). The effect on the energy equation is that the variations in the specific enthalpy (h) are smaller for a higher mass flux. For this reason, the fluid in the outer-layer tubes is fully condensed and sub-cooled at the exit (z = 0), while the inlet layer fluid is still at saturation temperature, as shown in figure 6 (a).

Maldistribution on the tube-side also affects the flow in the shell-side, through heat transfer. A higher tube-side mass flux gives a higher HTC and this represents a higher heat source to the shell-side fluid. This effect can be noticed in figure 6 (a), where the inner-layer shell-side fluid exits as super-heated vapor at z/L=1, while the outer-layer fluid exits at saturation temperature. In addition, a higher heat source increases the vapor content, producing a higher pressure drop, as figure 6 (b) shows. This pressure difference produces a net cross-flow from the outer to the inner layer, and the outer layer flux at the exit is 0.59 kg/m^{2}s (0.87%) lower that at inlet.

The effect on performance can be expressed in term of the total heat duty. In this case, the heat duty is Q = 547.75 kW, i.e. 0.97 % less than the reference value. The effect on heat duty is further studied in a parametric analysis, i.e. varying μ_T, for N = 2, 3 and 4 layers.

In addition to a maldistribution parameter, a distribution profile is required for extending the analysis to N layers. The usual model used is the one given by Bassiouny and Martin [21], originally developed for plate-type heat exchangers, which proposes two profiles a *cosh*-type profile if more flow goes through the inner channels, and if the outer channels receive more flow, a *cos*-type profile applies. However, this model assumes is only valid for large number of channels, which is not the case on this work, since only a few layers are considered.

In this work it is assumed that more flow goes through the inner layers, and a simple linear profile is proposed, as follows:

$$(GA)_T^j = (GA)_T^{AVG}\left[1+\mu_T\left(1-2\frac{j-1}{N-1}\right)\right] \tag{16}$$

The layers are listed $j = 1,\ldots, N$ from inside to outside. Figure 7 shows the heat duty for $N = 2$, 3, and 4 for different values of μ_T, considering the linear profile expressed in eq. (16).

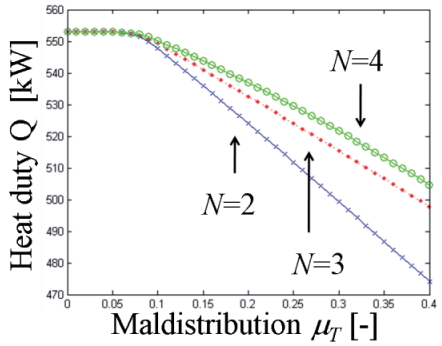

Fig. 7 Evolution of Q against μ_T. N = 2, 3 and 4 layers. Linear profile.

According to fig. 7, maldistribution reduces the performance in all cases. Its effect is negligible for small values of μ_T, reaching a 5% reduction of Q^{REF} for μ_T = 0.2. A maximum maldistribution of $\mu_T^{MAX} = 0.4$ was considered in this work, with a reduction of 14.3% in Q.

When more layers are considered, the absolute differences between two adjacent layers are smaller for a given value of μ_T. As a consequence, the effect on performance is also smaller, as shown in figure 7. On the other hand, if N is reduced, smaller values of μ_T are expected, since the relative differences are reduced during the averaging procedure. As an example, a value of $\mu_T = 0.3$ for $N = 4$ would give $\mu_T = 0.2$ for $N = 2$.

It should be noticed that the consideration of radial layers implicitly assumes axial symmetry. This might not be valid for gravitational dominated horizontal flow, and large differences between layers will results from the homogenization procedure. For this reason, maybe horizontal layers should be considered instead of radial for such a case.

5. CONCLUSIONS

The steady-state TPHE problem was studied in this work within a homogenization approach. This model is based on describing the exchanger in term of several representative channels, or layers, which can exchange mass, momentum and energy. State-of-the-art models were used for considering pressure drop, heat transfer and cross-flow. The governing equations, based on mass, momentum and energy balances, were solved with an in-house solver based on the least squares spectral element method.

In this framework, a homogeneous reference case and two heterogeneous scenarios, namely deviations in shell-side hydraulic diameters and tube-side flow maldistribution were studied. Both scenarios were studied first for 2 layers and fixed parameters, and then were extended to more layers in a parametric analysis. The performance is studied in terms of heat duty.

A slightly larger value of D_{hS}^{outer} makes the pressure drop in this outer layer slightly lower, and this produces a net cross-flow to the inner layer. Small differences are found in the outlet pressure and mass fluxes. However, the effect on performance is negligible.

Tube-side flow maldistribution produces differences in the outlet temperature and pressure. It also affects the behavior of the shell-side flow, producing a net cross-flow towards the layer with the higher tube-side flow. In all cases, the performance is reduced. However, its effect is negligible, except for large values of the maldistribution parameter μ_T. A maximum reduction of 14.3 % of the reference value was noticed in this work.

The result of differences in pressure drop may seem surprising at first sight. However, there is experimental evidence of such differences inside the header in the order of magnitude of the dynamic head, and pressure is equalized further downstream. If larger differences were found, an equal-pressure-drop constraint should be incorporated, which is expected to result in flow redistribution, with preference through the low resistance flow paths.

The consideration of more layers reduces the effect of a given perturbation on both scenarios, because each layer represents a lower fraction of the total flow, and the absolute differences between layers are smaller. It should be also noticed that when different number of layers are considered, the working parameters are affected, as shown in section 4.2 with the maldistribution parameter μ_T.

REFERENCES

1. K. Stephan, *Heat Transfer in Condensation and Boiling*, Springer Verlag, Berlin and London (1992).
2. P.B.Whalley, *Boiling, Condensation and Gas-Liquid Flow*, Oxford University Press, Oxford and New York (1987).
3. J.R. Thome, J. El Hajal & A. Cavallini, "Condensation in horizontal tubes, part 2: new heat transfer model based on flow regimes", *International Journal of Heat and Mass Transfer*, **46**, pp. 3365-3387 (2003).
4. O. Zurcher, D. Favrat & J.R. Thome, "Evaporation of refrigerants in a horizontal tube: an improved flow pattern dependent heat transfer model compared to ammonia data", *International Journal of Heat and Mass Transfer*, **45**, pp. 303-317 (2002).
5. Y.G. Yohanis, O.S. Popel & S.E. Frid, "A simplified method of calculating heat flow through a two-phase heat exchanger", *Applied Thermal Engineering*, **25**, pp. 2321-2329 (2005).
6. P.R. Bobbili, B. Sunden & S.K. Das, "Thermal analysis of plate condensers in presence of flow maldistribution", *International Journal of Heat and Mass Transfer*, **49**, pp. 4966-4977 (2006).
7. C. Aprea & A. Maiorino, "Numerical analysis of an air condenser working with the refrigerant R407C", *Applied Thermal Engineering*, **27**, pp. 2592-2599 (2007).
8. J.M. Corberán & J. Gonzálvez, "Two-phase heat transfer analysis of evaporators", *Experimental Thermal and Fluid Science*, **26**, pp. 259-267 (2002).
9. A.C. Mueller & J.P. Chiou, "Review of various types of maldistribution in heat exchangers", *Heat Transfer Engineering*, **9 (2)**, pp. 36-50 (1988).
10. R.K. Shah & D.P. Sekulic, *Fundamentals of Heat Exchanger Design*, John Wiley and Sons, New Jersey (2002).
11. W.T. Sha, B.T. Shao & S.L. Soo, "Porous-media formulation for multiphase flow with heat transfer", *Nuclear Engineering and Design*, **82 (2-3)**, pp. 93-106 (1984).
12. N.E. Todreas & M.S. Kazimi, *Nuclear Systems II: Elements of Thermal Hydraulic Design*, Hemispher Pub. Corp., New York (1990).
13. B. Jiang, *The least-squares finite-element method. Theory and applications in computational fluid dynamics and electromagnetics*, Springer. Berlin (1998).

14. B. De Maerschalck & M. Gerritsma, "Least-squares spectral element method for non-linear hyperbolic differential equations", *Journal of Computational and Applied Mathematics*, **215**, pp. 357-367 (2008).
15. F. White, *Fluid Mechanics*, McGrawHill Series in Engineering, New York (1986).
16. J.G. Collier & J.R. Thome, *Convective Boiling and Condensation*, Clarendon Press, Oxford University Press, Oxford & New York (1994).
17. S.G. Kandlikar, "Heat transfer characteristics in partial boiling, fully developed boiling, and significant void flow regions of subcooled flow boiling", *Journal of Heat Transfer*, **120 (2)**, pp. 395-401 (1997).
18. Z.Rouhani, "Steady-State Subchannel Analysis", in *Two-Phase Flows and Heat Transfer with Application to Nuclear Reactor Design Problems*, edited by J.J. Ginoux, Hemisphere Pub. Corp., Washington & London (1978).
19. D.K. Chandraker, N.K. Maheshwari, D. Saha & V. Venkat Raj, "Experimental and analytical investigation on core flow distribution and pressure distribution in the outlet header of a PHWR", *Experimental Thermal and Fluid Science*, **27**, pp. 11-24 (2002).
20. D.J. Timoney & P.J. Foley, "Some effects of air flow maldistribution on performance of a compact evaporator with R134a", *Heat Recovery Systems & CHP*, **14 (5)**, pp. 517-523 (1994).
21. M.K. Bassiouny & H. Martin, "Flow distribution and pressure drop in plate heat exchangers. I: U-type arrangement", *Chemical Engineering Science*, **39 (4)**, pp. 693-700 (1988).

APPENDIX A

The nomenclature used in this work is listed in Table 1.

Table 1. Nomenclature used in this work

Symbol	**Meaning**	**SI unit**	**Symbol**	**Meaning**	**SI unit**
G	Mass flux	kg/(m^{2}s)	UP	Linear HTC	W/(K m)
V	Velocity	m/s	α	Local HTC	W/(K m^2)
z	Axial position	m	A	Cross-sectional area	m^2
τ	Shear stress	Pa	T	Temperature	K
ρ	Density	kg/m^3	m'	Cross-flow rate	kg/(s m)
D_h	Hydraulic diameter	m	Per	Perimeter	M
G	Gravity	m/s^2	λ	Thermal conductivity	W/(K m)
p	Pressure	Pa	T	Thickness	M
e	Specific energy	J/kg	β	Mixing parameter	-
h	Specific enthalpy	J/kg	K	Distributed resistance	-
Q	Heat duty	W	L	Length	M
μ	Maldistribution	-	N	Number of layers	-
Subindex			Supraindex		
S	Shell side		i,j	Radial layer	
T	Tube side		IN	Inlet value	
W	Wall		REF	Reference value	
ST	Shell-tube		MAX	Maximum value	
ij	From i to j		AVG	Average value	

Table 1. Nomenclature used in this work

Article 6

Pacio J.C. and Dorao, C.A. (2010)

A comparative analysis of computational models for solving one-dimensional heat exchangers problems

Submitted to the International Journal of Refrigeration (under review).

Is not included due to copyright

Article 7

Pacio J.C. and Dorao, C.A. (2011)

A review on heat exchanger thermal hydraulic models for cryogenic applications

Cryogenics **51**(7), pp. 366-379. doi:10.1016/j.cryogenics.2011.04.005.

Cryogenics 51 (2011) 366–379

Contents lists available at ScienceDirect

Cryogenics

journal homepage: www.elsevier.com/locate/cryogenics

Review

A review on heat exchanger thermal hydraulic models for cryogenic applications

Julio Cesar Pacio *, Carlos Alberto Dorao

Dept. of Energy and Process Engineering, Norwegian University of Science and Technology, NO-7491 Trondheim, Norway

ARTICLE INFO

Article history:
Received 10 November 2010
Received in revised form 3 April 2011
Accepted 12 April 2011
Available online 20 April 2011

Keywords:
Heat exchanger
Thermal hydraulic
Review

ABSTRACT

Heat exchangers are the main components in cryogenic processes. Thermo-economic considerations set the need for high-effectiveness equipment and accurate models. This situation is challenging due to the complex operating conditions and the fact that some physical effects, such as changes in fluid properties, flow maldistribution, axial conduction and heat leakage, cannot be neglected.

In this work a systematic review of the state of art and challenges in modeling cryogenic heat exchangers is presented. They include lumped parameters, distributed parameters and stream-evolution models. These formulations fail to take all relevant effects into account.

A general discussion on the performance of the reviewed models is presented. In general, more effects are included in the framework of numerical solution of discretized energy balance equation. Two main points stand out as not considered by the present models, namely the effects of pressure drop on heat transfer and the existence of partial flow mixing. These two effects are highly relevant for two-phase flow and multi-component applications, as in LNG processes.

Contents

* Corresponding author.
E-mail address: julio.pacio@ntnu.no (J.C. Pacio).

0011-2275/$ - see front matter © 2011 Elsevier Ltd. All rights reserved.
doi:10.1016/j.cryogenics.2011.04.005

Nomenclature

Abbreviations and Acronyms

CWHE	coil-wound heat exchanger
DPM	distributed parameters model
HE	heat exchanger
HTC	heat transfer coefficient
LHC	longitudinal heat conduction
LMTD	logarithmic mean temperature difference
LPM	lumped parameters models
MTD	mean temperature difference
NTU	number of thermal units [–]
PFHE	plate-fin heat exchanger
PPHE	perforated-plate heat exchanger
SEM	stream evolution model

Greek symbols

ΔT	local temperature difference (K)
ΔT_m	effective mean temperature difference (K)
ΔT_{lm}	logarithmic mean temperature difference (K)
η	heat exchanger efficiency (–)
ϕ	general scalar function of one or more variables
ε	heat exchanger effectiveness (–)

Physical variables

$\dot{m}$	mass flow rate (kg s^{-1})
Ψ	nondimensional effective mean temperature difference (–)
A	area (m^2)
C	heat capacity rate (W K^{-1})
C^*	heat capacity rate ratio (–)
c_p	specific heat capacity at constant pressure (J kg^{-1} K^{-1})
dA	differential area (m^2)
dQ	differential heat transfered (W)
dT	differential temperature (K)
E_n	heat exchanger *new effectiveness* (–)
F	correction factor for LMTD (–)
P	temperature effectiveness (–)
Q	heat transfered (W)
R	heat capacity rate ratio (–)
T	temperature (K)
U	overall heat transfer coefficient (W m^{-2} K^{-1})
W	mechanical power (W)

Subscripts

c	refers to the lower temperature level (hot)
h	refers to the higher temperature level (cold)
max	maximum value
min	minimum value

1. Introduction

Heat exchangers (HEs) are the main components in cryogenic processes. In air separation units and Liquefaction of Natural Gas (LNG) plants, they represent 20–30% of the investment costs [38]. In addition, their performance affects the sizing and design of other major equipments, namely compressors and their power drivers.

Thermodynamic considerations make cryogenic processes very sensitive to the HE performance. For example, Kanoglu et al. [53] predicted a reduction of 22% in the production of liquid if the HE effectiveness (ε) departs from the ideal value of 100% to a more practical one of 96.5%. In the case of liquefaction of helium, Atrey [10] calculated that 12% less liquid is obtained if ε is reduced from 97% to 95%, and Barron [13], Barron [15] stated that no liquid is produced if $\varepsilon < 85\%$.

An important consequence of HE under-performance is the need for modifications in the process to achieve the desired liquid production rate. The refrigeration capacity has to be increased, with the corresponding increase in power input, which is a major concern in cryogenics. The minimum ideal power input per unit of removed heat in a refrigeration circuit, given by the inverse Carnot cycle [20, ch. 10] can be computed according to (1). Given the usually low values of T_c, the mechanical-to-thermal power ratio W/Q given by (1) is relatively high. For this reason, the refrigeration capacity should be kept at a minimum, emphasizing the requirements for high HE performance.

$$\frac{W}{Q} = \frac{T_h - T_c}{T_c} \tag{1}$$

In short, if the HE has low performance, the production is reduced and large amounts of additional power input are required. This sets the need for high-effectiveness heat exchangers, in the order of $\varepsilon > 90\%$ [116]. This situation is reflected in the requirements for the accuracy of the models used for design, that are more demanding than for high-temperature applications. The design of traditional HEs, such as shell-and-tube, is rather well established for a large range of sizes and different processes [106]. The special features of cryogenic HE, however, make their formulation a challenging task. Usually this situation results in a particular design for the given application, since sizing is not as straightforward as for more traditional geometries.

This work intends to review the present models for cryogenic HE design. These models fail to consider some physical effects, such as flow distribution and axial thermal conduction, that can usually be neglected for other applications, but might dominate the performance in the case of cryogenic applications. This scenario has been noticed by several authors, and the available literature concerning these effects is reviewed in this work.

The structure of this work is as follows. Section 2 discusses the challenges in the modeling of cryogenic HE. The different equipment and geometries are presented in Section 3. Section 4 reviews the present available models for HE design. Section 5 deals with relevant effects reported in the reviewed literature. A critical discussion on the state-of-the-art on this subject is presented in Section 6. The conclusions of this work are summarized in Section 7.

2. Challenging features for modeling

As discussed in Section 1, cryogenic HE have large efficiency requirements. This makes their modeling a challenging issue. Two particular features are most demanding. First, the thermal processes used in cryogenic engineering present some complex elements, such as simultaneous heat exchange between multiple streams. Second, some physical effects that are usually neglected for high-temperature applications cannot be disregarded in the case of cryogenics. These two features are studied in detail in the following subsections.

2.1. Complex processes

A process for producing refrigeration at liquefied gas temperatures always involves some equipment at ambient temperature in which the gas is compressed and heat is rejected to a coolant [37, ch. 6]. In some cases, such as the Linde cycle, the working fluid is self-refrigerated after an expansion. In other cases, the use of a refrigerant is necessary, which needs to be cooled as well.

The complexity of the processes is more marked in the case of Liquefied Natural Gas (LNG) production. In this case, the aim for overall economic optimization resulted in the development of complex liquefaction processes that represent roughly half of the plant capital costs [34]. A comprehensive review on LNG technologies was presented by Brendeng and Hetland [19]. Around 80% of the installed capacity uses a propane-precooled mixed refrigerant process, licensed by Air Products and Chemicals, Inc. (APCI) [11]. Other cycles include optimized cascade, single mixed refrigerant and natural gas expanders.

As a consequence of the mentioned processes, the cryogenic HEs operate in challenging conditions. These include:

- Large temperature range. Starting from ambient temperature, cryogenic fluids need to be cooled to temperatures as low as 110 K (LNG), 77 K (nitrogen), 20 K (hydrogen) or 4 K (helium) to achieve liquid state at atmospheric pressure. In some refrigeration cycles, this is done in a cascade process. However, in other cases, as the single mixed refrigerant process, the entire range is covered in one single HE. This leads to problems such as large temperature gradients inside the exchanger, and the changes in fluid properties.
- Multiple streams. In LNG processes, both the natural gas and high-pressure refrigerant need to be cooled. This process presents some economical advantages if it is performed within the same HE. For this reason, plate-fin and coil-wound HE are used in these processes with three or four simultaneous streams.
- Boiling and condensation. Cryogenic processes present condensation of the working fluid, and evaporation of the low-pressure refrigerants to achieve high heat transfer rates. The change of phase presents some challenges to model heat transfer and pressure drop. These are usually modeled on the base of empirical correlations, which predict them with a large degree of uncertainty.
- Multi-component mixtures. Two important mixtures play important roles in cryogenics: air and natural gas. Pre-treated natural gas to be processed in a cryogenic plant is a mixture of several hydrocarbons and some minor contents of nitrogen. In addition, roughly 95% of the LNG plants use a multi-component mixture as a refrigerant [114]. Condensation and evaporations of mixtures is a challenging scenario to model, given the effects of mass resistances on heat transfer.
- Flow injection and removal. During the liquefaction of natural gas, heavier hydrocarbons are separated to meet the specifications. This is performed within the main cryogenic HE where the liquefaction takes place, resulting in localized changes in mass flow rates and composition of the streams.

2.2. Non-negligible effects

Traditional heat exchanger models neglect some effects [99, ch. 3.2] since they are not relevant for the typical required engineering accuracy. However, the high-effectiveness requirements for cryogenic HEs make necessary to take these effects into account. They include: changes in fluid properties, heat exchange with the surrounding (heat leakage), longitudinal thermal conduction in the wall, and flow maldistribution.

The relative importance of these effects is summarized in Fig. 1. For low-efficiency applications, all of them can be neglected. For higher effectiveness requirements, they all need to be considered, in increasing order of accuracy: changes in fluid properties, flow maldistribution, longitudinal conduction and heat leakage. These considerations depend on the particular operating conditions and cover relatively wide and approximate ranges.

Some of these effects have been addressed in literature for rating the performance of HE in simple processes involving single-phase flow. The studies reported in literature are reviewed in Section 5. However, no reports were found on applications to complex processes as those used for production of LNG. The following subsections present some details of these effects.

2.2.1. Changes in fluid properties

Barron [14] stated that the main distinctive feature of cryogenic heat transfer is that *all constants become variables*. For single-phase flow, the main effect is given by changes in the specific heat capacity. In the case of two-phase flow, this is accompanied by large variations in the heat transfer coefficient, as well as density and viscosity. For the analysis of high-temperature HEs, Kays and London [55] suggested the use of a constant value, corresponding to the physical properties evaluated at a mean temperature. However,

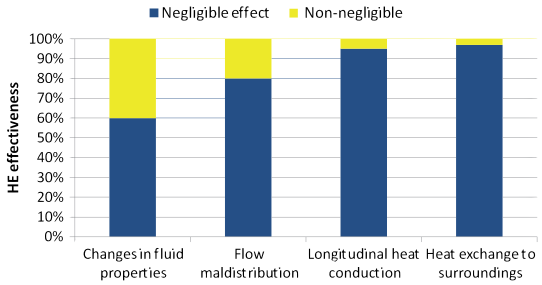

Fig. 1. Effects to be considered for a given design effectiveness.

this approach is not applicable for cryogenic applications. Soyars [101] stated that the use of this approximation for simulation of HE with helium below 15 K leads to mispredictions of 30–100% of the refrigeration heat load that can be achieved. Oonk and Hustvedt [74] found underpredictions of up to 12% on performance of helium HE between 4 and 20 K using this approach.

2.2.2. Flow maldistribution

In many scenarios, the flow distribution can deviate from design conditions, usually homogeneous. Mueller and Chiou [68] presented a comprehensive review on causes of maldistribution. They include mechanical issues such as fouling, fabrication tolerances, bypass and poor header performance, two-phase instabilities, and heat-transfer induced as a consequence of changes in viscosity or density. Flow maldistribution results in a deterioration of performance of single-phase HE [26,36,51], although this effect is only relevant for high efficiency equipment such as those used in cryogenics [68]. The effect on two-phase flow systems is more complicated, and both a reduction [79,102] and an increase [2,111] in performance have been observed.

2.2.3. Longitudinal thermal conduction

This effect reduces the local temperature difference between the working fluids and the separating wall, deteriorating the heat transfer. In the extreme case of infinite thermal conductivity, the performance of a balanced counterflow HE is reduced roughly by half, matching the co-current flow case [46, ch. 6]. This effect is more significant in small systems with short conduction lengths, such as perforated-plate, than in the large coil-wound (CWHE) and plate-fin (PFHE) heat exchangers.

2.2.4. Heat-in-leakage

Since cryogenic processes operate at much lower temperature than ambient, cryogenic equipment exchange heat with the surroundings. The development of multilayer insulations in the 1960s, with apparent thermal conductivity as low as 10–100 μW/(mK) [109] has reduced the heat-leakage to a practical minimum. However, when high-effectiveness equipment is required, this effect has to be considered.

3. Cryogenic heat exchangers. Types and geometries

Several types of heat exchangers have been used in cryogenic technology through its more-than-one-century-long history. They were described in detail by Barron [14,15]. In general, the selection of the geometry depends on the application. The decision should consider the operating pressure, mass flow rates, total heat duty, as well as operation and investment costs. In this section, the different geometries are reviewed from a modeling and design perspective.

To a broad extent, HE can be divided into two categories: recuperators and regenerators [99]. Both types are used for cryogenic applications. In a recuperator heat is transferred between the fluids through a separating wall. In a regenerator, both fluids alternately occupy the same physical space and thermal energy is stored and released from a matrix buffer material.

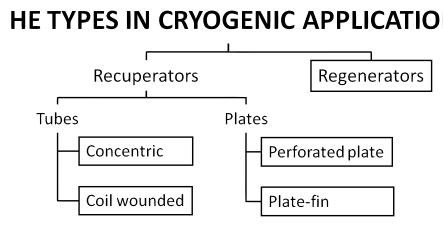

Fig. 2. Types of cryogenic heat exchangers.

The different types of recuperators used for cryogenic applications are summarized in Fig. 2, including tubular, plate-fin and perforated-plate HE. In particular, the first type can be subdivided into simple concentric-tube HE and more complex geometries with a multi-channel arrangement. The above mentioned types and geometries are studied in the following subsections, and the main features are summarized in Table 1.

A distinction should be made between HE for small-size and large-scale applications. The first ones require simple equipment that are easy to build and maintain and are dominated by the use of concentric-tube geometries (see Section 3.1), perforated-plate HE (see Section 3.4) and regenerators (see Section 3.5). On the other hand, the design of large-scale HE is more focused on minimizing the unit cost. Following this objective the selection of main HE for large cryogenic processes has been dominated by the coil-wound and plate-fin geometries [34]. They are studied in Sections 3.2 and 3.3, respectively.

3.1. Concentric tubes

Simple tubular HE used for small scale and laboratory applications are based in concentric-tubes geometries. A simple tube-in-tube exchanger was used by Linde in 1895 for the first-time liquefaction of air [89]. The efficiency can be improved with the use of a wire spacer that keeps the distance between tubes roughly constant. For more complex processes that involve multiple streams a multiple-concentric-tubes HE can be used. In this last geometry, several high-pressure streams flow inside parallel smaller tubes located inside a larger enclosing tube that contains the low-pressure stream.

From a model perspective, these geometries do not present major challenges. Since each stream flows in a single channel, no mixing needs to be considered. In addition, they are one-dimensional equipment in pure co-current or counter-current flow arrangement.

3.2. Coil wound

For large scale applications, the coil-wound heat exchanger (CWHE), also known as Giauque–Hampson HE is widely used. Layers of tubes are coiled around a central mandrel, which provides mechanical stability. Several tube-side streams can be used in the different layers, two or three being common in LNG processes, exchanging heat with a common shell-side stream. This feature represents a major comparative advantage to the more traditional shell-and-tube exchangers. They can be constructed in very large units, only limited in size by transportation issues [65]. The main disadvantage is that they are proprietary and expensive equipment, only manufactured by APCI and Linde Group [105].

The Collins-type HE [29] presents a similar geometrical arrangement. Similarly, successive layers of tubes are coiled around a central mandrel, and the low pressure stream has an helical flow-path around the tubes. The differences between both geometries are not large, they include the flow distribution devices and some mechanical support.

A major challenge in these last two geometries is the flow distribution on both tube and shell sides. For this reason, both tube spacing and length are kept almost constants.

3.3. Plate-fin

This type of HE consists of sets of layers of corrugated plates (usually made of aluminum) which serve as fins, and separating

Table 1
Summary of HE geometries. HTC = heat transfer coefficient. LHC = longitudinal heat conduction. Sources: [1,8,15,60].

	CWHE	PFHE	PPHE	Regenerators
Advantage(s)	Multifluid, robust to transients	Multifluid, low cost	High HTC	Good for only one working fluid
Disadvantage(s)	High cost	Sensitive to transients	Limited in size	Flow mixing
Scale	Large	Large	Small	Small
Heating surface density (m^2/m^3)	50–150	300–1000	up to 6000	up to 6500
Cost per unit duty	Very high	Medium	High	Low
Modeling challenges	Flow distribution	Fin efficiency	HTC and LHC	Matrix heat capacity

thin metal sheets. This configuration results in small flow passages and large extended surface area, which makes plate-fin heat exchangers (PFHE) very compact equipment. In addition, they can handle up to ten different streams in the same unit and very low temperature differences can be achieved. This results in lower capital and operation costs compared to traditional shell-and-tube-type HE [61]. For this reason they are used in several industries, covering large ranges of temperature and pressure, and many manufacturers produce them around the world, grouped in the *Brazed Aluminium Plate-Fin Heat Exchanger Manufacturers' Association* [4].

The main comparative advantages of PFHE over CWHE are the high compactness and lower cost per unit refrigeration duty [60]. However, PFHE are more limited in size and operating pressure [31].

A key issue in modeling and design of PFHE is the fin efficiency. Extensive research is focused on the specification of the fin geometry. Fin types include plain, triangular, perforated, serrated, among others.

3.4. Perforated plate

This type of HE has found extensive use for small scale refrigerators. A comprehensive review of the history and applications of perforated-plate HE (PPHE) is given by Venkatarathnam and Sarangi [116]. The geometry consists of several parallel perforated plates separated by spacers.

In this configuration, heat transfer in two directions needs to be considered. The main heat exchange between streams occurs laterally through the high-conductivity plates, usually copper or aluminum, acting as fins. Longitudinal heat conduction is avoided to some extent by the use of a relatively low-conductivity material for the spacers, such as stainless steel.

The periodic disruption of the flow when passing through the orifices provides high non-equilibrium heat transfer coefficient. At the same time this effect produces a relatively large pressure drop.

The consideration of longitudinal heat conduction is critical for the design of PPHE. Other main challenges for design are a proper estimation of the heat transfer coefficient, and the performance of the plates acting as fins.

3.5. Regenerators

Regenerators present a design that is conceptually different to the above mentioned geometries. In a regenerator both fluids occupy the same space alternately and the transfered heat is temporarily stored in a packing material, called the matrix. Therefore they run in a cyclic operation, storing and releasing energy from the matrix. A review on the historical development of regenerators and applications in cryogenics can be found in the book by Ackermann [1]. They are widely used for small-scale single-phase gas purposes.

The main advantage of regenerators is their extremely high area density, reaching up to 6500 m^2/m^3 [1]. The periodic flow reversal provides a self-cleaning mechanism. In spite of the inclusion of a switching device, they are generally simple to construct, resulting in a relatively low-cost component. An important disadvantage is the occurrence of some mixing between streams, since they alternately occupy the same physical space.

Considering that regenerators operate in a periodic mode, a key parameter for the transient modeling is the heat capacity of the matrix material. In addition, given the usually high operating frequencies the switching devices requires special considerations.

4. Heat exchanger models

This section deals with the present models used for thermal-hydraulic design of HEs. A complete analysis of a heat exchanger must consider mechanical and corrosion effects, and other issues as fabrication and shipping procedures should be taken into account. However, these effects exceed the scope of this review, limited to thermal-hydraulic models.

Heat exchanger thermal-hydraulic modeling involves the solution of two problems: rating and sizing [99]. Rating consists of evaluating the performance of an existing HE. Since all the relevant information is given (geometry, flow conditions), detailed models can be used. Sizing refers to the opposite problem, that is to select the proper HE geometry, flow arrangement and size to meet the specified performance within some given constraints. The geometry is still unknown, and for that reason simpler models are required.

A possible classification of the present HE models used for sizing is presented in Fig. 3. They can be grouped in three main categories: lumped parameters, distributed parameters and stream-evolution, which are further explained in detail in the following subsections and summarized in Section 4.4 and Table 2.

4.1. Lumped parameters models (LPM)

These models represent the basic design theory for HE and can be found in most textbooks [52,58,99]. They are based on the following energy balances for two single-phase streams:

$$C_c dT_c = U\,dA(T_h - T_c) \tag{2}$$

$$C_h dT_h = -U\,dA(T_h - T_c) \tag{3}$$

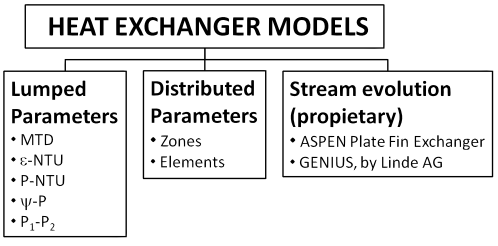

Fig. 3. Summary of models for sizing heat exchangers.

Table 2
Review of HE models. Evaluation of interesting effects for cryogenic and LNG applications. •: effect considered, ○: effect not considered.

Effect	LPM	DPM		SEM	
		Zones	Elements	ASPEN	GENIUS
Single-phase flow	•	•	•	•	•
Two-phase flow	○	•	•	•	•
Flow mixing (partial)	○	○	○	○	○
Flow mixing (complete)	•	•	•	•	•
Changes in fluid properties	○	○	•	•	•
Multiple streams	○	○	○	•	•
Multi-component mixture	○	•	•	•	•
Flow injection/removal	○	○	•	•	•
Heat-in-leakage	○	○	○	○	•
Axial thermal conduction	○	○	○	○	•
Flow maldistribution	○	○	○	•	○
Effect of pressure drop on heat transfer	○	○	○	○	○

where the heat capacity rate (C), defined as the mass flow rate ($\dot{m}$) times the specific heat (c_p) is used.

$$C = \dot{m}c_p \tag{4}$$

Eqs. (2) and (3) are integrated considering the following assumptions:

- Steady-state operating conditions.
- No heat transfer with the surroundings.
- Longitudinal heat conduction is negligible.
- Constant overall heat transfer coefficient.
- Constant heat capacity.

Following this integration, the HE is represented with two parameters: one for the physical size and another for the thermal performance. This category includes five different models [99, ch. 3], namely mean temperature difference (MTD), $\varepsilon - NTU$, $P - NTU$, $\Psi - P$ and $P_1 - P_2$. The first two methods are the most widely used for cryogenic applications. All these lumped parameters models (LPM) yield the same results, since they solve the same equations under identical assumptions. The only difference between them is the selection of the parameters. In general, lumped parameters models are meant to be used for single-phase flow with constant properties.

4.1.1. Mean temperature difference (MTD)

The local differential heat flux (dq) between streams is given by the product of the local temperature difference (ΔT), the differential area (dA) and an overall heat transfer coefficient (U), that is:

$$dq = U\Delta T\, dA \tag{5}$$

Integrating (5) and considering a constant heat transfer coefficient (HTC), an effective mean temperature difference (ΔT_m) can be considered as acting through the total area (A)

$$\Delta T_m = \frac{Q}{UA} \tag{6}$$

In the case of co-current or counter-current flow, the integration results in a logarithmic mean temperature difference ΔT_{lm}, defined as:

$$\Delta T_{lm} = \frac{(T_h - T_c)_{hot\ end} - (T_h - T_c)_{cold\ end}}{\ln[(T_h - T_c)_{hot\ end}/(T_h - T_c)_{cold\ end}]} \tag{7}$$

Since (7) applies to two of the most common flow arrangements, this method is also known as the logarithmic mean temperature difference (LMTD) method. For other geometries, a correction factor F, given by (8), is employed.

$$F = \frac{\Delta T_m}{\Delta T_{lm}} \rightarrow Q = UAF\Delta T_{lm} \tag{8}$$

ε-NTU. This method is widely used and is found in most textbooks on heat transfer. Its simplicity makes it very useful for the economic analysis of heat recovery. However, is of little help for the design engineer [104] if its assumptions are not fulfilled, which is a common scenario in cryogenic systems. The thermal performance is expressed in a dimensionless way using an effectiveness (ε) defined as the ratio of actual heat duty (Q) and the maximum achievable with the given inlet conditions (Q_{max}).

$$\varepsilon = \frac{Q}{Q_{max}} \tag{9}$$

The model uses two nondimensional parameters: the ratio of heat capacity rate of both fluids (C^*) and a number of thermal units (NTU) that relates the HTC and physical size area with the minimum heat capacity rate.

$$NTU = \frac{UA}{C_{min}} \tag{10}$$

$$C^* = \frac{C_{min}}{C_{max}} \tag{11}$$

For a given flow arrangement, the three variables ε, NTU and C^* are related, and two useful expressions can be obtained. On the one hand, (12) allows to rate the performance of a given HE. On the other hand, (13) gives the required size, in terms of NTU, for the design conditions. Basic forms of the solutions are available for both Eqs. (12) and (13).

$$\varepsilon = \phi(NTU, C^*, \text{flow arrangement}) \tag{12}$$

$$NTU = \phi(\varepsilon, C^*, \text{flow arrangement}) \tag{13}$$

P-NTU. This method employs two individual parameters for each stream. The first parameter, a number of thermal units, is defined for each stream as:

$$NTU_h = \frac{UA}{C_h}, \quad NTU_c = \frac{UA}{C_c} \tag{14}$$

The second parameter is a heat capacity rate ratio (R) for each stream:

$$R_h = \frac{C_h}{C_c}, \quad R_c = \frac{C_c}{C_h} \tag{15}$$

The thermal performance of the HE is evaluated with individual temperature effectiveness (P) defined as:

$$P_c = \frac{Q}{C_c\Delta T_{max}}, \quad P_h = \frac{Q}{C_h\Delta T_{max}} \tag{16}$$

According to this definition, the temperature effectiveness P is related to ε as given by (17)

$$P_c = \varepsilon \frac{C_{min}}{C_c}, \quad P_h = \varepsilon \frac{C_{min}}{C_h} \tag{17}$$

In general, for a given flow arrangement, P depends on the HE size and the heat capacity rate ratio, that is:

$$P_c = \phi_c(NTU_c, R_c, \text{flow arrangment}) \tag{18}$$

$$P_h = \phi_h(NTU_h, R_h, \text{flow arrangement}) \tag{19}$$

The comparative advantage of the P-NTU method is that, with the use of individual parameters, it is not necessary to identify the stream with the minimum heat capacity flow rate.

$\Psi - \mathbf{P}$. This method, first proposed by Mueller [67], introduces the parameter Ψ that represents a nondimensional effective mean temperature difference.

$$\Psi = \frac{\Delta T_m}{\Delta T_{max}} \tag{20}$$

This parameter is related to the previous models as:

$$\Psi = \frac{\varepsilon}{NTU} = \frac{P_c}{NTU_c} = \frac{P_h}{NTU_h} \tag{21}$$

The $\Psi - P$ method was introduced by Mueller [67] as a simpler graphical representation of the HE performance.

$\mathbf{P_1} - \mathbf{P_2}$. Roetzel and Spang [93] proposed this method as a simpler way of graphical representation of the HE performance. It does not introduce new parameters, but recommends the use of the temperature effectiveness of both streams.

4.1.2. Other efficiencies

Clayton [27] proposed the use of a two new parameters to rate the HE performance. They are a HE efficiency η and a *new effectiveness* E_n.

The first one is the ratio of the actual heat transfer rate to the one that would be achieved if both fluids had an infinite specific heat. It is always $\eta < 1$. Its use is advantageous for small-size exchangers, since in this case $\eta \to 1$, while $\varepsilon \to 0$, thus reducing the relative sensitivity to uncertainties. With these considerations, a boiler-condenser system has an efficiency of $\eta = 1$.

A *new effectiveness* E_n is defined as the ratio of the actual heat transfer to the one obtained by direct mixing. According to this definition, it can take values larger than unity. In particular, an infinite co-current flow HE would have $E_n = 1$, and a balanced infinitely large counter-current flow case would give $E_n = 2$. The use of this new effectiveness identifies more clearly the balanced heat capacity flow rates case as an optimal design, as opposite to the $\varepsilon - NTU$ method, which indicates that ε is larger when C^* is lower.

4.2. Distributed parameters models (DPM)

These models are based on dividing the HE in elements of variable size and applying a lumped parameters model in each of them; the $\varepsilon - NTU$ and MTD being the most common ones. The application of a LPM is then restricted to a small region where the assumptions listed above in Section 4.1 are better fulfilled. They are widely used for applications with complex flow arrangements, such as air conditioning systems and heat pumps. This can be done at two different levels: zones or elements [49]. Optimal results are obtained using a mixed approach.

4.2.1. Zones

Evaporators and condensers are usually divided in three zones: single-phase liquid, two-phase and single-phase vapor. This approach applies a lumped parameter model over the whole two-phase region, where its assumptions (listed in Section 4.1) are not strictly valid. In particular, the assumption of constant HTC is only applicable to a certain extent in scenarios where the thermal resistance is dominated by the single-phase stream. For this reason, this approach has been used by several authors for modeling air-cooled condensers and air-heated evaporators [30,35,69]. Orth et al. [75] further divided each zone into elements.

4.2.2. Elements

The heat exchanger is divided in elements of some given physical length, in a geometry-oriented approach. This approach is useful for complex geometries like air conditioning and heat pump systems with multiple tube passes in several directions [33,59]. Since this model is not flow-oriented, the transition between single- and two-phase is not intrinsically considered, which may lead to some numerical problems. These issues can be solved by reducing the element size to a tube-segment, as proposed by several authors [80,112], therefore reducing the size of the transition element, although this scenario is only conditionally stable. Iu et al. [48] further divided the transition elements into two zones, in a mixed geometric- and flow-oriented approach.

4.3. Stream evolution models (SEM)

SEM are based on steady-state one dimensional mass, momentum and energy balance equations for each individual stream. This feature makes them appropriate for multi-stream heat exchangers, which are often used in cryogenic applications, in particular for LNG processes. The inclusion of the mass balance allows the evaluation of the individual compositions of vapor and liquid in boiling and condensation of mixtures, and the momentum equation is used to evaluate the pressure drop. While a one-dimensional analysis is simple and fast, heterogeneous behavior through the cross section is neglected.

These models are usually implemented into proprietary software, and their key features are related to the correlations used for fluid properties and heat transfer and pressure drop characteristics. Two proprietary programs are reviewed in this section: *Aspen Plate Fin Exchanger* ®, offered by AspenTech® and *GENIUS*, developed by Linde AG. Other models, such as the one proposed by Fredheim et al. [39], are designed as user-defined subroutine integrated into a process simulator.

4.3.1. Aspen plate fin exchanger®

ASPENTech [9] offers this commercial software for simulation of PFHE, that can be integrated into its proprietary process simulator. Some relevant features include:

- Pressure drop is evaluated in detail, including the localized effects in distributors, headers and nozzles. However, its consequences on heat transfer are not considered, since it is computed *a posteriori*.
- Flow maldistribution can be considered to a certain extent in a layer-by-layer simulation mode. The evolution of each layer is modeled individually, given an imposed flow distribution profile, that can be either linear or parabolic. However, it should be noticed that the usual flow distribution for plate-type geometries are cosine or hyperbolic cosine profiles, as reported by Bassiouny and Martin [16], Bassiouny and Martin [17]. In addition, this approach does not consider interaction between layers.

This code represents a powerful tool for the modeling of PFHE, with the advantage of its integration to a process simulator. Although it considers several effects, a complete description of the HE is not achieved, as discussed in Section 4.4 and Table 2.

4.3.2. GENIUS, by Linde AG

This program, presented by Steinbauer and Hecht [103], was developed an tested by Linde AG to model CWHE. Although this program is not commercially available, it is used by one of the only two manufacturers of CWHE. Some important features include:

- Local heat transfer coefficients (HTC) and pressure gradients are used, evaluated with the local fluid properties. However, the HTC is only dependent on the local enthalpy and the wall temperature, neglecting the effects of changes in pressure (inlet value is assumed).
- Heat losses and heat feed can be considered. To our knowledge, this is the only code that includes heat exchange with the ambient. However, no details in geometrical location of the heat source/sink can be incorporated. In cryogenic systems, this exchange occurs in the outer part of the HE, producing temperature and densities heterogeneities in the shell-side flow that lead to some degree of flow mixing.
- Cross-sectional averaged temperatures are used. In addition, a mean fluid velocity is considered. This means that the HE is modeled at a stream-by-stream level, and not layer-by-layer.

The first version was released in 1993 and since then large efforts were focused on developing and testing correlations against reported literature and measurements performed in Linde AG laboratories. Although this gives an extensive level of validation to the code, it implies that all the physical effects that are not considered by the model, are implicitly taken into account by the correlations.

4.4. Summary. Features for cryogenic applications

Table 2 summarizes the HE models introduced in this section and their consideration of physical effects relevant for cryogenic applications. Some important conclusions can be extracted from this table:

1. All models are capable of modeling complete flow mixing. This can be simply done by using averaged values in a one-dimensional analysis. However, flow mixing is not always complete, and a partial mixing analysis would require a two- or three-dimensional model, which none of them considers. In the case of multi-component mixtures, this situation may lead to mass concentration profiles that affect the heat transfer performance.
2. The consequences of pressure drop on heat transfer is neglected in all cases. The importance of this effect is discussed in Section 6.
3. The most advanced models (stream evolution category) are proprietary. Furthermore, some of them are not commercially available.
4. The model given by ASPENTech [9] is the only one that considers flow maldistribution in a layer-by-layer approach. All layers are considered to be identical except for the mass flow rate. This allows to evaluate the consequence of a given distribution profile and cannot be used for predicting the existence of flow maldistribution.

In summary, present heat exchanger models are not capable of considering all physical effects relevant for cryogenic and LNG applications.

5. Other effects reported in literature

Section 4.4 highlights the limitations of the available models to consider all relevant effects. This situation has been noticed by several authors. The present section reviews the available literature on improvements to these models. This research has been focused in the main effects that should not be neglected, as described in Section 2.2, that is:

1. Changes in fluid properties.
2. Flow maldistribution in parallel channels.
3. Longitudinal thermal conduction.
4. Heat exchange with the surroundings (heat leakage).

The following subsections cover the state-of-the-art on these effects. Section 5.5 describes the literature on combination of these four effects. Finally, the review described in this section is summarized in Tables 3–8.

5.1. Changes in fluid properties

Distributed parameters and stream-evolution models, discussed in Sections 4.2 and 4.3, deal with this effect in a discretized approach. Some other approaches have been reported in literature, for example the use of averaged or effective values, and are reviewed in this section.

For single-phase flow HE design, the most relevant effects are given by the specific heat capacity and the overall heat transfer coefficient (HTC). Most research has been focused on their separate effect. The combination of both effects has been studied by Roetzel [90]. He recommended the use of suitable averaged values based on the calculation at two points. Following this work, Peters [77] included the variation of HTC in length due to laminar flow development. However, this author recognized that no reasonably simple procedure is successful when large variations are present. While most published works were limited to co-current and counter-current flow arrangements, Roetzel [91] extended this study to crossflow HE, considering both length and temperature effects.

5.1.1. Specific heat capacity

Kays and London [55] suggested the use of constant values for the fluid properties in a recuperator, evaluated at the mean temperature. This approach is valid when the variation is limited to a factor of 2. However, this is usually not the case in cryogenic systems. Chowdhury and Sarangi [24] studied the case of supercritical hydrogen in the temperature range 300–80 K and 300–40 K, where the specific heat varies by a factor 4. They observed that the use of a harmonic mean specific heat gives good results for balanced flow HE, but present some deviations for unbalanced, high NTU cases. The same approach (harmonic mean) was proposed by Sahoo and Sarangi [94] for the analyisis of regenerators. They observed that the overall effectiveness is correctly calculated, however this method does not satisfactorily predict the temperature profiles.

Kumar and Sarangi [57] noted that the use of averaged constant properties fails to predict the location of points with minimum temperature difference (pinch points). This pinch points occur when the heat capacity flow ratio C_h/C_c varies from a value of less than unity to one larger than unity, or vice versa. This situation is likely to occur in cryogenic systems with a close-to-balanced design. In this case, the authors recommend a finite-difference solution. The considered working fluids were both normal- and para-hydrogen.

Soyars [101] studied a cryogenic helium HE using discretized $\varepsilon - NTU$ and LMTD models. The author noticed that the $\varepsilon - NTU$ approach relies on the estimation of the heat capacity flow. In close-to-balanced design condition, a poor estimation of the heat capacity may lead to sections of the HE with a value of ε larger than unity. This situation is not physical, and leads to an erroneous sizing of the HE. For this reason, the author recomended the use of a discretized LMTD method.

Table 3
Summary of available literature on the effects of variations in specific heat capacity.

Method	Observations	Reference(s)
Use c_p at mean temperature	Up to a factor 2 variation	[55]
Harmonic mean (recuperators)	Up to a factor 4 variation. Misleading results for unbalanced, high NTU cases	[26]
Harmonic mean (regenerators)	Predicts well ε, but the temperature profiles are incorrect	[94]
Distributed parameters	LMTD preferred over $\varepsilon - NTU$	[101]
Finite-difference	Identifies pinch points	[57]

Table 4
Summary of available literature on the effects of variations in heat transfer coefficient.

Method	Observations	Reference(s)
Review (1977)	Widely studied for single-phase	[41]
Logarithmic mean of $U \times \Delta T$	For linear functions $U(T_c, T_h)$ in counter-flow arrangement	[28]
Arithmetic mean of $U \times \Delta T$	For linear functions $U(T_c, T_h)$ in multipass flow arrangements	[18,40,110]
Four-points integration	For polynomial or power-law functions $U(\Delta T)$, 1% uncertainty	[100]
Non-linear energy equations	General functions $U(T, \Delta T)$	[54]

Table 5
Summary of available literature on the effects of flow maldistribution.

Method	Observations	Reference(s)
Divide the HE in two sections, step profile	Flow mixing improves performance	[36]
Heat transfer coefficient depends on fluid velocity	2% change in ε compared to [36]	[82]
Axial dispersion	Transient analysis	[92,95]
Plate condensers	Optimum number of plates	[84–87]
Transverse heat conduction	Similar effect to flow mixing in [36]	[51]
Equal pressure drop constraint	Secondary maldistribution further reduces performance	[76]

Table 6
Summary of available literature on the effects of longitudinal heat conduction.

Method	Observations	Reference(s)
Review (1994)	Most relevant in counter-current	[98]
Pioneer work, non-dimensional	Maximum effect for balanced, high NTU.	[56]
Conduction in outer wall	Less severe than in inner wall	[115]
Regenerators (conduction in fluid)	Only significant for high reduced length HE	[96]
Regenerators (conduction in matrix)	Gives optimum value for charging time	[32]

Table 7
Summary of available literature on the effect of heat exchange to the surroundings.

Method	Observations	Reference(s)
Heat exchange to only one stream	Some graphical results. For cryogenics, heat exchange to the cold fluid is more severe	[12,24,78,97]
Heat exchange to both streams	Counter-current flow arrangement is less affected	[6,5]
Uniform heat source	Analytical solution, useful as a guideline	[72,3]
P-NTU method	If $C_c < C_h$, an optimum NTU exists	[62–64]

Table 8
Summary of available literature on combined effects.

Method	Observations	Reference(s)
Flow maldistribution and LHC	Tend to eliminate each other for high NTU, and augment each other for low NTU	[21,81]
Heat exchange to surroundings at one end, and LHC	An optimum value for NTU is found to exist	[44,71]
Changes in fluid properties, LHC and heat exchange to surroundings	Computing their effect simultaneously or separated gives similar results, within ±10%	[43,72]

5.1.2. Heat transfer coefficient (HTC)

This effect has been studied as early as 1933 by Colburn and de du Pont [28]. They presented an analytical solution for the counter-current flow case where the overall HTC varies linearly with the temperature of one of the fluids, keeping all other fluid properties constant. This approach uses a logarithmic mean combined function of HTC and temperature difference. This means that the average HTC is calculated on the basis of the extreme values.

Gardner and Taborek [41] presented an up-to-date review of HE models with variable HTC. For counter-current flow, the model

given by Colburn and de du Pont [28] is recommended. The use of an arithmetic mean of product of HTC and temperature difference have been suggested by Bowman et al. [18] for a general multipass flow arrangement, assuming a linear dependence of the HTC on temperature. Its use has been found to be satisfactory by later authors [40,110] within an accuracy range of ±10%. For general functional dependencies of the HTC, the method of Kao [54], based on solving simultaneous non-linear energy balance equations, is recommended.

Recently, Sharqawy and Zubair [100] presented numerical and analytical solutions for more complex variations of the HTC. They studied polynomial and power-law dependences on the local temperature difference and compared the results with experimental data available in the literature. These authors recommend the use of a four-points numerical integration which predicts the required surface area within a 1% uncertainty.

5.2. Flow maldistribution in parallel channels

Extensive research on this field was focused on modeling and design of distribution headers to improve the flow distribution. However, flow maldistribution can occur for several reasons other than header performance, summarized by Mueller and Chiou [68]. Since maldistribution occurs in most practical cases, its effect on HE performance must be quantified. In general, most authors agree that this effect is negligible for low-effectiveness HE.

The effects on high-effectiveness HE, as used in cryogenics, was first studied by Fleming [36]. In particular, he studied a counter-flow HE where one side is uniformly distributed and the other one is not. This latter stream with maldistribution is modeled as a fraction F_L of the channels with lower-than-average flow and a fraction $1 - F_L$ with higher-than-average flow. The model assumptions include a constant HTC, independent of the velocity, which is reasonably valid only for fully developed laminar flow. He presented results in terms of ε and an effective value of NTU, which can be reduced to less than half of the design value. The situation is improved if the uniform side is completely and continuously mixed, as an idealization of shell-and-tube or coil-wound geometries. The main conclusion of this work is that, for high-effectiveness cryogenic applications, there is very little to be gained from increasing the design NTU of a HE, but rather the flow distribution should be improved.

Rao and coworkers studied the effect on plate-type HE in several articles [84–87]. They considered the flow distribution profile suggested by Bassiouny and Martin [16], Bassiouny and Martin [17]. Their study includes the dependence of HTC on velocity, and the analysis of single- and multi-pass HE for single-phase laminar flow as well as condensers. Their results indicate that the Z-type exchangers are more severely affected by maldistribution. In addition, they noticed that increasing the number of plates improves the performance only up to certain optimum point. Further increase produces a higher extent of maldistribution, which result in a reduction of performance.

Roetzel and Ranong [92] introduced an hyperbolic axial dispersion for the steady-state analysis of HE with flow maldistribution. In this framework, they studied the response to imposed distribution profiles. The selected profiles were linear and quadratic. The existence of back-flow in some channels was also considered. This model was later extended to transient analysis [95].

A cross-flow arrangement was considered by Ranganayakulu [82]. They investigated the influence of changes in the HTC as a consequence of the variations in the velocity. According to their results, this influence is limited to a 2% effect on the effectiveness ε, compared to a simpler model, asumming constant HTC. The deterioration of thermal performance was studied considering four different flow distribution profiles.

Jung and Jeong [51] studied the effect of transverse heat conduction in single-body HE for counter-current single-phase flow. This condition provides some extent of thermal coupling between the different channels. The consequence is similar to that of flow mixing, that is, provides a more homogeneous temperature profile, thus reducing the effect of flow maldistribution in performance. This situation is interesting for the design of anisotropic equipment, such as perforated-plate HE.

Recently, Pacio and Dorao [76] presented a numerical analysis including the momentum equation for two-phase flow. They concluded that the pressure-drop coupling between channels is expected to produce a secondary maldistribution that further reduces the HE performance.

5.3. Longitudinal heat conduction (LHC)

The work by Hennecke [45] indicates that LHC in a single-phase fluid can usually be neglected, except when the Prandtl number is very low, which is the case for liquid metals. In cryogenic systems, then, LHC is only considered to occur in the wall. The effect of finite LHC is to flatten the wall temperature distribution, thus reducing the performance of a given HE.

A comprehensive review on this subject is given by Shah [98]. In this work, the author stated that the effect of LHC is negligible for co-current flow, since in this case the temperature gradient in the wall is small. In addition, this effect is the largest for cross-flow HE, given the two-dimensional profiles. For this reason, the research list on cross-flow arrangement is long [22,47,83,117,118]. However, this type of exchangers is frequently used for applications within a lower range of effectiveness, usually $\varepsilon < 0.8$. The consideration of this effect is most relevant for counter-current flow.

In this scenario, the work by Kroeger [56] stands out as a comprehensive analysis for a wide range of operating conditions. The effect of LHC on HE performance is more important with increasing number of thermal units, and it is maximum for a balanced operation, that is $C_h = C_c$. Results were obtained numerically and presented graphically and by means of approximate expressions. These results were later confirmed by Chowdhury and Sarangi [23] and Narayanan and Venkatarathnam [70].

Following the work by Kroeger, Venkatarathnam [113] considered LHC in perforated-plate HE. In this case, an axial conduction parameter is defined as a function of the number of spacers and their thermal conductivity.

Venkatarathnam and Narayanan [115] studied the LHC in the outer wall of a tube-in-tube HE. In general, they concluded that the degradation of performance is lower as compared to the LHC occurring in the inner wall. This result is a consequence of the lower temperature gradients. Finally, they recommended the use of the model given by Kroeger if the conduction in the inner wall is much higher than in the outer wall.

The effects of LHC have also been investigated in regenerators. Sarangi and Baral [96] considered the axial conduction in the fluid. In this case, this effect is relevant because of the eddy thermal conduction given by the flow through porous media. Solving transitory energy balances, the authors concluded that the consequences in performance are significant for high reduced-length HE. In their study case, the expected ineffectiveness was doubled by the effect of LHC.

The heat conduction in the matrix was considered by Das and Sahoo [32], using a similar procedure. Performing an optimization based on the second law of thermodynamics, the authors observed that, in order to improve the performance, the charging time should be increased to an optimum value. Cryogenic regenerators, however, are usually designed to operate at high frequency, thus resulting in a short charging period.

5.4. Heat exchange with the surroundings (heat leakage)

This effect might be beneficial if the objective is to cool down hot fluids (heat rejection) or heat up a cold stream, such as in regasification of LNG. However, in most cryogenic processes, the main goal is refrigeration below ambient temperature, and in these cases heat leakage has a negative effect.

The physical effect of heat-in-leakage depends on which stream is being heated. On the one hand, if the cold stream receives heat from the surroundings, the temperature difference (and heat exchange) between streams is reduced, and even temperature cross may occur. On the other hand the opposite situation occurs if heat is transfered from the environment to the warm stream, and the heat duty is increased. However, keeping in mind that the objective is to refrigerate the warm stream, its outlet temperature is higher than predicted by an adiabatic model. This situation reflects that the total heat duty (or, in dimensionless form, the HE effectiveness ε) is not sufficient to rate the performance.

The available literature on this subject is limited to single phase applications. Barron [12] studied a counter-current HE assuming constant fluid properties. In this framework, he presented non-dimensional heat transfer equations for the external heat transfer to the cold and hot fluids separately. His results showed that when the environmental temperature is greater than the temperature of the inlet hot fluid temperature, as in cryogenic applications, the heat transfer to cold fluid has a more pronounced effect on the HE performance.

Chowdhury and Sarangi [25] studied a double-pipe for cryogenic applications from a design perspective. In this geometry, only the stream flowing in the annulus interacts with the surroundings. They presented analytical solutions and an estimation of the reduction in the effective number of thermal units. This situation was later studied by Prasad [78] for high-temperature applications.

In some occasions, such as microminiature exchangers with thin insulations layers on both sides, both streams are subjected to simultaneous external heating. This situation was investigated by Ameel and Vitharana [6], Ameel [5] in co-current and counter-current flow arrangement. They presented analytical results considering non-dimensional conductance ratios and concluded that, when considering this effect, the counter-current arrangement gives a higher performance.

Seetharamu et al. [97] incorporated the effect of heat leakage in a tube-in-tube HE as a three-fluid exchanger where the third stream is ambient air at a constant temperature. Changes in fluid properties were also considered in a finite-element formulation. The author observed reduction of performance in all cases, and temperature cross when the hot fluid is cooled by heat transfer to the ambient.

Nellis and Pfotenhauer [73] presented analytical results for a counterflow HE with uniformly distributed heat load applied to one or both sides. However, this situation is not representative of cryogenic HE, that can be better represented by a constant ambient temperature scenario. Nevertheless, the analytical non-dimensional solutions are useful guidelines for the numerical analysis of arbitrary heat load profiles. A similar study was performed by Al-Dini and Zubair [3] for co-current flow arrangement.

Recently, Mathew and Hegab [62], Mathew and Hegab [63], Mathew and Hegab [64] studied microchannel HE in co- and counter-current flow with heat-in-leakage. Considering individual temperature effectiveness for each fluid, they concluded that the cold-side effectiveness is increased, while the hot-side effectiveness is reduced. For unbalanced flows, the results depend on which fluid has the lowest heat capacity rate. If this is the warm stream, the effectiveness is always increased with larger NTU. On the other hand, when the cold fluid has the lowest heat capacity flow rate, there is an optimum value of NTU that gives a peak maximum effectiveness.

5.5. Combined effects

The vast majority of the available literature is focused in only one of the four effects mentioned above. There are, however, some reported articles on the analysis of the combination of two or more of them. In all cases, they include the modeling of longitudinal heat conduction (LHC).

Chiou [21] attempted the combined effects of LHC and flow maldistribution for specific imposed distribution profiles. Ranganayakulu and Seetharamu [81] incorporated the effects of non-uniform inlet temperatures in the modeling of cross-flow HE. An interesting observation is that these three (LHC, flow maldistribution and temperature non-uniformities) combined effects on the deterioration of HE performance tend to eliminate each other in the regions of higher NTU, but tend to augment each other in the regions of lower NTU. Nevertheless, in all cases the performance is reduced, ranging from a few percent up to 30%.

Mehrabian et al. [66] studied the performance of a plate-HE with a finite-difference model that includes axial conduction in plates and flow channels and the dependence of viscosity on temperature. Their results show that LHC in the plates reduces the performance of the exchanger, while LHC in the flow channels improves it.

The most extensive research is dedicated to the combination of LHC and heat leakage. This can be divided in two categories. First, some authors assume constant physical properties and simulate the HE in a non-dimensional analysis. The second category is based on discretized energy balances that allow for the variation of fluid properties.

Included in the first category, the work by Narayanan and Venkatarathnam [71] investigated the performance of a Joule–Thompson recuperator with heat losses at the cold end due to its proximity to a low-temperature sink. In this scenario, the boundary condition at the wall is changed from adiabatic to conductive. Their results indicate that the hot fluid exits at a lower temperature. Gupta and Atrey [44] studied both effects, however without drawing general conclusions on their coupling. Their study concluded that increasing NTU can cause more degradation due to heat in leak and an optimum value of NTU is found to exist.

The second category is based in a discretized solution. Nellis [72] applied a finite-difference numerical approach to the modeling of axial conduction, parasitic heat loads, and property variations in a HE. The accuracy of separately calculating the important loss mechanisms in a high-effectiveness HE was found to give reasonable (within 10%) results as compared with the full model. Ghosh et al. [43] extended a simulation algorithm for multistream plate-fin HE presented earlier [42] to include LHC, heat exchange to the surrounding, and variable fluid properties.

6. Discussion on the state-of-the-art

Section 5 described the available literature on HE modeling. These can be considered advanced models, since they incorporate effects that are ignored by current models used for HE design, described in Section 4. In general, they can be divided in two categories: non-dimensional analysis and discretized equations.

The first category (non-dimensional analysis) consists of the analytical or numerical solution of dimensionless energy balances. They include the definition of axial conduction parameters and flow distribution profiles. Although this analysis is useful in a first stage of design, it is only applicable for simple cases with single-phase flow.

On the other hand, the vast majority of these models belong to the second category, namely the numerical solution of discretized energy balances. This approach can easily accommodate for

variation in fluid properties and heat transfer coefficients. In addition, more effects can be included with the consideration of energy balances in the wall. Following the same trend as in Table 2, more effects can be considered within this framework. The computational costs, however, are more demanding and for this reason advanced numerical methods, more efficient than the traditional finite-differences, will be needed. Examples of advanced methods used by some authors for the solution of HE include: first-order finite-element [81,83,88,97], spectral Galerkin [7,50], and collocation schemes [107,108]. In addition, the least-squares spectral elements method presents some potential advantages for its application to this problem.

Some general comments on the performance of available models for HE design were presented in Section 4.4 and Table 2, concluding that they fail to take into account all relevant effects. This situation is improved with the advanced models presented in Section 5. However, two points are not considered: first, the effects of pressure drop on heat transfer and second, partial flow mixing. Some remarks on these two points are presented next.

Changes in the working pressure affect the fluid physical properties and consequently, the heat transfer performance. While single-phase fluid properties are mainly dependent on the temperature, that is not always the case for two-phase flow. Of special interest for boiling and condensation applications are the variations in the saturation temperature. This situation can bring the temperature curves closer, thus reducing the total heat duty.

Flow mixing is neglected by some authors, while others assume a complete and continuous mixing. The practical case is an intermediate situation, producing temperature non-uniformities. The reason why this condition was not considered is because it cannot be successfully modeled by a one-dimensional formulation. Nevertheless, this effect is interesting for large shell-type HE, given that it affects the performance. In the case of multicomponent mixtures, partial mixing can also produce non-uniformities in the mass concentration profiles.

7. Summary

1. HE are key equipment in cryogenic systems. Thermodynamic and economic considerations set high-efficiency requirements which result in the need for accurate models. The state of the art on HE modeling for cryogenic applications is reviewed in this article.
2. Cryogenic systems involve two main challenges for the modeling of HE: complex processes and non-negligible physical effects. The complexity of the processes include large temperature ranges, multiple streams, two-phase flow and the use of multicomponent mixtures. The required accuracy is such that physical effects like changes in fluid properties, axial conduction, flow maldistribution and heat-in-leakage cannot be neglected.
3. The geometries used in cryogenic applications are summarized in Fig. 2 and Table 1. The selection of the HE type depends on the particular application. In this work, they were presented from a design-challenges perspective.
4. Present HE models used for design were reviewed. In general, they can be divided in three categories: lumped-parameters, distributed-parameters and stream-evolution. Their ability to consider relevant effect is summarized in Table 2. While the stream-evolution models are the most advanced, they are proprietary and, nevertheless, do not take all physical effects into account.
5. Extensive research covering the four above mentioned non-negligible effects is available in the open literature, resulting in state-of-the-art advanced models. In general, they can be divided into two categories: non-dimensional analysis and discretized energy equations. While most works were focused in only one of these effects, there are some published reports on their combination, indicating that no significant error is introduced by considering them separately.
6. The advanced models include more effects than those used for design. Nevertheless, two points are not considered: the effects of pressure drop on heat transfer and partial flow mixing. The variation on operating pressure is particularly important for two-phase flow, since it affects the saturation temperature. Flow mixing is neglected by some authors, while others assume a complete a continuous mixing. The practical case is an intermediate situation, producing temperature non-uniformities.

References

[1] Ackermann RA. Cryogenic regenerative heat exchangers. The international cryogenic monograph series. New York: Plenum Press; 1997.
[2] Aganda AA, Coney JER, Sheppard CGW. Airflow maldistribution and the performance of a packaged air conditioning unit evaporator. Appl Therm Eng 2000;20(6):515–28.
[3] Al-Dini S, Zubair SM. Effectiveness-NTU relations for parallel flow heat exchangers subjected to heat leak from outside. Heat Transfer Eng 2008;29(5):475–83.
[4] ALPEMA. The Standards of the Brazed Aluminium Plate-Fin Heat Exchanger Manufacturers' Association; 2000.
[5] Ameel TA. Parallel-flow heat exchangers with ambient thermal interaction. Heat Transfer Eng 2000;21(6):18–25.
[6] Ameel TA, Vitharana LH. Countercurrent heat exchangers with both fluids subjected to external heating. Heat Transfer Eng 1999;20(3):37–44.
[7] Amon CH, Mikic BB. Spectral element simulations of unsteady forced convective heat transfer: application to compact heat exchanger geometries. Numer Heat Transfer. Part A: Appl 1991;19(1):1–19.
[8] Anashkin O, Keilin V, Patrikeev V. Compact high efficiency perforated-plate heat exchangers. Cryogenics 1976;16(7):437–9.
[9] ASPENTech. Aspen plate fin exchanger; 2010. <http://www.aspentech.com/products/aspen-plate-fin.cfm>.
[10] Atrey MD. Thermodynamic analysis of collins helium liquefaction cycle. Cryogenics 1998;38(12):1199–206.
[11] Barclay M, Denton N. Selecting offshore LNG processes. LNG J 2005:34–6. October.
[12] Barron RF. Effect of heat transfer from ambient on cryogenics heat exchanger performance. Adv Cryogenic Eng 1984;29:265–72.
[13] Barron RF. Cryogenic systems. Monographs on cryogenics, 2nd ed., vol. 3. Oxford: Clarendon Press; 1985.
[14] Barron RF. Cryogenic heat transfer. Series in chemical and mechanical engineering. Philadelpia, PA: Taylor & Francis; 1999.
[15] Barron RF. Cryogenic technology. In: Ullmann's encyclopedia of industrial chemistry. Wiley-VCH Verlag GmbH and Co. KGaA; 2000.
[16] Bassiouny MK, Martin H. Flow distribution and pressure drop in plate heat exchangers – i u-type arrangement. Chem Eng Sci 1984;39(4):693–700.
[17] Bassiouny MK, Martin H. Flow distribution and pressure drop in plate heat exchangers – ii z-type arrangement. Chem Eng Sci 1984;39(4):701–4.
[18] Bowman R, Mueller A, Nagle W. Mean temperature difference in design. Trans ASME 1940;62:283–94.
[19] Brendeng E, Hetland J. State of the art in liquefaction technologies for natural gas. Ways of providing LNG for Transit Countries. In: Security of natural gas supply through transit countries. NATO science series II: mathematics, physics and chemistry, vol. 149. Netherlands: Springer; 2004. p. 75–102.
[20] Çengel YA, Boles MA. Thermodynamics. An engineering approach. New York: McGraw-Hill, Inc.; 1994.
[21] Chiou J. The advancement of compact heat exchanger theory considering the effects of longitudinal heat conduction and flow nonuniformity. In: Compact heat exchangers. History, technological advancement & mechanical design problems. ASME winter annual meeting, vol. 10, cited By (since 1996) 23. 1980. p. 101–21.
[22] Chiou JP. The effect of longitudinal heat conduction on crossflow heat exchanger. J Heat Transfer 1978;100(2):346–51.
[23] Chowdhury K, Sarangi S. Effect of finite thermal conductivity of the separating wall on the performance of counterflow heat exchangers. Cryogenics 1983;23(4):212–6.
[24] Chowdhury K, Sarangi S. The effect of variable specific heat of the working fluids on the performance of counterflow heat exchangers. Cryogenics 1984;24(12):679–80.
[25] Chowdhury K, Sarangi S. Performance of cryogenic heat exchangers with heat leak from the surroundings. Adv Cryogenic Eng 1984;29:273–80.
[26] Chowdhury K, Sarangi S. Effect of flow maldistribution on multipassage heat exchanger performance. Heat Transfer Eng 1985;6(4):45–54.
[27] Clayton DG. New concepts for heat exchanger performance. Heat Mass Transfer 1974;7:107–12.

[28] Colburn AP, de du Pont EI. Mean temperature difference and heat transfer coefficient in liquid heat exchangers. Ind Eng Chem 1933;25(8):873–7.
[29] Collins SC, Cannaday RL. Expansion machines for low temperature processes. London: Oxford University Press; 1958.
[30] Costa MM, Parise J. A three-zone simulation model for a air-cooled condensers. Heat Recov Syst CHP 1993;13(2):97–113.
[31] Crawford DB, Eschenbrenner GP. Heat transfer equipment for LNG projects. Chem Eng Process 1972;68(9):62–70.
[32] Das SK, Sahoo RK. Second law analysis of a cyclic regenerator in presence of longitudinal heat conduction in matrix. Heat Mass Transfer 1999;34:395–403. doi:10.1007/s002310050275.
[33] Domanski P, Didion D. Computer modeling of the vapor compression cycle with constant flow area expansion device. Technical Report 155. NBS Building Science Series; 1983.
[34] Finn AJ, Johnson GL, Tomlinson TR. Developments in natural gas liquefaction. Hydrocarb Process 1999;78(4):47–59.
[35] Fischer SK, Rice CK. A steady-state computer design model for air-to-air heat pumps. Technical Report ORNL/CON-80. Oak Ridge National Laboratory; 1981.
[36] Fleming RB. The effect of flow maldistribution in parallel channels of counterflow heat exchangers. Adv Cryogenic Eng 1967;12:352–62.
[37] Flynn TM. Cryogenic Engineering. Second, Revised ed. New York: Marcel Dekker; 2005.
[38] Fredheim AO, Heiersted RS. Possibilities for cost reductions in base-load. In: EUROGAS96. Proceedings from the European applied research conference on natural gas; 1996. p. 101–14 [TAPIR].
[39] Fredheim AO, Joerstad O, Owren G, Vist S, Neeras BO. COIL. a model for simulation of spiral wound LNG heat exchangers. In: Proceedings from world gas conference 2000, Nice; 2000.
[40] Gardner KA. Mean temperature difference in unbalanced-pass exchangers. Ind Eng Chem 1941;33(10):1215–23.
[41] Gardner KA, Taborek J. Mean temperature difference: a reappraisal. AIChE J 1977;23(6):777–86.
[42] Ghosh I, Sarangi SK, Das PK. An alternate algorithm for the analysis of multistream plate fin heat exchangers. Int J Heat Mass Transfer 2006;49(17–18):2889–902.
[43] Ghosh I, Sarangi SK, Das PK. Simulation algorithm for multistream plate fin heat exchangers including axial conduction, heat leakage, and variable fluid property. J Heat Transfer 2007;129(7):884–93.
[44] Gupta P, Atrey MD. Performance evaluation of counter flow heat exchangers considering the effect of heat in leak and longitudinal conduction for low-temperature applications. Cryogenics 2000;40(7):469–74.
[45] Hennecke DK. Heat transfer by hagen-poiseuille flow in the thermal development region with axial conduction. Heat Mass Transfer 1968;1:177–84. doi:10.1007/BF00751149.
[46] Hesselgreaves JE. Compact heat exchangers. Selection, design and operation. Amsterdam: Elsevier Science; 2001.
[47] Hettiarachchi HM, Golubovic M, Worek W. The effect of longitudinal heat conduction in cross flow indirect evaporative air coolers. Appl Therm Eng 2007;27(11–12):1841–8.
[48] Iu I, Weber N, Bansal P, Fisher D. Applying the effectiveness – NTU method to elemental heat exchanger models. ASHRAE Trans 2007;113(1):504–13.
[49] Iu IS. Development of air-to-air heat pump simulation program with advanced heat exchanger circuitry algorithm. Ph.D thesis. Oklahoma State University; 2007.
[50] Jen TC, Gutierrez G, Eapen S, Barber G, Zhao H, Szuba PS, et al. Investigation of heat pipe cooling in drilling applications. Part I: preliminary numerical analysis and verification. Int J Mach Tools Manuf 2002;42(5):643–52.
[51] Jung J, Jeong S. Effect of flow mal-distribution on effective NTU in multi-channel counter-flow heat exchanger of single body. Cryogenics 2007;47(4):232–42.
[52] Kakaç S, Pramuanjaroenkij A, Liu H. Heat exchangers: selection, rating, and thermal design. 2nd ed. London, New York: CRC Press; 2002.
[53] Kanoglu M, Dincer I, Rosen MA. Performance analysis of gas liquefaction cycles. Int J Energy Res 2008;32(1):35–43.
[54] Kao S. Analysis of multipass heat exchangers with variable properties and transfer rate. J Heat Transfer 1975;97(4):509–15.
[55] Kays WM, London AL. Compact heat exchangers. McGraw-Hill series in mechanical engineering. New York: McGraw-Hill Book Co.; 1964.
[56] Kroeger PG. Performance deterioration in high effectiveness heat exchangers due to axial heat conduction effects. Adv Cryogenic Eng 1967;12:363–72.
[57] Kumar KVR, Sarang S. On the performance of high-NTU heat exchangers with variable heat capacity of the working fluid. Heat Transfer Eng 1991;12(1):37–42.
[58] Kuppan T. Heat exchanger design handbook. Mechanical engineering. A series of textbooks and reference books, vol. 126. New York: Marcel Dekker Inc.; 2000.
[59] Liang SY, Wong TN, Nathan GK. Numerical and experimental studies of refrigerant circuitry of evaporator coils. Int J Refrig 2001;24(8):823–33.
[60] Linde AG. Aluminium plate-fin heat exchangers. Catalogue.
[61] Linde AG. Looking inside ... plate-fin versus coil-wound heat exchanger. Catalogue.
[62] Mathew B, Hegab H. Application of effectiveness-NTU relationship to parallel flow microchannel heat exchangers subjected to external heat transfer. Int J Therm Sci 2010;49(1):76–85.
[63] Mathew B, Hegab H. Modeling non-adiabatic parallel flow microchannel heat exchangers. Int J Therm Sci 2010;50:350–60.
[64] Mathew B, Hegab H. Performance of counterflow microchannel heat exchangers subjected to external heat transfer. Heat Transfer Eng 2010;31(3):168–78.
[65] McKeever J, Pillarella M, Bower R. An ever evolving technology. LNG Ind Spring 2008:44–9.
[66] Mehrabian M, Sheikhzadeh G, Khoramabadi M. Application of numerical methods to study the effect of axial conduction in plates and flow channels on the performance of plate heat exchangers. Int J Numer Methods Heat Fluid Flow 2006;16:67–83.
[67] Mueller AC. New charts for true mean temperature difference in heat exchangers. AIChE paper 10, 9th National Heat Transfer Conference; 1967.
[68] Mueller AC, Chiou JP. Review of various types of flow maldistribution in heat exchangers. Heat Transfer Eng 1988;9(2):36–50.
[69] Mullen CE, Bridges BD, Porter KJ, W-Hahn G, Bullard CW. Development and validation of a room air conditioning simulation model. Technical Report ACRC TR-116, Air Conditioning and Refrigeration Center, University of Illinois at Urbana–Champaign, Mechanical & Industrial Engineering Dept.; 1997.
[70] Narayanan SP, Venkatarathnam G. Performance degradation due to longitudinal heat conduction in very high NTU counterflow heat exchangers. Cryogenics 1998;38(9):927–30.
[71] Narayanan SP, Venkatarathnam G. Performance of a counterflow heat exchanger with heat loss through the wall at the cold end. Cryogenics 1999;39(1):43–52.
[72] Nellis GF. A heat exchanger model that includes axial conduction, parasitic heat loads, and property variations. Cryogenics 2003;43(9):523–38.
[73] Nellis GF, Pfotenhauer JM. Effectiveness-NTU relationship for a counterflow heat exchanger subjected to an external heat transfer. J Heat Transfer 2005;127(9):1071–3.
[74] Oonk RL, Hustvedt DC. The effect of fluid property variations on the performance of cryogenic helium exchangers. Adv Cryogenic Eng 1986;31:415–22.
[75] Orth L, Zietlow DC, Pedersen CO. Predicting refrigerant inventory of HFC 134a in air cooled condensers. Technical Report ACRCTR-34. Air Conditioning and Refrigeration Center, University of Illinois, Mechanical & Industrial Engineering Dept; April 1993.
[76] Pacio JC, Dorao CA. A study of the effect of flow maldistribution on heat transfer performance in evaporators. Nucl Eng Des 2010;240(11):3868–77.
[77] Peters DL. Heat exchanger design with transfer coefficients varying with temperature or length of flow path. Heat Mass Transfer 1970;3:220–6.
[78] Prasad RC. Analytical solution for a double-pipe heat exchanger with non-adiabatic condition at the outer surface. Int Commun Heat Mass Transfer 1987;14(6):665–72.
[79] Rabas T. The effect of tubeside maldistribution on the thermal performance of condensers used in multistage flash distillation plants. Desalination 1985;55:515–28.
[80] Ragazzi F, Pedersen CO. Modular-based computer simulation of an air-cooled condenser. Technical Report ACRC TR-07. Air Conditioning and Refrigeration Center, University of Illinois at Urbana–Champaign; 1991.
[81] Ranganayakulu C, Seetharamu KN. The combined effects of longitudinal heat conduction, flow nonuniformity and temperature nonuniformity in crossflow plate-fin heat exchangers. Int Commun Heat Mass Transfer 1999;26(5):669–78.
[82] Ranganayakulu C, Seetharamu KN, Sreevatsan KV. The effects of inlet fluid flow nonuniformity on thermal performance and pressure drops in crossflow plate-fin compact heat exchangers. Int J Heat Mass Transfer 1996;40(1):27–38.
[83] Ranganayakulu C, Seetharamu KN, Sreevatsan KV. The effects of longitudinal heat conduction in compact plate-fin and tube-fin heat exchangers using a finite element method. Int J Heat Mass Transfer 1997;40(6):1261–77.
[84] Rao BP, Das SK. Effect of flow distribution to the channels on the thermal performance of the multipass plate heat exchangers. Heat Transfer Eng 2004;25(8):48–59.
[85] Rao BP, Kumar PK, Das SK. Effect of flow distribution to the channels on the thermal performance of a plate heat exchanger. Chem Eng Process 2002;41(1):49–58.
[86] Rao BP, Sunden B, Das SK. An experimental and theoretical investigation of the effect of flow maldistribution on the thermal performance of plate heat exchangers. J Heat Transfer 2005;127(3):332–43.
[87] Rao BP, Sunden B, Das SK. Thermal analysis of plate condensers in presence of flow maldistribution. Int J Heat Mass Transfer 2006;49(25–26):4966–77.
[88] Ravikumaur S, Seetharamu K, Narayana PA. Finite element analysis of shell and tube heat exchanger. Int Commun Heat Mass Transfer 1988;15(2):151–63.
[89] Robertson JM. Heat exchange equipment for the cryogenic process industry. In: Taborek J, Hewitt GF, Afgan N, editors. Heat exchangers. Theory and practice. Hemisphere Publishing Corporation; 1983. p. 469–93.
[90] Roetzel W. Dimensioning heat exchangers with regard to variable heat transfer coefficients and heat capacities. Heat Mass Transfer 1969;2:163–70 [in German].
[91] Roetzel W. Heat exchanger design with variable transfer coefficients for crossflow and mixed flow arrangements. Int J Heat Mass Transfer 1974;17(9):1037–49.
[92] Roetzel W, Ranong CN. Consideration of maldistribution in heat exchangers using the hyperbolic dispersion model. Chem Eng Process 1999;38(4–6):675–81.
[93] Roetzel W, Spang B. Verbessertes diagramm zur berechnung von wärmenbertragern. Heat Mass Transfer 1990;25:259–64 [in German].

[94] Sahoo R, Sarangi S. Effect of temperature-dependent specific heat of the working fluid on the performance of cryogenic regenerators. Cryogenics 1985;25(10):583–90.
[95] Sahoo RK, Roetzel W. Hyperbolic axial dispersion model for heat exchangers. Int J Heat Mass Transfer 2002;45(6):1261–70.
[96] Sarangi S, Baral H. Effects of axial conduction in the fluid on cryogenic regenerator performance. Cryogenics 1987;27(9):505–9.
[97] Seetharamu K, Quadir G, Zainal Z, Krishnan G. FEM analysis of multifluid heat exchangers. Int J Numer Methods Heat Fluid Flow 2004;14(2):242–55.
[98] Shah RK. A review of longitudinal wall heat conduction in recuperators. J Energy Heat Mass Transfer 1994;97:453–4.
[99] Shah RK, Sekulič DP. Fundamentals of heat exchanger design. New Jersey: John Wiley and Sons; 2003.
[100] Sharqawy MH, Zubair SM. Heat exchangers design under variable overall heat transfer coefficient: improved analytical and numerical approaches. Heat Transfer Eng 2010;31(13):1051–6.
[101] Soyars WM. The applicability of constant property analysis in cryogenic helium heat exchangers. Adv Cryogenic Eng 1991;37A:217–23.
[102] Srihari N, Rao BP, Sunden B, Das SK. Transient response of plate heat exchangers considering effect of flow maldistribution. Int J Heat Mass Transfer 2005;48(15):3231–43.
[103] Steinbauer M, Hecht T. Optimised calculation of helical-coiled heat exchanger in LNG plants. In: EUROGAS96. Proceedings from the European applied research conference on natural gas, TAPIR; 1996. p. 223–8.
[104] Taborek J. Evolution of heat exchanger design techniques. Heat Transfer Eng 1979;1(1):15–29.
[105] Tariq S. LNG technology selection. Hydrocarb Eng 2004;9(2):71–6.
[106] TEMA. Standards of the Tubular Exchanger Manufacturers Assosiacion; 2007
[107] Thyageswaran S. Analysis of multi-pass evaporators using orthogonal collocation. Int J Refrig 2008;31(2):204–16.
[108] Thyageswaran S. Thermo-hydraulic predictions for multi-pass evaporators by orthogonal collocation using a new flow pattern map. Appl Therm Eng 2009;29(2–3):601–6.
[109] Tien CL, Cunnington GR. Cryogenic insulation heat transfer. In: Thomas J, Irvine Francis, Hartnett JP, editors. Advances in heat transfer, vol. 9. Academic Press; 1973. p. 349.
[110] Tiller FM, Kahl LF, Ramalho RS. Improved formulas for heat transfer calculations in multipass exchangers. J Chem Eng Data 1963;8(3):285–8.
[111] Timoney DJ, Foley PJ. Some effects of air flow maldistribution on performance of a compact evaporator with R134a. Heat Recov Syst CHP 1994;14(5):517–23.
[112] Vardhan A, Dhar PL. A new procedure for performance prediction of air conditioning coils. Int J Refrig 1998;21(1):77–83.
[113] Venkatarathnam G. Effectiveness-Ntu relationship in perforated plate matrix heat exchangers. Cryogenics 1996;36(4):235–41.
[114] Venkatarathnam G. Cryogenic mixed refrigerant processes. New York: Springer; 2008.
[115] Venkatarathnam G, Narayanan SP. Performance of a counter flow heat exchanger with longitudinal heat conduction through the wall separating the fluid streams from the environment. Cryogenics 1999;39(10):811–9.
[116] Venkatarathnam G, Sarangi S. Matrix heat exchangers and their application in cryogenic systems. Cryogenics 1990;30(11):907–18.
[117] Yuan P, Kou H-S. The effect of longitudinal wall conduction in a three-fluid crossflow heat exchanger. Numer Heat Transfer, Part A: Appl: Int J Comput Methodol 1998;34(2):135–50.
[118] Yuan P, Kou H-S. The comparison of longitudinal wall conduction effect on the crossflow heat exchangers including three fluid streams with different arrangements. Appl Therm Eng 2001;21(18):1891–907.

Article 8

Pacio J.C. and Dorao, C.A. (2011)

Modeling two-phase heat exchanger performance in the annular-mist flow regime considering entrainment and deposition phenomena

In Proceedings of ASME-JSME-KSME Joint Fluids Engineering Conference 2011, July 24-29, 2011, Hamamatsu, Shizuoka, Japan. Paper ID: AJK2011-10013.

Is not included due to copyright

Article 9

Pacio J.C. and Dorao, C.A. (2011)

Design considerations for the sizing of high-effectiveness two-phase flow heat exchangers

In Proceedings of the 23rd IIR International Congress of Refrigeration, August 21-26, 2011, Prague, Czech Republic. Paper ID: 476.

ID: 476

DESIGN CONSIDERATIONS FOR THE SIZING OF HIGH-EFFECTIVENESS TWO-PHASE FLOW HEAT EXHANGERS.

J. PACIO [(*)], C. DORAO [(**)]
Norwegian University of Science and Technology, Kolbjørn Hejes vei 1b, Trondheim, 7491, Norway,
Fax: +47-73591640. [(*)] julio.pacio@ntnu.no, [(**)] carlos.dorao@ntnu.no

ABSTRACT

Two-phase flow heat exchangers are main components in refrigeration, cryogenic and liquefaction processes, since thermo-economic considerations make low-temperature processes very sensitive to their performance. Current models used for design, based on integrated or discretized energy balances, fail to take into account all the relevant physical effects. In this work, a tube-in-tube exchanger is studied on the base of differential mass, momentum and energy balances, thus accounting for changes in pressure which affect the saturation temperature. Three numerical examples are presented, involving evaporators and condensers. The present model predicts up to larger area than traditional discretized models for condensers, and smaller for evaporators. These results can be explained by observing the temperature profiles. In addition, the reduction of performance if the heat exchanger is under-sized is evaluated. Finally, co-current and counter-current flow arrangements are compared.

1. INTRODUCTION

Heat exchangers (HE) are main components in refrigeration, cryogenic and liquefaction processes. Thermo-economic considerations make low-temperature processes very sensitive to the HE performance. For example, Kanoglu *et al.* (2008) predicted a reduction of 22% in the liquefaction rate of air if the HE effectiveness (ε) departs from the ideal value of 100% to a more practical one of 96.5%. In the case of liquefaction of helium, Atrey (1998) calculated that 12% less liquid is obtained if ε is reduced from 97% to 95%. In general, no liquid is produced if $\varepsilon < 85\%$ (Barron, 1985). In order to compensate for this drop in liquefaction rates, some modifications to the refrigeration cycle might be necessary, such as an increase in the working pressures ratio, thus increasing the overall power consumption.

In short, HEs for low-temperature applications have high-effectiveness requirements. This situation leads to the design of large and expensive equipment, which, in the case of Liquefaction of Natural Gas (LNG) plants, can represent up to 20-30% of the investment costs (Fredheim and Heiersted, 1996). In addition, the heat transfer process affects the sizing of other major equipments, namely compressors and drivers. Therefore a proper sizing of the high performance HE plays a major role in the capital investments of the process, setting the need for more accurate predicting models.

Two-phase flow HEs are widely used in refrigeration cycles for both boiling and condensation purposes. For example, in LNG processes, hydrocarbon mixtures are used as boiling refrigerant in the main cryogenic HE in which the condensation of natural gas takes place. In air conditioning and heat pump systems, the low pressure heat transfer occurs in the evaporator, and the heat rejection stage at low pressure takes place in the condenser, as shown in Fig. 1a.

An accurate description of high-effectiveness heat transfer equipment is limited, in particular for two-phase flow applications, and their sizing is a challenging task due to two main reasons. First, the determination of a two-phase heat transfer coefficient is a complex task depending on semi-empirical models. In boiling flows, bubble nucleation and forced convection must be accounted for, and large variations of the heat transfer coefficient occur within the two-phase region. Second, for the required degree of accuracy, some physical effects should not be neglected. In the case of high-effectiveness HE, in the order of $\varepsilon > 90\,\%$ the performance is dominated by other mechanisms (Venkatarathnam and Sarangi, 1990) including heat

exchange with the surroundings, axial conduction, flow maldistribution in parallel channels, and variations in the fluid properties.

Current models used for HE design are based on integrated energy balances, expressed in terms of dimensionless parameters such as effectiveness and number of thermal units which are only recommended for single phase flow. In the case of two-phase flow, these models can be improved by dividing the exchanger in smaller sections where the model assumptions are more valid. Nevertheless these models fail to take into account all the relevant physical effects.

The objective of this work is to investigate the performance of current HE models for the sizing of high-effectiveness equipment. An advanced model is presented that incorporates the coupled momentum balance equation. This allows to account for pressure drop and its effect on heat transfer. Three cases are considered and the sizing of different models is compared. On the base of these results, the consequences of undersizing in the performance are studied. Finally, optimal geometrical and physical design characteristics are investigated.

In general, several types of geometries can be selected for HE design, including plate-type, shell-and-tube and coil-wounded (Kakaç and Liu, 2002). Without loss of generality, a simple geometry was selected for this work, in particular a double-pipe HE, as sketched in Fig. 1b. This type of HE is especially suitable for small heat-transfer area applications, because of their simple cleaning and maintenance. The present analysis can be extended to other geometries.

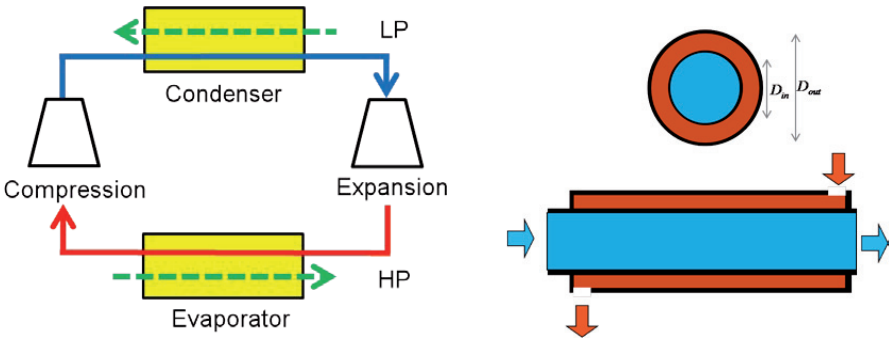

Figure 1. a) Vapour compression refrigeration cycle. b) Double-pipe heat exchanger geometry

2. THE TWO-PHASE HEAT EXCHANGER PROBLEM AND PRESENT MODELS

The HE problem consists on analyzing the thermal evolution of interacting streams within a given geometry. It involves the solution of two problems: rating and sizing (Shah and Sekulic, 2003). Rating consists on evaluating the performance of an existing HE. Since all the relevant information is given (geometry, flow conditions) detailed models can be used. Sizing refers to the opposite problem, that is, to select the proper HE geometry, flow arrangement and size to meet the specified performance within some given constraints. The geometry is still unknown, and for that reason simpler models are required.

Present HE models used for thermal design can be divided into three broad categories: lumped parameters (zero-dimensional), distributed parameters (nodal approach) and stream evolution (one-dimensional).

2.1. Lumped parameters models (LPM)

The basic design theory for HEs is given by this type of models. Examples of this category are the classic Mean Temperature Difference and ε-NTU methods, which can be found in most textbooks on heat transfer. They are based on integrated energy balances for steady-state condition and with the assumption of constant fluid properties. The HE is considered as a single unit with bulk parameters, and inputs and outputs are related in a zero-dimensional approach. Finally, the HE is represented with two parameters: one for the physical size and another for the thermal performance.

Considering that all lumped parameters models involve the solution of the same equation with equal

assumptions, they all yield the same results. The ε-NTU model is considered in this work. In this case, the number of thermal units (*NTU*) represents the physical size and the effectiveness (ε) gives the thermal performance as the ratio of the actual heat transferred and the maximum achievable with the given inlet conditions. The application of this method to an evaporator yields the relation given by Eq. 1. The required physical area A to fit the performance ε can be straightforwardly obtained from Eq. 1, where U is the overall heat transfer coefficient and C_{min} the heat capacity flow of the single-phase stream.

$$\varepsilon = 1 - \exp(-NTU), \text{ with } NTU = U\,A/C_{min} \tag{1}$$

2.2. Distributed parameters models (DPM)

These models consist on a nodal approach: the exchanger is divided into smaller units and a lumped parameter model is used in each of them, thus fulfilling better the LPM assumptions. These methods allow considering the variations in fluid properties and heating transfer coefficient in an iterative procedure, at the extent of a larger computational cost.

This discretization can be done at two different levels (Iu *et al*., 2007): into zones according to the refrigerant phase state or elements of a given physical size. Orth *et al*. (1995) further divided each zone into elements. This last approach is considered in this work, applying a ε-NTU method in each element.

2.3. Stream evolution models (SEM)

In general, one-dimensional models can be considered as an extension of nodal formulations. For this reason, SEMs are sometimes referred as fully distributed models. The main difference in this last category is the inclusion of the continuity and momentum, thus accounting for changes in velocity and pressure. This formulation has been applied to transient analysis of heat pump systems (Jia *et al*., 1995; Junge and Radermacher, 1997; Nyers and Stoyan, 1994). However, no application was reported for steady-state analysis and design. In other words, they were applied for the rating of existing equipment, and not for the sizing problem. The reason for this situation is probably that these more complex formulations require an established geometry, flow arrangement and size

In this work, a steady-state SEM is applied to the sizing problem. Geometry and flow arrangements are established first, and the required size to fit the target performance is obtained in an iterative approach. The governing equations are steady-state mass, momentum and energy balances for both cold and hot streams. However, the mass balance has a trivial solution, i.e. constant flux $G=\rho V$, where ρ is the fluid density and V its velocity. Therefore, it is only implicitly considered to account for the changes in velocity as a consequence of the variations in density. The problem is then governed by the momentum (Eq. 2) and energy (Eq. 3) balances for the cold and hot fluid as follows

$$\begin{aligned} &\frac{d}{dz}\left(\frac{G^2}{\rho}+p\right)_{cold} + \rho_{cold} g + \frac{4}{Dh_{cold}}\tau_{cold} = 0 \\ &\pm\frac{d}{dz}\left(\frac{G^2}{\rho}+p\right)_{hot} + \rho_{hot} g + \frac{4}{Dh_{hot}}\tau_{hot} = 0 \end{aligned} \tag{2}$$

$$\begin{aligned} &G_{cold}\frac{dh_{cold}}{dz} = \frac{4}{Deq_{cold}}U\left(T_{hot}-T_{cold}\right) \\ &\pm G_{hot}\frac{dh_{hot}}{dz} = -\frac{4}{Deq_{hot}}U\left(T_{hot}-T_{cold}\right) \end{aligned} \tag{3}$$

where z is the axial position, g the gravity in the axial direction, p the fluid pressure, Dh the hydraulic diameter, τ the frictional shear stress, h the fluid enthalpy, Deq the equivalent diameter, U the overall heat transfer coefficient, h the fluid enthalpy and T its temperature. The ± allows to account for both co-current (+) and counter-current (-) flow arrangements. All fluid physical properties, e.g. density, and local temperature for each fluid are given by the local thermodynamic state (p,h).

In addition, shear stress (τ) and heat transfer coefficient (U) are modeled on the base of semi-empirical

correlations that are further developed in the following subsections. Finally, the governing equations are solved with proper inlet boundary conditions.

2.4. Pressure drop models

In order to accommodate the effects of multiphase flow, a two-phase multiplier $\Phi_L^2=\tau/\tau_L$ is introduced for modeling the shear stress, and τ_L is computed on the base of a friction factor f_L, which is obtained according to the Haaland formula for smooth tubes (White, 1986), where the subindex L indicates liquid properties.

$$f_L = \left[\frac{1}{1.8\log(\mathrm{Re}_L/6.9)}\right]^2 \rightarrow \tau_L = f_L \frac{G^2}{2\rho_L} \rightarrow \tau = \tau_L \Phi_L{}^2 \tag{4}$$

For single-phase liquid $\Phi_L^2=1$ and for single-phase vapor $\Phi_L^2= (f_G\rho_L)/(f_L\rho_G)$. The Friedel correlation (Whalley, 1987) is used for Φ_L^2 in the two-phase region.

2.5. Heat transfer models

In a steady-state analysis, the heat transfer coefficient (U) is computed on the basis of thermal resistances: shell-side and tube-side convective heat transfer, and thermal conduction in the wall, i.e.:

$$\frac{1}{D_{in}U} = \underbrace{\frac{1}{D_{in}\hat{h}_{tube-side}}}_{\text{inside convection}} + \underbrace{\frac{1}{(D_{in}+2\mathrm{t})\hat{h}_{hot}}}_{\text{outside convection}} + \underbrace{\frac{\ln(1+2t/D)}{2k_W}}_{\text{wall conduction}} \tag{5}$$

Different correlations were used for computing the local inner and outer heat transfer coefficients, depending on the enthalpy range. In general, the formulas recommended by Collier and Thome (1994) were used, namely Gnielinsky, and Pethukov-Popov for single phase flow (depending on Reynolds number range), Shah for boiling flow, and Akers for condensation. In addition, the three-region subcooled boiling model by Kandlikar (1997) was incorporated. For all of them, see Ghiaasiaan (2007).

3. NUMERICAL EXAMPLES. SIZING OF THREE CASES

The predictions of the three models introduced in the previous section (DPM, LPM and SEM) are compared for three numerical examples. First, a water-cooling evaporator is considered where the cold fluid is boiling and the hot stream is single-phase liquid. Second, a water-cooled condenser is studied. In this case, the hot fluid is condensing and the cold stream is single-phase liquid. Finally, a more complex case is analyzed, where the cold stream is evaporating and the hot one is condensing.

In all three cases, the geometry is established as a counterflow double-pipe HE, sketched in Fig. 1b. The inner diameter is set at D_{in} = 5 mm, and the outer one at D_{out} = 10 mm. The tube material is copper (high thermal conductivity, k_W = 410 W m^{-1} K^{-1}) and the wall thickness is t = 0.5 mm. Taking into account that this geometry is usually employed for small-capacity applications, the mass flow rates in the following examples are small, in the order of a few grams per second.

3.1. Water-cooling evaporator

In this type of equipment, the objective is to cool down water by means of evaporating a refrigerant. In particular, the horizontal counter-flow of evaporating R134a inside the tube (entering at 275 K and 3.5 bar, saturation temperature 278K) and liquid water outside (303K, 1 bar) is studied. The mass flow rates are 5.0 and 20.0 g/s, respectively; resulting in mass fluxes of roughly G_{cold} = 250 kg m^{-2} s^{-1} and G_{hot} = 400 kg m^{-2} s^{-1}.

The required tube length to obtain a given target effectiveness for this case as predicted by the three different models is presented in Fig. 2. As could be expected, the required length L increases with the desired effectiveness ε. In fact, a sharp increase is noticed for $\varepsilon > 0.9$, which corresponds to the point when the refrigerant is fully evaporated. Further heat transfer occurs in single-phase gas region, which has a lower heat transfer coefficient, and thus a larger area (tube length) is required. Both DPM and SEM models account for this situation, however this is not reflected in the prediction of the LPM. Lumped parameter models (LPM) consider a constant averaged value for the heat transfer coefficient, thus do not reflect this sharp change.

Observing that $L_{LPM} > L_{DPM}$, it seems that LPM underestimates the average heat transfer coefficient, thus over predicting the required length up to more than double the one given by the DPM.

It is also observed in Fig. 2a that in all cases DPM predicts a slightly larger tube length than SEM. Although this difference can be negligible for lower effectiveness, the highlighted results for $\varepsilon = 0.99$ indicate that it can be up as high as 15%. The main difference between these two models is that SEM includes the momentum equation. Pressure drop affects all fluid saturated properties, among them its saturation temperature. This means that there is a temperature glide in the phase-change region, as observed in Fig. 2b, which indicates the temperature profiles for the extreme case ε=0.99. The cold temperature decline due to pressure drop gives a larger temperature difference, thus increasing the heat transfer performance. As a consequence, a smaller length is required to fulfill a required efficiency. Given the exponential-type dependence of ε on L (see Eq. 1), this effect is larger for high values of ε, close to unity.

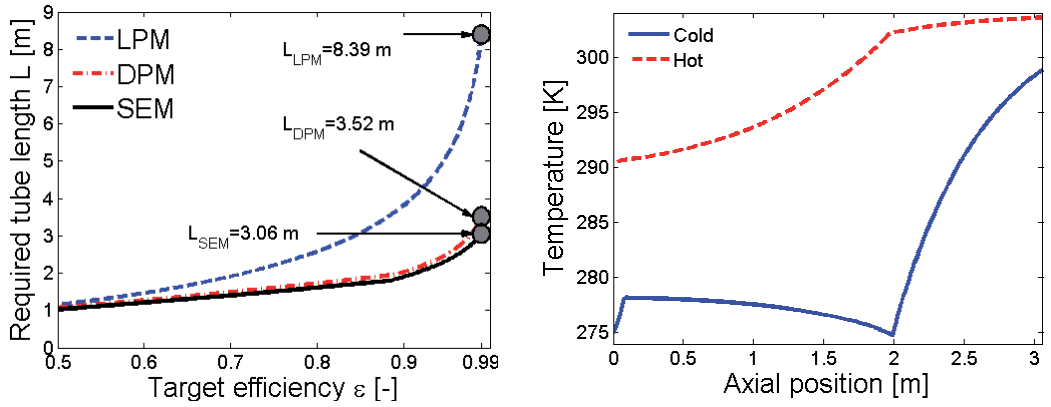

Figure 2. Results for the water-cooler evaporator case a) Sizing predictions. Highlighted results for ε=0.99 b) Temperature profiles for ε=0.99. Axial position is measured from the cold fluid inlet.

3.2. Water-cooled condenser

The objective in this type of HE is to condensate a gas flow by means of exchanging heat to cooling water. In particular, the horizontal counter-flow of condensing R134a inside the tube (entering at 303 K and 6.7 bar, saturation temperature 298K) and liquid water outside (283K, 1 bar) is studied. The mass flow rates are the same as in the previous case, that is 5.0 and 20.0 g/s for R134a and water, respectively; resulting in mass fluxes of roughly G_{cold} = 250 kg m^{-2} s^{-1} and G_{hot} = 400 kg m^{-2} s^{-1}. The results are presented in Figs. 3a and 3b.

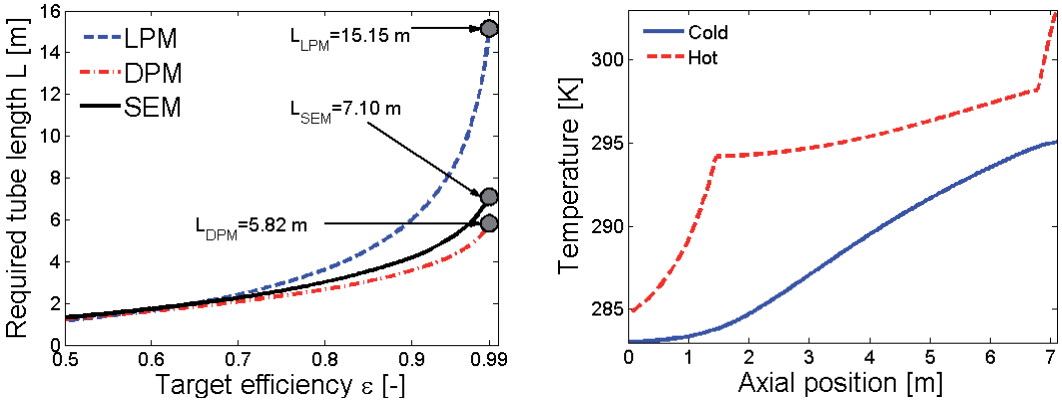

Figure 3. Results for the water-cooled condenser case a) Sizing predictions. Highlighted results for ε=0.99 b) Temperature profiles for ε=0.99. Axial position is measured from the cold fluid inlet.

As in the previous case, LPM over predict the required length compared to the other two models, more than

doubling their predictions for high values of ε. It is also observed in Fig. 3a that in all cases DPM predicts a smaller tube length than SEM, resulting is the opposite behavior as the previous case. This difference, that cab can be up to 20% for the highlighted results, is once again a consequence of pressure drop, which affects saturations temperature. In this case (see Fig. 3b), the temperature of the hot fluid declines as a consequence of pressure drop giving a lower temperature difference, thus reducing the heat transfer performance and predicting a larger required tube length.

3.3. Evaporation and condensation on the same unit

The previous two examples indicate that pressure drop can increase the heat transfer performance when considered in an evaporating flow, or decreasing in the case of a condenser. In this section, a mixed case is studied, where the hot fluid is condensing and the cold one is boiling. In particular, the vertical counter-flow of evaporating R134a inside the tube (entering at 280 K and 4.0 bar, saturation temperature 282) and condensing propane outside (293K, 7 bar, sat. temp. 286.5 K) is analyzed. The mass flow rates are 2.0 and 1.1 g/s, respectively; resulting in mass fluxes of roughly G_{cold} = 100 kg m^{-2} s^{-1} and G_{hot} = 16 kg m^{-2} s^{-1}.

Two flow configurations are considered: cold stream flowing upwards and hot downwards (Fig. 4a), and vice versa (4b). Gravitational effects produce a pressure increase for the stream flowing downwards, and a decrease for the one flowing upward. Since both LPM and DPM do not account for pressure drop, their predictions are equal for both cases. The prediction of SEM, however, indicates that the performance of case a (cold up, hot down) is increased by effects of pressure drop and a smaller tube length is required. The opposite behavior is noticed for case b (cold down, hot up). In short, making *good* or *bad* use of the available pressure drop, there can be up to 1 meter difference (roughly 20%) on the required length.

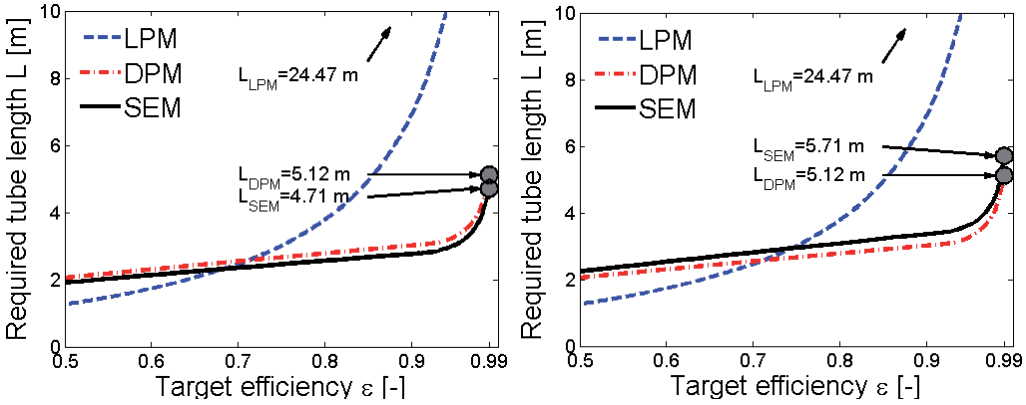

Figure 4. Sizing predictions for the third case: vertical counterflow of evaporating R134a and condensing propane. Highlighted results for ε=0.99 a) Cold upward, Hot downward. b) Cold downward, hot upward.

4. CONSEQUENCES OF UNDERSIZING

It is observed from the numerical examples presented in the previous section that different models predict different tube lengths. On the one hand, if the selected model predicts a larger value of L than actually required, the target performance is fulfilled and the use of this model is a conservative assumption. This is the case of Lumped Parameter Models (LPM), which overpredicts the required length in almost all cases (except for low efficiency cases in example 3.3). Although this overprediction is conservative, it can have a dramatic effect on the costs, since it exceeds the predictions of SEM by more than 100% and up to 400%.

On the other hand, if the selected model predicts a lower value of L, the required performance is not achieved. This is the case of the DPM model for the example 3.2. (condenser), where, by not considering the effects of pressure drop, it predicts a smaller length than SEM. Then, for example, a HE sized using the DPM model for operating at a target efficiency of ε = 0.99, will have an actual value of ε = 0.968, according to SEM. Or, if designed for ε = 0.90 using DPM, it will operate at ε = 0.853. Further numerical values can be obtained directly from Fig. 3a.

Although these differences may seem small, it should be reminded that for low temperature applications, high-effectiveness equipment is required, and a small degree of underperformance can have a large effect in overall system behavior, negatively affecting the power consumption, or liquefaction rate.

5. DESIGN CHARACTHERISTICS: FLOW ARRANGEMENT

It is well established that, for single phase flow, the counter-current flow arrangement gives the highest heat transfer performance (Incropera and DeWitt, 1996). In addition, the flow arrangement is considered irrelevant for evaporators and condensers. However, this might not always be the case if the effects of pressure drop are taken into account. Observing the temperature profiles for the evaporator example (Fig. 2b), it is noticed that in the phase-change region, the cold fluid temperature is decreasing while its enthalpy is increasing. This situation can be understood as a negative heat capacity (although the changes in temperature are not strictly related to those in enthalpy, but to the pressure drop), and in this region the temperature profiles are similar to those characteristic of co-current flow.

Figure 5 presents results for the evaporator example from section 3.1, comparing the performance of co-current (solid lines) and counter-current (dashed) flow arrangements. The sizing predictions using the SEM model, see Fig. 5a, indicate that, over a wide range of ε, the co-current flow arrangement requires a smaller tube length L, which means that has a higher performance.

Once again, this result can be explained by analyzing the temperature profiles, as shown in Fig. 5b. In the co-current flow arrangement, the temperature difference is initially large, and thus also the heat transfer rate. For this reason, the vapor content in the cold fluid increases rapidly, producing larger pressure drop, and consequently larger reduction of the saturation temperature (the cold fluid reaches its inlet temperature again at 1.5 m for co-current, and at 1.8 m for counter-current). In addition, the heat transfer rate to the liquid phase is larger, thus producing evaporation earlier and increasing the average heat transfer coefficient. Finally, observing both profiles it is noticed that full evaporation is not achieved in the counter-current flow arrangement, while overheated vapor is obtained using the co-current scheme.

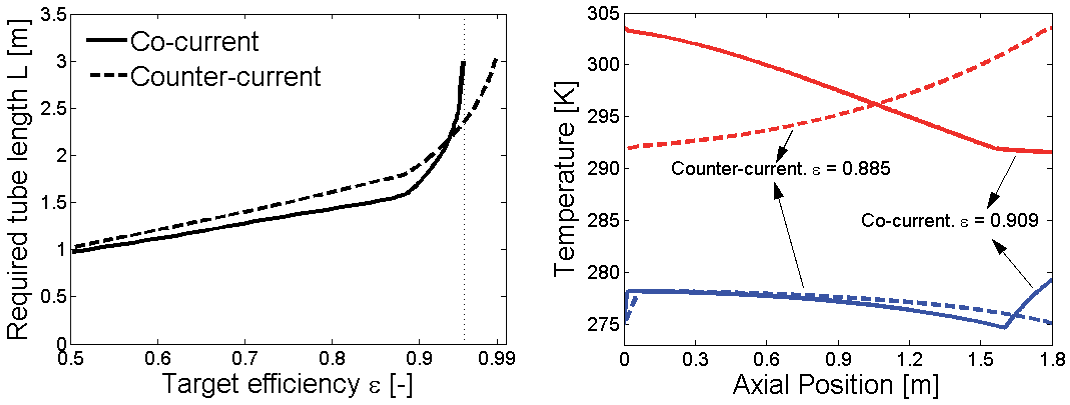

Figure 5. Comparison of co-current and counter-current flow for the evaporator example a) Sizing predictions with SEM. b) Temperature profiles for L=1.8 m.

However, in the high-effectiveness region $\varepsilon > 0.93$, the situation is reversed, and higher performance is obtained with the counter-current flow. The reason for this is that, after full evaporation of cold fluid, the problem becomes one of a single-phase HE, and then this well-known result is recovered. In a co-current flow arrangement, the maximum performance is achieved when both fluids exit at the same temperature, and then 100% effectiveness cannot be achieved. In fact, the plot in Fig. 5a indicates an asymptotic approach towards a final value of $\varepsilon = 0.955$. If a higher effectiveness is required, a counter-current flow arrangement is necessary.

6. CONCLUSIONS

Three different models for the sizing of two-phase heat exchangers are considered in this work: lumped and distributed parameters (LPM and DPM), and stream-evolution models (SEM). While the two first ones are based on energy balances, the last one includes the momentum balance equations, and thus it accounts for pressure drop and its effect on heat transfer, mainly through the changes in saturation temperature. In this framework three numerical examples are studied: a water-cooler evaporator, a water-cooled condenser and a mixed evaporator/condenser where both types of phase change are present.

In all cases, a double-pipe geometry was considered. The LPM, which considers only an average heat transfer coefficient that is in fact underestimated, predicts a too large tube length. This value can be up to four or five times the value predicted by SEM.

In the case of the evaporator, the DPM overpredicts the required tube length when compared to the SEM by up to 15%. Consequently, their use is conservative since there is no danger of undersizing. The opposite behavior is noticed for the condenser, with underpredictions of up to 20%. The consequences of undersizing can result in a reduction of efficiency than can be relevant for low-temperature applications

Finally, the characteristics of different flow arrangements for design are analyzed. Contrary to single-phase HE experience, the co-current flow arrangement can give higher performance in a wide range of target efficiency. Nevertheless, it has an asymptotic value of efficiency lower than unity, and counter-current flow arrangement is preferred for higher effectiveness equipment.

7. REFERENCES

1. Atrey MD. 1998, Thermodynamic analysis of Collins helium liquefaction cycle. *Cryogenics*. 38(12): 1199-1206.
2. Barron RF. 1985, *Cryogenic Systems*, Clarendon Press, Oxford, Second Ed., 507 p.
3. Collier JG, Thome JR. 1994, *Convective Boiling and Condensation*, Clarendon Press, Oxford, 596 p.
4. Fredheim AO, Heiersted RS. 1996, Possibilities for cost reduction in base-load LNG plants. *Proc. European Applied Research Conference on Natural Gas*, TAPIR: 101-114.
5. Ghiaasiaan SM. 2007, *Two-Phase Flow, Boiling, and Condensation In Conventional and Miniature Systems*, Cambridge University Press, Cambridge, 613 p.
6. Incropera FP, DeWitt DP. 1996, *Fundamentals of Heat and Mass Transfer*, John Wiley and Sons, New York, Fourth Ed., 886 p.
7. Iu I, Weber N, Bansal P, Fisher DE. 2007, Applying the effectiveness-NTU method to elemental heat exchanger models, *ASHRAE Transactions* 113(1): 504-513.
8. Jia X, Tso CP, Chia PK, Jolly P. 1995, A distributed model for prediction of the transient response of an evaporator, *Int. J. Refrig.*18(5): 336-342.
9. Judge J, Radermacher R. 1997, A heat exchanger model for mixtures and pure refrigerant cycle simulations, *Int. J. Refrig.* 20(4): 244-255.
10. Kakaç S, Liu H. 2002, *Heat Exchangers: Selection, Rating, and Thermal Design*, CRC Press, London Second Ed., 501 p.
11. Kandlikar SG. 1997, Heat transfer characteristics in partial boiling, fully developed boiling, and significant void flow regions of subcooled flow boiling, *J. Heat Transfer* 120(2):395-401.
12. Kanoglu M, Dincer I, Rosen MA. 2008, Performance analysis of gas liquefaction cycles, *Int. J. Energy Research* 32(1): 35-43.
13. Nyers J, Stoyan G. 1994, A dynamical model adequate for controlling the evaporator of a heat pump, *Int. J. Refrig.* 17(2): 101-108.
14. Orth LA, Zietlow DC, Pedersen, CO. 1995, Predicting Refrigerant Inventory of R134a in Air-Cooled Condensers, *ASHRAE Transactions* 101(1): 1367-1375.
15. Shah RK, Sekulic DP. 2003, *Fundamentals of Heat Exchanger Design*, John Wiley and Sons, New Jersey, 941 p.
16. Venkatarathnam G, Sarangi S. 1990, Matrix heat exchangers and their application in cryogenic systems, *Cryogenics* 30(11): 907-918.
17. Whalley PB. 1987, *Boiling, Condensation and Gas-Liquid Flow*, Clarendon Press, Oxford, 320 p.
18. White FM. 1986, *Fluid Mechanics*, McGraw-Hill, New York, Second Ed. 826 p.

References

[1] Abadzic, E. E. and H. W. Scholz (1972). Coiled tubular heat exchangers. *Advances in Cryogenic Engineering 18*, 42–51. Cited on page 23.

[2] Ablanque, N., C. Oliet, J. Rigola, C. Pérez-Segarra, and A. Oliva (2010). Two-phase flow distribution in multiple parallel tubes. *International Journal of Thermal Sciences 49*(6), 909 – 921. Cited on page 149.

[3] Ackermann, R. A. (1997). *Cryogenic Regenerative Heat Exchangers*. The International Cryogenic Monograph Series. New York: Plenum Press. Cited on page 25.

[4] Adamsson, C. (2009). *Dryout and Power Distribution Effects in Boiling Water Reactors*. Ph. D. thesis, Royal Insititute of Technology (KTH), Sweden. Cited on page 198.

[5] Adamsson, C. and H. Anglart (2010). Influence of axial power distribution on dryout: Film-flow models and experiments. *Nuclear Engineering and Design 240*(6), 1495 – 1505. Cited on pages 194 and 209.

[6] Aganda, A. A., J. E. R. Coney, and C. G. W. Sheppard (2000). Airflow maldistribution and the performance of a packaged air conditioning unit evaporator. *Applied Thermal Engineering 20*(6), 515 – 528. Cited on pages 29 and 149.

[7] Ahmad, M., G. Berthoud, and P. Mercier (2009). General characteristics of two-phase flow distribution in a compact heat exchanger. *International Journal of Heat and Mass Transfer 52*(1-2), 442 – 450. Cited on page 149.

[8] Al-Dini, S. and S. M. Zubair (2008). Effectiveness-ntu relations for parallel flow heat exchangers subjected to heat leak from outside. *Heat Transfer Engineering 29*(5), 475–483. Cited on pages 28, 39, and 42.

[9] Alipchenkov, V., R. Nigmatulin, S. Soloviev, O. Stonik, L. Zaichik, and Y. Zeigarnik (2004). A three-fluid model of two-phase dispersed-annular flow. *International Journal of Heat and Mass Transfer 47*(24), 5323 – 5338. Cited on page 193.

[10] Allen, D. H. (2001). Homogenization principles and their application to continuum damage mechanics. *Composites Science and Technology 61*(15), 2223 – 2230. Cited on page 48.

[11] ALPEMA (2000). The Standards of the Brazed Aluminium Plate–Fin Heat Exchanger Manufacturers' Association. Cited on page 24.

[12] Ameel, T. A. (2000). Parallel-flow heat exchangers with ambient thermal interaction. *Heat Transfer Engineering 21*(6), 18–25. Cited on pages 28, 39, and 41.

[13] Ameel, T. A. and L. H. Vitharana (1999). Countercurrent heat exchangers with both fluids subjected to external heating. *Heat Transfer Engineering 20*(3), 37–44. Cited on pages 28, 39, and 41.

[14] Amon, C. H. and B. B. Mikic (1991). Spectral element simulations of unsteady forced convective heat transfer: application to compact heat exchanger geometries. *Numerical Heat Transfer. Part A: Applications 19*(1), 1–19. Cited on page 64.

[15] Anderson, A. R. A. (2007). A hybrid multiscale model of solid tumour growth and invasion: evolution and microenvironment. In *Single-Cell-Based Models in Biology and Medicine*. Basel: Birkhuser Verlag AG. Cited on page 46.

[16] Andradóttir, S. (2007). *Simulation Optimization*, pp. 307–333. John Wiley & Sons, Inc. Cited on page 136.

[17] Andreani, M. and G. Yadigaroglu (1992). Difficulties in modeling dispersed-flow film boiling. *Heat and Mass Transfer 27*, 37–49. Cited on pages 229, 231, and 237.

[18] Andreani, M. and G. Yadigaroglu (1994). Prediction methods for dispersed flow film boiling. *International Journal of Multiphase Flow 20*(Supplement 1), 1 – 51. Cited on page 223.

[19] Arcadis Geraghty & Miller, I. (1998). Guidebook for evaluating, selecting, and implementing fuel choices for transit bus operations. Technical Report Transit Cooperative Research Program (TCRP). Report 38, Transport Research Board, Washington D. C. Cited on page 20.

[20] ASPENTech (2010). Aspen Plate Fin Exchanger. Available online at `http://www.aspentech.com/products/aspen-plate-fin.cfm`. Cited on pages 35 and 36.

[21] Atrey, M. D. (1998). Thermodynamic analysis of Collins helium liquefaction cycle. *Cryogenics 38*(12), 1199 – 1206. Cited on page 22.

[22] Awad, M. and Y. Muzychka (2008). Effective property models for homogeneous two-phase flows. *Experimental Thermal and Fluid Science 33*(1), 106 – 113. Cited on page 51.

[23] Azzopardi, B. J. (1985). Drop sizes in annular two-phase flow. *Experiments in Fluids 3*, 53–59. Cited on pages 236 and 237.

[24] Azzopardi, B. J. (1996). Prediction of dryout and post-burnout heat transfer with axially non-uniform heat input by means of an annular flow model. *Nuclear Engineering and Design 163*(1-2), 51 – 57. Cited on page 200.

[25] Bach, W., W. Foerg, M. Steinbauer, R. Stockmann, and F. Voggenreite (2001). Spiral wound heat exchangers for LNG baseload plants. In *13th International Conference of Exhibition on Liquefied Natural Gas*. Cited on page 147.

[26] Baker, C., E. Agyingi, E. Parmuzin, F. Rihan, and Y. Song (2006). Sense from sensitivity and variation of parameters. *Applied Numerical Mathematics 56*(3-4), 397 – 412. Selected Papers, The Third International Conference on the Numerical Solutions of Volterra and Delay Equations. Cited on page 110.

[27] Baldissera, P. and C. Delprete (2008). Deep cryogenic treatment: A bibliographic review. *The Open Mechanical Engineering Journal 2*, 1–11. Cited on page 19.

[28] Balio, J. L., A. E. Larreteguy, A. C. Lorenzo, A. G. Padilla, and F. R. de Andrade Lima (2001). The differential perturbative method applied to the sensitivity analysis for waterhammer problems in hydraulic networks. *Applied Mathematical Modelling 25*(12), 1117 – 1138. Cited on page 110.

[29] Barbosa Jr., J. R., T. Kandlbinder, and G. F. Hewitt (2000). A study of dryout in annular flow of single component hydrocarbons and their mixtures. *Multiphase Science and Technology 12*(3-4), 265–293. Cited on page 204.

[30] Barclay, M. and N. Denton (2005). Selecting offshore LNG processes. *LNG Journal October*, 34–36. Cited on page 26.

[31] Barron, R. F. (1984). Effect of heat transfer from ambient on cryogenics heat exchanger performance. *Advances in Cryogenic Engineering 29*, 265 – 272. Cited on pages 39 and 41.

[32] Barron, R. F. (1985). *Cryogenic Systems* (Second ed.), Volume 3 of *Monographs on Cryogenics*. Oxford: Clarendon Press. Cited on page 22.

[33] Barron, R. F. (1999). *Cryogenic Heat Transfer*. Series in Chemical and Mechanical Engineering. Philadelpia, PA: Taylor & Francis. Cited on page 27.

[34] Bassiouny, M. K. and H. Martin (1984a). Flow distribution and pressure drop in plate heat exchangers–I: U-type arrangement. *Chemical Engineering Science 39*(4), 693 – 700. Cited on pages 35 and 154.

[35] Bassiouny, M. K. and H. Martin (1984b). Flow distribution and pressure drop in plate heat exchangers–II: Z-type arrangement. *Chemical Engineering Science 39*(4), 701 – 704. Cited on pages 35 and 154.

[36] Becker, K. M., C. H. Ling, S. Hedberg, and G. Strand (1983). An experimental investigation of post-dryout heat transfer. Technical Report KTH-NEL-33, Department of Nuclear Reactor Engineering, Royal Institute of Technology. Cited on page 225.

[37] Bell, K. (1988). Two-phase flow regime considerations in condenser and vaporizer design. *International Communications in Heat and Mass Transfer 15*(4), 429 – 448. Cited on page 53.

[38] Bennett, A., G. Hewitt, H. Kearsey, and R. Keeys (1968). Heat transfer to steam–water mixtures flowing in uniformly heated tubes in which the critical heat flux has been exceeded. *Proceedings of the Institute of Mechanical Engineering (London) 182*(3), 258–267. Cited on pages 194, 226, 237, 239, and 240.

[39] Bourgat, J. (1979). Numerical experiments of the homogenization method. In R. Glowinski, J. Lions, and I. Laboria (Eds.), *Computing Methods in Applied Sciences and Engineering, 1977, I*, Volume 704 of *Lecture Notes in Mathematics*, pp. 330–356. Springer Berlin / Heidelberg. Cited on page 48.

[40] Bowman, R., A. Mueller, and W. Nagle (1940). Mean temperature difference in design. *Trans. ASME 62*, 283 – 294. Cited on pages 38 and 41.

[41] BP (2010, June). Statistical review of world energy. Cited on page 20.

[42] Brandt, A. (2001). Multiscale scientific computation: Review 2001. In *Multiscale and Multiresolution Methods*, pp. 1–96. Springer Verlag. Cited on pages 47 and 49.

[43] Brendeng, E. and J. Hetland (2004). State of the art in liquefaction technologies for natural gas. Ways of providing LNG for Transit Countries. In *Security of Natural Gas Supply through Transit Countries*, Volume 149 of *NATO Science Series II: Mathematics, Physics and Chemistry*, pp. 75–102. Springer Netherlands. Cited on page 26.

[44] Brevi, R. and M. Cumo (1971). Quality influence in post-burnout heat transfer. *International Journal of Heat and Mass Transfer 14*(3), 483 – 489. Cited on page 224.

[45] Brewster, M. E. and G. Beylkin (1995). A multiresolution strategy for numerical homogenization. *Applied and Computational Harmonic Analysis 2*(4), 327 – 349. Cited on page 48.

[46] Byun, H. and N. Kim (2011). Refrigerant distribution in a parallel flow heat exchanger having vertical headers and heated horizontal tubes. *Experimental Thermal and Fluid Science 35*(6), 920 – 932. Cited on page 149.

[47] Cacuci, D. G. (2010). Sensitivity and uncertainty analysis of models and data. In Y. Azmy and E. Sartori (Eds.), *Nuclear Computational Science*, pp. 291–353. Springer Netherlands. Cited on page 110.

[48] Canuto, C., M. Y. Hussaini, A. Quarteroni, and T. A. Zang (2006). *Spectral Methods. Fundamentals in Single Domains.* Springer. Cited on pages 67 and 77.

[49] Castrillo, L. S. (2004). Application of perturbative method for the sensitivity analysis of two-phase flows. In G. Buscaglia, E. Dari, and O. Zamonsky (Eds.), *Mecánica Computacional*, Volume 23, pp. 1–20. Biblioteca Digital de Teses e Dissertaes da UFPE. In portuguese. Cited on page 110.

[50] Çengel, Y. A. and M. A. Boles (1994). *Thermodynamics. An Engineering Approach* (Second ed.). New York: McGraw–Hill, Inc. Cited on pages 22 and 120.

[51] Chandraker, D. K., N. K. Maheshwari, D. Saha, and V. V. Raj (2002). Experimental and analytical investigations on core flow distribution and pressure distribution in the outlet header of a PHWR. *Experimental Thermal and Fluid Science 27*(1), 11 – 24. Cited on page 159.

[52] Chen, J. C. (1966). Correlation for boiling heat transfer to saturated fluids in convective flow. *Industrial & Engineering Chemistry Process Design and Development 5*(3), 322–329. Cited on page 59.

[53] Chen, J. C. (1986). A short review of dispersed flow heat transfer in post-dryout boiling. *Nuclear Engineering and Design 95*, 375 – 383. Cited on pages 223 and 224.

[54] Chen, J. C., F. T. Ozkaynak, and R. K. Sundaram (1979). Vapor heat transfer in post-CHF region including the effect of thermodynamic non-equilibrium. *Nuclear Engineering and Design 51*(2), 143 – 155. Cited on pages 225 and 227.

[55] Chen, L., Y. Tian, and T. Karayiannis (2006). The effect of tube diameter on vertical two-phase flow regimes in small tubes. *International Journal of Heat and Mass Transfer 49*(21-22), 4220 – 4230. Cited on page 5.

[56] Cheng, L., G. Ribatski, and J. R. Thome (2008). Two-phase flow patterns and flow-pattern maps: Fundamentals and applications. *Applied Mechanics Reviews 61*(5), 050802. Cited on page 196.

[57] Chowdhury, K. and S. Sarangi (1983). A second law analysis of the concentric tube heat exchanger: optimisation of wall conductivity. *International Journal of Heat and Mass Transfer 26*(5), 783 – 786. Cited on page 39.

[58] Chowdhury, K. and S. Sarangi (1984a). The effect of variable specific heat of the working fluids on the performance of counterflow heat exchangers. *Cryogenics 24*(12), 679 – 680. Cited on pages 27 and 37.

[59] Chowdhury, K. and S. Sarangi (1984b). Performance of cryogenic heat exchangers with heat leak from the surroundings. *Advances in Cryogenic Engineering 29*, 273–280. Cited on pages 28, 39, and 41.

[60] Chowdhury, K. and S. Sarangi (1985). Effect of flow maldistribution on multipassage heat exchanger performance. *Heat Transfer Engineering 6*(4), 45–54. Cited on pages 29 and 40.

[61] Chun, J.-H., W.-J. Lee, C. Park, and U.-C. Lee (2003). Development of the critical film thickness correlation for an advanced annular film mechanistic dryout model applicable to MARS code. *Nuclear Engineering and Design 223*(3), 315 – 328. Cited on page 199.

[62] Chung, J. N. and S. I. Olafsson (1984). Two-phase droplet flow convective and radiative heat transfer. *International Journal of Heat and Mass Transfer 27*(6), 901 – 910. Cited on pages 226 and 231.

[63] Clayton, D. G. (1974). New concepts for heat exchanger performance. *Heat and Mass Transfer 7*, 107–112. Cited on page 33.

[64] Clift, R., J. R. Grace, and M. E. Weber (1978). *Bubbles, Drops and Particles*. New York: Academic Press. Cited on pages 203 and 234.

[65] Colburn, A. P. and E. I. de du Pont (1933). Mean temperature difference and heat transfer coefficient in liquid heat exchangers. *Industrial & Engineering Chemistry 25*(8), 873–877. Cited on pages 38 and 41.

[66] Collier, J. G. and J. R. Thome (1994). *Convective Boiling and Condensation*. Oxford, New York: Clarendon Press, Oxford University Press. Cited on pages 55 and 82.

[67] Collis, S. S. (2001). Monitoring unresolved scales in multiscale turbulence modeling. *Physics of Fluids 13*(6), 1800–1806. Cited on page 47.

[68] Costa, M. M. and J. Parise (1993). A three-zone simulation model for air-cooled condensers. *Heat Recovery Systems and CHP 13*(2), 97 – 113. Cited on page 34.

[69] Crawford, D. B. and G. P. Eschenbrenner (1972). Heat transfer equipment for LNG projects. *Chemical Engineering Process 68*(9), 62–70. Cited on page 24.

[70] da Silva Lima, R. J., J. M. Quibn, and J. R. Thome (2009). Flow boiling in horizontal smooth tubes: New heat transfer results for R-134a at three saturation temperatures. *Applied Thermal Engineering 29*(7), 1289 – 1298. Selected Papers from the 10th UK National Heat Transfer Conference, Edinburgh, Scotland, September 10-11, 2007. Cited on pages xviii, 214, and 215.

[71] Dallman, J., J. Laurinat, and T. Hanratty (1984). Entrainment for horizontal annular gas-liquid flow. *International Journal of Multiphase Flow 10*(6), 677 – 689. Cited on page 202.

[72] Das, S. K. and R. K. Sahoo (1999). Second law analysis of a cyclic regenerator in presence of longitudinal heat conduction in matrix. *Heat and Mass Transfer 34*, 395–403. Cited on pages 39 and 41.

[73] de Andrade Lima, F. R., C. A. B. de Oliveira Lira, and A. Gandini (1993). Sensitivity analysis of thermohydraulic systems via heuristic generalized perturbation theory (HGPT) methods. *Annals of Nuclear Energy 20*(10), 679 – 690. Cited on page 110.

[74] de Andrade Lima, F. R., A. Gandini, A. Blanco, C. A. B. O. Lira, E. S. G. Maciel, A. C. M. Alvim, F. C. Silva, P. F. F. Melo, W. F. L. Frana, J. L. Balio, A. E. Larreteguy, and A. Lorenzo (1998). Recent advances in perturbative methods applied to nuclear engineering problems. *Progress in Nuclear Energy 33*(1-2), 23 – 97. Cited on page 110.

[75] de Bertodano, M. A. L., C.-S. Jan, and S. G. Beus (1997). Annular flow entrainment rate experiment in a small vertical pipe. *Nuclear Engineering and Design 178*(1), 61 – 70. Cited on page 202.

[76] Deen, N. G., M. van Sint Annaland, and J. A. M. Kuipers (2004). Multi-scale modeling of dispersed gas-liquid two-phase flow. *Chemical Engineering Science 59*(8-9), 1853 – 1861. Complex Systems and Multi-scale Methodology. Cited on page 47.

[77] Didi, M. B. O., N. Kattan, and J. R. Thome (2002). Prediction of two-phase pressure gradients of refrigerants in horizontal tubes. *International Journal of Refrigeration 25*(7), 935 – 947. Cited on page 96.

[78] DiNapoli, R. N. (1986). Evolution in LNG project costs and estimation techniques for new projects. In *8th International Conference on Liquefied Natural Gas*. Cited on page 23.

[79] Domanski, P. and D. Didion (1983). Computer modeling of the vapor compression cycle with constant flow area expansion device. Technical Report 155, NBS Building Science Series. Cited on page 34.

[80] Dorao, C., M. Fernandino, H. Jakobsen, and H. Svendsen (2009). hp-adaptive spectral element solver for reactor modeling. *Chemical Engineering Science 64*(5), 904 – 911. Cited on page 64.

[81] Dorao, C. and H. Jakobsen (2008). hp-adaptive least squares spectral element method for population balance equations. *Applied Numerical Mathematics 58*(5), 563 – 576. Cited on page 64.

[82] Dorobantu, M. and B. Engquist (1998). Wavelet-based numerical homogenization. *SIAM Journal on Numerical Analysis 35*(2), pp. 540–559. Cited on page 48.

[83] Dougall, R. S. and W. M. Rohsenow (1963). Film boiling on the inside of vertical tubes with upward flow of the fluid at low qualities. Technical Report 9079-26, Massachusetts Institute of Technology, Heat Transfer Laboratory. Cited on page 224.

[84] Duffy, P. and A. Kandalov (1996). *Tupolev. The man and his aircraft*. Warrendale, Pa: SAE International. Cited on page 20.

[85] Dukler, A. E. and Y. Taitel (1986). Flow pattern transitions in gas-liquid systems: measurement and modeling. In G. F. Hewitt, J. M. Delhaye, and N. Zuber (Eds.), *Multiphase Science and Technology*, Volume 2, Chapter 1, pp. 1–96. Hemisphere Pub. Corp. Cited on page 197.

[86] Dupont, V., J. R. Thome, and A. M. Jacobi (2004). Heat transfer model for evaporation in microchannels. Part II: comparison with the database. *International Journal of Heat and Mass Transfer 47*(14-16), 3387 – 3401. Cited on page 198.

[87] E, W. and B. Engquist (2003). The heterogeneous multiscale methods. *Communications in Mathematical Science 1*(1), 87–132. Cited on pages 45 and 49.

[88] Eason, E. D. (1976). A review of least–squares methods for solving partial differential equations. *International Journal for Numerical Methods in Engineering 10*, 1021–1046. Cited on page 64.

[89] Engquist, B. and O. Runborg (2002). Wavelet-based numerical homogenization with applications. In *Lecture Notes in Computational Science and Engineering*, pp. 97–148. Springer. Cited on page 48.

[90] Era, A., G. Gaspari, A. Hassid, A. Milani, and R. Zavattarelli (1966). Heat transfer data in the liquid deficient region for steam-water mixtures at 70 kg/cm^2 flowing in tubular and annular conduits. Technical report, Centro Informazioni Studi Esperienze, Milan (Italy). Cited on page 240.

[91] Finn, A. J., G. L. Johnson, and T. R. Tomlinson (1999). Developments in natural gas liquefaction. *Hydrocarbon Processing 78*(4), 47–59. Cited on pages 23 and 26.

[92] Fischer, S. K. and C. K. Rice (1981). A steady–state computer design model for air–to–air heat pumps. Technical Report ORNL/CON-80, Oak Ridge National Laboratory. Cited on page 34.

[93] Fleming, R. B. (1967). The effect of flow maldistribution in parallel channels of counterflow heat exchangers. *Advances in Cryogenic Engineering 12*, 352–362. Cited on pages 29, 38, 41, 43, 148, and 168.

[94] Flynn, T. M. (2005). *Cryogenic Engineering* (Second, Revised ed.). New York: Marcel Dekker. Cited on pages xix and 19.

[95] Foerg, W. (2002). History of cryogenics: the epoch of the pioneers from the beginning to the year 1911. *International Journal of Refrigeration 25*(3), 283 – 292. Cited on page 18.

[96] Forslund, R. P. (1967). *Thermal non-equilibrium in dispersed flow film boiling in a vertical tube.* Ph. D. thesis, Massachusetts Institute of Technology. Cited on page 226.

[97] Forslund, R. P. and W. M. Rohsenow (1966). Thermal non-equilibrium in dispersed flow film boiling in a vertical tube. Technical Report 75312-44, Massachusetts Institute of Technology, Heat Transfer Laboratory. Cited on page 226.

[98] Fraas, A. P. (1989). *Heat exchanger design* (Second ed.). New York: Wiley. Cited on page 153.

[99] Fredheim, A. O. (1994). *Thermal Design of Coil-Wound LNG Heat Exchangers.* Ph. D. thesis, Norwegian Institute of Technology. Cited on page 24.

[100] Fredheim, A. O. and R. S. Heiersted (1996). Possibilities for cost reductions in base–load LNG plants. In *EUROGAS96. Proceedings from the European Applied Research Conference on Natural Gas*, pp. 101–114. TAPIR. Cited on page 23.

[101] Fredheim, A. O., O. Joerstad, G. Owren, S. Vist, and B. O. Neeras (2000, June). COIL. A Model for Simulation of Spiral Wound LNG Heat Exchangers. In *Proceedings from World Gas Conference 2000, Nice*. Cited on page 35.

[102] Fu, M. C., F. W. Glover, and J. April (2005). Simulation optimization: a review, new developments, and applications. In *Proceedings of the 37th conference on Winter simulation*, WSC '05, pp. 83–95. Winter Simulation Conference. Cited on page 136.

[103] Gabriel, P., J. Y. Harrington, G. L. Stephens, and T. L. Schneider (1998). Adjoint perturbation method applied to two-stream radiative transfer. *Journal of Quantitative Spectroscopy and Radiative Transfer 59*(1-2), 1 – 24. Cited on page 110.

[104] Gage, A. A. (1998, March). History of cryosurgery. *Seminars in Surgical Oncology 14*(2), 99–109. Cited on page 19.

[105] Gall, J. (1957). Fluorine-derived chemicals as liquid propellants. *Industrial and Engineering Chemistry 49*(2), 1131–1132. Cited on page 20.

[106] Ganapathysubramanian, B. and N. Zabaras (2008). Modeling multiscale diffusion processes in random heterogeneous media. *Computer Methods in Applied Mechanics and Engineering 197*(43-44), 3560 – 3573. Stochastic Modeling of Multiscale and Multiphysics Problems. Cited on page 47.

[107] Gandini, A. (1967). A generalized perturbation method for bi-linear functionals of the real and adjoint neutron fluxes. *Journal of Nuclear Energy 21*(10), 755 – 765. Cited on page 111.

[108] Gandini, A. (1987). Generalized perturbation theory (GPT) methods. a heuristic approach. *Advances in Nuclear Science and Technology 19*, 205–380. Cited on pages 111 and 114.

[109] Gandini, A. (2001). HGPT based sensitivity time-dependent methods for the analysis of subcritical systems. *Annals of Nuclear Energy 28*(12), 1193 – 1217. Cited on page 111.

[110] Ganic, E. and W. Rohsenow (1977). Dispersed flow heat transfer. *International Journal of Heat and Mass Transfer 20*(8), 855 – 866. Cited on pages 233 and 234.

[111] Gardner, K. A. (1941). Mean temperature difference in unbalanced-pass exchangers. *Industrial & Engineering Chemistry 33*(10), 1215–1223. Cited on pages 38 and 41.

[112] Gardner, K. A. and J. Taborek (1977). Mean temperature difference: A reappraisal. *AIChE Journal 23*(6), 777—786. Cited on pages 38 and 41.

[113] George, C. M. and D. M. France (1991). Post-CHF two-phase flow with low wall-superheat. *Nuclear Engineering and Design 125*(2), 97 – 109. Cited on page 250.

[114] Ghiaasiaan, S. M. (2007). *Two-Phase Flow, Boiling, and Condensation In Conventional and Miniature Systems*. Cambridge University Press. Cited on pages 51, 57, 82, 95, and 221.

[115] Gill, L. E., G. F. Hewitt, and P. M. C. Lacey (1964). Sampling probe studies of the gas core in annular two-phase flow–II : Studies of the effect of phase flow rates on phase and velocity distribution. *Chemical Engineering Science 19*(9), 665 – 682. Cited on page 50.

[116] Giménez, M. O., M. A. Schlamp, and F. R. A. Lima (2003). Sensitivity analysis of the aerosols transport equation. *Annals of Nuclear Energy 30*(12), 1247 – 1266. Cited on page 110.

[117] Govan, A., G. Hewitt, D. Owen, and T. Bott (1988). An improved CHF modeling code. In *2nd U.K. National Heat Transfer Conference, Glasgow*. Cited on page 197.

[118] Groeneveld, D. (1975). Post-dryout heat transfer: Physical mechanisms and a survey of prediction methods. *Nuclear Engineering and Design 32*(3), 283 – 294. Cited on pages 223 and 224.

[119] Groeneveld, D. and G. Delorme (1976). Prediction of thermal non-equilibrium in the post-dryout regime. *Nuclear Engineering and Design 36*(1), 17 – 26. Cited on pages 224, 225, and 231.

[120] Groeneveld, D. C. (1972). The thermal behavior of a heated surface at and beyond dryout. Technical Report AECL-4309, Atomic Energy of Canada Limited. Cited on page 224.

[121] Gungor, K. and R. Winterton (1986). A general correlation for flow boiling in tubes and annuli. *International Journal of Heat and Mass Transfer 29*(3), 351 – 358. Cited on pages 58 and 59.

[122] Gungor, K. E. and R. H. S. Winterton (1987). Simplified general correlation for saturated flow boiling and comparison of correlations with data. *Chemical Engineering Res 65*, 148–156. Cited on page 59.

[123] Guo, Y. and K. Mishima (2002). A non-equilibrium mechanistic heat transfer model for post-dryout dispersed flow regime. *Experimental Thermal and Fluid Science 26*(6-7), 861 – 869. Cited on pages 230, 232, 233, and 237.

[124] Gupta, P. and M. D. Atrey (2000). Performance evaluation of counter flow heat exchangers considering the effect of heat in leak and longitudinal conduction for low-temperature applications. *Cryogenics 40*(7), 469 – 474. Cited on pages 28, 40, and 42.

[125] Hackbusch, W. (1985). *Multi-grid methods and applications*, Volume 4 of *Springer series in computational mathematics*. Berlin: Springer. Cited on page 48.

[126] Hadaller, G. and S. Banerjee (1969). Heat transfer to superheated steam in round tubes. Technical report, AECL. Cited on page 231.

[127] Hajibeygi, H., G. Bonfigli, M. A. Hesse, and P. Jenny (2008). Iterative multiscale finite-volume method. *Journal of Computational Physics 227*(19), 8604 – 8621. Cited on page 48.

[128] Harshbarger, D. S. and C. W. Bullard (2000, August). Finite element heat exchanger simulation within a Newton-Raphson framework. Technical Report ACRCTR-171, Air Conditioning and Refrigeration Center, University of Illinois, Mechanical & Industrial Engineering Dept. Cited on page 64.

[129] Hennecke, D. K. (1968). Heat transfer by Hagen-Poiseuille flow in the thermal development region with axial conduction. *Heat and Mass Transfer 1*, 177–184. Cited on page 39.

[130] Hesselgreaves, J. E. (2001). *Compact heat exchangers. Selection, design and operation*. Amsterdam: Elsevier Science & Technology Books. Cited on page 29.

[131] Hewitt, G. (1982). Prediction of pressure drop in annular flow by phenomenological modeling. In G. Hetsroni (Ed.), *Handbook of Multiphase Systems*, pp. 62–75. Hemisphere Pub. Corp. Cited on page 200.

[132] Hewitt, G. and D. Roberts (1969). Studies of two-phase flow patterns by simultaneous X-ray and flash photography. Technical report, Atomic Energy Research Establishment, Harwell (England). Cited on page 221.

[133] Hewitt, G. F. (1987). Experimental dataset no. 12: annular flow evaporation. *Multiphase Science and Technology 3*(1-4), 368–377. Cited on page 204.

[134] Hewitt, G. F. and A. H. Govan (1990). Phenomenological modeling of non-equilibrium flows with phase change. *International Journal of Heat and Mass Transfer 33*(2), 229 – 242. Cited on pages xvii, 200, 201, and 202.

[135] Hill, Wayne S.; Rohsenow, W. M. (1982). Dryout droplet distribution and dispersed flow film boiling. Technical Report 85694-105, Massachusetts Institute of Technology, Heat Transfer Laboratory. Cited on pages 227 and 238.

[136] Holman, J., P. Jenkins, and F. Sullivan (1972). Experiments on individual droplet heat transfer rates. *International Journal of Heat and Mass Transfer 15*(8), 1489 – 1495. Cited on pages 233 and 234.

[137] Horstemeyer, M. F. (2010). Multiscale modeling: A review. In J. Leszczynski and M. K. Shukla (Eds.), *Practical Aspects of Computational Chemistry*, pp. 87–135. Springer Netherlands. Cited on page 46.

[138] Hou, T. and Y. Efendiev (2009). *Multiscale Finite Element Methods. Theory and Applications*, Volume 4 of *Surves and tutorials in the applied mathematical sciences*. Springer. Cited on page 48.

[139] Hoyer, N. (1998). Calculation of dryout and post-dryout heat transfer for tube geometry. *International Journal of Multiphase Flow 24*(2), 319 – 334. Cited on pages 225 and 240.

[140] Hughes, T. J., L. Mazzei, and K. E. Jansen (2000). Large eddy simulation and the variational multiscale method. *Computing and Visualization in Science 3*, 47–59. Cited on page 47.

[141] Hynek, S. J., W. M. Rohsenow, and A. E. Bergles (1969). Forced-convection, dispersed-flow film boiling. Technical Report DSR 70586-63, Massachusetts Institute of Technology, Heat Transfer Laboratory. Cited on pages 225 and 240.

[142] Iloeje, O. C. (1975). *A study on wall rewet and heat transfer in dispersed vertical flow*. Ph. D. thesis, Massachusetts Institute of Technology. Cited on page 233.

[143] Incropera, F. P. and D. P. DeWitt (1996). *Fundamentals of Heat and Mass Transfer* (4th ed.). New York: John Wiley and Sons. Cited on pages 48, 104, 214, 226, 230, 231, and 261.

[144] Ishii, M. and M. A. Grolmes (1975). Inception criteria for droplet entrainment in two-phase concurrent film flow. *AIChE Journal 21*(2), 308–319. Cited on page 200.

[145] Ishii, M. and T. Hibiki (2006). *Thermo–fluid dynamics of two–phase flow*. Springer Science and Business Media, Inc. Cited on pages 50 and 192.

[146] Iu, I., N. Weber, P. Bansal, and D. Fisher (2007). Applying the effectiveness–NTU method to elemental heat exchanger models. *ASHRAE Transactions 113*(1), 504–513. Cited on page 34.

[147] Iu, I. S. (2007). *Development of air–to–air heat pump simulation program with advanced heat exchanger circuitry algorithm*. Ph. D. thesis, Oklahoma State University. Cited on page 34.

[148] Janssen, E. and J. A. Kervinen (1975). Film boiling and rewetting. Technical Report NEDO-20975, General Electric Co. Cited on page 240.

[149] Jayanti, S. and M. Valette (2004). Prediction of dryout and post-dryout heat transfer at high pressures using a one-dimensional three-fluid model. *International Journal of Heat and Mass Transfer 47*(22), 4895 – 4910. Cited on pages 236 and 237.

[150] Jen, T. C., G. Gutierrez, S. Eapen, G. Barber, H. Zhao, P. S. Szuba, J. Labataille, and J. Manjunathaiah (2002). Investigation of heat pipe cooling in drilling applications. Part I: preliminary numerical analysis and verification. *International Journal of Machine Tools and Manufacture 42*(5), 643 – 652. Cited on page 64.

[151] Jenny, P., S. H. Lee, and H. A. Tchelepi (2003). Multi-scale finite-volume method for elliptic problems in subsurface flow simulation. *Journal of Computational Physics 187*(1), 47 – 67. Cited on page 47.

[152] Jeong, H. Y. and H. C. No (1996). Modelling for post-dryout heat transfer and droplet sizes at low pressure and low flow conditions. *International Communications in Heat and Mass Transfer 23*(6), 767 – 778. Cited on page 221.

[153] Jha, A. R. (2006). *Cryogenic Technology and Applications*. Burlington, Massachusets: Butterworth-Heinemann. Cited on page 19.

[154] Jia, X., C. P. Tso, P. K. Chia, and P. Jolly (1995). A distributed model for prediction of the transient response of an evaporator. *International Journal of Refrigeration 18*(5), 336 – 342. Cited on page 96.

[155] Jiang, B. N. (1998). *The Least-Squares Finite Element Method. Theory and applications in computational fluid dynamics and electromagnetics*. Berlin, New York: Springer. Cited on pages 64, 71, and 80.

[156] Jiang, B.-N. and L. A. Povinelli (1990). Least-squares finite element method for fluid dynamics. *Computer Methods in Applied Mechanics and Engineering 81*(1), 13 – 37. Cited on page 64.

[157] Jiang, L., Y. Efendiev, and I. Mishev (2010). Mixed multiscale finite element methods using approximate global information based on partial upscaling. *Computational Geosciences 14*, 319–341. Cited on page 49.

[158] Jiao, B., L. m. Qiu, J. l. Lu, and Z. h. Gan (2009). Liquid film dryout model for predicting critical heat flux in annular two-phase flow. *Journal of Zhejiang University - Science A 10*, 398–417. Cited on pages 193, 196, 199, and 248.

[159] Judge, J. and R. Radermacher (1997). A heat exchanger model for mixtures and pure refrigerant cycle simulations. *International Journal of Refrigeration 20*(4), 244 – 255. Cited on page 96.

[160] Jung, J. and S. Jeong (2007). Effect of flow mal-distribution on effective NTU in multi-channel counter-flow heat exchanger of single body. *Cryogenics 47*(4), 232 – 242. Cited on pages 29, 38, and 41.

[161] Kakaç, S. and B. Bon (2008). A review of two-phase flow dynamic instabilities in tube boiling systems. *International Journal of Heat and Mass Transfer 51*(3-4), 399 – 433. Cited on pages 59, 148, 161, and 178.

[162] Kakaç, S. and H. Liu (2002). *Heat Exchangers: Selection, Rating, and Thermal Design* (Second ed.). London, New York: CRC Press. Cited on page 30.

[163] Kandlikar, S. G. (1990). A general correlation for saturated two-phase flow boiling heat transfer inside horizontal and vertical tubes. *Journal of Heat 112*(1), 219–228. Cited on pages 58 and 59.

[164] Kandlikar, S. G. (1997). Heat transfer characteristics in partial boiling, fully developed boiling, and significant void flow regions of subcooled flow boiling. *Journal of Heat Transfer 120*(2), 395–401. Cited on pages 57 and 82.

[165] Kandlikar, S. G. and W. J. Grande (2003). Evolution of microchannel flow passages–thermohydraulic performance and fabrication technology. *Heat Transfer Engineering 24*(1), 3–17. Cited on page 5.

[166] Kanoglu, M., I. Dincer, and M. A. Rosen (2008). Performance analysis of gas liquefaction cycles. *International Journal of Energy Research 32*(1), 35–43. Cited on page 22.

[167] Kao, S. (1975). Analysis of multipass heat exchangers with variable properties and transfer rate. *Journal of Heat Transfer 97*(4), 509–515. Cited on pages 38 and 41.

[168] Karniadakis, G. E. and S. J. Sherwin (2005). *Spectral/hp element methods for computational fluid dynamics* (Second ed.). Numerical mathematics and scientific computation Oxford science publications. Oxford: Oxford University Press. Cited on page 68.

[169] Kataoka, I., M. Ishii, and K. Mishima (1983). Generation and size distribution of droplet in annular two-phase flow. *Journal of Fluids Engineering 105*(2), 230–238. Cited on page 237.

[170] Kattan, N., J. R. Thome, and D. Favrat (1998). Flow boiling in horizontal tubes: Part 1—development of a diabatic two-phase flow pattern map. *Journal of Heat Transfer 120*(1), 140–147. Cited on pages 54 and 197.

[171] Kawara, Z., I. Kataoka, A. Serizawa, Y. J. Ko, and O. Takahashi (1998). Analysis of forced convective CHF based on two–fluid and three–fluid model. In J. S. Lee (Ed.), *Heat Transfer 1998, Proceedings of Eleventh International Heat Transfer Conference, Kyongju, Korea*, Volume 2, pp. 103–108. Taylor & Francis. Cited on pages 194 and 203.

[172] Kays, W. M. and A. L. London (1964). *Compact heat exchangers* (Second ed.). McGraw-Hill series in mechanical engineering. New York: McGraw-Hill Book Co. Cited on pages 27, 37, and 40.

[173] Kayser-Herold, O. and H. G. Matthies (2005, August). Least-squares FEM literature review. Technical Report 2005–05, Institute of Scientific Computing. Technical University Braunschweig. Brunswick, Germany. Cited on page 64.

[174] Kee, R. J., P. Korada, K. Walters, and M. Pavol (2002). A generalized model of the flow distribution in channel networks of planar fuel cells. *Journal of Power Sources 109*(1), 148 – 159. Cited on page 154.

[175] Kellner, K. and R. G. Scurlock (1971). Cryogenics and its applications. *Review of physics in technology 2*(25), 25–38. Cited on page 18.

[176] Kendall, G. E. and W. M. Rohsenow (1978). Heat transfer to impacting drops and post critical heat flux dispersed flow. Technical Report 85694-100, Massachusetts Institute of Technology, Heat Transfer Laboratory. Cited on page 233.

[177] Kishore, B. N. and S. Jayanti (2004). A multidimensional model for annular gas-liquid flow. *Chemical Engineering Science 59*(17), 3577 – 3589. Cited on page 193.

[178] Klimenko, V. (1990). A generalized correlation for two-phase forced flow heat transfer–second assessment. *International Journal of Heat and Mass Transfer 33*(10), 2073 – 2088. Cited on pages 58 and 59.

[179] Koizumi, Y., T. Ueda, and H. Tanaka (1979). Post dryout heat transfer to R-113 upward flow in a vertical tube. *International Journal of Heat and Mass Transfer 22*(5), 669 – 678. Cited on pages 240 and 247.

[180] Kolev, N. I. (2007). *Multiphase Flow Dynamics 2. Thermal and Mechanical Interactions* (3 ed.). Springer. Cited on pages 194, 199, and 203.

[181] Kroeger, P. G. (1967). Performance deterioration in high effectiveness heat exchangers due to axial heat conduction effects. *Advances in Cryogenic Engineering 12*, 363–372. Cited on pages 29, 39, 40, 41, and 181.

[182] Kumar, K. V. R. and S. Sarangi (1991). On the performance of high–Ntu heat exchangers with variable heat capacity of the working fluid. *Heat Transfer Engineering 12*(1), 37 – 42. Cited on pages 37 and 41.

[183] Kuppan, T. (2000). *Heat Exchanger Design Handbook*, Volume 126 of *Mechanical Engineering. A Series of Textbooks and Reference Books*. New York: Marcel Dekker, Inc. Cited on page 30.

[184] Kurti, N. (1970). Low temperature terminology. *Cryogenics 10*(3), 183 – 185. Cited on page 18.

[185] Kutateladze, S. S. (1961). Boiling heat transfer. *International Journal of Heat and Mass Transfer 4*, 31 – 45. Cited on pages 58 and 59.

[186] Lahey, R. T. and D. A. Drew (2001). The analysis of two-phase flow and heat transfer using a multidimensional, four field, two-fluid model. *Nuclear Engineering and Design 204*(1-3), 29 – 44. Cited on page 193.

[187] Lahey, Jr., R. T. (2005). The simulation of multidimensional multiphase flows. *Nuclear Engineering and Design 235*(10-12), 1043 – 1060. Cited on page 193.

[188] Lalot, S., P. Florent, S. K. Lang, and A. E. Bergles (1999). Flow maldistribution in heat exchangers. *Applied Thermal Engineering 19*(8), 847 – 863. Cited on pages 148 and 149.

[189] Laverty, W. F. and W. M. Rohsenow (1964). Film boiling of saturated liquid flowing upward through a heated tube : high vapor quality range. Technical Report 75312-44, Massachusetts Institute of Technology, Heat Transfer Laboratory. Cited on page 226.

[190] Lee, K. and D. J. Ryley (1968). The evaporation of water droplets in superheated steam. *Journal of Heat Transfer 445*, Paper 68–HT–11. Cited on page 230.

[191] Lee, K.-W., S.-J. Baik, and T.-S. Ro (2000). An utilization of liquid sublayer dryout mechanism in predicting critical heat flux under low pressure and low velocity conditions in round tubes. *Nuclear Engineering and Design 200*(1-2), 69 – 81. Cited on pages 197 and 198.

[192] Lee, S. I. and H. C. No (2007). Assessment of an entrainment model in annular-mist flow for a three-field trac-m. *Nuclear Engineering and Design 237*(4), 441 – 450. Cited on page 203.

[193] Lee, S. K. and S. H. Chang (2008). Experimental study of post-dryout with r-134a upward flow in smooth tube and rifled tubes. *International Journal of Heat and Mass Transfer 51*(11-12), 3153 – 3163. Cited on page 204.

[194] Leinhard V, J. H. and J. H. Leinhard IV (2011). *A heat transfer textbook* (4 ed.). Phlogiston Press. Cited on page 2.

[195] Lemmon, E. W., M. L. Huber, and M. O. McLinden. (2007). *NIST Standard Reference Database 23: Reference Fluid Thermodynamic and Transport Properties-REFPROP, Version 8.0*. Gaithersburg: National Institute of Standards and Technology, Standard Reference Data Program. Cited on page 20.

[196] Lewins, J. (1965). *Importance, the Adjoint Function*. Oxford, New York: Pergamon Press. Cited on page 111.

[197] Liang, S. Y., T. N. Wong, and G. K. Nathan (2001). Numerical and experimental studies of refrigerant circuitry of evaporator coils. *International Journal of Refrigeration 24*(8), 823 – 833. Cited on page 34.

[198] Linde, A. G. Aluminium plate–fin heat exchangers. Catalogue. Cited on pages xiii, xix, 24, and 25.

[199] Linde, A. G. Looking inside ... plate–fin versus coil–wound heat exchanger. Catalogue. Cited on page 24.

[200] Ling, C. H., K. M. Becker, S. Hedberg, and G. Strand (1971). Temperature distribution for the post-burnout regime in a round tube. Technical Report KTH-NEL-16, Royal Institute of Technology, Laboratory of Nuclear Engineering, Stockholm. Cited on page 237.

[201] Liu, W. K., E. G. Karpov, and H. S. Park (2006). *Nano mechanics and materials : theory, multiscale methods and applications*. Wiley. Cited on page 47.

[202] Liu, Z. and R. Winterton (1991). A general correlation for saturated and subcooled flow boiling in tubes and annuli, based on a nucleate pool boiling equation. *International Journal of Heat and Mass Transfer 34*(11), 2759 – 2766. Cited on pages 58 and 59.

[203] LNGpedia (2010). LNG Statistics. Available online at `http://www.lngpedia.com/lng-statistics/`. Cited on pages xiii and 21.

[204] Lockhart, R. W. and R. C. Martinelli (1949). Proposed correlation of data for isothermal two-phase, two-component flow in pipes. *Chemical Engineering Progress 45*(1), 39–48. Cited on pages 96 and 197.

[205] Lunati, I., M. Tyagi, and S. H. Lee (2011). An iterative multiscale finite volume algorithm converging to the exact solution. *Journal of Computational Physics 230*(5), 1849 – 1864. Cited on page 49.

[206] Maerschalck, B. D. and M. Gerritsma (2008). Least-squares spectral element method for non-linear hyperbolic differential equations. *Journal of Computational and Applied Mathematics 215*(2), 357 – 367. Cited on pages 64 and 83.

[207] Maggio, F., G. Mazzarella, and C. Pitzianti (2004). Least squares spectral element method for 2D Maxwell equations in the frequency domain. *International Journal of Numerical Modelling: Electronic Networks, Devices and Fields 17*, 509–522. Cited on page 64.

[208] Maharudrayya, S., S. Jayanti, and A. Deshpande (2005). Flow distribution and pressure drop in parallel-channel configurations of planar fuel cells. *Journal of Power Sources 144*(1), 94 – 106. Cited on page 154.

[209] Manteuffel, T. A. and K. J. Ressel (1998). Least-squares finite-element solution of the neutron transport equation in diffusive regimes. *SIAM Journal on Numerical Analysis 35*(2), pp. 806–835. Cited on page 64.

[210] Marathe, S. S. and R. L. Webb (2008). Prediction of dryout vapor quality for annular two-phase flow in tubes. *Applied Thermal Engineering 28*(7), 691 – 698. Cited on page 197.

[211] Marchitto, A., F. Devia, M. Fossa, G. Guglielmini, and C. Schenone (2008). Experiments on two-phase flow distribution inside parallel channels of compact heat exchangers. *International Journal of Multiphase Flow 34*(2), 128 – 144. Cited on page 149.

[212] Marchuk, G., V. Shutyaev, and G. Bocharov (2005). Adjoint equations and analysis of complex systems: Application to virus infection modelling. *Journal of Computational and Applied Mathematics 184*(1), 177 – 204. Special Issue on Mathematics Applied to Immunology. Cited on page 110.

[213] Mathew, B. and H. Hegab (2010a). Application of effectiveness-ntu relationship to parallel flow microchannel heat exchangers subjected to external heat transfer. *International Journal of Thermal Sciences 49*(1), 76 – 85. Cited on pages 39 and 42.

[214] Mathew, B. and H. Hegab (2010b). Performance of counterflow microchannel heat exchangers subjected to external heat transfer. *Heat Transfer Engineering 31*(3), 168 – 178. Cited on page 39.

[215] Mathew, B. and H. Hegab (2011). Modeling non-adiabatic parallel flow microchannel heat exchangers. *International Journal of Thermal Sciences 50*(3), 350 – 360. Nano, Micro and Mini Channels. Cited on pages 39 and 42.

[216] Mayinger, F. and R. Schnittger (1988). Post-dryrout heat transfer in tubes with uniform and circumferentially nonuniform heating. In M. V. Krishna Murthy, V. M. Krishna Sastri, and P. K. Sarma (Eds.), *Current research in heat and mass transfer: a compendium and a Festschrift for Professor Arcot Ramachandran*, pp. 157–165. Berlin: Springer. Cited on page 240.

[217] McAdams, W. (1954). *Heat Transmission* (3 ed.). New York: McGraw–Hill, Inc. Cited on page 231.

[218] McGinnis III, F. K. and J. Holman (1969). Individual droplet heat-transfer rates for splattering on hot surfaces. *International Journal of Heat and Mass Transfer 12*(1), 95 – 108. Cited on pages 233 and 234.

[219] McKeever, J., M. Pillarella, and R. Bower (2008). An ever evolving technology. *LNG Industry Spring*, 44–49. Cited on page 24.

[220] Mikhailov, M. D. and M. N. Özişik (1981). Finite element analysis of heat exchangers. In S. Kakaç, A. E. Bergles, and F. Mayinger (Eds.), *Heat Exchangers. Thermal–Hydraulic Fundamentals and Design.*, pp. 461–479. Hemisphere Pub. Corp. Cited on page 64.

[221] Milashenko, V., B. Nigmatulin, V. Petukhov, and N. Trubkin (1989). Burnout and distribution of liquid in evaporative channels of various lengths. *International Journal of Multiphase Flow 15*(3), 393 – 401. Cited on pages 198, 199, and 200.

[222] Mishima, K. and M. Ishii (1984). Flow regime transition criteria for upward two-phase flow in vertical tubes. *International Journal of Heat and Mass Transfer 27*(5), 723 – 737. Cited on page 196.

[223] Mitsutake, T., S. Morooka, K. Suzuki, S. Tsunoyama, and K. Yoshimura (1990). Void fraction estimation within rod bundles based on three-fluid model and comparison with x-ray CT void data. *Nuclear Engineering and Design 120*(2-3), 203 – 212. Cited on page 193.

[224] Moose, R. and E. Ganic (1982). On the calculation of wall temperatures in the post dryout heat transfer region. *International Journal of Multiphase Flow 8*(5), 525 – 542. Cited on pages 232 and 234.

[225] Mori, H., S. Yoshida, K. Phishi, and Y. Kakimo (2000). Dryout quality and post-dryout heat transfer coefficient in horizontal evaporator tubes. In E. W. P. Hahne, W. HEidemann, and K. Spindler (Eds.), *Third European Thermal Sciences Conference*, pp. 839–844. Cited on page 212.

[226] Mörk-Mörkenstein, P. and H. Herkenrath (1967). Wärmeübergang an Wasser bei erzwungener Strömung im Gebiet des kritischen Druckes unter hohen Heizflächenbelastungen (Heat transfer in forced flow of water near the critical pressure at high heat flux). *Chemie Ingenieur Technik 39*(5-6), 250–253. In German. Cited on page 240.

[227] Mueller, A. C. (1967). New charts for true mean temperature difference in heat exchangers. AIChE paper 10, 9th National Heat Transfer Conference. Cited on page 33.

[228] Mueller, A. C. and J. P. Chiou (1988). Review of various types of flow maldistribution in heat exchangers. *Heat Transfer Engineering 9*(2), 36–50. Cited on pages 29, 147, 148, 149, 158, and 168.

[229] Mukhopadhyay, M. (2007). *Fundamentals of cryogenic engineering*. New Delhi: Prentice Hall of India. Cited on page 19.

[230] Mullen, C. E., B. D. Bridges, K. J. Porter, G. W-Hahn, and C. W. Bullard (1997). Development and validation of a room air conditioning simulation model. Technical Report ACRC TR–116, Air Conditioning and Refrigeration Center, University of Illinois at Urbana–Champaign, Mechanical & Industrial Engineering Dept. Cited on page 34.

[231] Myint, W., S. Hosokawa, and A. Tomiyama (2007). Shapes of single drops rising through stagnant liquids. *Journal of Fluid Science and Technology 2*(1), 184–195. Cited on page 228.

[232] Narayanan, S. P. and G. Venkatarathnam (1998). Performance degradation due to longitudinal heat conduction in very high NTU counterflow heat exchangers. *Cryogenics 38*(9), 927 – 930. Cited on page 39.

[233] Nellis, G. F. (2003). A heat exchanger model that includes axial conduction, parasitic heat loads, and property variations. *Cryogenics 43*(9), 523 – 538. Cited on pages 40 and 42.

[234] Nellis, G. F. and J. M. Pfotenhauer (2005). Effectiveness-NTU relationship for a counterflow heat exchanger subjected to an external heat transfer. *Journal of Heat Transfer 127*(9), 1071–1073. Cited on pages 39 and 42.

[235] Nishikawa, K., S. Yoshida, H. Mori, and H. Takamatsu (1983). An experiment on the heat transfer characteristics in the post-burnout region at high subcritical pressures. *Nuclear Engineering and Design 74*(2), 233 – 239. Cited on pages 225 and 240.

[236] Nyers, J. and G. Stoyan (1994). A dynamical model adequate for controlling the evaporator of a heat pump. *International Journal of Refrigeration 17*(2), 101 – 108. Cited on page 96.

[237] Oblow, E. M. (1978). Sensitivity theory for reactor thermal-hydraulics problems. *Nuclear Science and Engineering 68*, 322–337. Cited on page 110.

[238] Okawa, T. and I. Kataoka (2005). Correlations for the mass transfer rate of droplets in vertical upward annular flow. *International Journal of Heat and Mass Transfer 48*(23-24), 4766 – 4778. Cited on pages 200 and 203.

[239] Okawa, T., T. Kitahara, K. Yoshida, T. Matsumoto, and I. Kataoka (2002). New entrainment rate correlation in annular two-phase flow applicable to wide range of flow condition. *International Journal of Heat and Mass Transfer 45*(1), 87 – 98. Cited on page 200.

[240] Okawa, T., A. Kotani, I. Kataoka, and M. Naitoh (2004). Prediction of the critical heat flux in annular regime in various vertical channels. *Nuclear Engineering and Design 229*(2-3), 223 – 236. Cited on pages 197 and 202.

[241] Oonk, R. L. and D. C. Hustvedt (1986). The effect of fluid property variations on the performance of cryogenic helium exchangers. *Advances in Cryogenic Engineering 31*, 415–422. Cited on page 27.

[242] Orth, L., D. C. Zietlow, and C. O. Pedersen (1993, April). Predicting refrigerant inventory of HFC 134A in air cooled condensers. Technical Report ACRCTR-34, Air Conditioning and Refrigeration Center, University of Illinois, Mechanical & Industrial Engineering Dept. Cited on page 34.

[243] Orth, L. A., D. C. Zietlow, and C. O. Pedersen (1995). Predicting refrigerant inventory of R134a in air-cooled condensers. *ASHRAE Transactions 101*, 1367–1375. Cited on page 98.

[244] Parter, S. V. (1999). On the Legendre–Gauss–Lobatto points and weights. *Journal of Scientific Computing 14*, 347–355. Cited on page 69.

[245] Paske, J. M., P. Papadopoulos, C. M. George, D. M. France, and W. J. Minkowycz (1992). Steady-state post-critical heat flux heat transfer to a refrigerant. *Journal of Thermophysics and Heat Transfer 6*, 314–320. Cited on pages 223 and 250.

[246] Pederson, C. O. (1967). *The dynamics and heat transfer characteristics of water droplets impinging upon a heated surface*. Ph. D. thesis, Carnegie Institute of Technology. Cited on page 232.

[247] Peng, S. (2008). Heat flux effect on the droplet entrainment and deposition in annular flow dryout. *Communications in Nonlinear Science and Numerical Simulation 13*(10), 2223 – 2235. Cited on page 199.

[248] Peters, D. L. (1970). Heat exchanger design with transfer coefficients varying with temperature or length of flow path. *Heat and Mass Transfer 3*, 220–226. Cited on page 37.

[249] Plummer, D. N. (1974). Post critical heat transfer to flowing liquid in a vertical tube. Technical Report 72718-91, Massachusetts Institute of Technology, Heat Transfer Laboratory. Cited on pages 225 and 250.

[250] Prasad, R. C. (1987). Analytical solution for a double-pipe heat exchanger with non-adiabatic condition at the outer surface. *International Communications in Heat and Mass Transfer 14*(6), 665 – 672. Cited on page 41.

[251] Premoli, A., D. Francesco, and A. Prima (1970). An empirical correlation for evaluating two-phase mixture density under adiabatic conditions. In *European Two-Phase Flow Group Meeting, Milan, Italy*. Cited on page 51.

[252] Proot, M. M. J. (2003). *The least-squares spectral element method theory, implementation and application to incompressible flows*. Ph. D. thesis, Delft University of Technology. Cited on page 79.

[253] Proot, M. M. J. and M. I. Gerrtisma (2002). Least-squares spectral elements applied to the Stokes problem. *Journal of Computational Physics 181*(2), 454 – 477. Cited on page 64.

[254] Pupko, V. Y. (1966). Use of adjoint functions in investigations of heat conduction and transfer processes. *Journal of Engineering Physics and Thermophysics 11*, 136–139. Cited on page 110.

[255] Quadir, G. A., G. M. Krishnan, and K. N. Seetharamu (2002). Modeling of wire-on-tube heat exchangers using finite element method. *Finite Elements in Analysis and Design 38*(5), 417 – 434. Cited on page 64.

[256] Quibén, J. M. and J. R. Thome (2007). Flow pattern based two-phase frictional pressure drop model for horizontal tubes, Part II: New phenomenological model. *International Journal of Heat and Fluid Flow 28*(5), 1060 – 1072. Cited on page 96.

[257] Rabas, T. (1985). The effect of tubeside maldistribution on the thermal performance of condensers used in multistage flash distillation plants. *Desalination 55*, 515 – 528. Cited on pages 29 and 149.

[258] Ragazzi, F. and C. O. Pedersen (1991). Modular–based computer simulation of an air–cooled condenser. Technical Report ACRC TR–07, Air Conditioning and Refrigeration Center, University of Illinois at Urbana–Champaign. Cited on page 34.

[259] Ranganayakulu, C. and K. N. Seetharamu (1999). The combined effects of longitudinal heat conduction, flow nonuniformity and temperature nonuniformity in crossflow plate-fin heat exchangers. *International Communications in Heat and Mass Transfer 26*(5), 669 – 678. Cited on pages 40, 42, and 64.

[260] Ranganayakulu, C., K. N. Seetharamu, and K. V. Sreevatsan (1996). The effects of inlet fluid flow nonuniformity on thermal performance and pressure drops in crossflow plate-fin compact heat exchangers. *International Journal of Heat and Mass Transfer 40*(1), 27 – 38. Cited on pages 38 and 41.

[261] Ranganayakulu, C., K. N. Seetharamu, and K. V. Sreevatsan (1997). The effects of longitudinal heat conduction in compact plate-fin and tube-fin heat exchangers using a finite element method. *International Journal of Heat and Mass Transfer 40*(6), 1261 – 1277. Cited on page 64.

[262] Rao, B. P. and S. K. Das (2004). Effect of flow distribution to the channels on the thermal performance of the multipass plate heat exchangers. *Heat Transfer Engineering 25*(8), 48–59. Cited on pages 38 and 41.

[263] Rao, B. P., P. K. Kumar, and S. K. Das (2002). Effect of flow distribution to the channels on the thermal performance of a plate heat exchanger. *Chemical Engineering and Processing 41*(1), 49 – 58. Cited on page 38.

[264] Rao, B. P., B. Sunden, and S. K. Das (2005). An experimental and theoretical investigation of the effect of flow maldistribution on the thermal performance of plate heat exchangers. *Journal of Heat Transfer 127*(3), 332–343. Cited on page 38.

[265] Rao, B. P., B. Sunden, and S. K. Das (2006). Thermal analysis of plate condensers in presence of flow maldistribution. *International Journal of Heat and Mass Transfer 49*(25-26), 4966 – 4977. Cited on pages 38, 41, and 149.

[266] Ravikumaur, S., K. Seetharamu, and P. A. Narayana (1988). Finite element analysis of shell and tube heat exchanger. *International Communications in Heat and Mass Transfer 15*(2), 151 – 163. Cited on page 64.

[267] Revellin, R., P. Haberschill, J. Bonjour, and J. R. Thome (2008). Conditions of liquid film dryout during saturated flow boiling in microchannels. *Chemical Engineering Science 63*(24), 5795 – 5801. Cited on page 198.

[268] Richlen, S. L. and K. G. Condie (1976). Comparison of post-CHF heat transfer correlations to tube data. Technical Report SRD-134-76, Idaho National Engineering Laboratory. Cited on page 224.

[269] Richtmyer, R. D. (1967). *Difference methods for initial-value problems*. New York: Interscience Publishers. Cited on page 76.

[270] Robertson, J. M. (1983). Heat exchange equipment for the cryogenic process industry. In J. Taborek, G. F. Hewitt, and N. Afgan (Eds.), *Heat Exchangers. Theory and Practice*, pp. 469–493. Hemisphere Publishing Corporation. Cited on page 17.

[271] Rodríguez, M. and M. Díaz (2007). Dynamic modelling and optimisation of cryogenic systems. *Applied Thermal Engineering 27*(7), 1182 – 1190. Cited on page 64.

[272] Roetzel, W. (1969). Berücksichtigung veränderlicher Wärmeübergangskoeffizienten und Wärmekapazitten bei der Bemessung von Wärmeaustauschern (Dimensioning heat exchangers with regard to variable heat transfer coefficients and heat capacities). *Heat and Mass Transfer 2*, 163–170. In German. Cited on page 37.

[273] Roetzel, W. (1974). Heat exchanger design with variable transfer coefficients for crossflow and mixed flow arrangements. *International Journal of Heat and Mass Transfer 17*(9), 1037 – 1049. Cited on page 37.

[274] Roetzel, W. and B. Spang (1990). Verbessertes Diagramm zur Berechnung von Wärmeübertragern (Improved diagram for the calculation of heat exchangers). *Heat and Mass Transfer 25*, 259–264. In German. Cited on page 33.

[275] Rohsenow, W. M. (1988). Post dryout heat transfer prediction method. *International Communications in Heat and Mass Transfer 15*(4), 559 – 569. Cited on page 232.

[276] Saha, P. (1980). A nonequilibrium heat transfer model for dispersed droplet post-dryout regime. *International Journal of Heat and Mass Transfer 23*(4), 483 – 492. Cited on pages 227, 232, and 237.

[277] Sahoo, R. and S. Sarangi (1985). Effect of temperature-dependent specific heat of the working fluid on the performance of cryogenic regenerators. *Cryogenics 25*(10), 583 – 590. Cited on pages 37 and 40.

[278] Saito, T., E. D. Hughes, and M. W. Carbon (1978). Multi-fluid modeling of annular two-phase flow. *Nuclear Engineering and Design 50*(2), 225 – 271. Cited on pages 193 and 203.

[279] Saitoh, S., H. Daiguji, and E. Hihara (2007). Correlation for boiling heat transfer of R-134a in horizontal tubes including effect of tube diameter. *International Journal of Heat and Mass Transfer 50*(25-26), 5215 – 5225. Cited on page 198.

[280] Sami, S. M. (1988). An improved numerical model for annular two-phase flow with liquid entrainment. *International Communications in Heat and Mass Transfer 15*(3), 281 – 292. Cited on pages 193 and 203.

[281] Sarangi, S. and H. Baral (1987). Effects of axial conduction in the fluid on cryogenic regenerator performance. *Cryogenics 27*(9), 505 – 509. Cited on pages 39 and 41.

[282] Scurlock, R. (1990). A matter of degrees: A brief history of cryogenics. *Cryogenics 30*(6), 483 – 500. Cited on page 18.

[283] Scurlock, R. G. (1992). Introduction. In R. G. Scurlock (Ed.), *History and origins of cryogenics*, Volume 8 of *Monographs on cryogenics*, pp. 1–47. Oxford Science Publications. Cited on pages 18 and 22.

[284] Secondi, F., C. Adamsson, and J.-M. Le Corre (2009). An assessment on entrainment correlations for the dryout prediction in BWR fuel bundles. In *Proceedings of the 13th International Topical Meeting on Nuclear Reactor Thermal Hydraulics*. Cited on page 201.

[285] Seetharamu, K., G. Quadir, Z. Zainal, and G. Krishnan (2004). FEM analysis of multifluid heat exchangers. *International Journal of Numerical Methods for Heat and Fluid Flow 14*(2), 242–255. Cited on pages 39, 41, and 64.

[286] Sha, W. T., B. Chao, and S. Soo (1984). Porous-media formulation for multiphase flow with heat transfer. *Nuclear Engineering and Design 82*(2-3), 93 – 106. Cited on page 173.

[287] Shah, M. (1979). A general correlation for heat transfer during film condensation inside pipes. *International Journal of Heat and Mass Transfer 22*(4), 547 – 556. Cited on page 55.

[288] Shah, M. M. (1982). Chart correlation for saturated boiling heat transfer: equations and further study. *AS 88*(1), 185–196. Cited on pages 58 and 59.

[289] Shah, R. K. (1994). A review of longitudinal wall heat conduction in recuperators. *Journal of Energy, Heat and Mass Transfer 97*, 453–454. Cited on pages 39 and 41.

[290] Shah, R. K. and D. P. Sekulić (2003). *Fundamentals of Heat Exchanger Design*. New Jersey: John Wiley and Sons. Cited on pages 23, 26, 29, 30, 31, 148, 257, and 260.

[291] Sharqawy, M. H. and S. M. Zubair (2010). Heat exchangers design under variable overall heat transfer coefficient: Improved analytical and numerical approaches. *Heat Transfer Engineering 31*(13), 1051–1056. Cited on pages 38 and 41.

[292] Shiferaw, D., T. Karayiannis, and D. Kenning (2009). Flow boiling in a 1.1 mm tube with R134a: Experimental results and comparison with model. *International Journal of Thermal Sciences 48*(2), 331 – 341. Nano Micro Mini Channels and Computational Heat Transfer. Cited on page 198.

[293] Soyars, W. M. (1991). The applicability of constant property analysis in cryogenic helium heat exchangers. *Advances in Cryogenic Engineering 37 A*, 217–223. Cited on pages 27, 37, and 40.

[294] Srihari, N., B. P. Rao, B. Sunden, and S. K. Das (2005). Transient response of plate heat exchangers considering effect of flow maldistribution. *International Journal of Heat and Mass Transfer 48*(15), 3231 – 3243. Cited on pages 29 and 149.

[295] Stefanov, Z. and K. A. Hoo (2003). A distributed-parameter model of black liquor falling film evaporators. Part I. Modeling of a single plate. *Industrial & Engineering Chemistry Research 42*(9), 1925–1937. Cited on page 64.

[296] Stefanov, Z. I. and K. A. Hoo (2004). Distributed parameter model of black liquor falling-film evaporators. Part 2. Modeling of a multiple-effect evaporator plant. *Industrial & Engineering Chemistry Research 43*(25), 8117–8132. Cited on page 64.

[297] Steinbauer, M. and T. Hecht (1996). Optimised calculation of helical–coiled heat exchanger in LNG plants. In *EUROGAS96. Proceedings from the European Applied Research Conference on Natural Gas*, pp. 223–228. TAPIR. Cited on page 35.

[298] Steiner, D. and J. Taborek (1992). Flow boiling heat transfer in vertical tubes correlated by an asymptotic model. *Heat Transfer Engineering 13*, 43–69. Cited on pages 58, 59, and 214.

[299] Stevanovic, V. and M. Studovic (1995). A simple model for vertical annular and horizontal stratified two-phase flows with liquid entrainment and phase transitions: one-dimensional steady state conditions. *Nuclear Engineering and Design 154*(3), 357 – 379. Cited on pages 193 and 203.

[300] Stickel, E. (1987). On the Fréchet derivative of matrix functions. *Linear Algebra and its Applications 91*, 83 – 88. Cited on page 113.

[301] Sugawara, S. (1990). Droplet deposition and entrainment modeling based on the three-fluid model. *Nuclear Engineering and Design 122*(1-3), 67 – 84. Cited on pages 193 and 203.

[302] Sun, G., G. Hewitt, and V. Wadekar (2004). A heat transfer model for slug flow in a horizontal tube. *International Journal of Heat and Mass Transfer 47*(12-13), 2807 – 2816. Cited on pages 58 and 59.

[303] Takada, N. and A. Tomiyama (2006). A numerical method for two-phase flow based on a phase-field model. *JSME International Journal Series B Fluids and Thermal Engineering 49*(3), 636–644. Cited on page 47.

[304] Tariq, S. (2004). LNG technology selection. *Hydrocarbon Engineering 9*(2), 71–76. Cited on page 24.

[305] Tatterson, D. F., J. C. Dallman, and T. J. Hanratty (1977). Drop sizes in annular gas-liquid flows. *AIChE Journal 23*(1), 68–76. Cited on pages 236 and 237.

[306] Tekin, E. and I. Sabuncuoglu (2004). Simulation optimization: A comprehensive review on theory and applications. *IIE Transactions 36*(11), 1067–1081. Cited on page 136.

[307] TEMA (2007). Standards of the Tubular Exchanger Manufacturers Assosiacion. Cited on page 262.

[308] Teyssedou, A., A. Tapucu, M. Gekinli, and M. Merilo (1989). Axial mass flow distribution in two laterally interconnected channels with blockages. *International Journal of Multiphase Flow 15*(4), 605 – 626. Cited on pages xvii and 178.

[309] Thome, J. R. (2005). Update on advances in flow pattern based two-phase heat transfer models. *Experimental Thermal and Fluid Science 29*(3), 341 – 349. Third European-Japanese Two-Phase Flow Group Meeting. Cited on page 59.

[310] Thome, J. R. (2006). Engineering databook III, Wolverine Tube, Inc. Available online at `http://www.wlv.com/products/databook/db3/DataBookIII.pdf`. Cited on page 220.

[311] Thonon, B. (2005). Advanced and high-performance heat exchangers for the hydrocarbon–processing industries. *Heat Transfer Engineering 26*(5), 73–84. Cited on page 23.

[312] Thyageswaran, S. (2008). Analysis of multi-pass evaporators using orthogonal collocation. *International Journal of Refrigeration 31*(2), 204 – 216. Cited on page 64.

[313] Thyageswaran, S. (2009). Thermo-hydraulic predictions for multi-pass evaporators by orthogonal collocation using a new flow pattern map. *Applied Thermal Engineering 29*(2-3), 601 – 606. Cited on page 64.

[314] Tien, C. L. and G. R. Cunnington (1973). Cryogenic insulation heat transfer. In J. Thomas Francis Irvine and J. P. Hartnett (Eds.), *Advances in Heat Transfer*, Volume 9, pp. 349. Academic Press. Cited on page 28.

[315] Tiller, F. M., L. F. Kahl, and R. S. Ramalho (1963). Improved formulas for heat transfer calculations in multipass exchangers. *Journal of Chemical & Engineering Data 8*(3), 285–288. Cited on pages 38 and 41.

[316] Timoney, D. J. and P. J. Foley (1994). Some effects of air flow maldistribution on performance of a compact evaporator with R134a. *Heat Recovery Systems and CHP 14*(5), 517 – 523. Cited on page 29.

[317] Todreas, N. E. and M. S. Kazimi (1990). *Nuclear Systems II: Elements of Thermal Hydraulic Design*. Taylor and Francis. Cited on page 173.

[318] Tong, L. and Y. Tang (1997). *Boiling Heat Transfer and Two-phase Flow* (Second ed.). Series in Chemical and Mechanical Engineering. Washington, D.C.: Taylor and Francis. Cited on pages xiii, 51, 52, 54, 95, and 96.

[319] Tribbe, C. and H. M. Mller-Steinhagen (2000). An evaluation of the performance of phenomenological models for predicting pressure gradient during gas-liquid flow in horizontal pipelines. *International Journal of Multiphase Flow 26*(6), 1019 – 1036. Cited on page 96.

[320] Ueda, T. (1979). Entrainment rate and size of entrained droplets in annular two-phase flow. *Bulletin of JSME 22*(171), 1258–1265. Cited on page 236.

[321] Ueda, T. and Y. Isayama (1981). Critical heat flux and exit film flow rate in a flow boiling system. *International Journal of Heat and Mass Transfer 24*(7), 1267 – 1276. Cited on page 198.

[322] Unal, C., K. Tuzla, A. F. Cokmez-Tuzla, and J. C. Chen (1991). Vapor generation rate model for dispersed drop flow. *Nuclear Engineering and Design 125*(2), 161 – 173. Cited on page 225.

[323] Usachev, L. N. (1964). Perturbation theory for the breeding ratio and for other number ratios pertaining to various reactor processes. *Journal of Nuclear Energy. Parts A/B. Reactor Science and Technology 18*(10), 571 – 583. Cited on page 114.

[324] Ustinov, E. A. (2001). Adjoint sensitivity analysis of radiative transfer equation: temperature and gas mixing ratio weighting functions for remote sensing of scattering atmospheres in thermal ir. *Journal of Quantitative Spectroscopy and Radiative Transfer 68*(2), 195 – 211. Cited on page 110.

[325] Vardhan, A. and P. L. Dhar (1998). A new procedure for performance prediction of air conditioning coils. *International Journal of Refrigeration 21*(1), 77 – 83. Cited on page 34.

[326] Varone Jr., A. F. and W. M. Rohsenow (1986). Post dryout heat transfer prediction. *Nuclear Engineering and Design 95*, 315 – 327. Cited on pages 231, 232, 238, 240, and 249.

[327] Venkatarathnam, G. (2008). *Cryogenic Mixed Refrigerant Processes*. New York: Springer. Cited on page 20.

[328] Venkatarathnam, G. and S. P. Narayanan (1999). Performance of a counter flow heat exchanger with longitudinal heat conduction through the wall separating the fluid streams from the environment. *Cryogenics 39*(10), 811 – 819. Cited on pages 29, 39, 40, and 42.

[329] Venkatarathnam, G. and S. Sarangi (1990). Matrix heat exchangers and their application in cryogenic systems. *Cryogenics 30*(11), 907 – 918. Cited on pages 22 and 25.

[330] Villadsen, J. V. and W. E. Stewart (1967). Solution of boundary-value problems by orthogonal collocation. *Chemical Engineering Science 22*(11), 1483 – 1501. Cited on page 64.

[331] Vist, S. and J. Pettersen (2004). Two-phase flow distribution in compact heat exchanger manifolds. *Experimental Thermal and Fluid Science 28*(2-3), 209 – 215. The International Symposium on Compact Heat Exchangers. Cited on page 152.

[332] Wachters, L. H. J., L. Smulders, J. R. Vermeulen, and H. C. Kleiweg (1966). The heat transfer from a hot wall to impinging mist droplets in the spheroidal state. *Chemical Engineering Science 21*(12), 1231 – 1238. Cited on page 233.

[333] Wallis, G. B. (1969). *One-dimensional Two-phase Flow*. New York: McGraw-Hill. Cited on pages 196 and 203.

[334] Wang, J. (2008). Pressure drop and flow distribution in parallel-channel configurations of fuel cells: U-type arrangement. *International Journal of Hydrogen Energy 33*(21), 6339 – 6350. Cited on page 154.

[335] Wang, J. (2010). Pressure drop and flow distribution in parallel-channel configurations of fuel cells: Z-type arrangement. *International Journal of Hydrogen Energy 35*(11), 5498 – 5509. Cited on page 154.

[336] Wang, S. and J. Weisman (1983). Post-critical heat flux heat transfer: A survey of current correlations and their applicability. *Progress in Nuclear Energy 12*(2), 149 – 168. Cited on pages 223, 224, and 234.

[337] Wattelet, J. (1994). Heat transfer flow regimes of refrigerants in a horizontal-tube evaporator. Technical Report 55, Air Conditioning and Refrigeration Center. College of Engineering. University of Illinois at Urbana-Champaign. Cited on pages 53 and 192.

[338] Webb, S. W. and J. C. Chen (1982). Vapor generation rate in nonequilibrium convective film boiling. In *Proceeding of the 7th International Heat TRansfer Conference, Munich*, Volume 4, pp. 437–442. Cited on page 225.

[339] Wegrzyn, J. and M. Gurevich (2000, June). Liquefied natural gas for trucks and buses. Conference SAE/TPS-2000-91-2210, Brookhaven National Lab, Upton, NY (US). Cited on page 20.

[340] Wen, M.-Y., C.-H. Lee, and J.-C. Tasi (2008). Improving two-phase refrigerant distribution in the manifold of the refrigeration system. *Applied Thermal Engineering 28*(17-18), 2126 – 2135. Cited on page 149.

[341] Whalley, P., P. Hutchinson, and G. Hewitt (1974). Calculation of critical heat flux in forced convection boiling. In T. Mizushina et al. (Eds.), *Proceedings of the 5th International Heat Transfer Conference, Tokyo, Japan*, pp. 290–294. Cited on page 193.

[342] Whalley, P. B. (1987). *Boiling, Condensation, and Gas-liquid Flow*. Oxford, New York: Clarendon Press, Oxford University Press. Cited on pages 55 and 96.

[343] White, F. M. (1986). *Fluid Mechanics* (2nd ed.). New York: McGraw-Hill. Cited on pages 97, 203, and 235.

[344] Williams, W. C. (2011). If the Dittus and Boelter equation is really the McAdams equation, then should not the McAdams equation really be the Koo equation? *International Journal of Heat and Mass Transfer 54*(7-8), 1682 – 1683. Cited on page 231.

[345] Winterton, R. H. S. (1998). Where did the Dittus and Boelter equation come from? *International Journal of Heat and Mass Transfer 41*(4-5), 809 – 810. Cited on page 231.

[346] Wojtan, L., T. Ursenbacher, and J. R. Thome (2005a). Investigation of flow boiling in horizontal tubes: Part i–a new diabatic two-phase flow pattern map. *International Journal of Heat and Mass Transfer 48*(14), 2955 – 2969. Cited on pages 204 and 212.

[347] Wojtan, L., T. Ursenbacher, and J. R. Thome (2005b). Investigation of flow boiling in horizontal tubes: Part II–development of a new heat transfer model for stratified-wavy, dryout and mist flow regimes. *International Journal of Heat and Mass Transfer 48*(14), 2970 – 2985. Cited on page 213.

[348] Woldesemayat, M. A. and A. J. Ghajar (2007). Comparison of void fraction correlations for different flow patterns in horizontal and upward inclined pipes. *International Journal of Multiphase Flow 33*(4), 347 – 370. Cited on pages xix, 51, and 52.

[349] Wolsky, A. M., E. J. Daniels, R. F. Giese, J. B. L. Harkness, L. R. Johnson, D. M. Rote, and S. A. Zwick (1989). *Applied superconductivity*. Noyes Data Corp. Cited on page 17.

[350] Würtz, J. (1978, April). An experimental and theoretical investigation of annular steam-water flow in tubes and annuli at 30 to 90 bar. Technical Report 372, Risø National Laboratory. Cited on page 204.

[351] Yang, A. and W. Marquardt (2009). An ontological conceptualization of multiscale models. *Computers & Chemical Engineering 33*(4), 822 – 837. Cited on page 59.

[352] Yang, J., D. Groeneveld, L. Leung, S. Cheng, and M. E. Nakla (2006). An experimental and analytical study of the effect of axial power profile on chf. *Nuclear Engineering and Design 236*(13), 1384 – 1395. Cited on pages 194 and 209.

[353] Yao, G. F. and S. M. Ghiaasiaan (1996). Wall friction in annular-dispersed two-phase flow. *Nuclear Engineering and Design 163*(1-2), 149 – 161. Cited on page 203.

[354] Yoder, Graydon L.; Rohsenow, W. M. (1980). Dispersed flow film boiling. Technical Report 85694-103, Massachusetts Institute of Technology, Heat Transfer Laboratory. Cited on pages 227, 231, 235, and 237.

[355] Yoo, S. J. and D. M. France (1996). Post-CHF heat transfer with water and refrigerants. *Nuclear Engineering and Design 163*(1-2), 163 – 175. Cited on pages 223 and 250.

[356] Yue, X. and W. E (2005). Numerical methods for multiscale transport equations and application to two-phase porous media flow. *Journal of Computational Physics 210*(2), 656 – 675. Cited on page 48.

[357] Yuen, M. C. and L. W. Chen (1978). Heat-transfer measurements of evaporating liquid droplets. *International Journal of Heat and Mass Transfer 21*(5), 537 – 542. Cited on page 230.

[358] Zhao, J. and L. Liu (2007). Solution of radiative heat transfer in graded index media by least square spectral element method. *International Journal of Heat and Mass Transfer 50*(13-14), 2634 – 2642. Cited on page 64.

[359] Zuber, N. and F. W. Staub (1966). Stability of dry patches forming in liquid films flowing over heated surfaces. *International Journal of Heat and Mass Transfer 9*(9), 897 – 905. Cited on page 51.

[360] Zun, I. (2002). Phase discrimination vs. multiscale characteristics in bubbly flow. *Experimental Thermal and Fluid Science 26*(2-4), 361 – 374. Cited on page 47.